



**4TH INTERNATIONAL WORKSHOP
ON THE PHYSICS OF
COMPRESSIBLE
TURBULENT MIXING**

**29 March - 1 April 1993
Cambridge, England**

FRONT COVER: Iso-surface for 0.99 volume fraction low density fluid in direct numerical simulation of Rayleigh-Taylor instability - D. Youngs, 1991.

The Proceedings of the
**4TH INTERNATIONAL WORKSHOP
ON THE PHYSICS OF
COMPRESSIBLE
TURBULENT MIXING**

Edited by

P.F. Linden, D.L. Youngs & S.B. Dalziel

Printed by

Cambridge University Press,
Cambridge, England

Scientific Committee

Didier Besnard,
Centre d'Etudes de Limeil-Valenton,
Department MA/MCN,
94195 Villeneuve St. Georges
Cedex, FRANCE.

Alfred Buckingham,
Lawrence Livermore Nat. Lab.,
PO Box 808, L-16
Livermore
CA 94550, USA.

James Glimm,
Dept. of Applied Mathematics,
State University of New York at
Stony Brook, Stony Brook,
New York 11794-3600 USA.

Jean-François Haas,
Centre D'Études de Limeil-Valenton,
94195 Villeneuve St Georges,
Cedex, FRANCE.

Yury Kucherenko,
All Union Research Institute of
Technical Physics,
454070, Chelyabinsk-70,
PO Box 245 RUSSIA.

Daryl Landeg,
Atomic Weapons Establishment,
Foulness,
Southend-on-Sea,
EssxSS3 9XE., UK.

Marcel Lesieur,
Institut de Mécanique de Grenoble
BP 68,
38402 St. Martin d'Herès Cedex,
FRANCE.

Evgenij Meshkov,
All Union Scientific Research Inst.
of Experimental Physics,
607200, Arzamas - 16,
Gorkii Region, RUSSIA.

Viviane Rupert,
Lawrence Livermore National Lab.,
PO Box 808 L-022,
Livermore,
California 94550 USA.

Bernard Sitt,
Centre D'Études de Vaujours-
Moronvilliers,
B.P. 7,
77181 Courtry, FRANCE.

Brad Sturtevant,
Graduate Aeronautical Labs.,
California Institute of Technology,
Pasadena,
California 91125 USA.

Sergey Zaytsev
The Krzhizhanovsky Power
Engineering Inst. ENIN,
Leninsky Prospect, 19
117071 Moscow, RUSSIA.

Organising Committee

Kate Anstee,
DAMTP,
Silver Street,
Cambridge CB3 9EW UK.

Stuart Dalziel,
DAMTP,
Silver Street,
Cambridge CB3 9EW UK.

Paul Linden,
DAMTP,
Silver Street,
Cambridge CB3 9EW UK.

David Youngs,
AWE,
Building E3 Aldermaston,
Reading RG7 4PR, UK.

Preface

The 4th International Workshop on the Physics of Compressible Turbulence was held at Downing College, Cambridge over a four day period at the end of March 1993. Approximately 100 scientists attended from around the world, with strong representations from France, Russia, the UK, and the US. This Workshop follows on from a sequence of Workshops held previously at Princeton and Pleasanton in the US and Royamont in France at approximately two year intervals. A total of 62 papers including both oral and poster presentations were presented over the four day period of the meeting.

In recent years much of the stimulus for the work on compressible turbulence has come from a desire to understand the interactions of shock phenomena with density variations within a fluid. These shocks may be induced intentionally by imposing a sharp pressure change on a fluid or may arise naturally in turbulent flow at high Mach number. The interaction of the large pressure gradients with the density gradients produces baroclinic generation of vorticity and the subsequent motion develops into a number of characteristic structures. The most simple form of this interaction occurs when a planar shock passes through a density interface between two fluids. Under these circumstances small random perturbations are unstable and grow as a result of the instantaneous baroclinic torque experienced as the shock interacts with the density discontinuity. This instability is known as Richtmyer-Meshkov instability and can be thought of as a variant on the more classical Rayleigh-Taylor instability which occurs when pressure variations are produced by continuous acceleration such as a gravitational field. In the latter case the baroclinic generation of vorticity occurs continuously whenever the higher pressure exists in the less dense fluid, such as when dense fluid overlies less dense fluid.

Despite the differences in detail, particularly of the forcing of the turbulent flow that develops, these instabilities have much in common and consequently considerable attention has been paid in recent years to examining the similarities between the two forms of instability. These two classical flow situations provide a means of analysing the transition to turbulence from the linear instability regime, and also provide a mechanism for studying turbulent mixing in compressible and stratified flows. Considering them as archetypes for the kinds of interactions that take place in compressible turbulence in general then enables the basic instabilities to be used as building blocks for the study of complex compressible turbulent flows. In addition to these effects, compressible turbulence is often affected by gravitational forces and so the effects of density stratification when the gravitational field is stabilising also play an important part in the mixing processes.

This dynamics of Richtmyer-Meshkov and Rayleigh-Taylor instabilities then underlies the basic theme of the meeting which was devoted to an examination of these questions. The papers in the meeting were then divided into 6 sections concerned with:

- Rayleigh-Taylor mixing
- Richtmyer-Meshkov mixing
- Shear and vortex flows
- Theoretical and empirical models
- Laser-driven instability experiments
- Converging flows

One of the main questions of practical interest is how much mixing occurs in these flows between the fluids as a result of the various instabilities that are observed. As a consequence much of the emphasis was on experimental work involving diagnostic techniques for analysing flow within a shock tube and also in other stratified scenarios. Despite considerable efforts over recent years it is still very difficult to make unambiguous measurements of these flows

particularly as averaging problems cause difficulties in resolving the details of the flow structures. However, some progress has been made in terms of phenomenological modelling and detailed turbulence modelling. There have been some significant improvements in the ability to predict experimental behaviour for a range of flows using sophisticated numerical codes. The ability of the turbulence models used by codes to predict accurately the mixing processes and to parameterise them at small scales depends heavily on the ability to tune the models according to appropriate data. Consequently the meeting provided a healthy discussion about the interactions between models and experiments.

The wide participation in this conference is possible largely due to the generous sponsorship of this meeting by Cray Research (UK), the European Research Community on Flow Turbulence and Combustion (ERCOTAC), The Ministry of Defence and the Royal Society.

Contents

I Rayleigh-Taylor mixing

Treatment of experimental data on determination of mixing velocity in the self-similar case, <i>V.I. Anisimov & A.V. Polionov</i>	1
Mixing front growth in RT and RM instabilities <i>R. Castilla & J.M. Redondo</i>	11
Perturbations and coherent flow in Rayleigh-Taylor instability <i>S.B. Dalziel</i>	32
Turbulent hydrodynamic mix experiment <i>G. Dimonte, B. Remington, P. Stry, E. Burke, P. Crowley, R. Hawke, J. Morrison & A. Susoeff</i>	42
Existence, uniqueness and physical selection of asymptotically steady-states solutions in the theory of the Rayleigh-Taylor instability <i>N.A. Inogamov & A.V. Chekhlov</i>	50
Experimental study of asymptotic stage of gravitational turbulent mixing of thin liquid layers of different densities <i>Yu.A. Kucherenko, S.I. Balabin & A.P. Pylaev</i>	57
Behaviour of gravitational turbulent mixing region under conditions leading to separation <i>Yu.A. Kucherenko, V.E. Neuvazhayev & A.P. Pylaev</i>	70
Rayleigh-Taylor instability in solids <i>A.I. Lebedev, P.N. Nisovtsev, V.A. Rayevsky</i>	81
Parallel computation of three dimensional Rayleigh-Taylor instability in compressible fluids through the front tracking method and level set methods <i>X.L. Li, J. Grove & Q. Zhang</i>	94
Rayleigh-Taylor and Kelvin-Helmholtz mixing in a large eddy simulation model <i>T. McAbee</i>	105
Wave processes effect on the dynamics of turbulent mixing at liquid layer surface accelerated by compressed gas <i>N.V. Nevmerzhitsky, E.E. Meshkov, A.G. Ioilev, I.G. Zhidov, I.G. Pylev & S.S. Sokolov</i>	112
Two and three dimensional analysis of nonlinear Rayleigh-Taylor instability <i>D. Ofer, J. Hecht, D. Shvarts, Z. Zinamon, S.A. Orszag & R.L. McCrory</i>	119
Experimental study into the stabilization effect in gravitational turbulent mixing development on an inclined boundary <i>N.V. Pfitzyna, Yu.A. Kucherenko, V.I. Chitaikin & A.P. Pylaev</i>	129

Rayleigh-Taylor mixing due to unstable thermal stratification: preliminary experimental results <i>D.M. Snider & M.J. Andrews</i>	144
Instability calculations for the LEM driver at LLNL <i>P. Stry, G. Dimonte, B. Remington, E. Burke & W.P. Crowley</i>	156
Direct three-dimensional numerical simulation of mixing by Rayleigh-Taylor instability <i>D.L. Youngs</i>	167
The study of Rayleigh-Taylor instability in continuous interface <i>S.G. Zaytsev, E.I. Chebotareva & S.N. Titov</i>	178
II Richtmyer-Meshkov mixing	
The influence of the shock interaction with an interface between the two gas flows of different densities on the intensity of mixing <i>A. Aleshin, S. Zaytsev & E. Lazareva</i>	188
X-ray measurements of shock-induced mixing at an air/xenon interface <i>R. Bonazza & B. Sturtevant</i>	194
Numerical simulations and experiments on physics of high Mach number shockwave - turbulent flow interactions <i>A.C. Buckingham & J. Grun</i>	201
Multidimensional numerical simulation of transition to turbulence in Richtmyer-Meshkov instability <i>V.V. Demchenko & A.M. Oparin</i>	207
The application of front tracking to the simulation of shock refraction and shock accelerated interface mixing <i>J.W. Grove, Y. Yang, Q. Zhang, D.H. Sharp, J. Glimm, B. Boston & R. Holmes</i>	213
Experimental study of instability growth patterns of a shock-accelerated, thin fluid layer <i>J.W. Jacobs, D.G. Jenkins, D.L. Klein & R.F. Benjamin</i>	223
The laser sheet as a quantitative diagnostic in shock tube experiments <i>D. Landeg, M. Philpott, I. Smith & A. Smith</i>	230
Freeze-out and the failure of Richtmyer's prescription <i>K.O. Mikaelian</i>	240
Non-linear stage in development of perturbations of interfaces between liquids under joint action of impulsive and constant accelerations <i>V.Ye. Neuvazhayev & I.E. Parshukov</i>	250
Richtmyer-Meshkov instability in a vertical shock-tube <i>G. Rodriguez, I. Galametz, H. Croso & J.-F. Haas</i>	260
Multidirectional laser technique for Richtmyer-Meshkov mixing experiments <i>A. Touat, I. Chemouni, G. Jourdan, L. Labracherie & L. Houas</i>	270

Vortex deposition and evolution of perturbed 3D Richtmyer-Meshkov environments <i>N.J. Zabusky & R. Samtaney</i>	276
Richtmyer-Meshkov instability for two- and three-dimensional interfaces <i>S. Zaytsev, A. Aleshin & E. Lazareva</i>	291
The initiation and the development of Richtmyer-Meshkov instability in continuous interface <i>S.G. Zaytsev, E.I. Chebotareva & S.N. Titov</i>	297
III Shear and vortex flows	
The effects of turbulence and viscosity on structure of thin vortex rings <i>S.M. Bakhrahk, N.S. Darowa, G.V. Zharowa, V.A. Zhmailo & V.P. Stazenko</i>	306
Simple models of stratified and compressible entrainment <i>R.E. Breidenthal</i>	313
A combined theoretical and numerical study of three dimensional jet mixing <i>E.F. Brown, J.E. Burr, S.L. Huang & T.B. Mutter</i>	322
Direct simulation of a shock-induced mixing layer <i>J.A. Greenough & J.B. Bell</i>	332
Response of a sheared density interface to periodic forcing <i>G.A. Lawrence, L.G. Guez, F.K. Browand & S.P. Haigh</i>	343
Compressibility effects on the dynamics of shear layers <i>M. Lesieur, P. Comte & Y. Fouillet</i>	351
Late-time turbulent mixing of a high density gas bubble in a shocked air flow ($M_s = 1.14$) <i>M. Philpott, A.V. Smith, N.W. Cowperthwaite & D.L. Youngs</i>	366
On shock polar analysis and analytical expressions for vorticity deposition in shock-accelerated density-stratified interfaces <i>R. Samtaney & N.J. Zabusky</i>	372
IV Theoretical and empirical models	
Modelling turbulent mixing where do we stand? <i>D. Besnard</i>	384
Towards a better hydro for dynamic mix calculations <i>J. Binstock</i>	399
Comparison of two turbulent diffusion-dissipation models via similarity methods <i>C. Cherfils</i>	413
Towards a quasi-linear closure for compressible turbulence <i>J.A.H. Futterman and W.P. Dannevik</i>	421

Kinetic energy of multimode Rayleigh-Taylor and Richtmyer-Meshkov instabilities <i>A.K. Harrison</i>	432
Description of transitional layer effect in simulations with $k\epsilon$ -model <i>V. Neuvazhaev, A. Polionov & V. Yakovlev</i>	444
Properties of the $k\epsilon$ -model for turbulent mixing <i>V.E. Neuvazhayev</i>	449
Asymptotic behaviour of a thin interlayer after passing a shock wave <i>V.E. Neuvazhayev</i>	461
Calculation of gravitational turbulent mixing in non-automodel flows <i>V.V. Nikiforov</i>	478
Mixture separation in the framework of $Hk\epsilon$ -model <i>A. Polionov & V. Yakovlev</i>	497
Application of a two-dimensional turbulence model <i>D.L. Youngs, B.C. Hankin & N.W. Cowperthwaite</i>	500
V Laser-driven instability experiments	
Effects of surface finish on the hydrodynamic evolution of surfaces exposed to thermal radiation <i>A. Caruso & V.A. Pais</i>	508
The AWE/LLNL NOVA planar foil mix experiment. Comparison with calculation <i>N.W. Cowperthwaite, T.J. Goldsack & D.L. Youngs</i>	519
Richtmyer-Meshkov experiments on Nova at high compression <i>G. Dimonte, B. Remington & E. Frerking</i>	525
Multimode and 3D Rayleigh-Taylor experiments on Nova <i>B.A. Remington, S.V. Weber, S.W. Haan, J.D. Kilkenny & R.J. Wallace</i>	533
VI Converging flows	
Hydrodynamic instability modelling for ICF <i>S.W. Haan</i>	539
Calculations of instability growth in cylindrical implosions <i>N.M. Hoffman, J. B. Beck & W.W. Hsing</i>	545
Three dimensional hydrodynamic calculations with adaptive mesh refinement of the evolution of Rayleigh-Taylor and Richtmyer-Meshkov instabilities in converging geometry: multi-mode perturbations <i>R.I. Klein, J. Bell, R. Pember and T. Kelleher</i>	554
Richtmyer-Meshkov and Rayleigh-Taylor instabilities inducing a turbulent flow during a cylindrical implosion <i>M. Legrand & N. Toqué</i>	568

Turbulent mixing development investigation with converging jelly rings <i>E.E. Meshkov, N.V. Nevmerzhitsky, V.G. Rogachev & I.G. Zhidov</i>	578
The importance of shear strength for development of disturbances and instability during acceleration, convergence and retardation of shells <i>V.A. Ogorodnikov, A.G. Ivanov, G. Ya. Karpenko, A.D. Kovtun, A.A. Demidov & L.A. Tolstikova</i>	586
Effect of nonuniform implosion on high gain ICF targets <i>H. Takabe & T. Ishii</i>	596

I

Rayleigh-Taylor mixing

Treatment of Experimental Data on Determination of Mixing Velocity in the Self-Similar Case

V.I. Anisimov, A.V. Polionov
All-Russia Research Institute of Technical Physics
P.O. Box 245, 454070, Chelyabinsk-70, Russia

Abstract

There has been substantiated in this work on the basis of general features of self-similar motions and practically applied the way for determining the self-similar slope coefficient α by considering the dependence of $L^{1/2}$ on $\int g^{1/2} dt$, which supposes the dependence of acceleration on time to be known. The acceleration drop-time relations have been computed on the basis of the developed physical model for experiments performed at SOM and EKAP installations¹. It is shown that the accepted way of processing makes an error in α determination 1.3÷2 times less and introduces an essential correction for the α - value up to 80%.

The shown conclusions were obtained when processing the experimental data with the densities relation $n = 3$. But when processing the experiments with the densities relation $n = 20$ the scatter in points was so large that the error in determination of the slope appeared to be greater by a factor of ten that evidenced about an additional error source not allowing here to reveal advantages of the processing way proposed.

Introduction

One of the main gravitational turbulence characteristics is the rate of the turbulent mixing development in the self-similar case. Dependence of the mixing zone width on time is described by the expression:

$$L = \alpha(A) \frac{gt^2}{2},$$

where α - coefficient depending only on the densities relation characterized by the Atwood number: $A = \frac{\rho_1 - \rho_2}{\rho_1 + \rho_2}$.

A great number of experimental works^{1,2,3,4} is devoted to determination of the α value. The main difficulty in its determination is the finite time of the evolution into the self-similar mode. Therefore, it is expedient to choose such a way for processing the experimental data which would allow to determine the self-similar slope value with the highest accuracy.

Different authors apply various ways for determination of α :

according to the L - S relation, where $S = \int_0^t dt' \int_0^{t'} g dt - 1$, L versus

$$X = \frac{\rho_1 - \rho_2}{\rho_2 + \rho_1} \left[\int_0^t g^{1/2} dt \right]^2 - 2, L^{1/2} \text{ versus } S^{1/2} - 3, L^{1/2} \text{ versus } \int g^{1/2} dt -$$

4,5. In the present work an additional substantiation of the last way for the determination of the self-similar slope coefficient is given. There is appeared in this way that the α value is determined in some moment of time through the value of acceleration at the moment $\alpha \sim \frac{1}{g}$, that is why it is necessary to know exactly the behavior of acceleration in time for experiments where it is not constant. However, information on acceleration behaviour at the installations SOM and EKAP designed for gravitational mixing study is rather uncertain. In the given work, the dependencies of acceleration on time are determined for experiments performed at the installations SOM and EKAP by computation on the basis of the developed physical model taking into account the structural features of the given installations.

§1 Substantiation of the way for determinating the self-similar slope coefficient

The self-similar turbulent mixing occurs between two semi-infinite fluids with different densities in the gravitational field when initiating the mixing from infinitesimal initial perturbations in case of absence of viscosity, surface tension and other factors characterized by dimensional constants. In this case it is not possible to form the combination with time and distance dimensionality from the parameters characterizing the problem that is the condition of self-similarity ⁶. For this case self-similar variable is equal to $\xi = \frac{x}{gt^2}$, where x , t - spatial and time coordinates, g - acceleration of the gravitational field applied. All the parameters including the mass concentration $C(\xi)$ are dependent on this variable. It is possible to determine the number $\Delta\xi$ corresponding to mass concentration change in the mixture, for example, from 0.01 to 0.99: $\Delta\xi = \xi(0.99) - \xi(0.01)$, where $\xi(C)$ is the inverse function of $C = C(\xi)$ mentioned above. Further we shall determine the mixing zone width at the given moment as a distance where the average mass concentration is changed from 0.01 to 0.99: $L = x(0.99) - x(0.01)$, where $x(0.99)$ is determined from equation $C\left\{\frac{x}{gt^2}\right\} = 0.99$ (analogously to $x(0.01)$). By using the number $\Delta\xi$ determined above we also can obtain the expression $L = \Delta\xi \cdot gt^2$

describing the mixing zone width dependence on time. This expression is usually written as

$$L = \alpha \cdot \frac{gt^2}{2}, \quad (1)$$

where α is the so-called self-similar slope coefficient determined empirically. Experimental data include as a rule the measurements of the mixing zone width L_{exp} and the transfer distance $S = \frac{gt^2}{2}$ corresponding to this width. The coefficient α is then determined as follows:

$$\alpha_{exp} = \frac{dL_{exp}}{dS}. \quad (2)$$

This way would be good if one succeeded in realizing the self-similar mixing from the very beginning. However, due to the effects of viscosity, surface tension and finite dimensions of initial perturbations the development of mixing in the initial section takes place more rapidly as compared with the self-similar one. Therefore, the self-similar state (i.e. such a state of the mixture which in no manifestations differs from the mixture state obtained under the strictly self-similar development) with a certain width L is reached earlier than it would be obtained if the self-similar motion were realized from the very beginning, i.e. the further self-similar motion takes place as if it were

$$\text{with some shift in time } t_0: L_{exp} = \alpha \cdot \frac{g(t+t_0)^2}{2}.$$

Since in the transfer distance S we do not take into account an indefinite time shift the determination of the experimental value α according to the formula (2) leads to an additional error

tending to zero only asymptotically: $\alpha_{exp} = \frac{d \alpha \frac{g(t+t_0)^2}{2}}{dS} = \alpha(1 + \frac{t_0}{t})$, i.e. in spite of the fact that the experimental data relates to the self-similar state which have been already reached the α_{exp} value determined by this way appears to be overevaluated.

On the other hand, from the expression (1) it is possible to obtain the relation for mixing zone growth velocity with time not entering explicitly into it : $\frac{dL}{dt} = \sqrt{2agL}$. Hence we obtain the expression defining α only through parameters characterizing the self-similar state:

$$\alpha = 2 \left[\frac{dL^{1/2}}{g^{1/2} dt} \right]^2 \quad (3)$$

When defining α by this way we obtain the true value of α as soon as the self-similar state is reached.

The expression (3) may be generalized for the case of a weak dependence of acceleration on time. The typical time of the changing must be much larger as compared with the characteristic

time of the turbulent motion $\dot{g} \gg \frac{1}{\sqrt{2k}}$, where l - typical scale of motion, k - kinetic energy of turbulence which can be estimated from potential energy change - $k = \frac{1}{12} AgL$. By assuming $l = 0.25L$ we find that the velocity of changing in g under which the self-similar state is conserved should satisfy the following condition:

$$\dot{g} \ll \sqrt{\frac{8Ag^3}{3L}} \quad (4)$$

If this condition is satisfied we can determine the self-similar slope coefficient according to the expression (3) by plotting the dependence of $L_{exp}^{1/2}$ on $Y = \int g^{1/2} dt$ and finding the derivative $\frac{dL_{exp}}{dY}$ equal to $\sqrt{\frac{\alpha}{2}}$.

§2 Determination of the acceleration-time relation for the installations SOM and EKAP

As opposed to the Rocket-Rig apparatus AWE (UK) where acceleration is kept to be constant, at the installations for studying gravitational turbulence in our Institute (EKAP, SOM) there is a drop in pressure connected with structural features of these installations.

For a more rigorous determination of the gravitational turbulence characteristics as well as for comparing experimental results obtained at different installations, one needs to determine the form of dependence of drop in acceleration on time.

The construction of SOM and EKAP installations described in the work ¹ represents a gas accelerator where an ampoule with fluids under study is accelerated under the pressure of a gas expanding adiabatically from the specified initial volume V_0 and pressure P_0 .

The equation of motion for the ampoule will have the form:

$$Mg = \sigma(P - P_1) + Mg_0 - F_{res}$$

where M - mass of the ampoule, σ - cross-section area of the measuring channel, g_0 - free fall acceleration, P - pressure of expanding gas, $P_1 = \text{const}$ - pressure in front of the ampoule, F_{res} -

resistance force assumed to be equal to Kv^2 , v - velocity of the ampoule motion, K - empirical coefficient, S - way passed by the ampoule.

$$\text{Since } g \equiv \frac{d^2S}{dt^2} = \frac{d\dot{S}}{dS} \frac{dS}{dt} = \frac{dv^2}{2dS}, \text{ then}$$

$$\frac{dv^2}{dS} = \frac{\sigma}{M} (P - P_1) + 2g_0 - \frac{2K}{M} v^2. \quad (5)$$

For the EKAP installation we have $P = \left[\frac{P_0}{1 + \frac{\sigma S}{V_0}} \right]^\gamma$, P_0 - initial pressure in the gas accelerator reservoir.

From (5) we obtain

$$\frac{dS}{dt} \equiv v = \exp\left\{-\frac{KS}{M}\right\} \sqrt{\int_0^S \exp\left\{\frac{2KS}{M}\right\} \left\{ \frac{2\sigma}{M} \left[\frac{P_0}{1 + \frac{\sigma S}{V_0}} \right]^\gamma - P_1 \right\} + 2g_0} dS}.$$

From here we determine $S(t)$, $v(t)$, and $g(t)$.

The coefficient K characterizing the resistance force will be chosen by comparing the acceleration $g(t)$ obtained by us with the experimentally measured dependence amiably placed at our disposal in Yu. Kucherenko's laboratory. For the EKAP installation $K = 12$.

For the SOM installation the proper allowance must be made for changing the pressure P in the gas accelerator reservoir as a consequence of adiabatic gas expansion and the leakage of some gas mass from the gas accelerator reservoir due to a clearance between the ampoule and the measuring probe tube. In this case we have the following differential equation for the pressure P :

$$\frac{dP}{dt} = \left[\frac{\partial P}{\partial V} \frac{dV}{dt} \right]_M + \left[\frac{\partial P}{\partial M} \frac{dM}{dt} \right]_V, \text{ where} \quad (6)$$

$$\frac{\partial P}{\partial V} = \left[\begin{array}{l} \text{from adiabatic} \\ \text{equation} \end{array} \right] = -\gamma \frac{P_0}{V_0} \frac{1}{\left\{ 1 + \frac{\sigma S}{V_0} \right\}^{\gamma+1}},$$

$$\frac{dV}{dt} = \sigma \cdot \dot{S},$$

$$\frac{\partial P}{\partial M} = \left[\begin{array}{l} \text{from equation of} \\ \text{state and} \\ \text{adiabatic equation} \end{array} \right] = \gamma \frac{P_0^\gamma P^{1-\gamma}}{M_0 \left\{ 1 + \frac{\sigma S}{V_0} \right\}}, \quad M_0 - \text{initial gas mass}$$

in gas accelerator reservoir,

$$\frac{dM}{dt} = -D \cdot \rho \cdot u = \left[\begin{array}{l} \text{from Bernoulli} \\ \text{and adiabatic} \\ \text{equations} \end{array} \right] = -D \cdot \sqrt{\frac{2\gamma}{\gamma-1} \left[\frac{P}{P_0} \right]^\gamma \frac{M_0}{V_0} P \left[1 - \left[\frac{P_1}{P} \right]^{1-\gamma} \right]}, \quad \rho,$$

u - density and velocity of gas outflow, D - empirical coefficient proportional to the clearance area.

By solving the set of differential equations (5), (6), we find $S(t)$, $v(t)$, and $g(t)$. The numerical solution of the obtained equations was realized on PC.

Coefficients K and D were chosen so as to describe identically the experimental trajectory data amiably placed at our disposal in Yu. Kucherenko's laboratory. For the SOM installation $K = 1$, $D = 2$. Dependence of acceleration on time is plotted in Fig.1, 2

for the EKAP and SOM installations in experiments described in work ¹.

§3 Determination of the self-similar slope coefficient

The obtained dependencies $g(t)$ are used for describing the experiments ¹. Plots of L vs S are reproduced in Fig. 3 from the work ¹. In Fig.4 the plots of $L^{1/2}$ vs $\int g^{1/2} dt$ have been built. It can be seen that in the last case the experimental points are closer to a straight line than in the first case, however, an objective estimation of the error in self-similar slope coefficient determination is required. This method for determining an error can be obtained on the basis of the general theorems in the probability theory and consists in the following (obtained by Dr. V. Bekhterev).

Let it be a priori known that X and Y must be connected by the linear relation $Y = \alpha X + \beta$. The parameters α and β are determined by the method of least squares through the values X_i , Y_i measured experimentally:

$$\alpha = \frac{\sum(X_i - \frac{\sum X_i}{n}) \cdot Y_i}{\sum X_i (X_i - \frac{\sum X_i}{n})}, \quad \beta = \frac{\sum Y_i}{n} - \alpha \cdot \frac{\sum X_i}{n}.$$

The parameters α and β appear to be the functions of random arguments X_i , Y_i and the determination of their r.m.s. deviations becomes possible. For the parameter α :

$$\sigma^2(\alpha) = \frac{\sum(X_i - \frac{\sum X_i}{n})^2 (\beta + \alpha X_i - Y_i)^2}{\left[\sum X_i (X_i - \frac{\sum X_i}{n})\right]^2 - \sum(X_i - \frac{\sum X_i}{n})^2 \left[\frac{1}{n} \sum X_i (X_i - \frac{\sum X_i}{n}) + (X_i - \frac{\sum X_i}{n})^2\right]} \quad (7)$$

The values of the self-similar coefficients obtained for experimental data shown in Fig. 3, 4 are given in Table 1:

$\frac{\rho_2}{\rho_1}$	measuring technique	α	processing L(S)	processing $L^{1/2}$ vs $\int g^{1/2} dt$
3	light	$\alpha _t$	0.062 ± 0.002	0.060 ± 0.002
		$\alpha_{t }$	0.064 ± 0.004	0.054 ± 0.003
		α	0.126 ± 0.006	0.113 ± 0.003
	X-ray	$\alpha _t$	0.039 ± 0.005	0.036 ± 0.004
		$\alpha_{t }$	0.044 ± 0.004	0.037 ± 0.003
		α	0.083 ± 0.008	0.073 ± 0.006
20	light	$\alpha _t$	0.139 ± 0.005	0.087 ± 0.005
		$\alpha_{t }$	0.268 ± 0.022	0.139 ± 0.012
		α	0.407 ± 0.025	0.226 ± 0.015
	X-ray	$\alpha _t$	0.119 ± 0.006	0.105 ± 0.010
		$\alpha_{t }$	0.214 ± 0.015	0.193 ± 0.021
		α	0.333 ± 0.020	0.298 ± 0.030

It can be seen that the error in determination of α when using the dependence of the $L^{1/2}$ on $\int g^{1/2} dt$ relation is made 1.3÷2 times less ($n = 3$). It should be noted that due to applying of statistical approach to processing of measurements results which is described in ⁶ and what is suggested to be used for the further refinements this error will be made even smaller. The experimental error in the self-similar slope coefficient determination is so great at $n = 20$ that it does not allow to reveal the advantage of the processing way proposed.

Conclusion

In the given work:

1. The necessity is substantiated for determining the self-similar slope coefficient α by the dependence of $L^{1/2}$ on $\int g^{1/2} dt$.

2. On the basis of the physical principles and structural features of the installations the dependencies of acceleration drop on time have been obtained for experiments performed at SOM and EKAP installations.

3. By using the obtained dependence $g(t)$ the self-similar slope coefficient α has been determined in coordinates with the $L^{1/2} - \int g^{1/2} dt$ relation. It is shown that the adopted way of processing makes the error in determination of α 1.3±2 times less and introduces an essential correction for the value of α up to 80%.

At $n = 20$ the experimental error in the determination of the self-similar slope coefficient is so great that it does not allow to reveal the advantage of the proposed way for processing.

References

1. Yu. Kycherenko, S. Balabin, A. Pylaev and others Experimental study of the gravitational turbulent mixing 3rd International Workshop on the Physics of Compressible Turbulent Mixing, Royaumont, France, 1991r.
2. V. Smeeton, D. Youngs Experimental Investigation of Turbulent Mixing by Rayleigh-Taylor Instability. AWE report.
3. A. Vasilenko, O. Byriakov, V. Olhovskaia and others Experimental study of gravitational instability and turbulization of the flow on the noble gases boundary. 2rd International Workshop on the Physics of Compressible Turbulent Mixing, Pleasanton, 1989r.
4. I. Zhidov, E. Meshkov, N. Nevmerzhitsky Experimental investigation of the mixing dynamics on the unstable boundaries accelerate fluid layers. Preprint ФИАИ № 56.
5. A. Polionov To determine of the self-similar slope coefficient on gravitational turbulent mixing development. 2rd International Workshop on the Physics of Compressible Turbulent Mixing, Pleasanton, 1989r.
6. V. Anisimov, A. Polionov The Statistical model of the turbulent mixing zone and its applying for the experiments analysis 2rd International Workshop on the Physics of Compressible Turbulent Mixing, Pleasanton, 1989r.

Fig.1 Dependence of acceleration on time for EKAP inst.

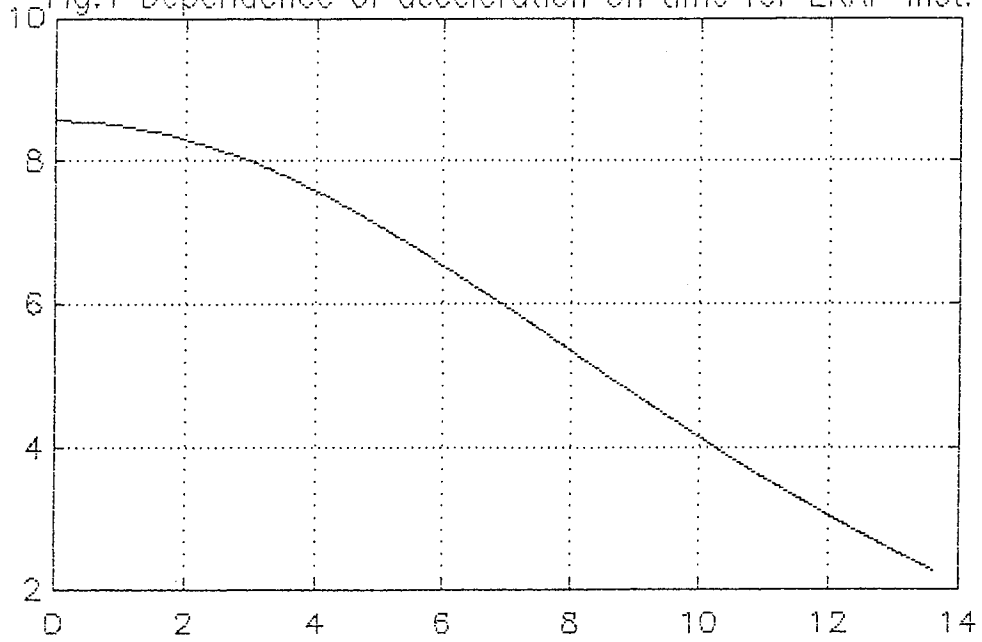
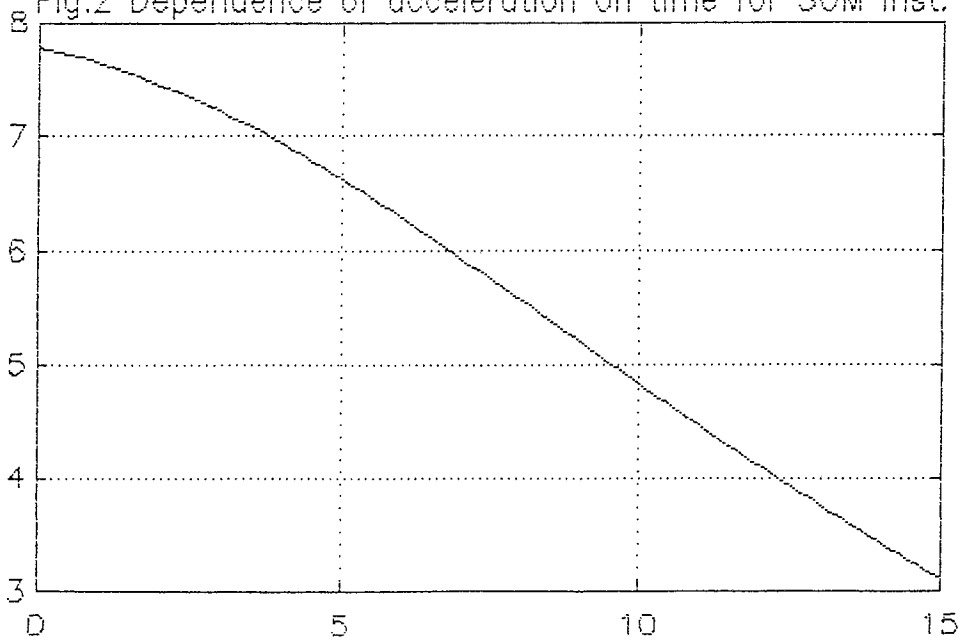
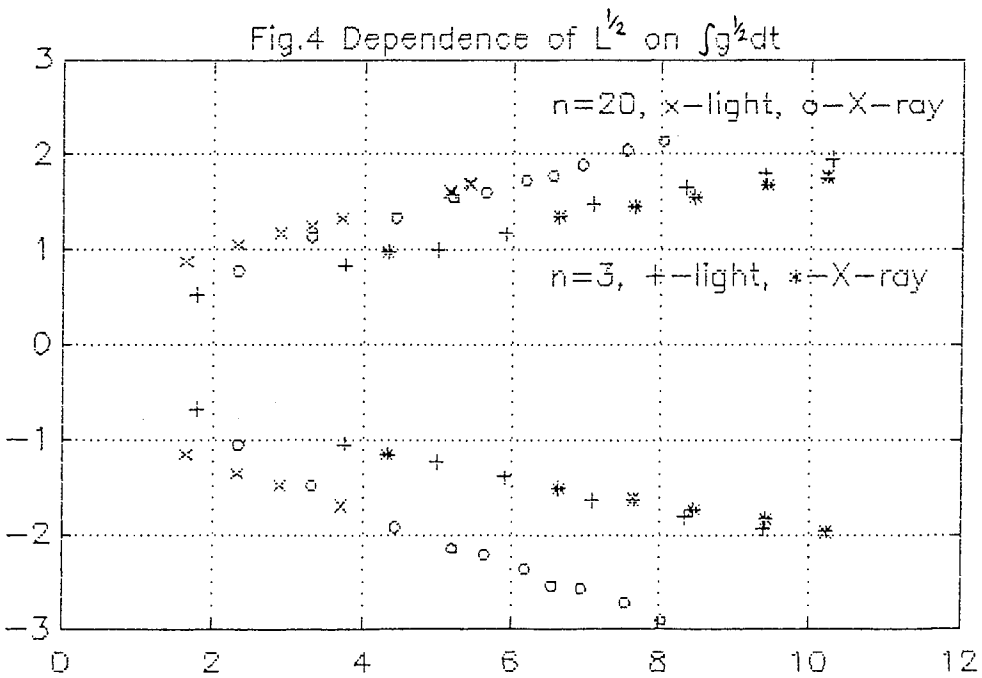
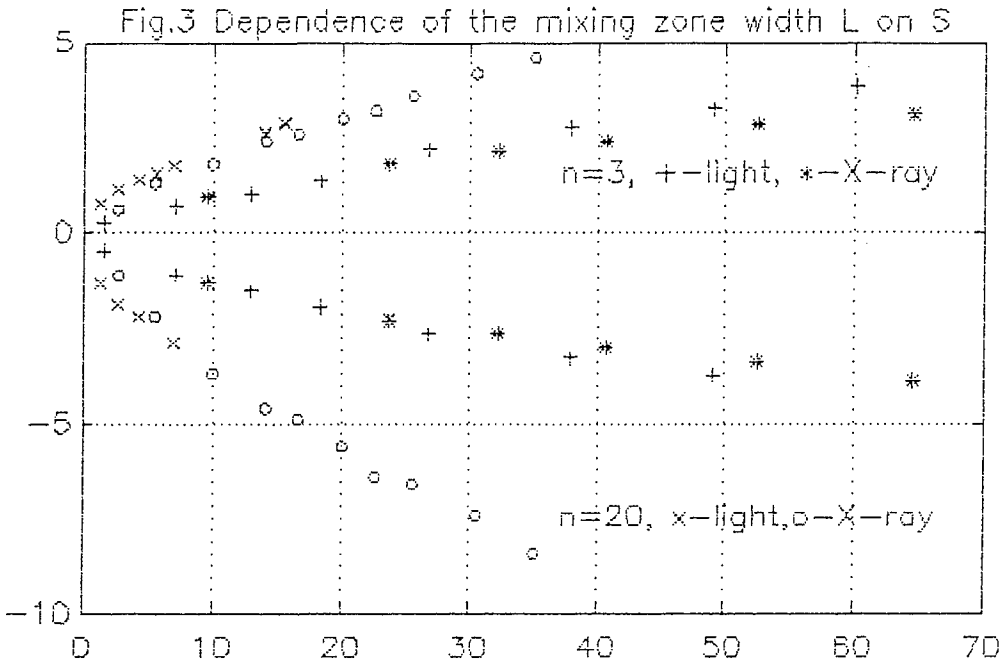


Fig.2 Dependence of acceleration on time for SOM inst.





Mixing Front growth in RT and RM instabilities

Roberto Castilla * † & José M. Redondo *

† Department d'Astronomia i Meteorologia, Diagonal, 647.
Universitat de Barcelona, Barcelona 08028, Spain.

* Department de Física Aplicada, Jordi Girona 31.
Universitat Politècnica de Catalunya, Barcelona 08034, Spain

Abstract

The dependence of the proportionality constant of the quadratic time growth law of the nonlinear mixing zone in Rayleigh-Taylor experiments on several parameters is considered in this work. If different initial perturbations are taken into account and the effect of the large scale initial perturbation is subtracted from the growth of the mixing interface, then a varying proportionality constant is obtained for low Atwood numbers.

Some related experiments on the effect of impulse acceleration on the Richtmyer-Meshkov instability is also presented. A two-fluid density interface between mercury and water or brine and oil is suddenly accelerated by the impact on a cushioned surface after it has attained free fall velocity on a carriage system. The structure of the resulting spikes and bubbles are analyzed giving statistics of their amplitude and maximum growth.

Some preliminary results of a numerical model solving the Boussinesq equations in a 2D configuration are presented, both for the RT and RM instabilities. The two situations are modelled by modifying the value of the effective gravitational acceleration in time.

1. Introduction

The instability of an interface between two superposed fluids of different density is unstable when the light fluid is accelerated towards the heavy fluid. The instability produced is known as Rayleigh-Taylor (RT) instability, and in its simplest forms occurs when a layer of dense fluid is placed on top of a less dense layer in a gravitational field. A related instability, known as the Richtmyer-Meshkov (RM) instability takes place when the acceleration is produced by a shock. We may thus interpret the RM instability as a RT one, when the acceleration has the time dependence of a Dirac delta function. A combination of both instabilities would take place when there are variations of the acceleration driving the flow with time.

In large Reynolds number flows, the RT instability forms a turbulent front and, after an initial linear growth described by Taylor (1950), is independent of the initial conditions

when the front growth may be expressed as

$$\delta = cgAt^2 \quad , \quad (1)$$

where δ is the width of the growing region of instability, g is the gravitational acceleration and A is the Atwood number defined by

$$A = \frac{\rho_1 - \rho_2}{\rho_1 + \rho_2} \quad . \quad (2)$$

The value of the constant c , has been investigated experimentally and its value for experiments at different values of the Atwood number, A , does not show large variations in fully developed flows. Values of c previously obtained experimentally have been in the range (0.03 - 0.035) (Read and Youngs 1984) in experiments with three dimensional effects and large density differences between the two fluids, $A \geq 0.5$. Linden & Redondo (1991) measured c for values of A in the range 1×10^{-4} to 5.0×10^{-2} and found values of $c = 0.035 \pm 0.005$. Numerical calculations in two dimensions (Youngs 1984) have given values of c in the range 0.02 - 0.025. The lesser values (Read 1984) have been explained in terms of two dimensional effects inhibiting the growth of the large scale.

The universality of the t^2 growth of the thickness of the mixing zone between the two layers (1) over a wide range of Atwood numbers suggests that the flow develops a self-similar state. The initial lengthscale of the RT instability is set by the initial density difference and the molecular properties of the fluid.

The work of Rattafia (1964) examined the growth of instability, using the classification of Colwey (1962) in low and medium Atwood number growth. Rattafia used a downwards accelerated interface between benzil alcohol and water with $A = 0.06$, and the growth was considered to be initially exponential following a $\cosh(t)$ law, and linear after mixing occurred. The advance of the front is a function of the instability wavelength for high Atwood numbers and large accelerations. Lewis (1950) used interfaces between air and water and glycerine and benzene, in a small apparatus of plane dimensions 6.35×1.27 cm. He proposed the relationship between the advance velocity of the interface, V_z and the size of the instability λ as

$$V_z = 0.39(\lambda g')^{1/2} \quad . \quad (3)$$

Allred & Blount (1953) used air-water with an acceleration equal to g in a large apparatus of 46×46 cm in plan, they proposed

$$V_z = \frac{2}{\sqrt{23}}(\lambda g')^{1/2} \quad . \quad (4)$$

Emmons (1959) and Cole & Tankin (1972) used various interfaces using a general fit

$$V_z = C(\lambda g')^{1/2} .$$

and Corradini (1978) for much higher accelerations introduced the effect of the size of the apparatus, L . If there is a dominant scale λ due to external forcing, like the two dimensional perturbation produced by the removal of the plate, there will be a competition between the growth at the small scales and at large scales.

In most of the above mentioned experiments, the advance of the front does not become fully turbulent so there is an identifiable wavelength of the fastest growing instability. For fully turbulent RT the dependence on the lengthscale is weak due to the nonlinear interactions between the different scales.

Fully turbulent experiments with longer time history of the RT front have been made by Read & Youngs (1983) who used a rocket propelled box accelerated downwards in order to create the RT instability. They found values of c between 0.03 and 0.035. They compared the advance of the well mixed front between a three dimensional and a two dimensional thin box observing higher values of c in the three dimensional box. Burrows, Smeeton & Youngs (1984) and Smeeton & Youngs (1987) used the same experimental apparatus and confirmed their earlier results. They also investigated three layer and tilted tank configurations.

Andrews (1986) found the same quadratic dependence on time of the advance of the front, but with a lower value of $c = 0.02$, this reduction could be attributed to the two-dimensionality of his experiments and the influence of the lateral walls as he used a $36 \times 25 \times 0.5$ cm box.

The numerical experiments of Youngs' (1984, 1989, 1990) mentioned above for both two dimensional and three dimensional turbulent RT front growth indicate that the three dimensionality produces a decrease in the rate of advance of the front, this suggests the importance of 3-D mixing. The numerical model of Andronov *et al* (1984) also suggest large three dimensional effects, with a breaking of the structure of the front in non-connected regions. The numerical model of Youngs (1990) also shows a range of interacting scales at the nonlinear RT front.

Zufiria (1988) explained the constant acceleration of the front in terms of bubble competition. If there is an initial front of equivalent bubbles, each of them tries to occupy the maximum possible space, the smaller bubbles will have a reduced speed and its companions will gain more space and will grow more. His simple two dimensional model gave values of c between 0.024 and 0.028 for twenty initial bubbles.

Both from experiments and numerical calculations described above, the importance of the three dimensional structure in the advance of the front has been highlighted. The acceleration of the front seems to be controlled by the turbulent mixing produced by the front and the instabilities it generates.

The outline of the paper is as follows. In section 2 we describe the two experiments. In section 3 we describe the numerical model used. In sections 4 and 5 we present the experimental results on the advance of the marked interface for the RT and RM fronts. In section 6 we present some results of the numerical model. In section 7 we describe the fractal nature of the instability fronts and finally we discuss the results and present some conclusions.

2. Experimental apparatus

2.1 RT experiments

The experiments consist of a release of a dense fluid superimposed on a lighter fluid, one of which is dyed, separated by a thin barrier in a tank. The tank is made of perspex and has a height, H of 50 cm, length, L 40 cm and width, W 20 cm. The two fluids are initially separated by a removable sheet of aluminium 1.5 mm thick in the center of the tank. See Linden & Redondo (1991) for more details. Fresh water is placed in the lower half of the tank, the aluminium sheet sliding in tight fitting grooves, is pushed across, sealed with silicone grease, then the dense brine is placed on top.

2.2 RM experiments

The experimental apparatus used is shown in figure 1, a perspex box of dimensions 10 cm \times 15 cm \times 1 cm slides on a carriage system consisting of two metal bars 120 cm long on a frame. A plastic foam layer is placed at the bottom of the carriage, in order to avoid damage to the box. A density interface is formed inside the perspex box, using different fluids. The two fluid density interface between mercury (Hg) and water or brine and oil is suddenly accelerated by the impact on a cushioned surface after it has attained free fall velocity on a carriage system. The cushion thickness could be varied in order to model different impulsive forces. A sharp deceleration models a R-M instability while a slower one models R-T instability.

A camera with a fast shutter was controlled by a trigger consisting of two aluminium foils, which opened the shutter at a preset time after the contact of the perspex box with the foam cushion. Video tapes of the experiments were also taken, and some of these digitized in order to track the evolution of the interface between the two fluids.

The range of Atwood numbers studied vary between 0.9998 for the Hg - air interface and 0.36 for the brine-fresh water interface, the interface between Hg and water ($A = 0.863$)

was studied in detail, and the evolution of the fronts in time measured.

3. Numerical Model

Some results of a numerical model solving the Boussinesq equations in a 2D configuration are presented, both for the RT and RM instabilities. The two situations are modelled by modifying the value of the effective gravitational acceleration in time.

The numerical model has been described in detail by Rees (1987) so only some features will be mentioned here. It is based on a L.E.S. with a numerical scheme that integrates the 2D Boussinesq equations

$$\begin{aligned} \frac{\partial u}{\partial t} + u \frac{\partial u}{\partial x} + w \frac{\partial u}{\partial z} &= -\frac{\partial \pi}{\partial x} - \frac{\partial P_0}{\partial x} + 2 \frac{\partial}{\partial x} \left[\nu \frac{\partial u}{\partial x} \right] + \frac{\partial}{\partial z} \left[\nu \frac{\partial u}{\partial z} + \nu \frac{\partial w}{\partial x} \right] , \\ \frac{\partial v}{\partial t} + u \frac{\partial v}{\partial x} + w \frac{\partial v}{\partial z} &= -\frac{\partial P_0}{\partial y} + \frac{\partial}{\partial x} \left[\nu \frac{\partial v}{\partial x} \right] + \frac{\partial}{\partial z} \left[\nu \frac{\partial v}{\partial z} \right] , \\ \frac{\partial w}{\partial t} + u \frac{\partial w}{\partial x} + w \frac{\partial w}{\partial z} &= -\frac{\partial \pi}{\partial z} + B + 2 \frac{\partial}{\partial z} \left[\nu \frac{\partial w}{\partial z} \right] + \frac{\partial}{\partial x} \left[\nu \frac{\partial u}{\partial z} + \nu \frac{\partial w}{\partial x} \right] , \\ \frac{\partial \vartheta}{\partial t} + u \frac{\partial \vartheta}{\partial x} + w \frac{\partial \vartheta}{\partial z} &= \frac{\partial}{\partial x} \left[\kappa \frac{\partial \vartheta}{\partial x} \right] + \frac{\partial}{\partial z} \left[\kappa \frac{\partial \vartheta}{\partial z} \right] , \end{aligned} \quad (5)$$

with the incompressibility condition

$$\frac{\partial u}{\partial x} + \frac{\partial w}{\partial z} = 0 , \quad (6)$$

where u , v , and w are the velocity components. The eddy viscosity ν was determined by a mixing length hypothesis

$$\nu = \ell^2 S , \quad (7)$$

where S is the 2D deformation tensor and ℓ is a mixing length set constant or inversely proportional to the distance from the interface. Gravity is modified by the Atwood number in the shock models.

4. Experimental results for the RT instability

If the dependence of the proportionality constant of the quadratic time growth law of the non-linear mixing zone in Rayleigh-Taylor experiments on the initial perturbations is taken into account and the effect of the large scale perturbation is subtracted from the growth of

the mixing interface, then a varying proportionality constant is obtained for low Atwood numbers.

In the process of removing the plate, the instability produced by the vortex sheet trailing behind the plate edge, produces a large amplitude wave, and this initial instability produces an additional initial vertical velocity, V_z which depends inversely on the Atwood number. Plotting the coefficient of the quadratic law for the growth of the RM interface as a function of the reduced gravity $g' = 2Ag$, we see in figure 2 a decrease in the value of $2c$ between 0.17 and 0.06: note that the commonly quoted constant is half of this value.

The small scales produced as the RT instability develops, see figure 3, are analyzed using fractal analysis.

5. Experimental results for the RM instability

As the instability develops, sharp peaks shoot up from the dense layer upwards, as the interface is suddenly decelerated. See figure 4 for two photographs of the Hg-air interface.

The evolution of the RM front was measured both from the video tapes and the photographs and some digitized video images were used to measure the relative widths of the spikes, but no dependence was found on the Atwood number.

In figure 5 a series of digitized interfaces are shown. In figure 6 a plot of the distance from the maximum extent of the disturbed interface to the initial interface are plotted versus non-dimensional time. $L = 15$ cm is the height of the perspex box. The initial growth for three experiments shown in figure 6 is approximately linear, after reaching a maximum height, gravity pulls back the unstable interface, at the same time, resonant interactions between the side walls take place. In the figure circles indicate a high impact velocity and triangles a low one.

Figure 7 shows a plot of the maximum extent of the RM front before the unstable fluid falls back, as a function of the Atwood number.

6. Numerical model results

The RT and the RM instabilities have been studied with the numerical model described above. A 32×32 mesh grid was used, an initially unstable interface was set up. In the RM model, gravity was 'switched off' after a short time.

Figure 8 shows the evolution of a RT front for non dimensional times $t/T = 1, 2, 3$ and 4 the density isolines are plotted in an elevation view.

The growth of the mean thickness of the mixed region is quadratic in time, in agreement with the experiments. If RM fronts are modelled using a reduction in gravitational acceleration, the growth is linear initially.

7. Fractal dimension as function of time

The structure of a blob shows a relatively sharp head with small scales developing at the sides due to what seems to be shear instability very similar to the Kelvin-Helmholtz instabilities. The formation of the blobs with their secondary instabilities produces a turbulent cascade after 1 to 2 non-dimensional time units, which can be studied by the growth of the fractal dimension in the front.

Fractal analysis can be used on the images obtained by LIF in which a thin sheet is illuminated. The range of distortions to the interface by the fluid instabilities may be investigated using the definition of the fractal dimension D , Mandelbrot (1972), as

$$D = \frac{\log N}{\log(l/e)} \quad , \quad (8)$$

where N is the number of self similar parts found at a scale e .

It has been suggested Vassilicos & Hunt (1990), Redondo (1990) that fractal analysis allows a better discrimination of the lengthscales involved in a self-similar cascade type of process than the spectral analysis, because for an inertial subrange to be identified, the ratio between the largest, ℓ and the smallest, η , wavelengths in the process, has to be larger when using spectral analysis by a factor depending on the fractal co-dimension, viz.

$$\left(\frac{\ell}{\eta}\right)^E - D_E \quad , \quad (9)$$

for a power spectrum and

$$\frac{\ell}{\eta} \quad , \quad (10)$$

for visual (fractal) analysis.

This additional information which we are able to extract from the direct visual images is related to the fact that a larger separation between the scales is needed when performing a cross-correlation of the velocity fields. A relationship between the fractal dimension of a material line in the flow and the scalar power spectrum β for three dimensional flows can be shown to be

$$D = 3 + \frac{1 - \beta}{2} \quad , \quad (11)$$

or

$$D = 4 - \beta \quad , \quad (12)$$

depending on the assumptions made, see Redondo & Linden (1990), Vassilicos (1990). If the scalar is advected by the velocity field, then some information on the velocity power

spectrum can be investigated by geometrical means analysing the fractal structure of the RT or RM instability fronts.

The number of self-similar parts was calculated by means of a box counting algorithm. This method divides the image into smaller and smaller boxes of dimension e , and counts the number N of the boxes through which the edge of the interface passes. The fractal dimension D_2 , where the sub-index indicates that the embedding space is a plane, is calculated with the expression (8) given above. Plots are made of $\log N$ against $\log(1/e)$, and if the surface is self-similar or fractal, the points will lie on a straight line with slope D_2 . There is a predominance of two scales that correspond to the bubble size and the dominant KH instability on the sides. Nevertheless, averaging different regions of the mixing front (different bubbles or different experiments at the same non-dimensional time) the fractal dimension, can take into account the statistical nature of the mixing processes.

The development of the full fractal structure takes approximately 1 to 2 non dimensional time units for the range of effective accelerations used in the RT experiments Linden & Redondo (1991) ($20 > g' > 10 \text{ cms}^{-2}$). At earlier times only the linear RT scales and the disturbances imposed by the withdrawal of the plate are present. The fractal dimension then remains approximately constant until the influence of the bottom of the tank and the subsequent stable stratification reduces the dimension again. The time development of the fractal dimension is shown in figure 9 for a typical experiment. The open squares indicate the evolution of the mean fractal dimension, for an elevation view. Here the two dimensionality produced by the removal of the plate, reduces the fractal dimension until $T = 1.25$, after which it follows a similar pattern as for side views.

The LIF visualisation method is restricted by the width of the light sheet (assuming at these small scales the structure is isotropic). Thus we are unable to resolve motions on scales less than 2 mm, which exceeds the Kolmogorov scale. On the other hand, as noted earlier the smallest scales observed initially at the interface edge were larger than the 2 mm resolution scale suggesting that the flow is not fully developed until after some time. The nondimensional time for the front to reach the bottom of the tank is 2.7 T, but at least 1T is needed for the flow to become turbulent. Thus can be thought of as a transition between the initial growth dominated by the bubble competition and the fully turbulent regime.

The increase in contact area due to the fractal appearance of the front should be taken into account in order to relate the molecular mixing across the front with the multiple scales interacting there.

Considering that at least statistically a fractal dimension gives an indication of the convolutions of the interface, the times at which the fractal dimension is large will be the

most efficient in terms of local mixing.

We can estimate the area taking into account the fractal convolutions in the range $(\ell - \xi)$ in terms of the area measured in an euclidean sense at size ℓ , A_ℓ , as

$$A_f = A_\ell \left(\frac{\xi}{\ell} \right)^{2-D} . \quad (13)$$

See Mandelbrot (1979) for a wider discussion on line and area measures.

In order to estimate in our experiments the contact area between the two fluids and the area increase with time from the evolution of the fractal dimension we can substitute the value of the fractal as it evolves in time. The maximum growth in area found is

$$\frac{A_f}{A_\ell} = \left(\frac{\xi}{\ell} \right)^{-0.3} \quad (14)$$

which gives a value of 2.66 using $\xi = 2$ mm, (the visual limit), and $\ell = 100$ mm, (blob size) typical values after $T = 1$.

As the turbulent RT front evolves, ℓ the size of a typical blob, which is assumed to be proportional to the integral lengthscale of the turbulence, increases up to a fraction of the tank size, L .

8. Discussion and conclusions

The evolution of the maximum advance of the RT and RM fronts with non dimensional time, defined as

$$T = \left(\frac{Ag}{H} \right)^{1/2} t , \quad (15)$$

agrees with previous work.

The RM instability grows initially in a linear way until the restoring effect of gravity dominates, as

$$\delta = c'(A)t . \quad (16)$$

The similarity solution

$$\delta = L_o^{1-p} (A\Delta Ut)^p , \quad (17)$$

indicated by Youngs (1989) is masked by the effect of gravity pulling back the unstably stratified layer.

The RT instability, as described in Linden & Redondo (1991) grows quadratically

$$\delta = c(A)Agt^2 \quad . \quad (18)$$

The results of the RM experiments are influenced by surface tension between the different fluids used, only in the case of water and brine, is its effect negligible.

The effect of gravitational impulse due to the shock seems a simple way of studying the structure of RM and RT instabilities as well as the effect of boundary effects. The main inconvenience is the restoring effect of gravity after the instability sets in.

The numerical calculations show overall agreement with the advance of the front modeling the gravitational acceleration in order to account for the effect of the shock. More work is needed in order to reflect Atwood number dependence.

Acknowledgements

We would like to thank P.F. Linden and D.L. Youngs for their support and S. Dalziel for his help with the digitizing system DigImage. This work was partly supported by the MOD.

References

- Allred J.C. & Blount G.H. (1953) "Experimental studies of Taylor instability". Los Alamos Scientific Laboratory report LA-1600.
- Andrews M.J. (1986) "Turbulent mixing by Rayleigh-Taylor instability" PhD Thesis CFDU/86/10 Imperial College of Science & Technology, London.
- Andronov et.al. (1984) "Numerical experiment of Rayleigh - Taylor instability" preprint Novosibirsk. Acad. Nauk.
- Cole R.L. & Tankin (1972) " Experimental study of Taylor instability". *Phys. Fluids* 16 (11), 1810-1820.
- Crowley W.P. (1962) Lawrence Livermore Laboratory report UCRL-72650.
- Corradini M.L. (1978) " Heat transfer and fluid flow aspects of fuel-coolant interactions" PhD thesis M.I.T.
- Daly B. J.(1969) " Numerical study of the effect of surface tension on interface instability". *Phys. Fluids* 12 (7), 1340-1354.
- Emmons H.W., Chang C.T. & Watson B.C. (1960) " Taylor instability of finite surface waves" *J. Fluid Mech.* 7, 417-425.

Lewis D.J., (1950) "The instability of Liquid surface when accelerated in a direction perpendicular to their planes" *Proc. Royal Soc.* 202 A, 81 - 90.

Linden P.F. Redondo J.M. & Caulfield C.P. (1990) "Molecular mixing in Rayleigh-Taylor Instability" *Proceedings Workshop on the physics of compressible turbulent mixing.* Princeton 1988. Ed. A.C. Buckingham.

Linden P.F. & Redondo J.M. (1991) "Molecular mixing in Rayleigh-Taylor instability. Part 1. Global mixing". *Phys. Fluids.* 5 (A), 1267-1274.

Linden P.F., Redondo J.M. and Youngs D. (1993) "Comparison of numerical calculations and experiments in Rayleigh-Taylor instability." submitted to *J. Fluid Mech.*

Mandelbrot B.B. (1972) "Fractals, form, chance and dimension". Ed. W. Freeman, San Francisco.

D.H.Sharp,(1984) "An overview of Rayleigh-Taylor Instability",*Physica* 12D ,3

Smeeton V.S. and Youngs D.L.(1987)"Experimental Investigation of Turbulent mixing by Rayleigh-Taylor instability, part 3" AWE Report O 35/87.

Ratafia M. (1964) "Experimental investigation of Rayleigh-Taylor instability". *Phys. Fluids* 16 (8), 1207-1210.

Read K.I. and Youngs D. Y.,(1983) "Experimental investigation of turbulent mixing by Rayleigh-Taylor instability" AWE Report 011/83.

Read K.I.(1984) "Turbulent mixing by Rayleigh-Taylor instability" AWE Report 002/84.

Redondo J.M. and Linden P.F.(1990) "Geometrical observations of turbulent density interfaces" *Proceedings of IMA conference Mathematics and computation of deforming surfaces.* Cambridge 19 Dec 1988. Eds D.G. Dritshel, J.C.R. Hunt & R. Perkins.

Redondo J.M. and Linden P.F.(1990) "Mixing produced by Rayleigh-Taylor instabilities" *Proceedings of Waves and Turbulence in stably stratified flows,* IMA conference. Leeds 18 Dec 1989. Ed. J. King and S.D. Mobbs. IMA. Oxford.

Taylor G.I.(1950) *Instability of superimposed fluids,* *Proc. Royal Soc*

Turner S. (1973),"Buoyancy effects in fluids",*Cambridge University Press.*

Vassilicos. C. (1990) "Relations between the geometry of an interface and the structure of turbulent velocity fields" Ph.D. Thesis , University of Cambridge.

Vassilicos C. & Hunt (1990) "Fractal dimensions and spectra in turbulence", manuscript, DAMTP. U Cambridge.

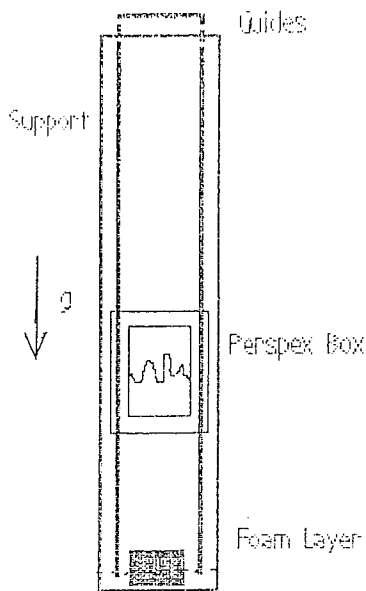
Youngs D.L.(1984) "Numerical simulation of turbulent mixing by Rayleigh-Taylor instability", *Physica D*, 12.

Youngs D.L. (1989) "Modelling turbulent mixing by Rayleigh-Taylor instability". *Physica D* 37, 270-287.

Youngs D.L. (1990) "Three dimensional numerical simulation of turbulent mixing by Rayleigh-Taylor instability" Submitted to *Phys. Fluids*.

Youngs D.L. (1991) "Simulation of turbulent mixing by Rayleigh-Taylor instability affected by a two dimensional perturbation"

Zufiria J.A. (1988) "Bubble competition in Rayleigh-Taylor instability". *Phys. Fluids* 31 (3), 440-446.



Experimental Apparatus

Fig. 1 - Diagram of the experimental apparatus used for the Richtmyer - Meshkov instability study. The perspex box is allowed to fall until it hits the foam, and stops, producing an upwards shock.

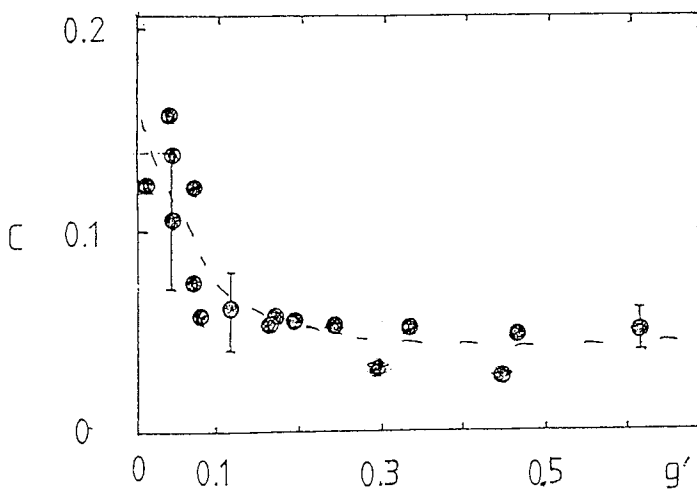
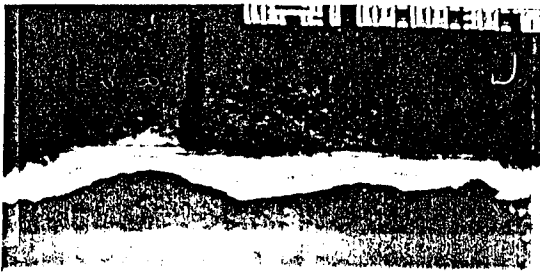


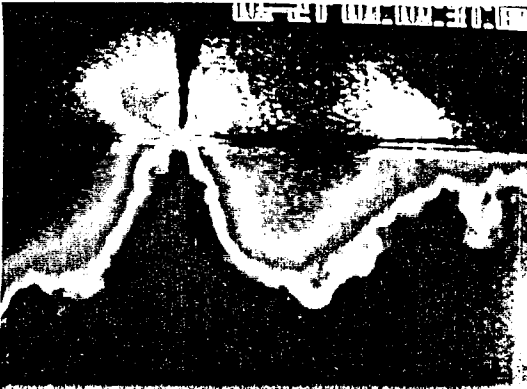
Fig. 2 - Plot of the constant c of the quadratic time dependence of the growth of the Rayleigh - Taylor front as a function of the reduced gravity.



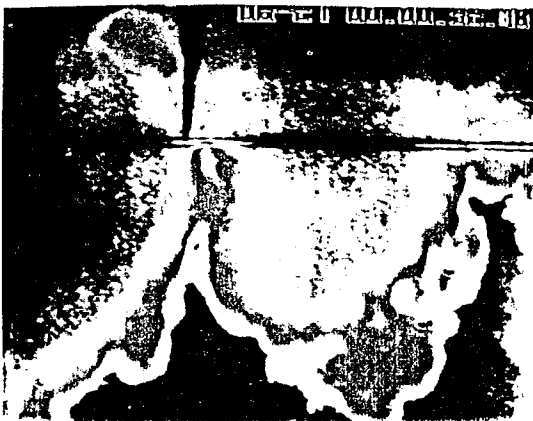
a)



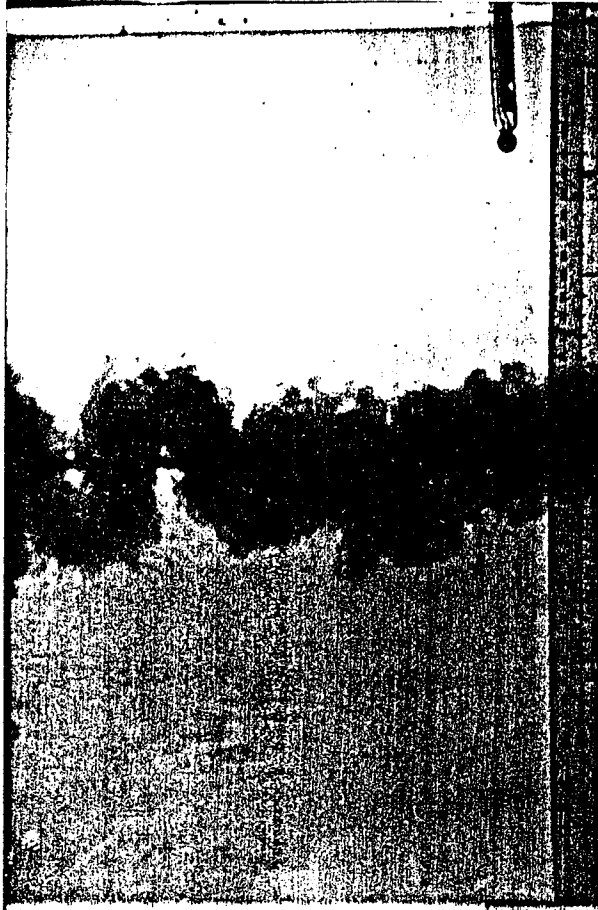
b)



c)

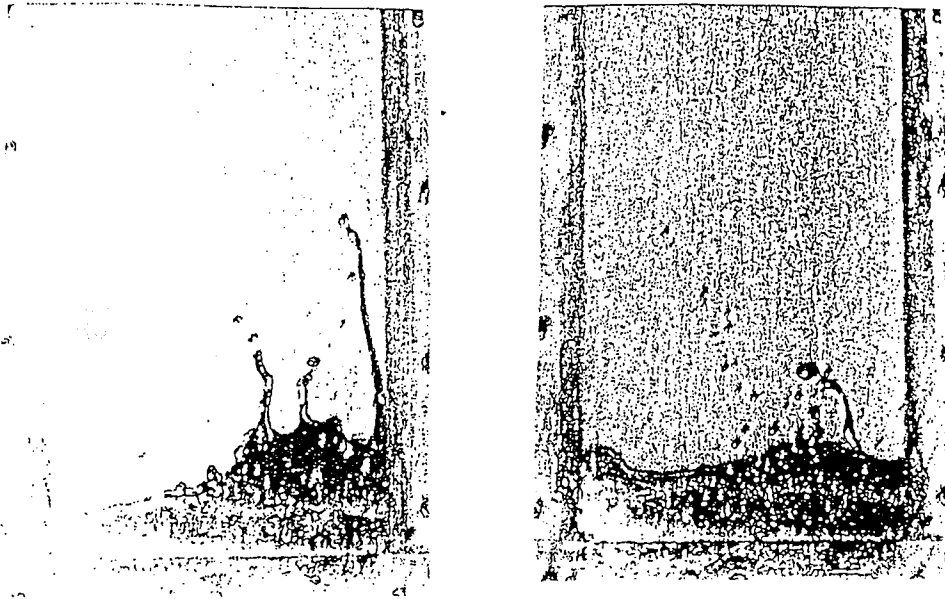


d)



e)

Fig. 3 - Digitized images of the advance of the RT mixing front, at non - dimensional times of $T=0.1$, 1 , 2 and 3. Dye colouring, integrated across the width of the tank is the visualization method shown here.

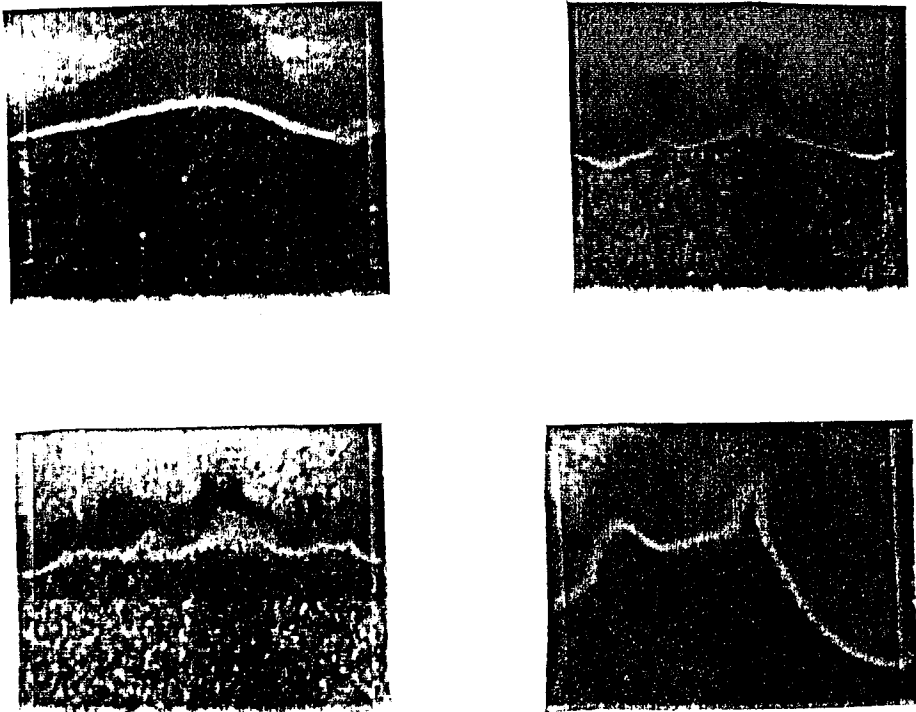


a)

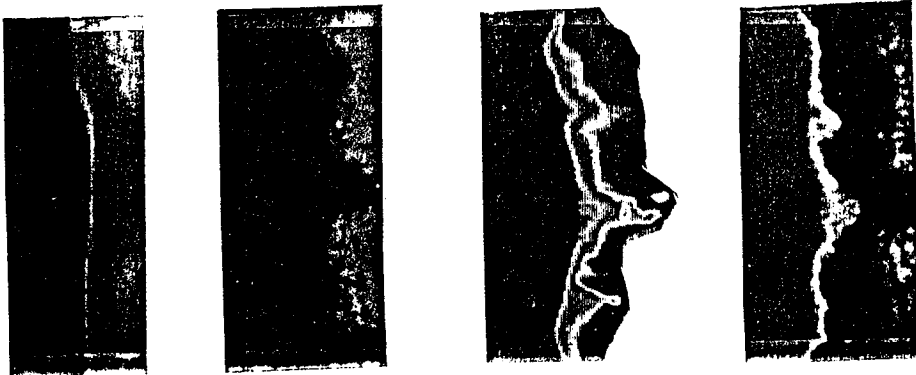


b)

Fig. 4 - Photographs of the Mercury - air interface, for two different experiments, the spikes have rounded shapes, due to the high surface tension. a) Black and white photographs , b) Colour digitization of the interface.



a)



b)

Fig. 5 - Different digitized interfaces arising from the RM instability, the periodic appearance of spikes is clearly seen. a) brine - fresh water interfaces. b) Different false colours used in order to enhance the structure of the interface.

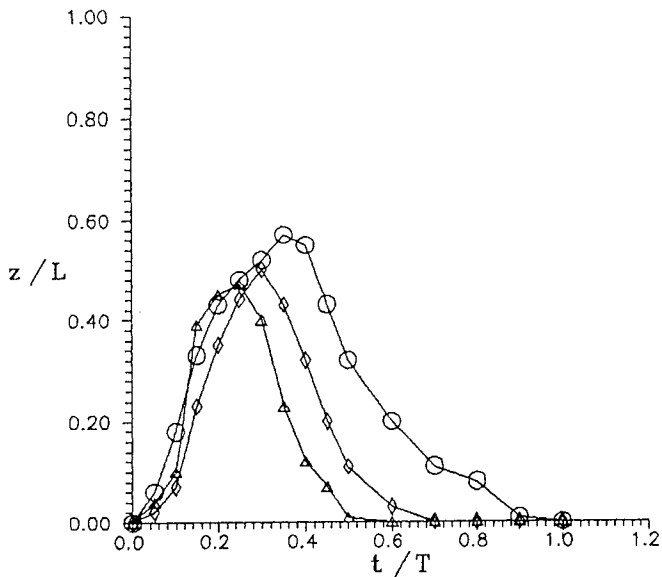


Fig. 6 - Non dimensional distance advanced by the RM front versus non-dimensional time, $t/T \times 10$, where $T = (Ag/L)^{1/2}$. The initial growth, after a delay due to the foam, the growth is linear, until restoring gravity reduces the extent of the instabilities, the tails are due to oscillations of the interfaces. \circ indicates water on air experiments, \diamond oil on air and \triangle Hg on air.

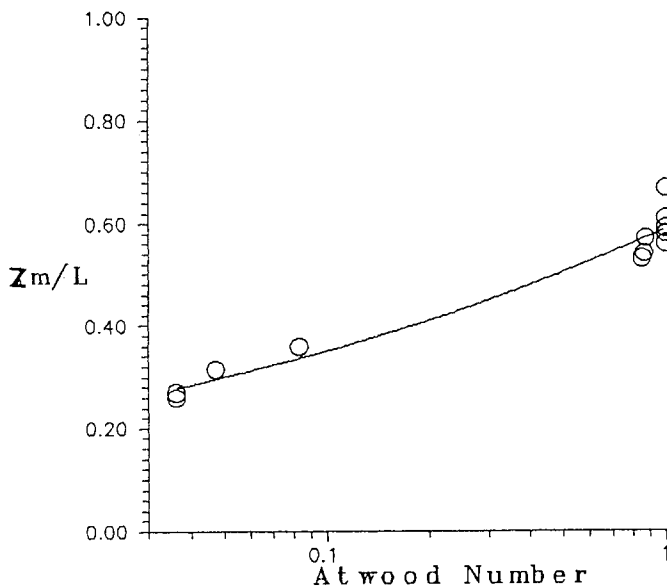


Fig. 7 - Variation of the maximum extent of the interface as a function of the Atwood number, for the different substances used to form the interfaces.

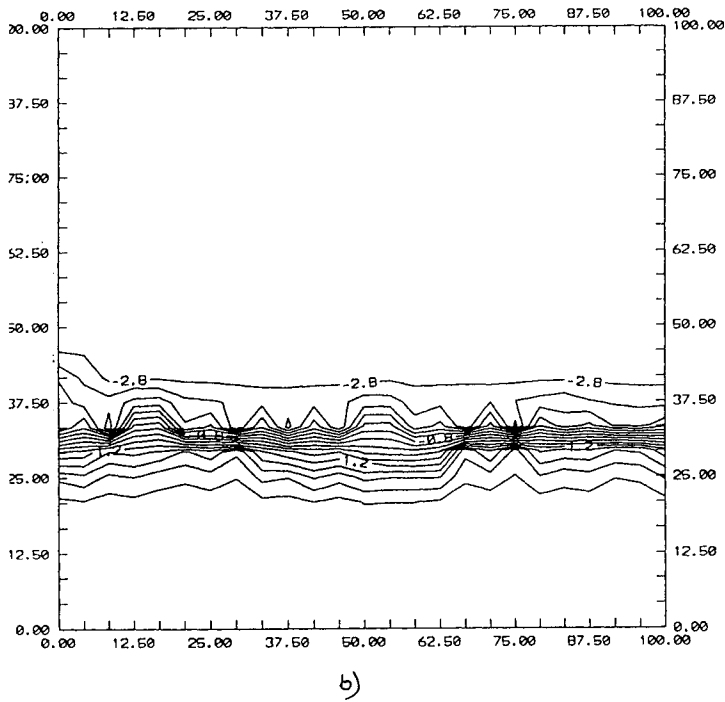
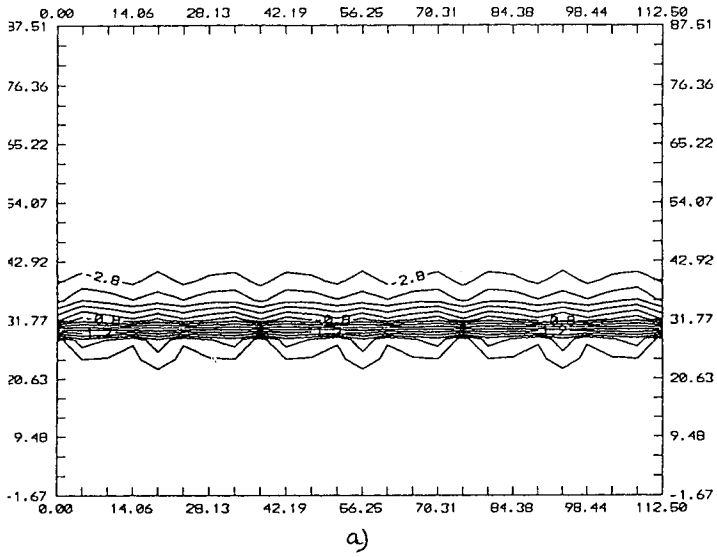
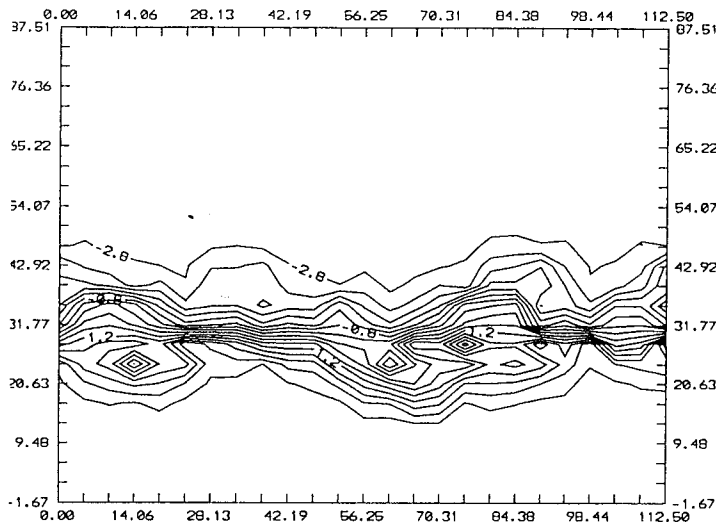
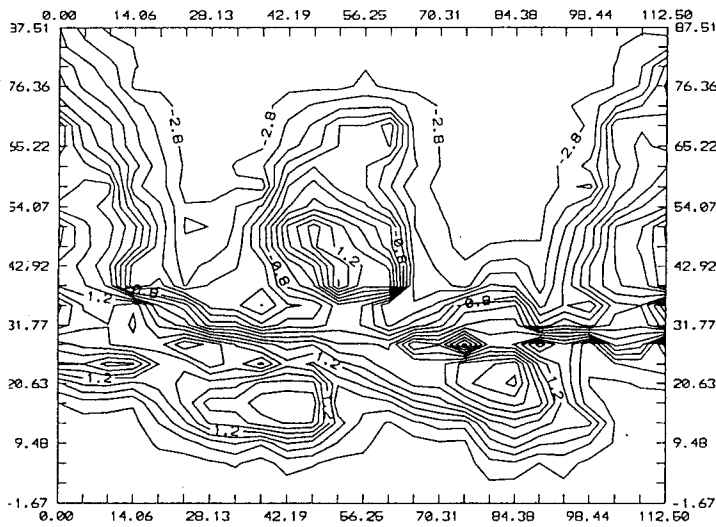


Fig. 8



c)



d)

Fig. 8 - Evolution of a RT instability in time , a) $t/T = 1$, b) $t/T = 2$, c) $t/T = 3$ and $t/T = 4$.

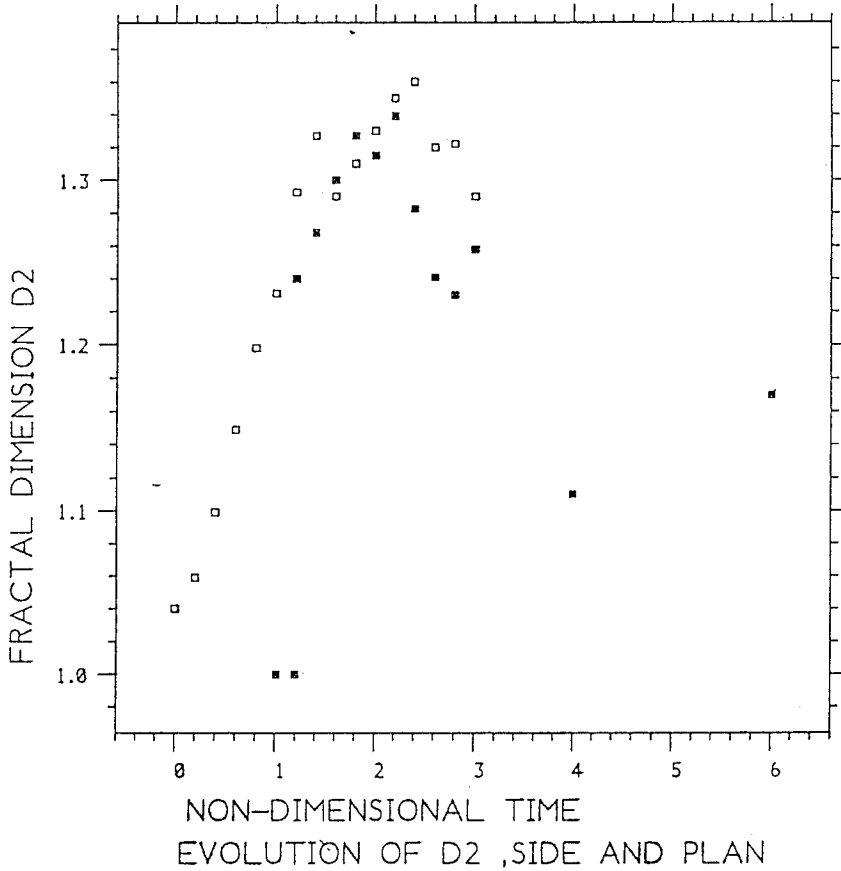


Fig. 9 - Evolution of the fractal dimension with non-dimensional time for the RT experiment, most experiments showed a similar behaviour. The RM experiments showed smaller values of the fractal dimension, mostly due to surface tension effects.

Perturbations and coherent flow in Rayleigh-Taylor instability

Stuart B. Dalziel

Department of Applied Mathematics and Theoretical Physics
University of Cambridge, Silver Street, Cambridge CB3 9EW, ENGLAND
Phone: (44)(223)337840; Fax: (44)(223)337918; E-mail: sd103@amtp.cam.ac.uk

ABSTRACT

In this paper we explore the effects of initial perturbations and enclosed geometry as found in a set of simple experiments performed in the laboratory using a gravitationally unstable system. The aim of this work is to attempt to quantify the relatively large differences in the growth rate found previously in such experiments when compared with rocket experiments or numerical codes.

1. Introduction

One of the simplest experimental systems which exhibits Rayleigh-Taylor instability is that where a homogeneous layer of dense fluid overlies a similar layer of less dense fluid. Initially the two layers are separated by a horizontal barrier. The instability starts when the barrier is removed with gravity providing the acceleration driving the instability. In the experiments reported in this paper we utilise salt water for the denser fluid and a solution of fresh water and propan2ol for the less dense fluid. The alcohol is added to the fresh water in order to match the refractive index of this layer with that of the dense layer. The alcohol has the additional effect of reducing the density of the less dense layer, increasing the density ratio for a given weight of salt added to the dense layer. Typically these experiments are performed with Atwood numbers

$$A = \frac{\rho_1 - \rho_2}{\rho_1 + \rho_2} \quad (1)$$

in the range 10^{-4} to 10^{-2} , where ρ_1 is the density of the upper (denser) layer and ρ_2 the density of the lower layer.

The removal of the barrier always produces some initial perturbation to the flow. These perturbations, and how they affect the subsequent flow are the principal focus of this paper. The perturbations are analysed using a combination of experimental techniques to give both qualitative and quantitative descriptions of the flow. These descriptions are compared with previous experiments and with the numerical solutions of Youngs (1991, 1993).

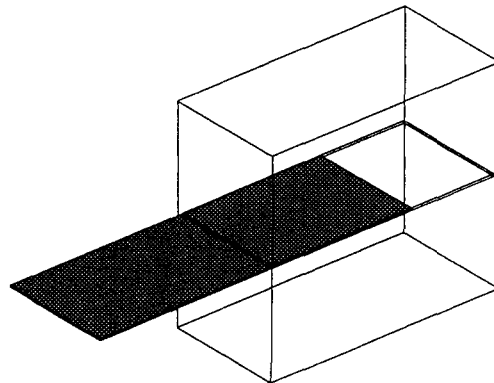


FIGURE 1: Schematic of experimental apparatus showing the original solid barrier.

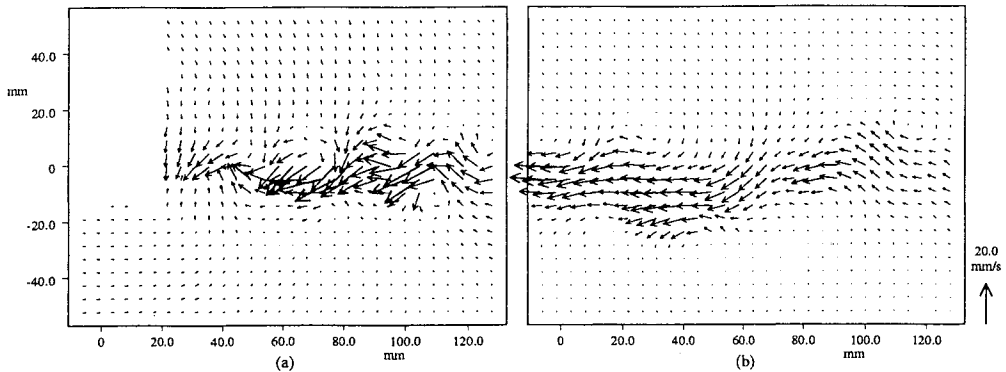


FIGURE 2: Velocity field produced by the withdrawal of the simple, solid barrier. (a) Flow field at $t=1s$: the barrier interrupts the light sheet preventing velocity vectors from being obtained in the upper left quadrant of the view. (b) Flow field at $t=4s$.

This paper is divided into three main sections plus conclusions in addition to this introduction. In section 2 we consider the original box and simple, solid barrier utilised in these and earlier experiments (Linden & Redondo, 1991). A new composite barrier, originally suggested by Lane-Serff (1989, p. A-7) is introduced and the flow analysed in section 3. In section 4 we consider the flow when a modified version of the barrier of section 3 is utilised. Finally we present our conclusions in section 5.

2. Original barrier

In this section we shall consider briefly the initial perturbations produced by the original barrier used in these experiments and earlier experiments by Linden & Redondo (1991). Figure 1 shows a schematic view of the tank with this barrier installed. The tank measures 400mm long, 200mm wide and 500mm deep. The barrier is located at mid-depth, 250mm above the tank floor. The barrier consists of a single sheet of stainless steel 1.65mm thick with a square trailing edge. The barrier runs in grooves machined into the walls of the tank and is removed through a slit in one of the end walls. Rubber seals are used to prevent leakage around the barrier. The barrier is removed manually by simply pulling it out.

As noted by Linden & Redondo (1991), shear boundary layers are generated on the upper and lower surfaces of the barrier as it is removed. The wake that is left behind is unstable, rapidly forming wave-like disturbances. Figure 2 shows the velocity field produced by the wake of the barrier in a homogeneous system. In this case we can see the flow in a two dimensional slice near the centre of the tank. The slice is oriented such that we can see the vertical component of the velocity and the horizontal parallel with the direction of plate withdrawal. The velocity field has been determined using the particle system developed by the author and described in Dalziel (1992, 1993a, 1993b).

We can clearly see the growth of the instability on the wake from a simple wave-like flow in figure 2a to a more complex vortical flow in figure 2b. The flow in this example is relatively weak as the barrier was withdrawn very slowly (approximately 4s to remove it). The flow in the wake is much more vigorous and turbulent when the barrier is removed more rapidly. In typical experiments the barrier was removed in between 0.5s and 2s, although it is possible to withdraw it in as little as 0.2s.

Arguably more important is the secondary effect of the wake as it is stripped off the barrier at the side wall through which the barrier is removed. The fluid carried along by the barrier is turned to form wall jets directed vertically away from the barrier at the end wall of the tank. These jets have been seen to penetrate into the upper and lower layers of the flow much more rapidly than the growing Rayleigh-

Taylor instability. These have been seen to have a marked affect on the flow, at least in the early stages.

The third and final part of the perturbation introduced by this simple barrier is possibly the most important. Continuity and the incompressibility of water require that the volume removed from the tank by the withdraw of the barrier must be compensated for by a net downward movement of the upper free surface. This is particularly important just as the barrier is started to be removed. At this stage the only way of filling the void left by the withdrawn barrier is by fluid moving down from the upper layer with a velocity

$$w_{trailing} = U_{barrier} \frac{\partial D}{\partial \hat{x}}, \quad (2)$$

where $w_{trailing}$ is the velocity of the upper layer immediately behind the trailing edge of the barrier, $U_{barrier}$ is the velocity at which the barrier is withdrawn and D is the thickness of the barrier as a function of its length \hat{x} . As noted above, the simple solid barrier has a square trailing edge, so $\partial D/\partial \hat{x} \rightarrow \infty$ at the trailing edge and so $w_{trailing}$ is singular at that point. The net result of this is that the upper layer crashes down on the exposed lower layer, providing an impulse at one end of the tank. As the barrier is removed further, it becomes possible for some of the lower layer fluid to rise up to replace the volume removed by the barrier (a corresponding down flow occurring elsewhere in the tank), allowing the initial impulse to set up a large scale overturning motion in the tank. This is observed in the experiments as the upper layer *always* reaches the bottom of the tank first at the end where the barrier is first removed from and reaches the top of the tank first at the end where the barrier is last removed from. The large scale overturning motion associated with this is always in the same direction.

We shall not consider experiments with this simple barrier in this paper. Instead we refer to reader to Linden & Redondo (1991) and Castilla & Redondo (1993). In the next section we shall consider the development of the flow when the two layers are initially separated by a more complex barrier which attempts to reduce the initial perturbations.

3. Composite barrier

Lane-Serff (1989, p. A-7) suggested an alternative form of barrier which eliminates most of the shear between the barrier and the fluid above and below it. Such a barrier is shown schematically in figure 3. The barrier consists of a thin, hollow stainless steel plate through which two pieces of nylon fabric are passed. One piece of nylon fabric is stretched along the top of the stainless steel plate to be attached to the tank wall just above the plate at the point where the plate is withdrawn from the tank. The second piece of nylon fabric is stretched along the underside of the hollow plate and also attached to the tank wall. Overall the construction of the hollow plate (laminated from two pieces of 0.6mm stainless steel and separated by thin strips of the same material) and nylon fabric is approximately 2.4mm thick.

In principle this barrier is removed by withdrawing the nylon fabric through the plate at a speed (relative to the box) twice as fast as that at which the barrier is withdrawn from the box. Except for the

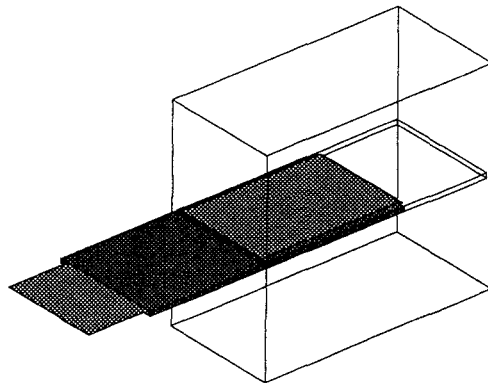


FIGURE 3: Schematic of tank with composite barrier showing the stainless steel plates (dark grey) and nylon fabric (light grey).

point where the nylon passes around the end of the plate, there is no shear between the fluid above (or below) the barrier and the nylon fabric. All the shear is confined between the nylon fabric and the stainless steel plate.

3.1 TRAILING JET

Dalziel (1993b) presents some preliminary results using this composite barrier. The initial growth of the structures on the unstable interface once the barrier was removed was observed to be dominated by a two-dimensional mushroom-like structure with a 20mm wave length. In contrast the linearly most unstable mode (Chandrasekhar, 1961, p. 447) and initial three-dimensional growth occur with a wave length of approximately 2mm.

By adding small, neutrally buoyant particles to the flow it may readily be seen that this two dimensional structure is formed by inviscid instabilities on a two-dimensional jet. The existence of this jet is somewhat surprising as it is produced by the barrier and directed in the opposite direction to the withdrawal of the barrier. This jet is formed by the nylon fabric dragging fluid with it as it is suddenly being pulled into the end of the stainless steel plate as the barrier passes a given point. The fluid being pulled up from the lower layer and down from the upper layer collide and transfer their energy into a horizontal flow away from the trailing edge of the barrier.

Figure 4 shows a typical example of the jet-like flow produced in a homogeneous flow by the barrier when it is withdrawn very slowly (approximately 4s for complete withdrawal). The velocity field is obtained from the particle tracking system mentioned earlier. The structure of the jet and subsequent instability are readily apparent in the two snap-shots. The instability is driven by the coupling between the two inflection points in the velocity profile (one above the barrier and one below). Analysis of jets with a similar structure (*e.g.* Tatsumi & Kakutani, 1958) suggest the jet is unstable whenever the Reynolds number (based on the width of the jet) exceeds some value of order one.

While we have removed the wake, wall jets and related instabilities discussed in the previous section, we still have a medium wave-length perturbation, albeit somewhat weaker than that for a simple solid barrier. Experiments with and without stratification have shown that the large scale overturning mode caused by the square trailing edge of the barrier is still present. The question is can we do any better? In section 4 we shall consider a method of reducing the large scale overturning and eliminating the jet. Before doing so, however, we shall look briefly at the early stages of evolution with the jet produced by the composite barrier.

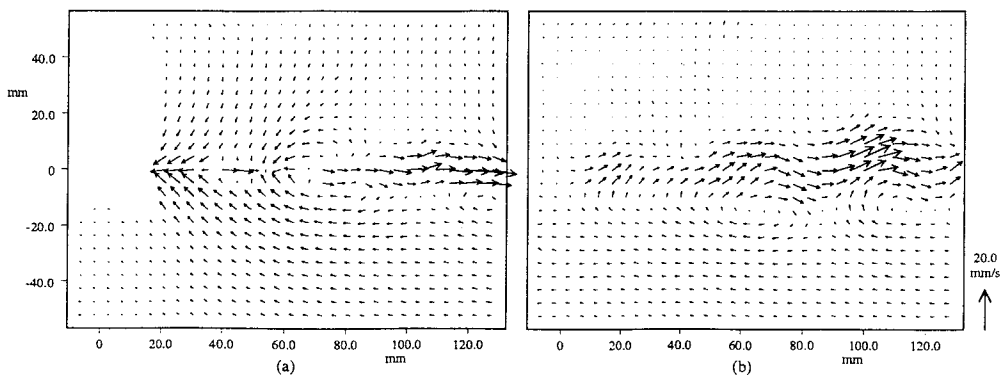


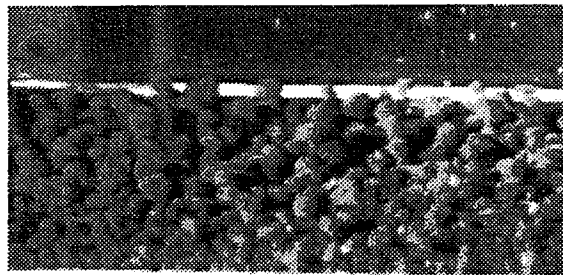
FIGURE 4: Velocity field produced by the withdrawal of the composite barrier (no trailing wedge). (a) Flow field at $t=1$ s: the barrier interrupts the light sheet preventing velocity vectors from being obtained in the upper left quadrant of the view. (b) Flow field at $t=4$ s.

It is relatively easy to reduce the strength of the jet when compared with that in figure 4 and the flows presented by Dalziel (1993b). Since the aforementioned experiments were undertaken, it has been discovered that the trailing edge of the barrier had been damaged by difficulties in during the preliminary phase of experimentation. The damage combined a slight opening and misalignment of the trailing edge with curvature along the length of the barrier. The result of this damage was the production of a stronger two-dimensional jet behind the barrier than is the case for an undamaged barrier. More recent experiments with a replacement barrier produce a much weaker jet. The growth rate of instabilities on this jet is much slower, leading to very little energy being supplied to the Rayleigh-Taylor instability in the 20mm wave length range.

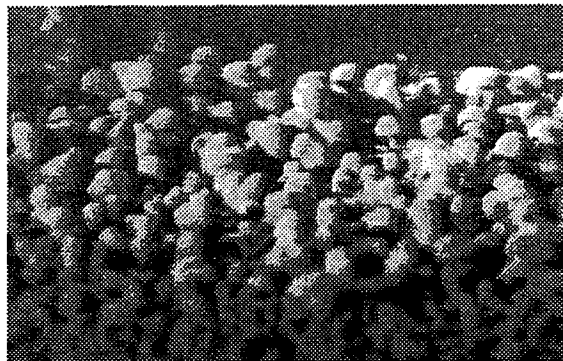
3.2 PERSPECTIVE VIEW

Figure 5 shows a series of perspective views of the early stages of the growth of the instability. The upper layer contains salt water as normal. A high concentration mixture of textile dyes (Terasil Red G and Solophenyl Turquoise Br1) and sodium fluorescein was added to the lower layer. The Atwood number for this flow was not measured, but is estimated at 5×10^{-4} .

The flow was illuminated by an arc lamp and viewed by a video camera looking through the end of the tank at an angle of approximately 30° above the horizontal. The textile dyes served to prevent light penetrating more than approximately 0.3mm into the lower layer fluid, while the fluorescein gave the interface between the upper and lower layer a bright, solid appearance. The views are similar to those presented by Dalziel (1993b), but have a different scale and slightly different view point. The mixture of dyes also differs from these earlier experiments, although the overall effect is similar. Note the qualitative similarity between these images and the simulation of Youngs (1992, personal communication) on the cover of this volume.



(a)



(b)



(c)

FIGURE 5: Perspective view of the early evolution of the instability using the composite barrier without a trailing wedge. Times are measured from the start of the withdrawal process. (a) $t=2s$. (b) $t=3s$. (c) $t=4s$.

The interface immediately behind the barrier at $t=2s$ ($\tau = (Ag/H)^{1/2}t \approx 0.2$, where τ is the dimensionless time, g is the gravitational acceleration and H the depth of the tank) is shown in figure 5a. The rapid development of small, three-dimensional structures is readily apparent. The length scale of the smallest of these structures is comparable with the 2mm of linear theory. There is only a very faint indication of any two-dimensional motion due to the jet. Not apparent in these images although present in this experiment is the large scale overturning mentioned earlier.



FIGURE 6: Schematic showing a trailing wedge installed behind the composite barrier.

Interaction between the small structures leads to the development of increasingly larger bubbles of less dense fluid rising into the denser upper layer. Figure 5b shows the development at $t=3s$ ($\tau=0.3$) and figure 5c at $t=4s$ ($\tau=0.4$). As the flow approaches the Boussinesq limit, we may expect similar structures to be penetrating downward, carrying dense fluid into the lower layer.

4. Trailing wedge

A simple method of eliminating the two-dimensional jet produced by the composite barrier is to simply block it with some obstruction. Clearly this obstruction needs to be relatively small and streamlined so that it does not itself contribute a significant wake. If we utilise an asymmetric wedge to block the unwanted jet, such as the one illustrated in figure 6, then in addition to blocking the jet, we will lower the upper layer relatively gently onto the lower layer by removing the singularity in $\partial D/\partial \hat{x}$ in equation (2).

4.1 WAKE

The presence of the wedge effectively blocks the two-dimensional jet produced by the pulling together of the nylon fabric. The disadvantages of such a wedge is that shear boundary layers are generated on the two surfaces. On the lower surface this is not too much of a problem as the length of the wedge is relatively small. On the upper surface, however, the boundary layer is relatively thick due to the divergence of the flow down the wedge and separation of the boundary layer. The end result is an asymmetric wake and the introduction of a preferred sign for the vortices it generates.

A series of experiments with no stratification but a fluorescent dye in one of the two layers has shown that with the trailing wedge there is very little energy transferred to a large scale overturning when compared to the same conditions without a trailing wedge. Thus the introduction of the wedge offers a substantial improvement in the perturbation at the largest scales. In contrast the perturbation is greater at smaller scales where the roll up of the asymmetric wake is apparent.

4.2 PERSPECTIVE VIEW

Figure 7 shows a series of perspective views from the same view point and at the same times as those shown in figure 5. The Atwood number is similar (although again not measured), and the speed at which the barrier was withdrawn is also similar. In the early stages (figure 7a) the flow is clearly much more two-dimensional than that in the absence of the trailing wedge. The separated wake on the upper side of the wedge drags the growing structures in the direction of the withdrawal. A relatively strong two-dimensional component is also introduced with the structures overall being more regular than when there was no wedge.

The initial structure persists during the initial growth phase as the length scale of the bubbles increases (figures 7a & 7b). Note that in this case we do not expect the downward moving bubbles of

denser fluid to be identical to the bubbles of light fluid we can see due to the asymmetry of the wake behind the wedge. Observations suggest, at least at the qualitative level, that differences in the development of the flow with the wedge remain until quite late in the development of the instability.

Given the stronger, medium-scale, approximately two-dimensional initial perturbation introduced by the wedge, it is tempting to discard the wedge and simply use the composite barrier of section 3. There is, however, one substantial improvement introduced by the wedge: the removal of the large scale overturning. It is felt that the initiation of the large scale overturning has a more profound influence on the overall development of the instability than the relatively small scale effects of the wake. Further data, however, is needed to confirm this hypothesis.

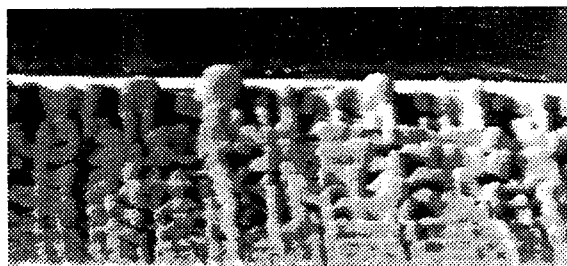
4.3 GROWTH RATE

An ensemble of experiments with $A=2.1 \times 10^{-3}$ has been analysed to determine the growth of the mixed region. The data was obtained by adding sodium fluorescein to the upper layer and illuminating the flow throughout the central 50% of the length and width of the tank. After digitising a time series of images of the flow and correcting the images for non idealisations in the experimental set-up, the horizontal mean intensity was calculated as a function of depth. This function was then averaged over the eight experiments in the ensemble to produce the profile in figure 8. Finally this profile was analysed to determine the 95% lower layer/5% upper layer mix point.

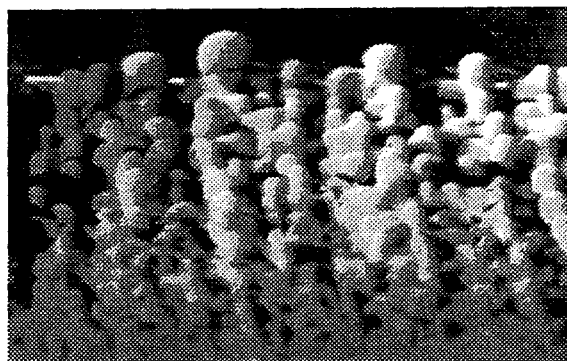
Figure 9 plots the square root of the penetration of the dense fluid into the lower layer as a function of time. The nearly straight line relationship gives clear evidence of the

$$h_1 = \alpha A g t^2 + h_0 \quad (3)$$

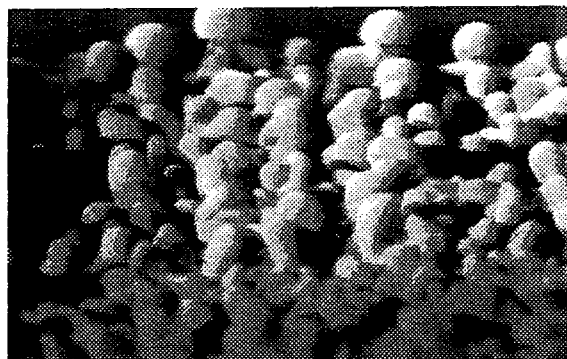
growth rate expected for these flows. Here h_1 is the penetration of the dense fluid into the lower layer, α the constant of proportionality and h_0 some measure of the amplitude of the initial



(a)



(b)



(c)

FIGURE 7: Perspective view of the early evolution of the instability using the composite barrier with a trailing wedge. Times are measured from the start of the withdrawal process. (a) $t=2s$. (b) $t=3s$. (c) $t=4s$.

perturbation. A least squares fit to the initial phase of the growth ($\tau < 1.4$) yields a value $\alpha \approx 0.075$ for the growth rate. This is broadly in line with the earlier experiments of Linden & Redondo (1991) at larger Atwood numbers (they found that at Atwood numbers in the range of these experiments the flow was dominated by the initial perturbation and yielded much larger values of α), but significantly larger than the $\alpha \approx 0.04$ to 0.05 suggested by the numerical work of Youngs (1991) or the $\alpha \approx 0.06$ of rocket experiments with immiscible fluids.

Youngs (personal communication, 1993) has recently adapted his numerical model to include in a simple manner both the structure of the initial perturbation and the time required to complete the withdrawal of the barrier. This simulation included the effects of rigid lateral end walls. The penetration was then measured using an algorithm equivalent to that used experimentally. The dot-dash line in figure 9 summarises the results. In the early stages there is moderate agreement between the numerical and experimental penetrations with similar effective value of α . However later (after $\tau \approx 1.3$) the experimental growth rate increases whereas the numerical growth rate decreases.

5. Conclusions

In this paper we have explored briefly various methods of reducing the amplitude and altering the form of the initial perturbation to simple, gravitationally unstable laboratory experiments. We have seen that the withdrawal of a barrier introduces perturbations on a range of length scales, and have indicated that perturbations on some scales are more important to the subsequent development of the flow than perturbations on other scales.

Attempts to model numerically the basic form of the initial perturbations have met with only limited success. There remain relatively large discrepancies between the growth rate of the mixing region for experiments and simulations. The question then is what is the cause of these

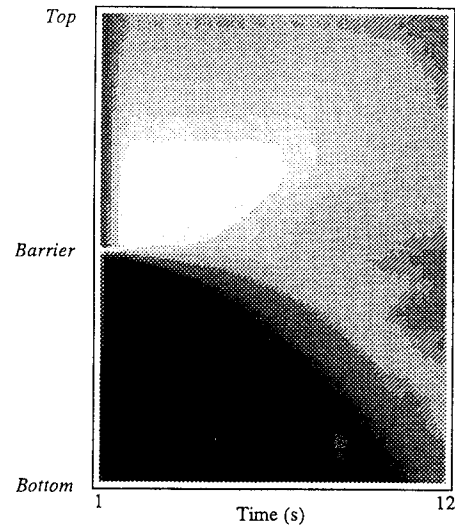


FIGURE 8: Ensemble mean of horizontal mean intensity of LIF images as a function of time.

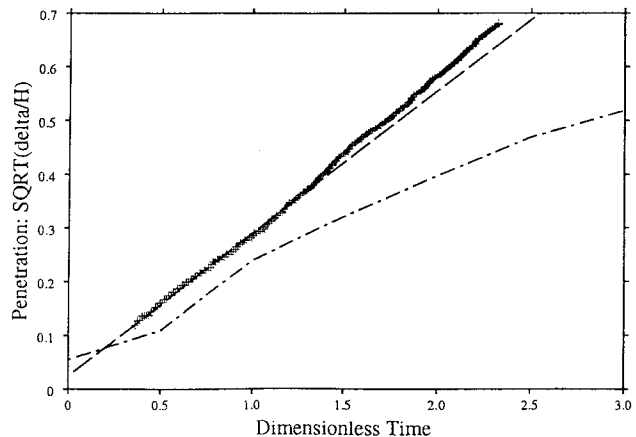


FIGURE 9: Penetration of dense fluid into the lower. The crosses indicate the measured values and the dashed line a least squares fit to the experimental data. The dot-dash line gives the penetration from a numerical model of this flow (Youngs, personal communication, 1993).

differences? Are they due to precise details of the initial perturbations, geometrical aspects of the experiments which are not being modelled in an appropriate manner, or fundamental problems with the way these flows are modelled?

It is clear that further work is required to determine where the differences arise. It is too early to reach a firm conclusion. Instead we shall present a list of some of the candidates to be considered:

Incomplete modelling of initial perturbation. The initial perturbation is typically modelled as a simple displacement of the interface. In contrast, in the experiments the perturbation starts off in the velocity field, rapidly leading to coherent, vortical structures slightly displaced from the initial interface position. This coherence may lead to a lesser amount of mixing at the molecular level than is achieved in the simulations, allowing more of the initial potential energy to be converted to kinetic energy and increasing the apparent value of α .

Effects of finite geometry. The finite horizontal tank geometry enters the problem in two ways. The first is its interaction with the initial perturbation at the scale of the tank. For example the large scale overturning observed in experiments without a trailing wedge is due to the coupling between the initial downward motion of the upper layer and the two end walls of the tank. The second effect is the blocking of the larger eddies (Hunt & Graham, 1978) and subsequent change in the structure of the turbulence within one integral length scale of the wall. This has been modelled to a limited extent in the recent simulations by Youngs (personal communication, 1993), but the overall influence on the flow is unresolved.

Resolution and subgrid modelling. The controversy as to whether direct numerical simulation (DNS, with its implicit subgrid-scale modelling) or large eddy simulation (LES, with explicit subgrid-scale modelling) is more appropriate continues to be an issue. Both approaches have their limitations. Youngs used the DNS approach for the simulations mentioned earlier, assuming that the flow is perfectly mixed at scales smaller than the numerical grid. This is likely to lead to an over estimate of the molecular mixing in the presence of strongly coherent structures and subsequent underestimate of α .

Physical parameters. The Atwood number for these experiments - $O(10^{-3})$ - is substantially smaller than the $A=0.2$ used in Youngs' simulations. It is not clear at present just how universal the growth rate is at very low Atwood numbers. The other physical parameters are also approximated: the Reynolds number for the experiments is relatively low, yet the simulations are nominally inviscid (although an artificial numerical viscosity is present).

It is clear that further experimental and numerical work is required to address these questions. The ongoing development of improved experimental diagnostics and refinement of numerical techniques should aid our search for an understanding of these flows. It is critical that groups running numerical simulations do not lose sight of experimental reality. Equally it is essential for experimentalists to make use of the ideas and insights gained from simulations.

Acknowledgements

The author is grateful to David Youngs (AWE, Aldermaston) for his interest in this work and supplying the numerical results used in this paper. This work has been supported by the UK Ministry of Defence under contract number NUC/21A/194801.

References

- Castilla, R. & Redondo, J.M. (1993): Mixing front growth in R-T and R-M instabilities; *in this volume*.
 Chandrasekhar, S. (1961): *Hydrodynamic and hydromagnetic stability*; Oxford University Press, Oxford, 652 pp.

- Dalziel, S.B. (1992): Decay of rotating turbulence: some particle tracking experiments; *Appl. Scien. Res.* **49**, 217-244.
- Dalziel, S.B. (1993a): Decay of rotating turbulence: some particle tracking experiments; in *Flow visualization and image analysis*, 27-54. Ed. F.T.H. Nieuwstadt; Kluwer, Dordrecht.
- Dalziel, S.B. (1993b): Rayleigh-Taylor instability: experiments with image analysis; *Dyn. Atmos. Oceans*, in press.
- Hunt, J.C.R. & Graham, J.M.R. (1978): Free stream turbulence near plane boundaries; *J. Fluid Mech.* **84**, 209-235.
- Lane-Serff, G.F. (1989): *Heat flow and air movement in buildings*, PhD Thesis, DAMTP, University of Cambridge, 131pp.
- Linden, P.F. & Redondo, J.M. (1991): Molecular mixing in Rayleigh-Taylor instability. Part 1: global mixing; *Phys. Fluids A* **3**, 1269-1277.
- Tatsumi, T. & Kakutani, T. (1958): The stability of a two-dimensional laminar jet; *J. Fluid Mech.* **4**, 261-275.
- Youngs, D.L. (1991): Three-dimensional numerical simulation of turbulent mixing by Rayleigh-Taylor instability; *Phys. Fluids A* **3**, 1312-1320.
- Youngs, D.L. (1993): Direct three-dimensional numerical simulation of mixing by Rayleigh-Taylor instability; *in this volume*.
-

Turbulent Hydrodynamic Mix Experiment *

Guy Dimonte, Bruce Remington, Pete Stry, Gene Burke, Pat Crowley, Ron Hawke, Jim Morrison, Allan Susoeff, Lawrence Livermore National Laboratory, Livermore, CA 94550.

We describe an experiment to investigate the development of turbulent mix in hydrodynamically unstable systems. The Rayleigh-Taylor instability is investigated by accelerating fluids similar to AWE's seminal rocket rig experiment but using a linear electric motor (LEM) to achieve arbitrary acceleration and deceleration profiles up to 10^3 times earth's gravity. Elements of the Richtmyer-Meshkov instability are investigated with impulsive acceleration profiles. The initial interfacial perturbations will be characterized and varied from single mode to fully random wavenumber spectra. The fluids are ~ 8 cm in size and can accommodate the large range in scales (~0.05-5 cm) required to study turbulence. In addition to the conventional shadowgraphy and radiography, we will deploy two modern diagnostics: (1) laser induced fluorescence (LIF) to measure the wavenumber spectrum of the interfacial perturbations and the mix mass distribution and (2) particle image velocimetry (PIV) to measure the turbulent velocity distribution and its anisotropy. The experiments will be compared to multi-dimensional hydrodynamic simulations and used to develop simple 1D models.

*Work performed under the auspices of the U.S. Department of Energy by Lawrence Livermore National Laboratory under contract number W-7405-ENG-48.

New Mix Experiment to Test 2D Simulation (ALE) codes and 1D Mix Models (k - ε)



Approach to Turbulance

Displacement >> fluid size >> shortest scale mix length
 250 >> 10 >> .05 cm

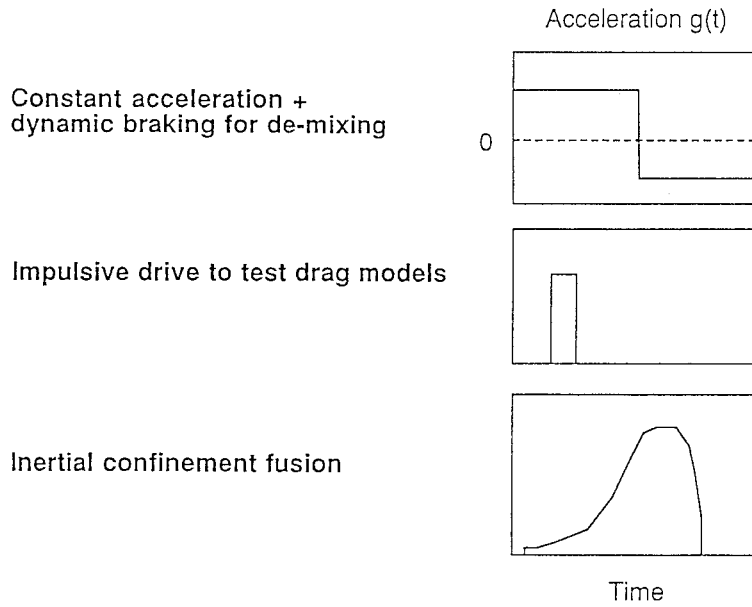
Provide variable acceleration to generalize self-similar model

$$h \sim \left[\int \sqrt{g(t')} dt' \right]^2 + O(dg/dt) + O(g < 0) + \text{Drag}$$

Apply modern diagnostics

Insensitive to edge
 Modal content in addition to mix width
 Turbulent energy

Pulse shaping can be used to generalize self-similar models



Modern Techniques in New Turbulent Mix Experiment



Linear electric motor (LEM)

Propulsion with variable acceleration
Deceleration for "de-mixing"

Laser induced fluorescence (LIF)

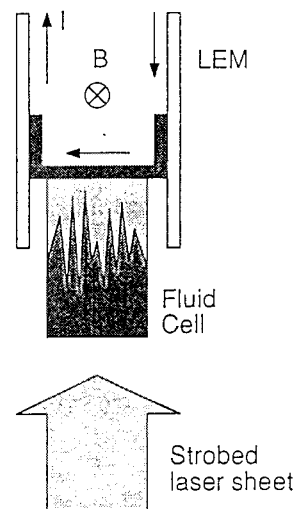
2D images with high spatial resolution

Particle imaging velocimetry (PIV)

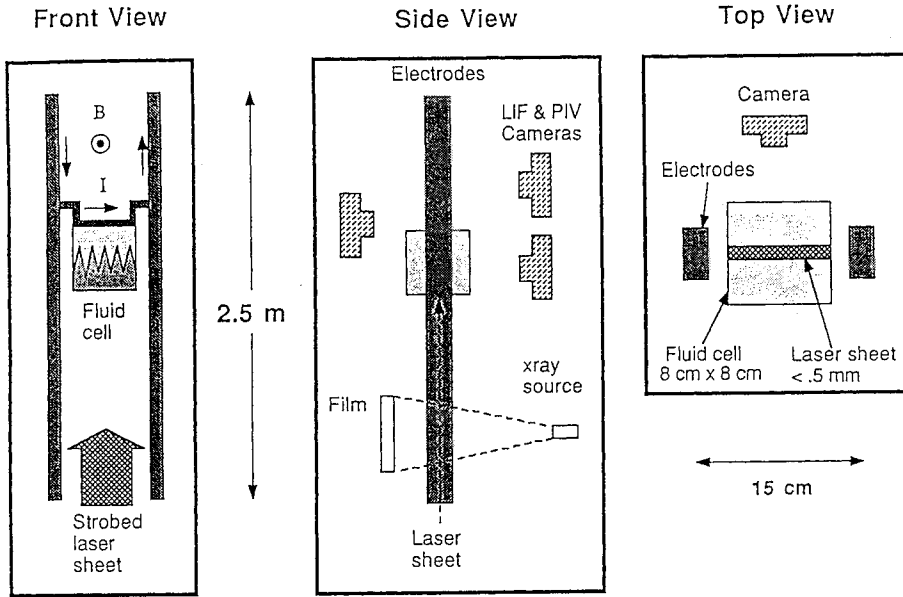
Direct measure of turbulent energy

Radiography

Turbulent mix distribution



Schematic of Turbulent Hydrodynamic Mix Experiment (THyMX)



Linear Electric Motor (LEM) Provides Variable Acceleration



Electromagnetic force on armature

$$Mg = IDB$$

Augmentor coil produces magnetic field

$$B \sim \mu N I_a / D$$

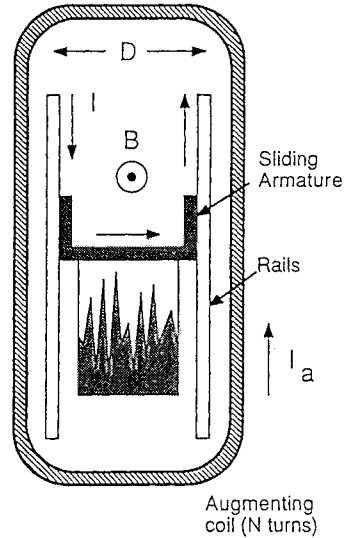
Acceleration

$$g \sim \mu N I_a / M \sim 100 g_0$$

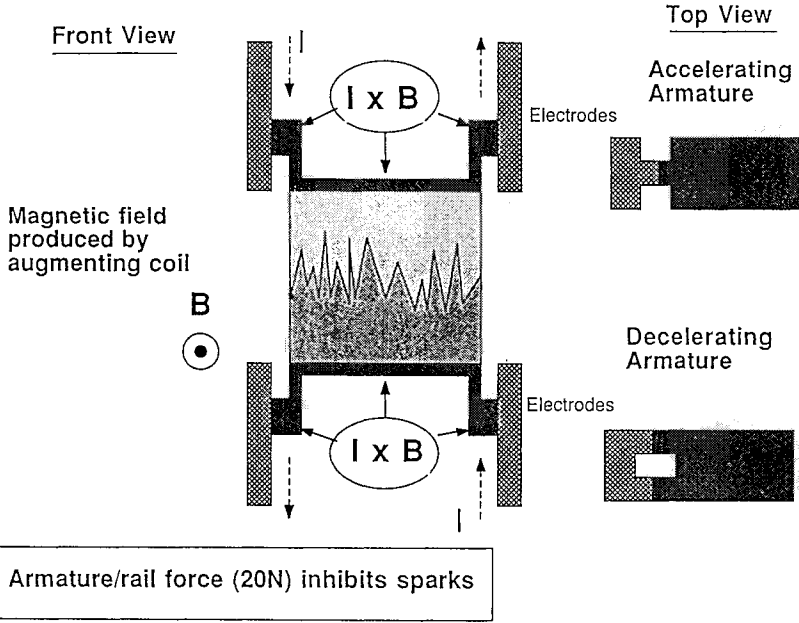
$I \sim 15 \text{ kA}$, $N I_a \sim 100 \text{ kA-T}$, $M \sim 2 \text{ kg}$

Deceleration similar but in reverse

Acceleration varied electrically $g \sim I^2(t)$



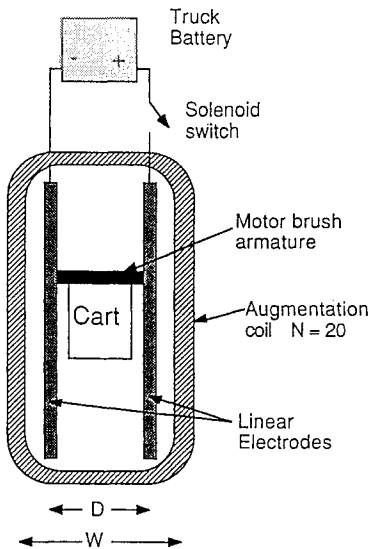
Armature Designed so that Magnetic Forces Aid Electrical Contact to Linear Electrodes



Simple Prototype LEM Demonstrates Principle Quantitatively



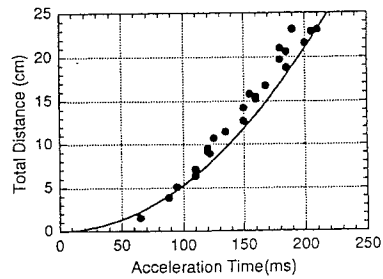
Prototype LEM



Measurements confirm calculations

$$g = \mu N I^2 D / WM \sim 0.75 g_0$$

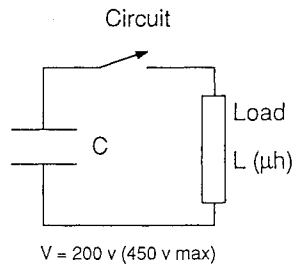
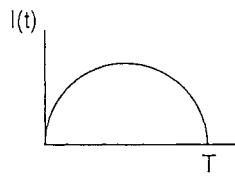
I = 300 amps, M = 100 g, WD = 2,
Friction coefficient = 0.3



Acceleration History Varied by Changing Circuit Parameters



	Short Pulse	Long Pulse
g / g_0	1000	100
T (ms)	6	45
Length (cm)	10	70
Drift (cm)	230	100
Rail		
C (f)	0.4	1.4
L (μ h)	8	150
I (kA)	45	18
Augmentor (N = 8, C = 2.8 f)		
L (μ h)	20	600
I _a (kA)	50	12
B (kG)	30	8

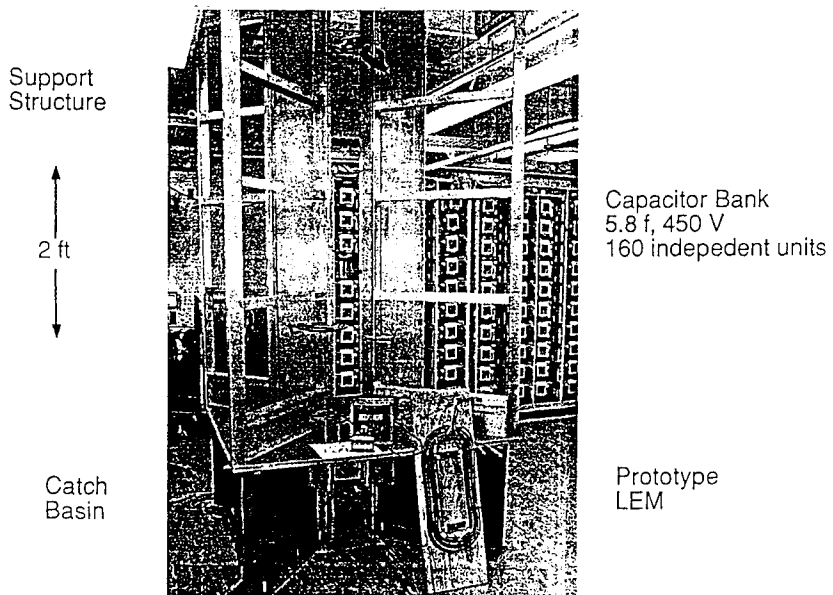


Total energy ~ 500 kJ in 160 independent capacitor modules

Supporting Structure for Linear Electric Motor (LEM) in March, 1993



Trajectory ↓



Support Structure

2 ft

Catch Basin

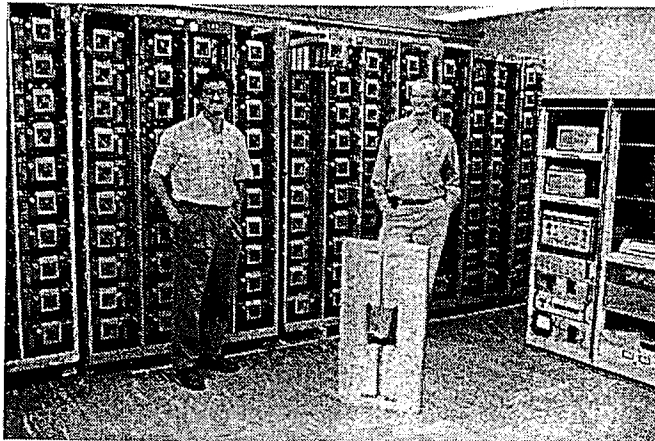
Capacitor Bank
5.8 f, 450 V
160 independent units

Prototype LEM

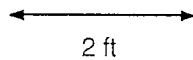
Capacitor Bank for Linear Electric Motor (LEM) in March, 1993



5.8 f, 450 V (580 kJ) in 160 independent units



Diagnostic Rack



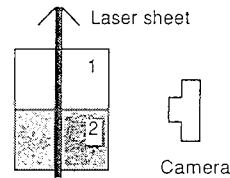
Top support for I-beams

Laser Induced Fluorescence (LIF) to Measure Fluid Density Distribution



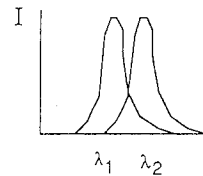
Laser sheet excites dye in heavy fluid

- Nd:YAG lasers @ 532 nm
- 100 Hz, 100 mJ/pulse
- < 0.5 mm thick



Dye is excited at λ_1 and radiates at λ_2

- Intensity \sim dye \sim fluid density
- 10:1 dynamic range



Compare 2D profiles directly with simulations
 10-20 frames per shot

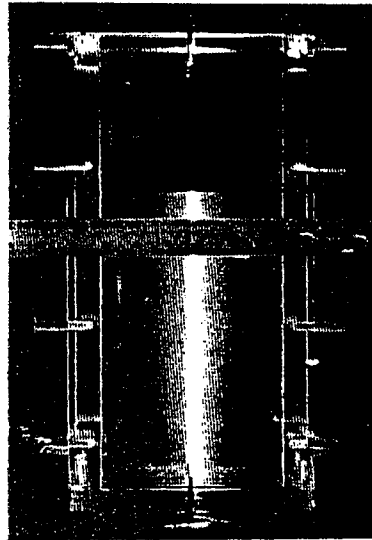
Laser Sheet for LIF and PIV



Face-on View



Side-on View



Particle Image Velocimetry (PIV) to Measure Turbulent Velocity Field



Mix buoyant 20 μm test particles in fluid

~ 10 particles/ sq. mm within laser sheet

Laser sheet

Double pulse laser for each exposure

$dt = dr / v \sim 5 - 20 \mu\text{s}$

Use 2 independent lasers

Displacements from correlating particle pairs

Interrogation cell is 1 sq. mm (10 particles)

5000 cells / image , 5-10 frames / shot

Automated analysis system (TSI)



Turbulent energy and vorticity obtained from velocity field

System Checkout Begins in Summer, Experiments Late in 1993



Mechanical system for LEM

Design nearly complete

Assembly underway

Electrical System

Capacitor bank being refurbished

Controls being designed

Diagnostics

Lasers ordered

Optimizations with low power Argon laser

Design of electrical diagnostics - current, acceleration, position, etc.

Pulsed radiography with Kucherenko (Chelyabinsk)

Existence, Uniqueness and Physical Selection of Asymptotically Steady-States Solutions in the Theory of the Rayleigh-Taylor Instability

N.A.Inogamov

Landau Institute for Theoretical Physics, Russian Academy of Sciences

E-mail: ITF0@cpd.Landau.free.msk.su (in subject: for Inogamov)

Fax: (095) 938 2077, Phone: (095) 137 3244

Address: GSP-1, 117940, Moscow, Kosigin street 2, Russian Federation

A.V.Chekhlov

Program in Applied and Computational Mathematics, Princeton University,

E-mail: chekhlov@acm.princeton.edu

Address: 2nd Floor Fine Hall, Washington Road, Princeton, NJ, 08544, USA

March 1993

Abstract

Using an algebraic method, based on truncation of both Fourier and Taylor series for the complex potential, together with a 2D hydrodynamic code, the existence and realization of a one-parameter family of bubbles are considered. Approximate analytical solutions of the Euler equations up to $O(z^{14})$ are obtained and compared with simulation results. It is shown that the sequence of such approximate solutions converges, giving accurate data about the one-parameter family of possible bubbles. Results of simulation show that bubbles with the smallest radius of curvature at the tip are realized from the whole family.

In recent years there has been a noticeable increase in interest in the problems of Rayleigh-Taylor-type instabilities. This is due to their many important applications in astrophysics [1], high density energy physics and inertial confinement fusion [2], physics of explosions [3] and shock waves [4]. Also such attention is induced by the fundamental importance of hydrodynamic studies in the generation of vorticity by a nonhomogeneous external force (the baroclinic generation of vorticity). The theory of the steady-state solutions [5] in such problems is of primary concern because it is believed that their subharmonic (modulational) instability and breakdown of periodicity due to this instability govern generation of coherent structures in the turbulent mixing layer [6].

Let us proceed with these solutions. We will describe an approximate algebraic method which allows us at least formally to construct any desirable high-order approximation to the steady-state solution. The complex velocity potential has the following expansion, truncated at

the N -th term:

$$f(z) = \sum_{n=1}^N f_n(e^{inz} - inz - 1), \quad f = \phi + i\psi, \quad z = x + iy, \quad (1)$$

where f_n are real coefficients. The axes x and y are oriented so that $\vec{g} = \{0, -g\}$, all the lengths are nondimensionalized by $1/k$, time by $1/\sqrt{gk}$. The expansion (1) satisfies homogeneous conditions if $y \rightarrow +\infty$ and has a stagnation point at $z = 0$. One may use (1) to get the stream function $\psi = \psi(x, y)$ and pressure distribution $p = p(x, y)$. We normalize ψ and p such that $\psi(0, 0) = 0, p(0, 0) = 0$. Assume that the zero stream line $y_\psi(x)$ and line of zero pressure $y_p(x)$ are analytical functions of x around $x = 0$. Then their Taylor expansions in x , truncated at the M -th terms, are:

$$y_\psi(x) = \sum_{m=1}^M \psi_m x^{2m}, \quad y_p(x) = \sum_{m=1}^M p_m x^{2m}, \quad \psi_m = \psi_m(\vec{f}), \quad p_m = p_m(\vec{f}), \quad \vec{f} = \{f_1, \dots, f_N\}. \quad (2)$$

Kinematic and dynamic boundary conditions will be satisfied with the truncation error $O(x^{2(M+1)})$ on every solution \vec{f} of the following system of algebraic equations:

$$U_m(\vec{f}) = 0, \quad U_m = \psi_m - p_m, \quad m = 1, \dots, M. \quad (3)$$

This system has M equations and N unknowns \vec{f} . After some equivalent transformations expressions for the first 6 functions $U_m(\vec{f})$ can be written as:

$$\begin{aligned} U_1 = 3b_2^3 - b_3, \quad U_2 = 95b_2b_3^2 - 90b_2^2b_4 + 3b_5, \quad U_3 = -27615b_2^2b_3^3 + 8645b_2^2b_4 - 630b_2b_4^2 - \\ 189b_2^2b_6 + 3b_7, \quad U_4 = 8922865b_3^5 - 9341640b_2b_3^3b_4 + 1460340b_2^2b_3b_4^2 - 2520b_4^3 + 51870b_2^2b_6 - \\ 4536b_2b_4b_6 - 324b_2^2b_8 + 3b_9, \quad U_5 = 39891967325b_2b_3^6 - 45637831575b_2^2b_3^4b_4 + \\ 3407298300b_3^5b_4^2 - 116745300b_2b_3b_4^3 + 231453810b_2b_3^3b_6 - 44033220b_2^2b_3b_4b_6 + 41580b_2^2b_6 + \\ 12474b_2b_6^2 - 378990b_2^2b_8 + 11880b_2b_4b_8 + 495b_2^2b_{10} + 9b_{11}, \quad U_6 = -79407535453400b_2^2b_3^7 + \\ 22731508875075b_2^2b_3^5b_4 + 1261025973900b_2b_3^4b_4^2 - 1139115978000b_2^2b_3^3b_4^3 + 6675669000b_3b_4^4 - \\ 420194742660b_2^2b_3^2b_6 - 27239612400b_2^2b_3b_4b_6 + 5618913300b_2b_3b_4^2b_6 + 206756550b_2^2b_3b_6^2 - \\ 972972b_4b_6^2 + 756704520b_2b_3^3b_8 + 208648440b_2^2b_3b_4b_8 - 463320b_4^2b_8 - 277992b_2b_6b_8 - \\ 444015b_3^2b_{10} - 77220b_2b_4b_{10} - 2106b_2^2b_{12} + 9b_{13}, \end{aligned} \quad \text{where we denote: } b_l = \sum_{n=1}^N n^l f_n. \quad (4)$$

Also we will need such characteristics as the velocity $V = -b_1$ and radius of curvature $R = 1/b_2^2$ of bubble at the tip.

It is possible to show the following properties of the system (4). For $N \geq M$ a complex solution \vec{f} of (4) exists and $-\vec{f}, \vec{f}^*, -\vec{f}^*$ are also solutions of (4), where $*$ means complex conjugation. (4) always has the trivial solution $\vec{f} = \vec{0}$. By physically relevant we mean real nontrivial solutions of (4) with $V > 0$. The cases $M = 1, 2$ give 3 and 9 complex roots respectively with only one physically relevant. If $M \geq 3$ multiple real physically relevant solutions appear. We will call solutions in the $N = M$ -case pointwise, M -th order. In the $N = M + 1$ -case the solutions depend on 1 parameter and we will call them as one-parameter solutions, of order M . Pointwise and one-parameter solutions are closely related: pointwise of order $M > 1$ lies in the intersections of one-parameter solutions of order $M - 1$ and M , being seen as functions of the same parameter. A pointwise solution of order 1 lies in the maximum of the family of order 1. A notable fact is that despite the strongly nonlinear character of the system (4), in

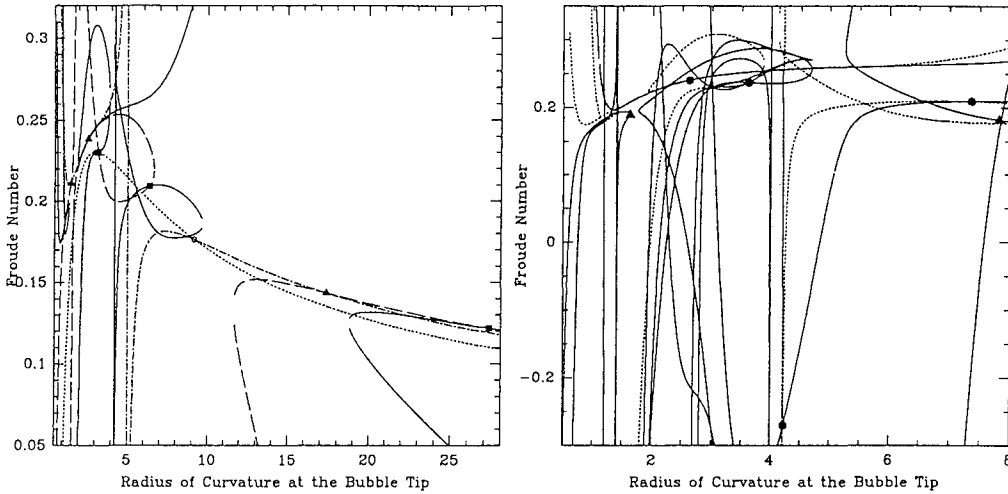


Figure 1: One-parameter and pointwise solutions for $M = 1-4$ cases. Dotted curve, solid circles - $M = 4$; circle - $M = 1$; dot-dash curve and empty circle - $M = 5$; solid triangles - $M = 6$. $M = 2$, long dash curve, triangles - $M = 3$; solid curve and squares - $M = 4$.

the orders $M \leq 4$ solutions in radicals can be obtained. This can be done through the use of the observation that the major part of the nonlinearity of (4) is concentrated in the $b_2^p b_3^q$ -type terms. Then, using as a set of unknowns $\{V, R, b_2, b_3, f_4, \dots, f_N\}$ instead of \vec{f} , the system to be solved can be strongly simplified. Due to limited space we will present here only one-parameter solutions for $V = V(R)$ in the lowest orders 1 - 3:

$$\begin{aligned}
 M = 1: \quad V &= \frac{3(R-1)}{2R\sqrt{R}}; \quad M = 2: \quad V = \frac{5(4R^3 - 27R^2 + 36R - 19)}{12(R-5)R^{5/2}}; \\
 M = 3: \quad V_{1,2} &= \frac{5(\beta \pm (R-3)\sqrt{\gamma})}{\alpha}, \quad \alpha = 336R^{7/2}, \quad \beta = -4389 + \\
 &5509R - 2385R^2 + 477R^3 - 20R^4, \quad \gamma = 2061577 - 3686760R + \\
 &2476306R^2 - 802480R^3 + 138105R^4 - 11976R^5 + 400R^6. \quad (5)
 \end{aligned}$$

Solutions for $M \geq 5$ are not expressible in radicals and we found $M = 5$ one-parameter solution and $M = 5, 6$ pointwise solutions numerically using Newton's iterations with multiprecision arithmetic. A good deal of information about the solutions obtained can be seen from their graphical representation on the real $(Fr = V/\sqrt{2\pi}, R)$ -plane (Fr-Froude number). In Figs. 1,2 we put together pointwise and complete one-parameter solutions for different values of M . Due to the fact, that for each value of R there are two values of $b_2 = \pm 1/\sqrt{R}$, two solutions symmetric with respect to R -axis, $\pm V(R)$ can be found. We present the solution corresponding to $b_2 = -1/\sqrt{R}$. Fig. 1 shows the cases $M = 1-4$; cases $M = 4, 5$ are shown in Fig. 2. The

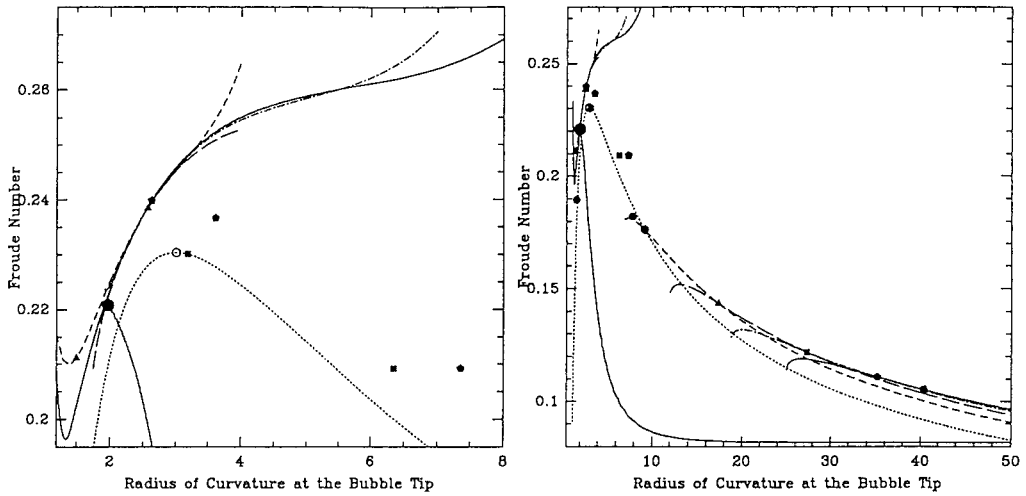


Figure 3: Converging branches in $M = 1 - 6$ cases (a) around the limiting point and (b) general view. Curves notations: dot- $M = 1$, dash- $M = 2$, long dash- $M = 3$, dot-dash - $M = 4$, solid- $M = 5$. Solid curve, approaching family from below is taken from DNS and is parametrized by time. Pointwise solutions: empty circle- $M = 1$, solid circle- $M = 2$, solid M -polygons- $M > 2$ and large solid circle corresponds to steady-state in DNS.

dependences $V(R)$ in Fig. 1,2 show that solutions for $M \geq 3$ are essentially nonunique and illustrate other properties noted above as well.

Let us make a note on convergence, which turned out to be nonhomogeneous in R . Really, in the above-considered cases $M \leq 6$ (the same is in the general case) two intervals of R : $\{R_{min}, R_{max}\}$ (where $R_{min} \approx 1.97$, $R_{min} = R_{crit}$, $R_{max} = R_{max}(M)$) and $\{R_{max,2}, +\infty\}$, $R_{max,2} = R_{max,2}(M)$ were found to give faster convergence of one-parameter solutions than other regions of R . A general view of the converging branches, extracted from Fig. 1,2, together with all the pointwise solutions found, are shown in Fig. 3(a) and 3(b). Fig. 3(a) gives closer look at the region surrounding the limiting point. A general view of larger interval in R is shown in Fig. 3(b). Concrete data on the convergence of one-parameter solutions at $R = 2.21$ are shown in the table below. The relative difference (RD) between two successive approximations drops from 4.54 at $M = 2$ to 0.0260 at $M = 5$ at an exponential rate. Similar rate of convergence is observed for other values of R inside the above defined intervals of R , see Figs.1-3, also see the table 3 in preprint of Landau Inst. by N.A.Inogamov and A.V.Chekhlov for more details on the convergence in the Fourier coefficients, [5].

M	Fr(2.21)	RD, %
1	0.22039	
2	0.23087	4.54
3	0.23000	0.378
4	0.23043	0.187
5	0.23037	0.0260

The direct numerical simulation (DNS) was based on an Eulerian finite-difference code for an incompressible ideal fluid in 2D. For the time stepping a modification of the well-known [7] artificial compressibility method to the case of nonstationary motion of a nonhomogeneous fluid

was used. The implicit semidiscrete scheme used is:

$$\frac{u_i^{n+1} - u_i^n}{\tau} + (\nabla, u_i^n \bar{u}^n) = -\frac{p_{x_i}^{n+1}}{\rho^n} + g_i, \quad i = 1, 2;$$

$$\beta(p^{n+1} - p^n) + (\nabla, \bar{u}^{n+1}) = 0, \quad \frac{\rho^{n+1} - \rho^n}{\tau} + (\nabla, \rho^n \bar{u}^{n+1}) = 0, \quad (6)$$

which was solved through the use of approximate factorization with total operation count per time step of $O(NM)$, where N and M are the numbers of grid points in each space direction. In (6) $\beta = O(1)$ and τ are scheme parameters. For the nonlinear terms in (6) a TVD-type scheme in each of the coordinate directions was used. The truncation error in such an approximation is $O(\tau, h^2)$ in the smooth regions, where τ and h are the time and space discretization parameters. Convergence and other questions related to similar approximations for the case of a homogeneous fluid are treated in [7]. A set of test runs showed sufficient efficiency and accuracy of our code.

Calculations were performed with nonzero density of the lower fluid, which does not correspond directly to what was assumed above.

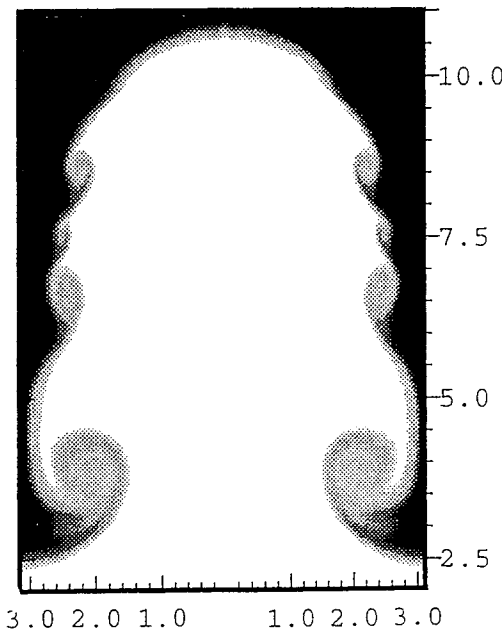


Figure4: Typical flow picture taken from DNS: heavy fluid is black and light is wight, density ratio $\mu = 0.05$. Symmetric bubble has a perfectly smooth top with convective-type instability on the sides. Shape and velocity of its tip are stationary. Only the part of computational domain occupied by the bubble is shown.

But in the cases with sufficiently small ratio of densities in the lower versus upper fluids $\mu \leq 0.1$, it was found that vortex motion induced both by the shear-layer instability on the sides of the bubble and processes of mushroom generation in the jets at large enough times almost do not affect local properties of the bubble top. One can say that the flow reaches a quasi-steady-state in the sense that the region around the bubble tip is almost in a steady-state with nonstationary processes occurring only in the jets and in the vortex region, which at large enough times will be far away from the bubble. A density plot is shown in Fig.4. This run was performed with density ratio $\mu = 0.05$ and initial velocity perturbation amplitude $V_0 \sqrt{k/g} = 0.2$, which is approximately 3 times less than the expected steady-state velocity; the time depicted in Fig. 4 is $t \sqrt{gk} \approx 5.1$. Initially the shape of the contact surface was taken to be flat. The upper and lower boundaries are rigid walls, right and left-lines of symmetry. The computational grid contained 100 cells per half period in x -direction and 400 cells in y . Data taken from a set of runs were compared with those given by the above algebraic method. Due to the lack of space we will just note that very good agreement was obtained in the first three Fourier coefficients. Situation here is similar to one with the Froude number.

The Fourier coefficients computed from DNS very accurately fit the points on the one-parametric curves, where the value of R is minimal. The characteristic dependence of $F\tau(t)$, $R(t)$ with the time t as a parameter, taken from DNS, is shown in Fig. 3, where $F\tau = V/\sqrt{2\pi g(1-\mu)/k}$ and V is the dimensional bubble tip velocity. As the time t goes from 0 to 5.1, the nondimensional radius of curvature R goes from $+\infty$ to its minimal value 1.97 ± 0.02 . The end-point corresponding to this value of R is the steady-state in which the local Froude number is 0.221 ± 0.004 .

Let us conclude with a brief summary of the results obtained. On the basis of an algebraic method we constructed a sequence of approximations converging to a unique one-parameter family of possible exact solutions, with bubbles which were assumed to be analytic at the tip. The solution from this family is uniquely specified whenever the value of R is given. Approximations of two different types (pointwise and one-parameter) approximately exponentially converge to the family. The existence of the solution of boundary-value problem discussed here follows from the convergence of approximations. Precise data on how this one-parameter family looks were obtained, including the first 5–6 Fourier coefficients f_n . In the high-resolution DNS the bubble corresponding to the end-point with the minimal radius of curvature at the tip was realized.

References

- [1] S.A.Grebenev and R.A.Sunyaev, Pis'ma A.Zh., 13, 945 (1987). [Sov. Astron. Lett., 13, 397 (1987)]; D.Arnett and B.Fryxell, Astroph. J., 341, L63 (1989); M.Den et al. KEK Prog. Rep., 89, 173 (1990); I.Hachisu et al., *ibid*, p.185; F.D.Kahn in: Planetary Nebulae IAU Symp. No.103; D.Reidel Publ. Comp., p.305, (1982); B.Fotner, F.Lamb and G.Zylstra in Numerical Astroph. Proc. Symp. in honor J.Wilson, Univ. Illinois, J.M.Centrella et al ed., Jones and Bartlett Publ., Inc., Boston etc., (1985), Ch.2; J.Arons and S.M.Lea, Astroph. J., 207, 914 (1976).
- [2] H.Takabe, K.Mima, L.Monteierth and R.L.Morse, Phys. Fluids, 28, 3676 (1985); E.G.Gamaly, A.P.Favorsky and A.O.Fedianin et al., Laser Part. Beams, 8, 299 (1990); S.Atzeni, *ibid*, 9, 233 (1991).
- [3] S.I.Anisimov, Ya.B.Zel'dovich, N.A.Inogamov and M.F.Ivanov, in: "Shock waves, explosions and detonations". New York, AIAA Prog. in Astron. Aeron. Series, AIAA, 87, 218 (1983).
- [4] V.A.Andronov, S.M.Bachrach, E.E.Meshkov et al., Zh. Eksp. Teor. Fiz., 71, 806 (1976) [Sov. Phys. JETP 44, 424 (1976)]; S.G.Zaitsev et al., Dokl. Akad. Nauk SSSR 283, 94 (1985) [Sov. Phys. Dokl. 30, 579 (1985)]; D.L.Youngs, Phys. 12D, 32, (1984); D.Besnard and J.-F.Haas in: "Current topics in shock waves", 17th ISSWST, Y.Kim ed., A.I.P. Conf. Proc. 208 (1990); K.O.Mikaelian, Phys. Fluids, 2A, 592 (1990).
- [5] D.Layzer, Astroph. J., 122, 1 (1955); P.R.Garabedian, Proc. Roy. Soc. London, 241A, 423 (1957); G.Birkhoff and D.Carter, J. Math. Mech., 6, 769 (1957); H.J.Kull, Phys. Rev. Lett., 51, 1434 (1983); J.-M.Vanden-Broeck, Phys. Fluids, 27, 1090 (1984); N.A.Inogamov, "About stationary solution connected with RTI", in: "Problems of dynamics and stability of plasma", Moscow Inst. of Phys. and Technology (MFTI), Moscow, pp. 115-124 (1990); N.A.Inogamov, A.V.Chekhlov and A.Yu.Dem'yanov, Proc. 3rd Intern. Workshop on the "Phys. of Compr. Turb. Mixing", Royaumont, France, pp. 423-426 (1991); N.A.Inogamov, JETP Lett., 55, 521 (1992); N.A.Inogamov and A.V.Chekhlov, "Stationary solutions in

the theory of RTI", Preprint of Landau Inst. for Theor. Phys. (ITF) of Acad. of Scien., Chernogolovka, 140p. (1992); N.A.Inogamov and A.V.Chekhlov, Dokl. Akad. Nauk, 328, 311 (1993) [publ. in Engl. by the A.I.P., Sov. Phys. Dokl.]; S.I.Anisimov and N.A.Inogamov, "Studies in phys. of high energy density", Preprint of Landau Inst. for Theor. Phys. (ITF) of Acad. of Scien., Chernogolovka, 62p. (1993).

- [6] N.A.Inogamov, Pis'ma Zh. Tekh. Fiz., 4, 743 (1978) [Sov. Tech. Phys. Lett., 4(6), 299 (1978)]; C.Gardner et al., Phys. Fluids, 31, 447 (1988); J.A.Zufria, *ibid*, p.440.
- [7] R.Temam, Navier-Stokes equations. Theory and numerical analysis, Studies in Math. and its Appl., Vol.2, J.-L.Lions et al ed., North-Holland Publ. Comp., Amsterdam, N.Y., Oxford, 1979; D.Kwak et al., AIAA J. No. 3, 390 (1986).

EXPERIMENTAL STUDY OF ASYMPTOTIC STAGE
OF GRAVITATIONAL TURBULENT MIXING OF THIN LIQUID LAYERS
OF DIFFERENT DENSITIES

Yu.A.Kucherenko, S.I.Balabin, A.P.Pylaev

PHYSICAL DIVISION

Institute of Technical Physics

454070, Chelyabinsk-70, P.O. 245, Russia

Perspective laser targets for thermonuclear fusion as a rule consist of several layers of different substances. Very often during such targets operation the layers turbulent mixing related to the Rayleigh-Taylor instability even at the first stages of compression involves the entire substance of one of the layers. The typical situation is when thickness of the layer which is turbulized is less than thickness of the surrounding layers. Therefore determination of behavior of such turbulized thin layers matter is of practical interest.

Theoretical research of thin layers mixing was carried out in the works [1,2] on the basis of semi empirical models of turbulent mixing. Mixing of a thin layer immersed into a medium of different density under influence of acceleration g_1 was considered. In this case one of the layer boundaries appears to be

stable, and at the other boundary the turbulent mixing of the substances takes place. In the work [2] asymptotic expressions for dimension $h_1(t)$ (or $h_2(t)$) of region involved in turbulent mixing are obtained. For dimension $h_1(t)$ at mixing of light layer having density ρ_1 and initial thickness h_{10} the following expression was obtained:

$$\frac{h_1(t)}{h_{10}} = b_1 \cdot \sqrt{2 \frac{n-1}{n}} \cdot \left(\frac{S}{h_{10}} \right)^{1/2} \quad (1)$$

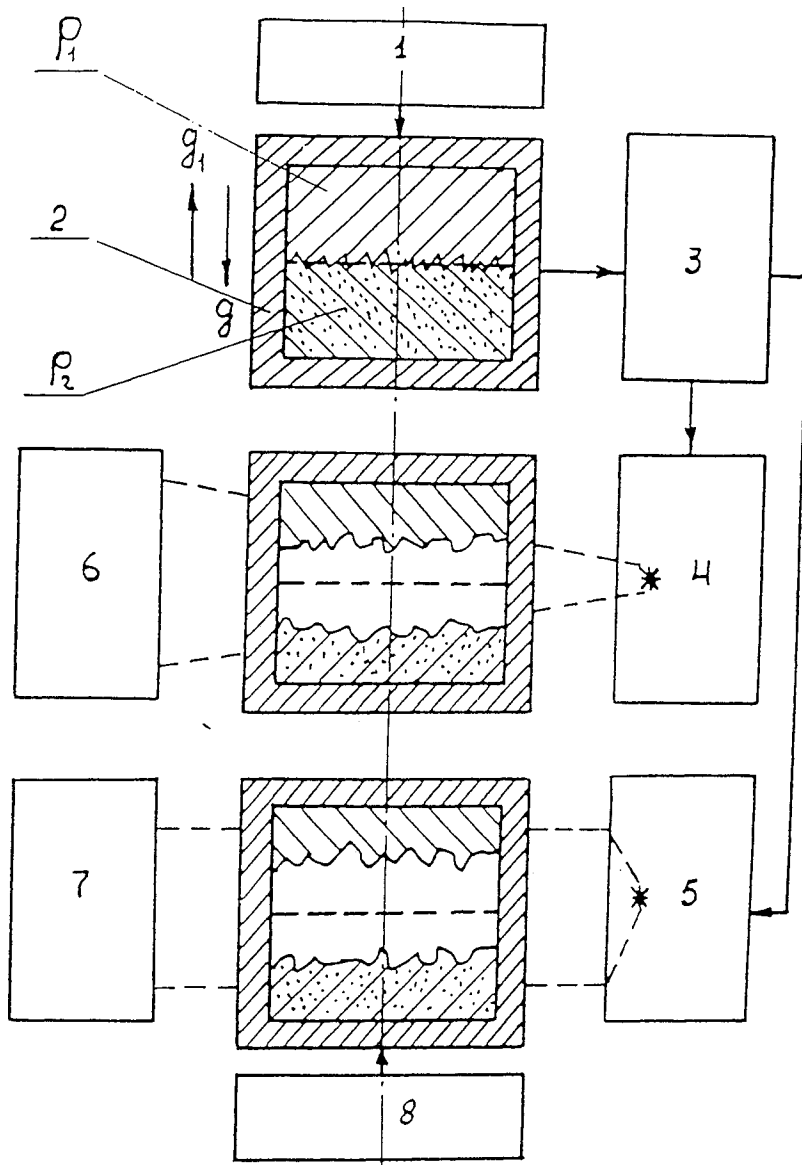
For dimension $h_2(t)$ at mixing of heavy layer having density ρ_2 and initial thickness h_{20} we obtained the following expression:

$$\frac{h_2(t)}{h_{20}} = b_2 \cdot \sqrt{2 \frac{n-1}{n}} \cdot \left(\frac{S}{h_{20}} \right)^{1/2} \quad (2)$$

In formulas (1) and (2) $S = g_1 t^2 / 2$, $n = \rho_2 / \rho_1$, and constants b_1 and b_2 are subject to experimental determination.

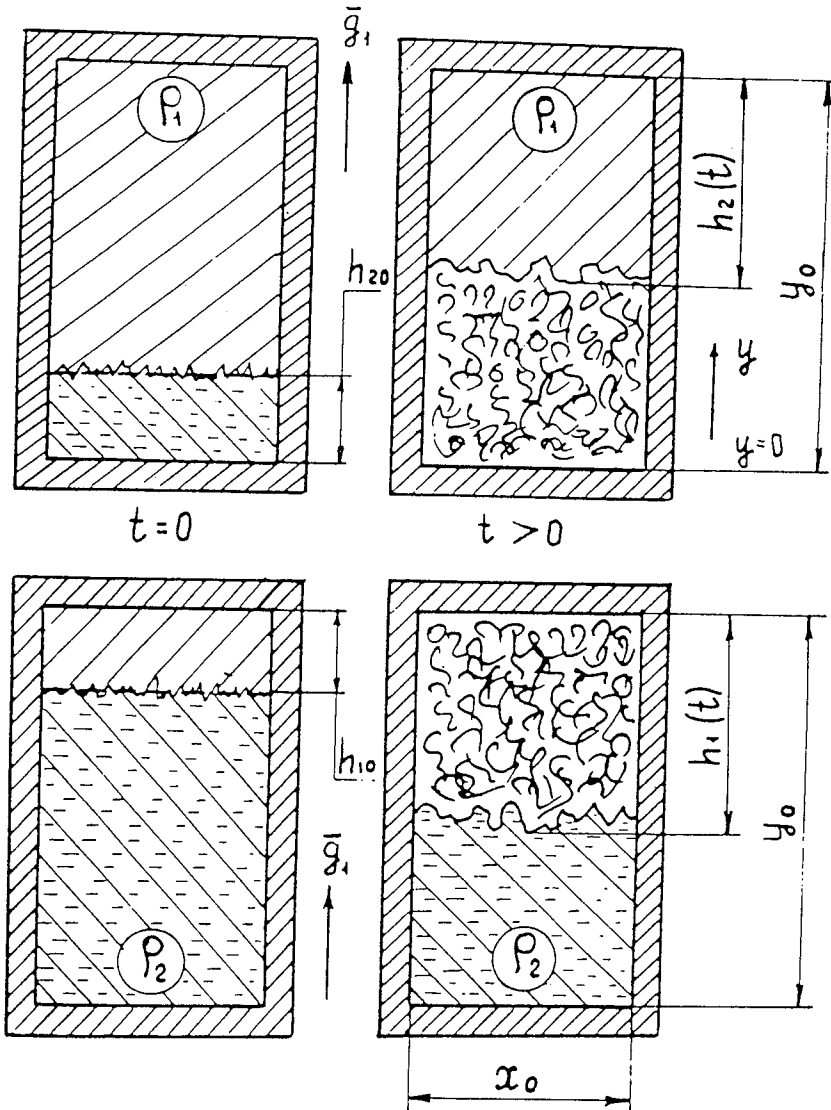
The turbulent mixing with thin liquid layers was studied experimentally in the work [3]. The experiments were carried out under conditions when both boundaries of the layer were unstable. The experiments goal was to determine decrease of two liquids mixing velocity attained by introduction of thin layer of a third liquid between them. In the work presented investigation of plane thin layers mixing under conditions when one boundary is stable is carried out.

Velocity of thin layers mixing after the whole substance of the layer was involved into the mixing was determined at modeling installations EKAP and SOM [4]. The experiments were carried out according to the well-known setup (see fig.1). Two liquids of different densities ρ_1 and ρ_2 ($\rho_2 > \rho_1$) were placed in a vessel - sample container, and small random disturbances were created at contact boundary between the liquids. The sample was accelerated



- | | |
|--------------------------|-------------------------|
| 1. GAS ACCELERATOR | 6. X-RAY IMAGE RECORDER |
| 2. AMPOULE | 7. PHOTORECORDER |
| 3. TRAJECTORY TRANSDUCER | 8. DAMPING DEVICE |
| 4. PULSE X-RAY CELL | |
| 5. PULSE SOURCE | |

FIG. 1 DIAGRAM FOR PERFORMING EXPERIMENTS



h_{10}, h_{20} - THICKNESSES OF LIGHT AND HEAVY LIQUID LAYERS
 $h_1(t), h_2(t)$ - MEAN VALUES OF THE TURBULIZED LAYER THICKNESS

FIG.2 SCHEME FOR PERFORMING MEASUREMENTS

by gas accelerator in direction of the earth gravity field \vec{g} . Process of development of instability and gravitational turbulent mixing was developing under influence of artificial gravity field \vec{g}_1 directed from the heavy liquid to the light one. As the sample container was moving along the accelerator bore X-ray chambers (of EKAP installation) or photo recorders (of installation SOM) were triggering, that made it possible to obtain either X-ray image or photographic image of the mixing region. After the acceleration the sample container got into a shock-mitigation device which enabled to decelerate and catch the sample containers without their construction damage.

The experiments were carried out using the following liquids: benzene, water, solution of zinc chloride, solutions of salts of thallium, mercury. It made it possible to carry out research at densities ratio $n = \rho_2/\rho_1 = 3; 4; 6; 13.5$ at different initial thicknesses of light layers h_{10} and heavy layers h_{20} (see fig.2). At the installation EKAP we used sample containers with $x_0 = 50$ mm and $y_0 = 130$ mm, and at the installation SOM with $x_0 = 64$ mm and $y_0 = 120$ mm. Besides that to determine influence of decrease of the acceleration g_1 and surface tension upon the mixing process special experiments were carried out. In these experiments the acceleration decrease changed by the factor of 2 (experiments with $n = 3$, light method), and the surface tension was brought to zero (experiments with $n = 4$, X-ray method, and surface tension coefficient $\sigma = 0$). The main initial data for all the experiments are shown in table 1.

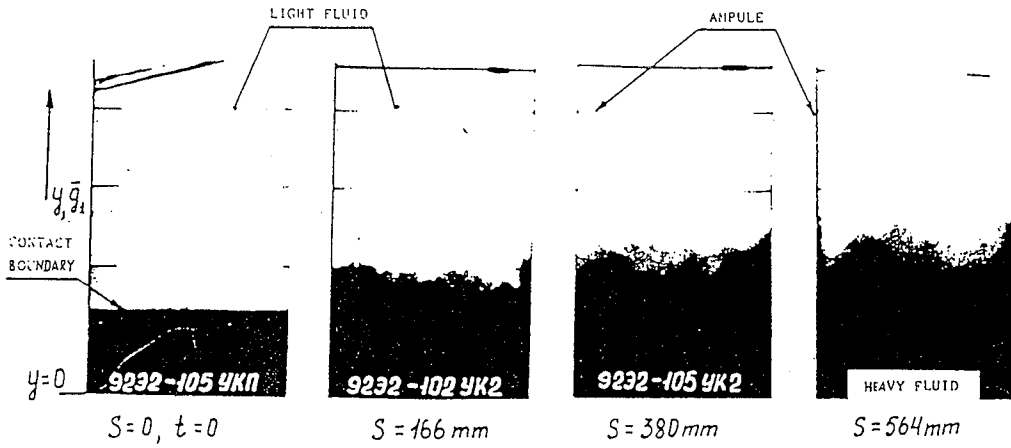


FIG. 3 TYPICAL X-RAY IMAGES OF THE MIXING REGION

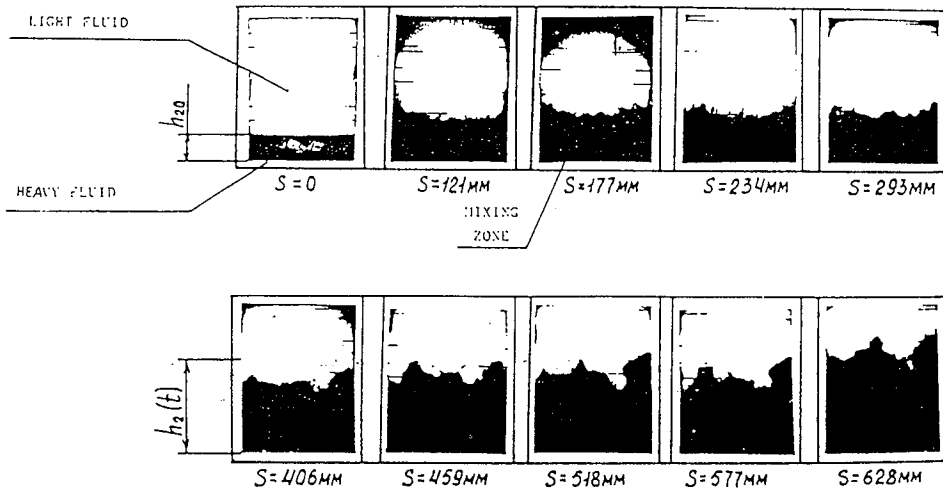


FIG. 4 CHARACTERISTIC PHOTOGRAPHIC IMAGES OF THE MIXING REGION

Table 1

Method	n	h_{20} , mm	h_{10} , mm	g_{10}/g
EKAP	3	4	-	$0.9 \cdot 10^3$
		8	-	
		20	-	
SOM	3	8	-	$0.72 \cdot 10^3$
		10	-	
		20	-	
		30	-	
EKAP	4	8	-	$(0.6-3.5) \cdot 10^3$
EKAP	6	8	-	$0.9 \cdot 10^3$
EKAP	13.5	8	-	$3 \cdot 10^3$
		16	-	
SOM	3	-	8	$0.72 \cdot 10^3$
		-	15	
		-	25	
		-	35	

In the experiments we determined displacement $S = \int_0^t \int_0^\tau g_1(\tau) d\tau dt$ of contact boundary by the moment of obtaining image of the mixing region. By the photographic images (see fig.4) we determined dimensions $h_1(t)$ and $h_2(t)$ of the mixing region measuring position of the mixing front which corresponded to zero concentration of the layer substance. By X-ray images (see fig.3) we determined dimension $h_2(t)$ measuring position of the mixing front which corresponded to concentration equal to 0.02. Besides that, by semitone X-ray images for $n=3$ we determined distribution of

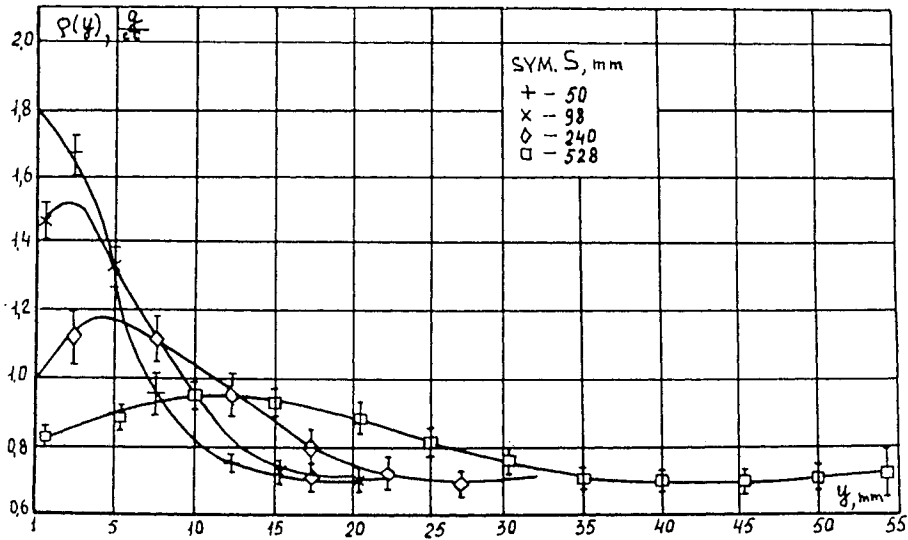


FIG. 5. DISTRIBUTION OF AVERAGE MATTER DENSITY IN THE MIXING ZONE FOR $h_{20} = 4$ mm AND $n = 3$.

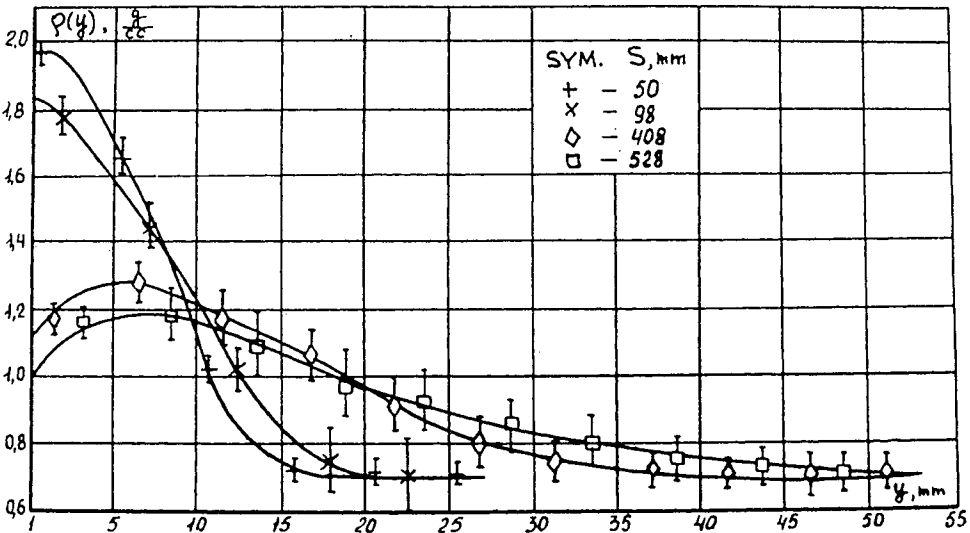
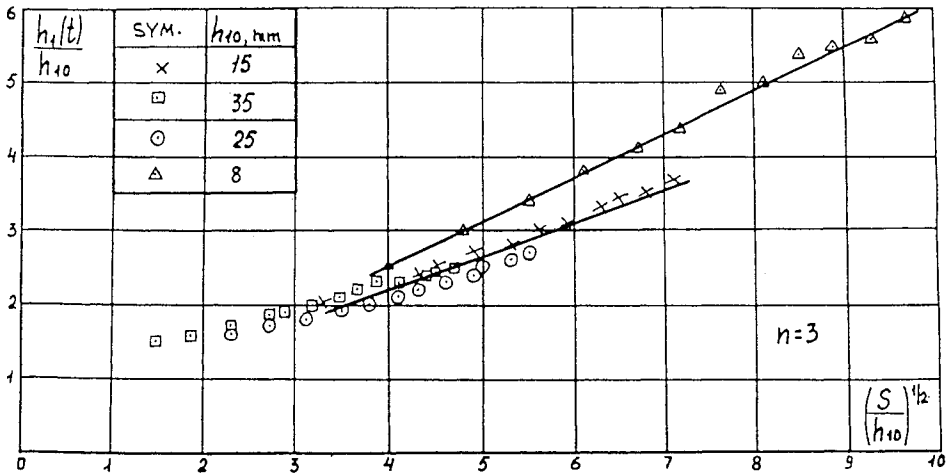
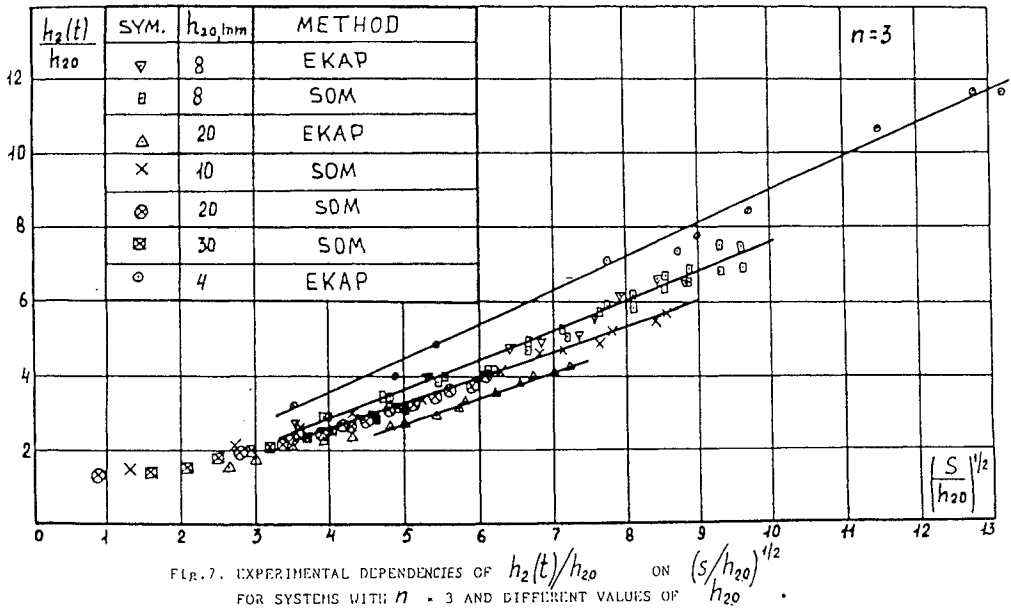


FIG. 6 DISTRIBUTION OF THE SUBSTANCE AVERAGE DENSITY IN THE MIXING ZONE FOR $h_{20} = 8$ mm, $n = 3$

Kucherenko, Balabin & Pylaev



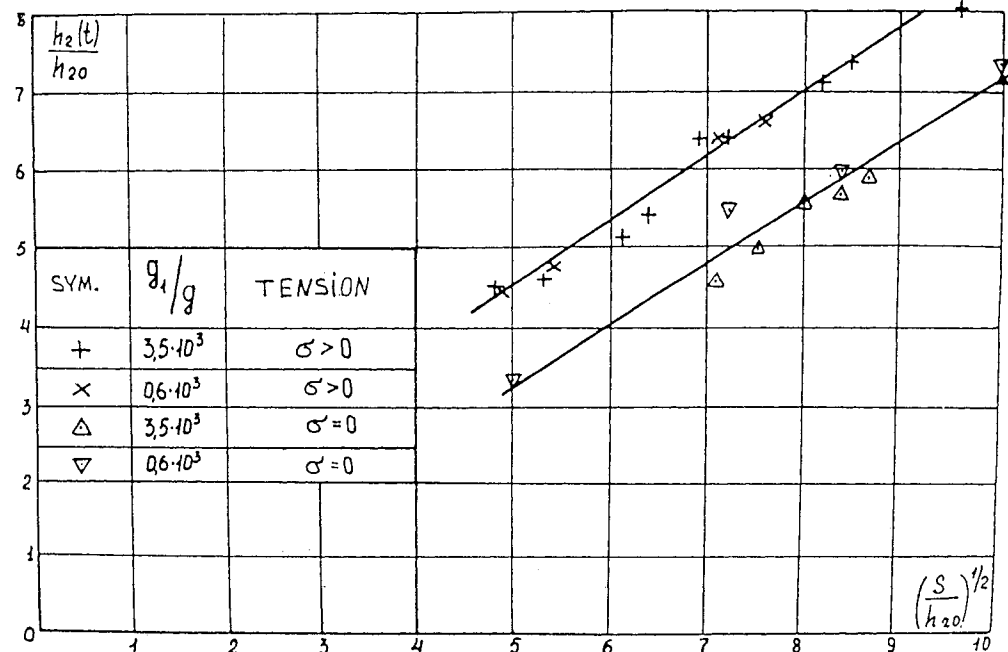


FIG. 9. EXPERIMENTAL DEPENDENCIES OF $h_2(t)/h_{20}$ ON $(S/h_{20})^{1/2}$ FOR EXPERIMENTS WITH $n = 4$ AND $h_{20} = 9$ mm.

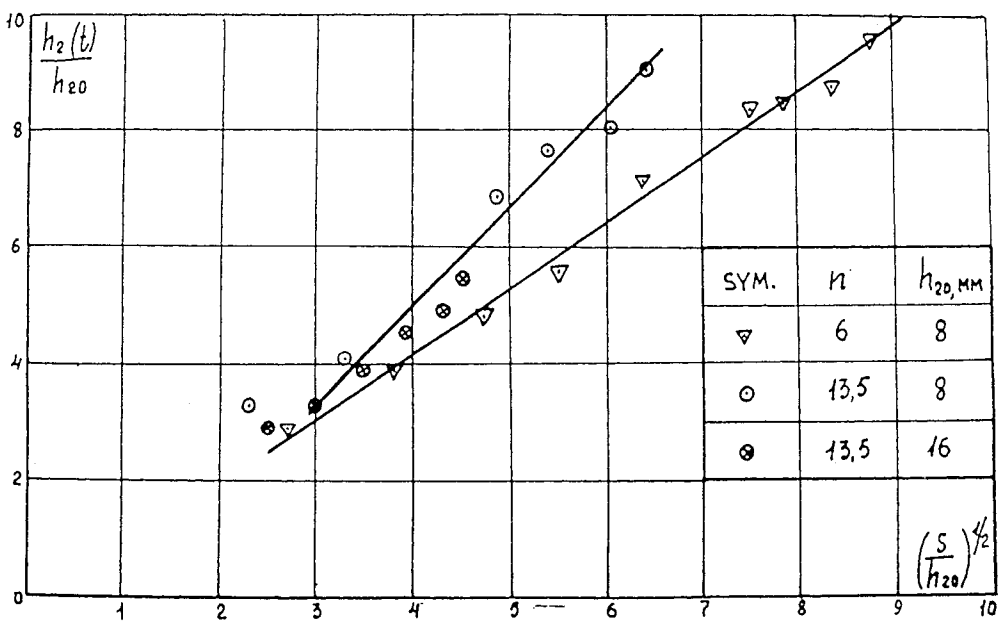


FIG. 10. EXPERIMENTAL DEPENDENCIES OF $h_2(t)/h_{20}$ ON $(S/h_{20})^{1/2}$ FOR SYSTEMS WITH $n = 6$ AND $n = 13.5$.

average density $\rho(y)$ of the mixture for different values of the parameter S (see fig.5,6).

Average values of quantities h_1/h_{10} ; h_2/h_{20} for the experiments with different values of n are shown in fig.7, 8, 9, 10. The averaging was carried out over 15 experiments at the installation SOM, and over 4-10 experiments at the installation EKAP.

The experimental results on the dependences determination come to the following.

FOR DENSITIES RATIO $n=3$:

1. All groups of the experiments beginning with $(S/h_{20})^{1/2} > 3$ are well described by linear dependences. In this case mixing is going on at constant non-dimensional velocity which is determined as

$$v_{21} = \frac{d(h_2/h_{20})}{d(S/h_{20})^{1/2}} \quad (\text{analogously to } v_{12}).$$

2. Velocity v_{21} beginning with $h_{20} > 8$ mm doesn't depend upon initial thickness of the layer and equals $v_{21} = 0.69$.

3. The fact that experimental points for $h_{20} = 20$ mm obtained by the X-ray method lie lower can be explained by different method of finding the mixing front.

4. For $h_{20} \leq 8$ mm $v_{21} > 0.69$. It can be explained by the fact that at such thicknesses within the time when the mixing front attains rigid wall ($y=0$) the developing mixing is only at the first stage [4]. It is confirmed by the fact that separation processes which are observed in this case are displayed more quickly for the layers with $h_{20} = 4$ mm than for the layers with $h_{20} = 8$ mm (see fig.5,6).

5. The velocity v_{12} beginning with $h_{10} > 8$ mm doesn't depend upon initial thickness of the layer and equals $v_{12} = 0.43$.

6. The obtained experimental results do not depend upon the acceleration decrease.

FOR DENSITIES RATIO $n = 4$:

1. Insoluble and mutually soluble liquids used in the experiments gave approximately the same value $v_{21} = 0.81$.
2. Displacement of the experimental points at $\sigma = 0$ is stipulated by delay in the mixing development [4].
3. The obtained results do not depend upon initial acceleration g_{10} .

FOR DENSITIES RATIO $n = 6$ and $n = 13.5$:

1. For $(S/h_{20})^{1/2} > 3$ values for velocities v_{21} were determined which equal $v_{21} = 1.12$ for $n = 6$ and $v_{21} = 1.69$ for $n = 13.5$. The obtained experimental data enabled to determine coefficients b_1 and b_2 in the formulas (1) and (2) (see table 2).

Table 2

n	Layer	v_{12}	v_{21}	b_1	b_2
3	heavy	-	0.69	-	0.35
4		-	0.81	-	0.33
6		-	1.12	-	0.35
13.5		-	1.69	-	0.34
3	light	0.43	-	0.37	-

Thus, the research carried out enabled to investigate the asymptotic stage of gravitational turbulent mixing and determine constants of semi empirical theory of mixing.

In conclusion the authors express gratitude to their colleagues R.I.Ardashova, V.D.Murzakov, S.I.Onufrienko, V.N.Popov for assistance in conduct of the experiments, and to A.V.Pavlenko and O.E.Shestochenko for their help in the experiments processing.

REFERENCES

1. S.Z.Belen'ky, E.S.Fradkin

Theory of Turbulent Mixing. Proceedings of DIAM named after Lebedev, v.29, 1965.

2. V.E.Neuvazhaev

Property of model of turbulent mixing of interface between accelerated liquids with different densities, PMTF, No 5, 1983.

3. V.S.Smeeton, D.L.Youngs

Experimental Investigation of Turbulent Mixing by Rayleigh-Taylor instability, III, AWE Report 0-35/87, 1988.

4. Yu.A.Kucherenko, L.I.Shibarshov, V.I.Chitaikin, S.I.Balabin, A.P.Pylaev

Experimental Study of the Gravitational Turbulent Mixing Self-Similar Mode, Report at III International Workshop of Physics of Turbulent Mixing, France, 1991.

BEHAVIOUR OF GRAVITATIONAL TURBULENT
MIXING REGION UNDER CONDITIONS
LEADING TO SEPARATION

Yu.A.Kucherenko, V.E.Neuvazhayev, A.P.Pylaev

INSTITUTE OF TECHNICAL PHYSICS
454070, Chelyabinsk-70, P.O. 245, Russia

Abstract

Experimental and theoretical study of gravitational turbulent mixing on the boundary of two incompressible liquids having different densities under conditions when accelerated motion of the boundary is changed into the decelerated one has been carried out. At the initial moment the liquids are placed so that during the phase of the accelerated motion the turbulent mixing caused by Rayleigh-Taylor instability is taking place. In the decelerated phase the process of separation is under development. At the same time the turbulent mixing region is decreasing and, as the

experiments show, the size of the mixing region is decreasing according to the law which has universal character.

The dependence of the mixing region size on the initial densities relation and the value of the acceleration has been determined theoretically. On the basis of the carried out experiments the constant α_s has been calculated which characterizes the intensity of the mixing region decrease. Compared with the constant $\alpha_m=0.07$, characterizing the intensity of the turbulent mixing region width increase at the unstable stage of the motion, the constant $\alpha_s=0.01$. The process of the mixing region width decrease is proceeding one seventh as fast as that of its growth.

1. INTRODUCTION. Turbulent mixing and separation which are developing on contact boundaries between two media having different densities during their non-stationary motion exert the marked influence on the dynamics of the targets compression in the inertial thermonuclear fusion problem. Thus, at the first stage of the targets compression the contact boundary is subjected to the so-called gravitational instability or Rayleigh-Taylor instability when the light matter accelerates the more heavy one (ρ_1 - density of the light matter, ρ_2 - density of the heavy matter). The development of the small initial perturbations on the contact boundary leads to the distortion of the interface between media and to the appearance of the region of turbulent mixing between the light and heavy matters with the region size growing in time. At the second stage of the decelerated motion the separation processes are developing in the mixing region when acceleration changes its sign and motion becomes stable.

The stage of the unstable motion has been well studied [1-4]. The independent investigations of the turbulent mixing performed at this stage showed that in the self-similar turbulence case the non-dimensional growth rate of the mixing region size L_{12} in the heavy medium has the form:

$$\frac{dL_{12}}{dS} = 2\alpha_m A ,$$

where α_m - constant of mixing, $A = \frac{\rho_2 - \rho_1}{\rho_2 + \rho_1}$ - Atwood number. The

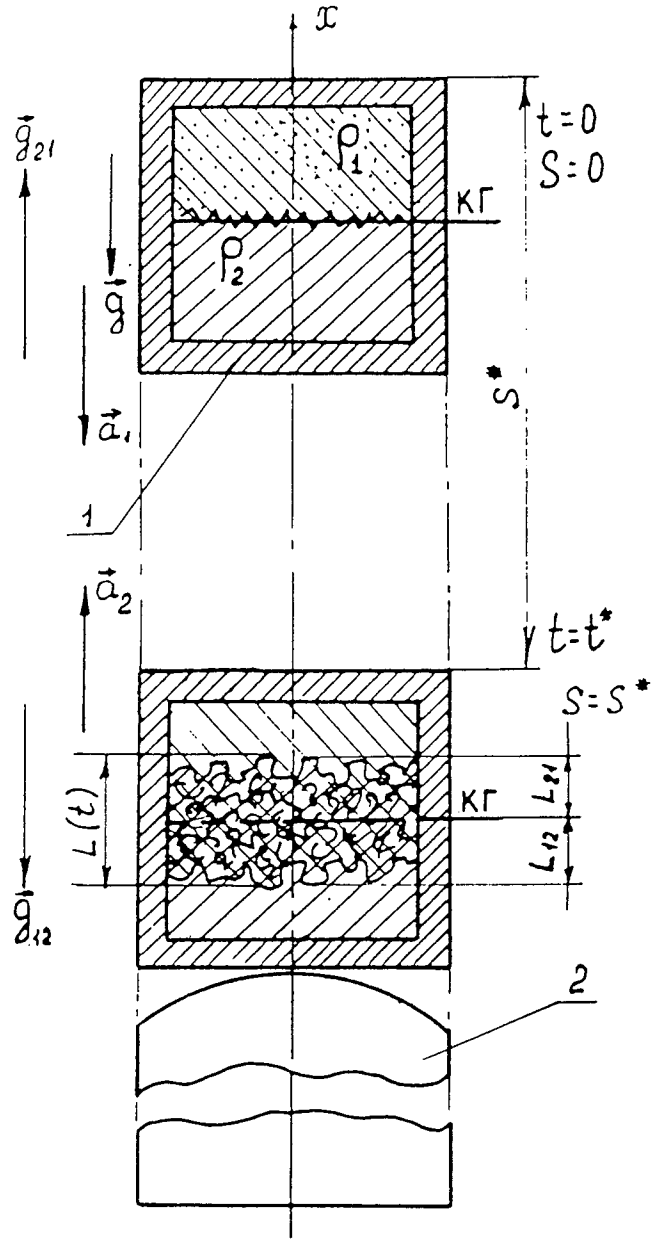
parameter $S = \frac{g_{21} t^2}{2}$, where g_{21} - acceleration. It was experimentally found that the constant $\alpha_m = 0.07$ [2], [3].

The stable stage of motion is less studied. It is especially related to the experimental and theoretical investigations of the separation processes between components in the turbulent mixing region. In the first publication concerning this problem [5] it was experimentally established that for $A=0.27$ the turbulent mixing region width is decreasing at the stable stage. In the present work, on the basis of a semiempirical k-model [6], the law of the mixing region development at the stable stage is obtained in the form:

$$\sqrt{L_{12}(t)} = \sqrt{L_{12}(t_c)} - \sqrt{\alpha_s A g_{12}(t-t_c)} \quad (1)$$

where g_{12} - acceleration at the second stage, t_c - instant of time when the mixing region size reaches its maximum value. Experiments performed for $A=0.5$ substantiated formula (1) and allowed to determine the coefficient α_s .

2. EXPERIMENTAL INVESTIGATION. The non-stationary motion of fluids and the gravitational turbulent mixing arising as a result of this motion were studied by using the modelling installation SOM [3]. Fluids having different densities ρ_1 and ρ_2 ($\rho_2 > \rho_1$) were placed in an ampoule (vessel) (see Fig.1). In the gravitational field \vec{g} the light fluid was just over the heavy one. On the contact boundary between these fluids the random initial perturbations of the solid surfaces roughness type were artificially generated. At a



1. AMPOULE
2. DEVICE FOR CHANGING THE SIGN OF ACCELERATION

FIG. 1 SCHEME FOR PERFORMING EXPERIMENTS ON SEPARATION

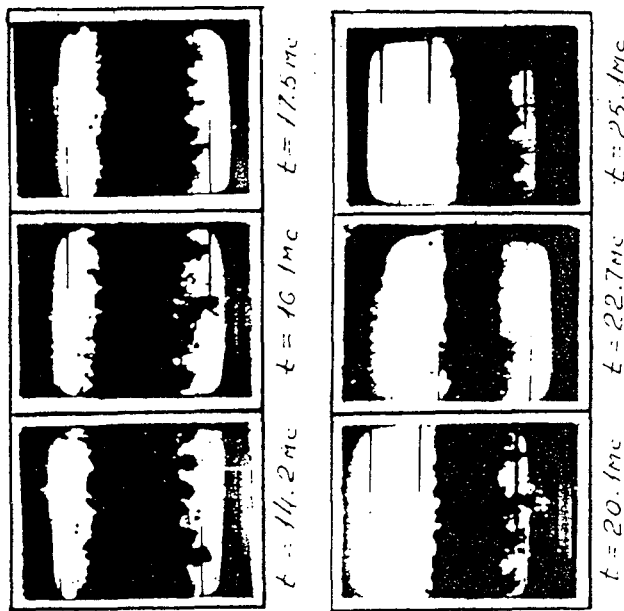


FIG. 2 TYPICAL PHOTOGRAPHIC IMAGES OF THE MIXING REGION AT THE STAGE OF DECELERATED MOTION

certain instant of time ($t=0$) the ampoule begins to accelerate in the direction \vec{g} (with acceleration $a_1(t)$). In the process of acceleration, in the coordinates connected with the ampoule, an unstable system is realized with an artificial gravitational field \vec{g}_{21} directed from the heavy fluid to the light one (the unstable motion stage). In the contact boundary region the process of the instability and turbulent mixing development was studied by applying light techniques. Such parameters as acceleration a_1 , the way $S = \int_0^t \int_0^t a_1(\tau) d\tau$, passed by the contact boundary up to the moment of photographic images obtaining, average sizes L_{21} , L_{12} of regions involved into the turbulent motion in the light and heavy fluids were experimentally determined.

At a certain instant of time t^* (at $S=S^*$) the ampoule found itself in the inverter where reversing of the acceleration sign took place. From this moment on the stage of decelerated motions begins with acceleration $a_2(t)$. At this stage the artificial gravitational field \vec{g}_{12} is directed from the light fluid to the heavy one (the stable motion stage). Starting from some instant of time t_0 the separation process develops with decreasing the size α of the region involved into mixing (see Fig.2). In order to exclude the effect of viscosity and surface tension [7] all experiments were performed for the initial values of accelerations $a_{10} \gg g$, $a_{20} \gg g$ (with $g_{21}=a_1$; $g_{12}=a_2$). At the stable motion stage the experimental investigation into the developed turbulent mixing region behaviour was performed with liquids, such as petrol ($\rho_1=0.69 \text{ g/cm}^3$) and zinc chloride solution ($\rho_2=2.04 \text{ g/cm}^3$, $n=\rho_2/\rho_1=3$).

Two series of experiments have been performed for two different values of S^* . The series included five groups of experiments (15-20 experiments in each group) differing in the values of accelerations g_{21} and g_{12} (see Table 1).

Table 1.

Group No	1	2	3	4	5	6	7	8	9	10
$\frac{g_{21}}{g}$	305	305	483	483	483	276	276	440	440	440
$\frac{g_{12}}{g}$	93	140	93	140	186	93	140	93	140	186
S^*, cm	$S^* = 36.0$					$S^* = 13.6$				

The characteristic relations for the way S , accelerations g_{21} , g_{12} and the size $L=L_{12}+L_{21}$ of the region involved into mixing versus time are shown in Fig.3 for one group of experiments. After reversing the acceleration sign at $t^*=8.2$ ms the size of the mixing region kept growing. Beginning just from the moment $t_c=16.6$ ms the mixing region size is decreasing. This is the consequence of the separation of heavy and light fluids particles differing in scales. Experimental results for $t > t_c$ are presented in Fig.4 for all groups of experiments. The coordinates in which processing of the experiments has been performed were chosen in terms of formula (1). Formula (1) has been generalized for the case of slowly changing acceleration when $d\sqrt{L_{12}}/d\sqrt{S'} = -\sqrt{2\alpha_s A}$, where $S' = \int_{t_c}^t g_{12}(\tau) d\tau$.

Straight lines have been built by the least-square technique according to experimental points corresponding to $t > t_c$. It can be seen that at the separation stage the experimental data in total are well described by the straight lines having an identical slope

$\frac{d\sqrt{L_{12}}}{d\sqrt{S'}} = -0.103$. From here we find that the constant separation $\alpha_s = 0.01$ for the densities relation $n=3$.

Processing of experiments presented in [5] has been performed at our request by V.G.Yakovlev who applied the technique mentioned

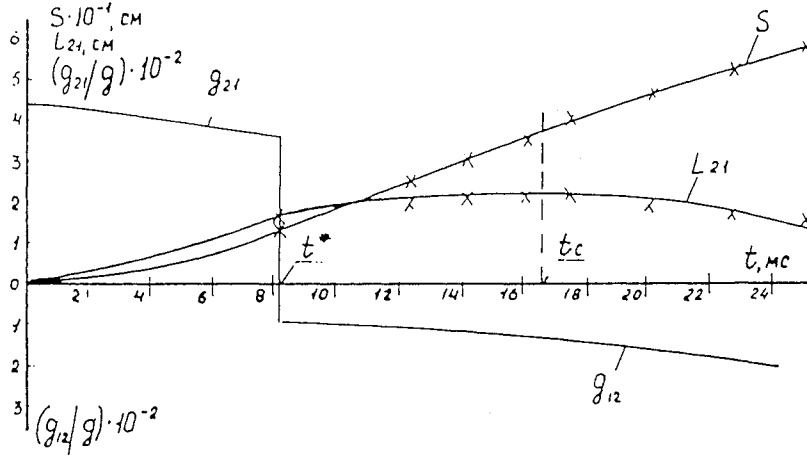


FIG. 3 PLOT OF DISPLACEMENT S , ACCELERATIONS g_{21}, g_{12} AND TURBULENT MIXING REGION SIZE L_{21} VS TIME (THE 8th SERIES OF EXPERIMENTS)

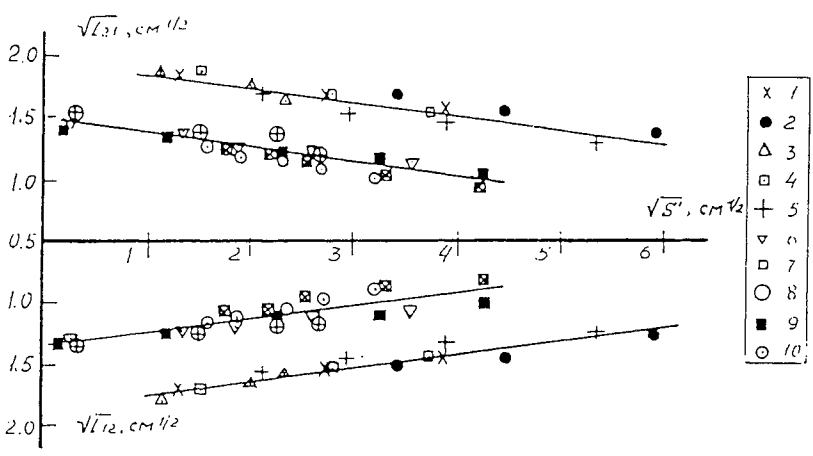


FIG. 4 PLOT OF $\sqrt{L_{12}}, \sqrt{L_{24}}$ VS PARAMETER \sqrt{S} AT THE STAGE OF SEPARATION

above. For $A=0.27$ an analogous numerical value has been obtained for the constant α_s .

3. THEORETICAL INVESTIGATIONS. Allowance for the acceleration sign change within the limits of the known approximate k-model [6], [8] leads to the statement of a new ks-model consisting in the following. For $t \leq t_c$ the k-model based on the equation of balance for the kinetic turbulence energy $\bar{v}^2/2$ is applied:

$$\frac{d\bar{v}^2}{dL} + 4k_0 \frac{\bar{v}^2}{L} = \frac{g_{21} A}{2\eta_1} \Phi(\eta_1); \quad \eta_1 = \frac{z}{\sqrt{\pi}} \quad (2)$$

$$\frac{dL}{dt} = 8\eta_1^2 \alpha_m \bar{v}; \quad k_0 = 1.25 + \frac{\Phi(\sqrt{2} \eta_1)}{12\sqrt{2}} A^2 \quad (3)$$

$$\Phi(\eta) = \frac{2}{\sqrt{\pi}} \int_0^\eta \exp(-\eta^2) d\eta, \quad (4)$$

but for the determination of the average mixture density $\rho(x)$ the following equations of the diffusion type are used:

$$\frac{\partial \rho}{\partial t} = \frac{\partial}{\partial x} \left[D \frac{\partial \rho}{\partial x} \right], \quad D = \alpha_m L \bar{v}. \quad (5)$$

On the assumption that \bar{v} depends only on time the solution of Eq.(5) has the form:

$$\rho = \frac{\rho_1 + \rho_2}{2} + \frac{\rho_2 - \rho_1}{2} \Phi \left[\frac{2\eta_1 x}{L} \right] \quad (6)$$

The solution of Eq.(2) is written as follows:

$$\bar{v}^2 = \begin{cases} \frac{\Phi(\eta_1)g_{21}AL}{2\eta_1^2(1+4k_0)} & \text{for } 0 \leq t \leq t^* \\ \bar{v}^2(t^*) + \frac{\Phi(\eta_1)g_{12}AL}{2\eta_1^2(1+4k_0)} \left[1 - \left[\frac{L(t^*)}{L} \right]^{1+4k_0} \right] & \text{for } t^* < t \leq t_c \end{cases}$$

$$L = \begin{cases} \frac{8\alpha_m^2 \eta_1^2 \Phi(\eta_1) g_{21} A t^2}{1+4k_0} & \text{for } 0 \leq t \leq t^* \\ L^* \leq L(t) \leq L_c & \text{for } t^* < t \leq t_c \end{cases}$$

$$t_c = t^* + \frac{1}{4\eta_1 \alpha_m} \sqrt{\frac{2(1+4k_0)}{\Phi(\eta_1)g_{12}}} [L_c - L(t^*)]$$

For describing the separation in case of $t > t_c$ the following transfer equation is applied:

$$\frac{\partial \rho}{\partial t} = - \sqrt{\alpha_s} \sqrt{\frac{2g_{12}L}{(\rho_2 - \rho_1)(\rho_2 + \rho_1)}} (\rho_1 + \rho_2 - 2\rho) \frac{\partial \rho}{\partial x} \quad (7)$$

The analysis of equations of the model [2], [5] performed for the case of incompressible fluids leads to the similar equation. Density distribution (6) at the moment $t=t_c$ can be used as the initial data. Equation for width will be determined from the condition on the characteristic and will be written as

$$\frac{d\sqrt{L}}{dt} = - \sqrt{2\alpha_s g_{12} A} \cdot \Phi(\eta_1) \quad (8)$$

with initial conditions $L=L^0$ under $t=t_0$. The integration of Eq (7) leads to formula (1).

4. CONCLUSION Thus, the results obtained during experimental and theoretical investigations into the separation of matters in the gravitational turbulent mixing region at the stable motion stage can be used for solving the inertial thermonuclear fusion problems.

References

1. S.Z.Belen'ky, E.S.Fradkin Sb."Trudy FIAN im.Lebedeva", [In Russian], 1965, 29, pp.207-238.
2. Youngs D.L. Physica, 1984, D 12, p.19.
3. Yu.A.Kucherenko, L.I.Shibarshov, V.I.Chitaikin, S.I.Balabin, A.P.Pylaev Experimental investigation into self-similar mode of gravitational turbulent mixing. Transactions of the 4th International Conference on Turbulent Mixing Physics, France, 1991, p.427.
4. N.N.Anuchina, Yu.A.Kucherenko, V.E.Neuvazhayev, V.N.Ogibina, L.I.Shibarshov, V.G.Yakovlev Mekhanika zhidkosti i gaza, [In Russian], №6, pp.157-160.
5. Youngs D.L. Physica, 1989, D 37, pp.270-287.
6. V.E. Neuvazhayev, DAN SSSR, 1975, 5, pp.1053-1056.
7. Yu.A.Kucherenko, G.G.Tomishev, L.I.Shibarshov Experimental investigation into gravitational turbulent mixing, VANT, seriya: teoreticheskaya i prikladnaya fizika, [In Russian], Issue 1, 1988, p.13.
8. V.E. Neuvazhayev PMTF, 1992, 1, p.38-42.

RAYLEIGH-TAYLOR INSTABILITY IN SOLIDS.

A.I. Lebedev, P.N. Nisovtsev, V.A. Rayevsky.

ALL-RUSSIA SCIENTIFIC RESEARCH INSTITUTE OF EXPERIMENTAL PHYSICS. (607200, Arzamas-16, Nizhny Novgorod region, Russia).

REPORT FOR THE 4 INTERNATIONALE WORKSHOP ON THE PHYSICS OF COMPRESSIBLE TURBULENT MIXING (Cambridge, England, 29 March-1 April 1993).

ABSTRACT

The results of theoretical prediction and experimental investigations of Rayleigh-Taylor instability in strong substances are summarized.

The instability has been found to grow as a function of strength, the wavelength and initial amplitude of the perturbation, layer depth, the pressure value and time dependence at the accelerated layer boundary. The substance strength may result in complete suppression of short-wavelength perturbation instability. As shown experimentally, three-dimensional perturbations in strong layer, unlike perfect fluid case, may have lower growth rate than the two-dimensional.

Simple analytical expressions have been derived to estimate the strong layer instability.

INTRODUCTION.

The classical Rayleigh-Taylor instability situation is that of perturbation growing at the surface of a plate (or shell) accelerated by pressure applied on its one surface [1]. As the instability grows this would eventually result in complete disintegration of the accelerated layer. For perfect fluid or gas layer acceleration, the perturbation would grow turbulently, and the turbulent zone would have its width increasing as square law

$$H_t = \alpha g t^2$$

where g is the acceleration, α -- constant.

The development of Taylor instability in strong substances is impeded by shear stresses caused by the medium deformation. The substance strength can substantially increase the "lifetime" and maximum achievable velocity of the accelerating liners.

The experiments to investigate Taylor instability in solids were pioneered by G.S. Barnes [4],[5]. In 1987 Ye. Meshkov and N. Nevmergitsky observed the stabi-

lizing effects of strength in the experiments on a jelly layer being accelerated by gas detonation products. J. Miles [2] was the first to estimate theoretically the strength effects in terms of perfectly elastic substance model. From [2], unstable are only the perturbations having wavelengths above a certain critical

$$\lambda > \lambda_c = \frac{6 \cdot \pi \cdot G_F}{g \cdot \rho} = \frac{6 \cdot \pi \cdot C^2}{g} \quad (1)$$

where G is the shear modulus of substance, ρ - the substance density and C is the shear wave velocity. Evidently, Miles erroneously considered this criterion (1) as independent of the layer depth: while this is generally wrong.

A more accurate solution for elastic half-space has been obtained by S. Bakhrahk and N. Kovalev [3]

$$\lambda_c = \frac{4 \cdot \pi^2 \cdot C}{g} \quad (2)$$

By D. Drucker's theory whatever the wavelength, and with the initial perturbation amplitude below a certain critical value

$$\Delta H < \Delta H_c = \frac{2 \cdot \sigma_T}{\rho \cdot g} \quad (3)$$

the surface would be stable [4], (σ_T - the yield strength).

This statement was verified by J. Barnes et. al. [4], [5] who performed experiments to study Taylor instability for aluminum plates.

However, as our theoretical prediction have shown (VNIIEF reports of 1987, 1988, [8], [9]), D. Drucker's theory is only valued for very short wavelengths ($\lambda \ll \lambda_c$), while that by Miles only holds for very small initial perturbation and large layer depths ($H \gg \lambda$). Generally, instability depends on both the initial amplitude and wavelength of the perturbations, and also on the pressure history, at the layer boundary. The same inference results from the data obtained by A. Robinson and G. Swegle [9].

The paper summarizes the investigations carried out by the authors in 1987-91.

1. ANALYICAL STUDY.

In some cases, elastoplastic model is applicable in representation of strong medium strain. From the thin-shell theory, we have derived equations accounting for small perturbations developing in the perfectly elastic layer of substant acceleration driven by the unilaterally applied pressure $P = \rho \cdot g \cdot H$ were H is the depth of layer.

The equations of motion have been derived in coordinates accelerated linearly

with the non-perturbed layer surface. Y axis is normal to the surface, X axis lying therein. the equation are written for the layer depth averaged displacement U_x and U_y of substance in X and Y - directions. for initial difference in layer depth $\Delta H(x) = \Delta H_0 \sin(kx)$ these equations take the form

$$\frac{\partial^2 U_x}{\partial t^2} = 4 \cdot C^2 \cdot \frac{\partial^2 U_x}{\partial x^2} - g \cdot \frac{\partial U_y}{\partial x} \tag{4}$$

$$\frac{\partial^2 U_y}{\partial t^2} = g \cdot \frac{\partial U_x}{\partial x} - \frac{(C \cdot H_{ef})^2}{3} \cdot \frac{\partial^4 U_y}{\partial x^4} - g \cdot \frac{\Delta H}{H_{ef}}$$

where C is the shear wave velocity, $H_{ef} = \frac{\sqrt{3} \cdot (1 - \exp(-\frac{KH}{\sqrt{3}}))}{K}$, $K = \frac{2 \cdot \pi}{\lambda}$.
 The eq.(4) have the following solutions

$$U_x = \frac{\Delta H_0}{H_{ef}} \cdot \frac{K \cdot g^2}{\omega_1^2 - \omega_2^2} \cdot \left(\frac{\cos(\omega_1 t) - 1}{\omega_1^2} - \frac{\cos(\omega_2 t) - 1}{\omega_2^2} \right) \cdot \cos(K \cdot x)$$

$$U_y = \frac{\Delta H_0}{H_{ef}} \cdot \frac{g}{\omega_1^2 - \omega_2^2}$$

$$\times \left(\left(1 - \frac{4 \cdot (C \cdot K)^2}{\omega_1^2} \right) \cdot (\cos(\omega_1 t) - 1) - \left(1 - \frac{4 \cdot (C \cdot K)^2}{\omega_2^2} \right) (\cos(\omega_2 t) - 1) \right)$$

$$\times \sin(K \cdot x)$$

natural frequencies ω_1 and ω_2 being found from the equation

$$\omega_{1,2}^2 = \frac{1}{2} \cdot \left((C \cdot K)^2 \left(4 + \frac{(KH_{ef})^2}{3} \right) \right) \tag{6}$$

$$\sqrt{(C \cdot K)^4 \cdot \left(1 + \frac{(KH_{ef})^2}{3} \right)^2 + 4 \cdot \left((Kg)^2 - \frac{4(KC)^4 \cdot (KH)^2}{3} \right) p n}$$

The higher frequency, ω_1 , consistent with stable oscillations of the layer. The

lower frequency, ω_2 , represents the system stability and may become imaginary. In this case the perturbations would grow exponentially

$$U_x \sim U_y \sim \exp(\text{Im}(\omega_2) \cdot t)$$

The critical wavelength λ_c , where $\omega_2 = 0$, defines stability boundary of the elastic layer. Eqs.(4), (6) result in the transcendental equation for

$$\lambda_c = \frac{4 \cdot \pi \cdot C^2}{g} \cdot \left(1 - \exp\left(\frac{-2 \cdot \pi \cdot H}{\sqrt{3} \cdot \lambda_c}\right) \right) \tag{7}$$

or approximately

$$\lambda_c \equiv \frac{8 \cdot \pi \cdot C^2}{g \cdot \left(1 + \sqrt{1 + \frac{8 \cdot \sqrt{3} \cdot C^2}{g \cdot H}} \right)} \equiv \frac{\lambda_\infty}{g \cdot \left(1 + \sqrt{1 + \frac{8 \cdot \sqrt{3} \cdot C^2}{g \cdot H}} \right)}$$

Clearly, the half space ($H \rightarrow \infty$) (9),(10) go into Miles formula (1) $\lambda_\infty = \frac{4 \cdot \pi \cdot C^2}{g}$, while for thin layer

$$H \ll \frac{8 \cdot \sqrt{3} \cdot C^2}{g}$$

into the equation $\lambda_c = 2 \cdot \pi \cdot \left(\frac{4}{3}\right)^{1/4} \cdot \sqrt{\frac{H}{g \cdot C^2}}$.

Fig.1 shows in nondimensional coordinates λ_c as a function of layer depth. Evidently, the resulting equation (9) agrees well with numerical calculations in a perfectly elastic approximation.

For steady-state conditions ($\lambda < \lambda_c$), the range of stress intensity depends on the initial amplitude and how close λ is to λ_c

$$\sigma_1 \sim \frac{\Delta H_0}{\lambda/\lambda_c - 1} \tag{8}$$

Real substances cannot have infinite stress intensity. It has been assumed, that the elastoplastic payer would become unstable when stress intensity reaches the yield strength σ_T .

As expected, if this is the case, then the perturbations would further grow without bound plastically despite that $\lambda < \lambda_c$. this assumption has the instability criterion in the form

$$\Delta H > \Delta H_c(\lambda) = \frac{2 \cdot \sigma_T \cdot \left(1 - 0.86 \exp\left(\frac{-2\pi H}{\sqrt{3} \cdot \lambda}\right) \right) \left(\left(1 - \exp\left(\frac{-2\pi H}{\sqrt{3} \cdot \lambda}\right) \right)^2 - (\lambda/\lambda_\infty)^2 \right)}{\rho \cdot g} \tag{9}$$

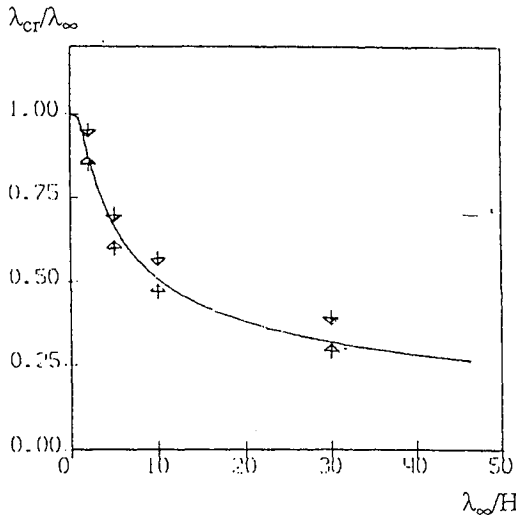


Fig. 1. $\lambda_{cr}/\lambda_{\infty}$ versus λ_{∞}/H .
 ▲▼ - numerical calculations.
 ▲ - stable conditions.
 ▼ - unstable conditions.

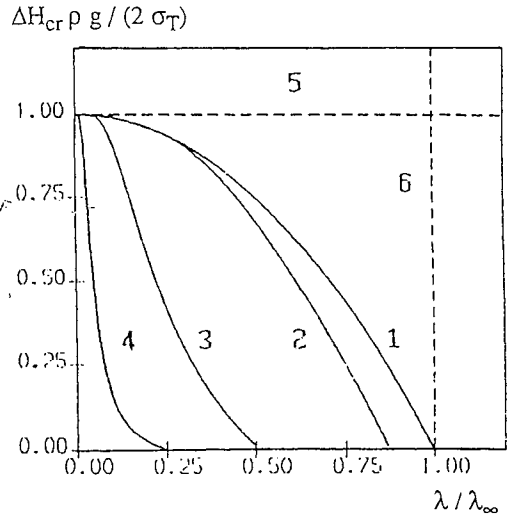


Fig. 2. Critical perturbation amplitude as a function of wavelength.
 1 - $H = \infty$, 2 - $H/\lambda_{\infty} = 0.5$, 3 - $H/\lambda_{\infty} = 0.1$,
 4 - $H/\lambda_{\infty} = 0.02$, 5 - Drucker's solution,
 6 - Miles' solution.

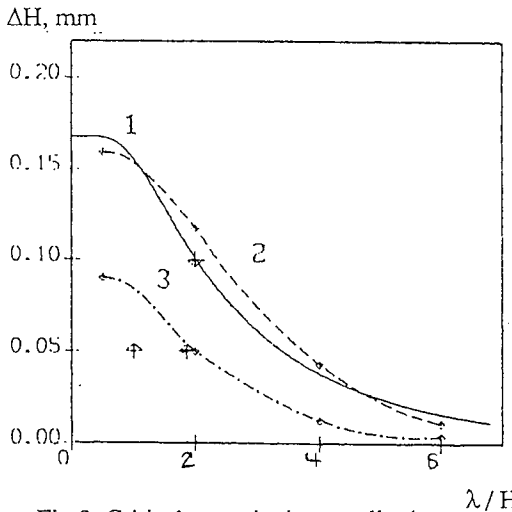


Fig. 3. Critical perturbation amplitude as a function of wavelength for aluminum plate in Barnes' experiments.
 1 - formula (9), 2 - numerical calculations in terms of noncompressibility assumption,
 3 - numerical calculations in terms of compressibility, ▲▼ experi. points., ▲ - stable conditions, ▼ - unstable conditions.

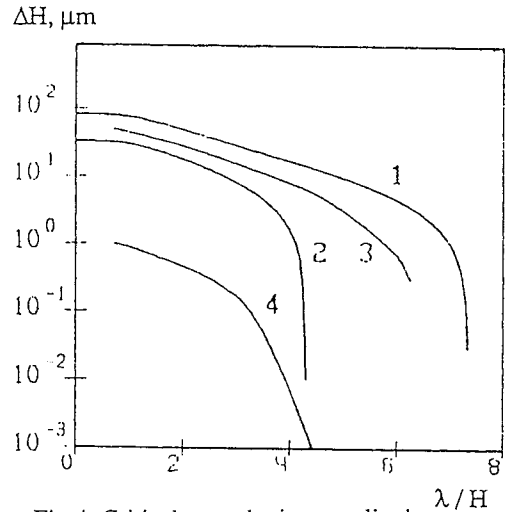


Fig. 4. Critical perturbation amplitude versus wavelength for various driving pressures at the interface.
 1 - formula (9) $P = 20$ GPa,
 2 - formula (9) $P = 50$ GPa,
 3 - numerical predictions $P = 20$ GPa,
 4 - numerical predictions $P = 50$ GPa.

Fig.2 shows instability boundaries related with the criterion (9) for various layer depths.

For $\lambda \ll 2\pi H$ and $\lambda \ll \lambda_c$, eq. (9) would go into the Drucker criterion (3). the Miles instability criterion (2)

$$\lambda > \lambda_\infty = \frac{4\pi C^2}{g}$$

is only valid for thick $H \gg \lambda_\infty$ when the initial perturbation amplitude is small,

$$\Delta H_0 \ll \frac{2\sigma_T}{\rho g}.$$

Fig. 3 shows a calculated stability boundary for aluminum plate 2.5 mm thick accelerated by pressure $P=100$ kbar, as in Barnes' experiments [4]. The calculations used the following constant values: $\rho = 2.71 \text{ g/cm}^3$, $G = 300$ kbar, $\sigma_T = 3.3$ kbar. The figure also includes the numerically calculated curves and Barnes' experimental data.

By virtue of the layer incompressibility assumption, the resulting equations are valid for pressure and compressions that are not high. Fig.4 gives the boundary curves obtained from our equation (9) and numerical elastoplastic calculation for higher pressures.

2. NUMERICAL STUDY.

The numerical calculation were performed in an elastic-plastic approximation. Equations of motion were solved in Lagrangian coordinates using "Dinamika 2" code widely employed in VNIIEF. The calculations were made for growing in a steel layer having depth $H = 2\text{mm}$ at it was accelerated by pressure unilaterally approach thereto. Fig.5 shows this pressure as a function of time, Pressure front rise time was varied in wide range, i.e. $\tau_f = 0.4 - 7 \mu\text{s}$. The least time value was taken such that no shock wave should be generated in loading. The maximum pressure taken by the calculations was 50 GPa, i.e. 30 times the yield strength that was considered equal to $\sigma_T = 1.5$ GPa. The equation of state was taken identical to the Mie-Gruneisen's minus thermal component.

$$P = \frac{\rho_0 C_0^2}{n} \cdot \left(\left(\frac{\rho}{\rho_0} \right)^n - 1 \right)$$

with the parameters $\rho_0 = 7.85 \text{ g/cm}^3$, $C_0 = 3.8 \text{ km/s}$, $n = 5$. The shear modulus was considered equal to $G=77$ GPa. Sinusoidal perturbations were driven at both layer surfaces.

$$\Delta V = \begin{cases} -a_0 \cdot \cos(K \cdot x) & \text{upper-surface} \\ a_0 \cdot \sin(K \cdot x) & \text{lower-surface} \end{cases}$$

with $a_0 = 3.3 \mu\text{m}$.

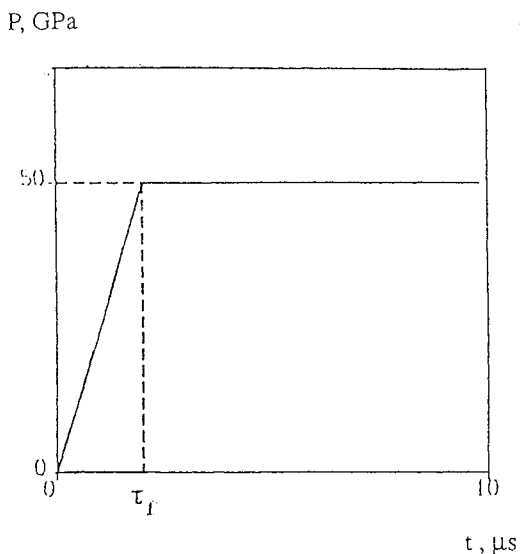


Fig. 5. Pressure history at the plate surface

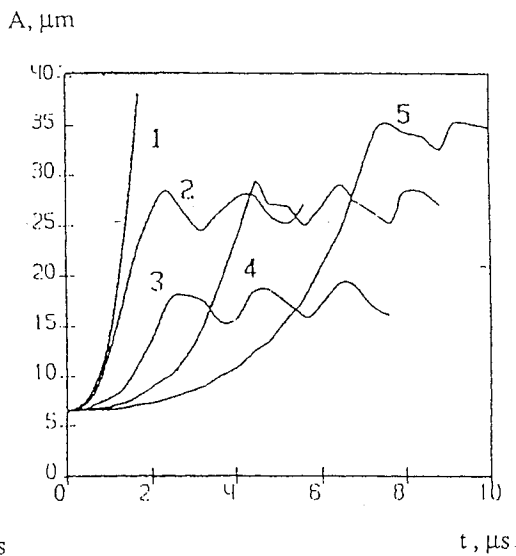


Fig. 6. Time dependences of perturbation amplitudes for different rise times τ_f , $\lambda=0.4\text{cm}$
 1 - $\tau_f = 0.5 \mu\text{s}$, 2 - $\tau_f = 0.7 \mu\text{s}$, 3 - $\tau_f = 2.0 \mu\text{s}$,
 4 - $\tau_f = 4.0 \mu\text{s}$, 5 - $\tau_f = 7.0 \mu\text{s}$.

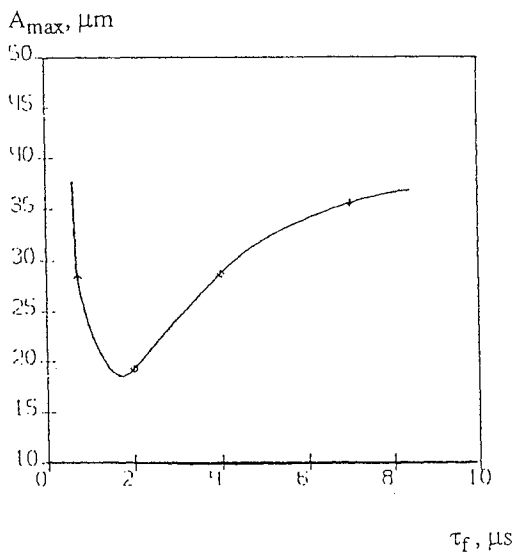


Fig. 7. Maximum perturbation amplitude as a function of τ_f

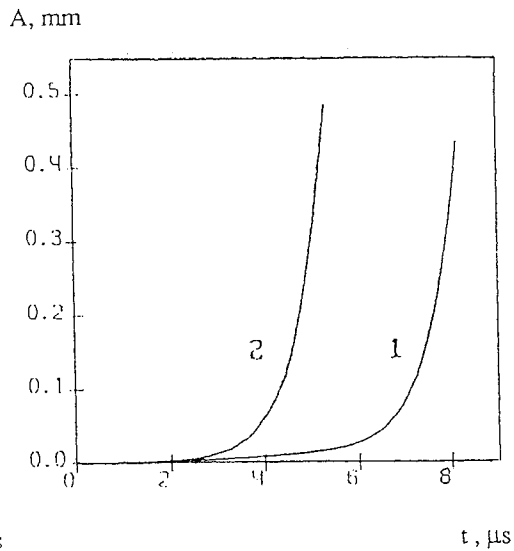


Fig. 8. Time dependences of perturbation amplitude, $\lambda = 0.8 \text{ cm}$.
 1 - involving strength, 2 - no strength.

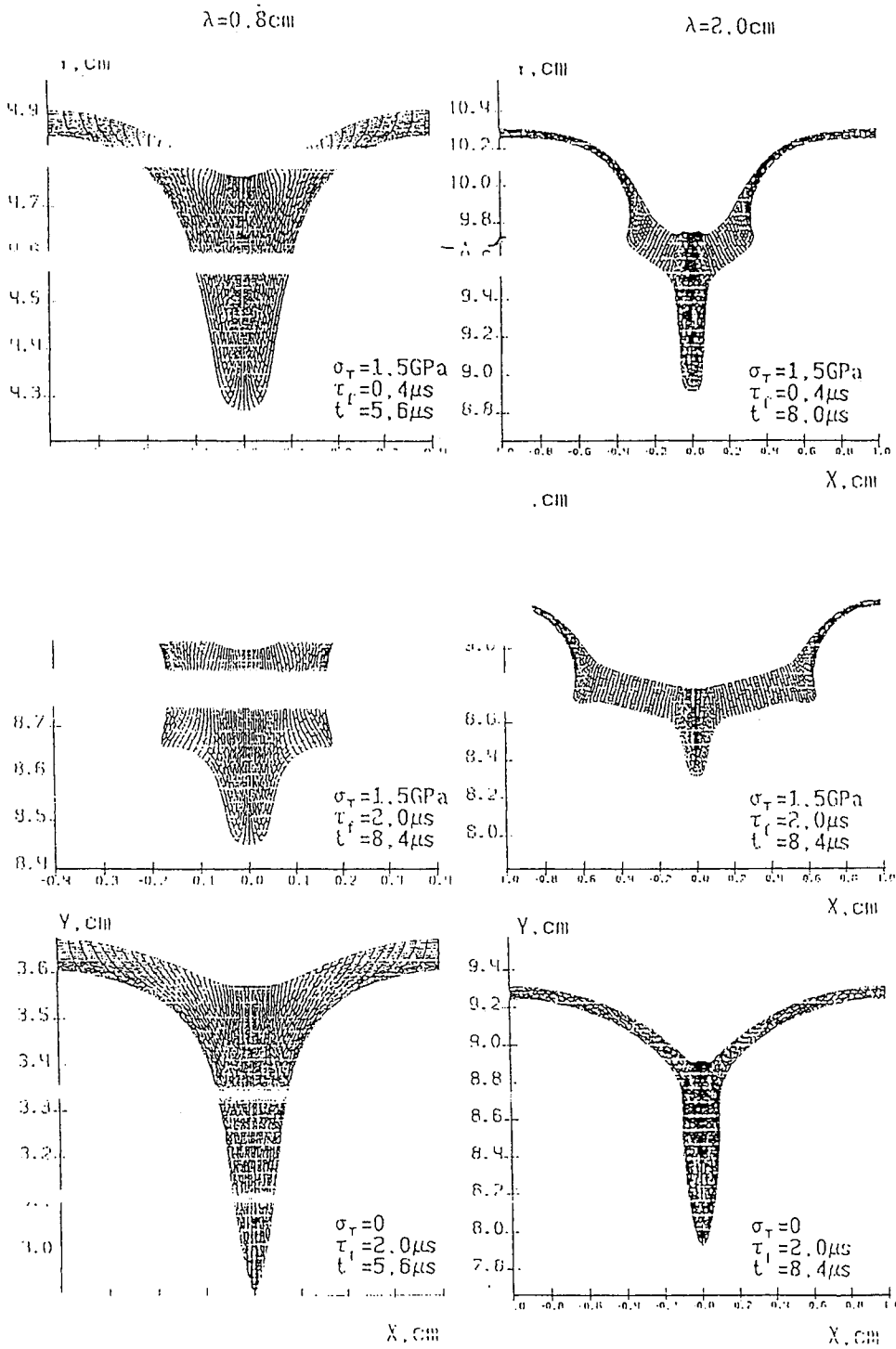


Fig. 9. Typical perturbation configurations.

Fig.6 shows perturbation amplitudes in the driven surface $A(t) = V_{\max} - V_{\min}$ for perturbation wavelength $\lambda = 0.4$ cm. and τ_f of various values. As is evident from the plots, the system becomes unstable when $\tau_f < 0.5$ μs . For $\tau_f > 0.7$ μs , the amplitude first increases and then begins fluctuating about some mean value. Maximum oscillation amplitude versus driving pressure rise time is shown in fig.7. Perturbations of the wavelength $\lambda > 0.8$ cm are completely unstable for any pressure front rise time. Fig.8 gives growth rate histories of perturbations of $\lambda = 0.8$ cm. wavelength with and without strength present. Worth mentioning is the influence of the pressure pulse rise time on the perturbation configurations, fig. 9.

For short pulse rise times the perturbations have a configurations near sinusoidal which is typical for perfect fluid, while with longer $\tau > 2\mu\text{s}$ the configuration becomes more complex with local maxima occurrence observed.

Another significant peculiarity with the strong layer instability is the relationship between the two-dimensional and three dimensional perturbation growth rates. Perfect fluid is known to have three-dimensional perturbations growth faster than the two-dimensional. As Ye. Meshkov and associates have established in jelly experiments, single three-dimensional perturbations have growth rates twice as high as the two-dimensional. We have carried out calculations similar to the above mentioned, but for the axisymmetric geometry to simulate a three-dimensional perturbation amplitude for different wavelength in two- and three- dimensional cases. As seen from the figure, for short wavelengths three-dimensional perturbations grow significantly slower than two-dimensional ones.

3.EXPERIMENTS AND RESULTS.

Experiments were performed in a set up that was very much like that of Barnes'[5], though involving longer wavelength. Additionally, there was testing for instability relationship between two-dimensional and three-dimensional perturbations.

The aluminum plate 1.5 mm thick was accelerated by gaseous detonation products of high explosive separated from the plate by a 15 mm vacuum gap. Thus, the plate was driven without generating shock waves. The calculated pressure history at the plate interface is shown in fig. 10. Perturbations were machined in the driven surface as longitudinal triangular grooves. the surface was machined in the same way crosswise to produce three-dimensional perturbations. Accordingly, these three-dimensional perturbations were configured as pyramids. Perturbation values during the plate motion were measured using flash X-ray techniques.

The typical radiographs are shown on fig.14, Fig.11 shows experimental data for two-dimensional perturbations in the driven plate surfaces. As seen from the plots, perturbation growth rates as well as plate stability depend on both the wavelengths and initial amplitudes of perturbations. Figs.12 summarize experimental results on

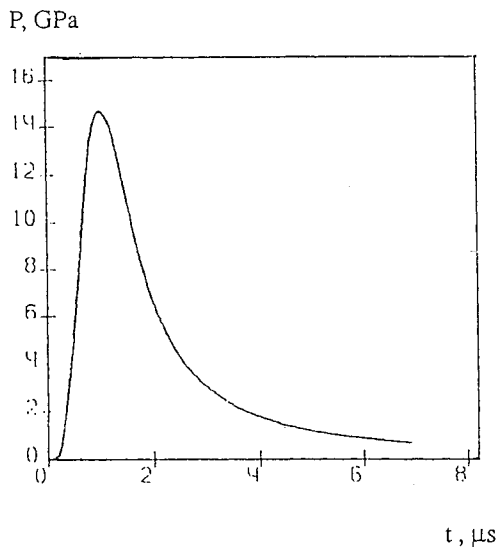


Fig. 10. Pressure history at the plate surface.

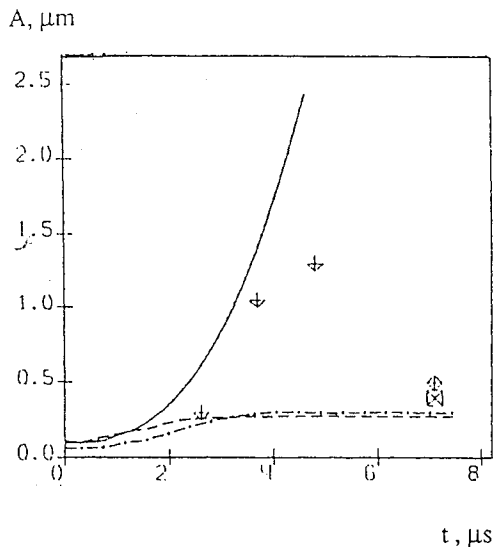


Fig. 11. Time dependences of perturbation amplitude. Lines - calc's, points - experiment

∇ - $\lambda=4\text{mm}$, $A_0=0.1\text{mm}$;
 \blacklozenge - $\lambda=4\text{mm}$, $A_0=0.05\text{mm}$;
 \square - $\lambda=2\text{mm}$, $A_0=0.1\text{mm}$.
 A, mm

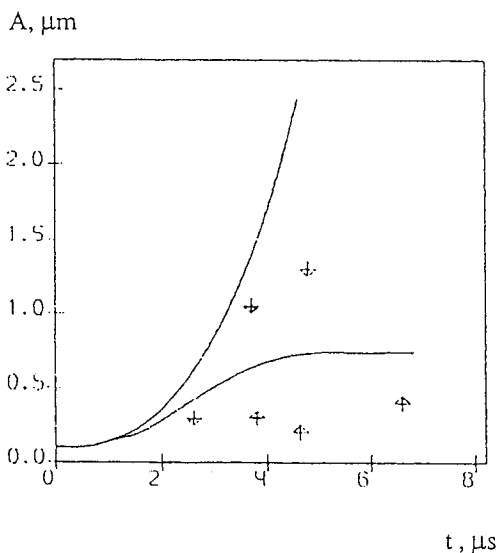


Fig. 12. Time dependences of perturbation amplitude. $\lambda = 4\text{mm}$, $A_0=0.1\text{mm}$.

∇ - two - dimensional experimental points ,
 \blacktriangle - three - dimensional experimental points.

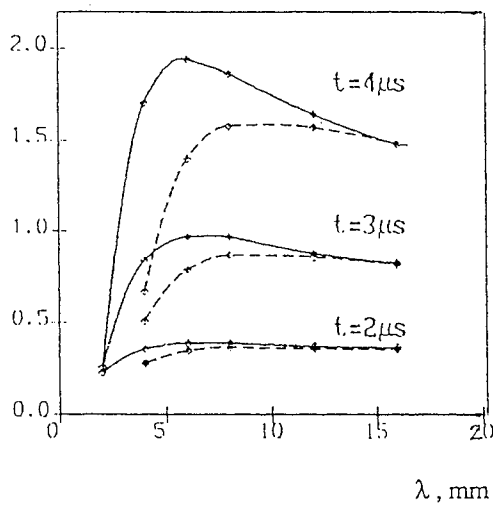


Fig. 13. Perturbation amplitude versus wavelength at different times.

— Two - dimensional,
 - - - Three dimensional.

three and two-dimensional perturbations, with the same amplitudes and wavelengths. As seen from the figure, for the range of parameters of interest three-dimensional perturbations are growing more slowly than the two-dimensional.

Numerical simulation of the experiments has been performed using elastic plastic method with the yield strength linearly dependent on driving pressure.

$$\sigma_T = 0.2 \cdot (1 + 0.2 \cdot P)$$

$$[\sigma_T] = GPa; [P] = GPa$$

The calculated time dependences of perturbation amplitude are given in figs.11,12,13.

4.CONCLUSIONS AND DISCUSSION.

The studies have shown that perturbations growth rate to depend on elastic-plastic material properties, driving pressure and its history at the media interface, and the wavelength and initial amplitude of perturbation. For comparatively small initial perturbations, the instability in the range of rather short wavelengths ($\lambda < \lambda_c$) can be fully suppressed even with the driving pressure applied to the payer being an order of magnitude as high as the yield strength. Perturbation of wavelengths above critical ($\lambda > \lambda_c$) are completely unstable.

The simple equation obtained to determine λ_c versus elastic properties of material, values of acceleration and depth layer, agrees rather well with numerical calculation and experiments.

The instability criterion for elastic-plastic layer, which specifies the upper bound of initial perturbation amplitude, is valid for not too high a driving pressure at the interface, i.e. low material compression ($\frac{P}{\rho_0} < 1.2$).

The perturbation growth pattern has been found to be strongly dependent on the plate loading rate (\dot{P}). As \dot{P} is increasing, stable perturbations may change over to unstable regime. This effect can be accounted for by the following explanation. When the layer is driven, a compression wave is propagating therein. After this wave has come out to the free surface, a rarefaction wave starts travelling in the opposite direction, this being followed by several more compression and rarefaction waves generated. The perturbation growth is restrained by deviatoric stress components. When the compression and rarefaction waves exceeding in amplitude the yield strength have passed through the payer, the material goes over to another state. The total stress intensity is limited by yield stress, therefore the stress component restraining the perturbation growth decreases. Thus, the sequence of waves passing through the layer results in reduced stabilizing effects of strength. Apparently, there

is a specific plate loading rate for each particular case, where maximum stability is achieved. The layer loading rate also strongly effects perturbation configurations. For high \dot{P} , the perturbation configuration is slightly different from the perfect fluid case. When \dot{P} is comparatively low, perturbation configuration is largely different from the sinusoidal and characterized by the occurrence of additional peaks.

Unlike the perfect fluid instability case, strong layer has three-dimensional perturbations growing more rapidly than the two-dimensional for relatively short wavelengths.

At the interface of physically read layer of material there would always exist perturbation of any wavelengths. Therefore, the acceleration of this layer whatever its strength is an unstable process, and then a certain "lifetime" of a thin smooth

($H < \lambda_c, H \ll \frac{\sigma_T}{\rho \cdot g}$) can be estimated as follows

$$\tau_1 = \sqrt{\frac{\pi \cdot \lambda_c}{g}} \cdot \ln\left(\frac{2\pi H}{\Delta H_0}\right).$$

1. Taylor, G. I. Proc. Roy. Soc. 1950. Vol. 201, N1065, P. 192.
2. Miles, J.W. General Atomic Rep. GAMO-7335, 1960.
3. Bakhrakh, C.M., Kovalev, N.P., Material 5 All-Union Conference on numerical methods ..., Novosibirsk p. 15-23, 1978.
4. Barnes, J.F., Blevitt, P.J., McQueen, R.K., et. al. J. Appl. Phys. Vol. 45, No.2, p.727-732, 1974
5. Barnes, J.F., Janney, D.H., London, R.K. et.al. Ibid. Vol 51, p.4687, 1980.
6. Drucker, D.C., Mechanics Today, Vol. 5 Pergamon Press, p.37-47.
7. Robinson, A.C., Swegle, J.W., J. Appl. Phys., Vol. 66 p.2838-2872.
8. Lebedev, A.I., Nizovtsev, P.N., Raeyevskii, V.A., BANT cep. Teor. prikl. phiz. 1991.
9. Nizovtsev, P.N., Raeyevskii, V.A., Ibid. Bwep. Z. p.11-17 1991.

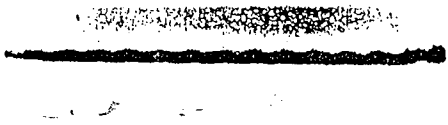
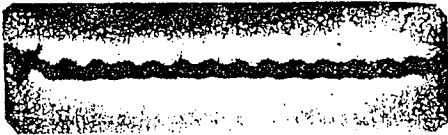


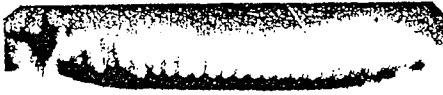
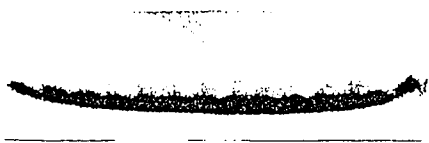
λ , mm	A_0 , mm	T, μ s	The radiographs
4.0	0.1	2.6	
		3.7	
		4.8	
		7.6	
2.0	0.1	6.8	
4.0	0.05	6.8	

Fig. 14.

Parallel Computation of Three Dimensional Rayleigh-Taylor Instability in Compressible Fluids through The Front Tracking Method and Level Set Methods

X. L. Li

Computer and Information Science Department
Indiana University-Purdue University at Indianapolis
Indianapolis, IN 46202

J. Grove

Q. Zhang

Department of Applied Mathematics and Statistics
SUNY at Stony Brook
Stony Brook, NY 11794

ABSTRACT

Computation of three dimensional Rayleigh-Taylor instability in compressible fluids is performed on a MIMD computer. In this paper we will present our study using two numerical methods, the front tracking method and the level set method. We will discuss algorithms used in the 3D front tracking method and parallel implementation using this method. This includes 3D interface partition, unstructured grid generation and parallel coordination of the program. Our algorithms using level set method include application of a second order TVD scheme with a full parallelization to the 3D Euler equations. The computational programs will be used for a 3D study of bubble evolution in the Rayleigh-Taylor instability and for large scale simulation of a 3D random fluid interface. The objective of this research is to compare the numerical solutions with the experimental results by Taylor and Youngs.

1. Lagrangian and Eulerian Approaches

Rayleigh-Taylor instability is an interface instability. Two fluids are separated by an unstable boundary across which the density changes sharply. Due to the importance of the density discontinuity in Rayleigh-Taylor instability, numerical methods used to solve the problems must focus on the evolution of the fluid interface. We consider two methods, which have been used in the past few years, to study the dynamical interface motion. The first method is the Lagrangian method, which is known as the front tracking method. The interface motion is characterized by the motion of individual points on the interface. The velocity of these points are calculated by the solution of a Riemann problem in the direction normal to the interface. The front points are propagated according to the contact velocity in the Riemann solution. To ensure uniformity of the interface points and the correct topological structure of the interface, the front

geometry has to be described and correctly resolved.

Another method, due to Osher and Sethian, applies the Eulerian approach to describe the fluid interface. Instead of considering the interface as a collection of points, this method considers a level set function in the whole space; the interface is just a special level surface of this function in the space. The embedded interface together with the whole level set function moves as a special physical quantity with the fluid and may be reconstructed at any time.

These two methods can be illustrated by the following examples in one dimensional space. Given the velocity of a mass point $v = v(x, t)$, the position of the mass point can be described by the equation of motion

$$\frac{dx}{dt} = v(x, t), \quad (1.1)$$

subject to the initial condition $x(0) = x_0$. On the other hand, the motion of the mass point can be described by a PDE

$$u_t + vu_x = 0. \quad (1.2)$$

If at the initial time $u(x_0, 0) = u_0$, the subsequent position of the mass point can be found by solving $u(x(t), t) = u_0$, where $u(x, t)$ is the solution of PDE (1.2) at time t . This is obvious because solutions of Eq. (1.1) are the characteristics of the hyperbolic PDE Eq. (1.2). The method using Eq. (1.1) is the Lagrangian approach and the method using Eq. (1.2) is the Eulerian approach to describe the motion of the mass point initially at x_0 .

2. The 3D Front Tracking Method

2.1. Outline

Front tracking method in 3D applies the same principle as the 2D front tracking method. It separates the fluids according to their components and applies finite difference method to each component of the fluids. The fluid interface is described by a set geometrical surfaces (curves in 2D) and each point on the surface is propagated by the solution of a Riemann problem.

Among difficulties in extending 2D front tracking method to 3D front tracking method are:

- (a). Description of the 3D interface,
- (b). 3D unstructured grid near interface,
- (c). 3D state interpolation and coupling,
- (d). Normal propagation and tangential flux,
- (e). Resolution of interface tangling,
- (f). Parallelization.

2.2. 3D Fluid Interface and Interior Coupling

The 3D interface data structure contains a global interface structure, surface data structure and surface element structure and is a superset of the 2D interface data structure.

Delaunay triangulation is used to construct an unstructured volume grid for interpolation of states near fluid interface.

- (a). Theorem: Given a set S of N points in space, for each point p_i in S , there is a locus of points in the space that are closer to p_i than any other point of S . The boundaries of these loci form the Voronoi diagram. The plane dual of the Voronoi diagram is the Delaunay triangulation of the set S
- (b). Incremental Method for Delaunay Triangulation
 - (i). Select any four points to make the first tetrahedral as the base Delaunay triangulation.
 - (ii). For an existing Delaunay triangulation, test a new point.
 - (iii). List all tetrahedrals whose circumsphere enclose the new point.
 - (iv). If the list is null (outside), connect the new point with all visible sides of the convex hull to form a new Delaunay triangulation.
 - (v). Else, destroy all inner boundaries of listed tetrahedrals and connect the new point to all the remaining sides to form new Delaunay triangulation.

2.3. The Reason for 3D Front Tracking

The 3D front tracking method gives an active description of the fluid interface. The level set method, even with a second order ENO method, still has a density diffusion of about five computational mesh blocks across the interface. The front tracking method is intended to maintain the physical discontinuity throughout the numerical computation by applying the Riemann solution at the interface. The geometry of the fluid interface will make it easy to compute functions such as surface curvature and to implement surface physical quantities such as surface tension.

3. The Level Set Method

3.1. Mathematical Model

The 3D inviscid Euler equations for compressible gases are:

$$\frac{\partial \rho_j}{\partial t} + \frac{\partial(\rho_j u_j)}{\partial x} + \frac{\partial(\rho_j v_j)}{\partial y} + \frac{\partial(\rho_j w_j)}{\partial z} = 0$$

$$\frac{\partial}{\partial t} [\rho_j (E_j)] + \frac{\partial}{\partial x} [\rho_j u_j (E_j + P_j)] + \frac{\partial}{\partial y} [\rho_j v_j (E_j + P_j)] + \frac{\partial}{\partial z} [\rho_j w_j (E_j + P_j)] = \rho_j w_j g.$$

$$\frac{\partial \rho_j u_j}{\partial t} + \frac{\partial(\rho_j u_j^2 + P)}{\partial x} + \frac{\partial(\rho_j u_j v_j)}{\partial y} + \frac{\partial(\rho_j u_j w_j)}{\partial z} = 0$$

$$\frac{\partial \rho_j v_j}{\partial t} + \frac{\partial(\rho_j u_j v_j)}{\partial x} + \frac{\partial(\rho_j v_j^2 + P)}{\partial y} + \frac{\partial(\rho_j v_j w_j)}{\partial z} = 0$$

$$\frac{\partial \rho_j w_j}{\partial t} + \frac{\partial(\rho_j u_j w_j)}{\partial x} + \frac{\partial(\rho_j v_j w_j)}{\partial y} + \frac{\partial(\rho_j w_j^2 + P)}{\partial z} = \rho_j g$$

The polytropic equation of state used below is:

$$P = (\gamma_j - 1)\rho_j(E_j - 1/2(u_j^2 + v_j^2 + w_j^2))$$

The equation of the level function is:

$$\psi_t + u\psi_x + v\psi_y + w\psi_z = 0.$$

At any time, the fluid interface is given by:

$$\psi(x, y, z, t) = 0$$

3.2. Numerical Method

The conservation form of the 3D Euler equations are:

$$\mathbf{q}_t + \mathbf{F}_x^1 + \mathbf{F}_y^2 + \mathbf{F}_z^3 = \mathbf{H}$$

The one-step finite difference equation can be written as

$$\mathbf{q}^{n+1} = \mathbf{q}^n + \Delta t (L^1(\mathbf{q}^n) + L^2(\mathbf{q}^n) + L^3(\mathbf{q}^n) + H(\mathbf{q}^n))$$

The ENO calculation of the net flux in i -direction gives

$$L^i = (F^i)_x$$

$$F^i = \frac{1}{2}(f(q_L) + f(q_R)) - \frac{1}{2} \int_{q_L}^{q_R} |A(q)| dq$$

where A is the 5×5 matrix

$$A = \begin{bmatrix} 0 & 1 & 0 & 0 & 0 \\ u(K-H) & H - (\gamma-1)u^2 & (1-\gamma)uv & (1-\gamma)uw & \gamma u \\ K - u^2 & (3-\gamma)u & (1-\gamma)v & (1-\gamma)w & (\gamma-1) \\ -uv & v & u & 0 & 0 \\ -uw & w & 0 & u & 0 \end{bmatrix},$$

and $K = 1/2(u^2 + v^2 + w^2)$

The matrix A has five eigenvalues, $u + c$, $u - c$, u , u , u . The right eigenvectors of the matrix A are:

$$T = \begin{bmatrix} 1 & 1 & 1 & 1 & 1 \\ H + uc & H - uc & K & K & -2v^2 & K & -2w^2 \\ u + c & u - c & u & u & u \\ v & v & v & -v & v \\ w & w & w & w & -w \end{bmatrix}.$$

The second order TVD scheme in time is:

$$\mathbf{q}^{n+1} = \mathbf{q}^n + \frac{1}{2}(\mathbf{m}_1 + \mathbf{m}_2)$$

where

$$\mathbf{m}_1 = \Delta t L(\mathbf{q}^n)$$

$$\mathbf{m}_2 = \Delta t L(\mathbf{q}^n + \mathbf{m}_1)$$

The CFL condition is:

$$\Delta t \leq \frac{2}{3} \max(|u|/\Delta x + |v|/\Delta y + |w|/\Delta z + c\sqrt{1/\Delta x^2 + 1/\Delta y^2 + 1/\Delta z^2})^{-1}.$$

3.3. Reconstruction of 3D Interface

The three dimensional fluid interface can be reconstructed at any time using the level function $\psi(x, y, z, t)$. Such a reconstruction can be used for illustration of the time dependent surface. Ultimately, we will be interested in the geometric structure of the interface because it is our intention to separate the fluid components and apply the finite difference solver to each domain individually. This will enable us to increase the resolution of the discontinuity using concepts from the front tracking method.

Triangulation of the surface is performed within each computational mesh block. Since each vertex point of the mesh block can have two different signs of ψ , there are total of 2^8 different topological configurations possible for a given block. Through rotation, we can group them into 12 basic types of configurations. Each basic type of configuration is triangulated accordingly.

3.4. Numerical and Experimental Comparison.

We have simulated the 3D bubble motion with variation of the following dimensionless parameters: the Atwood number

$$A = \frac{\rho_2 - \rho_1}{\rho_2 + \rho_1},$$

the compressibility

$$M^2 = g \lambda / c_b^2$$

and the bubble aspect ratio

$$a_p = \frac{\lambda_y}{\lambda_x}.$$

The 3D single bubble simulations have been compared with the experimental result by Taylor:

$$V_b = C \sqrt{gAR}$$

where C is a dimensionless constant ($C = 0.49$ for a 3D bubble with $A = 1$).

Preliminary simulation of bubble envelop in 3D randomly perturbed Rayleigh-Taylor instability has also been attempted to compare with the experiments by Read and Youngs.

$$h_{av}(t) = \alpha Agt^2$$

3.5. Results from numerical simulation.

(1). Table 1 shows the results of simulation of 3D single bubble velocity on different Atwood number.

A	0.33	0.67	0.82	1
C	0.36	0.46	0.50	0.49
C/\sqrt{A}	0.63	0.56	0.55	0.49

Table 1. Results of single bubble simulation with varying Atwood numbers. The last column represents data give by Taylor for incompressible fluids.

(2). Table 2 shows the results of simulation of 3D single bubble velocity on different aspect ratio.

a_p	1	1.5	2	∞
V_{term}	0.13	0.11	0.10	0.08
C	0.50	0.42	0.37	0.30
C/\sqrt{A}	0.55	0.46	0.41	0.33

Table 2. Numerical results of simulations with different a_p .

(3). Figure 3-5 show the fluid interfaces of a single bubble, single spike and bubble envelop respectively.

4. Domain Decomposition for Parallelization

Both the memory and the CPU time of a 3D computation in fluid dynamics suggest the use of a parallel computer. This is especially true if we wish to use the 3D code to study random interface chaotic mixing of the two fluids in the late stage of Rayleigh-Taylor instability. The initial random surface may contain large numbers of unstable modes. A refined computational mesh is required to give a high resolution of each participating mode. In our study, a domain decomposition method is used to distribute the load of the computation into many parallel processors of a MIMD computer, each with its own memory and CPU.

Figure 1 shows the parallelization algorithm. Assume N_c is the total number of processors used for the computation. The overall computational domain is decomposed into $n_x \times n_y$ sub domains, where

$n_x \times n_y = N_c$. For each subdomain, the rectangular mesh of states is extended by a buffer zone with the width of two mesh blocks, so that the computation of the interior states at each boundary point does not have to reference points in its neighboring subdomain. States in buffer zones are initially copied from the corresponding mesh blocks in neighboring subdomains. At each computational time step, the buffer states are updated at synchronization points. There are several synchronization points for a time step. For the level set method, the first synchronization point is after the computation of m_1 and the second one is after the computation of q^{n+1} . Since the computation of ψ is one step, only one synchronization is needed for updating ψ in the buffer zone.

References

- [1] I.-L. Chern, J. Glimm, O. McBryan, B. Plohr, and S. Yaniv, *Front Tracking for Gas Dynamics*, J. Comp. Phys., 62, 83, 1986.
- [2] C. Gardner, J. Glimm, O. McBryan, R. Menikoff, D. H. Sharp, and Q. Zhang, "The Dynamics of Bubble Growth for Rayleigh-Taylor Unstable Interfaces", *Phys. Fluids*, 31, 447, 1988.
- [3] J. Glimm, X. L. Li, Q. Zhang, R. Menikoff, and D. H. Sharp, "Statistical Theories of Rayleigh-Taylor Instability for Compressible Fluids", *Advances in Compressible Turbulent Mixing*, Springer-Verlag, 85, 1992.
- [4] J. Glimm and O. McBryan, "A Computational Model for Interfaces", *Adv. Appl. Math.*, 6, 422, 1985.
- [5] W. Mulder, S. Osher, and J. Sethian, "Computing Interface Motion in Compressible Gas Dynamics", *J. Comp. Phys.*, 100, 209, 1992.
- [6] S. Osher and J. Sethian, "Front Propagation with Curvature-Dependent Speed: Algorithm Based on Hamilton-Jacobi Formulations", *J. Comp. Phys.*, 79, 12, 1988.
- [7] K. I. Read, "Experimental Investigation of Turbulent Mixing by Rayleigh-Taylor Instability", *Physica* 12D, 45, 1984.
- [8] J. A. Sethian, "Numerical Algorithms for Propagating Interfaces: Hamilton-Jacobi Equations and Conservation Laws", *J. Differential Geometry*, 31, 131, 1990.
- [9] C. W. Shu, and S. Osher, *J. Comp. Phys.*, 83, 32, 1989.
- [10] G. I. Taylor, *Proc. Royal Soc. London*, A201, 192, 1950.

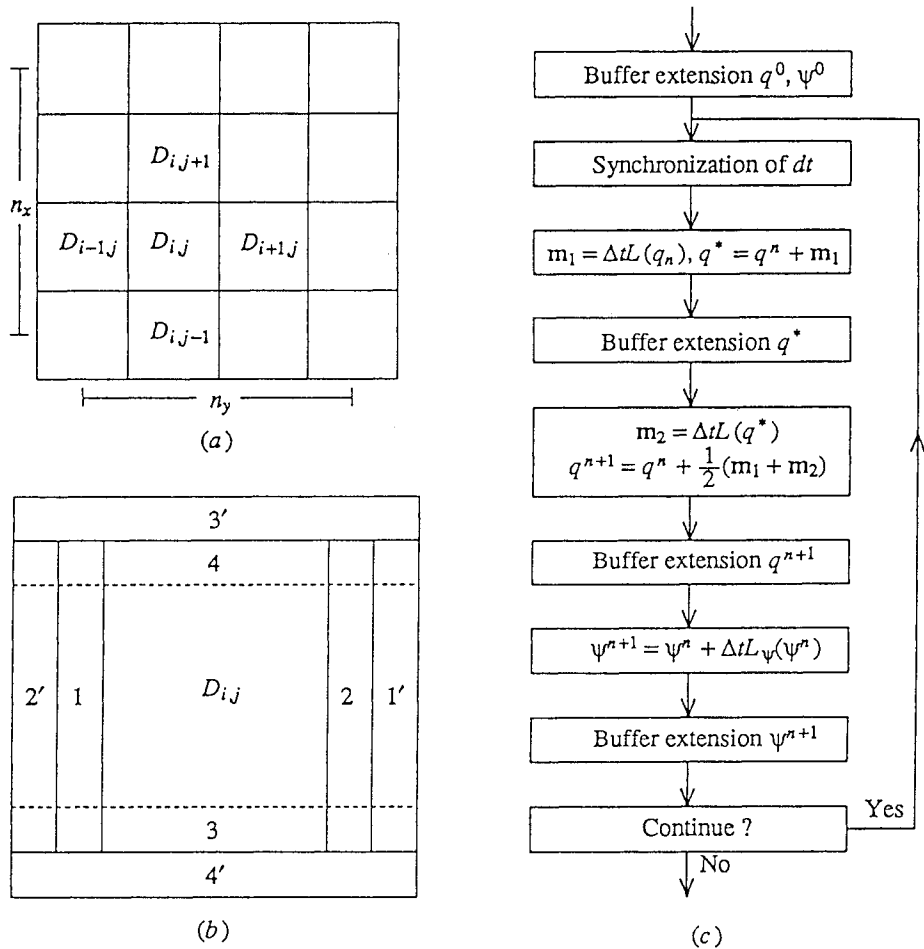


Figure 1. Parallelization diagrams for 3D interior solvers. Figure 1(a) shows the division of processors for the whole computational domain. Total of $n_x \times n_y$ nodes are used. Each node is used to compute a 3D subdomain. Every subdomain D_{ij} has its x -neighbours $D_{i-1,j}$ and $D_{i+1,j}$ and y -neighbours $D_{i,j-1}$ and $D_{i,j+1}$. Figure 1(b) shows the buffer extension and update. Data in region 1 and 2 are first sent to its left and right neighbours respectively, while data in 2' and 1' are received from its left and right neighbours. Then data in 3 and 4 are sent to its lower and upper neighbours and data in 4' and 3' are received from its lower and upper neighbours. Figure 1(c) shows the program flow chart of the second order TVD scheme.

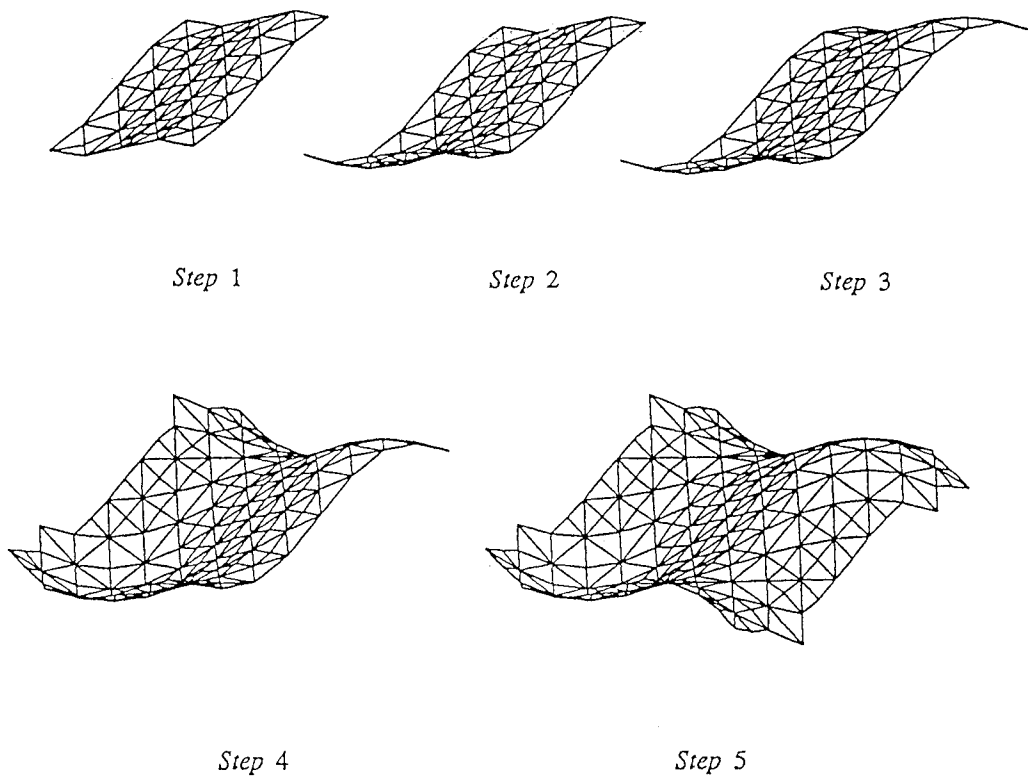


Figure 2. Procedures of interface buffer expansion in 3D front tracking method. Steps 1-3 show the interface expansion in x -direction and steps 4-5 show the continuing expansion in y -direction.

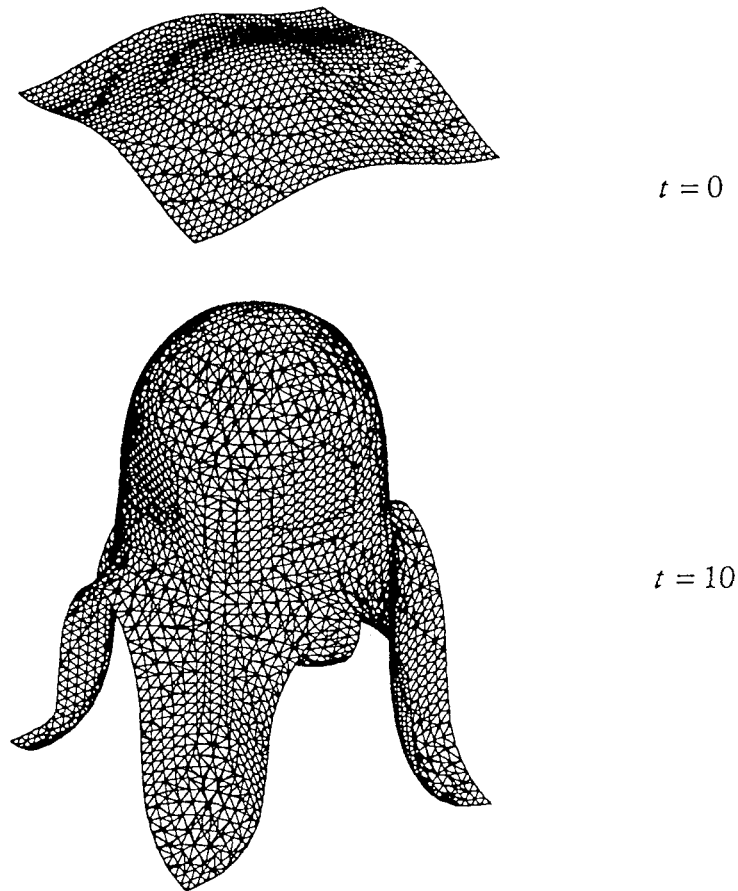


Figure 3. Simulation of interface evolution of Rayleigh-Taylor instability using the 3D level set method. This picture shows the bubble of light fluid rising to the ceiling. The bubble reaches a terminal velocity at about $t = 8$. The computational mesh is $30 \times 30 \times 60$.

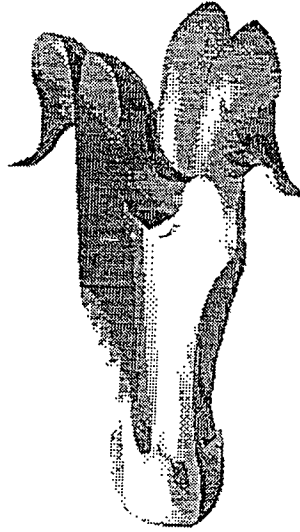


Figure 4. The elongated spike at late time of the simulation ($t = 12$). The aspect ratio a_p is 1.5. The bubble front tends to be unstable and broke into two modes. The tip of the spike shows the roll-up of the heavy fluid.

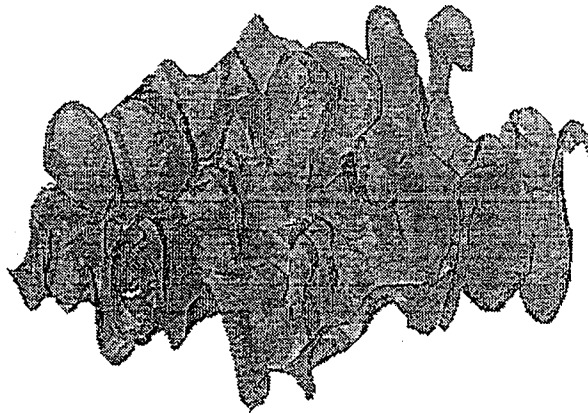


Figure 5. Fluid interface in simulation of randomly perturbed Rayleigh-Taylor instability. The simulation is performed on an Intel/IPSC-860 hypercube using $4 \times 4 = 16$ nodes. The computational mesh in each subdomain is $10 \times 10 \times 120$ and the total computational domain has a combined $40 \times 40 \times 120$ computational mesh. The average compressibility in this case is $M^2 = 0.2$ and the Atwood number is $A = 0.33$ (density ratio $D = 2$). The acceleration coefficient α (Eq. 4.2) of the maximum bubble envelop for each subdomain is given in Table 4. The global average is $\bar{\alpha} = 0.066$.

Rayleigh-Taylor and Kelvin-Helmholtz mixing in a large eddy simulation model

T. McAbee, Lawrence Livermore National Laboratory

Outline of the Problem

- 1) We take the objectives of mix or turbulence modelling to be the coupling of unresolved scales of interaction between fluids to the resolved scales.
- 2) We assume that the Navier-Stokes equations are the correct equations of motion, and that we simply have not resolved all scales of interaction in our numerical simulations.
- 3) We wish to model various instabilities, such as Rayleigh-Taylor, Kelvin-Helmholtz, or Richtmyer-Meshkov, by introducing subgrid-scale couplings into the Navier-Stokes equations. We adopt an approach known as a Large Eddy Simulation (LES) and develop a one-equation turbulence model to express the temporal and spatial development of mix.
- 4) Lastly, we may choose to relax assumption (2) above and introduce symmetry-breaking terms into the model through direct feedback of turbulent energy into resolved perturbations in the velocity field.

Some Definitions

μ_t is the turbulent viscosity coefficient.
 S_{ct} is the turbulent Schmidt number (relates viscosity to mass diffusion).
 Pr_t is the turbulent Prandtl number (relates viscosity to energy diffusion).
 Δ is the local length scale for turbulence, here taken as the local mesh size.
 A_t and C_B are coefficients for the creation of turbulent energy through shear forces (Kelvin-Helmholtz) and buoyancy forces (Rayleigh-Taylor) respectively.
 D_t controls the rate of dissipation of turbulent energy back into internal.
 α_{BS} is the coefficient for the Perturbative Backscatter model.
 β_{BS} controls the time-rate for feedback from the Perturbative Backscatter model.

Description of the Example Calculations

Mixing in Rayleigh-Taylor unstable situations is illustrated by a series of 2-D and 3-D numerical simulations. Calculations have been performed on an Eulerian hydrodynamics code which utilizes a non-diffusive advection scheme to preserve density gradients.

The initial conditions for all calculations use two regions of uniform density ideal gas, $\rho = 1$ to the left and $\rho = 2$ to the right, with adiabatic index $\gamma = 5/3$. Initial internal energies are determined such that gravitational equilibrium is attained (gravity accelerates to the left in all figures). A gravitational constant $g = 1$ is assumed. $P = (\gamma - 1)\rho e$.

Two methods are used to establish perturbations in the velocity field, which result in unstable flow of matter.

- 1) The Perturbative Backscatter model is used to seed perturbations based on the development of turbulent energy, K . The LES model describes the temporal and spatial evolution of this K -field.
- 2) An initial velocity perturbation is made at the fluid interface, using the magnitude of perturbations suggested by the Perturbative Backscatter model, but neglecting the LES model in the subsequent development of instability growth. In this approach the initial velocity perturbation is of equal magnitude, but random direction at each node. Thus, one degree of freedom exists in the 2-D simulations, while two exist in 3-D.

The growth rates of instabilities are similar for methods 1 and 2 above. A noticeable feature is the enhancement of growth rate in 3-D (by about 20%) relative to 2-D Cartesian or cylindrical geometries. This is in agreement with earlier calculations and experiments by D. Youngs and the AWE group.

Fundamental Equations

K-Equation

$$\frac{\partial}{\partial t}(\bar{\rho}K) + \frac{\partial}{\partial x^i}(\bar{\rho}K\bar{U}^i) = \frac{\partial}{\partial x^i} \left(\mu_t \frac{\partial K}{\partial x^i} \right) - \bar{P} \frac{\partial \bar{U}^i}{\partial x^i} + \Sigma_{ij} \frac{\partial \bar{U}^i}{\partial x^j} - \frac{D_t \bar{\rho} K^2}{\Delta} - S_{BS} + F_{BC}$$

Internal Energy Equation

$$\frac{\partial}{\partial t}(\bar{\rho}\bar{\epsilon}) + \frac{\partial}{\partial x^i}(\bar{\rho}\bar{\epsilon}\bar{U}^i) = \frac{\partial}{\partial x^i} \left(\frac{\mu_t}{P_{rt}} \frac{\partial \bar{\epsilon}}{\partial x^i} \right) - \bar{P} \frac{\partial \bar{U}^i}{\partial x^i} + \frac{D_t \bar{\rho} K^{3/2}}{\Delta} - F_{BC}$$

Momentum Equation

$$\frac{\partial}{\partial t}(\bar{\rho}\bar{U}_j) + \frac{\partial}{\partial x^i}(\bar{\rho}\bar{U}_j\bar{U}^i) = - \frac{\partial}{\partial x^j}(\bar{P} + P_t) + \frac{\partial \Sigma_{ij}}{\partial x^i} + R_j^{BS}$$

Continuity Equation

$$\frac{\partial \bar{\rho}}{\partial t} + \frac{\partial}{\partial x^i}(\bar{\rho}\bar{U}^i) = 0$$

Mass Species Equation

$$\frac{\partial}{\partial t}(\bar{\rho}\bar{X}_\alpha) + \frac{\partial}{\partial x^i}(\bar{\rho}\bar{X}_\alpha\bar{U}^i) = \frac{\partial}{\partial x^i} \left(\frac{\mu_t}{S_{ct}} \frac{\partial \bar{X}_\alpha}{\partial x^i} \right)$$

Mass Fraction

$$X_\alpha = \rho_\alpha / \rho$$

Turbulent Viscous Stress Tensor

$$\Sigma_{ij} = \mu_t \left(\frac{\partial \bar{U}_j}{\partial x^i} + \frac{\partial \bar{U}_i}{\partial x^j} - \frac{2}{3} \delta_{ij} \frac{\partial \bar{U}^i}{\partial x^i} \right)$$

Turbulent Pressure

$$P_t = \frac{2}{3} \bar{\rho} K$$

Rayleigh-Taylor and Kelvin-Helmholtz Instability Sources

Mixing Layer Depth

$$h_{RT} = \alpha_{RT} \left(\frac{\rho_1 - \rho_2}{\rho_1 + \rho_2} \right) g t^2$$

Buoyancy Source Term

$$F_{BC} = -C_B \bar{\rho} \Delta \frac{\nabla (\bar{\rho} - \bar{\rho}_{ad})}{\bar{\rho}} \cdot \frac{\nabla \tilde{P}}{\bar{\rho}} \sqrt{K + \beta_{RT}^2}$$

$$\beta_{RT} = \alpha_{RT} \Delta \frac{\nabla (\bar{\rho} - \bar{\rho}_{ad})}{\bar{\rho}} \cdot \frac{\nabla \tilde{P}}{\bar{\rho}} (dt)$$

Mixing Layer Depth:

$$h_{KH} = \alpha_{KH} |U_1 - U_2| t$$

Turbulent Viscosity Coefficient:

$$\mu_t = A_t \Delta \bar{\rho} \sqrt{K + \beta_{KH}^2}$$

$$\beta_{KH} = \alpha_{KH} \Delta \text{curl}(\bar{U})$$

Perturbative Backscatter Model

We wish to feed turbulent effects into the resolved scale with a magnitude characteristic of the turbulent energy and on a time scale associated with some turbulent eddy frequency.

Our objective is to remove the close coupling of the single-equation turbulence model from the arbitrary length scale which the model assumes.

Postulate:

- 1) a local scalar velocity perturbation, $\delta\text{-velocity} = \alpha_{BS} K^{1/2}$
- 2) this local scalar perturbation is randomly oriented in space; this is accomplished by choosing an angle (only one in 2D) randomly over 2π and distributing the perturbation by sine and cosine of this angle to each direction
- 3) a characteristic turbulent eddy time $\tau = \beta_{BS} \Delta / K^{1/2}$
- 4) perturbations are made only on local time scales of order τ , which evolves in time and space with the turbulent K field

Assumption (4) is carried through by evaluating a temporal perturbation probability at each node in each cycle, given by

$$P = 1 - e^{-dt/\tau}$$

If a random number is less than the probability P the perturbation is made.

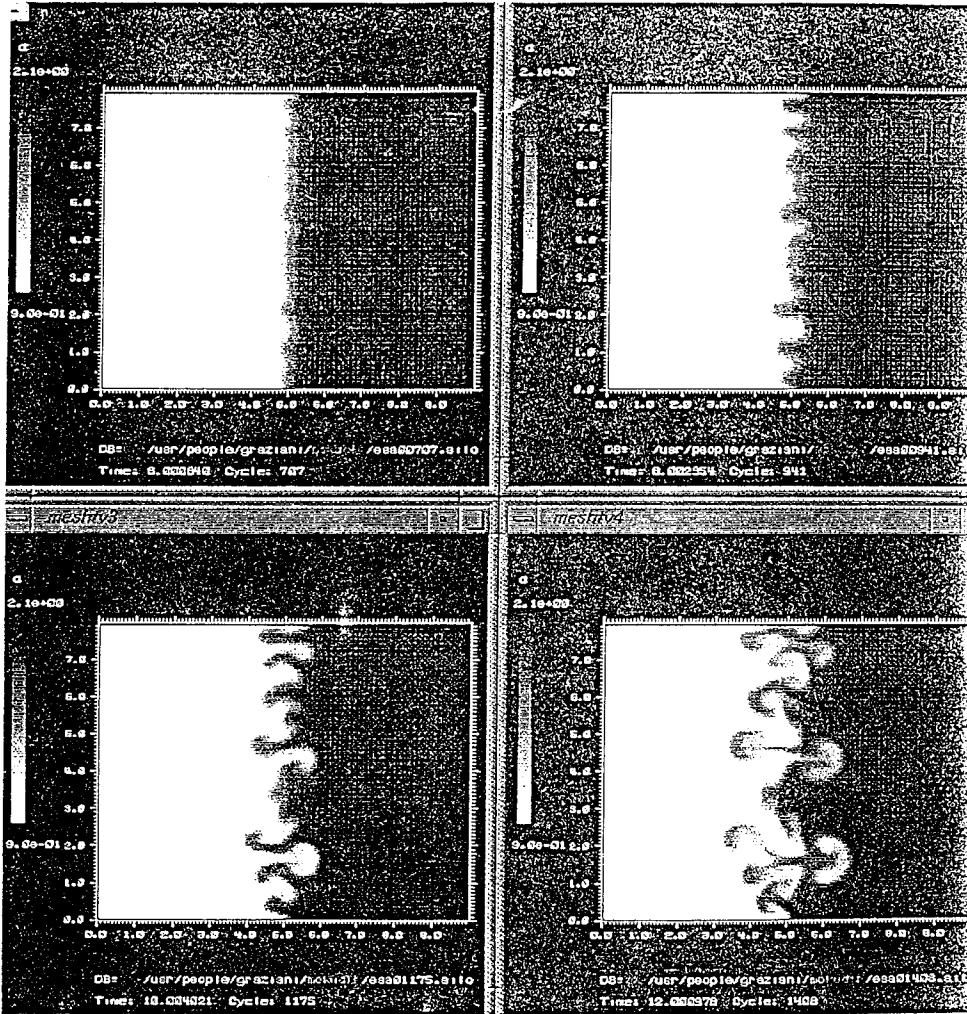


Figure 1: Rayleigh-Taylor instability growth in an LES model with Perturbative Backscatter. $G = 1 \text{ cm}/\mu\text{s}^2$, $A_t = 1/3$; times are 6 - 12 μs . The resolution scale is uniform 0.1 cm in the x- and y-directions (Cartesian coordinates). Figures 1-3 indicate the near independence of mix depth on resolution. This results from use of Perturbative Backscatter in a 1-Equation LES model.

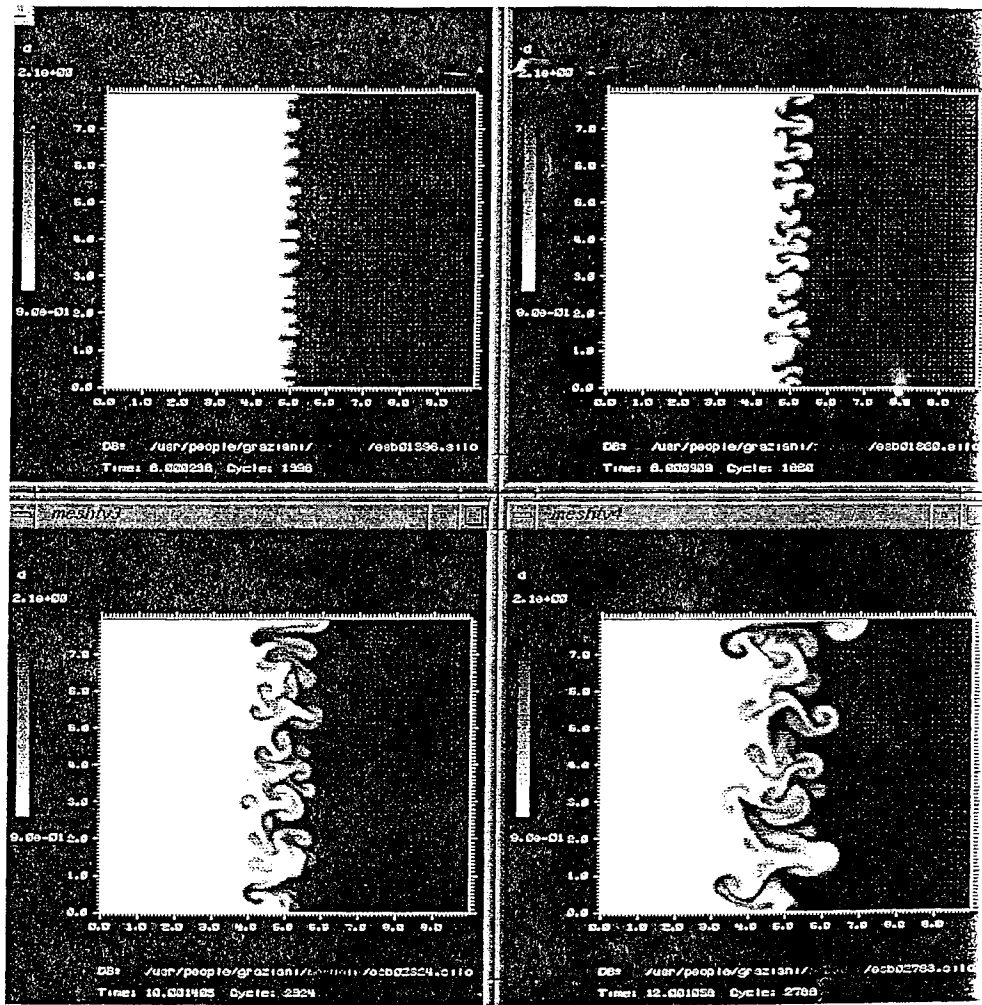


Figure 2: Rayleigh-Taylor instability growth in an LES model with Perturbative Backscatter. $G = 1 \text{ cm}/\mu\text{s}^2$, $A_t = 1/3$; times are 6 - 12 μs . The resolution scale is uniform 0.05 cm in the x- and y-directions (Cartesian coordinates).

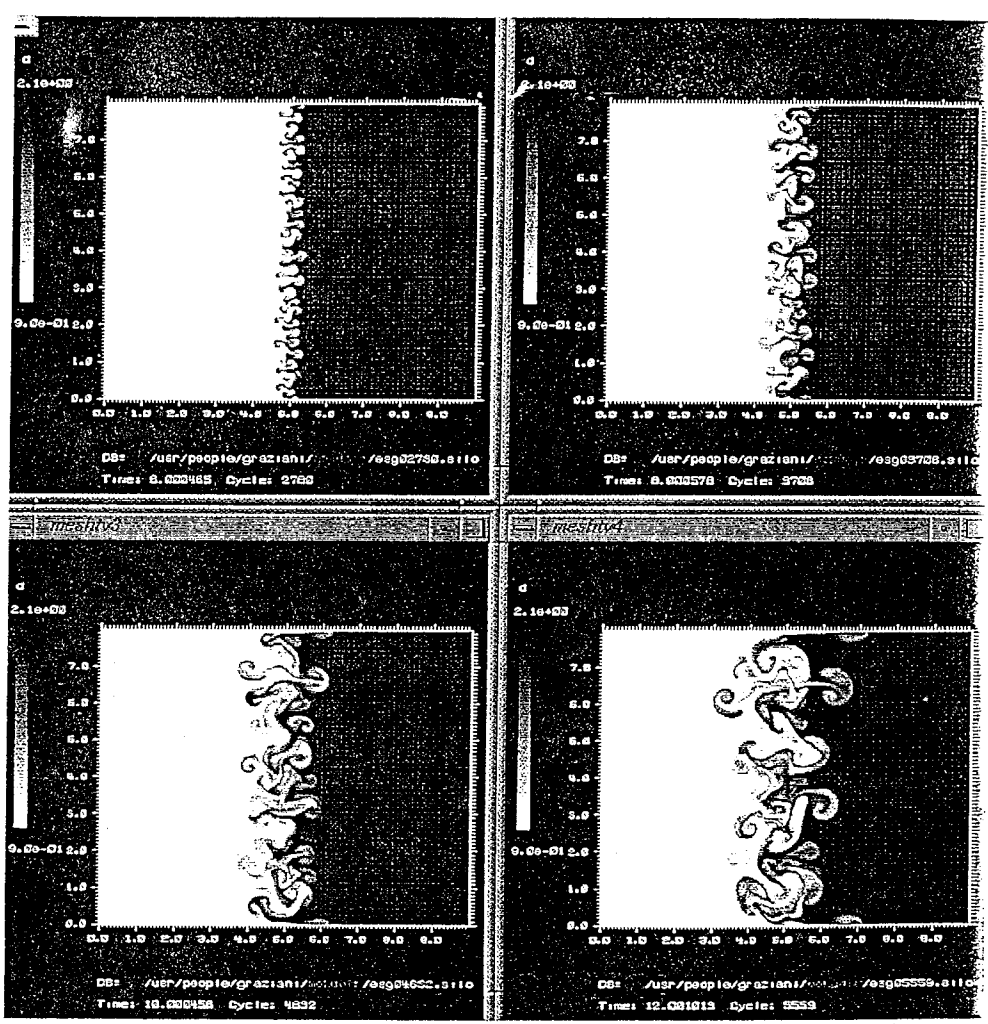


Figure 3: Rayleigh-Taylor instability growth in an LES model with Perturbative Backscatter. $G = 1 \text{ cm}/\mu\text{s}^2$, $A_t = 1/3$; times are 6 - 12 μs . The resolution scale is uniform 0.025 cm in x- and y-directions (Cartesian coordinates).

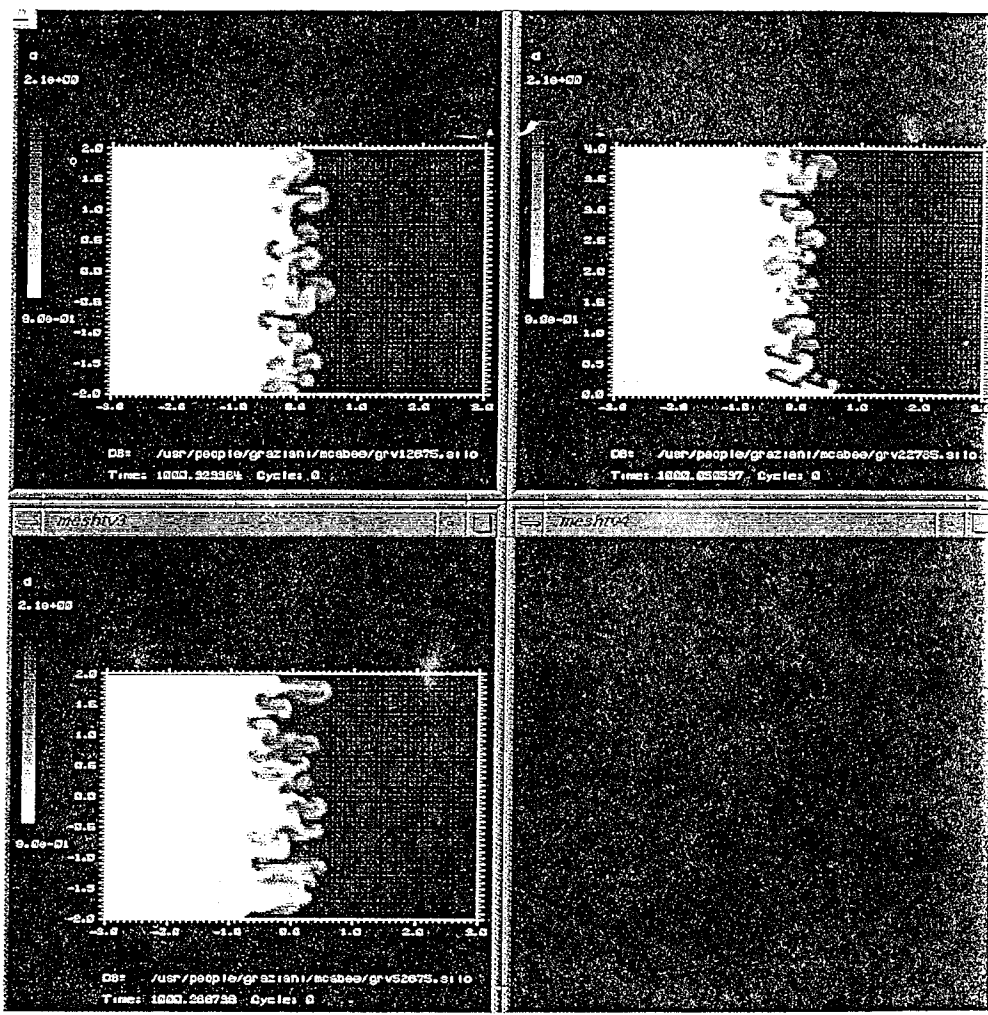


Figure 4: Rayleigh-Taylor instability growth from a seeded velocity perturbation as a function of geometry. A randomly oriented velocity perturbation at the interface, with constant magnitude $0.0001 C_s$, is set at $t = 0$. Frame 1 is for 2D x-y geometry, Frame 2 for 2D r-z, and Frame 3 for 3D x-y-z. All calculations were performed on one Eulerian hydrodynamics code which used a non-diffusive remap treatment to preserve density gradients.

WAVE PROCESSES EFFECT
ON THE DYNAMICS OF TURBULENT MIXING AT
LIQUID LAYER SURFACE ACCELERATED BY COMPRESSED GAS

N.V.Nevmerzheritsky, F.F.Meshkov, A.G.Ioilev, I.G.Zhidov, I.G.Pylev,
S.S.Sokolov

Russian Federal Nuclear Center
All-Russian Research Institute of Experimental Physics
607200, Arsamas, Nizhnii Novgorod region
-Russia

INTRODUCTION

If the interface between two different density fluids acceleratively moves, the acceleration being directed from the lighter fluid (with ρ_2 density) to the heavier one (ρ_1), then the first becomes unstable (RT-instability [1,2]). RT-instability development leads to the turbulent mixing of fluids at the unstable interface [3-7].

In the case of ideal fluids and $g = \text{const}$ the mixing zone width (L) and the depth of the light fluid penetration into the heavier one (h_1) must grow with time as:

$$L = \alpha A g t^2 \quad \text{and} \quad h_1 = \alpha_1 A g t^2 = 2\alpha_1 A S,$$

where $A = (\rho_1 - \rho_2) / (\rho_1 + \rho_2)$, S - the path made the interface, t - time, and α и α_1 - empirical constants.

The results of experimental investigations of the turbulent mixing associated with RT-instability development [4,5,7] confirm these dependencies, although various authors have obtained different values of α_1 (from 0.04 to 0.07).

Results of experimental investigation of the turbulent mixing zone (TMZ) development at the interface of jelly layer (jelatine solution in water) accelerated by explosion products (EP) of the explosive gas mixture (EGM) were reported in [8]; in this case, the value of $\alpha_1 \approx 0.12$ was obtained. Results of experimental investigation of the TMZ evolution at the surfaces of liquid layers (with different thicknesses) accelerated by compressed gas under different initial pressures were reported in [9], the value of $\alpha_1 \approx 0.053 - 0.126$ were obtained; the relation between α_1 value and the average pressure gradient value in the layer was observed. This observations leads to possibility of wave processes in a liquid layer effects on the TMZ evolution.

The experimental data presented in this paper confirm the suggestion [9] of the wave processes effects on the dynamics of the mixing zone.

EXPERIMENTAL TECHNIQUES.

The experimental set up (Fig.1) was similar to that of experiments described in [8]. The water layer WL was placed in the $4 \times 4 \text{ cm}^2$ square channel with PMMA walls. The layer was held in the channel by means of the plate PJ hermetically sealed around the periphery by jelatine jelly. The confined volume of chamber CH was filled with EGM - acetylene - oxygen mixture ($\text{C}_2\text{H}_2 + 2.5\text{O}_2$) by multiple pumping thereof through gas inlets. The lower end of outlet channel OC was open.

EGM in the chamber was detonated at 64 points located

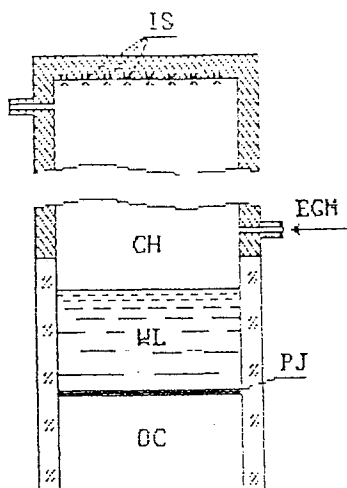


Fig.1 Scheme of the experimental apparatus.

Designations: CH - chamber, EGM - explosive gas mixture, IS - ignition system, WL - water layer, PJ - plate, OC - outlet channel.

uniformly across the chamber upper end section. EP accelerated water layer downwards, RT-instability developed at the EP - water interface, resulting in the formation of TMZ growing in width with time.

In experiments the chamber height (H_{ch}) and water layer thickness (H_{w1}) were varied.

The layer acceleration and TMZ evolution at the unstable interface were registered by frame and slit streak cameras. In the second case, the shadow graph techniques were used.

Some experiments involved pressure measurements near the stable layer surface using piezoelectric pressure gauges.

In the experiments, the initial average EP pressure varied insignificantly, but shock and rarefaction waves passed through TMZ.

The effects of these waves on the TMZ evolution dynamics were the subject of the investigation.

RESULTS AND DISCUSSION

The chamber height H_{ch} (500 - 40mm) and water layer thickness H_{w1} (25 - 65mm) were varied in experiments.

Fig.2,a shows the frame camera record for the experiment with $H_{ch} = 500\text{mm}$ and $H_{w1} = 29\text{mm}$ (No. 689). Fig.2,b shows the streak camera record for the experiment with $H_{ch} = 120\text{mm}$ and $H_{w1} = 25\text{mm}$ (No. 612), which was obtained by shadow method. In Fig.2,c one can see the frame camera record for the experiment with $H_{ch} = 40\text{mm}$ and $H_{w1} = 65\text{mm}$ (No. 710).

The streak camera record (Fig.2,b) shows detonation and shock waves in EP and a sequence of acoustic waves W passing through the water layer as it is accelerated by EP. When the detonation wave has reached the water layer interface, the shock waves run into EP and the layer. Having passed through the layer, the shock wave refracts at the layer-air interface - the sound wave runs into the air, and rarefaction wave runs into the layer. When the latter reflects from the water - EP interface, a weak shock wave returns into the layer, etc. At the background of this wave sequence attenuating with time, clearly prominent are the waves appearing in the layer, when shock waves in EP reflect from it, and arriving at the layer interface at the times $t_2 \approx 0.18$, $t_3 \approx 0.4$ и $t_4 \approx 0.64$ ms as measured from the time when the detonation wave reaches the layer interface. Fig.3 shows the pressure record $P(t)$ near the lower (stable) layer interface obtained by piezoelectric gauge in the experiment No. 558 ($H_{ch} = 120$, $H_{w1} = 25$ mm).

On this record, there are pressure pulses correlating in time with the times of shock waves arriving at the layer interface in EP in experiment No. 612, standing out at the background of small-scale pressure oscillations with the period of $\sim 30 \mu\text{s}$ (due to acoustic waves



Fig. 2 Mixing zone development of the water layer surface, accelerated by explosion products: (EP) of explosive gas mixture. a) Frame camera record (Exp.N 689, Hch 500, Hw 29mm). b) Streak camera record (Exp.N 612, Hch 120, Hw 25mm). c) Frame camera record (Exp.N 710, Hch 40, Hw 65mm). Designated terms: CH - channel; WL - water layer; PJ - plate; OC - out let channel; ML - mixing layer; LW - detonation wave; Sep - shock wave in the EP; U1, U2, U3, U4 - waves of going into water layer of detonation and shock waves; W - rarefaction and rarefaction waves in water layer. Time in milliseconds.

in water layer).

The frame camera record of experiment No. 689 (Fig.2,a) shows the change in the TMZ image when a shock wave has passed through TMZ ($t \geq 0,98$ ms) - TMZ gets somehow cleared up. Changing of TMZ observed structure when a shock wave passed through it attracts attenuation. Shock wave may lead to changing of observed perturbations spectrum.

Thus, the results of the experiments show that shock and acoustic waves series attenuating in time passes through the layer (and TMZ).

The stable layer surface (X_1) position and TMZ front in the layer (X_2) as a function of time were determined from frame camera records. The depth of penetration of the lighter substance into the heavier one (h_1) was determined by the formula: $h_1 = H_{w1} - (X_2 - X_1)$. X_1 and X_2 measurement accuracy is ~ 0.3mm.

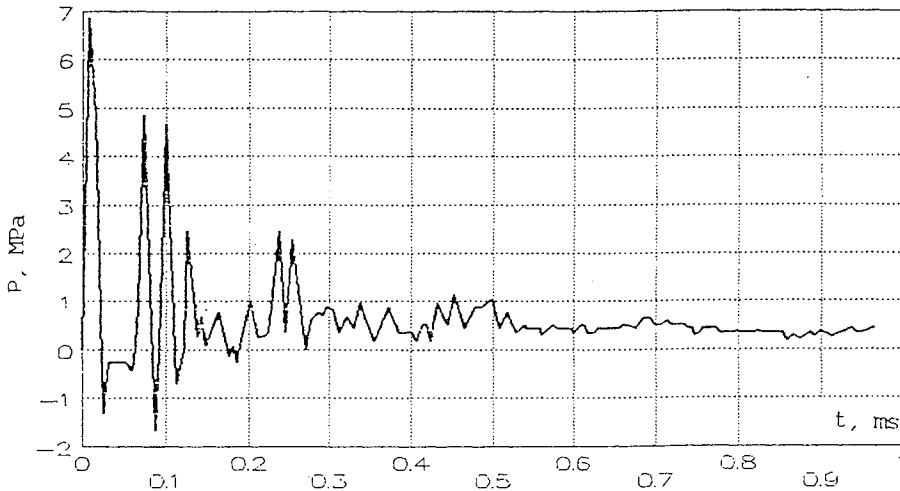


Fig.3. The pressure record $P(t)$ near the lower (stable) layer interface obtained of piezoelectric gauge in the experiment (No. 558, $H_{ch} = 120$, $H_{w1} = 25$ mm).

Fig.4,a shows dependencies of the path made by the layer, $S(t)$ ($S = X_1$); the layer acceleration $g(t)$ and $h_1(t)$ in experiment N 689. The measurement results for $S(t)$ were approximated by the 4th degree polynomial. The dependence $g(t)$ was obtained by double differentiation of the polynomial.

In the dependence $h_1(t)$, a step-like increasing at $t \approx 0.8$ ms is observed, which corresponds to the time of the first shock wave passing through TMZ from EP side (this time was determined from the streak records of the similar experiments). In this experiment, only one shock wave from EP side passed in the measurement duration due to the considerable chamber length ($H_{ch} = 500$ mm). In this case, the step-like increasing in the TMZ width is likely to be caused by turbulent mixing growing more intensively similarly to that observed when a shock wave passes through TMZ at gas-gas interface [10].

The observed small steps at times 0.25 and 0.55 ms are probably occasional and associated with measurements errors. In a set of analogous experiments the steps of this kind are not observed, the step-like increasing is observed only at the moments of the shock wave passes (from EP side) through TMZ.

For experiments involving variable (though constant in sign)

acceleration, the dependence h_1 is represented [4] as:

$$h_1 = \alpha_1 \cdot A \cdot \left(\int \sqrt{g} dt \right)^2 = \alpha_1 \cdot A \cdot (I(S))^2$$

Fig.4,b shows the dependence of $\sqrt{h_1}$ on $I(S)$ in experiment No. 689. The linear dependence approximating the experiment at one portion after the shock wave passed through TMZ, is shown here as well.

The results of analogous measurements for experiments with the chamber length $H_{ch} = 120\text{mm}$ (experiment N 559) and $H_{ch} = 40\text{ mm}$ (experiment N 710) are shown on Figs. 5,6. From the analysis of these results the following conclusions can be made: in these dependencies no step-like increasing is observed, which could be associated with shock waves passing through TMZ. As H_{ch} decreases, the frequency of shock waves coming to the layer interface from EP side increases, and recording equipment is likely failed to resolve these frequent sharp increasings. The latters would merge, thus resulting in the TMS growth rate increasing until attenuation of the wave processes. The TMZ growth rate decreases when waves are attenuated. In experiment No. 612 (and in No. 559), the attenuation time of wave processed as evaluated by the streak record is $t_{att} \approx 0.8\text{ ms}$. Correspondingly, in the dependence of $\sqrt{h_1}$ on $I(S)$ (Fig.5,b) for $I(S) \geq 6$, a significant TMZ growth rate decreasing is observed. In experiment No. 710, the same situation is observed: for $t_{att} \approx 0.4\text{ ms}$ TMZ growth rate starts to decrease when $I(S) \geq 2$ (Fig.6,b).

It should be noted, that a set of experiments (4-5) was performed for each of the cases described above and presented experimental results are typical examples chosen from each set.

The approximation of dependencies $\sqrt{h_1} \sim f(I(S))$ at portions 1) $t \leq t_{att}$ and 2) $t > t_{att}$ yields values $\alpha_1^{(1)}$ и $\alpha_1^{(2)}$, respectively. In experiment No. 559, the values $\alpha_1^{(1)} = 0.11$, $\alpha_1^{(2)} = 0.03$, were obtained. In experiment No. 710 these are $\alpha_1^{(1)} = 0.3 \pm 0.2$, $\alpha_1^{(2)} = 0.07 \pm 0.006$.

In other words, after the wave processes attenuation the turbulent mixing evolution reaches the mode approaching to a self-similar. The low $\alpha_1^{(2)}$ value in experiment 559 may be attributed to the errors associated with comparatively narrow range of values $I(S)$ the $\alpha_1^{(2)}$ value was determined from. Besides, more correct evaluation of α_1 in experiments of that kind, requires direct measurements of $g(t)$ dependency.

Unlike the above described experiments, in which the EGM detonation results in the sequences of shock waves, in the experiments presented in [9] the compressed gas accelerating the layer is immobile, but the initial stage of the layer acceleration is also related with a sequence of compression and rarefaction waves passing through them, thus possibly resulting in higher TMZ evolution rate. In the experiments presented in [9], α_1 measurements were performed for values $S \leq 16\text{ mm}$, which are significantly lower than S in the experiments described above. It is likely to be the cause of measuring in those experiment only $\alpha_1^{(1)}$ corresponding to wave processes in the layer, rather than measuring of α_1 values.

Thus, when liquid layer is accelerated by gaseous explosive mixture explosion products, three specific stages in the turbulent mixing zone evolution process can be distinguished.

1st stage - the initial perturbations growth and turbulent mixing zone formation. At this stage, the zone width growth is practically step like (for sufficiently high-level initial perturbations).

2nd stage - the turbulent mixing zone evolution at the unstable interface of the layer accelerated by the combined effects of explosion products pressure and a sequence of shock waves attenuating in time. At

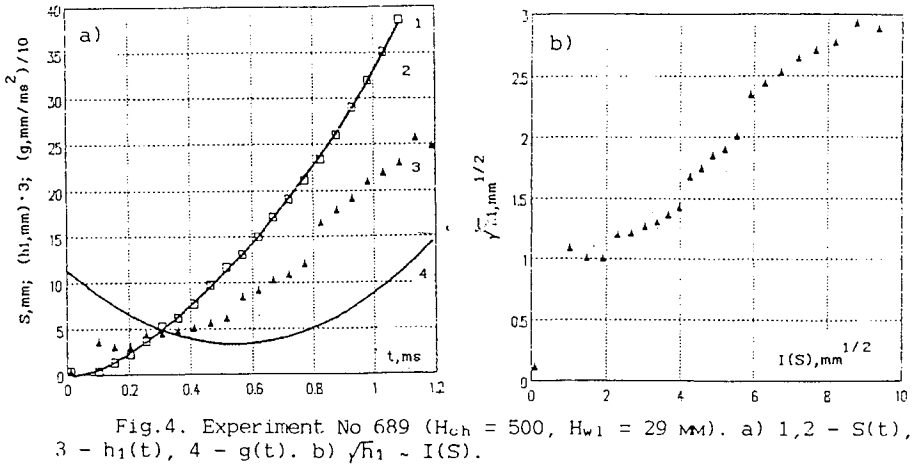


Fig.4. Experiment No 689 ($H_{ch} = 500$, $H_{w1} = 29$ mm). a) 1,2 - $S(t)$, 3 - $h_1(t)$, 4 - $g(t)$. b) $\sqrt{h_1} \sim I(S)$.

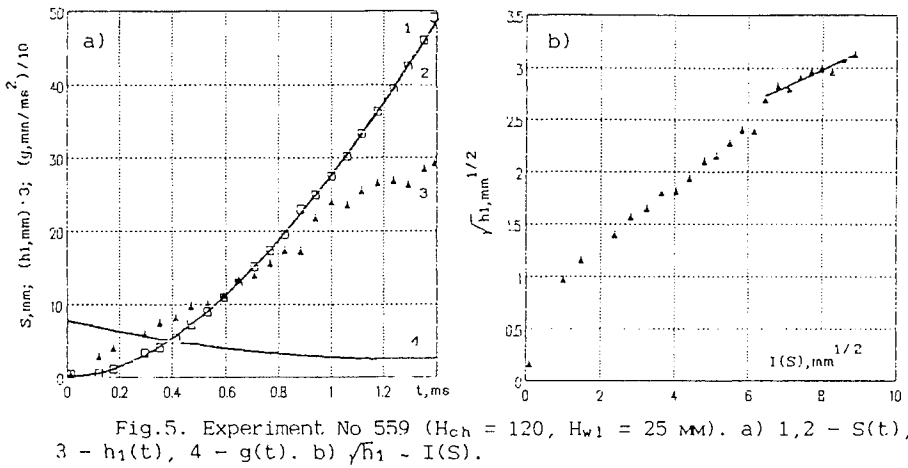


Fig.5. Experiment No 559 ($H_{ch} = 120$, $H_{w1} = 25$ mm). a) 1,2 - $S(t)$, 3 - $h_1(t)$, 4 - $g(t)$. b) $\sqrt{h_1} \sim I(S)$.

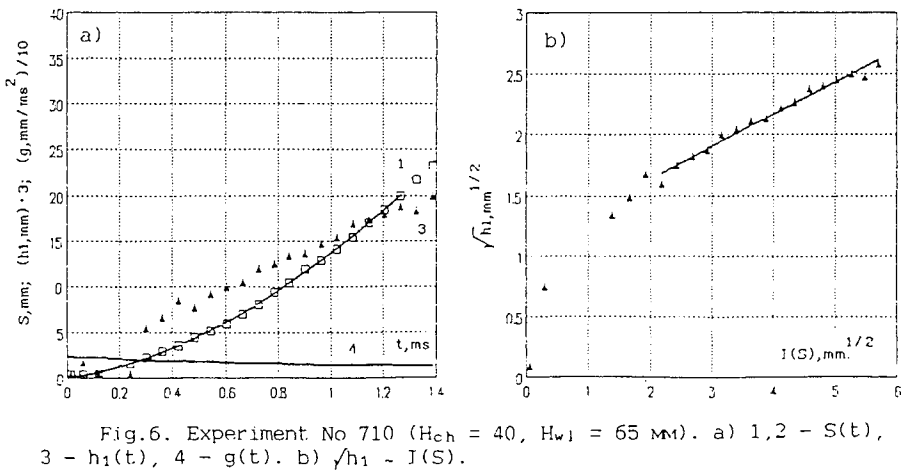


Fig.6. Experiment No 710 ($H_{ch} = 40$, $H_{w1} = 65$ mm). a) 1,2 - $S(t)$, 3 - $h_1(t)$, 4 - $g(t)$. b) $\sqrt{h_1} \sim I(S)$.

this stage, a high rate mixing zone growth ($\alpha_1 \geq 0.07$) is observed.

3rd stage - the mixing zone evolution reaches the mode, approaching the self-similar one, with value $\alpha_1 \approx 0.07$.

Furthermore, the time needed for turbulent mixing to approach the self-similar mode depends on the attenuation time of shock wave processes in liquids (gases) layers; the higher is the waves intensity and frequency of passage through the interface, the higher is the growth rate of the turbulent mixing zone width in the non-self-similar mode,

Presented results illustrate typical difficulties of self-similar turbulent mixing mode experimental realization.

REFERENCES

1. Lord Rayleigh, Proc. London Math. Soc., v.14, p.170, 1883.
2. G.I. Taylor. Proc. Roy. Soc., v.A201, p.192, 1950.
3. S. Belenky & E. Fradkin. Proc. of Phys. Inst. of Acad. of Sci., 29, 1965.
4. R. Read. Physica D12, p.45, 1984.
5. D. Youngs. Physica D37, p.270-287, 1989.
6. V.V. Nikiforov. Russian J. VANT (Problems of Atomic Sci. & Tech.). Ser. Theor. & Appl. Phys. Issue 1, p.3-8, 1985.
7. Y. Kucherenko, L. Shibarshov, V. Chitaikin, S. Balabin, A. Pylaev. 3rd Intl. Workshop on the Physics of Compressible Turbulent Mixing, Abbey of Royaumont (France)-June 17-19, p.427, 1991.
8. I.G. Zhidov, E.E. Meshkov, N.V. Nevmerzhitsky. Preprint No 56 Phys. Inst. of Acad. of Sci., p.63, Moscow, 1990.
9. E.E. Meshkov, N.V. Nevmerzhitsky. 3rd Intl. Workshop on the Physics of Compressible Turbulent Mixing, Abbey of Royaumont (France)-June 17-19, 1991, p.467.
10. V. Andronov, S. Bakhrakh, E. Meshkov, V. Mokhov, V. Nikiforov, A. Pevnitsky & A. Tolshnjakov. J. Exp. & Theor. Phys., 71, 2(8), p.806-811, 1976.

Two and Three Dimensional Analysis of Nonlinear Rayleigh-Taylor Instability

D. Ofer, J. Hecht, D. Shvarts

Physics Dept., Nuclear Research Centre Negev.

Z. Zinamon

Nuclear Physics Dept., Weizmann Institute of Science.

S.A. Orszag

Applied and Computational Math, Princeton University.

R.L. McCrory

Laboratory for Laser Energetics, University of Rochester.

Introduction

The linear stage of evolution of a single wavelength sinusoidal perturbation is well known and understood. During the last decade a large amount of work was devoted to the study of the late time evolution of the instability. At this nonlinear stage the perturbation evolves into the classical spike-bubble shape where the bubble reaches a constant terminal floating velocity and the spike accelerates downward. When the Atwood ratio is less than 1, there is an additional instability present that takes place along the sides of the spikes due to velocity shear. This instability, which is very similar to the classical Kelvin-Helmholtz instability, results in the formation of "hamerhead" shaped spikes which finally reach a constant velocity at late times.

The aim of this presentation is to report on some recent studies that were performed in order to further extend our understanding of the late time evolution of the RT instability. The issues reported here are:

- a) Two dimensional interaction of a small number of modes.
- b) Three dimensional single mode and two-mode-coupling evolution as compared with 2D results.
- c) RT evolution in three dimensional spherical geometry under conditions relevant to ICF targets.

Code descriptions

Our 2D code is LEEOR2D, a compressible ALE (Arbitrary Lagrangian Eulerian) hydro code into which we have incorporated an Interface-Tracking (IT) scheme similar to that presented by Youngs⁽¹⁾. The ALE scheme enables the code to take advantage of the benefits of both Lagrangian and Eulerian schemes. Each time-step is divided into two principal stages: (1) a Lagrangian stage in which mesh points flow with the physical material; (2) a rezone Eulerian stage in which the Lagrangian mesh is remapped to a more desirable mesh (specified by the user). In order to allow for the presence of more than one material in a problem and large fluid distortions, and still retain the full flexibility of the ALE scheme, we have added an IT scheme in the code. Each cell may contain an arbitrary number of materials. Basic material properties (such as density and internal energy) are stored separately, and the interface between materials in a cell is taken to be a straight line.

LEEOR3D is a direct generalization of LEEOR2D into three dimensions. Each computational cell is an 8 vertex box. The interface in the case of a mixed cell is a plane dividing the cell.

Mode-Coupling in Two Dimensions.

We study^[2] the interaction of a small number of modes in a two fluid RT instability at relatively late stages of development, i.e. the highly non-linear regime. We have identified strong interaction between modes that is both relatively long range in wave number space and also acts in both directions: short wavelengths affect long wavelengths and visa-versa.

In studying the interaction of mode pairs, we identify three distinct stages in the development of the inter-fluid mixing region: (i) the linear stage, in which each mode develops independently of other modes; (ii) the "ordered" non-linear stage, in which strong, highly non-linear interaction between modes is present but the flow remains relatively ordered and specific modes can still be identified and quantified; (iii) the "turbulent" stage, in which modal analysis (as defined in [2]) is no longer relevant and we have chosen to analyse statistical properties of the flow.

It has been found that during the second stage, mode pairs interact by suppressing the single mode growth rate, as compared with the growth rate of that mode when present alone. We have shown both how a long wavelength mode can suppress the growth of a short wavelength mode and visa versa. In each regime, the mechanism for suppression has been identified. The onset of suppression has been defined as the point when the suppressed mode has been reduced to 90% of the amplitude it attains when growing alone with the same initial amplitude. We have found that: (i) the onset of suppression occurs at a constant amplitude of the suppressing mode, regardless of the suppressed mode amplitude; (ii) the suppressing amplitude (of the suppressing mode) is of the form $a_{sup} = f(A)\sqrt{\lambda_1\lambda_2}$, where A is the Atwood ratio and $f(A)$ changes smoothly from 0.05 in the long suppressing short regime to about 0.15 in the short suppressing long regime (see Fig. 1).

In the short wavelength suppressing long wavelength regime, we have identified the cause of suppression to be a density gradient effect. The short wavelength bubble-spike structure creates an effective density gradient in which the long wavelength must grow. This reduces the exponential growth rate according to: $\gamma_{eff} = \sqrt{Ak_l g / (1 + k_l L)}$, where L is the effective gradient scale length found to be proportional to a_s^2/λ_s .

In the long wavelength suppressing short wavelength regime, the cause of suppression, in our opinion, is a shear effect in which the long wavelength flow field causes the short wavelength structures to flow laterally instead of vertically, thereby reducing their growth (see Fig. 2). This effect has not been observed when $A = 1$ at least for the duration of our simulation. This behaviour at $A = 1$ indicates that the main mechanism relevant to this phenomenon, at least for the time scales of our simulations, is probably the velocity shear, which is not present when $A = 1$, and not interface stretching. Comparison of the velocity of a linear-regime long wavelength mode to the non-linear-regime short wavelength velocity yields the empirical functional dependence of the onset for suppression on the wavelengths.

Multi-Mode Coupling

Of particular importance to ICF is the case where a broad band of short wavelength modes, representing the smaller scale laser and target inhomogeneities, appear with a discrete set of long wavelength modes, representing the large scale illumination nonuniformity. We have therefore extended our study on two mode coupling to the multi-mode case, especially cases in which some short wavelength modes (a band) interact with a single long wavelength mode. Fig. 3 shows such a case in which the initial modes are $l = 2$ and a band of $l = 11 - 20$, at both intermediate and late stages of the flow development. When more than one short wavelength mode are initially present, the analysis should distinguish between

two distinct mode interaction mechanisms: (i) the generation of a long wavelength mode through the interaction of two short wavelengths, as discussed by Haan^[3]; (ii) the non linear suppression of the long wavelength mode by the density gradient induced by the short wavelengths, as is described above^[2].

As regards to the first mechanism, we have found that Haan's second order mode coupling term (in which two modes generate additional modes with $l = l_1 \pm l_2$) can be extended much beyond his original estimates. We found that the formula suggested by Haan for a weakly non linear interaction can be used up to at least short wavelength amplitudes comparable to λ_s , and not merely $\sim 0.1\lambda_s$. We believe that this formula will be reasonably accurate as long as the long wavelength amplitude is small compared to its own wavelength.

After subtracting the contribution of the first mechanism to the long wavelength amplitude (including the correct phase), one is left with the effects of the second mechanism. We have found that one can generalise the above results, in which a single short wavelength mode is suppressing a long wavelength mode, to the case in which suppression is due to a band of short wavelength modes. The gradient length scale L is now defined by a sum a^2/λ of the short wavelength modes. We are currently working on further extending the definition of L to the late turbulent stage of flow development.

Three Dimensional Simulations and results.

We have performed 3D simulations of single-mode nonlinear growth, using the LEEOR3D code^[4]. Planar, 3D and cylindrical modes were compared. We found that the final bubble velocity of all 3D modes is the same, even for a 3D rectangular mode. In Fig. 4 the position of the bubble tip is plotted for the planar, square 3D mode ($k_x = k_y$), rectangular 3D mode ($k_x = 2k_y$) and cylindrical case in which the bubble is on the symmetry axis. It is seen that all 3D bubbles rise similarly, while the planar bubble is slower, consistent with Layzer's prediction for planar and cylindrical bubbles.

The final shape of the single wavelength perturbation was found to be of three possible forms^[4]: (i) symmetric checkerboard bubble-spike configuration with saddle points on the diagonals connecting next-nearest-neighbour bubbles or spikes; (ii) bubbles surrounded by a ridge of interconnecting spikes ("bubble-ridge" configuration^[5]); (iii) spikes surrounded by a valley of interconnecting bubbles ("spike-valley" configuration^[6]). Which late-time configuration is formed depends on the initial conditions, that imprint their shape on the late time shape, and the Atwood number. We have found that as the Atwood number rises the saddle-points, which have zero vertical velocity during the linear stage, tend to fall with the spikes (see Fig. 5). Since at high Atwood numbers these points fall down rapidly, an effective circular bubble is created from the original bubbles. This means that at high Atwoods a "bubble-ridge" shape will be formed even when the initial perturbation is symmetric with respect to bubbles and spikes (such as a single mode initial perturbation, as is shown in Fig. 5(b) for $A=0.9$).

The difference between the above three configurations can explain the different late time shape of the spherical geometry calculations presented by Town and Bell^[5] and by Sakagami and Nishihara^[6]. We have performed^[4] spherical geometry calculations similar to those of Town and Bell and Sakagami and Nishihara. Following Town and Bell we considered a perturbation with dodecahedral symmetry simulating the primary laser induced perturbation in a 12 beam ICF experiment (each beam at the centre of a pentagon). Fig. 6(a) shows the interface between the inner gas and outer layer when the bubbles are in the pentagon centres. Fig. 6(b) shows the same run but with spikes in the pentagon centres. One can see that the final shape of the interface takes the form of "bubble-ridge" configuration in the case when a bubble is initially present in the pentagon centre (Fig. 6(a)) and a "spike-valley" form when the initial perturbation is inverted (Fig. 6(b)). The fact that in this configuration two different geometries are created

is simply an effect of the asymmetry between bubbles and spikes in each of the initial perturbations and should not be related to the spherical geometry of the problem. The same effect can be seen in a two dimensional cylindrical case where a bubble or a spike are initially present on the symmetry axis, or in a three dimensional planar perturbation with hexagonal symmetry.

In contrast with the above case, the case presented by Sakagami and Nishihara consists of a single spherical mode. Their initial conditions consist of an $l=6, m=0$ to 5 single spherical harmonic mode and an Atwood number at peak compression of about 0.9. Fig. 7(a) shows our calculation results for the $l=6, m=4$ case. One can see that the structure created is approximately that of isolated bubbles surrounded by a ridge of interconnecting spikes ("bubble-ridge"), though there is still some reminder of the initial checkerboard structure. This shape remains when we invert the initial perturbation sign. As was explained in the planar case this fact is a result of the high Atwood number, which is about 0.9 in this case. Fig 7(b) shows for comparison the interface for the case $l=6, m=0$, which is essentially a two dimensional problem. Note the large difference between the three and two dimensional structure of the interface. This difference may be important when one is trying to simulate the failure of an ICF target due to laser nonuniformity.

Using the 3D code, we have calculated the two-mode interaction in cases of moderate wavelength ratios. It has been found that the three dimensional behaviour is qualitatively and quantitatively similar to the 2D results. In cases of a short wavelength mode suppressing a long wavelength mode, the amplitude for the onset of suppression (as defined above) was found to be of the form $f(A)\sqrt{\lambda_1\lambda_2}$ but with $f(A)$ larger than the value in two dimensions by about a factor of 2, qualitatively consistent with the observation that the onset of nonlinear effects in a single RT mode in 3D also occurs at a later stage (or larger amplitude) when compared to the 2D case.

We have also performed some preliminary simulations of random initial perturbations at low-resolution (about $30 \times 30 \times 60$). We found the value of α to be about 0.05 (5% to 95% volume fraction of a single fluid), similar to the value found in our 2D simulations of similar and higher resolutions^[7]. Youngs found for the high resolution two dimensional case $\alpha = 0.04 - 0.05$ ^[8] while for the three dimensional case he found $\alpha = 0.05 - 0.06$ ^[9] in the low resolution front tracking simulation and $\alpha = 0.03 - 0.04$ ^[10] in the high resolution miscible fluid simulation.

References

- [1] D.L. Youngs in "Numerical Methods for Fluid Dynamics", edited by M.J. Baines and K.W. Morton (Academic, New York, 1982).
- [2] D. Ofer, D. Shvarts, Z. Zinamon, S.A. Orszag, Phys. Fluids B. **4**, pp. 3549 (1992).
- [3] S.W. Haan, Phys. Fluids B **3**, pp. 2349 (1991).
- [4] J. Hecht, D. Ofer, D. Shvarts, S.A. Orszag, R.L. McCrory, "Analysis of 3D RT Instability", submitted for publication.
- [5] R.P.J. Town, A.R. Bell, Phys. Rev Lett. **67**, pp. 1863 (1991).
- [6] H. Sakagami, K. Nishihara, Phys. Rev. Lett. **65**, pp. 432 (1990).
- [7] N. Freed, D. Ofer, D. Shvarts, S.A. Orszag, Phys. Fluids A **3**, pp. 912 (1991).
- [8] D.L. Youngs, Physica D **12**, pp.32 (1984)
- [9] D.L. Youngs in "Advances in Compressible Turbulent Mixing", edited by W.P. Dannevik, A.C Buckingham and C.E. Leith, NTIS Conf-8810234 (1992).
- [10] D.L. Youngs, Phys. Fluids A **3**, pp. 1312 (1991).

Figure Captions

- 1) Suppressing amplitude for various mode pairs and Atwood numbers (A). A positive l_1/l_2 ratio indicates a large l mode suppressing a small l mode. A negative ratio indicates the reverse. The amplitude is normalised by multiplying by $\sqrt{l_1 \times l_2}$ in order to judge the accuracy of the $\sqrt{\lambda_1 \lambda_2}$ rule in the text. Note that $l = 2/\lambda$.
- 2) The mechanism whereby the long wavelength mode suppresses the growth of short wavelength "noise" (in this case a single short wavelength). One can see that the long wavelength shear flow tends to pull the short wavelength spikes laterally instead of vertically, resulting in a reduced small scale RMS. In this case $l_1 = 2$, $l_2 = 30$ and $A=0.5$. (a) Short wavelength spikes in the presence of a long wavelength shear flow. (b) The same short wavelength perturbation with no long wavelength mode present.
- 3) Suppression of a single long wavelength mode by a band of short wavelength modes. In this case $l_1 = 2$ and the band consists of $l_2 = 11 - 20$ with random initial amplitudes, $A=0.5$. (a) Intermediate times when mode analysis is relevant. (b) The late turbulent stage.
- 4) Bubble penetration in 4 single mode cases: square 3D ($k_x = k_y$), rectangular 3D ($k_x = 2k_y$), cylindrical bubble (from the 2D code) and planar 2D. One can easily note that the first three cases, with 3D effects, reach the same bubble velocity whereas the 2D planar case reaches a much lower asymptotic velocity.
- 5) Late stage single mode 3D profile for (a) $A=0.5$ and (b) $A=0.9$. Note that when $A=0.5$ the saddle points are roughly halfway between the bubble and spike penetration, whereas in $A=0.9$ the saddle point tends to fall with the spikes, essentially creating a circular spike "curtain" around the bubble.
- 6) Spherical perturbations with dodecahedral symmetry. Inversion of the perturbation can result in a: (a) bubble-ridge or (b) spike-valley structure.
- 7) Single mode spherical RT perturbations. Shown is the interface between the inner and outer fluids at late times. In these cases $A \sim 0.9$. (a) $l=6$, $m=4$: a typical fully 3D perturbation. (b) $l=6$, $m=0$: cylindrical symmetry or what a typical 2D calculation actually represents in 3D.

Figure 1

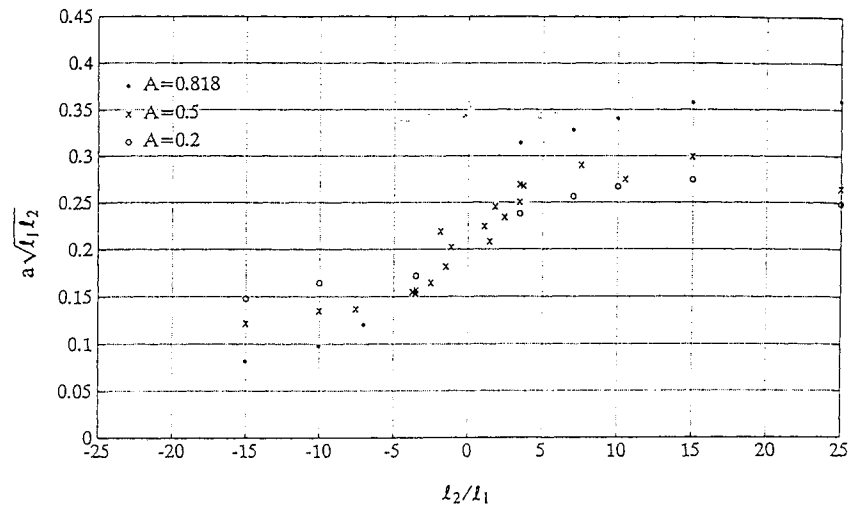


Figure 2(a)

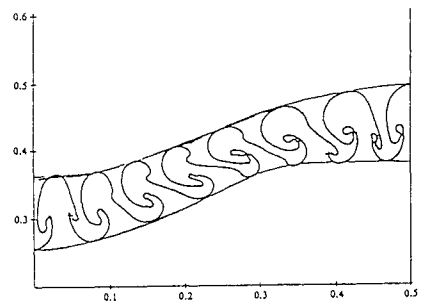
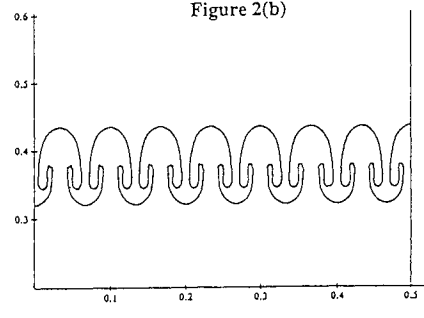
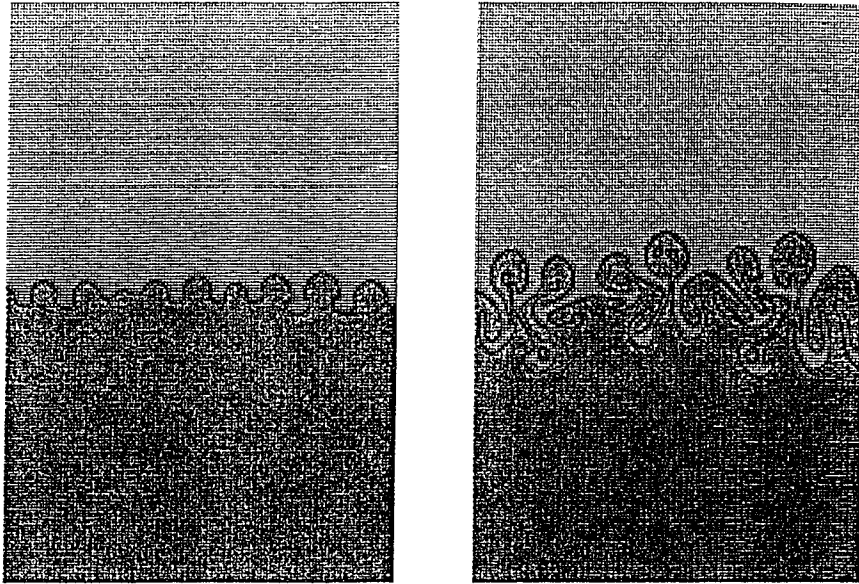


Figure 2(b)





(a)

(b)

Figure 3

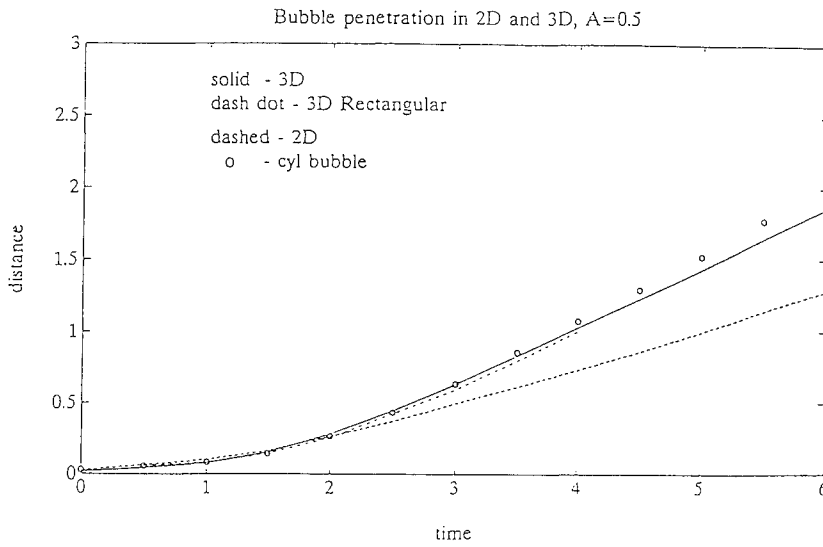


Figure 4

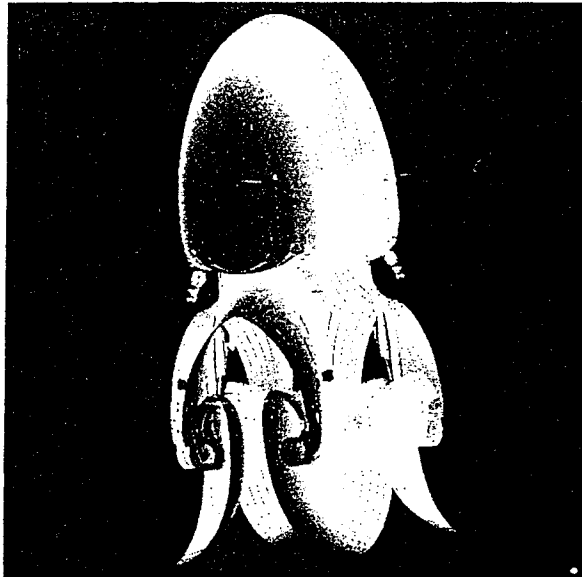


Figure 5a



Figure 5b

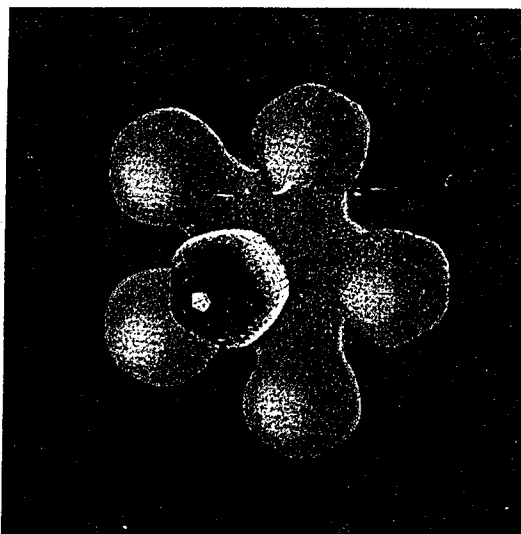


Figure 6a

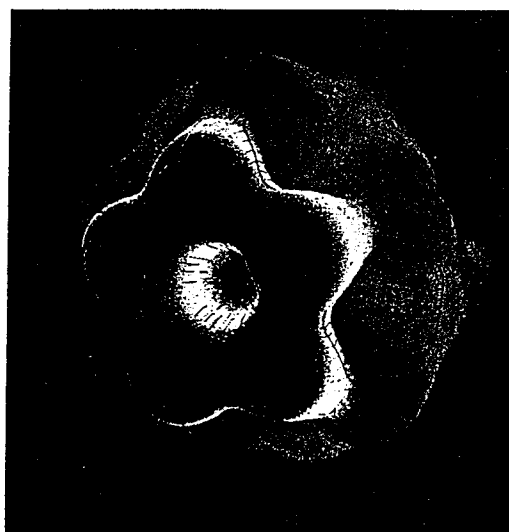


Figure 6b

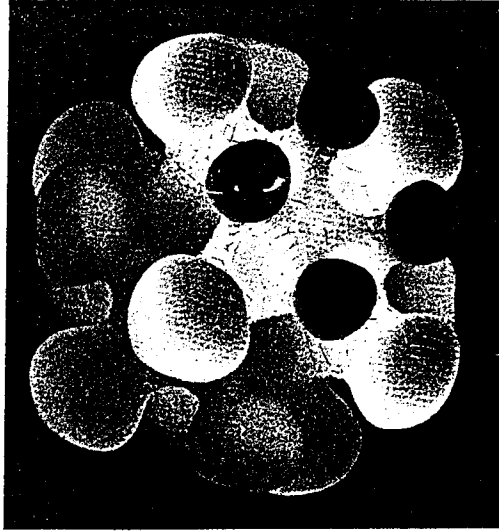


Figure 7a

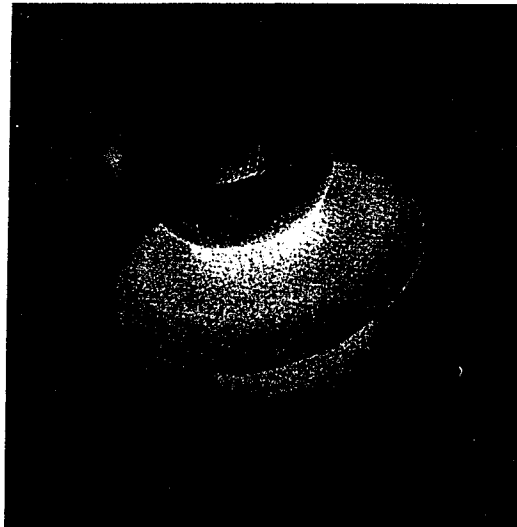


Figure 7b

EXPERIMENTAL STUDY INTO THE STABILIZATION EFFECT
IN GRAVITATIONAL TURBULENT MIXING DEVELOPMENT
ON AN INCLINED BOUNDARY

N.V.Ptitzyna, Yu.A.Kucherenko, V.I.Chitaikin,
A.P.Pylaev

PHYSICAL DIVISION
INSTITUTE OF TECHNICAL PHYSICS

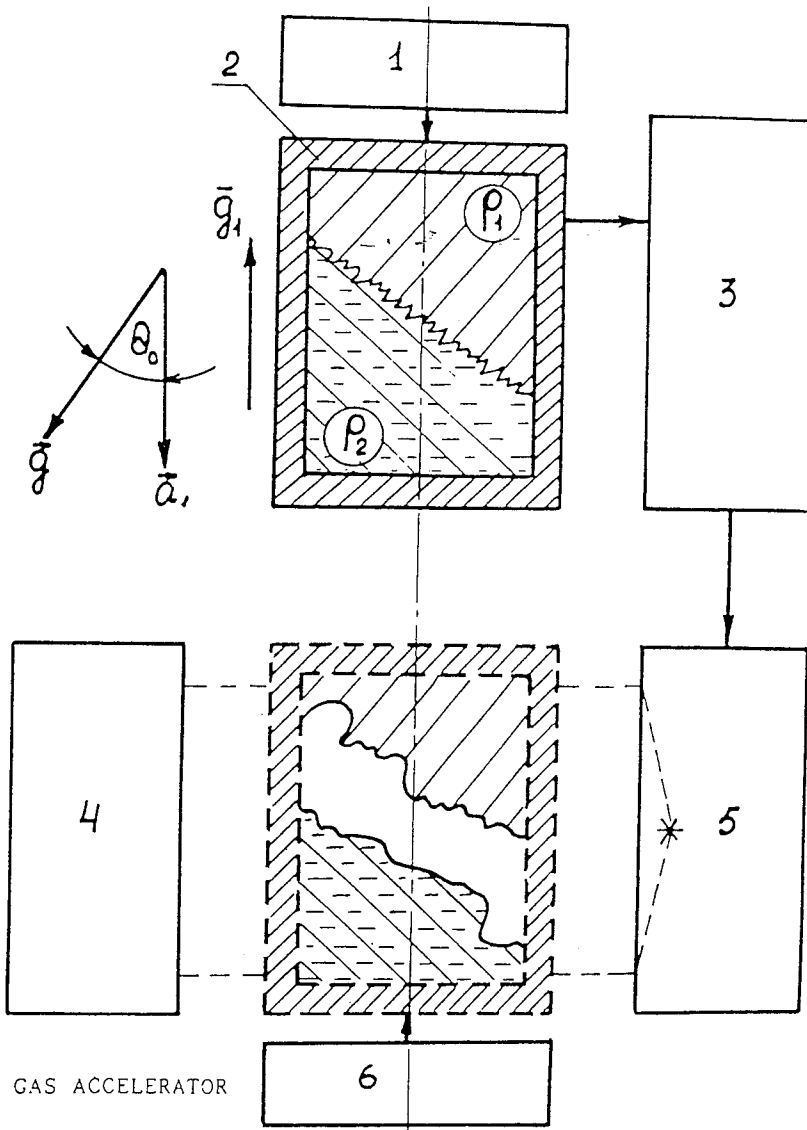
454070, Chelyabinsk-70, P.O.245, Russia

For a variety of reasons it is difficult to organize the compression of the multilayered targets designed for inertial thermonuclear fusion so that the arising flow is spherically symmetrical. This leads to the development of the turbulent mixing induced by the Rayleigh-Taylor instability under conditions when acceleration is not perpendicular to the contact boundary

between layers. In this case, it is possible to describe the development of the gravitational turbulent mixing between layers of different densities by using two-dimensional models of mixing. Experiments on investigation into the gravitational turbulent mixing on the inclined boundary can be a good verification and, in some cases, even calibration of these models.

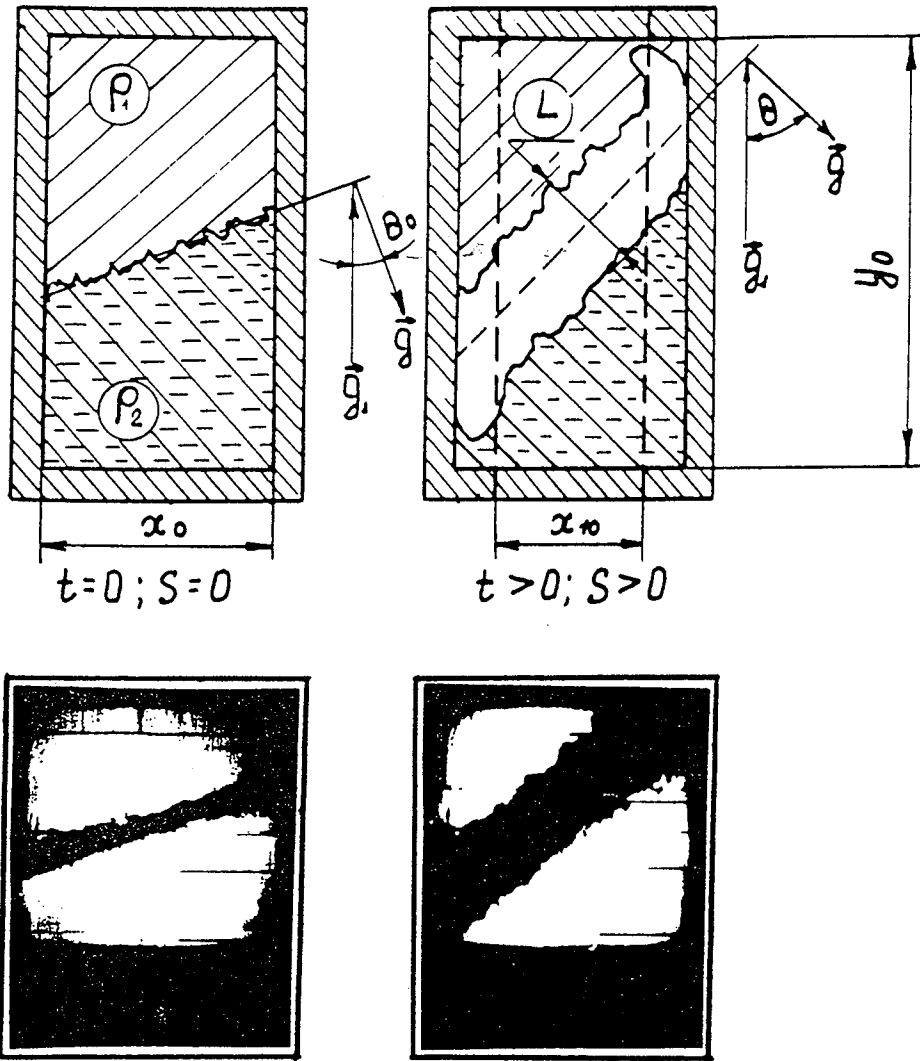
In works [1,2] the results of experiments on the turbulent mixing between fluids of different densities are given for the contact boundary being inclined to the direction of acceleration. Decrease in the turbulent mixing development rate is substantiated by the results of these works and can be considered as displaying of the stabilization effect. In the present work this effect has been experimentally studied at the installation SOM [3].

Experiments were performed according to the following block-diagram (see Fig. 1). An ampoule filled with two transparent fluids having different indices of light refraction was accelerated by means of a gas accelerator (densities of the light and heavy fluids were equal to ρ_1 and ρ_2 , respectively). 14 light channels being found along the path of the ampoule motion allowed to obtain the shadow photographic images of the turbulent mixing region in each experiment by photographic recording technique. The initial angle θ_0 of the contact boundary inclination forward to the artificial gravitational field \vec{g}_1 was obtained by inclining the gas accelerator and the damping device at the same angle. At



1. GAS ACCELERATOR
2. AMPOULE
3. TRAJECTORY TRANSDUCERS
4. PHOTORECORDER
5. PULSED LIGHT SOURCES
6. DAMPING DEVICE

FIG. 1 SCHEME FOR PERFORMING EXPERIMENTS ON TURBULENT MIXING



$L(t)$ - WIDTH OF THE TURBULENT MIXING ZONE

θ_0 - INITIAL ANGLE OF THE CONTACT BOUNDARY SLOPE

FIG. 2 SCHEME FOR PERFORMING MEASUREMENTS AND PHOTOGRAPHIC IMAGES OF THE AMPOULE

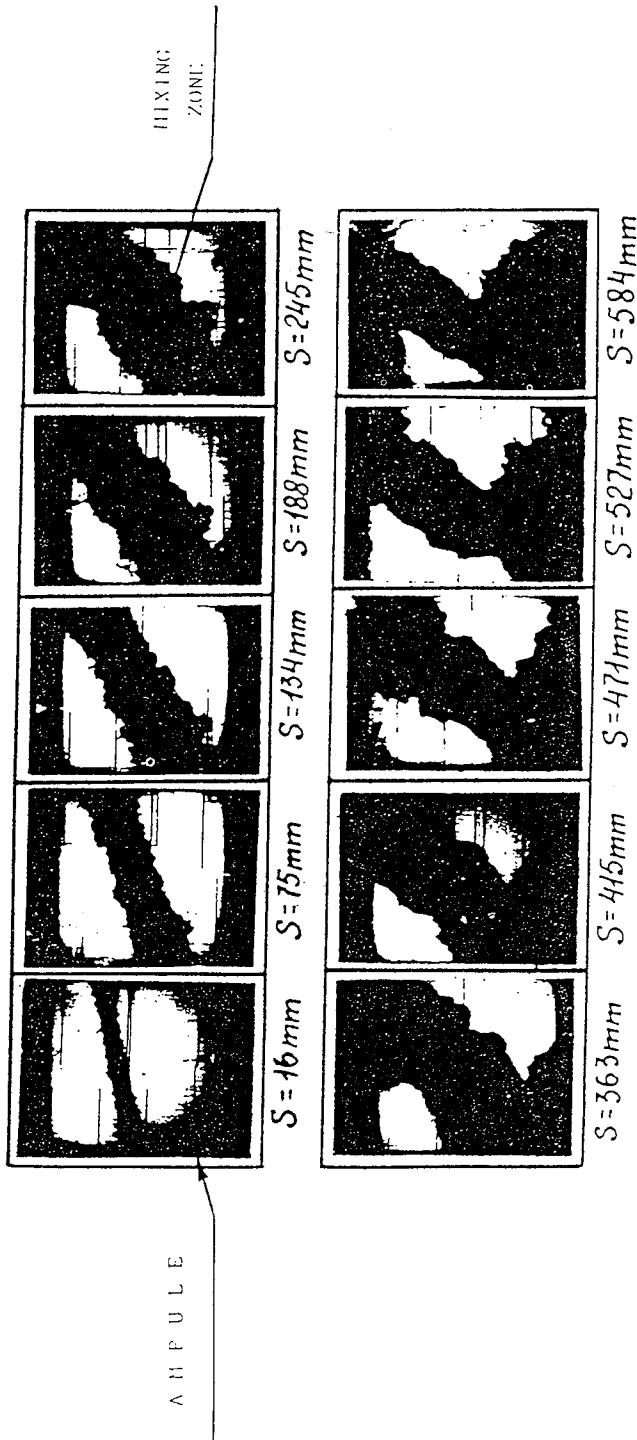


FIG. 3 TYPICAL PHOTOGRAPHIC IMAGES OF THE MIXING ZONE ON THE INCLINED CONTACT BOUNDARY WITH THE INITIAL ANGLE OF SLOPE $\theta_0 = 10^\circ$ (EXPERIMENTS WITH PETROL, — ZnCl2, SOLUTION)

the initial instant of time the contact boundary remained in the horizontal position with formation of the angle θ_0 with the direction of the ampoule in the gravitational field g . In each experiment the displacement of the contact boundary $S = \int_0^t dt \int_0^{\theta} g_1(\tau) d\tau$, the angle of the mixing region inclination $\theta(S)$ and the size of the mixing region $L(S)$ were measured at the moments for taking the photographic images (see Fig. 2). The values of L and θ were determined according to the photographic images of the mixing region in the ampoule centre when $x_{10} = 20-40$ mm. It is possible to consider that the turbulent mixing is developing between plane layers in this region.

In the experiments, petrol with density $\rho_1 = 0.69$ g/cm³ and zinc chloride solution with density $\rho_2 = 2.04$ g/cm³ (densities relation $n = 3$) were used as the fluids under study. Random initial perturbations having the geometry of the contact boundary were generated on the contact boundary. The spectral composition of initial perturbations had a maximum being found at the wave length equal to 2 mm. Six main groups of experiments differing in the values of the angle θ_0 have been performed with 15-20 experiments in each group. The experiments were carried out in ampoules with dimensions $x_0 = 64$ mm and $y_0 = 120$ mm. In all groups the initial acceleration of the ampoule was equal to $a_1 = 730g$.

The characteristic photographic images of the mixing region

obtained in one of the experiments are presented in Fig. 3. In all the experiments the largescale flow was observed near the side walls of the ampoule whereas in the centre of the ampoule the turn of the mixing region was noted in connection with this.

In Fig. 4 the relations of the average size L of the mixing region versus the parameter $S' = S \cos \theta_0$ are presented for all groups of experiments and in Fig. 5 - the angle θ of the mixing region rotation versus the same parameters S' . It can be seen that for all groups of experiments, with the exception of the group with $\theta_0 = 60^\circ$, the size of the mixing region is growing with increasing of the parameter S' until it reaches the maximum value L_{\max} (the effect of stabilization). In experiments with $\theta_0 = 60^\circ$ the value L_{\max} is not reached because prior to the moment the mixing region is in the vertical position with $\theta = 90^\circ$. From Fig.4 it can be seen that all the values of $L_{\max} = L_{\max}(S')$ are found on a straight line going out of the origin of coordinates. In Fig.6(a) the relations for $L_{\max} = L_{\max}(\theta_0)$ and $L_{\max} = L_{\max}(\hat{\theta})$ are shown where $\hat{\theta}$ is the current value of the angle θ allowing to reach L_{\max} . It can be seen that the difference $\hat{\theta} - \theta_0 = \text{const}$ for each value of L_{\max} . In order to determine this constant the relation $\hat{\theta} = \hat{\theta}(\theta_0)$ has been built in Fig. 6(b). All experimental points are described by the straight line $\hat{\theta} = \theta_0 + 36.4^\circ$. In the experiments with the initial angle $\theta_0 = 60^\circ$ the stabilization does not take place. This means that for all experiments with different

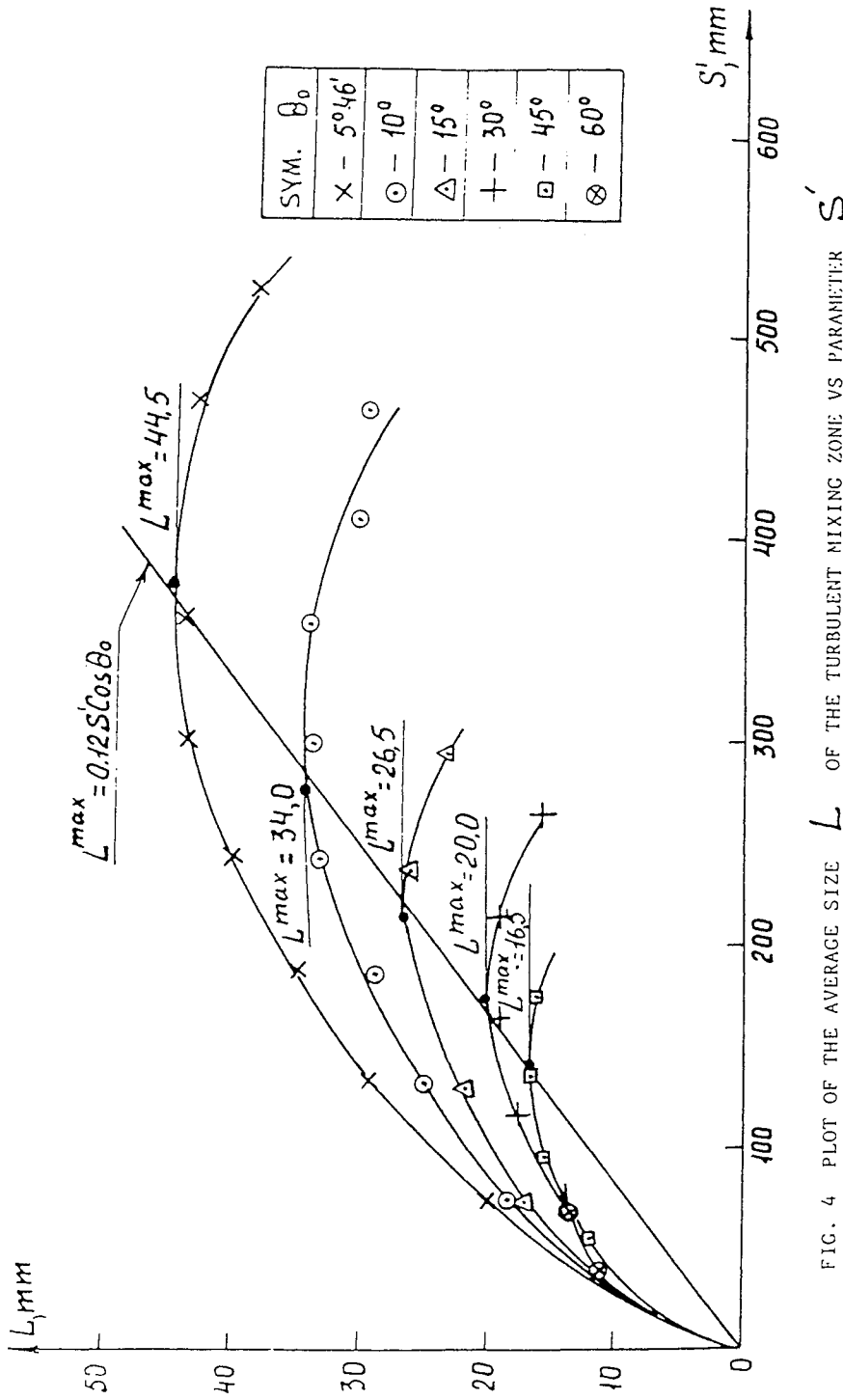


FIG. 4 PLOT OF THE AVERAGE SIZE L OF THE TURBULENT MIXING ZONE VS PARAMETER S' (EXPERIMENTS WITH $n = 3$)

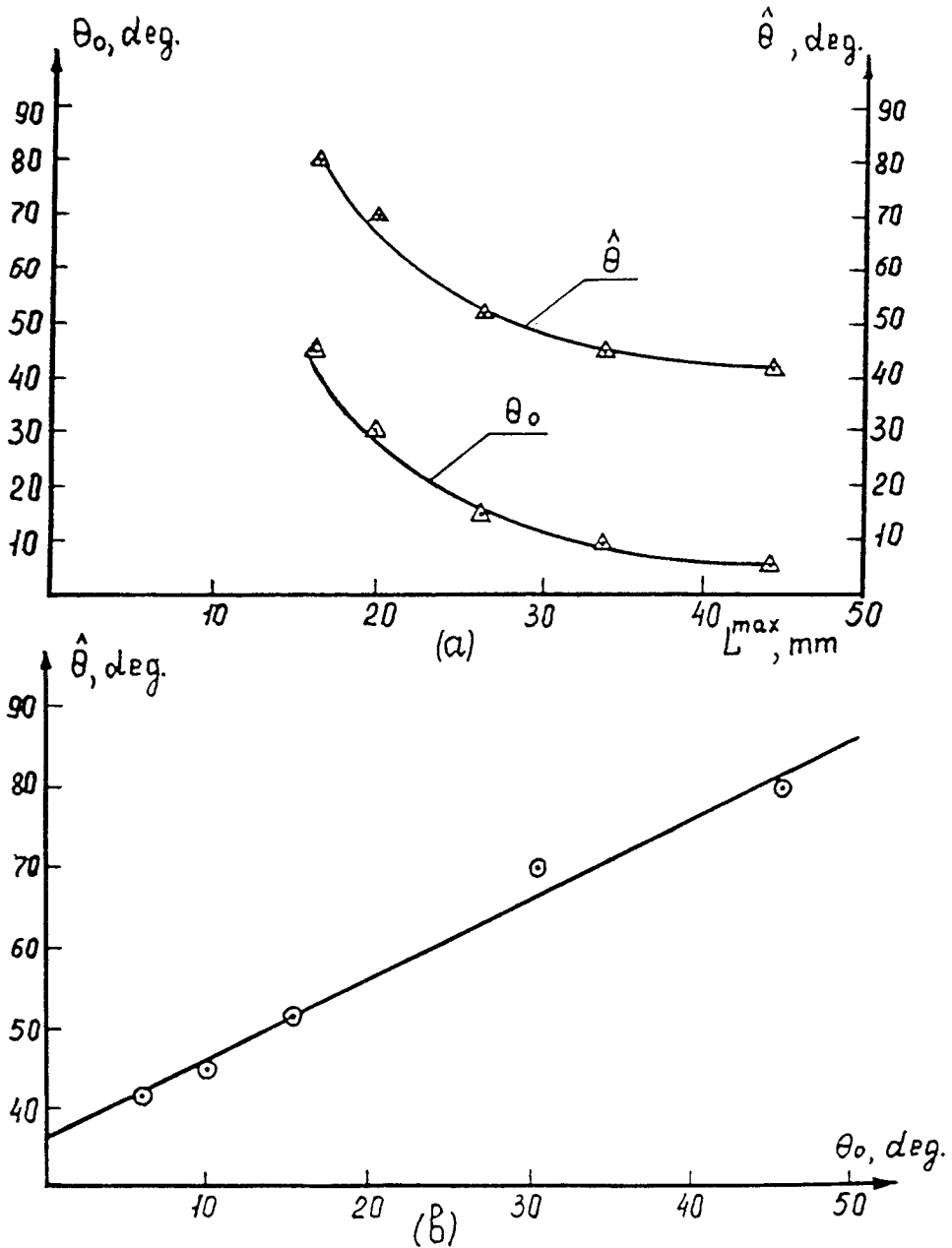


FIG. 6 (a) PLOT OF L^{max} VS θ_0 AND $\hat{\theta}$
 ($x_0 = 64$ mm)
 (b) PLOT OF $\hat{\theta}$ VS θ_0
 ($x_0 = 64$ mm)

values of the initial angle θ_0 the stabilization effect takes place only when the mixing region turns through the critical angle $\theta_0 = 36.4^\circ$ provided that the inequality $\theta_0 + \theta_c < 90^\circ$ is satisfied.

The obtained result supports the supposition made in the work [2] with respect to the mixing region extension as the reason for stopping the growth of the mixing region and its subsequent reduction. This extension reaches the critical value when the region turns through the angle θ_0 .

If one states that the critical angle θ_0 is of universal character for the densities relation $n = 3$, then a number of questions arises, in particular, whether the value of the critical angle θ_0 depends on the size x_0 of the ampoule. For solving this question the experimental results obtained by D.L.Youngs group in the work [1] for an ampoule with $x_0 = 150$ mm and $n = 2.9$ were used. Some experiments have been performed for the values of $\theta_0 = 5^\circ 46'$ as in one group of the experiments in the given work. If it is shown that in D.L.Youngs experiments stabilization must take place at the value of the angle $\hat{\theta}$ close to the value of this angle in our experiments then it will mean that the critical angle θ_0 is independent of the ampoule size x_0 .

For using the results of the work [1] it is necessary to determine the dependence of the angle of rotation θ on the parameter S for the ampoule with $x_0 = 150$ mm. Since we had no

ampoules of this size, such determination was realized by an indirect method. Three groups of experiments have been additionally performed with the ampoule sizes $x_0 = 50; 32; 16$ mm, the angles of the mixing region rotation θ were determined just in these ampoules. Relations $\theta(S)$ are given in Fig. 7(a). Within the range of values $S < 200$ mm the experimental points are well described by straight lines with the coefficients of the inclination $K = \frac{d\theta}{dS}$. The values of $K(x_0)$ are given in Fig. 7(b) where it can be seen that the rate of changing in the mixing region turn is the higher the smaller the ampoule size x_0 is. The values of $K(x_0)$ are described by a smooth curve. The evaluation of the K value equal to 0.05 for $x_0 = 150$ mm has been made by the second order splineextrapolation.

In Fig. 8 the relations $L(S)$ and $\theta(S)$ obtained in the given work for $\theta_0 = 5^\circ 46'$ and $x_0 = 64$ mm as well as the relation $L(S)$ from the work [1] for $\theta_0 = 5^\circ 46'$ and $x_0 = 150$ mm are shown. The relation $\theta(S)$ for $x_0 = 150$ mm obtained by the above mentioned evaluation and presented in the form of the straight line is also given in the same figure. It can be seen that for the ampoule with $x_0 = 150$ mm the value of L_{\max} will be reached as well as for the ampoule with $x_0 = 64$ mm and angle $\hat{\theta} = 42^\circ$. Hence, it is possible to make a conclusion that the value of the critical angle $\theta_0 = 36.4^\circ$ is independent of the ampoule size.

Experiments with $\theta_0 = 5^\circ 46'$, $\theta_0 = 15^\circ$ and the initial value

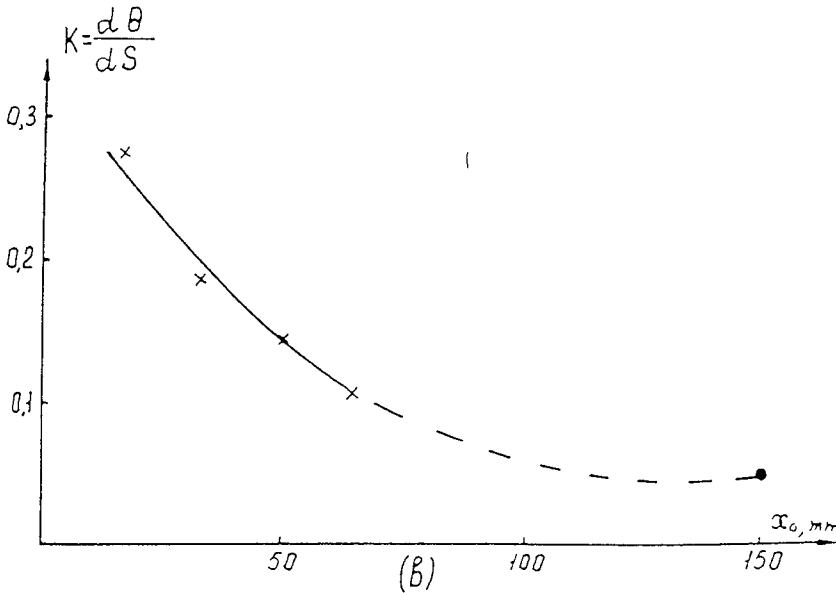
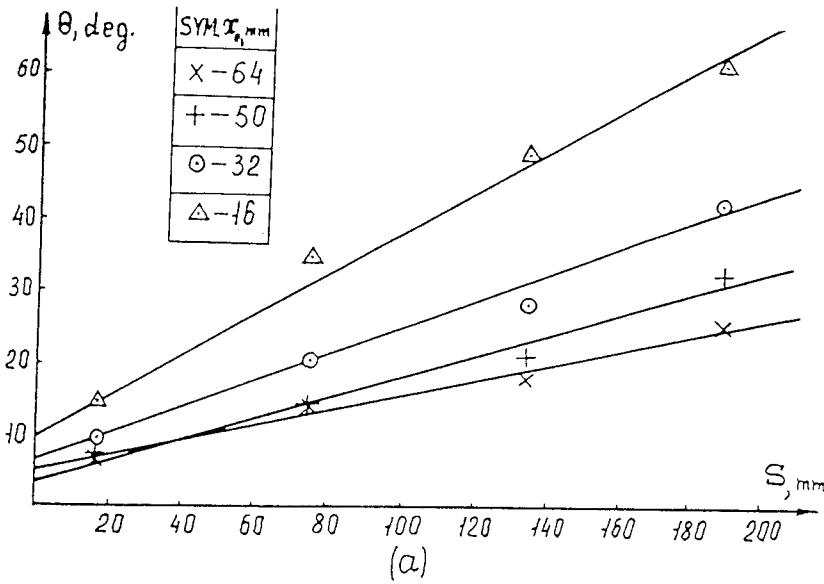


FIG. 7 (a) PLOT OF θ VS S FOR DIFFERENT VALUES OF α_0 .
 (b) PLOT OF ROTATION VELOCITY K VS α_0 .

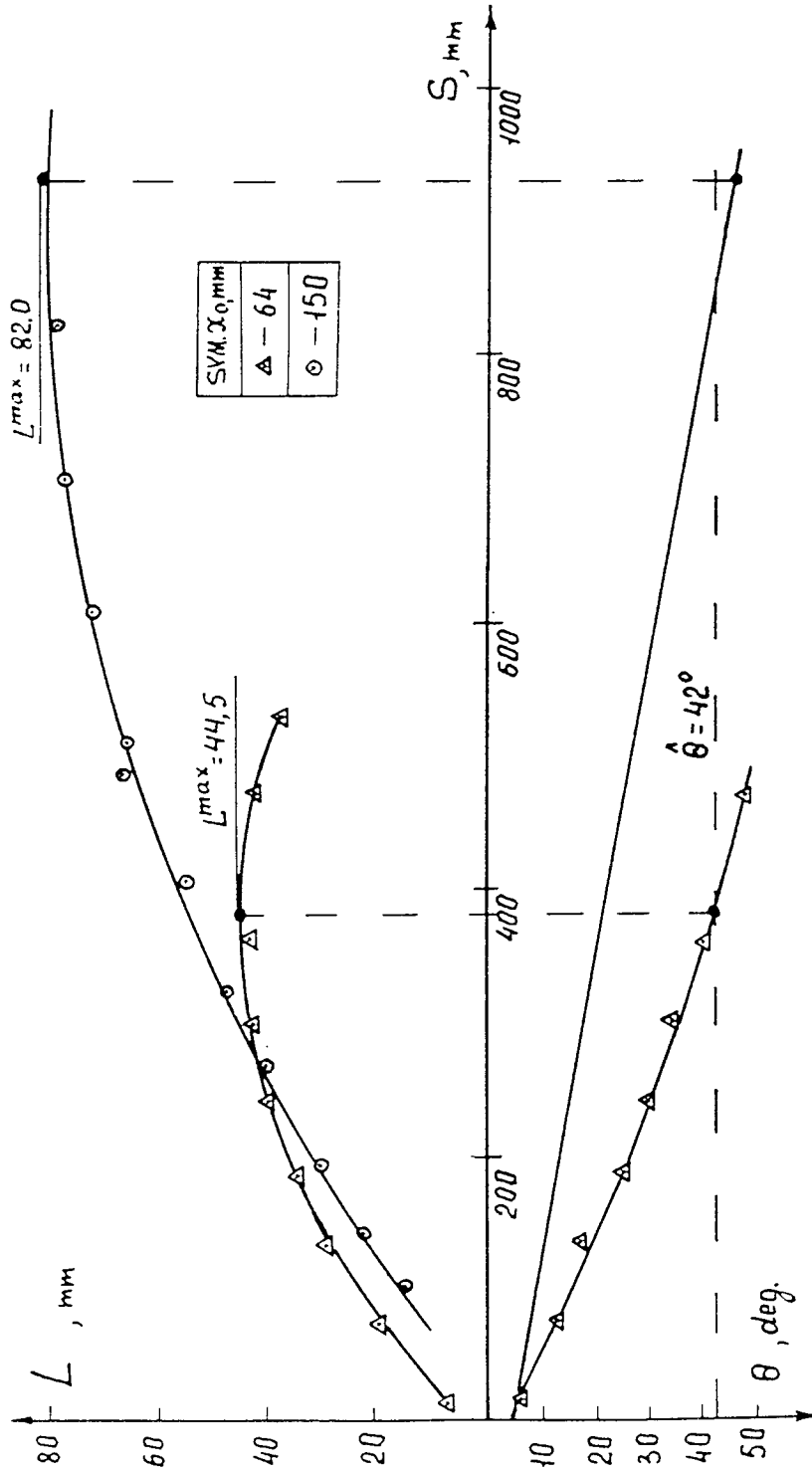


FIG. 8 PLOT OF L AND θ VS S FOR INITIAL ANGLE $\theta_0 = 5^\circ 46'$ FOR $\alpha_0 = 64$ mm AND $\alpha_0 = 150$ mm.

of acceleration $g_1(0) = 180g$ have been performed for the verification of the acceleration value influence on the development of the mixing region having an inclined contact boundary. Difference in the average values of L and θ from the same values in main groups of experiments were not found within the limits of errors in measurements.

Thus, in the work which has been carried out the stabilization effect in the evolution of the region of the gravitational turbulent mixing on the inclined contact boundary was revealed. This effect consists in the termination of the region sizes growth and arises when the mixing region turns through the critical angle $\theta_c = 36.4^\circ$ for the densities relation $n = 3$. The critical angle θ_c is independent of the ampoule width and the value of acceleration. The possible reason for stabilization is the extension of the mixing region when the latter turns through the critical angle.

References

1. D.L. Youngs. A two-dimensional turbulence model based on the equations of multiphase flow. The 3 - rd Zababahin Scientific Talks, Kishtim, USSR, 1992.
2. M.J. Andrews and D.B. Spalding. A simple experiment to investigate two-dimensional mixing by Rayleigh - Taylor instability. *Phys. Fluids A* 2 (6), 1990.
3. Yu.A. Kucherenko , L.I. Shibarshov, V.I. Chitaikin, S.I. Balabin, A.P. Pylaev. Experimental study of the gravitational turbulent mixing self-similar mode. 3 - rd International workshop on the physics of compressible turbulent mixing, Abbey of Royanmont, France, 1991.

Rayleigh-Taylor mixing due to unstable thermal stratification: Preliminary experimental results

Dale M. Snider and Malcolm J. Andrews
Texas A&M University
College Station, TX 77843-3123

Abstract

A new water channel experiment is used to study turbulent mixing by Rayleigh-Taylor instabilities as well as shear mixing by superimposing a velocity shear. The experiment can be operated to study buoyancy induced mixing, shear induced mixing, or combined buoyancy and shear mixing. The experiment is statistically steady and provides a long time period in which to study the mixing behavior and record data. Results presented are from preliminary experiments that use dye to visualize the mixing process.

Introduction

A Rayleigh-Taylor instability exists when a heavy fluid lies above a lighter fluid under the influence of gravity. The heavier fluid falls and the lighter fluid rises, which form vortices and turbulent mixing. This process occurs in nature, such as the "over turning" of a lake as its surface cools in the fall; clear air turbulence associated with atmosphere temperature inversion; and, in the ocean, from local salinity inversion due to shear. Rayleigh-Taylor mixing also occurs in a variety of industrial processes such as counter-gradient transport in engine cylinders with swirl; degradation of ICF capsules; and multiphase mixing in chemical engineering processes.

The objective of this study is to measure the amount of mixing due to buoyancy. By design, the amount of mixing due to shear and the amount of mixing from combined buoyancy and shear is also measured. This study will lead to a better understanding of fundamental mixing processes. Data collected will validate a two-fluid mixing model for practical engineering prediction, and will be provided to other researchers upon request.

The work presented here is from a preliminary study. Results from this work will improve on the experiment, the method of measurements, and the method of data reduction.

Viscous and buoyancy induced mixing background

Kelvin-Helmholtz instabilities arise between fluids with different mean velocities. The resulting free shear layers have been widely investigated both experimentally and numerically [1,2,3,4,5]. For low velocity differences, the flow is characterized by large structures (rollers) with little global mixing. As the difference in velocity increases or as the fluid progresses downstream, a mixture transition occurs where the mixing dramatically increases [3]. This increase in mixing has been attributed to the development of the instability of large eddies breaking down to small-scale eddies [7]. Experiments have shown that the flow reaches a self similar state away from the end of the splitter plate. Following Browand and Roshko [2], the mixing width can be defined by the linear relation:

$$h=b(x+x_0) \tag{1}$$

where x is the distance from the end of the splitter plate and x_0 is the virtual origin. Brown and Roshko reported that for a visually defined mixing layer of air the constant, b , is:

$$b=0.38(U_1-U_2)/(U_1+U_2). \tag{2}$$

Rayleigh-Taylor mixing occurs when a heavy fluid is above a light fluid. Buoyancy drives the mixing at the unstable interface. In principle, if the heavy and light fluids do not molecularly mix, the container with the mixture can be inverted (such that gravity acts in the opposite direction) and the original separated state can be recovered. If the heavy and light fluids molecularly mix then, at best, only a partial recovery of the starting condition can be obtained. In a Rayleigh-Taylor mixing process, the mixing width is described by a self-similar solution that is driven by the potential energy associated with a density difference [8]:

$$h = \alpha A g t^2 \tag{3}$$

where the Atwood number $A = (\rho_1 - \rho_2)/(\rho_1 + \rho_2)$; h is the width of the mixing layer; g is the acceleration due to gravity; and t is time.

For our experiment, the mixing width is transformed from a temporal form to a spatial form.

$$h = \frac{\alpha A g (x - x_0)^2}{V^2} \quad (4)$$

where V is the mean mixture velocity; x is the distance from the end of the splitter plate; and x_0 is the effective location for the start of the mixing layer. The constant, α , has been measured by Youngs [8] and other investigators, and found to be in the range 0.04 to 0.07. From a two-dimensional direct numerical study, Youngs [8,9] calculated α from 0.04 to 0.05. He postulated that two-dimensional constraints may inhibit the growth of large scale structures. From a numerical statistical study, Glimm, Li and Zhang [10] reported that α ranges from 0.05 to 0.066 for most cases. However, initial conditions were found to give a value as low as 0.038.

Experiment

The present water channel experiment contains an inlet and outlet plenum and a test channel as shown in Figure 1. The channel is made of 1.27 cm (0.5 in.) Plexiglas and has a full-flow cross section of 31.8 cm high by 30.5 cm wide. Two channels, one above the other, are formed by a horizontal splitter plate. The splitter plate separates the lower warm water from the cooler upper water. A vertical divider reduces the original channel to 16.5 cm wide by 31.8 cm deep (10.2 cm depth from floor to the horizontal splitter plate). The reduction was made by adding a plywood floor and a plywood back-wall. A pump supplies feed water to both channels from 568 liter tanks. The temperature in the bottom channel is regulated by adding hot water to the bottom channel feed line. A packed array of 0.64 cm diameter tubes are used to straighten the entering flow. Teflon-weave pads are located at the channel entrance and screens are placed after the array of tube straighteners.

The original experiment design called for back lighting. One modification, in working with the preliminary experiment, was the addition of a solid back-wall. This precluded back lighting, and

data presented here are from front lighting. In the future, the experiment will use back lighting. Back lit photographs will enable measurements of the mixture density based on light absorption passing through the mixing layer.

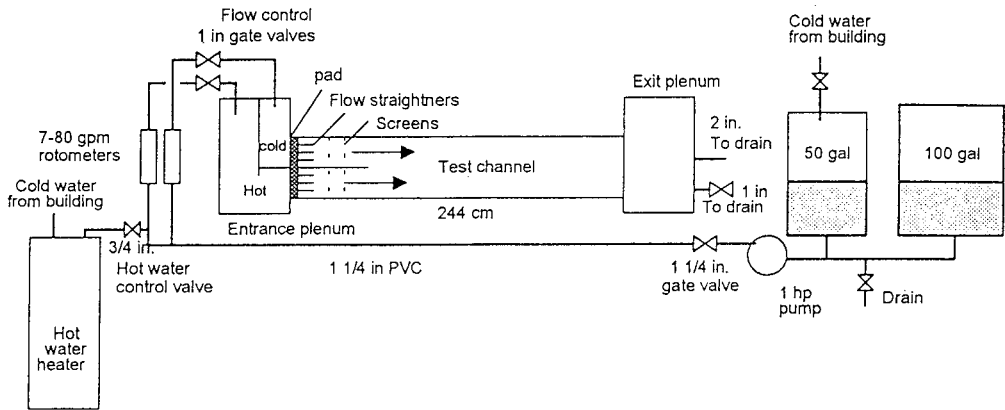


Figure 1. Experiment layout.

Measurements of mixing

Mixing is measured by adding nigrosene dye to one stream and photographing the resultant mixing. In tests with density differences between the upper and lower flows, the difference in index of refraction associated with strong density gradients, produce shadow graphs when exposed to a bright camera flash. The shadow graphs highlight the flow structures. As the fluid mixes, the mixture becomes a uniform gray and the shadows (strong density variation) decrease.

Photographs 1, 2 and 3 show shear layers. Following the practice of Brown and Roshko [2], the shear layer boundary is identified in the photographs by drawing a line tangent to the dark peaks along the dark-light mixture interface. The shear layer half width is measured from the tangent line to a line projected from the splitter plate.

When running the experiment with Rayleigh-Taylor mixing, the shadow graphs from density gradients mark the mixing region boundary. As seen from photograph 6, a distinctive interface can be seen where the shadow graphs end. The mixture width is measured between the upper and lower shadow graph peaks. If the dye is dark and hides part of the shadow graphs, as it does in photograph 5, then the half width is measured. The half width is measured from the peaks of the shadow graph boundary to a line projected from the splitter plate.

Shear and no buoyancy

A free shear layer is produced at the interface between two different velocity streams. No mixing occurs if the interface where the streams meet is seamless (no velocity difference). Photograph 1 shows a shear layer where the top and bottom velocities are close. Photographs 2 and 3 show shear layers for progressively larger velocity differences. The temperature of both streams is the same in these experiments.

The side-view flow characteristics are similar to visual data recorded in other studies on free shear layers [11]. With a negligible velocity difference there is little mixing. The shear layer grows faster as the velocity difference increases as seen from photographs 1 through 3. Large coherent structures (rollers) appear as the velocity increases. We have measured the constant defined in Equation 1 to be 0.4 and 0.45 for photographs 1 and 2, respectively. This compares favorably with the value of 0.38 measured by Brown and Roshko. Our values for the constants were from instantaneous measurements. Future work will use ensemble averages.

Buoyancy and no shear

Photographs 4, 5, and 6 show mixing from buoyancy alone. The flow rates for each channel are close. Warm water is supplied to the bottom channel and cool water is supplied to the top channel. Water density decreases as the temperature increases over the temperature range in these experiments. Photograph 4 shows that significant mixing occurs for even a small differential temperature (about 1° C), downstream of the splitter plate.

The density difference increases from photograph 4 to photograph 6. The mixing region expands faster at the larger density difference. The increased mixing results from the higher potential energy, associated with larger density difference, being released to kinetic energy.

Buoyancy induced mixing does not exhibit the big rollers that are seen in the shear mixing. Rayleigh-Taylor mushrooms can be seen in the photographs, and the size of flow structures increase downstream. The size of the flow structure is more pronounced at the lower density differences because of a lower Reynolds number and, consequently, lower levels of turbulence. Photograph 4 shows that the wave length of the largest structure is about 2.7 cm, in the interval from 15 to 34 cm from the end of the splitter plate. Bubble pairing occurs around 35 cm. Pairing occurs sooner at higher density differences. For the highest density difference (photograph 6), the short wave lengths, which are easily seen at the lower density difference run, are not apparent.

It is observed that the water downstream becomes a uniform gray. There is no well defined stratification of warm clear water above cool dyed water at the end of the test section. The warm and cool water have not switched places which suggest significant molecular mixing occurs.

Shadow graphs provide a convenient quantitative measure of the mixing layer bounds. In photograph 6, in the section marked **A** above the mixing layer, the water is cool and the same temperature as the upper channel. Similarly, the section marked **A** below the mixing region is at

uniform temperature and at the same temperature as the lower channel. The instantaneous shear layer seen in the photograph is well defined and can be measured. The mixing region shows a nonlinear growth. The measured mixture widths for photographs 4, 5 and 6 are compared to Equation 3 in Figure 2. The full mixture width for photograph 6 was measured using the shadow graph to determine the boundary. In photograph 5, the dye was thick and the half width was measured. The data lie between quadratic curves with a constant of 0.4 and 0.8. Future data reduction will use ensemble averaged digitized photographs.

Buoyancy and shear

Photographs 7 and 8 show runs where cool water flows over warm water but with the flows at a different velocity. Both cases show a high degree of mixing typical of buoyancy induced mixing alone. From examining the instantaneous pictures, the mixing width is greater with both buoyancy and shear (photograph 8) than with buoyancy only (photograph 7). Because the behavior is nearly the same, an averaging process is required to determine to what degree the velocity difference adds to the mixing.

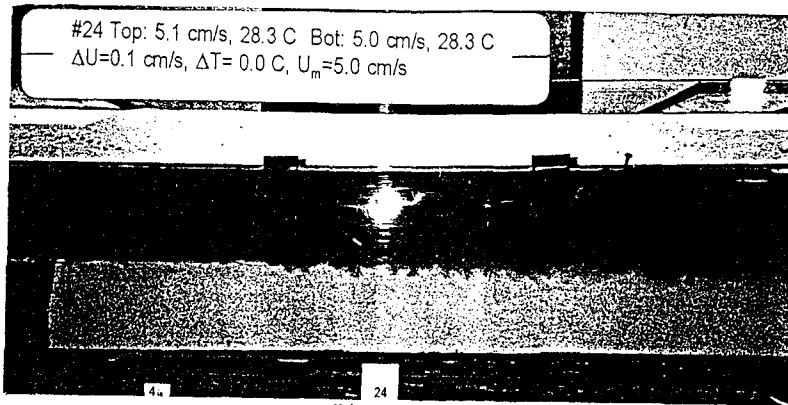
Conclusions

A statistically steady experiment has been developed that allows for independent control of buoyancy and shear driven mixing. Experimental data from our exploratory system show that we can reproduce characteristics of pure shear mixing layers and pure buoyancy driven mixing.

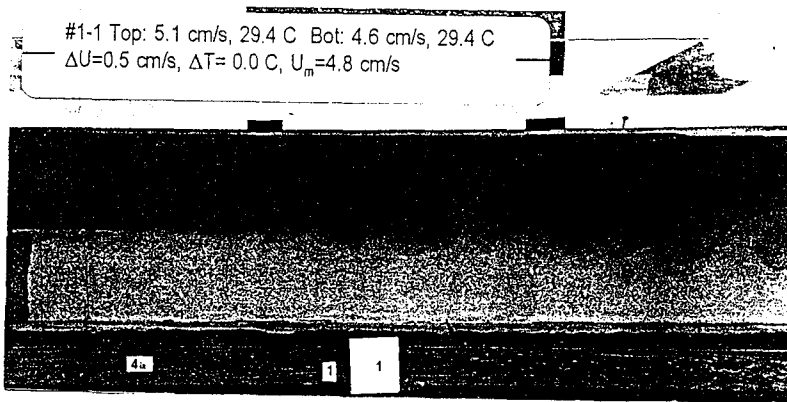
For combined buoyancy and shear mixing, preliminary results indicate that for the temperature differences in this study, buoyancy is the predominant driver for mixing. From this preliminary work, shear and buoyancy mixing appear to induce slightly faster mixing than buoyancy alone.

References

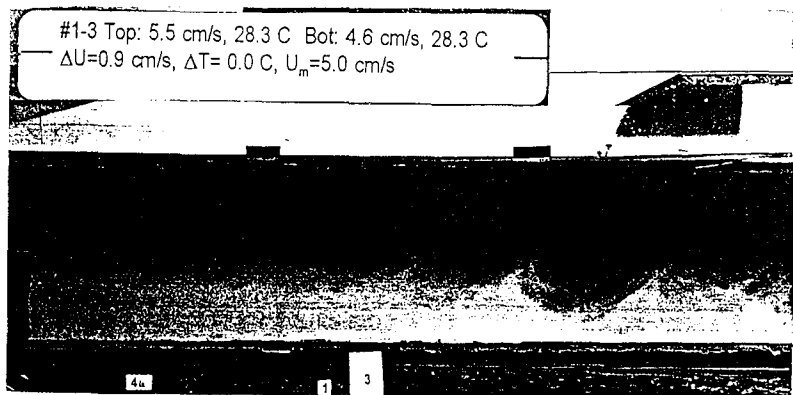
- 1 C. G. Koop, (1976), Instability and turbulence in a stratified shear layer, Ph.D. Thesis, Univ., South. Calif.
- 2 F. L. Brown and A. Roshko, (1974), On density effects and large structure in turbulent mixing layers," *JFM*, vol. 64, pp 775-816.
- 3 M. M. Koochesfahani and P. E. Dimotakis, (1986), "Mixing and chemical reaction in a turbulent liquid mixing layer," *JFM*, vol. 170, pp 83-112.
- 4 M. Lesieur, P. Comite, Y. Fouillet and A. Silveria, (1991), Three-dimensional numerical simulation of coherent structures in free-shear flows, *The Global Geometry of Turbulence*, Plenum Press, NY.
- 5 S. Tavoularis and S. Corrsin, (1987), "The structure of a turbulent shear layer embedded in turbulence," *Phys. Fluids* vol. 30, no. 10, pp 3025-3033.
- 6 M. M. Rogers and R. D. Moser (1992), "The three-dimensional evolution of a plane mixing layer: the Kelvin-Helmholtz rollup," *JFM*, vol. 243, pp 183-226.
- 7 A. Roshko, (1991), "The mixing transition in free shear flow," *The Global Geometry of Turbulence*, Plenum Press, NY.
- 8 D. L. Youngs, (1992), "Experimental investigation of turbulent mixing by Rayleigh-Taylor instability", *Advances in Compressible Turbulent Mixing*, International Workshop on the Physics of Compressible Turbulent Mixing, Conf-8810234, National Tech. Serv., U.U. Dept Com, 5285 Port Royal, Springfield, VA 22161, pp 607-626.
- 9 D. L. Youngs, (1984), "Numerical simulation of turbulent mixing by Rayleigh-Taylor instability," *Physica 12D*, pp 32-44.
- 10 J. Glimm, X. L. Li, Q. Zhang, (1992), "Statistical theories of Rayleigh-Taylor instabilities for compressible fluids," *Advances in Compressible Turbulent Mixing*, International Workshop on the Physics of Compressible Turbulent Mixing, Conf-8810234, National Tech. Serv., U.U. Dept Com, 5285 Port Royal, Springfield, VA 22161, pp 85-93.
- 11 J. C. Lasheras and H. Choi, (1988), "Three-dimensional instability of a plane free shear layer: an experimental study of the formation of the streamwise vortices," *JFM*, vol. 189, pp 53-86.



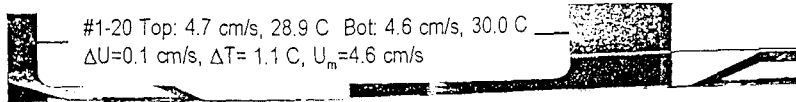
Photograph 1



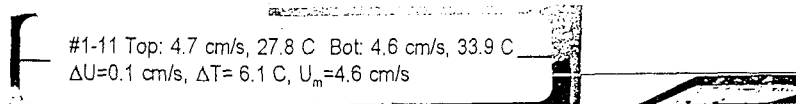
Photograph 2



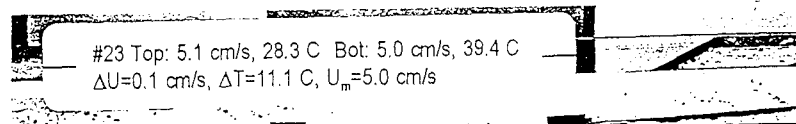
Photograph 3



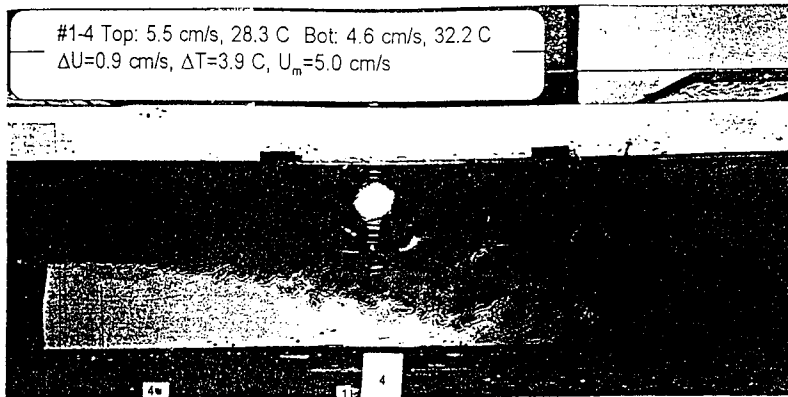
Photograph 4



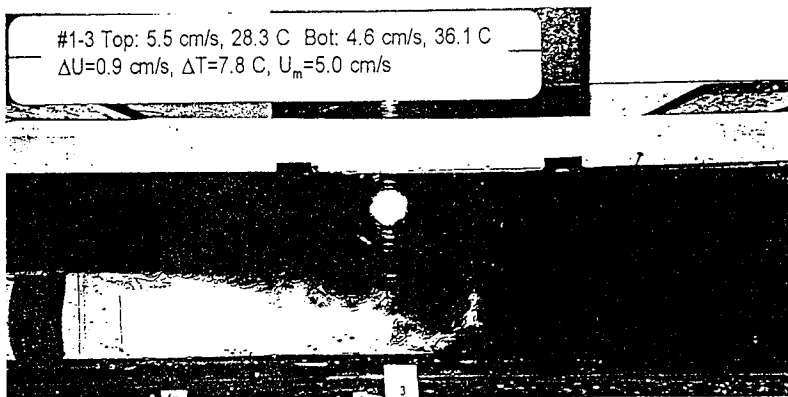
Photograph 5



Photograph 6



Photograph 7



Photograph 8

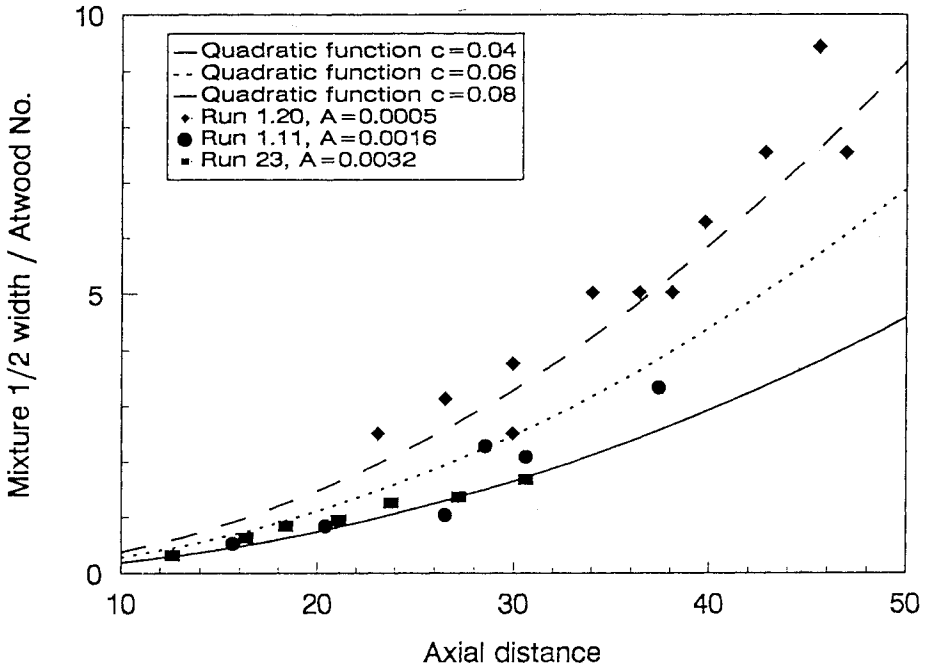


Figure 2. Mixing width along channel length.

Instability Calculations for the LEM Driver at LLNL

Peter Stry, Guy Dimonte, Bruce Remington
Eugene Burke and W. Patrick Crowley

Lawrence Livermore National Laboratory
Livermore, California 94550, U. S. A.

Abstract

The linear electric motor (LEM) at LLNL (see Dimonte *et al.*) will allow us to perform experiments similar to the AWE rocket rig experiments (Burrows, Smeeton, Youngs) but with a greater freedom to vary the acceleration, $g(t)$. Some sets of numerical simulations are presented here in support of these experiments, made with CALE, a 2D ALE code. Each set of simulations begins with a calculation of a corresponding AWE experiment to gain confidence in the code and calculational procedure. Certain experimental difficulties - the initial meniscus shape of the interface, drag along the sides of the tank, and the effect of variable accelerations, $g(t)$ - are treated calculationally and found not to have major detrimental effects. Finally, an acceleration profile with reversing sign of $g(t)$ is proposed to challenge simple models of turbulent mixing region (TMR) growth.

Introduction

The linear electric motor (LEM) being constructed at LLNL is described in detail in another report presented at this conference (see Dimonte *et al.*). This report describes some sets of numerical calculations made in support of hydrodynamic instability experiments we plan to perform with the LEM. All of these simulations were performed with CALE, a 2D arbitrary Lagrangian Eulerian (ALE) code capable of multi-material Eulerian flow and mixing and interface tracking on a sub-grid scale¹. The meshes were flat 2D and the equations of state were in Gruneisen form for these nearly incompressible flows.

An important first step in these simulations is testing the code and calculational methods against previous measurements. We are very fortunate to have available for that purpose an extensive series of well described mixing experiments performed by Youngs *et al.* at AWE^{2,3,4}. Whenever possible we begin a set of LEM simulations by calculating the corresponding AWE measurements.

Description of Calculations and Procedure

The simplest acceleration profile envisioned for the LEM is a constant acceleration of the experimental tank for a distance of one meter. To begin this first set of calculations, Fig. 1 shows the results of CALE applied to calculate some corresponding AWE measurements³. The data are from AWE experiments 54, 66 and 71 in which a tank containing an interface between CaCl₂ dissolved in water ($\rho=1.145$ g/cm³) and hexane ($\rho=.66$ g/cm³) was accelerated at about 45g₀. The agreement with the AWE experiments is reasonably good. Initial and final CALE meshes are shown in Fig 2. Allowing for a plane of symmetry, the mesh spans one half of the 2D projection of the 15x15x15 cm³ AWE tank.

The visible initial roughness of the initial interface in Fig. 2a points out the problem of initializing these calculations. For the liquids and accelerations considered the minimum wavelength for positive growth is determined physically by the surface tension, T,

$$\Lambda_c = 2\pi[T / (g (\rho_2 - \rho_1))]^{1/2} \quad (1)$$

and the maximum growth rate is at $\Lambda_{\max} = \sqrt{3} \Lambda_c$ ⁵. In a calculational mesh a "computational viscosity" is produced by a complicated mixture of explicit artificial viscosity and the incidental effects of solving the fluid motion equations in discrete form for finite cell size. The latter is dominant for the nearly incompressible flows considered here and determines a purely numerical "minimum wavelength" about equal to twice the mesh cell size. A further factor in these calculations is that the running time grows approximately as the inverse third power of the mesh spacing. Taking into account all these considerations, a practical way to initialize the calculations was found: adopting a mesh spacing of 1/4 Λ_{\max} in both directions at the interface and imposing there an initial random perturbation with maximum amplitude of 1/2 Λ_{\max} . This prescription was determined by numerical experiments, successively refining the mesh until adequate agreement with the data was reached. Even so, until the amplitude has a chance to grow to a few times Λ_{\max} , the calculations slightly under-predict the data. It should be emphasized that we regard this initialization prescription as a practical way of using our particular code to predict the LEM experimental results, not necessarily a general solution to the initialization problem.

Fig. 3 contains the CALE prediction for the final configuration of the 7x14x7 cm³ LEM tank after 1 m of acceleration at 100 g₀. The fluids are the same as the AWE tank in Fig 2 and the initialization method is as

described above. The LLNL LEM is designed to be capable ultimately of producing up to 300 g_0 accelerations for 1 m, but the initial experiments will be at lesser values.

CALE calculations also allows us to try to quantify the effects of two complicating factors in these experiments - the effects of drag on the fluid motions by the sides of the tank and the effect of the initial meniscus shape of the interface. Fig. 4 was produced by a calculation exactly the same as Fig. 3 except for additional features applied to attempt to model these complications. A meniscus 0.3 mm high and 0.5 mm wide was superimposed on the initial interface shape at the outer boundary of the mesh and a surface drag term was also applied there:

$$F/A = C_D \rho v^2 \quad (2)$$

where C_D , the drag coefficient, is .0065 corresponding to a Reynolds number of about 41,000, characteristic of the final, fully developed turbulence at the interface. The differences between Fig. 4 and Fig. 3 are slight and confined to the outer interface. This calculation points out an advantage of all such accelerated tank experiments relative to stationary tanks and shock tubes - boundary effects tend to be small because at least initially there is only slight relative motion of the fluids and the walls.

A slightly more complicated set of experiments planned for the LEM consists of an acceleration phase followed by coasting. Again we begin the set of simulations by calculating some corresponding AWE measurements⁴. Fig. 5 compares the AWE measurements of their experiments 107, 108 and 116 to results of CALE calculations. The fluids were the same as above, the accelerations were about 42 g_0 for 50 ms. followed by coasting. The agreement is again close. Our calculated instability amplitudes have a slightly more quadratic growth with time during the acceleration phase, closer to the simple formula (for constant g)²,

$$h = Y x_{\text{eff}} = Y \alpha g t^2 \quad (3)$$

where h is the penetration into the denser fluid, Y is the Youngs coefficient $\approx .07$, and α is the Atwood number.

Fig. 6 shows the simulated instability growth for an idealized form of the first acceleration-coasting experiments envisioned for the LLNL LEM: a constant acceleration of 1000 g_0 to 10 cm followed by a coasting phase to 1 or 2 m. The fluids are again the same. The top mesh plot was made at 5 ms, just after the acceleration was turned off, the bottom mesh plot was made at 25 ms when the tank reaches 1 m.

Once again we introduce an experimental complication - due to the time scale of the driving circuit, τ_s , the actual acceleration profile for these short pulses at the LEM will have the form:

$$g = g_{\max} \text{Sin} (\pi t/\tau_s) \tag{4}$$

The effect of this actual acceleration profile on the development of the turbulent mixing region at the interface can be judged by comparing Fig. 6, the ideal case, with Fig. 7 which was generated by the profile of Eq. (4) with parameters $g_{\max} = 1571. g_0$ and $\tau_s = 4.518$ ms. With those parameters the tank reaches 10 cm and begins coasting at the same time as for the idealized profile. The ratio of final mixing region thickness at 25 ms to that at 5 ms is the same in the two cases to within a few percent, but the absolute amplitudes in the $\text{Sin}(\pi t/\tau_s)$ acceleration case are about 20% lower. The ratio of amplitudes mainly determines the measured value of the drag coefficient, C_D , in simple predictive models like the BOLLE formula⁶:

$$\ddot{h} = 2Y(1 + 2C_D)\alpha g(t) - C_D \dot{h}^2/h \tag{5}$$

(with $g(t) = 0$ in the coasting phase). The smaller absolute amplitudes are roughly in line with the more general definition for x_{eff} given by David Youngs for the acceleration phase²:

$$x_{\text{eff}} = \alpha \left[\int \sqrt{g(t)} dt \right]^2 \tag{6}$$

While both acceleration profiles produce the same displacement of the tank, x_{eff} as defined in Eq. (6), is about 10% less for the acceleration profile of Eq. (4).

The final CALE simulation is of a LEM experiment with a $g(t)$ profile chosen explicitly to challenge the simple formulas for instability growth in Eq. (3), (6) and (5).

$$g(t) = \begin{array}{ll} 100 g_0 & t < 15 \text{ ms} \\ -300 g_0 & 15 \text{ ms} < t < 20 \text{ ms} \\ 100 g_0 & 20 \text{ ms} < t \end{array}$$

This profile is really just the constant 100 g_0 acceleration profile of Fig. 3. with the exception that the acceleration reverses for 5 ms, bringing the tank almost to a halt before resuming again. Practically this $g(t)$ could be implemented on the LEM by applying an additional augmentation coil. In

simulations the effect of reversing the acceleration is a period of demixing, analogous to the reversal of perturbation amplitudes for a shock traveling in the stable direction in Richtmyer-Meshkov instabilities. Fig. 8 shows the calculated behavior of the mixing region; the final amplitudes are much larger than for the simple constant 100 g_0 case..

Conclusions

The LLNL LEM seems capable of contributing valuable experimental data in aid of our understanding of the growth of Rayleigh-Taylor instabilities at fluid interfaces. In calculations none of the complications considered - menisci, surface drag on the sides of the tank, timescales of the driving circuit - seem to have greatly detrimental effects on the quality of the measurements.

References

1. Tipton, R. E.; CALE Users Manual, Copyright 1987-1992 The Regents of the University of California. All Rights Reserved.
2. Read, K. I. and Youngs, D. L.; AWRE Report No. O 11/83, "Experimental Investigation of Turbulent Mixing by Rayleigh-Taylor Instability" (1983).
3. Burrows, K. D., Smeeton, V. S., and Youngs, D. L.; AWRE Report No. O 22/84, "Experimental Investigation of Turbulent Mixing by Rayleigh-Taylor Instability II" (1984).
4. Smeeton, V. S. and Youngs, D. L.; AWE Report No. O 35/87, "Experimental Investigation of Turbulent Mixing by Rayleigh-Taylor Instability Part 3" (1987).
5. Chandrasekhar, S.; "Hydrodynamic and Hydromagnetic Stability", Sect. 92. (1961)
6. Crowley, W. P.; "Application of a Two-Equation Turbulence Mix Model" LLNL Report UCRL-98686 (1988)

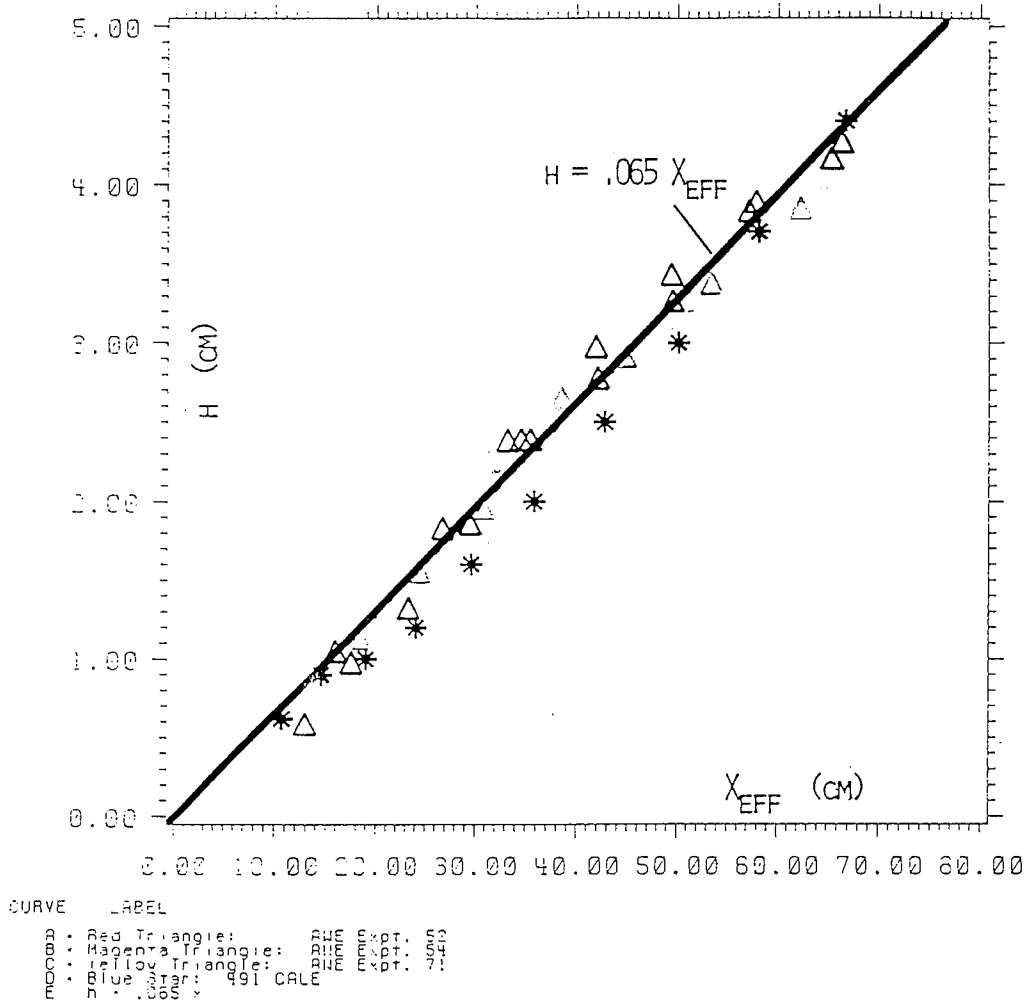


Figure 1. A comparison between CALE simulations and the results of AWE measurements for constant accelerations of a tank containing CaCl₂/H₂O - Hexane.

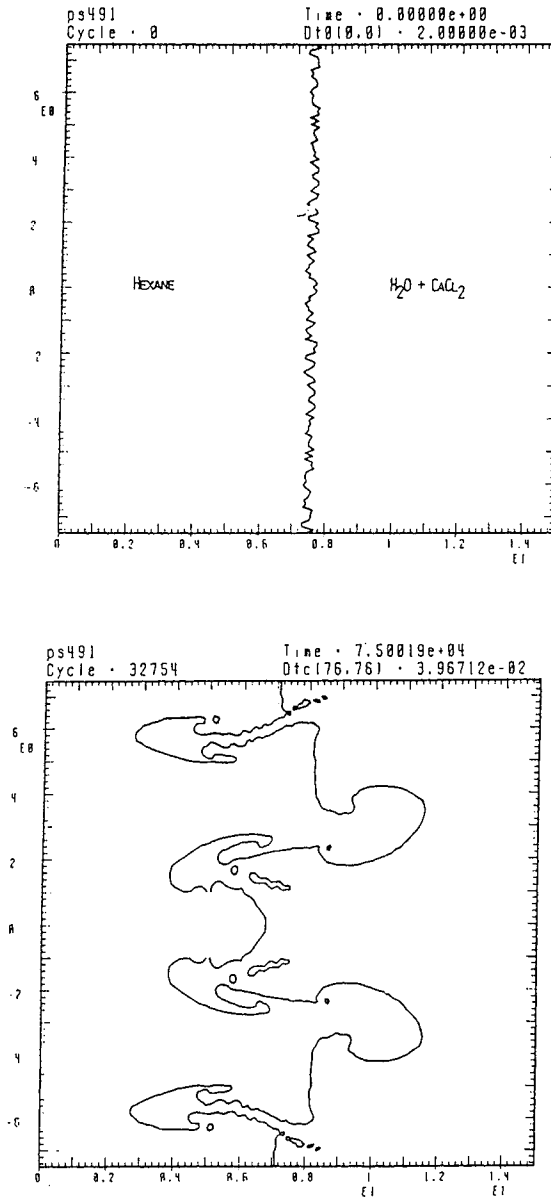


Figure 2. Initial and final meshes for the CALE simulation of the AWE experiments in Fig. 1.

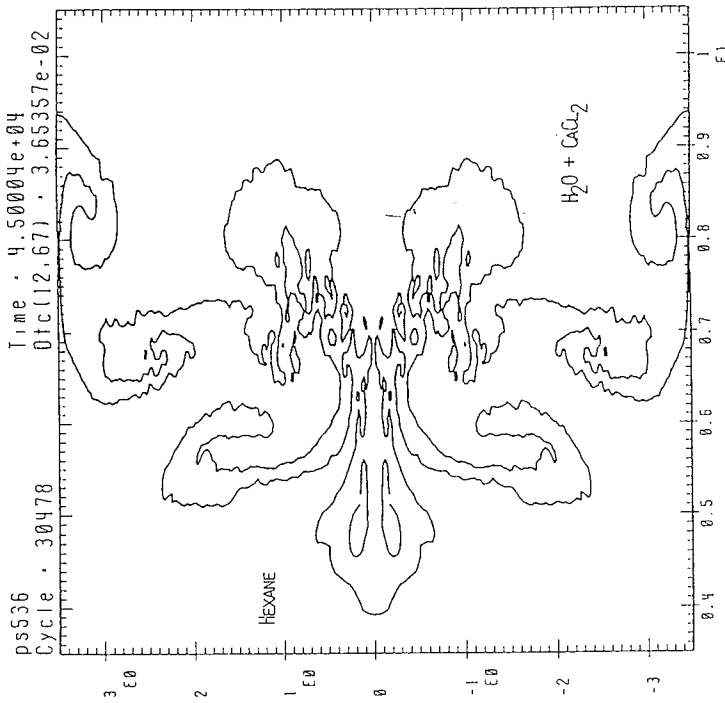


Figure 4. A comparison calculation to the calculation of Fig. 3: 1 m of 100 g acceleration of the LEM tank with additional complications of a meniscus at the surface and drag along the sides of the tank.

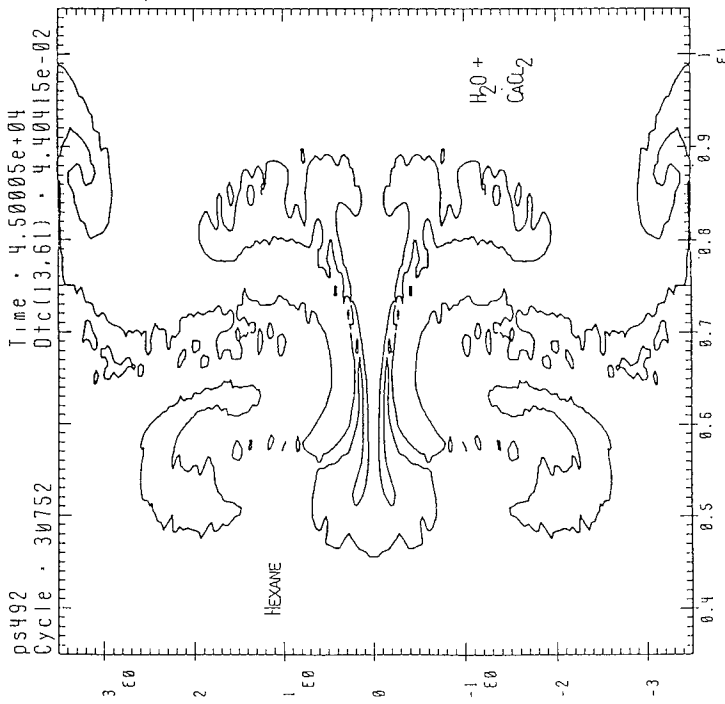


Figure 3. CALE prediction for one of the first proposed LEM experiments: a 100 g acceleration for 1 m of a 7x14x7 cm tank containing $\text{CaCl}_2/\text{H}_2\text{O}$ - Hexane.

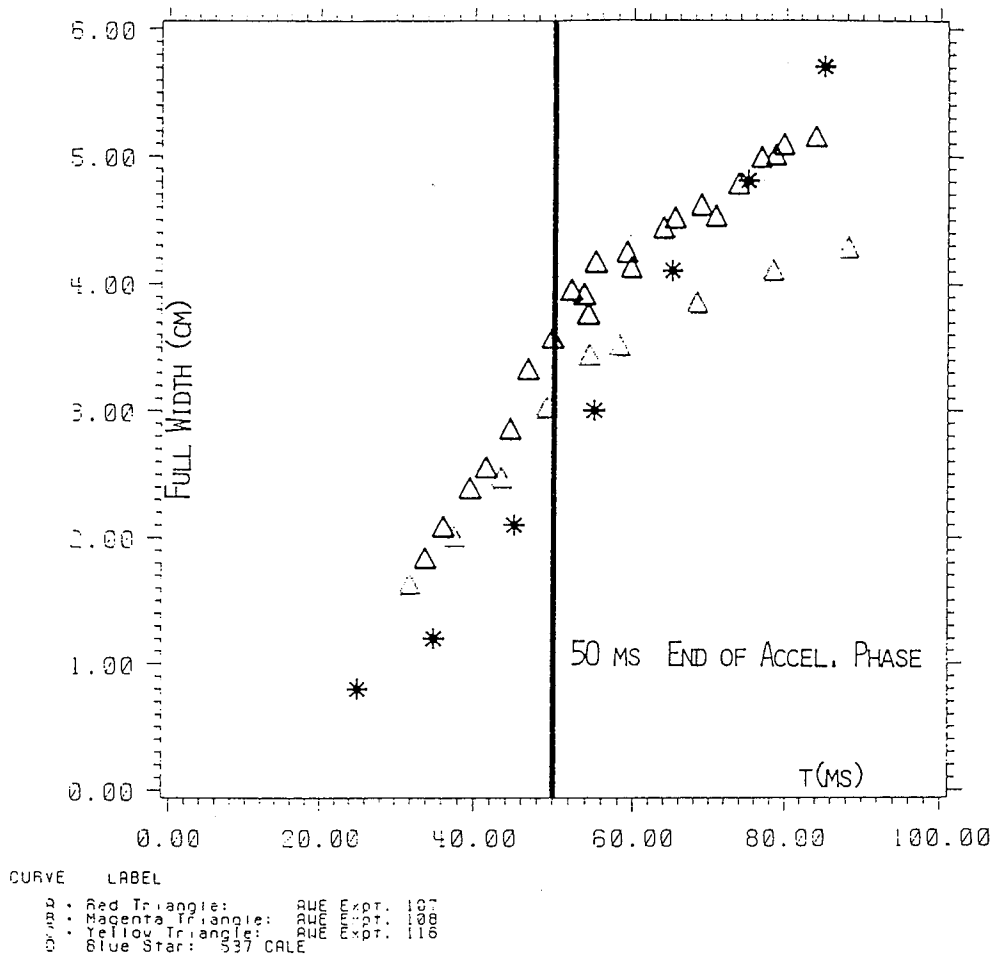


Figure 5. A comparison between CALE simulations and the result of AWE measurements for acceleration and coast experiments.

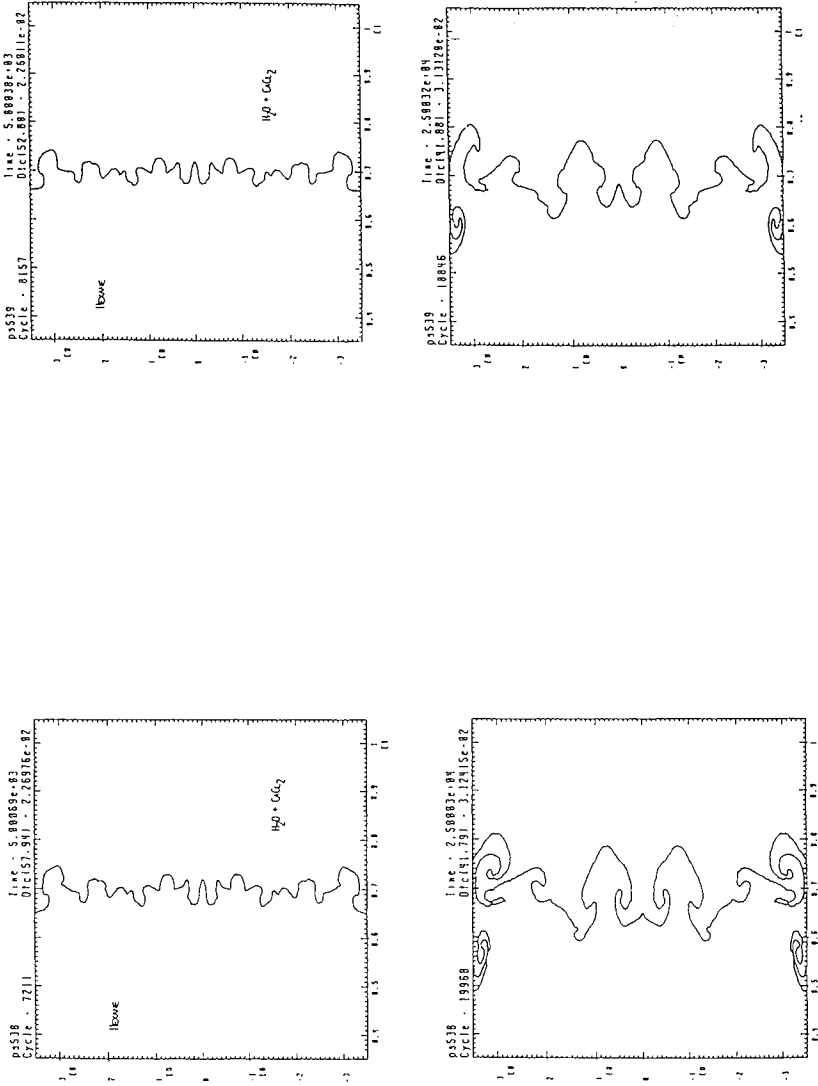


Figure 6. CALE simulation of the proposed LEM acceleration/coast experiment. The acceleration is 1000 g to 10 cm followed by coasting to 1 m. The mesh pictures are taken at 5 ms, just after the acceleration phase, and at 25 ms, the end of the coasting phase.

Figure 7. A comparison calculation to Fig 6, the LEM acceleration/coast experiment. Here the acceleration profile has a non-ideal shape governed by the timescale of the electrical circuitry: $g(t) = g_{max} \sin(\pi t / \tau_s)$.

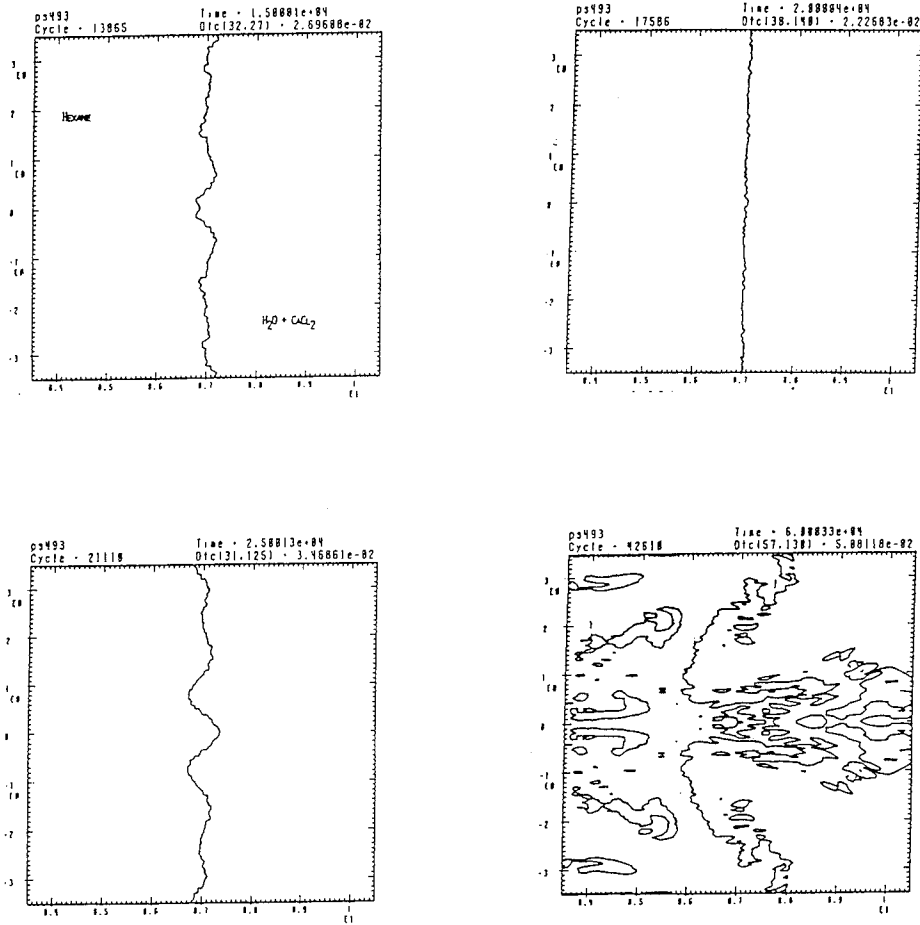


Figure 8. CALE simulations of an acceleration profile with a reversing sign of $g(t)$ chosen to challenge simple predictive formulas. The acceleration is a constant $100 g_0$ as in Fig. 3 and 4 except for a $-300 g_0$ phase from 15 to 20 ms.

DIRECT THREE-DIMENSIONAL NUMERICAL SIMULATION OF MIXING
BY RAYLEIGH-TAYLOR INSTABILITY

David L Youngs

Atomic Weapons Establishment
Aldermaston
Reading, Berkshire
United Kingdom

Introduction

If fluid of density ρ_1 rests on top of fluid of density $\rho_2 < \rho_1$ in a gravitational field g , perturbations at the interface between the two fluids grow due to Rayleigh-Taylor instability. In this paper the two fluids are assumed to be incompressible and g is constant. The two fluids are also assumed to be miscible.

For the case when there is a random multimode initial perturbation at the fluid interface the instability should evolve as follows [1]:-

Stage 1 : A perturbation corresponding to the most unstable wavelength, λ_m , appears. (λ_m may be determined by viscosity or surface tension.)

Stage 2 : When the perturbation of wavelength λ_m reaches a height of the order of $\frac{1}{2}\lambda_m$ its exponential growth rate slows down and longer wavelength perturbations begin to grow more rapidly.

Larger and larger structures appear. If these evolve from the non-linear interaction between smaller structures, then loss of memory of the initial conditions will tend to occur.

Stage 3 : Loss of memory of the initial conditions occurs. gt^2 is the only length scale of importance. Then the width of mixing zone is:-

$$\delta = F \left(\frac{\rho_1}{\rho_2} \right) \cdot gt^2$$

Larger and larger structures appear as time proceeds. The dominant wavelength λ_d at a given time may have evolved from

- or
- (A) the interaction between shorter wavelength structures
 - (B) an initial perturbation of wavelength λ_d

Loss of memory of the initial conditions will only occur if (A) applies. If large-amplitude long wavelength initial perturbations are present mixing may be enhanced.

Rayleigh-Taylor experiments at AWE, Foulness [2] indicated that the depth to which the instability penetrates the denser fluid 1 was given by

$$h_1 = \alpha A g t^2$$

where $A = \frac{\rho_1 - \rho_2}{\rho_1 + \rho_2}$, Atwood number

and $\alpha \sim 0.06$

Similar values of α were reported by Kucherenko et al [3]*. Andrews and Spalding [4] gave $\alpha = 0.04$ for a slim two-dimensional tank. Most other experimental estimates of α are higher. The 3D direct numerical simulation of Youngs [5] indicated $\alpha \sim 0.035$ to 0.04 , lower than most of the experimental results.

The aim of the present investigations is to use high-resolution 3D direct numerical simulation to calculate the value of α for the case when complete loss of memory of the initial conditions occurs.

TURMOIL3D

A simple 3D hydrocode, TURMOILD3D, is used to simulate turbulent mixing of two fluids. The equations solved are the Euler equations plus an equation for the mass fraction of fluid 1:-

$$\frac{\partial}{\partial t} (\rho m_1) + \text{div} (\rho m_1 \underline{u}) = 0$$

A perfect gas equation of state is used (different values of γ may be used for each fluid). The explicit compressible finite difference method is based on the method described by Youngs [6]. For each time step there is a Lagrangian phase followed by an advection (rezoning) phase. In the advection phase the monotonic method of van Leer is used for all fluid variables. This gives a robust numerical method which avoids spurious numerical oscillations. Many essential properties follow; the mass fraction m_1 remains in the interval $[0,1]$ and for the present near-incompressible application the density ρ remains in the interval $[\rho_1, \rho_2]$.

* Recent results presented at this workshop indicate lower values of α .

The monotonicity constraints in the van Leer method introduce numerical dissipation at high wavenumbers. A sub-grid eddy viscosity (or diffusivity) is not used as there is sufficient dissipation in the numerical method to provide the required high-wavenumber dissipation for turbulent flows (of both kinetic energy and density fluctuations). As a sub-grid model is not used, the method has been referred to here as "Direct Numerical Simulation" rather than "Large Eddy Simulation".

In the three dimensional calculations described here the density ratio is $\rho_1/\rho_2 = 3$. The initial density distribution is

$$\rho = \begin{cases} \rho_1 & x < \xi(y, z) \\ \rho_2 & x > \xi(y, z) \end{cases}$$

where ξ is the initial perturbation at $x = 0$. This is a random combination of Fourier modes with wavelengths in the range $4\Delta x$ to $8\Delta x$ and standard deviation $\langle \xi^2 \rangle^{1/2} = 0.08 \Delta x$. The size of the computational region is

$$\begin{aligned} -0.65 < x < 0.9 \\ 0 < y < 0.8 \\ 0 < z < 0.8 \end{aligned}$$

In the x -direction coarse meshes are used in the regions $x < -0.5$ and $x > 0.75$. The calculations are run up to the time when $h_1 = 0.5$. Gravity, in the x -direction, is chosen to give $gA = 1$. The initial pressure is high enough to ensure that the flow is almost incompressible.

Results are shown here for three calculations. Two calculations with different random numbers for the initial perturbation have been performed on the CRAY-YMP at AWE using $270 \times 160 \times 160$ meshes. A high-resolution calculation ($420 \times 256 \times 256$ meshes) has been performed by CRAY Research on a CRAY-YMP M92. This calculation used $\frac{1}{2}$ GW of memory.

Results from the 3D calculations

Figure 1 shows iso-surfaces for the fluid 1 volume fraction, $f_1 = (\rho - \rho_2)/(\rho_1 - \rho_2) = 0.99$, for one of the $270 \times 160 \times 160$ calculations. This shows the bubbles of light fluid penetrating the heavier fluid. The increase in bubble size with time is evident.

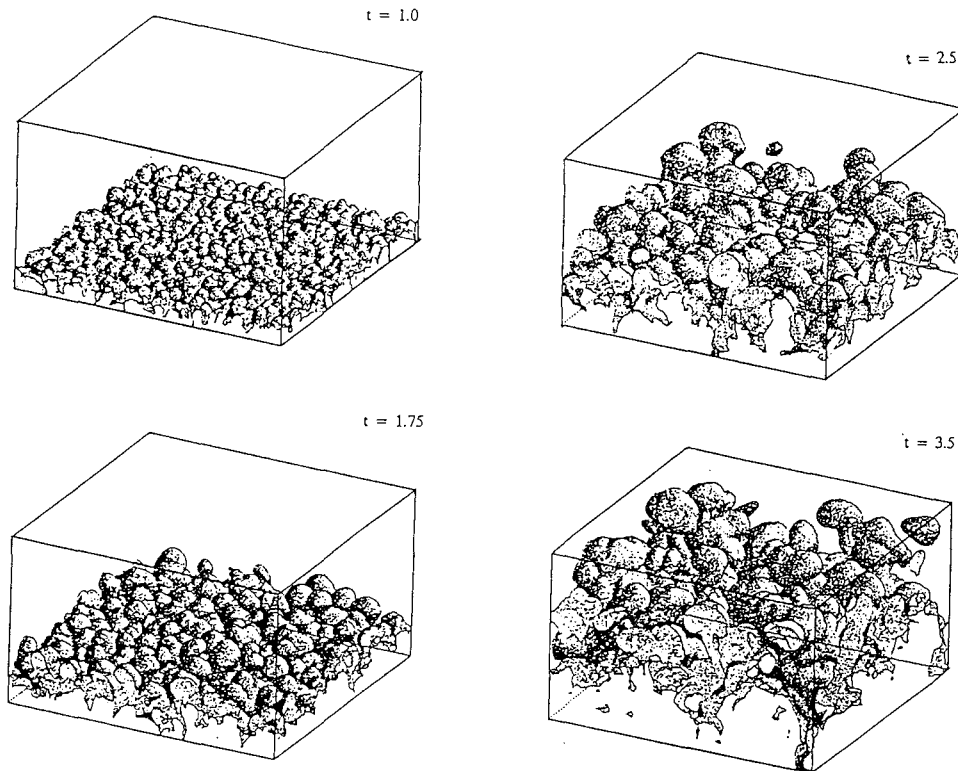


Figure 1: Iso-surfaces for $\overline{f_1}$ in the region $x < 0$. (x -axis vertically downwards.)

The width of the turbulent mixing zone has been quantified in two different ways. The penetrations of fluids 1 and 2, h_1 and h_2 are defined as the distances between the initial interface ($x = 0$) and the points when $\overline{f_1} = 0.99$ and 0.01 respectively. $\overline{f_1}(x)$ denotes the plane averaged value of f_1 . As in [4], an integral width may be defined as

$$W = \int \overline{f_1} \overline{f_2} dx$$

W is less susceptible to statistical fluctuations than h_1 and h_2 . The simulations indicate $h_1 \approx 3.3W$ and $h_2 \approx 3.8W$ at $\rho_1/\rho_2 = 3$. Figure 2 shows a plot of W versus Agt^2 for the three calculations. There is a high initial slope but at late times the slope of the graphs reaches a limiting value which is independent of the mesh size:-

$$W = 0.086 Agt^2 + \text{constant}$$

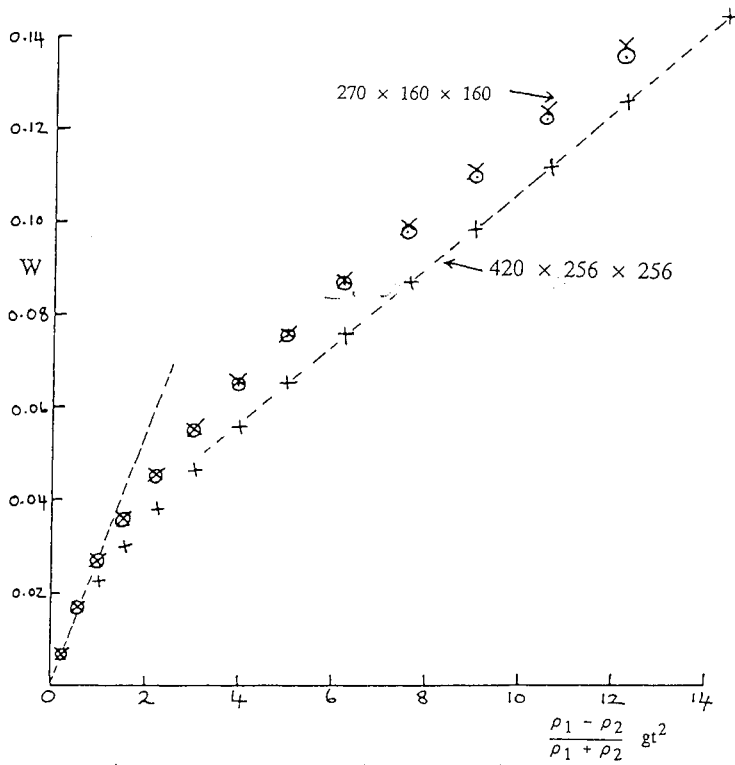


Figure 2: Integral width of mixing zone (W).

This implies $\alpha = 3.3 \times 0.86 \sim 0.03$, significantly less than the experimental values. The transition from the high initial slope to the lower final value depends on the mesh size and begins when $W \sim 6\Delta x$, ie, when the width turbulent mixing zone, $\delta = h_1 + h_2$, is about $40\Delta x$. The high initial slope is attributed to the inability to resolve the inertial range eddies in the early stages of the calculation. The transition occurs earlier in the finer mesh calculation; as a result the width of mixing zone is less at late time.

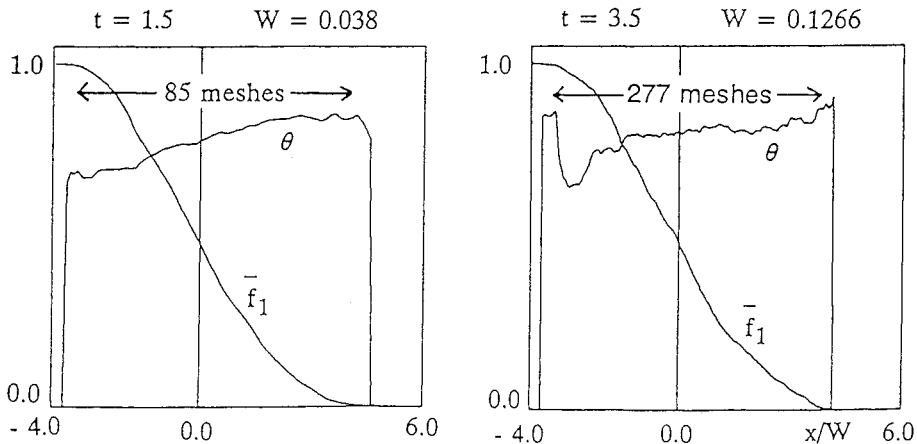


Figure 3: Profiles of fluid 1 volume fraction \bar{f}_1 and molecular mixing fraction θ

Average properties of the turbulent mixing zone are examined in order to show that the numerical simulation gives a self-similar behaviour. As in [5], the molecular mixing fraction for the plane layer $x = a$ constant is defined as

$$\theta(x) = \overline{f_1 f_2} / (\overline{f_1} \cdot \overline{f_2})$$

where the bar denotes the plane average. If there is no molecular mixing, ie, $f_1 = 0$ or 1 , then $\theta = 0$. On the other hand, if there are no concentration fluctuations in the plane $x = a$ constant, ie $f_1 = \overline{f_1}$ and $f_2 = \overline{f_2}$, then $\theta = 1$. Figure 3 shows plots of $\overline{f_1}$ versus x/W and $\theta(x)$ versus x/W for the $420 \times 256 \times 256$ calculation at $t = 1.5$ and $t = 3.5$. Figure 4 shows probability density functions at the same times for f_1 in the plane layers $x/W = -2.0, 0.0$ and $+2.0$. Results obtained at the two times are very similar. However, the resolution of the turbulent mixing zone has increased by a factor 3 from $\delta = 85\Delta x$ at $t = 1.5$ to $\delta = 277\Delta x$ at $t = 3.5$.

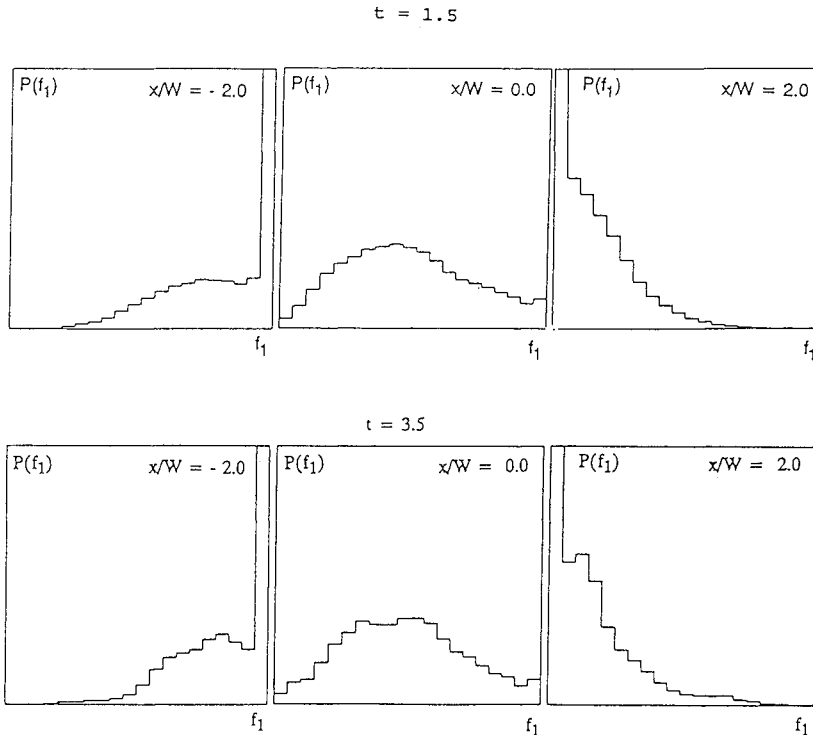


Figure 4: Probability density functions for f_1 in plane layers. (Fine mesh calculation.)

Integral properties of the turbulent mixing zone are also examined. The molecular mixing fraction for the mixing zone as a whole is defined as

$$\Theta = \int \overline{F_1 F_2} dx / \left(\int \overline{F_1} \overline{F_2} . dx \right)$$

K_x , K_y and K_z denote the total kinetic energy components and P denotes the loss of potential energy. In the advection phase kinetic energy is dissipated at high wavenumbers due to the numerical viscosity inherent in the numerical scheme. This is calculated explicitly and summed to give the total dissipation D . It should then follow that $P = K_x + K_y + K_z + D$. For the self-similar case Θ , D/P , K_x/P , etc, should attain constant values. In order to see if this is true, these quantities are plotted against $\Delta x/W$, which is a measure of the mesh resolution (Figure 5). Approximately constant values are obtained for $\Delta x/W < 0.1$, ie, $\delta > 70\Delta x$. There is some run-to-run variation for small $\Delta x/W$ (ie, at the end of the calculations). This is attributed to statistical fluctuations; at the end of the calculations the number of large scale structures over which the averaging takes place is reduced. The limiting values as $\Delta x/W \rightarrow 0$ give the values for the self-similar state. These are approximately:-

$$\begin{aligned} \Theta &= 0.80 \\ K_x / P &= 0.30 \\ K_y / P = K_z / P &= 0.10 \\ D / P &= 0.50 \end{aligned}$$

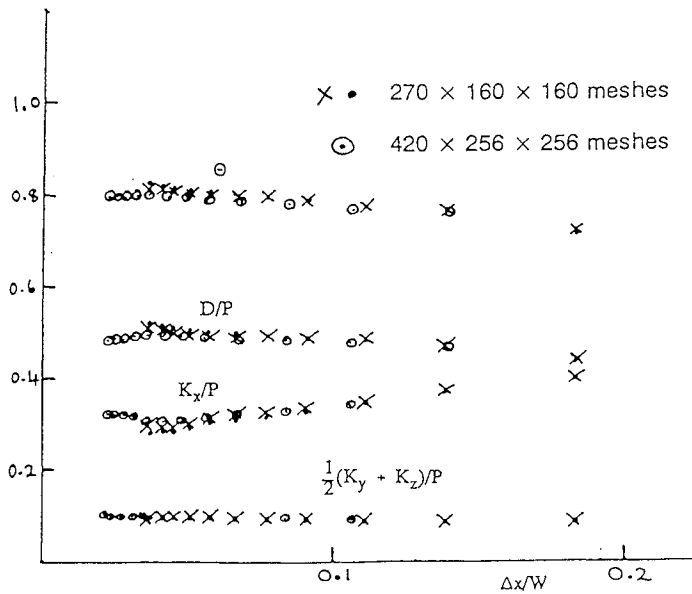


Figure 5: Integrated properties of the turbulent mixing zone versus mesh resolution.

The 3D simulations appear to have reached a self-similar state. As the initial wavelength was small, $\lambda = 4\Delta x$ to $8\Delta x$, loss of memory of the initial conditions should have occurred. However, $\alpha \sim 0.03$, lower than the observed values. This suggests that complete loss of memory of the initial conditions may not have occurred in the experiments, ie, mixing may have been enhanced by additional long wavelength perturbations. This possibility is considered in the next section.

The effect of additional long wavelength perturbations

An equation due to Layzer [7] is used to assess the effect of a single long wavelength perturbation:-

$$\xi(Y, z) = a_0 \cos \frac{2\pi Y}{\lambda}$$

the bubble penetration is given by

$$\frac{dh_1}{dt} = V, (2 + E) \frac{dV}{dt} = gA(1 - E) - C_D \frac{V^2}{\lambda}$$

$$\text{where } E = \exp \left\{ - \frac{6\pi h_1}{\lambda} \right\}$$

Layzer considered the case $A = 1$ and gave $C_D = 6\pi$. Then, at late time, the limiting bubble velocity is

$$V_\infty = \sqrt{\frac{g\lambda}{C_D}} = 0.23 \sqrt{g\lambda}.$$

At $\rho_1/\rho_2 = 3$, 2D simulation for a single wavelength initial perturbation indicates

$$V_{\max} \sim 0.26 \sqrt{gA\lambda}$$

Hence the Layzer equation may be empirically modified for the case when ρ_1/ρ_2 by setting

$$C_D = \frac{gA\lambda}{V_{\max}^2} = 14.8$$

In order to see if an additional long wavelength perturbation enhances mixing we compare the result of integrating the Layzer equation with the quadratic growth law, $h_1 = \alpha Agt^2$.

We define

$$\alpha^* = \frac{h_1 \text{ (from the Layzer equation)} - a_0}{Agt^2}$$

at time when $h_1 = \frac{1}{2}\lambda$

α^* is a function of a_0/λ . Values are given in Table 1 below.

Table 1: Values of α^*

a_0/λ	α^*
0.0005	0.028
0.001	0.033
0.002	0.038
0.005	0.047
0.01	0.055

If α^* is greater than the value of α for the case when complete loss of memory of the initial conditions occurs, then the long wavelength perturbation should enhance mixing. If, for the self-similar case, α is indeed as low as 0.03 then the results given in Table 1 suggest that mixing should be enhanced if

$$\frac{a_0}{\lambda} > 0.001$$

To check that this is reasonable, one of the calculations which used $270 \times 160 \times 160$ zones was repeated with an additional long wavelength perturbation having $\lambda = 0.2$ (ie, four wavelengths across the width of the computational region) and $a_0/\lambda = 0.002$. The bubble penetration, h_1 , is shown in Figure 6. Mixing is enhanced by about 20% at some stages during the calculation. This is approximately in agreement with the results of Table 1.

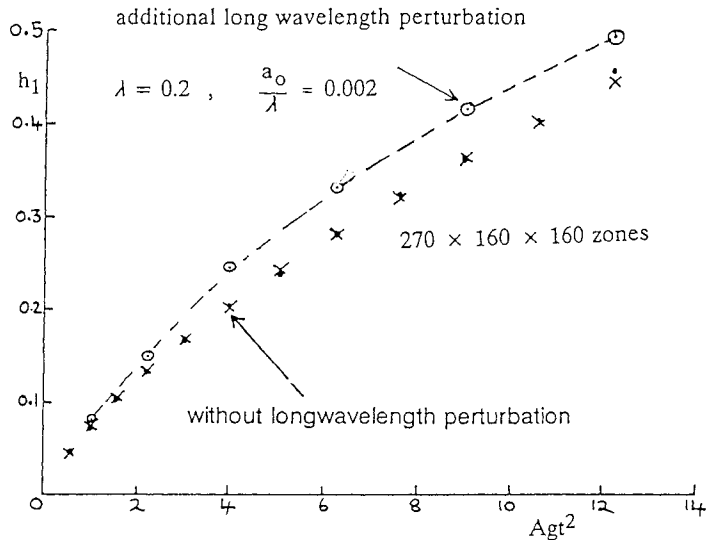


Figure 6: Effect of the additional long wavelength perturbation on bubble penetration (h_1).

Conclusions

Three dimensional numerical simulation shows that for the self-similar state where loss of memory of the initial conditions occurs, there is significant dissipation of density fluctuations and turbulent kinetic energy. The growth rate coefficient α is found to be approximately 0.03 at $\rho_1/\rho_2 = 3$. This is significantly less than most of the experimental values. If this low value is indeed correct, then the mixing rate will be very susceptible to additional long wavelength perturbations. The effect of such additional perturbations may explain the higher observed growth rates.

The uncertainty in the value of α is a major problem for the development of turbulence models (model coefficients are chosen to fit a given value of α). Hence values of α from independent three dimensional numerical simulations would be of great value. More carefully controlled Rayleigh-Taylor experiments with improved diagnostics are also needed.

Acknowledgements

I would like to thank Jan Wilson of CRAY Research (UK) Ltd for her assistance in running the high-resolution Rayleigh-Taylor simulation, and CRAY Research for providing computer time on the CRAY-YMP M92.

References

1. D L Youngs: "Numerical simulation of turbulent mixing by Rayleigh-Taylor instability". Physica 12D, p32 (1984)
2. D L Youngs: "Modelling turbulent mixing by Rayleigh-Taylor instability". Physica D37, p270 (1989)
3. Yu A Kucherenko, L I Shibarshov, V I Chitaikin, S I Balabin and A P Pylaev: "Experimental study of the gravitational turbulent mixing self-similar mode". Proceedings of the 3rd International Workshop on the Physics of Compressible Turbulent Mixing, Royaumont (1991)
4. M J Andrews and D B Spalding: "A simple experiment to investigate two-dimensional mixing by Rayleigh-Taylor instability". Phys Fluids A, 2, p922 (1990)
5. D L Youngs: "Three-dimensional numerical simulation of turbulent mixing by Rayleigh-Taylor instability". Phys Fluid A, 3, p1312 (1991)
6. D L Youngs: "Time-dependent multi-material flow with large fluid distortion", in Numerical Methods for Fluid Dynamics, Eds. K W Morton and M J Baines, Academic Press (1982)
7. D Layzer: "On the instability of superposed fluids in a gravitational field". Astrophysical J 122, p1 (1955)

The study of Rayleigh-Taylor instability in continuous interface

S.G. Zaytsev, E.I. Chebotareva and S.N. Titov

The Krzhizhanovsky Power Institute, Leninsky Pr.19, Moscow, 117071, Russia

Abstract

The Rayleigh-Taylor instability has been studied in a layer of finite thickness (continuous interface) between two gases of different densities. The interface was generated by removing the plate, initially separating the gases, from the channel, followed by mixing caused by molecular diffusion. Then in the upper part of the channel filled with an oxygen-hydrogen mixture (molecular weight $\mu=18.5$), a flame was ignited. A compression wave formed ahead of the flame front hit the continuous interface and drew it into accelerated motion down the channel. The lower part of the channel was filled with either argon ($\mu=38.9$) or helium ($\mu=4$). The motion of continuous interface was visualized by the interferometer. During the accelerated motion, perturbation grew in the fronts which separated the continuous interface from the "pure" gases. The amplitude a of the perturbations grew exponentially in time provided that $a < \lambda$ (λ is the perturbation wavelength). The growth rate in continuous interface was nearly half that in a discontinuous interface, for equal density ratios and accelerations.

Introduction

This paper represents the experimental studies on the evolution of a continuous interface between two gases of different densities accelerated in a direction perpendicular to the interface. In several theoretical and experimental papers [1,2] it has been reported, that the interface was unstable for $\nabla p \cdot \nabla \rho < 0$ (where p is the pressure and ρ is the density). Perturbations in the interface grew exponentially with an increment of $\gamma_0 = \sqrt{k g A}$ ($k = 2\pi\lambda^{-1}$ is the wave number), $A = (\rho_1 - \rho_2) / (\rho_1 + \rho_2)$ is the Atwood number, g is the acceleration under the gravity), if under these conditions the density changed discontinuously. The replacement of a discontinuous interface with a continuous one reduced the instability growth rate observed for the linear stage [3]. The significant effect of the density profile on the retardation of the instability evolution has been considered in [4].

To determine the influence of an interface on the instability evolution, an experimental set-up providing the generation of perturbed interfaces, has been developed. Interfaces were accelerated by a compression wave generated ahead of the flame front. An optical system with a Mach-Zehnder interferometer and a laser light source was used to record the process. A ruby laser was used in a flash mode which yielded from 10 to 12 pictures of the interface at 30 μ s intervals. The linear and transition regimes in the instability evolution, as well as the effect of the interface thickness, have been studied.

1. Experimental set-up.

The principal element of the set-up was a vertical channel with a cross-section of $7.2 \times 7.2 \text{ cm}^2$ (Figure 1). A measuring unit with walls made of optical glass has been mounted in the lower part of the channel. A quickly removable plate which divided the channel into two parts was in the field of view. Prior to experiment, both parts of the channel were evacuated and filled with different gases at the same pressure. The upper part of the channel was filled with an oxygen-hydrogen mixture ($\mu=18.5$), and the lower part was filled with an inert gas (Ar, Kr, Xe, He). The 2mm thick separating plate has been removed by a spring mechanism. The plate was removed from the channel at acceleration. The time of the complete removal of the plate ranged from 40 to 150 ms. The removal of the plate induced the generation of an interface between the oxygen-hydrogen mixture and inert gas. After the plate has left the channel, the combustible mixture was immediately ignited at the upper flange and a flame F rushed down the channel. A compression wave C_0 was generated ahead of the flame front. The compression wave was flat until its interaction with K_0 resulted in acceleration of K_0 down the channel. The distance between the point where the combustible mixture was ignited and the location of the plate was a little shorter than that required for a transformation of a travelling compression wave into a shock wave; K_0 was located in a field of acceleration growing steadily in time.

The system of coordinates used in this paper is given in Figure 1. A part of the channel between the cross-sections $x=\pm 5\text{cm}$ (except from the section $-0.15\text{cm} < x < +0.15\text{cm}$, containing the sliding plate and observed as a dark band in the interferograms) is in the field of view.

2. Generation of an interface after the plate removal

On the removal of the plate, the gases in the upper and lower parts of the channel started mixing. Monotony and undulatory interfaces could be generated by changing the pressure, combinations of gases and the speed of plate removal. Analysis of the experimental data has shown that the interface boundaries were monotonous lines with Reynolds numbers of $Re = ud\nu^{-1} < 40$ (u and d are the speed and thickness of the plate, respectively, and ν is viscosity). Undulatory perturbations appeared in the interface at $Re \cong 100$. Since the Reynolds numbers on the side of a heavy gas were always higher than those on the side of the light one, the interface surface adjacent to the heavy gas would be perturbed the first. The perturbations became the most pronounced when $y < 3 \text{ cm}$, i.e. where the plate speed was the highest. For $Re \gg 100$, the character of perturbations resembled a "Karman vortex street". For every combination of gases, the wavelength of the generated perturbations remained the same. Thus, for the combustible mixture/argon combination, $\lambda = 1.5 \pm 0.2 \text{ cm}$ and for the combustible mixture/xenon combination, $\lambda = 0.9 \pm 0.1 \text{ cm}$. The perturbation amplitudes ranged from less than a millimetre to 6mm within each experiment.

3. Determination of the density in continuous interface.

In order to determine how the density was distributed throughout the interface, the interference bands were aligned parallel to the sliding plate. Figure 2(a) represents a typical interferogram for the interface pattern, obtained for the oxygen-hydrogen mixture/argon combination. An interface with high $\nabla\rho$ is represented as a system of narrow interference bands of a varying width. The bands remained equidistant in pure gases. The value of the interference band shift in the interface is given by

$$K = \frac{(x_0 + n_i - 1)\delta - x_i}{\delta},$$

where x_0 is the coordinate of any unshifted band crossing the pure gas region, n_i is the number of the band in the interface ($i=1$ for the band with x_0 -coordinate), x_i is the coordinate of the n_i -band and δ is the interference band width in an unshifted state). Figure 2(b) shows the distribution pattern of the dimensionless density $\rho^* = (\rho - \rho_1) / (\rho_2 - \rho_1)$ along the x -axis for two cross-sections y_1 and y_2 . To determine the density, the temperature changes in the interface were neglected, and the oxygen/hydrogen ratio as this mixture was mixing with argon has been assumed to remain constant and equal to that in the upper part of the channel before ignition. Similar density distributions were obtained for the cross-section y_1 , which corresponded to the extreme points of the interface. The figure clearly demonstrates the monotonous change of density inside the interface. The interface surfaces were determined as the sets of points with $\rho^*=0.1$ and $\rho^*=0.9$. Figure 2(c) shows the interface determined as described above. The distance between the interface surfaces along the x -axis, $\Delta = x_B - x_C$, was taken to be the interface thickness. The time of mixing in each cross-section was determined by employing $y-t$ diagram of the plate travel. Figure 3 shows the growth of the interface thickness after the removal of the plate. The solid line in this figure is the design value of interface thickness dependent on molecular diffusion. A good agreement indicates that it is a molecular diffusion that principally controls the interface thickness. The perturbation amplitude a is the difference between the extreme points in the interface surface on the side of combustible mixture: $a = x_A - x_B$.

4. The interface evolution under acceleration.

When the compression wave hit the interface, it accelerated the latter along the x -axis. The acceleration was growing continuously with the interface moving along the visualised section of the channel. In most of experiments the acceleration ranged from 0 to $3-5.0 \times 10^7 \text{ cm/s}^2$. The continuous interface has been found to be gradually compressed when the compression wave passed from the light gas into the heavy one and vice versa. The monotonous character of the interfaces was not distorted within the field of view. To measure the thickness $\Delta(t)$ of the interface moving under the compression wave, the paths

ordinate axis, the interface thickness divided by that before the compression wave arrival is plotted. As can be clearly seen from the figure, by the moment the wave has left the field of view, the thickness Δ has decreased by 30%. A similar compression has been found for undulatory interfaces, when the compression wave passed from the heavy gas into the light one. This was the most evident when the lower part of the channel was filled with helium. Once the plate has been removed, with the heavy medium overlaying the light one in the gravitational field, the system becomes unstable. If the ignition was delayed, in the interferograms appeared bubbles and spikes, the characteristic elements of RT instability pattern. The first frame in Figure 5(a) shows the interface between the combustible mixture and helium 50ms after the withdrawal of the plate. The arrival of the compression wave changed the direction of acceleration, the system became unstable and the perturbation growth was stopped. As the interface moved across the field of view in the channel, the pattern in the first frame shrank, being gradually transformed into a layer with slightly perturbed surfaces (the second frame in figure 5(a)).

For experimental studies of the Rayleigh-Taylor instability evolution in a continuous interface accelerated by a compression wave, the lower part of the channel was filled with argon, provided that $Re > 100$. The interface was accelerated to $g \approx 2 \times 10^7 \text{ cm/s}^2$ by the compression wave, and within the time $t \approx 700 \mu\text{s}$ the interface covered 5cm of the field of view. In this case, the perturbation amplitude grew continuously, eventually exceeding the wavelength. The growth of the interface thickness caused by molecular diffusion did not exceed 1%. Figure 5(b) shows an interferometric pattern of the interface between the combustible mixture and argon for two instants of time.

In order to determine $a(2S)$ or $a(t)$ (S is the path length), the motion paths of points A and B were plotted and the value $a = x_A - x_B$ was determined for definite positions of the interface. Figure 6 represents the experimental curves of $\ln a(\sqrt{2S})$ for two patterns corresponding to different thickness of interface. This figure demonstrates an exponential amplitude growth for both perturbations at the initial stage, which was significantly retarded for $\alpha/\lambda > 0.3$. A comparison of recorded a with the interferometric patterns of perturbations has shown that the retardation was accompanied by distortions of the perturbation sinusoidal shape and by appearance of a spike, quickly producing a mushroom-like structure on its edge.

The straight lines 1* and 2* in the same figure show the exponential growth of amplitude with factor $\beta = \sqrt{Ak2S}$ for each pattern. The deviation of the calculated values from the experimental ones, caused by the replacement of a discontinuous interface with a continuous one, grew with the interface thickness. A model allowing to take into account the retardation of amplitude growth rate by introducing a growth reduction factor Ψ into exponential factor β was proposed in [5]: $\beta^* = \sqrt{Ak2S/\Psi}$. Ψ is a function of interface thickness and Atwood number. Figure 7 represents the theoretical and experimental values Ψ for different interface thicknesses. When analysing the experiments, Atwood number was assumed to be constant and equal to 0.365. The disposition of the experimental points higher than 1 has enabled us to assert unequivocally that the replacement of a discontinuous interface with a continuous one reduced the amplitude growth rate.

Experimental values Ψ obtained for $0.3\lambda < a < \lambda$ have shown an approximate agreement with the data calculated by the method proposed in [5] (solid line in Figure 7).

Acknowledgement

We would like to thank Dr J.F. Haas for his helpful advices and comments on the manuscript.

References

1. G.I. Taylor. The instability of liquid surfaces when accelerated in a direction perpendicular to their planes. Proc. Roy. Soc. London. Ser.A, 1950, vol. 201, No. 1065, pp. 192-196.
2. D.I. Lewis. The instability of liquid surfaces when accelerated in a direction perpendicular to their planes. Proc. Roy. Soc. London. Ser.A, 1950, vol. 202, No. 1065, pp. 81-96.
3. B.B. Chakraborty. Rayleigh-Taylor instability of heavy fluid. Phys. Fluids. 1975, vol. 18, No 8, p.1066.
4. E.I. Zababakhin and A.P. Ptitsyn. Limitations of convection instability. Voprosy Atomnoi Nauki i Tekhniki. 1988. No. 1.
5. R.E. Duff, F.H Harlow and C.W Hirt. Effects of diffusion on interface instability between gases. Phys. Fluids, 1962, vol. 5, No. 4, pp. 417-425.

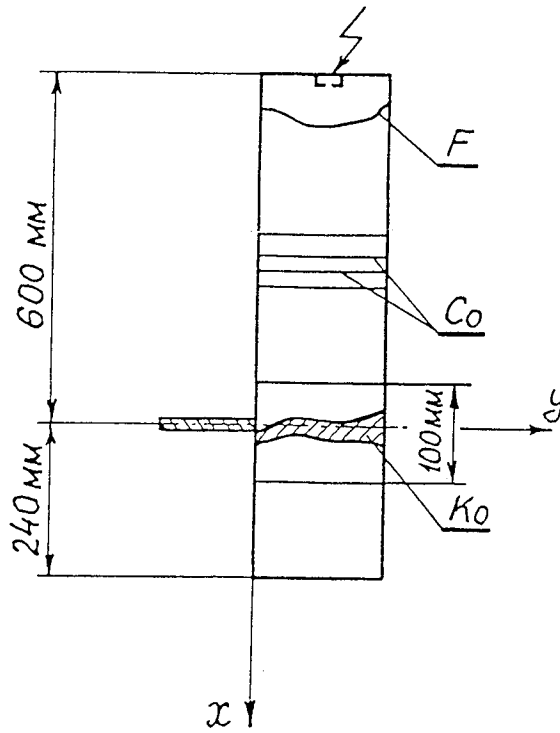


Fig. 1. A scheme of the set-up.

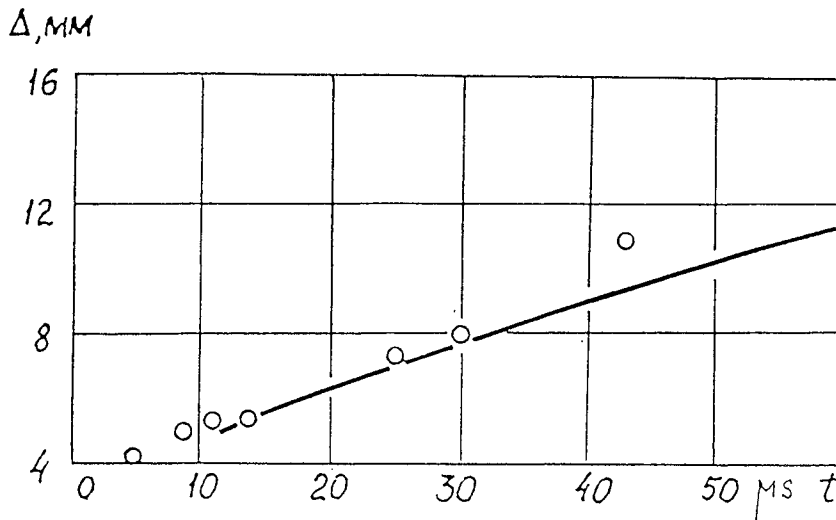


Fig. 3. Growth of the interface thickness due to diffusion.

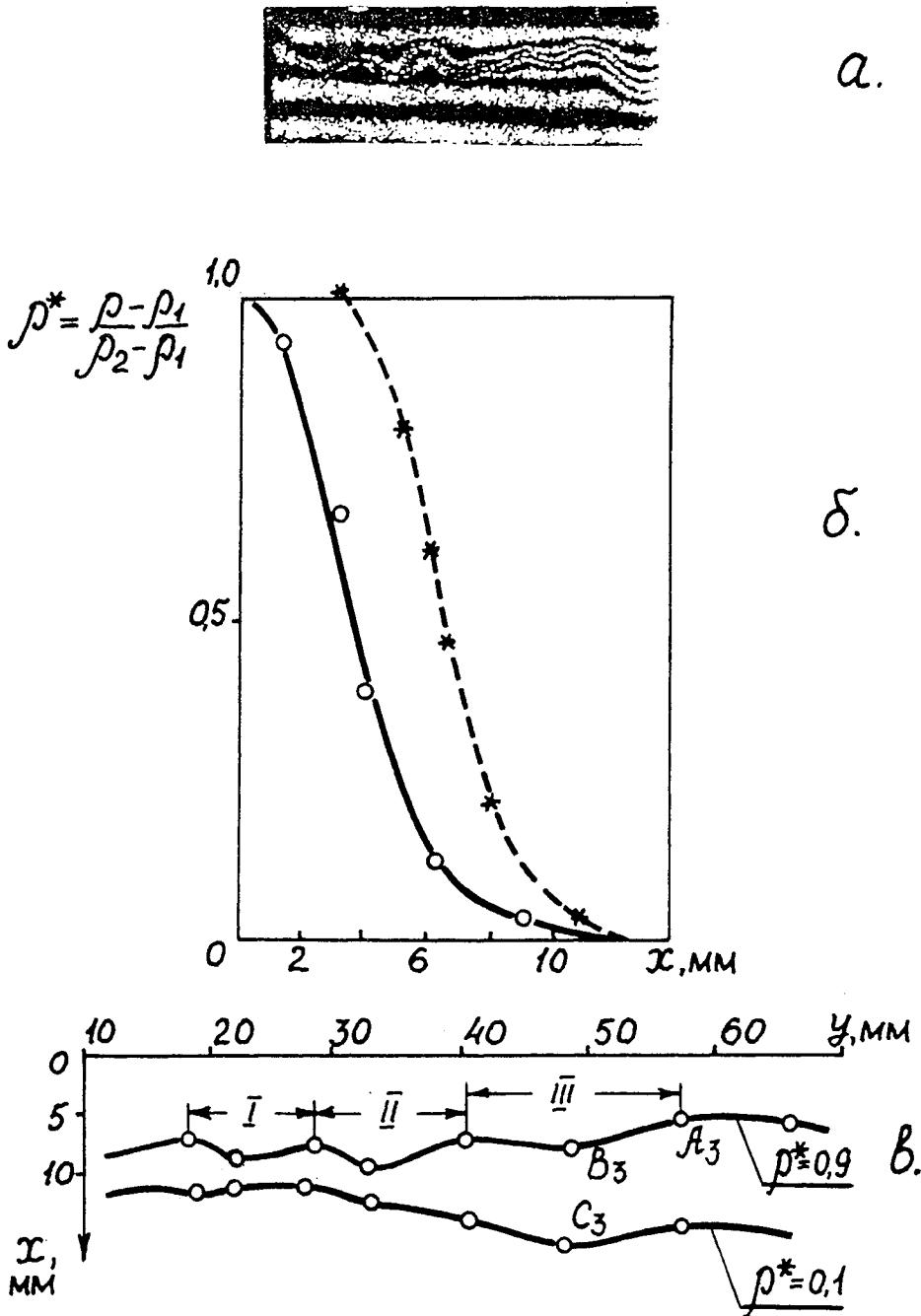


FIGURE 2: Determination of the interface parameters: (a) interferogram; (b) density distribution; (c) interfaces determined for $\rho^* = 0.1$ and $\rho^* = 0.9$.

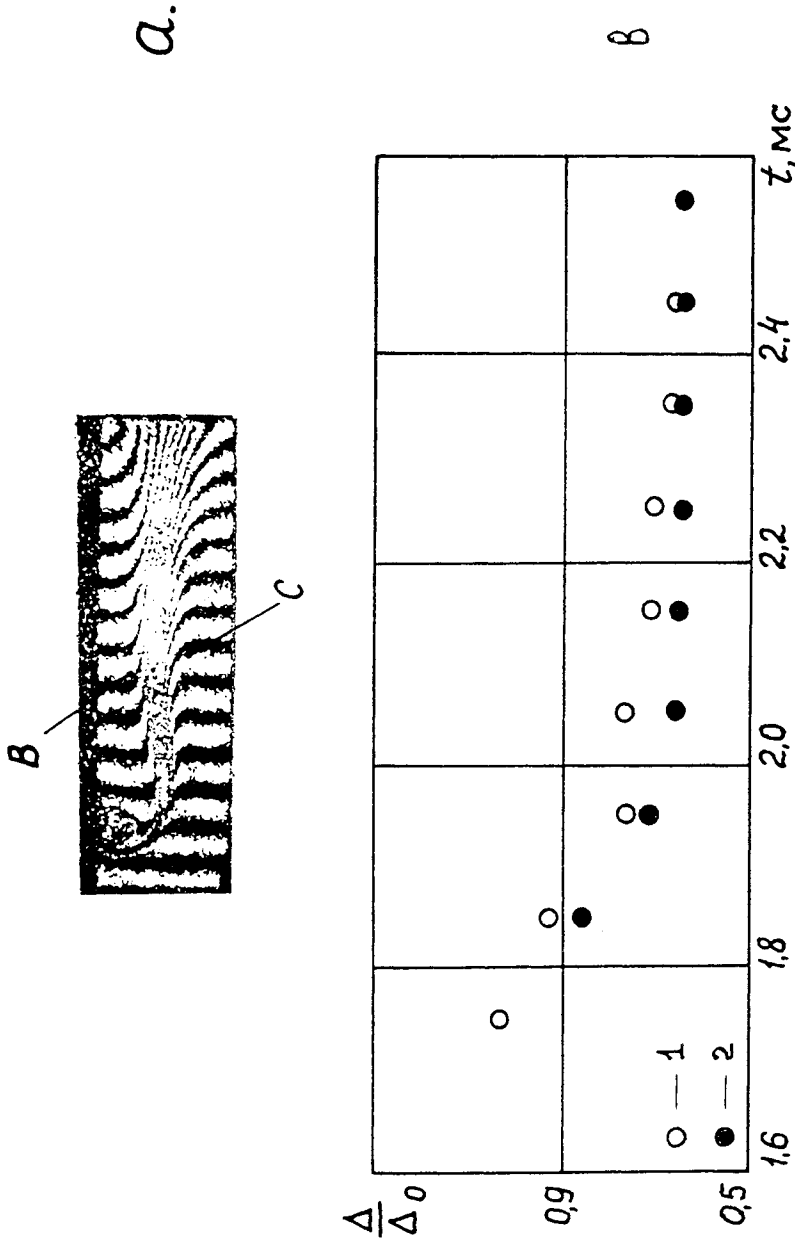


FIGURE 4: Compression of the interface moving along the channel: (a) monotonic interfaces; (b) 1 - $O_2+H_2 \rightarrow He$, 2 - $O_2+H_2 \rightarrow Ar$.

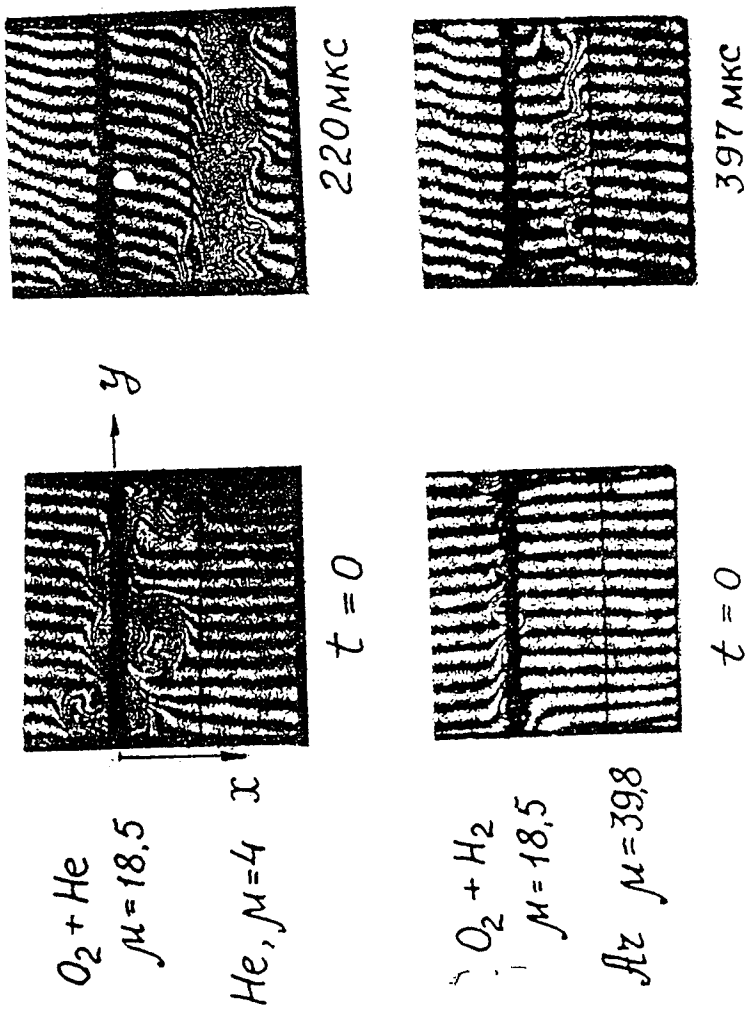


FIGURE 5: Interface evolution in the compression wave: (a) $O_2 + H_2 \rightarrow He$; (b) $O_2 + H_2 \rightarrow Ar$.

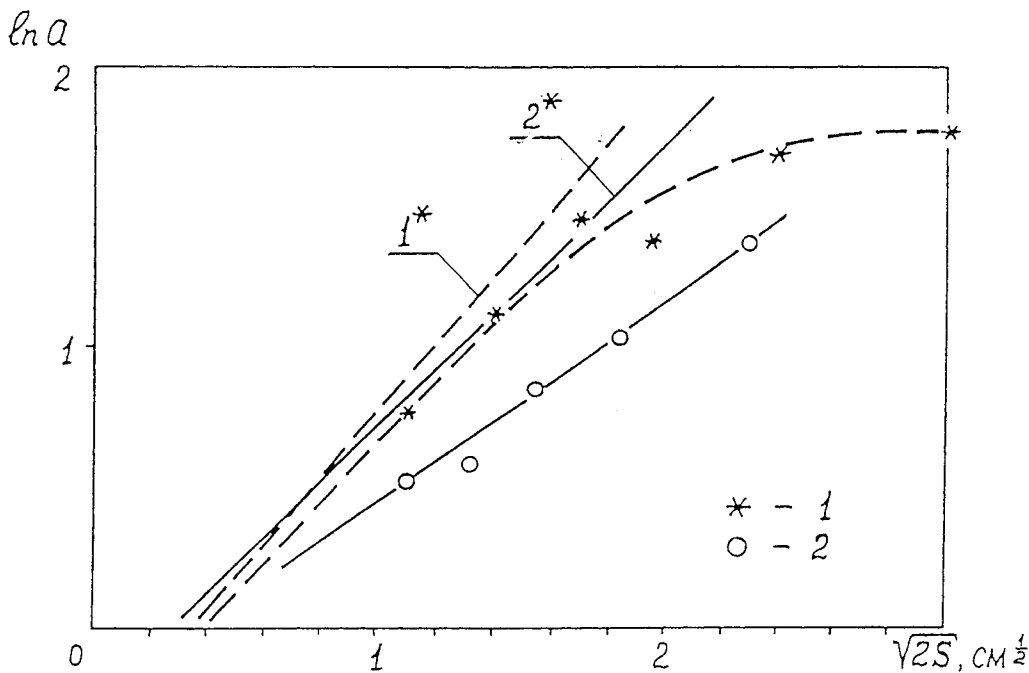


Fig. 6. The amplitude of the continuous interface versus the distance passed. The experiment: (1) $\Delta = 0.2$; (2) $\Delta = 0.9$. The calculation: (1*) $\Delta = 0.2$; (2*) $\Delta = 0.9$.

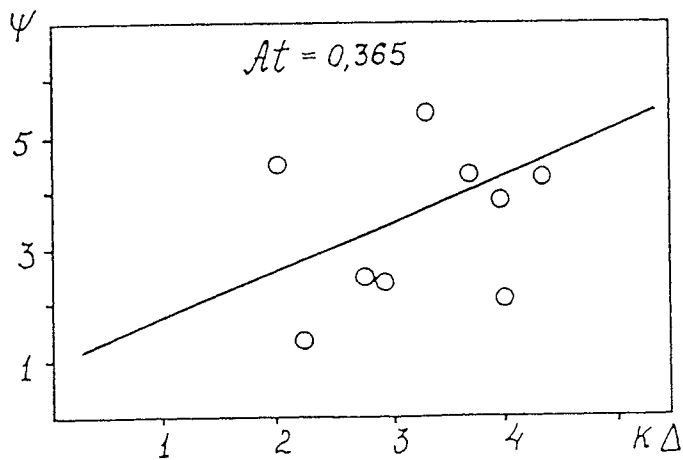


Fig. 7 The growth reduction factor Ψ versus $k\Delta$.

II

Richtmyer-Meshkov mixing

The influence of the shock interaction with an interface between the two gas flows of different densities on the intensity of mixing.

A. Aleshin, S. Zaytsev, E. Lazareva

The Krzhizhanovsky Power Institute, Leninsky Pr.19, Moscow, 117071, Russia

Abstract

A shock tube was used in an investigation of enhancement of the rate of turbulent mixing in the region of contact (interface) between two media of different densities after the shock passage through it, from a light gas into a heavy one. This process has been found to influence the decrease in the amount of a "pure" shock-compressed gas ("mass-defect") located between the end of the shock tube and the interface. We have determined that the curve of the "mass-defect" versus Atwood number had a maximum.

1. Introduction

The process of compression of targets by laser radiation during the stages of shell acceleration and deceleration is accompanied by hydrodynamic instabilities which finally result in mixing of the substance of the shell with the fuel. The interaction of the shock waves reflected from the target center with the region separating the shell from the fuel, is accompanied by the intensification of the mixing. This reduces the partial density of the fuel, and thus lowers the target gain [1,2]. The process of turbulent mixing in the interface between the media of different density moving at acceleration was studied in [3-7]. In [5-7], a simplified model of this process for 1D flows has been proposed and analytical expression for the thickness of interface has been found; the motion in the field of constant and impulsive acceleration induced by the shock passage through interface has been studied.

The experimental study of the mixing in the "shell-fuel" region in laser target is considered to be a very difficult task. The laws governing the development of this process can be investigated by experiments in shock tubes.

2. The experimental design

This paper represents an experimental investigation of the change in the thickness of interface resulting from the interaction of a shock with the interface. The shock passage from a light gas into a heavy one has been studied. The experiments has been carried out in an shock tube described in [9]. The diagnostics of the process was performed by a Topler method which allowed to determine the density gradients of the investigated flow. Topler schlieren pictures were made through the slit directed along the axis of driven section of the shock tube using a photograph film moving perpendicularly to the slit. The gases of different density filling the driven section of the shock tube were initially separated with 2.0 μm thick lvasan film. The incident shock wave travelling in gas A, broke the film and passed into gas B. The interface produced by the destruction of the film, separated the two flows of different density

and temperature. The used working gases helium, argon, krypton, xenon and their mixtures allowed to carry out the investigation for a wide range of Atwood numbers. The intensification of mixing in the interface interacting with the shock wave reflected from the end wall of a driven section has been studied as a function of the ratio of the densities of the two flows being in contact.

3. The results of experiment

Fig. 1 represents an (x,t) diagram obtained by analyzing the Topler pictures. The shock wave moving in gas A, hits the film separating gas A from gas B, and a refracted shock wave S appears in gas B. All the waves are denoted by a letter S with three lower indices. The first index shows the direction of wave motion relatively to the point of interaction with discontinuous interface: e - towards the interface, i - in the opposite direction. The second index is the number of point or region in the (x,t) diagram where interaction occurs: 1 - the interaction of initial shock wave with the film; 2 - the first interaction of the interface between the two flows. The third index identifies the gas in which the wave is moving. Other denotations: K_{ij} - the interface separating the two flows located between the points or regions i and j ; M - Mach number, $*$ - indicates the calculated values corresponding to the ones obtained by the 1D calculation, leaving the effect of laval film out of consideration (i.e. solving the Riemann problem at the interface). The initial conditions were chosen on the base of coincidence of experimental and calculated (x,t) diagrams within approximately 3% error of the experiment. Taking this into account, the initial pressure was chosen to be 380 mm Hg and Mach number of initial wave approximately 3.5.

The interaction of initial shock wave S_{e1a} generated in gas A with a film produced a refracted shock wave S_{i1b} in gas B. The flows of shock-compressed gases A and B were separated with the interface K_{12} . The wave S_{i1b} , reflecting from the end wall of driven section, generated a shock wave S_{e2b} moving towards the interface K_{12} . The interaction of S_{e2b} and K_{12} occurring in site 2 (Fig. 1), produced a refracted shock wave S_{i2a} , moving in gas A, a reflected shock wave S_{i2b} moving in gas B towards the end wall and an interface K_{23} . A more detailed analysis of the wave picture used can be found in [9]. Topler pictures were used to study estimate the thickness $L_{23}(t)$ of interface. This method allowed to determine the positions of the fronts K_{23}^b and K_{23}^a , separating K_{23} from gases B and A, respectively. It should be noted that, due to the employment of shadowgraphy, the fronts K_{23}^b and K_{23}^a were determined to be on different levels δ for different experiments, where $\delta = (\rho - \rho_b) / (\rho_a - \rho_b)$. This was taken into consideration in the process of analyzing the experimental data. The calculated position of the path of the interface K_{12}^* is located between the boundaries of the interface K_{12} (Fig. 1). The shock wave S_{i2b} observed in experiment had the front moving at supersonic speed. Topler pictures and pressure transducers disposed on a side wall of the channel identified the wave S_{i2b} as a shock wave, the intensity of which grew because of its overtaking by a compression wave ψ , appeared during the interaction of shock wave with the interface. The velocity of front approached the velocity of the shock wave S_{i2b}^* , determined by solving the problem of the S_{e2b} interaction with the interface K_{12}^* . Fig. 1 illustrates the position of K_{23}^* after this interaction. The preliminary discussion of the shock wave S_{i2a} properties was given in [9].

4. Discussion

As can be seen in Topler pictures demonstrating the interaction of shock wave with an interface, the thickness of interface sharply increases after the shock passage through the interface. By the moment of interaction of the S_{e2b} with K_{12} , the latter was assumed to be in the stage of advanced turbulence. This is confirmed by the structure of the interface in Topler pictures obtained by an instantaneous recording and by the "disappearance" of the shock wave front resulted from the random changes of the medium parameters in the interface. A model of turbulent mixing excited by an impulsive acceleration has been proposed in [5-7]. It has been assumed that the flows in contact were incompressible and the rate of pulsations was only a function of time. Analytical expressions have been obtained for the thickness of interface moving under acceleration. For impulsive acceleration generated by a shock wave, the interface thickness is expressed as follows:

$$L = L_0[(\nu + 8\alpha^2 \eta_0^2)U_0 A_2 t / L_0 + 1]^{8\alpha^2 \eta_0^2 / (\nu + 8\alpha^2 \eta_0^2)} \tag{1}$$

where λ and ν are empirical constants introduced into the model of the process; η_0 - constant depending on the criterion on the levels of dimensionless density $\delta(x)$ change used for the determination of the interface thickness):

for $\delta(x)$ - 0.02 and 0.98, $\eta_0=1.45$

for $\delta(x)$ - 0.1 and 0.9, $\eta_0=0.906$

where $u_0 = u_{i1b} - u_{i2b}$ are the velocities of the flows in the states $i2b$ and $i1b$ (in laboratory system of coordinates), respectively, obtained by solving the problem of the shock wave interaction with the interface K_{12} . $A_2 = cA_t$, A_t - Atwood number for the interface surface, c - the constant dependent on the character of density distribution in the interface.

$$c = \frac{(\rho_a + \rho_b)L}{\int_0^L \rho(x) dx}$$

For a symmetric density profile, $c=2$. The value of c obtained in experiment was 1.8 ± 0.4 , what testifies to a certain asymmetry of the density profile. This agrees with the results obtained in [5-7]. However, the accuracy of c determination does not allow to observe the growth of asymmetry of density profile. The using of experimentally measured functions $L_{23}(t)$ has allowed to determine the empirical constants. The influence of the initial conditions of experiment was taken into consideration. To perform the analysis, the following equation has been assumed to be correct for $L_{23}(t)$:

$$L_{23}(t) = L_0(Bt + 1)^n,$$

$$\text{where } B = \frac{\nu + 8\alpha^2 \eta_0^2}{L_0} U_0 c A_t, \quad n = \frac{8\alpha^2 \eta_0^2}{\nu + 8\alpha^2 \eta_0^2}$$

Combinations γ/α^2 and $\alpha^2 c A_t$ were determined by computing. Further, α and ν were determined using the value c mentioned above. α has been found to be 0.29 ± 0.02 , for all gas combinations within the deviation indicated. ν has been found to be considerably dependent on A_t and ρ_b , probably due, (i) to the simplifications of the model proposed in [5-7] and (ii) to not absolutely adequate application of this model for the regions with δ varying from 0.02 to 0.98 (in [5-7] it has been suggested to use the model for δ ranging from 0.1 to 0.9). Fig. 2 represents the experimental and calculated dependencies of $L_{23}(t)$.

As can be seen, the model suggested in [5-7], adequately describes the thickness of interface observed in experiment. This conclusion agrees with the data obtained in [10].

The paths of S_{i12} and K^b_{23} , recorded in Topler pictures, allowed to determine experimentally the loss of "pure" shock-compressed gas located between the end wall and K_{23} caused by the mixing of gases being in the states $i2a$ and $i2b$ in the interface. The loss of substance, or "mass-defect" was estimated for a definite time interval τ using the following equation:

$$\Delta = \frac{\Delta m}{m} = \frac{m(0) - m(\tau)}{m(0)} \quad (2)$$

where: τ is the time of acoustic wave propagation in the state $e2b$, from the site of S_{e2b} interaction with K_{12} , to the end wall, $t=0$ is the moment of S_{e2b}/K_{12} interaction; $m(0) = d\rho_{2b}$ - the mass of gas enclosed between the site of S_{e2b}/K_{12} interaction and the end wall; d - the distance from the site of the interaction to the end wall; $m(\tau)$ - the gas mass between the end wall and K^b_{23} for $t=\tau$

According to the model proposed in [5-7], the following equation may be used to describe the phenomenon of "mass-defect":

$$\Delta = \frac{L_0}{2d} \frac{\rho_{i2b}}{\rho_{e2b}} \left[\left(\frac{\nu + 8\alpha^2 \eta_0^2}{L_0} c A_t d \frac{U_0}{a_{e2b}} + 1 \right)^{\frac{8\alpha^2 \eta_0^2}{\nu + 8\alpha^2 \eta_0^2}} - 1 \right] \quad (3)$$

where a_{e2b} - sound speed in $e2b$.

Fig. 3 represents the values for "mass-defect", obtained in experiment and calculated from (3). As can be seen, the "mass-defect" depending on Atwood number, is maximal for $A_t=0.75$, in experiment and in calculations as well. We can suggest the following explanation of this finding: for the low A_t , the mixing in K_{23} is limited, because of the small difference in densities of the flows in contact, and for $A_t \rightarrow 0$, the reflected wave S_{e2b} carries and, therefore, transfers a smaller amount of kinetic

energy, comparing to the energy in interface, due to the higher density of interface ($\rho_a \ll \rho_b$). It should be noted that application of the model proposed in [5-7] for the region with d from 0.02 to 0.98 must result in overestimation of the "mass-defect", what can be seen in Fig. 3. This is due to the formal increase in kinetic energy of interface mixing. It may thus be concluded that the model proposed in [5-7] adequately describes the shock-induced process of turbulent mixing in interface separating gases of different density, but overestimates the intensity of mixing. Using the "mass-defect" experimentally measured for $A_t \rightarrow 0$, it appears possible to perform an independent determination of α with the model proposed in [5-7]. For $A_t \rightarrow 0$,

$$\Delta = \frac{\rho_{i2b}}{\rho_{e2b}} \frac{4\alpha^2 \eta_0^2}{a_{e2b}} c A_t U$$

This calculation gives $\alpha=0.25 \pm 0.04$. Thus, the values α obtained by two independent methods, have appeared to be very similar.

Acknowledgement

We wish to thank Dr J.F. Haas for the valuable discussion and constructive comments on the manuscript.

References

1. Yu.V.Afanasiev, N.G.Basov, E.G.Gamalii, V.B.Rozanov. 1976. Pis'ma v Zhurnal Eksperimentalnoi i Teoreticheskoi Fiziki, v.23, p.617.
2. V.A. Lykov, B.A.Murashkina, V.E.Neuvazhaev, L.I.Shibarshov, V.G.Yakovlev. 1979. Pis'ma v Zhurnal Eksperimentalnoi i Teoreticheskoi Fiziki, v.30, p.339.
3. C.Z. Belenkij, E.S Fradkin. 1965. Trudy Fizicheskogo Instituta Akademii Nauk, v.29,339.
4. N.N.Anuchina, S.M.Bakhrakh, A.V.Zabrodin, L.A.Pliner, I.D.Safronov. In: Investigation if hydrodynamic instability by computering. Ed. by The Keldysh Institute of applied Mathematics. 1981.p.108.
5. V.E.Neuvazhaev, V.G.Yakovlev.1983. Problemy Prikladnoi i Teoreticheskoi Fiziki, no.2, p.85.
6. V.E.Neuvazhaev.1981. Problemy Prikladnoi i Teoreticheskoi Fiziki, no.5, p. 81.
7. V.E.Neuvazhaev, V.G.Yakovlev.1984. Voprosy atomnoi nauki i tekhniki. Seriya: Metodiki i programmy chislennogo resheniya zadach matematicheskoi fiziki. issue 2(16), p. 17.

8. E.E.Meshkov. 1969. *Izvestiya Akademii Nauk SSSR. Ser. Mekhanika Zhidkosti i Gasa*,v.5, p.151.
9. S.G.Zaytsev, E.V Lazareva, V.V.Chernukha, V.M.Belyaev. 1985. *Doklady Akademii Nauk SSSR*, v.283, p.94.
10. V.A.Andronova, S.M.Bakhrakh, E.E.Meshkov, V.N.Mokhov, V.N.Nikiforov, A.V.Pervitskiy, A.I.Tolmyakov. 1976 *Zhurnal Eksperimentalnoi i Teoreticheskoi Fiziki*,v.71.
p. 806.
11. L.L.Vasiliev. *Shadographic methods*. Moscow. "Nauka". 1968.

X-Ray Measurements of Shock-Induced Mixing
at an Air/Xenon Interface

R. Bonazza * and B. Sturtevant

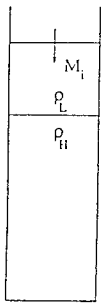
Graduate Aeronautical Laboratories

California Institute of Technology

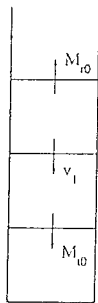
Pasadena, California 91125

A new experimental technique based on the absorption of X-rays by a high-Z gas has been developed and implemented in a vertical square shock tube for the study of shock-accelerated air/xenon interfaces. The interfaces are prepared by retracting a metal plate initially separating the two gases, prior to the release of the shock wave. The interfaces are of two types, quasi-sinusoidal and nominally flat, depending on the amount of time elapsed between the end of the plate retraction and the arrival at the interface of the shock wave. The amplitude of large wavelength (25–100 mm) perturbations on the interface, and the thickness of the interface are studied. An integral definition for the interface mean line due to Pham (Caltech Ph.D. Thesis, 1990) is adopted. A new integral definition for the interface thickness, which makes it feasible to study for the first time the thickness of quasi-sinusoidal interfaces, is proposed. X-ray images of the interfaces are obtained at increasing times after interaction with the incident shock, the reflected shock, and a subsequent series of weak waves reverberating between the interface and the shock tube end wall. The measured shape of the interface is decomposed into spatial modes for comparison with a modified linear theory of the Richtmyer-Meshkov instability. After interaction with the incident shock the measured *amplitude growth rate* of all modes is much smaller than those predicted by theory. After reshock the measured growth rate of the first mode disturbance is smaller than that predicted by theory but the higher modes grow faster than predicted. For multiple wave reverberations in a configuration with the interface initially closer to the shock tube end wall all modes show slower amplitude growth than predicted. The theoretical model (Brouillette and Sturtevant, 17th Shock Tube Symposium, 1989) accounts for the interface finite thickness through a growth reduction factor (Duff *et al.*, Phys Fl. 5, 417, 1962) and, in the case of multiple weak shocks, it assumes that the initial condition for the i th interaction is the superposition of the effects due to the $i - 1$ previous interactions. The initial values of the amplitude used in the calculations are the ones measured after passage of the incident shock. We speculate that the interaction of the reflected shock with the turbulent boundary layer behind the incident one generates random acoustical disturbances which reach the interface and cause the subsequent thickness growth. In the case of multiple interactions, the *thickness growth rates* of nominally flat interfaces are smaller than those previously found in a schlieren visualization experiment (Brouillette & Sturtevant, Physica D, 39, 248, 1989). In the case of two shock interactions, wall vortices generated by the interaction of the reflected shock with the wall boundary layer severely affect the measurements. A correction is proposed to account for this effect in the measurements of the interface thickness.

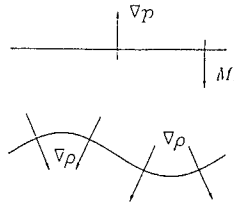
* Present address: Department of Nuclear Engineering, University of Wisconsin, Madison



t_1



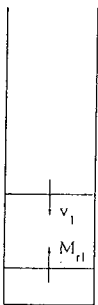
t_2



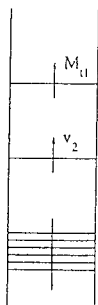
Incident Shock



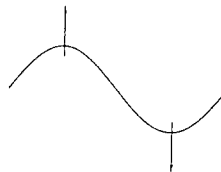
Vorticity Generation



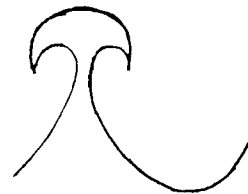
t_3



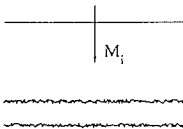
t_4



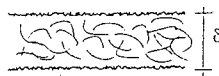
Linear Growth



Nonlinear Effects



$$\delta = f(A') [v] t$$

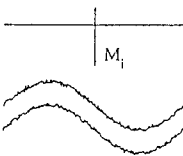


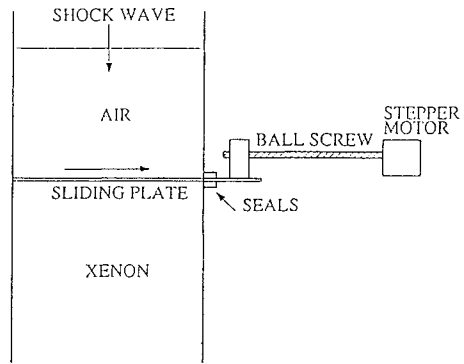
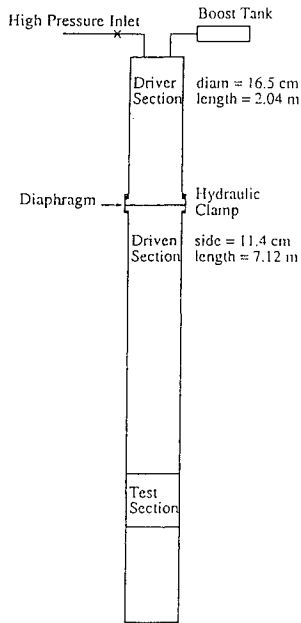
Objectives:

Develop quantitative densitometry technique
Density Field \rightarrow Density Interface

Measure interface distortion (instability)

Measure interface thickness (mixing)



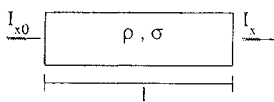


$\tau = 1.2$ s: Single Scale

$\tau = 8.0$ s: Multiscale (Random)

Why X-rays ?

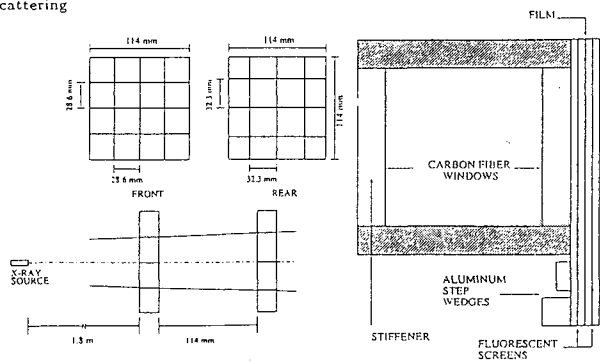
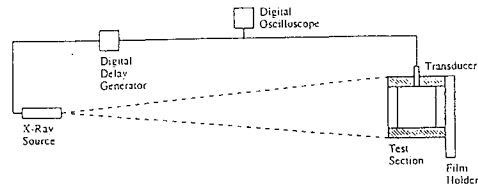
Density Field \rightarrow Density Interface



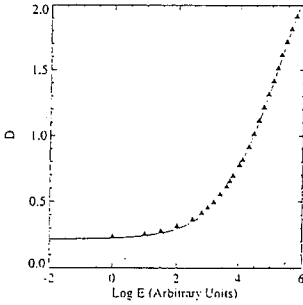
$$\frac{I_x}{I_{x0}} = e^{-\sigma(P_e)\rho l} \quad \sigma \begin{cases} \text{photoelectric} \\ \text{coherent scattering} \\ \text{incoherent scattering} \end{cases}$$

$$\frac{I_x}{I_{x0}} = e^{-\sigma(P_e) \int_0^l \rho(z) dz}$$

Film: $E = \int I_x dt$



$$D = \log \frac{I_{v0}}{I_v} \quad \begin{array}{c} | \\ I_v \\ | \\ I_{v0} \end{array} \text{ Film} \quad I_v \neq I_x$$



$$\frac{D - D_{min}}{D_{max} - D_{min}} = \frac{\tanh(p_1 \log E - \log E_0) + 1}{2}$$

Image Processing Issues

A. X-Ray Source

1. Spatial Nonuniformity
2. Temporal (Shot-to-Shot) Nonuniformity

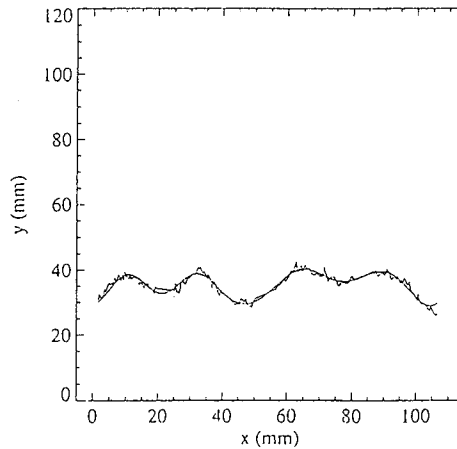
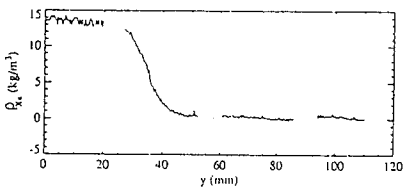
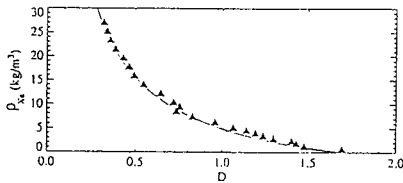
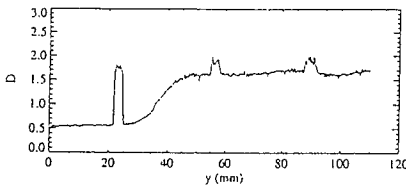
B. Digitization of the Negative

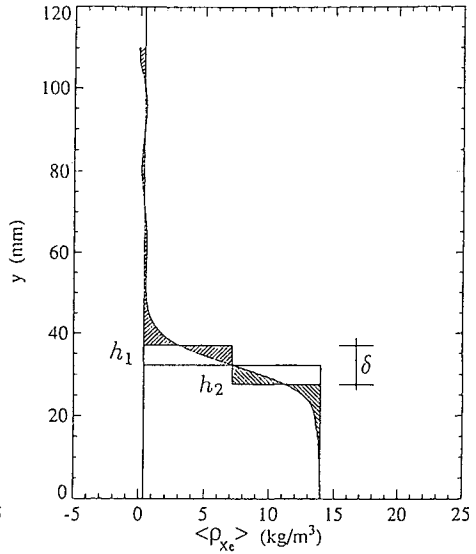
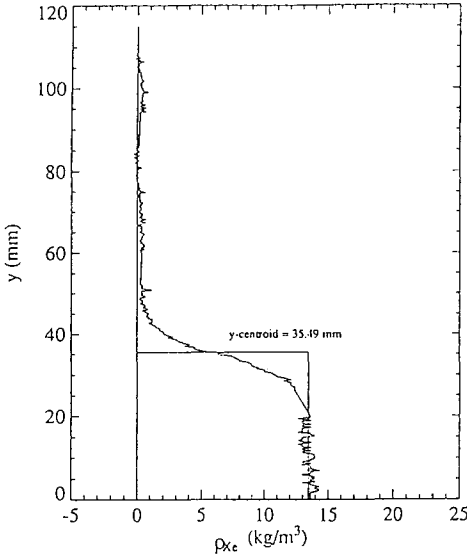
1. Temporal Fluctuations of CCD Output
2. Calibration of CCD Camera
3. Spatial Nonuniformity of Light Box
4. CCD Pixel Noise
5. Film Response (*D* vs. *E*)

Aluminum Thickness vs. Optical Density (each negative)

Xenon Density vs. Aluminum Thickness (once)

Xenon Density vs. Optical Density (each negative)



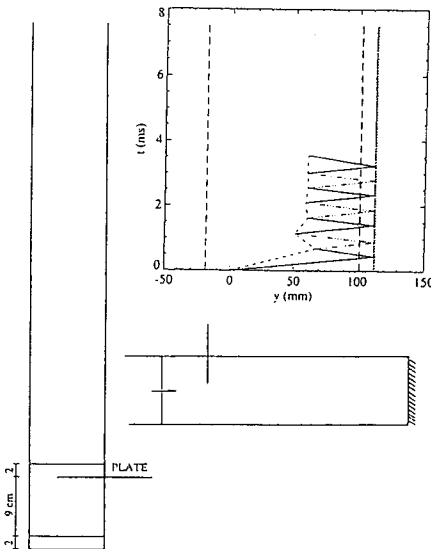


$$y_c(x) = \frac{\int_0^Y \rho(x,y) dy}{\rho_m(x)} \quad (\text{Pham, 1991})$$

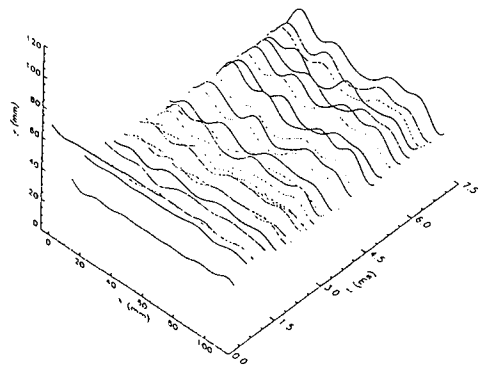
$$h_1 = \frac{1}{\rho_c} \int_{y_c}^Y \rho dy$$

$$h_2 = \frac{1}{\rho_m - \rho_c} \left(\rho_m y_c - \int_0^{y_c} \rho dy \right)$$

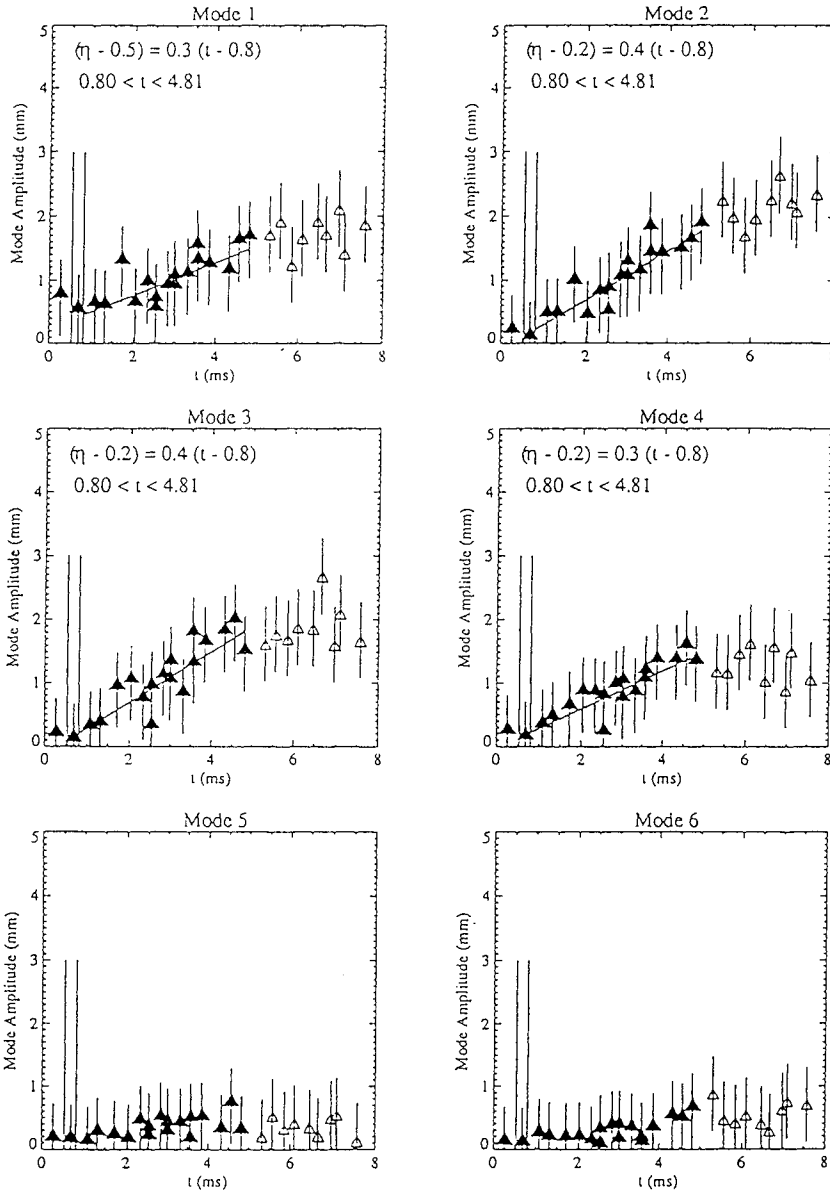
CEW $M_i = 1.32$

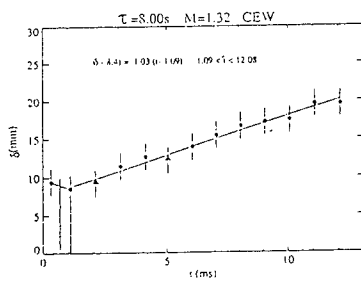
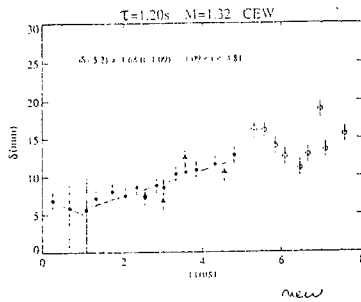


CEW $\tau = 1.2 \text{ s}$ $M_i = 1.32$



CEW $\tau = 1.2 \text{ s}$ $M_i = 1.32$





Conclusions

- New imaging and densitometry technique
- Mean interface shape
 - Modal decomposition
 - Modal growth rates after reflected shock and reverberations smaller than predicted
- Interface Thickness
 - Single scale interface:
 - New contribution
 - Multiscale interface:
 - Growth rates smaller than previously reported

Numerical simulations and experiments on physics of high Mach Number shockwave - turbulent flow interactions

Alfred C. Buckingham
Center for Compressible Turbulence
Lawrence Livermore National Laboratory
Mail Code L-321, P.O. Box 808
Livermore, California 94551, USA

Jacob Grun
Plasma Physics Division, Space Plasma Branch
Code 4784, Naval Research Laboratory
Washington DC 20375, USA

Precis'

When a shock moves into and interacts with an existing turbulent field, a substantial enhancement of the after-shock turbulent intensity and a simultaneous distortion and realignment of the tensor strain rate field and associated tensor stress field results. Component mixing, advective transport, and diffusion, as well as associated momentum and energy dissipation, are intensified over their pre-shocked levels. A combination of low pre-shocked turbulent intensity and strong shocks (e.g. shock Mach numbers substantially greater than one) produces the most pronounced interactive change in the turbulence level. In contrast, when a weak shock (Mach number only slightly greater than one) moves through relatively intense upstream turbulence, the turbulence change is modest but dynamical distortion and erratic motion of the shock front is much more pronounced.

It is a commonly held view that if the interactive shock Mach number is in the hypersonic range (shock Mach numbers equal to or greater than about 6), rapid reinforcement of shock strength at the front by non-linear pressure field interactions and consequent self-healing of shock front geometric irregularity would act to suppress front distortion and also suppress the influence of the shock interactions on the surrounding turbulence. In the present work, recent experiments, numerical large eddy simulations (LES), and analysis are presented which contradict this notion. This work suggests that pronounced shock front distortion and substantial interactive modification of the turbulence persists even for shocks propagating at shock Mach numbers well in excess of 100! This work is submitted for review and consideration as a presentation (by the first author) at the 4th International Workshop on the Physics of Compressible Turbulent Mixing to be held at Cambridge University, UK on 29 March - 1 April 1993.

Discussion

Information on the shock-turbulence interaction dynamics and accurate estimates of their influence on changes to turbulent transport are vital for modifying turbulence closure models and enhancing their reliability in predicting the turbulent transport, mixing, eddy diffusion and dissipation at realistically large Mach Numbers and Reynolds numbers and in the complicated configuration geometries that are of practical interest. Experience demonstrates that useful combinations of these flow and configuration conditions are nearly impossible to simulate and reproduce experimentally. Numerical simulation techniques and efficient, well-calibrated flow models must be developed, refined and applied.

This work emphasizes recent progress in investigating the physics of the interaction process using two dimensional large eddy simulations (LES) to supplement analysis of the experiments and a theoretical concept based on viscoelastic response and the turbulence eddy analogy to second viscosity to describe the apparent persistence of dynamic distortions to shock front structure at indefinitely large Mach numbers.

Many current example applications exist. These include supersonic/hypersonic flow field analysis, design, and materials selection, interior supersonic flow combustion analysis and design, predicting the dynamic evolution of laser driven target material mixing, ignition, and burning in inertial confinement fusion experiments in addition to the prediction of the fluid dynamics of thermal, plasma, radiation, and electromagnetic fields which may substantially influence astrophysical evolution processes.

Figure 1 provides some experimental evidence of the existence of pronounced interactive shock distortion and turbulent field alteration even for a very strong (Mach number > 100) spherical shock wave. This dark field shadowgraph record is one of a series of sequential flow realizations captured at very short exposure intervals (< 100 picoseconds) by image-intensification camera. The initial turbulent plume field may be seen at the right in the picture. The later arriving spherical shock front may be seen as a well defined smooth arc in the non-turbulent region at the center of the picture and as a highly distorted, thickened front where it crosses and interacts with the earlier initiated turbulent plume.

A 4-ns pulse from the 1.06- μm , 1 kJ Pharos III laser at the Naval Research Laboratory is focused onto the surface of a period-sized piece of target material placed in an ambient gas of optionally selected composition and background density. The laser heats the material to a few hundred eV, creating a powerful, miniature explosion. Depending on details of the experimental setup this explosion can initiate one or more shocks in the ambient gas or it may initiate the turbulent plume through which the shock propagates and interacts at a later stage.

Precision optical diffraction techniques of sequences of realizations provide a data base that is currently being analyzed with the aid of LES procedures. These experiments from Grun et al. (1991, 1992) provide a significant experimental data base and source for analysis of turbulent scale changes during shock transition, turbulence amplification, and quantitative information on directed shock to turbulence energy transfer and modal energy partition.

The Rotman (1991) results show some evidence of long period computational dissipation in the absence of a subgrid scale model while predicting an increase in the overall grid spectral energy content of about 20% following shock transition. The Buckingham (1991, 1992) results predict about an 85% increase in the kinetic energy while the experimental values at these flow conditions reflect a measured increase of about 150% where limited measurement site distributions may be reflected in this disparity. However, these results seem to confirm the utility of a formal procedure for modeling the influence of the non-resolvable subgrid scales even when using advanced, high resolution multi-grid shock capturing procedures for the resolved scales in LES.

Presently new developments in two-band dynamic eddy viscosity modeling for the subgrid scale influences by Germono, Piomelli, Moin, and Cabot (1991), extended for compressible flow by Moin, Squires, Cabot, and Lee (1991) are being implemented to improve the results of the LES in the near wall region, under the influence of stochastic subgrid scale stochastic backscatter, and in the neighborhood of the shock.

Acknowledgements

This is a report of work performed under the auspices of the U.S. Department of Energy by the Lawrence Livermore National Laboratory under Contract No. W-7405-Eng-48. The writer gratefully acknowledges the ideas, comments and suggestions that were developed in discussions with C. E. Leith, D. A. Rotman, and W. P. Dannevik during the course of this work.

References

- A. C. Buckingham, (1989), "Numerical Studies of Shock Wave Structure Sensitivity to Interactions with Turbulent Fields", *Numerical Methods in Laminar and Turbulent Flow, VI, (1)*, eds C. Taylor, P. Gresho, R. L. Sani, J. Hauser, Pineridge Press, Swansea, UK, 805.
- A. C. Buckingham, (1990), "Interactive Shock Structure Response to Passage through Turbulence", *AIAA Paper 90-1642*, (AIAA 21st Fluid and Plasma Dynamics Conf. Seattle, WA 18-20 June, 1990).
- A. C. Buckingham, (1991), "Shockwave Considerations for sub-grid closure modeling in turbulent large eddy simulations", *Proc. 3rd International Workshop on the Physics of Compressible Turbulent Mixing*, (Abbey of Royaumont, France, June 17 - 19, 1991), 155.
- A.C. Buckingham, (1992), "Large Eddy Simulation of Shockwave Passage Through Turbulence", MS in review for ASME Fluids Engineering Summer Meeting, June 20-23, 1993, Washington DC and for publication in *Journ. Fluids Engr.* Available pre-print, Lawrence Livermore National Laboratory, UCRL-111080.

- M. Germono, U. Piomelli, P. Moin, and W. H. Cabot, (1991), "A dynamic sub-grid scale eddy viscosity model", *Phys. Fluids A* 3 (7), 1760.
- J. Grun et al. (1991), "Instability of Taylor-Sedov Blast Waves Propagating Through a Uniform Gas", *Phys. Rev. Lett.* 66, 2378.
- J. Grun, C. K. Manka, B. H. Ripin, A. C. Buckingham, J. Resnick, and H. R. Burris, (1992), "Enhancement of Turbulence by a High Mach Number Shock", *Bull. Am. Phys. Soc.* 37, (6), 1478. To be published.
- J. Keller and W. Merzkirch, (1990), "Interaction of a normal shock wave with a compressible turbulent flow", *Experiments in Fluids* 8, 241.
- C. E. Leith, (1990), "Stochastic backscatter in a subgrid-scale model: Plane shear mixing layer", *Phys. Fluids A* 2 (3), 297,
- C. E. Leith, (1991), "Stochastic Backscatter in a Subgrid-Scale Model: 3D Compressible Flows", *International Workshop on Large Eddy Simulation*, eds. S. A. Orszag, T. A. Zang, Cambridge University Press, Cambridge, UK.
- P. Moin, K. Squires, W. Cabot, and S. Lee, (1991), "A dynamic subgrid-scale model for compressible turbulence and scalar transport", *Phys. Fluids A* 3 (11), 2746.
- D. A. Rotman, (1991), "Shock wave effects on a turbulent flow", *Phys. Fluids A* 3 (7), 1792.

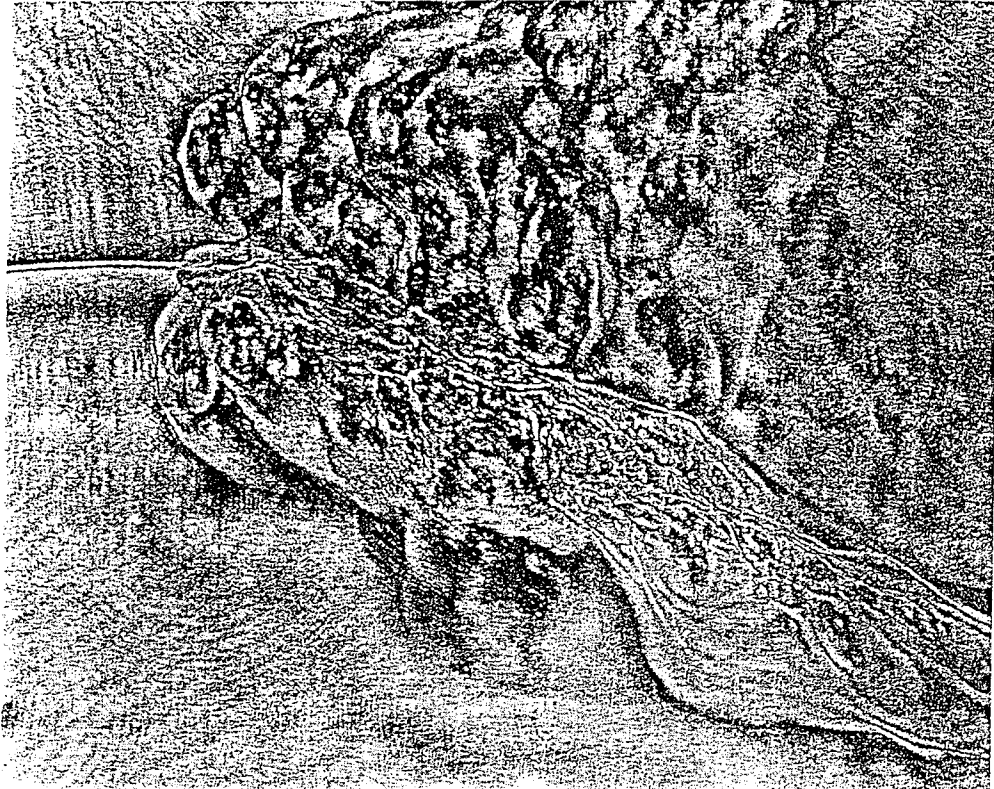


Figure 1. Dark field shadowgraph of a hypersonic spherical shock front (bottom) over-running but distorted by passage through pre-existing turbulence. Mach number > 100 , $Re \sim O(10^6)$, from experiments of Grun et al. (1992).

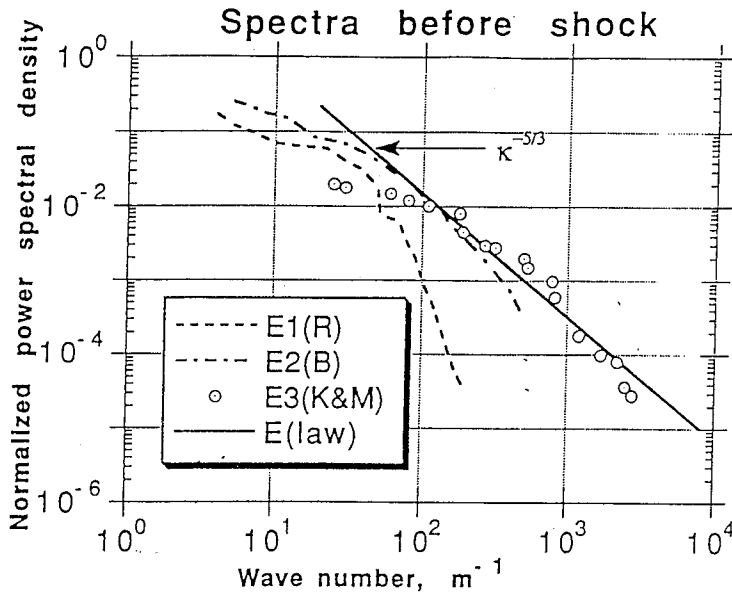


Figure 2. Normalized power spectral density of pre-shocked turbulent fields comparing the LES results of Rotman (1991) designated E1(R), the current LES results designated E2(B) and the experimental results of Keller and Merzkirch (1990) designated E3(K&M).

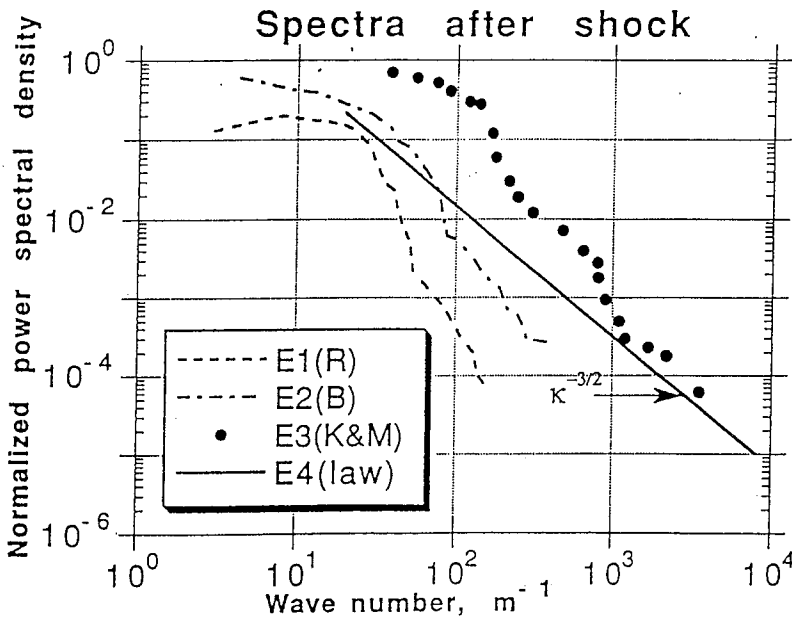


Figure 3. Normalized power spectral density of post-shocked turbulent field comparing the LES results of Rotman (1991) designated E1(R) the current LES results designated E2(B) and the experimental results of Keller and Merzkirch designated E3(K&M).

Multidimensional Numerical Simulation of Transition to Turbulence in Richtmyer-Meshkov Instability

V.V. Demchenko & A.M. Oparin

Moscow Institute of Physics and Technology

Dolgoprudny, Moscow Region, Russia

Abstract

The problem of perturbation growth and the development of turbulence in Richtmyer-Meshkov instability (RMI) is examined using the ideal compressible gas model (Euler equation system) for 2D and 3D systems. In 2D calculations the physical mechanics of transition to turbulence from the uniform flow behind the incident shock wave was observed. In the early stages mushroom-like structures form, coalesce and become turbulent. The 3D case of the nearly axisymmetrical contact discontinuity disturbance was also considered. The whole flat interface of two media was divided on identical square cells, and only the surface of the circle, inscribed into the cell square, was disturbed in the sine-like and axisymmetrical way.

Introduction

There are many physical phenomena in which turbulence is an essential part of the process. The investigation of turbulence is a very difficult problem both by experimental methods and by theoretical or numerical ones. Studying RMI development permits observations of the gradual transition from the laminar flow to a turbulent one, and enables explanation of the physical mechanics of this phenomenon. In this paper multidimensional numerical simulation is applied to study the linear, nonlinear, transmitted and turbulent stages of RMI on the example where $Ka \gg 1$. This situation is a more convenient than $Ka \ll 1$ as the turbulence arises earlier. The difference between 2D and 3D RMI development is also important part in the study.

1. 2D numerical simulation of transition to turbulence in RMI

Let us consider the dependence of RMI evolution with Mach number (2 to 5); the initial pressure (0 to 5 bar); the wave length (0 to 8 mm); and the perturbation amplitude of contact discontinuity (1cm). Also let us look at the gradual transition from laminar flow to the turbulent one. In that case the diffraction process is irregular. It means that the reflected shock wave is not planar but is curved. Before the end of the diffraction process, the reflected shock waves from the next wave length of contact discontinuity begin to interact between themselves on the minimum perturbation axis in helium. As a consequence the incident shock wave intensity increases and after stopping by diffraction

the secondary shock waves arise. (See fig. 1 at 5 mks). The interaction of the curved reflected shock waves and the secondary shock waves on the maximum perturbation axis in the xenon causes the appearance of some high pressure local domain (fig.1, 10 mks). In time these waves interact between themselves on the minimum perturbation axis in helium (fig. 1, 15 mks) and so on. Interaction of the secondary shock wave with the transmitted and reflected shock wave smoothes out their curved fronts. The movement of a slip line along the shock front causes the appearance of whirlwind isolines in the xenon (see fig. 2, 3 the thin lines at 30-60 mks). The domain of mass concentration of the helium from 0.1 to 0.9 is shown on fig. 1-3 by the 0.1 to 0.9 crosshatching. The thick lines on these figures are the isobars. It is seen that the mixing zones gradually merge. This means that in the experiment turbulence develops.

2. 3D numerical simulation of RMI

The results of the 3D numerical simulation are represented on the figures 4, 5 as the frames from a slide film. It is possible to define, at any instant in time for an arbitrary point in the domain of integration, the quantitative information about each of physical parameters of interest. The pressure in the local xenon domain is higher in the 3D numerical calculations than in 2D. This leads to the accelerated growth of the perturbation in 3D case.

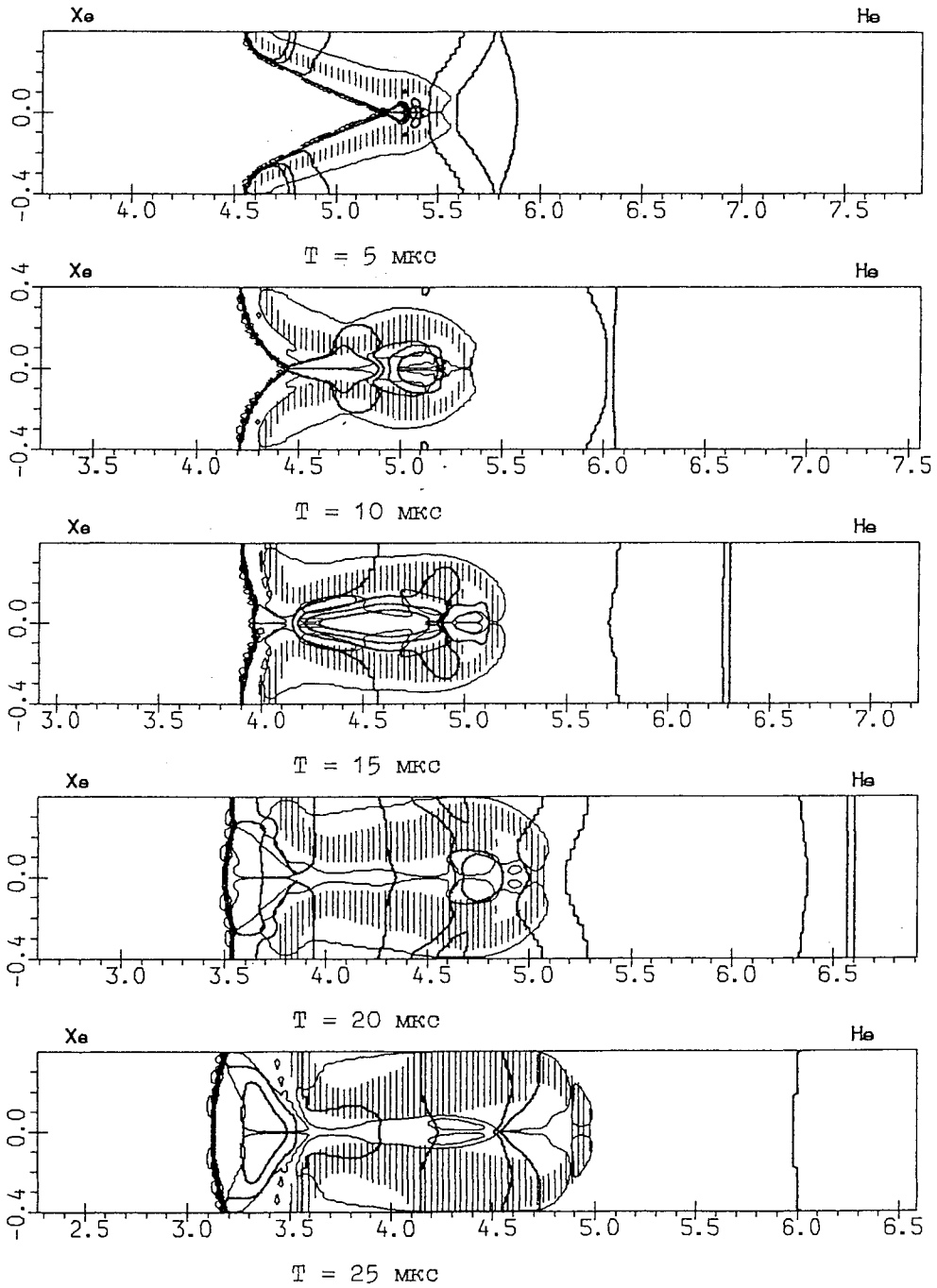


FIGURE 1

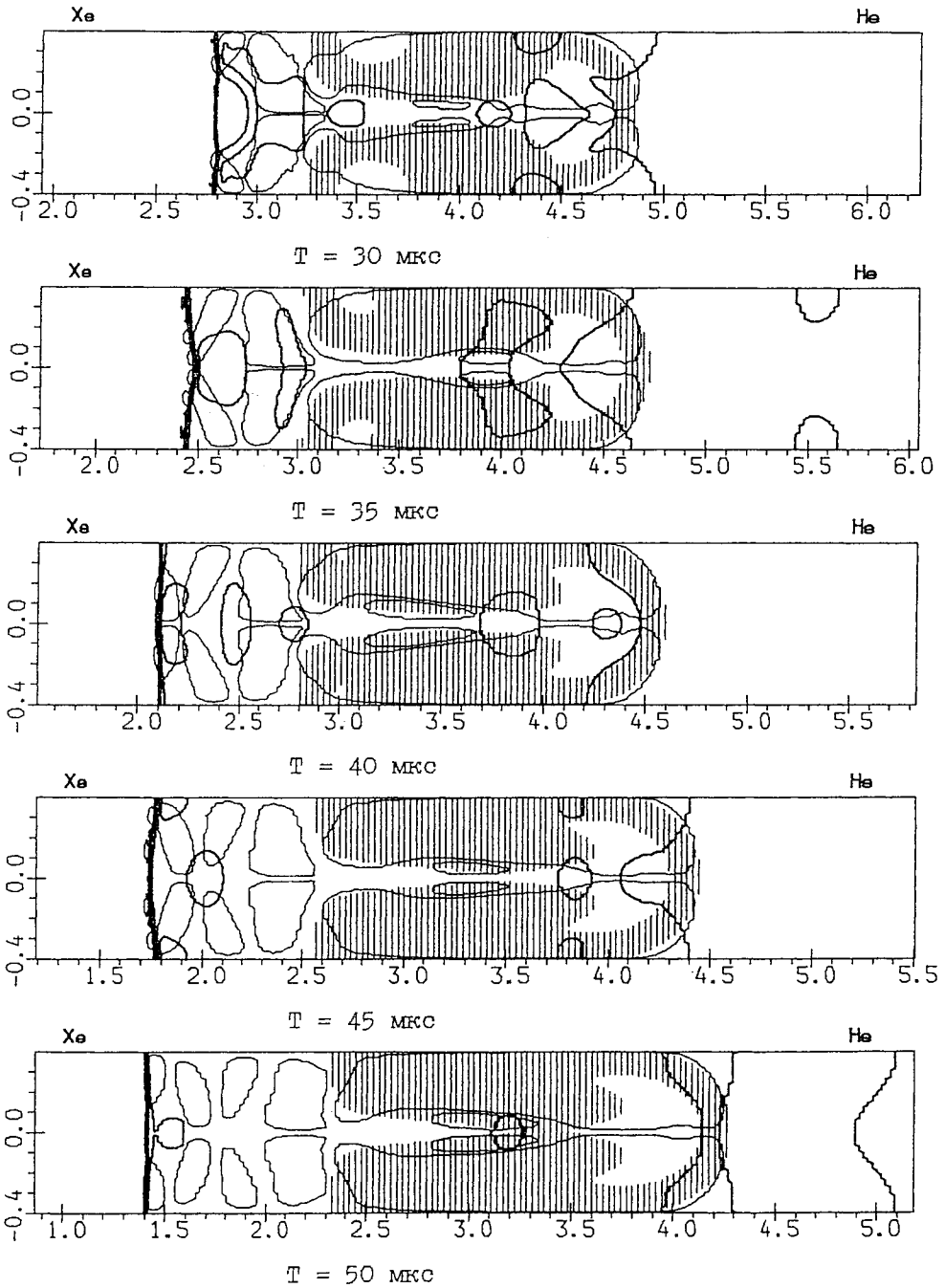
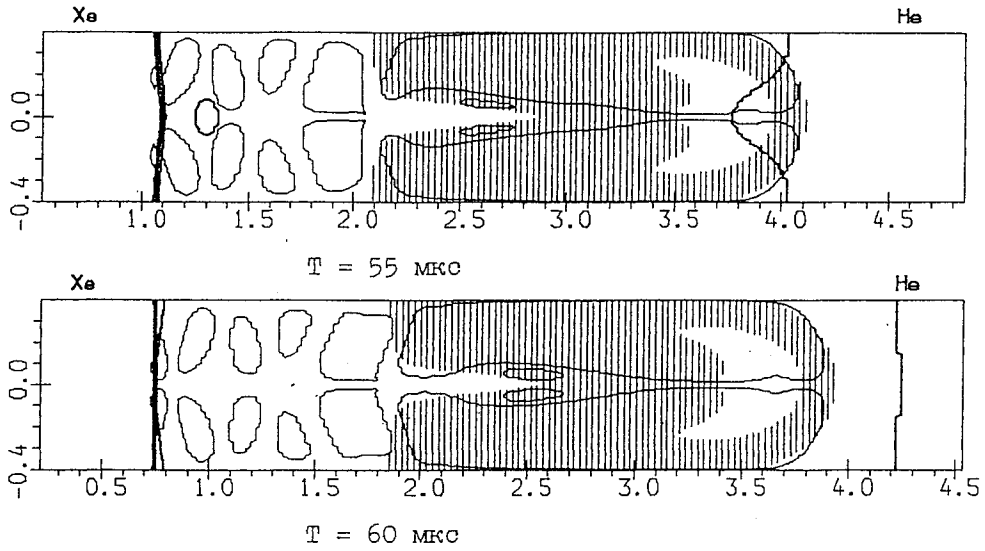


FIGURE 2



Штриховкой показана зона смешения
 (массовая концентрация He от 0.1 до 0.9),
 толстые линии — изобары,
 а тонкие — изолинии завихренности.

FIGURE 3

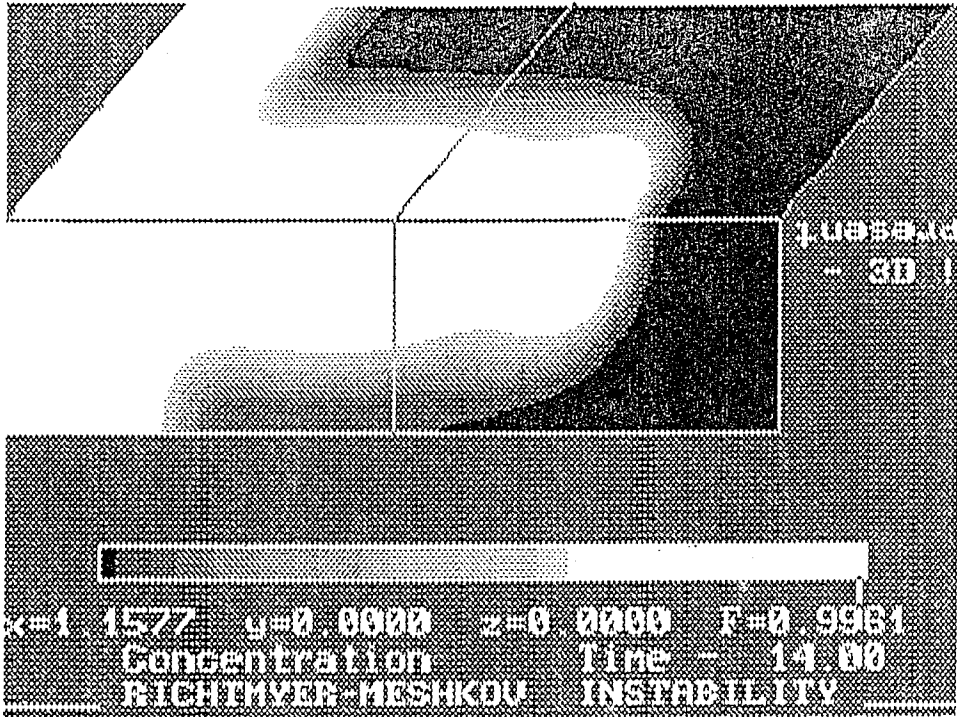


FIGURE 4

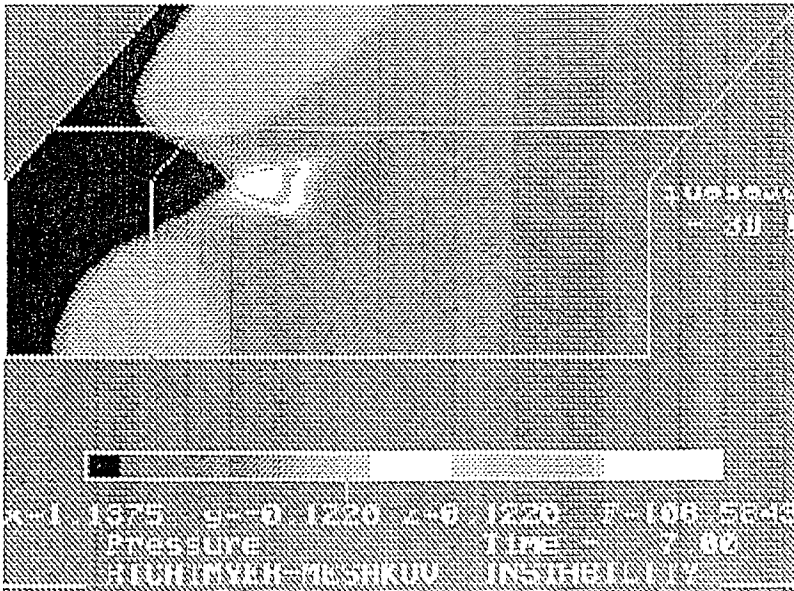


FIGURE 5

THE APPLICATION OF FRONT TRACKING TO THE SIMULATION OF SHOCK REFRACTIONS AND SHOCK ACCELERATED INTERFACE MIXING

JOHN W. GROVE^{1,2,3,5}, YUMIN YANG⁴, QIANG ZHANG^{4,6}, DAVID H. SHARP⁷,
JAMES GLIMM^{1,2,3,4}, BRIAN BOSTON, AND RICHARD HOLMES

ABSTRACT. We report new results on the Rayleigh-Taylor and Richtmyer-Meshkov instabilities. Highlights include calculations of Richtmyer-Meshkov instabilities in curved geometries without grid orientation effects, improved agreement between computations and experiments in the case of Richtmyer-Meshkov instabilities at a plane interface, and a demonstration of an increase in the Rayleigh-Taylor mixing layer growth rate with increasing compressibility, along with a loss of universality of this growth rate. The principal computational tool used in obtaining these results was a code based on the front tracking method.

1. INTRODUCTION

The mixing behavior of two or more fluids plays an important role in a number of physical processes and technological applications. We consider two basic types of mechanical (*i.e.*, non-diffusive) fluid mixing. If a heavy fluid is suspended above a lighter fluid in the presence of a gravitational field, small perturbations at the fluid interface will grow. This process is known as the Rayleigh-Taylor instability. One can visualize this instability in terms of bubbles of the light fluid rising into the heavy fluid, and fingers (spikes) of the heavy fluid falling into the light fluid. A similar process, called the Richtmyer-Meshkov instability [13, 15], occurs when an interface is accelerated by a shock wave. These instabilities have several common features. Indeed, Richtmyer's approach to understanding the shock induced instability was to view that process as resulting from an acceleration of the two fluids by a strong gravitational field acting for a short time.

We examine three separate aspects of the Rayleigh-Taylor and Richtmyer-Meshkov problems. Section 2 discusses direct numerical simulations of Richtmyer-Meshkov type problems using front tracking. Front tracking is an adaptive method which provides sharp resolution of distinct waves in fluid flows. This is accomplished by the use of a dynamically moving co-dimension one grid that follows the tracked wave fronts. Our conclusion is that front tracking is a valuable numerical method due to its ability to remove numerical diffusion, enhance the resolution of the computation, and reduce or eliminate grid orientation effects. Section 3 describes an analysis of the short term growth in the unstable modes of a shocked interface using a linearization of the Euler equations.

1991 *Mathematics Subject Classification.* 35L67, 76L05 .

Key words and phrases. Rayleigh-Taylor, Richtmyer-Meshkov, front tracking .

¹Supported in part by the U.S. Army Research Office through the Mathematical Sciences Institute of Cornell University under subcontract to SUNY Stony Brook, ARO contract number DAAL03-91-C-0027.

²Supported in part by the National Science Foundation Grant no. DMS-9201581

³Supported in part by the U. S. Army Research Office, grant no. DAAL03-92-G-0185.

⁴Supported in part by the Applied Mathematics Subprogram of the U.S. Department of Energy DE-FG02-90ER25084.

⁵Supported in part by the National Science Foundation Grant no. DMS-9057429

⁶Supported in part by the Oak Ridge National Laboratory subcontract 19X-SJ067V.

⁷Supported by U. S. Department of Energy

We compare the solution of the linearized equations with an impulsive model of the mixing process due to Richtmyer, and with numerical solutions of the full Euler equations. We show that for sufficiently small amplitudes of the perturbations in the fluid interface, the linear theory agrees with the numerical solutions to the fully nonlinear system. We noticed that in many cases the results of the impulsive model disagreed with the exact solution to the linearized equations. We also report in section 4 on recent work that has examined the role of compressibility in the Rayleigh-Taylor problem. It is shown that the mixing layer growth rate increases markedly with increasing compressibility and this effect is accompanied by a loss of universality. This is the first prediction of an important property of the Rayleigh-Taylor mixing layer outside of the range of existing experiments.

2. FRONT TRACKING SIMULATIONS OF SHOCK INDUCED SURFACE INSTABILITIES

The front tracking method represents a surface of discontinuity in a fluid flow as a sharp interface, thereby eliminating numerical diffusion. This results in a substantial increase in computational resolution, and a corresponding increase in efficiency, which has been utilized to increase the detail and scope of computations attempted. Moreover, front tracking can be combined with modern shock capturing methods to provide a computational tool of great flexibility for modeling flows dominated by shocks and fluid interfaces. The shock capturing provides a robust alternative to tracking when the interacting waves produce configurations that are too complicated to track, while tracking improves the ability of the shock capturing code to resolve secondary features of the flow. The general goal of our effort is to achieve a good balance between the increased resolution of the tracked wave fronts and the robustness of the shock capturing methods.

An important aspect of our front tracking code in simulations of the Richtmyer-Meshkov instability is its ability to handle interactions between tracked waves. It can automatically detect the collision of two wave fronts, analyze the resulting interaction, and modify the tracked wave data structures accordingly. References [4, 6, 9, 11, 12] describe the basic algorithms and provide details on the construction of our front tracking code.

Figure 1 shows a front tracking simulation of the acceleration of a perturbed circular interface by an expanding shock wave. The computation begins with a bubble of heavy fluid suspended in a lighter fluid. The two fluids are initially at rest, and the bubble interface is given a slight sinusoidal perturbation of the form $r = (r_0 + \epsilon \cos(n\theta))$, where (r, θ) are the polar coordinates of a point on the bubble interface. Here $r_0 = 0.8$, $\epsilon = 0.05$, and $n = 12$. Both fluids are modeled using a polytropic equation of state with $\gamma = 1.33$, and the density ratio across the bubble is 5. An expanding shock with ahead Mach number 6.6 (pressure ratio 50) is installed at a distance 0.3 from the origin. The entire computation takes place within a square of side 6.0 using a 200×200 grid.

At about time 0.19 the expanding shock reaches the bubble interface and is refracted into an inwardly directed rarefaction wave, and an outwardly directed transmitted shock. Note that we track both edges of the reflected rarefaction. Figure 1b shows the tracked wave configuration shortly after the expanding shock has passed through the bubble interface. By this point the average radius of the bubble interface is approximately twice its initial value and the ripples on the interface have experienced a phase inversion. Such an inversion is typical for interactions that produce reflected rarefactions.

Figure 1c shows the simulation just before the leading edge of the reflected rarefaction reaches the origin. The reflection of the rarefaction wave at the origin produces additional outwardly directed waves. These new waves are not tracked in our simulation, but are still reasonably well resolved by the shock capturing method.

Figure 1d shows the later time development of the bubble interface. Here the spikes of the heavy fluid being ejected into the lighter fluid outside have become quite elongated. We also see that the heads of the fingers are starting to pinch off. The velocity shear across the sides of the fingers is

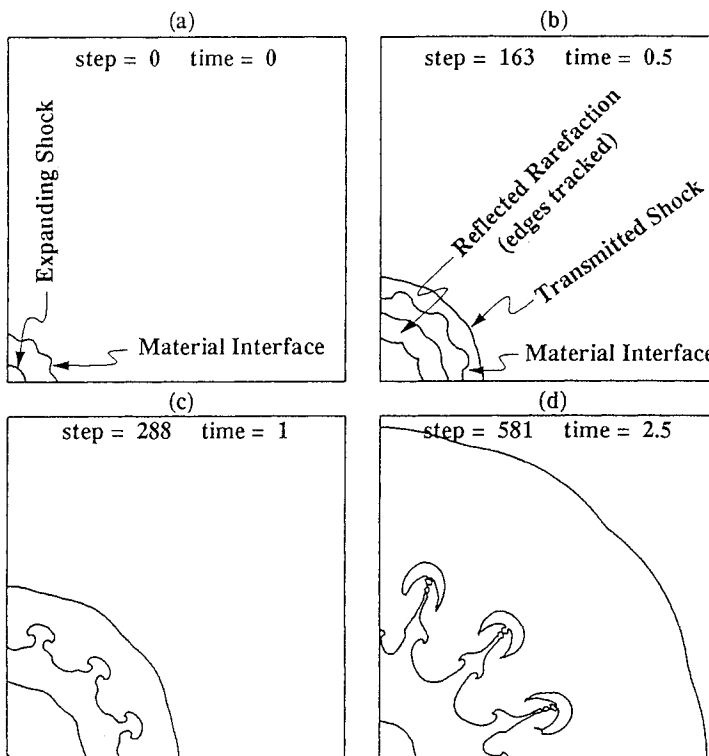


FIGURE 1. The acceleration of a perturbed circular interface by a shock wave. A significant advantage of front tracking is the improvement in the resolution of interface features not aligned with the finite difference grid. Note that even at late times the three fingers have nearly the same shape and extension.

substantial, which explains the production of the Kelvin-Helmholtz type roll up on the sides of the fingers.

This computation illustrates several important points. First is the ability of front tracking to reduce grid orientation effects on the fluid interface. Since the underlying rectangular grid is square, the effective grid size in directions diagonal to the grid is $\sqrt{2}$ times coarser than in directions parallel to the grid. Unless the grid is quite fine, this can produce a substantial degradation in the resolution of waves in these directions. This effect was cited, for example, in [1, 5] to explain the relatively faster growth of fingers aligned with the coordinate axes as compared to fingers oriented at oblique angles to the grid. We emphasize that there is very little indication of grid orientation effect in our computation. Since the initial data is periodic in θ with period $\pi/6$, each of the three spikes in figure 1 should be identical. In our simulation we see that there is only about a 2.5% difference in the elongation of the spikes at the latest time shown.

We also comment that the asymmetry in the Kelvin-Helmholtz roll up on the sides of the outer spikes appears to be due to an additional artificial mode that has been produced by the interaction of the tracked wave with the boundary. For efficiency we conducted these simulations using a quarter circular geometry with the axes of symmetry along the positive x and y axes replaced by reflecting boundaries. As implemented, this results in a slight loss of information at the boundaries, and can lead to the development of additional modes in such highly unstable problems as this one. We are currently investigating improved algorithms for the propagation of curves at reflecting walls

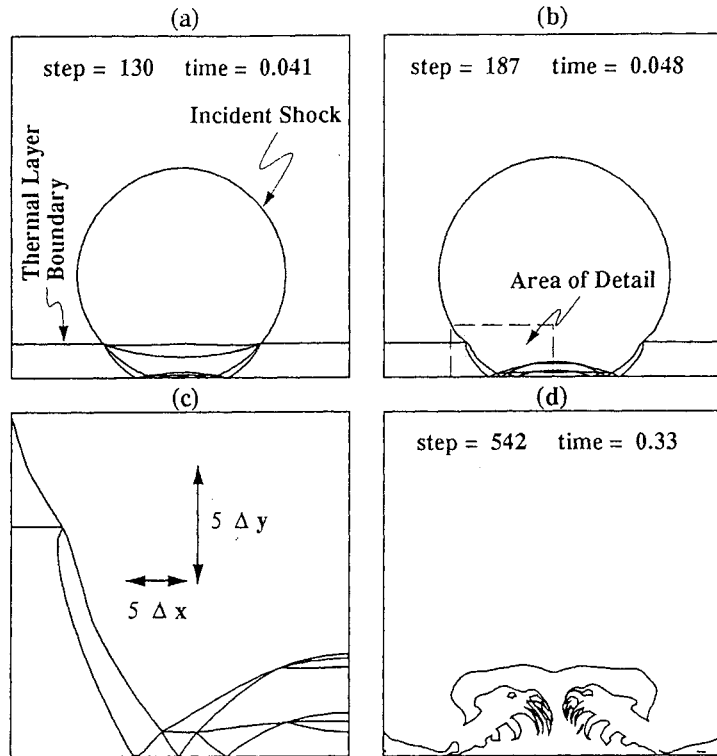


FIGURE 2. The interaction of a shock wave with a thermal boundary layer. Figures 2a-b show the early stages of the simulation which is dominated by multiple wave interactions. Figure 2c shows a detail from (b) illustrating the complexity of the tracked waves. Note that here the y coordinate has been scaled by a factor of two to improve the visibility of the multiple wave interactions. Figure 2d shows the late time formation of a central geyser in the layer.

which we hope will eliminate this extra mode.

Finally we observe that the expanding nature of the outgoing shock wave has an effect on the fluid interface quite similar to that of a gravitational acceleration which enhances the unstable behavior of the interface.

Figures 2 show a simulation of the acceleration of a thermal boundary layer by an expanding shock wave. Such a layer might, for example, be produced by radiant energy from the explosion that initiates the shock wave. This computation illustrate two important points. The first is the ability of the front tracking code to handle complex interactions between the tracked waves. The second is that a sharp resolution of these features is absolutely essential for obtaining the correct answer to the questions of interest here.

The layer is modeled as a region of warm gas bounded by the wall and a contact discontinuity. A circular, expanding shock wave is initiated at a distance from the wall of three times the width of the thermal layer, and an initial radius of half the thermal layer width. The fluid outside the shock is at rest, and the density ratio between the gas inside and outside the thermal layer is 0.5. An adiabatic exponent of $\gamma = 1.4$ is used for the equation of state. The pressure ratio across the shock is initially 10^5 , which gives an initial shock Mach number of 92.5. The collision between the shock and thermal layer produces a number of interesting wave interactions and bifurcations that

are all installed and handled automatically by our code.

When the incident shock hits the thermal layer, it produces a pair of connected shock refractions with reflected rarefactions. As the blast continues to expand, there is eventually a bifurcation in the structure of the two dimensional wave pattern created by the refraction of the blast wave through the thermal layer boundary. When this happens, the transmitted wave outruns the incident wave producing a precursor type configuration as described in [10]. In modeling this bifurcation we track the precursor shock and the original incident shock but not the reflected rarefactions. This explains the absence of the two middle wave edges between figures 2a and 2b, which only show the tracked waves in the simulation. This rarefaction is still present in the computation as a captured wave.

Figure 2c shows a detail from figure 2b of the reflection of the tracked waves near the wall. The expanding nature of these waves leads to an eventual bifurcation from a regular to a Mach type reflection that has been installed for the outermost pair of reflections in figure 2c. The thermal layer acts like a channel for the waves inside it leading to a series of multiple reflections. All of this complicated structure is resolved within a zone of only about 20×10 grid blocks. Eventually the dominant characteristics of the flow shift from wave interactions to chaotic mixing, and at some point we cease tracking all of the waves except the thermal boundary interface. Figure 2d shows the interface at late time.

3. THE RICHTMYER-MESHKOV INSTABILITY IN PLANE GEOMETRY

The extremely complex nature of the Richtmyer-Meshkov instability makes it essential to investigate simplified fluid configurations that can be used to interpret experiments and to validate numerical computations. We analyze here the case where a plane fluid interface at rest is accelerated by the passage of a single plane shock wave through the interface.

If we represent the interface position at time t by $y(x) = a(t) \cos kx$, a formula for the amplitude growth rate, $\dot{a}(t)$, was conjectured by Richtmyer [15] as

$$\dot{a}(t) = k\bar{u} \frac{\rho_+ - \rho_-}{\rho_+ + \rho_-} a(0+), \quad (3.1)$$

where \bar{u} is the average velocity of the contact surface after the interaction, ρ_+ and ρ_- are the post-shocked densities on the two sides of the contact, and $a(0+)$ is the perturbation amplitude immediately after the shock-contact interaction.

Formula (3.1), called the impulsive model, is based on the assumption that the main effect of the shock wave passing through the interface is to compress the fluids on either side of the interface and to give the fluid near the interface a push. It is also assumed that once the shock has passed through the interface the fluids are incompressible. Richtmyer verified his conjecture using a linearization of the Euler equations, and he demonstrated agreement between the impulsive model and the solution of the linearized equations for a small parameter range corresponding to the case of a reflected shock.

As a first step in our program we solved the linear equations numerically for a much broader range of parameters, including both the case of reflected shocks and rarefactions. Illustrative results are given in table 1. Our units are chosen such that $U_{i,s} = \rho_a = k = 1$, where $U_{i,s}$ is the speed of incident shock, ρ_a is the density of the state ahead of the incident shock, and k is the perturbation wave vector. We can also set $a(0-)$ to one since in the linear theory the growth rate, $\dot{a}(t)$, is proportional to this pre-shocked perturbation amplitude. The solution of the linearized equations is completely determined by four dimensionless parameters: the adiabatic exponents γ_1 and γ_2 , the pre-shocked density ratio ρ_1/ρ_2 , and the incident shock strength $(p_b - p_a)/p_b$. The subscripts 1 and 2 refer quantities on the incident and transmitted side of the fluid interface respectively, and a and b refer to the ahead and behind sides of the incident shock. For the reflected shock case we see points of agreement as well as disagreement between the impulsive model and the linear theory. The reflected rarefaction case showed substantial disagreement between the two theories.

Table 1a
Reflected Shock

	1.1	2.0	4.0	8.0	16.0
1.0	0.0052 0.011	0.049 0.080	0.11 0.14	0.16 0.18	0.18 0.18
0.5	0.011 0.013	0.070 0.080	0.11 0.12	0.12 0.13	0.11 0.11
0.05	0.0015 0.0015	0.0090 0.0092	0.013 0.013	0.013 0.014	0.012 0.012

(a)

Table 1b
Reflected Rarefaction

	0.91	0.5	0.25	0.125	0.0625
1.0	-0.0044 -0.0042	-0.014 -0.028	-0.025 -0.048	-0.12 -0.059	-0.26 -0.064
0.5	-0.011 -0.0068	-0.081 -0.047	-0.15 -0.077	-0.19 -0.086	-0.21 -0.080
0.05	-0.0016 -0.00078	-0.013 -0.0054	-0.026 -0.088	-0.037 -0.0099	-0.045 -0.0093

(b)

TABLE 1. Comparison of terminal velocities between the impulsive model and linear theory. The left column of table 1a shows the incident shock strength $[(p_b - p_a)/p_b]$, and the top row the pre-shocked density ratio (ρ_1/ρ_2) . The upper number in each entry is from the impulsive model, and the lower is the result of numerical simulations of the linear theory. The two adiabatic exponents are $\gamma_1 = \gamma_2 = 1.5$.

We have also compared the results of the linear theory to those obtained by simulation of the full Euler equations. This serves both to determine the range of validity of the linear theory and to validate the solution of the full Euler equations at small amplitudes.

Figures 3 and 4 show a comparison of the linear theory and the full Euler equations. In this problem the interface is accelerated by a shock moving from air to SF₆. The parameters were chosen to agree with those occurring in the experiments reported by Benjamin [2]. The density ratio of SF₆ to air at standard conditions is 5.1, and the adiabatic exponents were taken as $\gamma_{air} = 1.4$ and $\gamma_{SF_6} = 1.0394$. The initial amplitude, $a(0-)$, was 0.0637 times the period of the sinusoidal perturbation. Figure 3 shows a plot of the normalized amplitude of the fluid interface, $\alpha(t)/a(0-)$, after its acceleration by a shock with ahead Mach number $M_0 = 1.24$. Figure 4 shows the value of $\dot{\alpha}(t)/a(0-)$ for the same simulation together with the value calculated from the Benjamin's experiments [2]. The horizontal time axis in these figures is normalized so that $t = 0$ corresponds to the time at which the shock wave has completed its refraction through the interface.

Referring to the figures we emphasize the following points. First, for sufficiently small amplitudes the simulations of the linear theory and the full Euler equations agree. Second, the growth rate as determined by the solution of the full Euler equations is in substantial agreement with the experimentally measured growth rate. Third, the growth rate as predicted by the linear theory, which agrees with the impulsive model in this case, disagrees with experiment by a factor of approximately two.

In these figure we also compare front tracking calculations where all curves were tracked (incident, reflected and transmitted shock waves and material interface) and where only the material interface is tracked. We note that while the two nonlinear computations agree for much of the simulation they begin to diverge at late times.

In ongoing work we are investigating the case of reflected rarefactions, the effects of mass diffusion on the mixing rates, and exploring the interaction over a wide range of flow parameters.

4. THE INFLUENCE OF COMPRESSIBILITY ON THE GROWTH RATE OF A RAYLEIGH-TAYLOR MIXING LAYER

Previous investigations [7, 8, 16] reported on the behavior of the outer envelope of the bubbles produced by a Rayleigh-Taylor unstable interface. For incompressible or nearly incompressible flows, the height of this envelope is given by

$$h(t) = \alpha A g t^2, \tag{4.1}$$

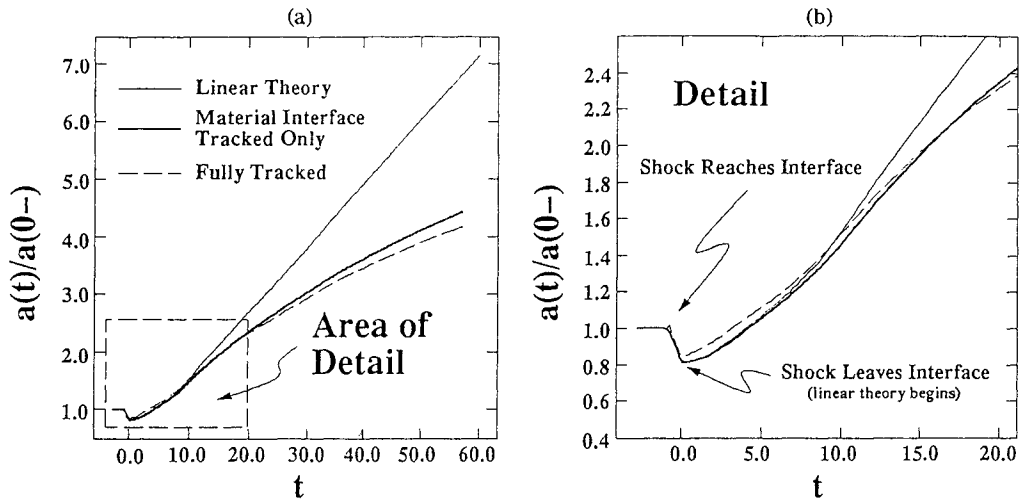


FIGURE 3. A comparison of three separate calculations of the amplitude, $a(t)/a(0-)$, of a shocked air-SF₆ interface. We see that the linear theory agrees with the nonlinear computations for sufficiently small amplitudes. Figure 3b shows a detail for early times in the computations.

where $A = (\rho_2 - \rho_1)/(\rho_2 + \rho_1)$ is the Atwood ratio of the densities of the two fluids, g is the gravitational acceleration, and $\alpha \approx 0.06$ is an approximately universal constant. We use $M^2 = \lambda g/c_h^2$ as a dimensionless measure of the compressibility, where λ is the wave length of the perturbation, and c_h^2 is the sound speed of the heavy fluid at the interface. The number α is universal in the sense that it is independent of both the thermodynamic properties of the two fluids, as well as the initial conditions at the unstable interface. This formula agrees with the experimental results of Read and Youngs [14].

Further justification of the validity of formula (4.1) was provided by analysis which established the existence of a renormalization group fixed point for a set of equations that approximate the fluid motion in terms of the dynamics of a statistical ensemble of elementary modes governed by pairwise interactions [8, 16]. Numerical solutions of this model gave a value for α in excellent agreement with both experiments and computations.

The above investigations, which were conducted for compressibilities $M^2 \leq 0.1$, have been extended to flows with moderate to large values of M^2 . We conducted a series of numerical simulations of Rayleigh-Taylor unstable flows for a variety of different parameter regimes and values of M^2 ranging from 0.1 to 1.0 [3]. Two significant observations were made on the basis of these numerical computations. The first is that α shows a marked dependence on M^2 , with the value of α for $M^2 = 1$ nearly two and a half times the value of the incompressible ($M^2 = 0$) limit of $\alpha_{incomp} = 0.06$. In general, α appears to be an increasing function of M^2 . The second observation was that α was no longer universal for larger values of M^2 , which is expressed by a dependence of α on the initial distribution of the perturbations on the unstable interface.

Table 2a summarizes the results of our investigation into the dependence of α on compressibility. The value of α , as summarized in the last column of table 2a, was computed by fitting the bubble height $h(t)$, as measured from an ensemble of N different numerical simulations, versus t^2 . Each individual simulation used a different set of random surface perturbations to act as seeds for the unstable modes, and the reported value of α is the statistical average of the individual α_i 's of the separate runs. For sample runs with $N > 1$ the root-mean-square (rms) is also reported. The other

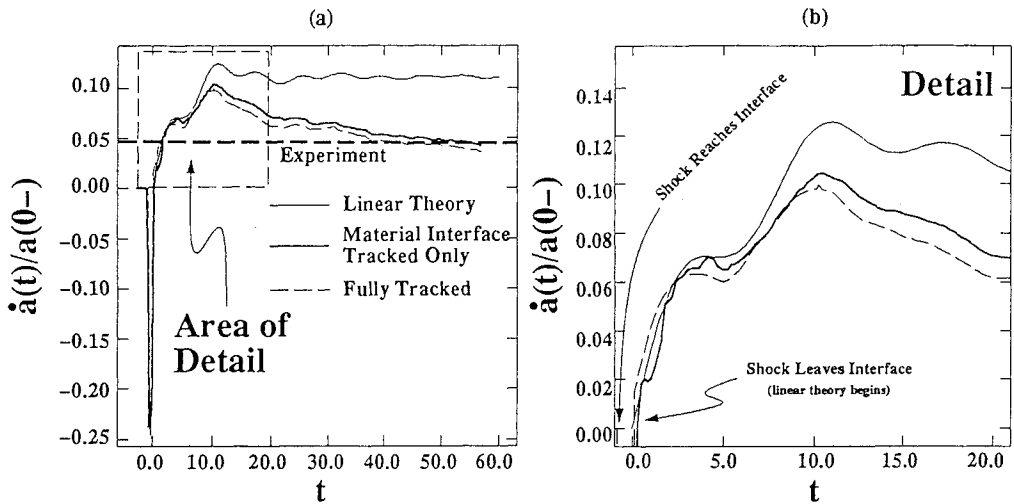


FIGURE 4. The rate of change, $\dot{a}(t)$, of the amplitude of a shocked air-SF₆ interface. The dark dashed line shows the measurement of $\dot{a}(t)/a(0-)$ obtained from the experiments of Benjamin [2] using the same flow parameters as used in this computation. The experimental number has been converted into dimensionless units as mentioned in the text.

columns of table 2 report respectively, the compressibility M^2 of the initial configuration, the grid sizes used for the simulation, the minimum and maximum of the fourier modes used to generate the initial random interface, the number of fourier modes ($k_{max} - k_{min} + 1$), and the number N of samples. In each sample, the amplitudes of the fourier modes were selected from independent Gaussian random variables.

The data reported in table 2a clearly indicate an increase in α for larger values of M^2 . We also note that for $M^2 = 0.5$, α is also dependent on the number of modes on the initial random surface.

We also compared the predicted values of α as computed from the renormalization group fixed point model with the numerical computations. These results are summarized in table 2b. We observe a dependence of α on M^2 , and note that the RG fixed point model begins to fail for larger values of M^2 .

5. CONCLUSION

This article summarizes recent work by members of our group on the modeling and analysis of unstable fluid interfaces. Our experience is that front tracking is an effective tool for the computation of these flows in two dimensions and allows us to achieve good resolution of complex flows even on relatively coarse grids.

To summarize, our principal conclusions are: front tracking substantially reduces grid orientation effects for computations in curved geometries, the solution of the linearized Euler equations agrees with numerical solutions of the full Euler equations for the Richtmyer-Meshkov problem at sufficiently small amplitudes, our front tracking simulation of the Richtmyer-Meshkov problem agrees with the experimental results of Benjamin, and the rate of growth of a Rayleigh-Taylor mixing layer increases with increasing compressibility.

Table 2a
The growth rate α for a Rayleigh-Taylor mixing layer.

Line	M^2	Domain	k_{max}	k_{min}	Modes	Samples	Modulation	α
1	.1	208 × 300	36	24	13	1	Yes	.062
2		208 × 300	18	6	13	1	Yes	.059
3		208 × 300	22	10	13	4	Yes	.066 ± .004
4		208 × 300	22	10	13	8	No	.068 ± .004
5		640 × 300	78	39	40	1	Yes	.072
6	.2	320 × 300	37	18	20	4	No	.084 ± .003
7	.3	320 × 300	37	18	20	4	No	.096 ± .004
8	.5	104 × 300	10	5	6	1	Yes	.0736
9		104 × 300	10	5	6	8	No	.099 ± .008
10		320 × 300	37	18	20	1	Yes	.105
11		320 × 300	37	18	20	8	No	.121 ± .006
12		320 × 300	28	9	20	1	Yes	.106
13		320 × 300	57	38	20	1	Yes	.106
14		640 × 300	74	35	40	1	Yes	.119
15		960 × 300	114	55	65	1	Yes	.123
16		1280 × 300	159	80	80	1	Yes	.116
17	1	640 × 300	74	35	40	1	Yes	.137
18		960 × 300	114	55	65	1	Yes	.144

Table 2b
A comparison of α to RG Theory

M^2	α_{comp}	α_{model}	error (%)
0.1	0.062-0.070	0.064-0.076	0
0.2	0.081-0.087	0.073-0.080	1
0.3	0.092-0.100	0.080-0.086	7
0.5	0.114-0.128	0.089-0.094	19
1.0	0.137-0.144	0.105-0.107	24

TABLE 2. Table 2a shows the results of our numerical computations of the growth rate α for a Rayleigh-Taylor mixing layer. A Comparison of α as predicted by numerical simulation vs. the renormalization group theory is shown in table 2b. This table is reproduced from reference [3].

ACKNOWLEDGMENTS

We wish to thank the other members of the front tracking group at the University at Stony Brook for their assistance in this project. In particular we thank Y. Deng, and Y. Chen who were two of the main contributors to the numerical computations discussed in section 4. Use of the Intel iPSC/860 located at Oak Ridge National Laboratory and NASA Ames is also gratefully acknowledged.

REFERENCES

1. D. Arnett, B. Fryxell, and E. Muller, *Instabilities and nonradial motion in SN 1987a*, Astrophysical J. **341** (1989), L63-L66.
2. R. Benjamin, *Experimental observations of shock stability and shock induced turbulence*, Advances in Compressible Turbulent Mixing (5285 Port Royal Rd. Springfield VA 22161) (W.P. Dannevik, A.C. Buckingham, and C.E. Leith, eds.), National Technical Information Service, U.S. Department of Commerce, 5285 Port Royal Rd. Springfield VA 22161, 1992, pp. 341-348.

3. Y. Chen, Y. Deng, J. Glimm, G. Li, D. H. Sharp, and Q. Zhang, *A renormalization group scaling analysis for compressible two-phase flow*, Phys. Fluids A, 1993, to appear.
4. I-L. Chern, J. Glimm, O. McBryan, B. Plohr, and S. Yaniv, *Front tracking for gas dynamics*, J. Comput. Phys. **62** (1986), 83-110.
5. B. Fryxell, E. Müller, and D. Arnett, *Instability and clumping in SN 1987a. I. early evolution in two dimensions*, The Astrophysical Journal **367** (1991), 619-634.
6. J. Glimm, J. Grove, W. B. Lindquist, O. McBryan, and G. Tryggvason, *The bifurcation of tracked scalar waves*, SIAM J. Comput. **9** (1988), 61-79.
7. J. Glimm, X. L. Li, R. Menikoff, D. H. Sharp, and Q. Zhang, *A numerical study of bubble interactions in Rayleigh-Taylor instability for compressible fluids*, Phys. Fluids A **2** (1990), no. 11, 2046-2054.
8. J. Glimm and D. H. Sharp, *Chaotic mixing as a renormalization group fixed point*, Phys. Rev. Lett. **64** (1990), 2137-2139.
9. J. Grove, *The interaction of shock waves with fluid interfaces*, Adv. Appl. Math. **10** (1989), 201-227.
10. ———, *A survey of the analysis of irregular shock refractions and its application to front tracking methods*, Proceedings of the Second Workshop on Hyperbolic Waves, Rio de Janeiro, Brazil, 1992.
11. ———, *Applications of front tracking to the simulation of shock refractions and unstable mixing*, J. Appl. Num. Math., to appear 1993, Proceedings of the U.S. Army Workshop on Adaptive Methods for Partial Differential Equations, ed. J. Flaherty, Rensselaer Polytechnic Institute, Troy, New York.
12. J. Grove and R. Menikoff, *The anomalous reflection of a shock wave at a material interface*, J. Fluid Mech. **219** (1990), 313-336.
13. E. E. Meshkov, *Instability of a shock wave accelerated interface between two gases*, NASA Tech. Trans. F-13 (1970), 074.
14. K. I. Read, *Experimental investigation of turbulent mixing by Rayleigh-Taylor instability*, Physica D **12** (1984), 45.
15. R. D. Richtmyer, *Taylor instability in shock acceleration of compressible fluids*, Comm. Pure Appl. Math **13** (1960), 297-319.
16. Q. Zhang, *Validation of the chaotic mixing renormalization group fixed point*, Phys Lett A **151** (1990), 18-22.

DEPARTMENT OF APPLIED MATHEMATICS AND STATISTICS, STATE UNIVERSITY OF NEW YORK AT STONY BROOK, STONY BROOK, NY 11794-3600

E-mail address: glimm@ams.sunysb.edu, grove@ams.sunysb.edu, ymy@ams.sunysb.edu, zhang@ams.sunysb.edu, boston@ams.sunysb.edu, holmes@ams.sunysb.edu

COMPLEX SYSTEMS GROUP, THEORETICAL DIVISION, LOS ALAMOS NATIONAL LABORATORY, LOS ALAMOS, NM 87545

E-mail address: dhs@t13.lanl.gov

Experimental study of instability growth patterns of a shock-accelerated, thin fluid layer

J. W. Jacobs

Department of Aerospace and Mechanical Engineering
University of Arizona, Tucson, AZ 85721

D. G. Jenkins, D. L. Klein, and R. F. Benjamin

Los Alamos National Laboratory
Los Alamos, NM 87545

We have discovered a remarkable set of flow patterns induced by shock acceleration of two nearby, perturbed interfaces. Using planar laser-induced fluorescence (PLIF), we observe three distinct patterns in the nonlinear evolution of Richtmyer-Meshkov (RM) instabilities associated with this flow. We observe two patterns dominated by vortex pairs and one pattern showing no vortex pairing (until late time) for initial conditions that are indistinguishable by measurement techniques available for our work. The flow is initiated by spatially periodic perturbations imposed on a “gas curtain” interacting with a planar shock wave. These flow patterns are not predictable nor controllable in our experiments. Our measurements appear to be the first observations of a shock-driven flow exhibiting characteristics of bifurcation. Results were recently published,¹ and more detailed results are forthcoming. We present here a brief description of the experiment, summary of results, and a vortex-based explanation of the phenomena.

Our technique for forming an interface between fluids is an improvement over previous methods using a membrane or gravitational stratification. The vertically-flowing “gas curtain” is a quasi-planar, laminar jet flowing transversely to the direction of shock-wave propagation (shown schematically in Fig. 1). The gas/gas interfaces on both sides of the jet are diffuse with thickness of only ≈ 1 mm. The technique is an extension of work with transverse cylindrical jets used to study vorticity production and evolution.²

We use a shock tube to produce a Mach 1.2 shock wave (in air) to impinge on the gas curtain. Essential parts of the test section are shown in Fig. 1. A schlieren system (not shown in Fig. 1) checked for stabilization of the jet before initiating the shock wave. The diagnostic technique uses PLIF flow visualization to observe the shock accelerated transversely-flowing gas jet.² The PLIF diagnostic consists of sheet illumination by a dye laser beam, and imaging by an intensified, gated CCD camera having a frame duration of

5 μs . We acquire only one frame per experiment, and use our judgement to assign it to one of the three patterns. Thus, the three patterns shown in Fig. 2 are representations of time sequences of each of the three patterns. However, each representation is an ensemble of many experiments. Future experiments will attempt to image multiple frames per experiment. The validity of this tracer-based method to image the flow at Mach 1.2 is confirmed by recent results of Budzinski,³ who used Rayleigh scattering to measure the same properties of shock-accelerated cylindrical jets as did Jacobs with PLIF.² Our attempts to use schlieren imaging to detect the free-stream flow patterns failed because optical distortion by boundary effects obscured the flow patterns in the free-stream region of interest.

The observed flow patterns evolve from a shock-accelerated SF₆ gas jet (i.e., the “gas curtain”) initially having a varicose cross-section, as shown in Fig. 1. The interfaces on both sides of the jet undergo Richtmyer-Meshkov instability when accelerated by a planar shock. Assuming the interfaces behave independently, one expects the first interface encountered by the shock, i.e., the air->SF₆ interface, to experience perturbation growth after shock compression, whereas one expects the second interface, i.e., SF₆->air, to invert phase before growing. Thus, the varicose cross-section is expected to transform into a sinuous cross-section with growing amplitude after phase inversion, if the interfaces grow independently. This occurs about 40% of the time as shown by the ensemble of PLIF images presented in the middle row of Fig. 2. However, some experiments produce mushroom-shaped profiles, characteristic of vortex pairing, either on the upstream side of the mean interface position, upper row of Fig. 2, or on the downstream side, lower row of Fig. 2. The “upstream mushrooms” occur about 50% of shots and the “downstream mushrooms” about 10%. For initial conditions which are indistinguishable by measurement techniques available for our work, we observe that the intermediate growth stage of this Richtmyer-Meshkov flow evolves unpredictably into one of three distinct sets of patterns during each experiment.

These phenomena can be described qualitatively by the dynamics of the vorticity in these flows, shown schematically in Fig. 3. Vorticity is produced by the misalignment of pressure and density gradients, sometimes referred to as the baroclinic generation of vorticity. Because the dominant pressure gradient is produced by the shock front, and the dominant density gradient is at the boundaries of the gas layer, vorticity produced by the shock interaction will lie on the boundaries of the layer, and will vary periodically along the layer as a row of distributed vortices having alternating sign. We postulate that the diffuse nature of the interfaces enables the vorticity at both interfaces to couple, and form

either a uniform distribution or pairing. The pairing is manifest as upstream and downstream mushrooms. The sinuous pattern would be produced by a more uniform distribution. Subtle asymmetries in the initial conditions may favor one of these three modes in each experiment. Because we do not observe upstream and downstream mushrooms in a single frame during the first millisecond of growth, we suggest that the pairing mechanism is a collective phenomenon. Our model is not yet precise enough to quantitatively estimate how much initial asymmetry is needed to induce pairing.

We have attempted to quantify these images by extracting the growth rate of the peak-to-peak perturbation. We measure the width, W , of the envelope enclosing the perturbed SF_6 layer; we do not measure the peak-to-peak amplitude of each wavelength. The W vs time data have considerable scatter. We have fit the experimental data to the function, $W = W_0 (1 + At)^n$, where we estimate the initial width, W_0 , and treat A and n as fitting parameters. We find that $n \approx 1/2$ for all three patterns. This result is preliminary, and must be compared with future multi-frame data.

•

Attempts to simulate these flows observed experimentally have been made at Los Alamos⁴ and Lawrence Livermore National Laboratories.⁵ These calculations find that initial upstream-downstream asymmetries of the perturbation amplitudes can produce sinuous-shaped and mushroom-shaped flow profiles. Also the Los Alamos calculations show that initially symmetric perturbations of sufficiently large amplitude can evolve into the mushroom-shape mode. These simulation results are preliminary and we expect that future calculations will elucidate the possible mechanisms causing this bifurcating flow.

In summary, we present flow visualizations showing a bifurcating flow associated with the Richtmyer-Meshkov instability of contiguous interfaces. The shock-accelerated gas curtain evolves into one of three distinct flow patterns in each experiment. The flows can be explained qualitatively in terms of shock-induced vorticity production and transport. Models, simulations, and multi-frame experiments are needed to understand these flows.

The shock tube experiments were performed at the Los Alamos National Laboratory, supported by US Department of Energy Contract W7405-ENG-36, following nozzle development at the University of Arizona. We are grateful to R. Reinovsky and H. Rogers for encouragement, to R. Haight for use of the intensified camera, and to C. Findley and D. Bannerman for technical assistance.

Figure captions

1. Experimental setup. The shock wave moves left to right at Mach 1.2. The illuminated cross-section, denoted I X-S, is the portion of the shock-accelerated gas jet that is illuminated by the laser sheet. The vertical jet is formed by the SF₆ nozzle, and SF₆ is removed in the exhaust plenum below the test section. The camera is an intensified CCD camera that captures one image per event.
2. Experimental data. Each row is a representation of a time sequence of a flow pattern. The upper row shows "upstream mushrooms," the middle row shows the sinuous pattern, and the lower row shows "downstream mushrooms." Each row is actually an ensemble of images from different events. Adjacent images are at $\approx 100 \mu\text{s}$ intervals.
3. The pressure gradient of the shock wave and the density gradient at the layer boundary (a) produces a vorticity distribution roughly approximated as a row of equally spaced vortices (b). The three observed patterns develop from slight differences in the initial vorticity distribution (shown greatly exaggerated). Nonuniform vortex spacings cause the vortices to pair (c and d). A more equally spaced distribution produces the sinuous shape (e).

References

- (a) Present address of D. G. Jenkins is University of Chicago.
- (b) Present address of D. L. Klein is University of California, Berkeley.
1. J. W. Jacobs, D. L. Klein, D. G. Jenkins and R. F. Benjamin, "Flow patterns in a shock-accelerated thin fluid layer," *Phys. Rev. Lett.* **70**, 583-6 (1993).
2. J. W. Jacobs, "Shock-induced mixing of a light-gas cylinder," *Journal of Fluid Mechanics* **234**, 629-49 (Jan. 1992).
3. J. M. Budzinski, "Planar Rayleigh scattering measurements of shock enhanced mixing," PhD. thesis, California Institute of Technology, 1992. A preliminary account is given in John M. Budzinski, Edward E. Zukoski, and Frank E. Marble, "Rayleigh scattering measurements of shock enhanced mixing," AIAA 92-3546, p. 1-15, proceedings of the 28th Joint Propulsion Conference and Exhibit (July 6-8, 1992, Nashville TN).
4. R. Gore, Los Alamos National Laboratory, private communication.
5. W. P. Crowley, Lawrence Livermore National Laboratory, private communication.

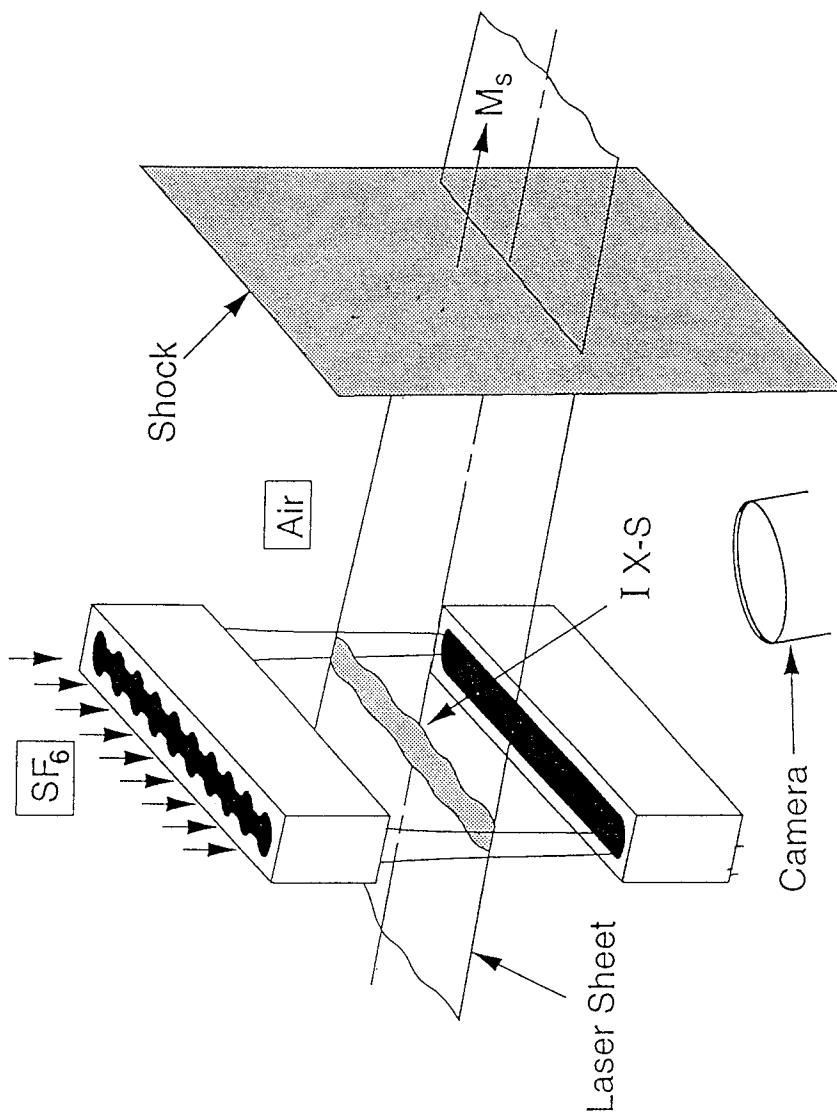


Figure 1

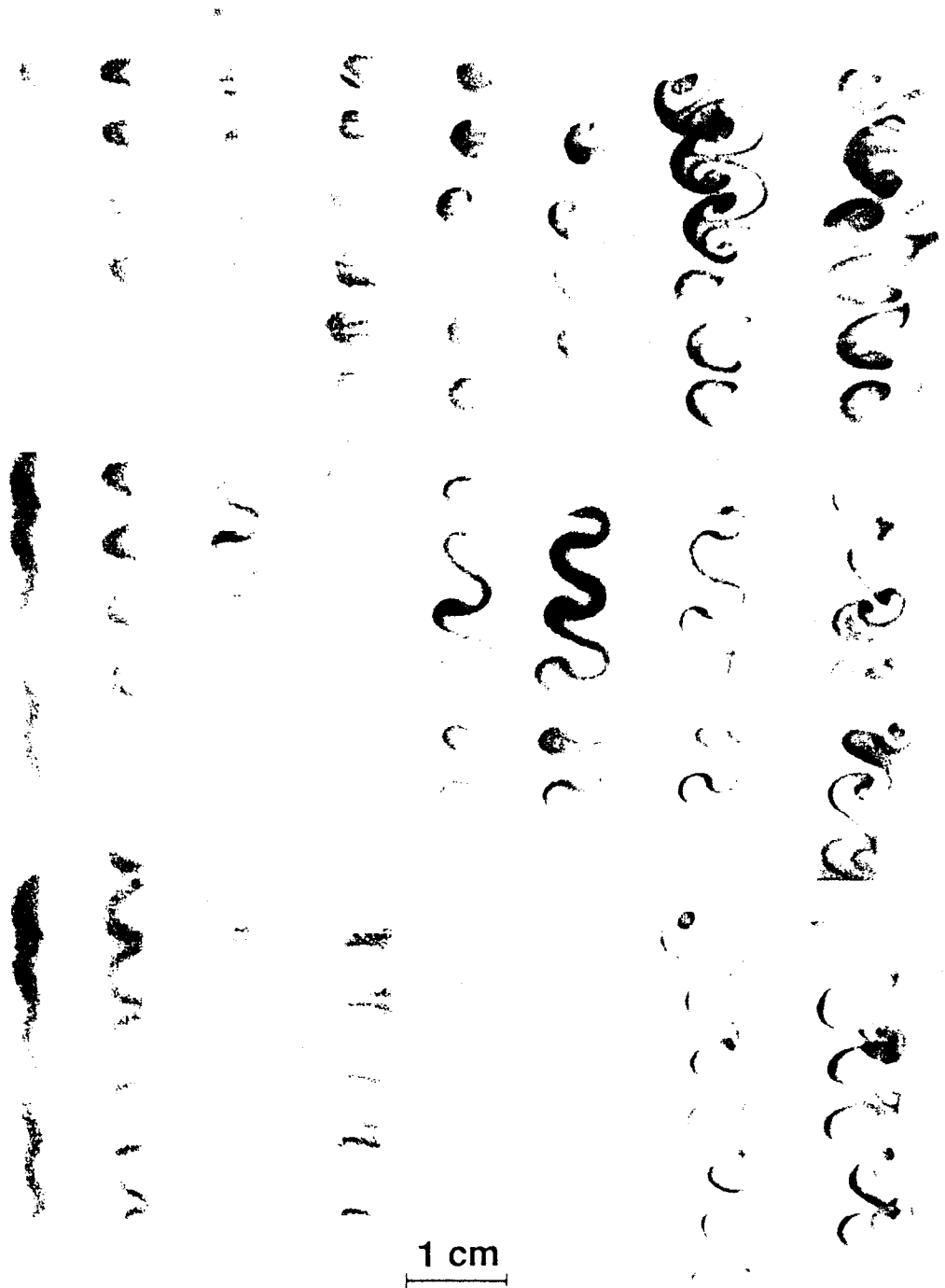


Figure 2

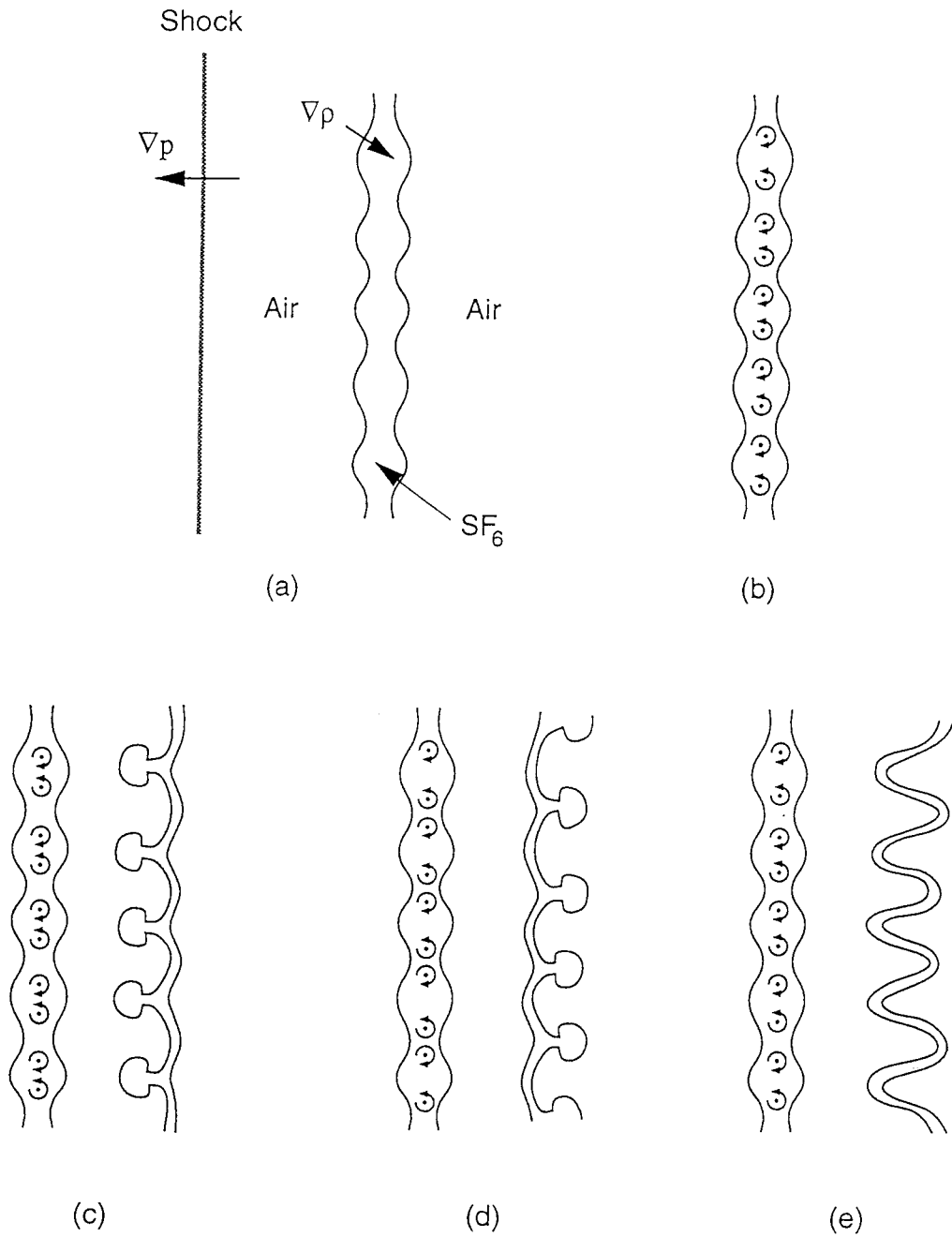


Figure 3

THE LASER SHEET AS A QUANTITATIVE DIAGNOSTIC
IN SHOCK TUBE EXPERIMENTS

Daryl Landeg, Martin Philpott,
Ian Smith, Alan Smith

AWE, Foulness, UK

INTRODUCTION

The aim of this study was primarily to improve the diagnostic techniques incorporated in shock tube compressible turbulent mixing studies. The report details the current status of experiments studying Richtmyer/Meshkov instabilities being performed at AWE(F) and describes a recently introduced improved visualisation method, based on a multiple frame laser sheet technique. Single frame laser sheet experiments were reported by Meshkov et al, Reference 1. Early evidence exists of the potential of the method to yield quantitative concentration data across the mixing zone width.

BRIEF DESCRIPTION OF THE SHOCK TUBE STUDIES

The experiments were based on the 8 x 2 inch shock tube (20 x 5 cm) and were similar to those described by Meshkov (References 1 and 2). A test cell was placed at the end of the expansion chamber just before the rigid end termination (Figure 1). This shock tube was operated so as to produce air shocks of 10 psi over-pressure (0.69 bar, $M = 1.26$) of duration 7 ms.

A schematic for the test cell is shown in Figure 2. The cell comprises three compartments separated by nitrocellulose membranes (approximately 1 micron thick). Compartments 2 and 3 are the active compartments, the principal interest being the mixing across membrane B. The incident shock travels from right to left in this schematic.

Two different configurations for membrane B have been studied (Figure 3). In the 1D planar case only small scale turbulent mixing should occur. For the 2D case a large sinusoidal perturbation is added: the aim was to investigate the effect of the large scale perturbation on the small scale turbulence. In previous experiments, Reference 1, using a nitrocellulose membrane it was found that the membrane did not readily fragment and this was overcome by using a wire grid as reported in Reference 3. The wires used here were in the form of a 4 mm square aperture grid of 0.025 mm diameter annealed tungsten wire in contact with and supporting the downstream side of membranes A and B. In addition to ensuring fragmentation after shock passage, the wire grid served to support membrane B and preserve the required initial configuration when the dense gas had been admitted. One flaw in this arrangement, to be corrected, is the failure to use a wire grid to prevent upstream bulging of membrane A. Experiments were done with and without wire grids.

Compartment 2 was filled with freon-12 seeded with olive oil particles generated in a TSI atomizer (model 9302), the average particle size being approx 0.8 micron (according to the accompanying product literature). Compartments 1 and 3 contained air. All three compartments were initially at atmospheric pressure. As shown in Figure 2, the laser sheet (approximately 1 mm thickness) entered the test-cell via the vertical slit window in the end-plate and passed down the centre of the observation section to encompass the full height of the shock tube.

VISUALISATION TECHNIQUE

For the studies described, the mix region was interrogated using the Mie/Tyndall scattering technique. The laser sheet defined a thin 2D plane as the test volume in which the experiment was studied. Seeded gas within this plane scattered the light which was collected and imaged onto a high speed camera (Cordin 35 mm drum camera). This method enabled the position of the seeded freon gas to

be tracked as it mixed with unseeded gas (air in these experiments). Using the following proportionality relationship, it is possible to make a quantitative assessment of the relative concentration of the seeded and unseeded gases away from the boundary layer and also of the increased mix region to be found at the shock tube walls.

$$P = \eta IN \Delta V \int \frac{\partial \sigma}{\partial \Omega} d\Omega \quad (\text{Reference 4})$$

P, collected power

N, number of scattering particles

η , efficiency factor related to optical system

ΔV , one volume element

I, illumination intensity

$\int \frac{\partial \sigma}{\partial \Omega} d\Omega$, integrated cross-section (function of scattering angles, assumed a constant).

The laser used for this study was an Oxford Lasers CU 15-A Cu Vapour pulsed laser. The choice of the Copper vapour laser was primarily due to the high pulse repetition rate (up to 30 kHz) available for this particular system. It has proved to be a very versatile and efficient diagnostic particularly when synchronised to the Cordin camera via Oxford Lasers N-shot recorder. The latter allows operation of the firing sequence shown in Figure 4. The system is capable of yielding up to 100 high quality photographic records (35 mm film) within the 4 ms duration of the event. The system functions without a camera shutter: the exposure time is simply the laser pulse duration (30 nanoseconds at 30 kHz); this effectively "freezes" the flow for recording the images.

Sample results (3 frames selected from 50 recorded) are shown in Figure 5 for each of two tests with plane and sinusoidally-perturbed membrane B supported in both cases by a wire mesh. Evidence of effective fragmentation of the membranes (maximum dimensions - 4 mm) at an early time is clearly visible.

At the time of reporting, we have established neither optimisation of the seeding level nor the illumination level for interrogation of the mix region. However, results from preliminary investigations have already revealed a great deal more information about the growth of the mix region than was previously possible using shadowgraph or Schlieren techniques. The validity of such refractive difference summation techniques is impaired due to the increased mix at the shock tube walls.

Because of the seeding and illumination problems in these initial experiments we are not yet able to report a detailed analysis on the mix region using our image processing system.

RESULTS

Sample results of the four types of test referred to are presented together with a comparison with 3D direct numerical simulation. As previously stated the photographic results obtained to date have suffered from non-ideal exposure levels due to seeding and illumination difficulties, limiting analysis to measurements made by eye. Consequently the only presentable results available relate to positional data, ie mix width and displacement; as yet, no concentration data.

The comparison is presented between the wired and non-wired cases for both the plane and sinusoidally perturbed cases, and further, a comparison between the experimental results and theoretical data

produced by the TURMOIL 3D calculations. Details of the calculations are summarised in Figure 6.

Figure 7a shows the experimental data (distance - time diagram) extracted from a test featuring initially plane (1D) WIRED membranes. As with the calculations, time zero corresponds to shock arrival at membrane A. The downstream mix-width bounded by X1 - X2 compares favourably with the calculated 0.01 and 0.99 volume fraction levels (ie f values, defined in Figure 6), particularly if it is accepted that the eye is not capable of such fine resolution and provides only an approximate result. In the lower part, changes in growth (at A, B, C) can be correlated with successive transmissions of the reflected shock through the mix region. At A and B, indication exists of the shock recompression of the mix region immediately prior to further growth. Of particular interest is the inclusion of the result from an equivalent 'NO WIRES' experiment. Significantly, its measured mix-width is only 50% of the 'WIRE' case.

[NB - In Figure 7a a small discrepancy in mix width is apparent warranting explanation: X1 and X2 data is based on mean boundary position over the full test-section height while δ refers to measurement over the central region for comparison with the 3D calculations].

The velocity of the freon/air interface after the passage of the first shock is slightly greater in the simulation than in the experiment. This discrepancy is currently being investigated.

Figure 7b shows the experimental data from an initially perturbed (2D) WIRED experiment.

At the end of the experiment the width of the small scale turbulent mixing zone δ is about $\frac{1}{2}$ of that in the 1D experiment.

Of particular interest is the problem experienced in analysing and determining boundaries for this class of experiment. At later times, there appeared to be freon entering the sheet ahead of the mixing zone (ie downstream of the downstream boundary). This suggested evidence of some non-symmetrical or wall effect influencing the flow. We had already postulated that boundary/wall effects were influencing our previous shadowgraph studies giving grounds for introducing the laser sheet technique. It had been assumed that the apparent increased mixing evident in the shadowgraph studies was confined to the tube wall and although it influenced the shadowgraph it did not encroach on the flow at the centre of the tube or adversely effect the experiment. We therefore decided to investigate the wall effects to assess their contribution, if any, to the mix zone at the centre of the shock tube.

To do this we switched from a vertical sheet to a horizontal sheet that spanned the width of the shock tube (2 inch): viewing was from a near-vertical direction via an angled mirror. Figure 8 shows a sample comparison from the film sequence between horizontal and vertical sheet images recorded on two NO-WIRE experiments at approximately the same time (1.7 ms). Two marked observations were noted. Firstly the membranes did not fragment. Secondly, severe edge effects were observed especially at membrane A. Of relevance in this comparison is the exclusion of the top and bottom extremities in the vertical sheet image; also, the established repeatability of the experiments so validating comparisons from different experiments. The result of the investigation revealed that without the wire mesh for support, membrane B initially assumed a convex bulge in the downstream direction. This bulging produced increased mixing at the tube wall which appeared to severely affect the experiment after approximately 1 millisecond. In contrast, the increased support afforded by a wire mesh appeared to suppress these wall effects thereby producing a far more satisfactory result.

Figure 9 shows plane sections from the TURMOIL calculations for the 1D and 2D cases at 2.5 ms and 3.5 ms. The intensity of shading is proportional to the freon mass per unit volume and such results will in the future be compared directly with the quantitative experimental analysis.

A brief comment can be offered on qualitative comparison with experimental data (up to 3.5 ms) from the WIRE experiments. Generally encouraging agreement exists regarding outline and shape of the more prominent structures of the mixing region. Of particular value is the insight provided by the calculations into the sensitivity of mix width to arbitrarily selected contour values (eg 0.01 and 0.99 volume fraction). In advance of the forthcoming experimental analysis, the requirement for accurate data is clearly evident.

CONCLUSIONS

The results for the NON-WIRED cases display a marked region of increased mix at the tube wall. In fact it would appear from our horizontal sheet work that the NON-WIRED membrane experiment is severely affected by the wall effects after approximately 1 ms. This, we believe, is inconsistent with boundary layer growth alone and is probably due mainly to the fact that the membrane breaks at the edges but does not fragment in the centre. The absence of wires also leads to some bulging of the membrane and this may enhance the edge effects. High mixing near the shock tube walls, attributed to a wall vortex, was also reported in Reference 5.

Although the wired experiments exhibit much closer correlation with the predicted results qualitatively, several anomalies still need to be addressed. The inclusion of wires may add a small wavelength perturbation to the gross perturbation. This may well be the reason for the apparent increased mix width. This is particularly noticeable in the plane membrane wired examples. Here the growth of the bubble/spike mix region has a periodicity similar to the wire grid spacing. This effect will need to be investigated: several null experiments are planned. The existence of a small wavelength perturbation may not be detrimental to the results provided the wavelength and amplitude can be quantified. Indeed the presence of a small scale perturbation may be beneficial in that the hydrocode runs require the addition of random small scale perturbation to induce mixing at plane interfaces. By accurately describing the interface we may be able to increase code confidence.

We feel that the adoption of the laser sheet method and in particular the use of a copper vapour laser system provides a significant improvement in shock tube visual diagnostics. The quality of the photographic records produced and the detail evident in them will allow us to quantitatively analyze the concentration throughout the mix region. Currently we are installing an appropriate hardware system back by image analysis software enabling us to develop a working system.

FUTURE WORK

Progress will continue with investigating those aspects of the laser sheet technique that will affect accuracy of the image analysis. These include uniformity of seeding, suitability of particle size, calibration of the optical system and use of a shock-tube of increased cross-section.

Longer term, a development of the above diagnostic technique is envisaged involving the use of a multiple laser sheet arrangement to permit pseudo-volumetric studies.

REFERENCES

1. Meshkov E E, Nikiforov V V and Tolshmyakov A I. About the Structure of Turbulent Mixing Layer at Two-Gas Interface, accelerated by Shock Waves. Proceedings of the 2nd International Workshop on the Physics of Compressible Turbulent Mixing, Pleasanton 1989.
2. Meshkov E E. Instability of a Shock Wave accelerated Interface between Two Gases. NASA Tech Tran. TTF-13074 (1970).
3. Smith A V. Turbulent Mixing in Shock Tube Experiments with a High Initial Perturbation. Proceedings of the 2nd International Workshop on the Physics of Compressible Turbulent Mixing, Pleasanton 1989.
4. Gad-El-Hak P 40. Lecture Notes in Engineering 1989 Springer Verlag.
5. Brouillette M and Sturtevant B. Experiments on the Richtmyer-Meshkov Instability: Small scale Perturbations on a plane Interface. Phys Fluids A5 916 p916 (1993).

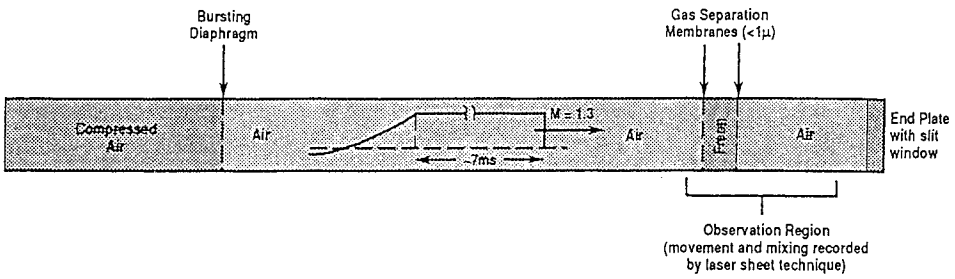


FIGURE 1. 8 x 2 inch SHOCK-TUBE

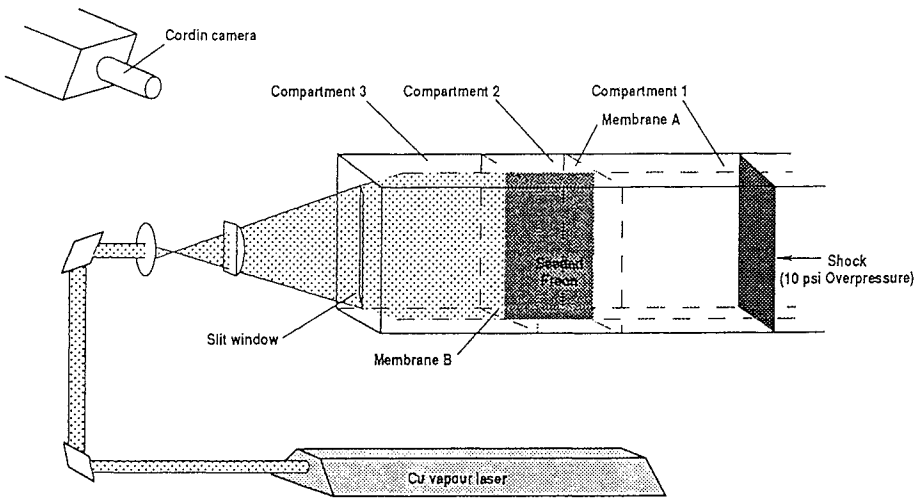


FIGURE 2. SCHEMATIC OF TEST CELL SHOWING LASER SHEET SET-UP

AS 7

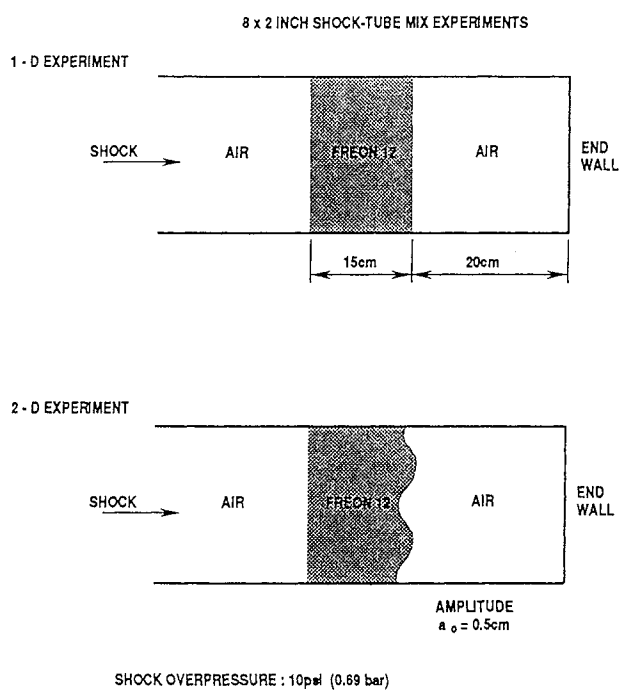


FIGURE 3. TEST CONFIGURATIONS FOR MIX EXPERIMENTS

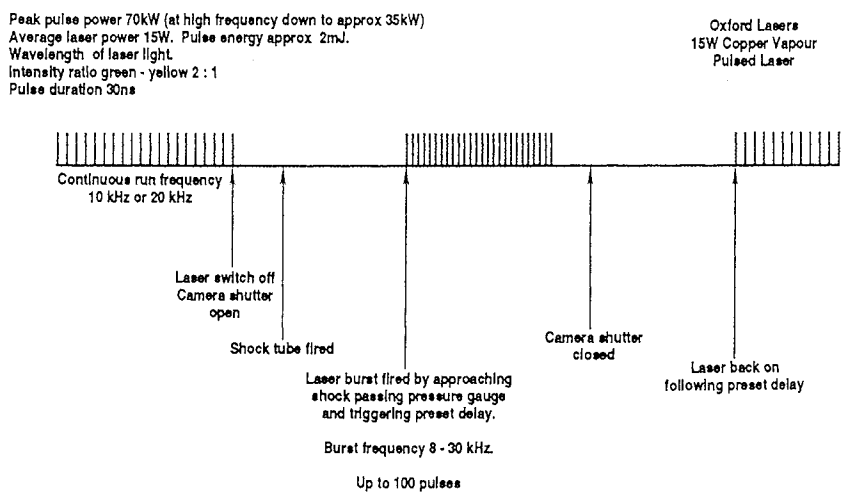


FIGURE 4. LASER FIRING SEQUENCE

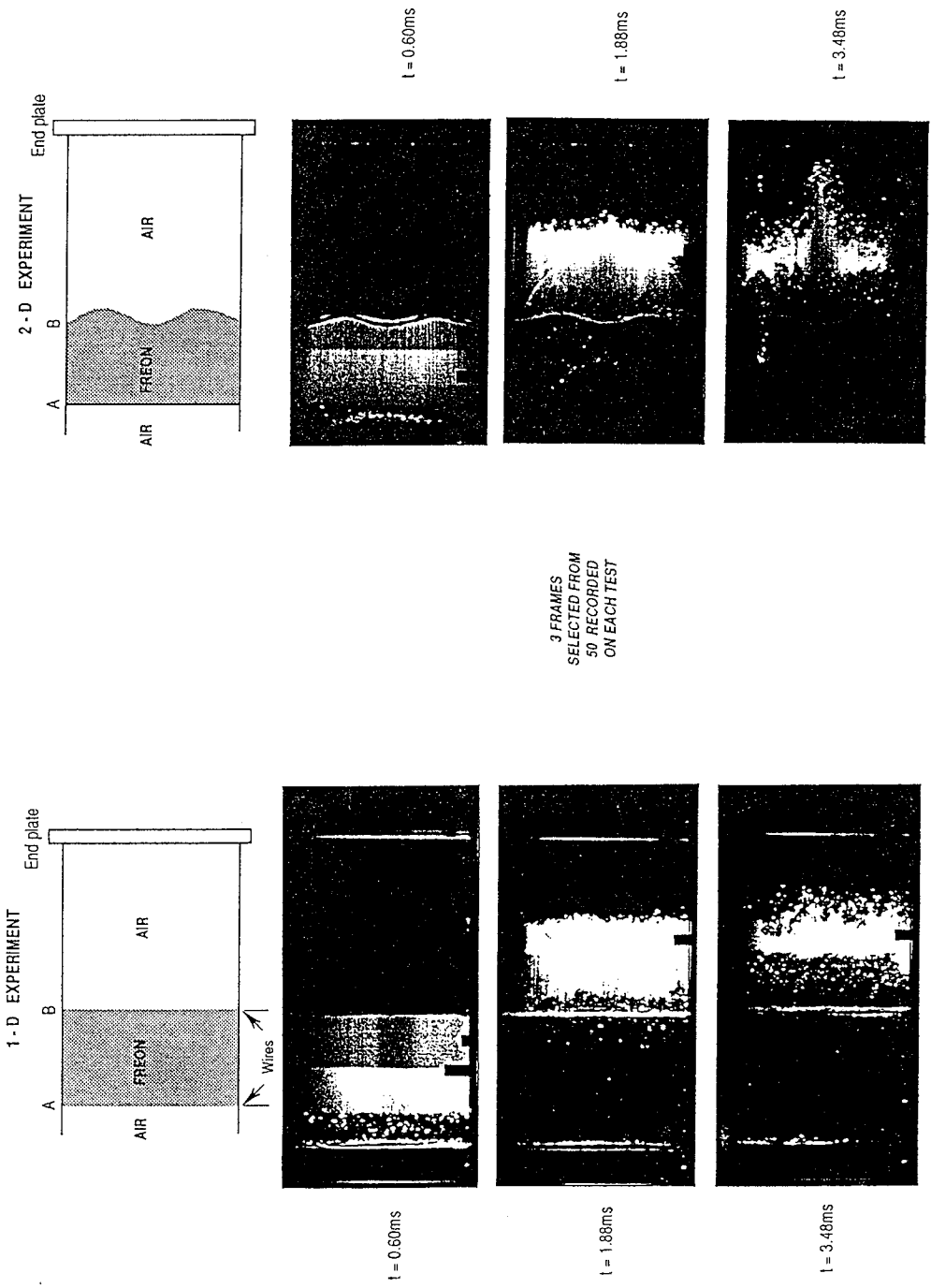
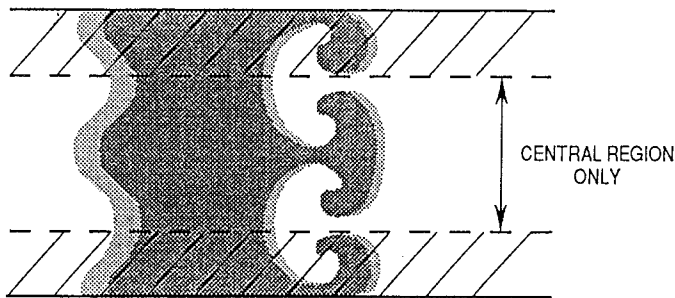


FIGURE 5. SAMPLE LASER SHEET RESULTS



MESH SIZE

320 x 160 x 80 ZONES

X - DIRECTION MESH MOVES WITH MEAN X - VELOCITY
(SEMI-LAGRANGIAN CALCULATION)

INITIAL CONDITIONS

COSINE PERTURBATION

$\lambda = 10.16\text{cm}$

$a_0 = 0.0 \text{ or } 0.5\text{cm}$

RANDOM SMALL SCALE PERTURBATIONS $\lambda \text{ min} = 0.5\text{cm}$

s.d. OF AMPLITUDE

$= 0.01 \lambda \text{ min}$

$= 0.005\text{cm}$

MEAN VOLUME FRACTION

$$\bar{f}(x) = \frac{\int f(x, y, z) dy dz}{\int dy dz}$$

$f(x, y, z)$ IS THE FREON VOLUME FRACTION.
MIX LIMITS FOR THE 1D CASE TAKEN TO BE
THE POINTS WHERE $\bar{f} = 0.01$ AND 0.99

FIGURE 6. TURMOIL 3-D CALCULATIONS

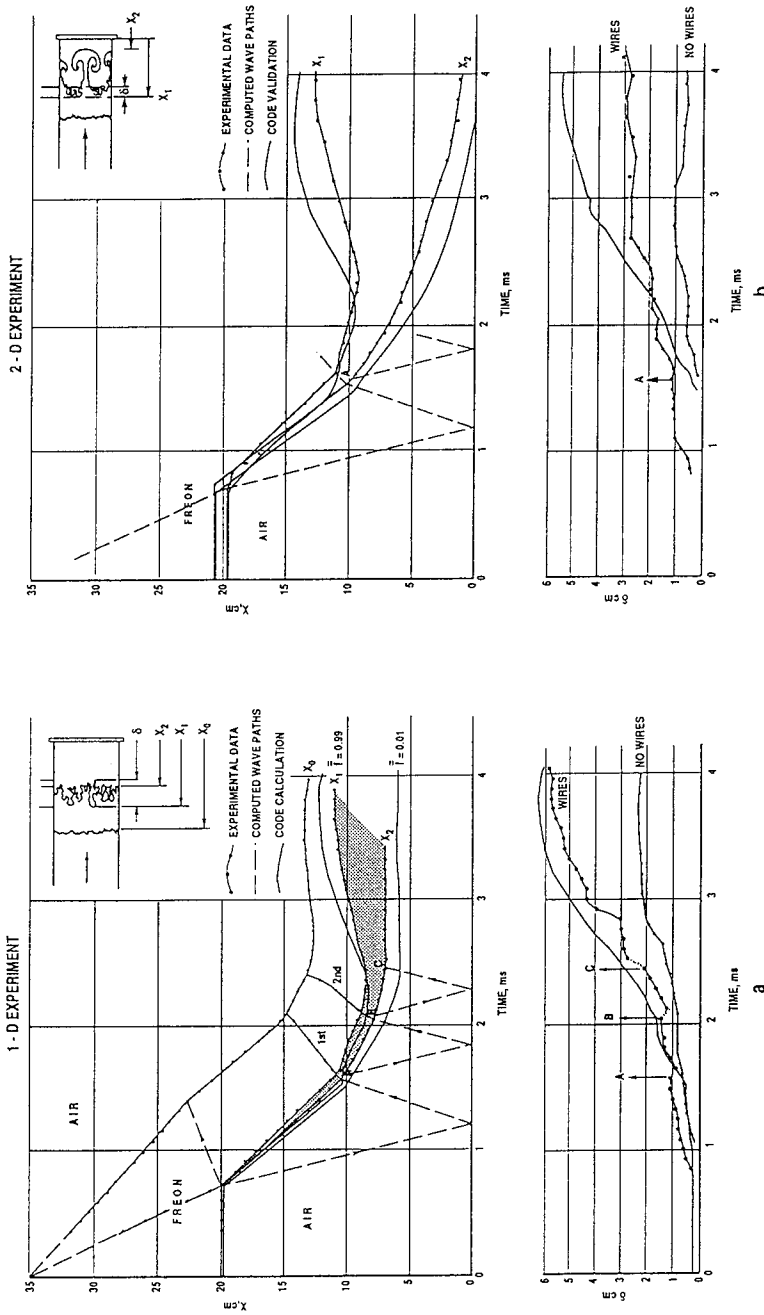


FIGURE 7a & b. EXAMPLES OF EXPERIMENTAL DATA FROM SINGLE TESTS COMPARED WITH TURMOIL 3-D CALCULATIONS

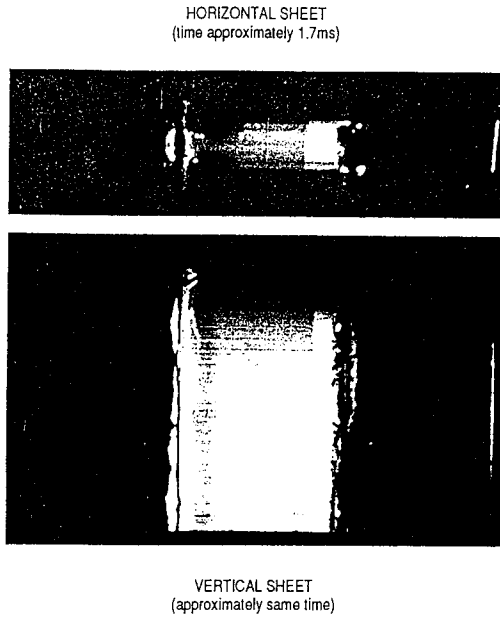
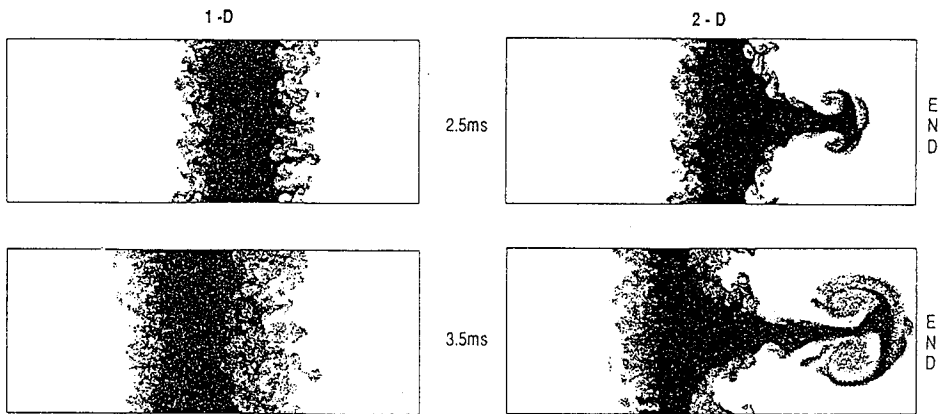


FIGURE 8. COMPARISON OF HORIZONTAL AND VERTICAL SHEET IMAGES



INTENSITY OF SHADING IS PROPORTIONAL TO FREON MASS PER UNIT VOLUME

FIGURE 9. TURMOIL CALCULATIONS FOR 1D AND 2D EXPERIMENT

FREEZE-OUT AND THE FAILURE OF RICHTMYER'S PRESCRIPTION

Karnig O. Mikaelian
 University of California
 Lawrence Livermore National Laboratory
 Livermore, California 94550

In the standard Richtmyer-Meshkov^{1,2} (RM) instability perturbations at a shocked interface grow after the passage of a shock. Freeze-out refers to the phenomenon whereby the perturbations do **not** grow, i.e., freeze-out, after the passage of a shock. This is fairly straightforward, at least theoretically (no experiments have been done so far) in a doubly shocked system: The first shock induces a growth which can be completely neutralized by a second shock, provided that the direction and the strength and timing of the second shock are properly chosen (see ref. 3). This type of double-shock freeze-out occurs in compressible as well as incompressible fluids, and is easy to understand.

Somewhat more subtle is single-shock freeze-out; in our pursuit of this phenomenon we found that in certain cases Richtmyer's prescription fails to give the correct growth rate.

Fig. 1 shows the system and our notation: An incident shock moves at speed W_i from fluid A into fluid B having densities ρ_A and ρ_B and specific heat ratios γ_A and γ_B respectively. The interface between A and B has a sinusoidal perturbation of wavelength λ and initial amplitude $\eta_0 \equiv \eta_{\text{before}}$. After the shock strikes the interface the perturbation $\eta(t)$ grows linearly in time at a rate given by

$$\frac{\dot{\eta}}{\eta_0 \Delta v k} = \text{NGR} = A_{\text{effective}} \tag{1}$$

where Δv is the jump velocity of the interface ($\Delta v = u_1 = u_2$ in Fig. 1), $k = 2\pi/\lambda$, and NGR stands for Normalized Growth rate, a dimensionless quantity. Eq. (1) is limited to the linear regime, i.e., $\eta k \ll 1$, the regime considered by Richtmyer.

The question is: What is $A_{\text{effective}}$? For incompressible fluids

$$A_{\text{effective}} = A_{\text{before}} = \frac{\rho_B - \rho_A}{\rho_B + \rho_A} \quad (2)$$

Of course $A_{\text{before}} = A_{\text{after}}$ and $\eta_{\text{before}} = \eta_{\text{after}}$ for incompressible fluids, i.e., the Atwood number as well as the amplitude immediately after the shock are the same as before the shock: There is no compression. In this case freeze-out becomes completely trivial: the NGR in Eq. (1) vanishes if and only if $\rho_B = \rho_A$, i.e., for identical fluids. The same is true for the Rayleigh-Taylor instability also.

The situation is not so trivial for compressible fluids: One can have $\rho_A = \rho_B$ with $\gamma_A \neq \gamma_B$. In fact Richtmyer's prescription for $A_{\text{effective}}$ is:

$$A_{\text{effective}} = A_{\text{after}} \times \text{Compression Factor} \\ = \left(\frac{\rho_1 - \rho_2}{\rho_1 + \rho_2} \right) \left(1 - \frac{\Delta v}{W_i} \right) \quad (3)$$

which he gave on the basis of three numerical examples.¹ His prescription was to use $A_{\text{after}} \eta_{\text{after}}$ instead of $A_{\text{before}} \eta_{\text{before}}$ in the classical incompressible result $\dot{\eta} = \Delta v k A \eta_0$ which he had obtained first by treating the shock as an instantaneous acceleration. In Eq. (3) $A_{\text{after}} = (\rho_1 - \rho_2) / (\rho_1 + \rho_2)$ and the compression factor is $\eta_{\text{after}} / \eta_0 = 1 - \Delta v / W_i$.

Therefore, we should expect freeze-out not when $A_{\text{before}} = 0$ (incompressible result), but when $A_{\text{after}} = 0$, according to Richtmyer's prescription. This is easy to achieve if fluid A is highly compressible (following Richtmyer we are considering cases where $\rho_A < \rho_B$): a highly compressible low density fluid can be shocked to a density equal to or greater than the density of a less compressible fluid even though the latter is initially more dense. Referring to Fig. 1, one can start with $\rho_A < \rho_B$ yet achieve $\rho_1 = \rho_2$ (freeze-out) or even $\rho_2 > \rho_1$ (Atwood number reversal) provided that fluid A is much more compressible than B.

An example with $\gamma_A=1.1$ and $\gamma_B=5/3$ is shown in Fig. 2 where we plot A_{after} and the compression factor as functions of ϵ for various initial Atwood numbers: $A_{\text{before}}=0.0, 0.25, 0.5, 0.75,$ and 0.95 . Here ϵ is a measure of shock strength,

$$\epsilon = 1 - \frac{p_0}{p_3},$$

related to the Mach number of the shock via

$$M_s = \sqrt{1 + \frac{\gamma_A + 1}{2\gamma_A} \left(\frac{\epsilon}{1-\epsilon}\right)}.$$

Clearly, for $\epsilon \rightarrow 0$ the compression factor $\rightarrow 1$ and $A_{\text{after}} \rightarrow A_{\text{before}}$. As ϵ increases A_{after} decreases because fluid A compresses more than fluid B and A_{after} , in some cases, passes through zero and is indeed negative at higher ϵ . The compression factor is always positive, as seen in Fig. 2b. If we concentrate on the case $A_{\text{before}}=0.5$, we see from Fig. 2a that $A_{\text{after}} \leq 0$ for $\epsilon \geq 0.87$. Therefore according to Richtmyer's prescription, Eq. (3), we should have freeze-out ($\dot{\eta}=0$) at $\epsilon=0.87$, and phase reversal ($\dot{\eta}<0$) at higher ϵ .

Direct numerical simulations, however, do **not** confirm this behaviour. In Figs. 3 and 4 we show the cases $\epsilon=0.87$ and $\epsilon=0.95$ respectively. Clearly, there is no freeze-out in Fig.3 nor phase reversal in Fig. 4. The time scale, microseconds, in these figures follow from setting $\rho_0 = \rho_{\text{atmosphere}}$ and $p_0 = p_{\text{atmosphere}}$, while the dimensions, centimeters, follow those of the CalTech shock-tube.⁴ We should point out, however, that such strong shocks cannot be generated at the CalTech shock-tube.

These and other examples given in ref. 5 show that Richtmyer's prescription fails in certain cases. The cause of this failure is not clear, and we emphasize that it is **not** the strength of the shock. In fact the examples which Richtmyer considered were strong shock problems, and they all agree with his prescription, which we also verified. An example of a weak shock, $\epsilon=0.4$, which does not agree with Richtmyer's prescription is given in ref. 5. For weak shocks his prescription can be written explicitly as

$$A_{\text{effective}} = A_{\text{before}} + \varepsilon F / \gamma_A + \text{terms of order } \varepsilon^2 + \dots \quad (4)$$

where

$$F = 2 \left[1 - R + 2 \frac{R(R-y^2)}{y(R+1)} \right] (R+1)^{-1} (y+1)^{-1}, \quad (5)$$

with the definitions $R \equiv \rho_B / \rho_A$ and $y \equiv (R \gamma_B / \gamma_A)^{1/2}$.

In contrast, we found that an analysis of the RM problem given by Fraley⁶ agreed with our simulations. Richtmyer's prescription and Fraley's analysis both give the correct limit, $A_{\text{effective}} \rightarrow A_{\text{before}}$ as $\varepsilon \rightarrow 0$, i.e., they both reproduce the expected leading term A_{before} in the expansion given in Eq. (4). The next term, however, is different; Fraley's expression for F, after correcting a misprint, is⁶

$$F = \left[(y-1)^2 + 4 \frac{R^2 + y^2}{y(R+1)} - 2R - 2y \right] (R+1)^{-1} (y+1)^{-1} \quad (6)$$

to be compared with Eq. (5).

Two cases naturally come to mind in comparing Eq. (5) with Eq. (6): When $\gamma_A = \gamma_B$, Eq. (5) gives

$$F(\gamma_A = \gamma_B) = -2(\sqrt{R} - 1)/(R+1) \quad (7a)$$

while Eq. (6) gives

$$F(\gamma_A = \gamma_B) = -(\sqrt{R} - 1)/(R+1), \quad (7b)$$

i.e., half of Eq. (7a). One must remember, however, that F is the coefficient of the ε/γ_A term in Eq. (4) for small ε and therefore can be easily masked if the leading term A_{before} is large.

The second case is $A_{\text{before}} = 0$, i.e., $R=1$, for which Eq. (5) gives

$$F(\rho_A = \rho_B) = -1 + \frac{1}{y} \quad (8a)$$

while Eq. (6) gives

$$F(\rho_A = \rho_B) = \left(-1 + \frac{1}{y}\right) \left(1 - \frac{y}{2}\right). \quad (8b)$$

Note that for $y=2$ Eq. (8a) gives -0.5 while Eq. (8b) gives 0 . Since the leading term $A_{\text{before}} = 0$, we conclude that $A_{\text{effective}}$ is negative according to Richtmyer's prescription while it is zero according to Fraley's analysis. Examples of this type are reported in ref. 5 where we did find freeze-out ($\dot{\eta} = 0$) for a case with $A_{\text{before}} = 0$ but $A_{\text{after}} \neq 0$.

In summary, we found a case of freeze-out which, according to Richtmyer's prescription, should not have been there: $\dot{\eta}=0$ while $A_{\text{after}} \neq 0$. Conversely, freeze-out cases expected from Richtmyer's prescription, i.e., $A_{\text{after}}=0$, did not exhibit freeze-out, an example of which is Fig. 3. Nor did the case of Atwood number reversal, Fig. 4, exhibit phase reversal. This lack of correlation between the sign of A_{after} and the sign of $\dot{\eta}$ is, we believe, definite proof that Richtmyer's prescription fails in certain cases. We should add that Fraley's analysis passed these tests, correctly showing where freeze-out should occur and where it should not. Equally if not more important is the fact that Richtmyer's prescription gives an accurate result in many cases, in particular for previous experiments, physical or numerical, starting of course with Richtmyer's own numerical experiments. There are 4 free variables in the RM problem: ρ_A/ρ_B , ε , γ_A and γ_B . Unfortunately we have no simple recipe for finding where in this 4-dimensional space Richtmyer's prescription is guaranteed to work. The combination of high Atwood numbers, weak shocks and high γ 's appears to be a safe bet.

ACKNOWLEDGMENT

This work was performed under the auspices of the U.S. Department of Energy by the Lawrence Livermore National Laboratory under Contract No. W-7405-ENG-48.

REFERENCES

- ¹R. D. Richtmyer, "Taylor instability in shock acceleration of compressible fluids," *Commun. Pure Appl. Math* **13**, 297 (1960).
- ²E. E. Meshkov, "Instability of the interface of two gases accelerated by a shock wave," *Fluid Dynamics* **4**, 101 (1969) (trans. from *Izv. Akad. Nauk SSSR, Mekh. Zhidk. Gaza* **5**, 151 (1969)).
- ³K. O. Mikaelian, "Richtmyer-Meshkov instabilities in stratified fluids," *Phys. Rev. A* **31**, 410 (1985).
- ⁴M. Brouillette, "On the interaction of shock waves with contact surfaces between liquids of different densities," Ph. D. Thesis, California Institute of Technology, 1989; R. Bonazza, "X-ray measurements of shock-induced mixing at an Air/Xenon interface," Ph. D. Thesis, California Institute of Technology, 1992.
- ⁵K. O. Mikaelian, "Freeze-out and the effect of compressibility in the Richtmyer-Meshkov instability," LLNL report UCRL-JC-112495 (January 1993).
- ⁶G. Fraley, "Rayleigh-Taylor stability for a normal shock wave-density discontinuity interaction," *Phys. Fluids* **29**, 376 (1986).

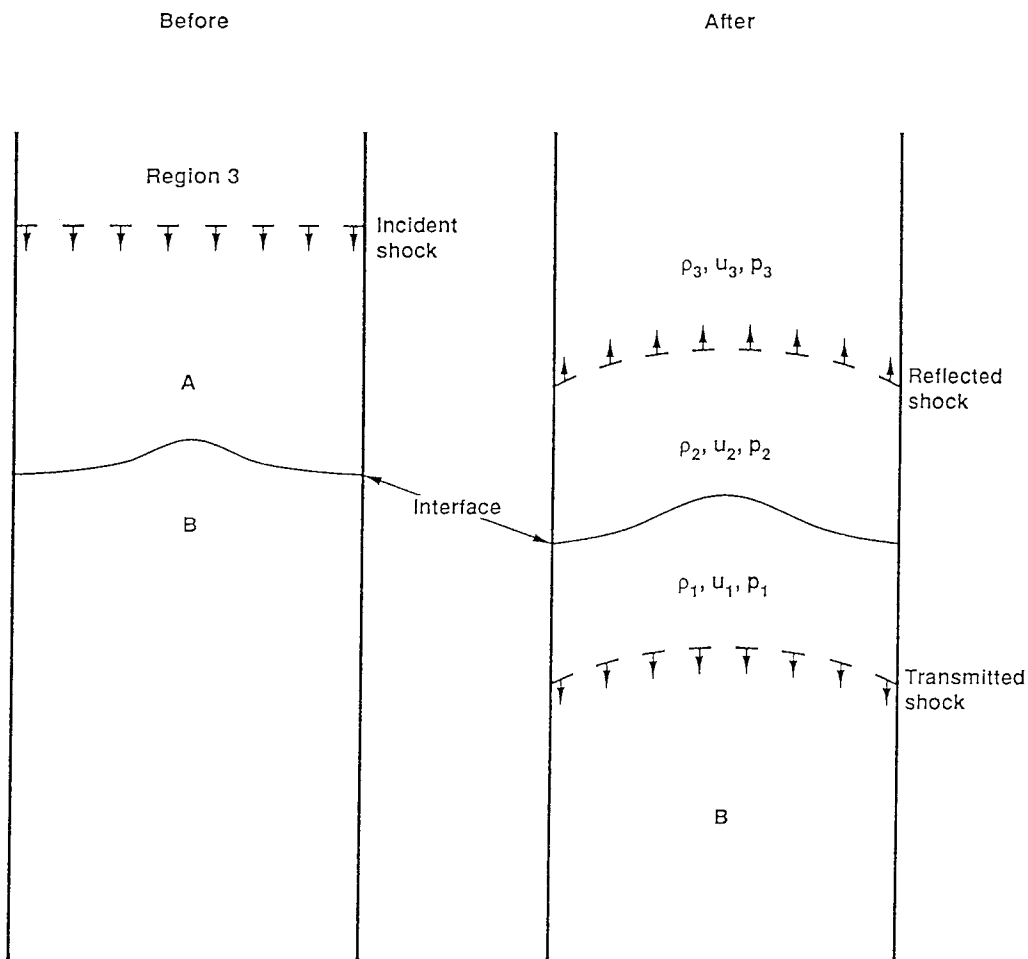


Fig. 1

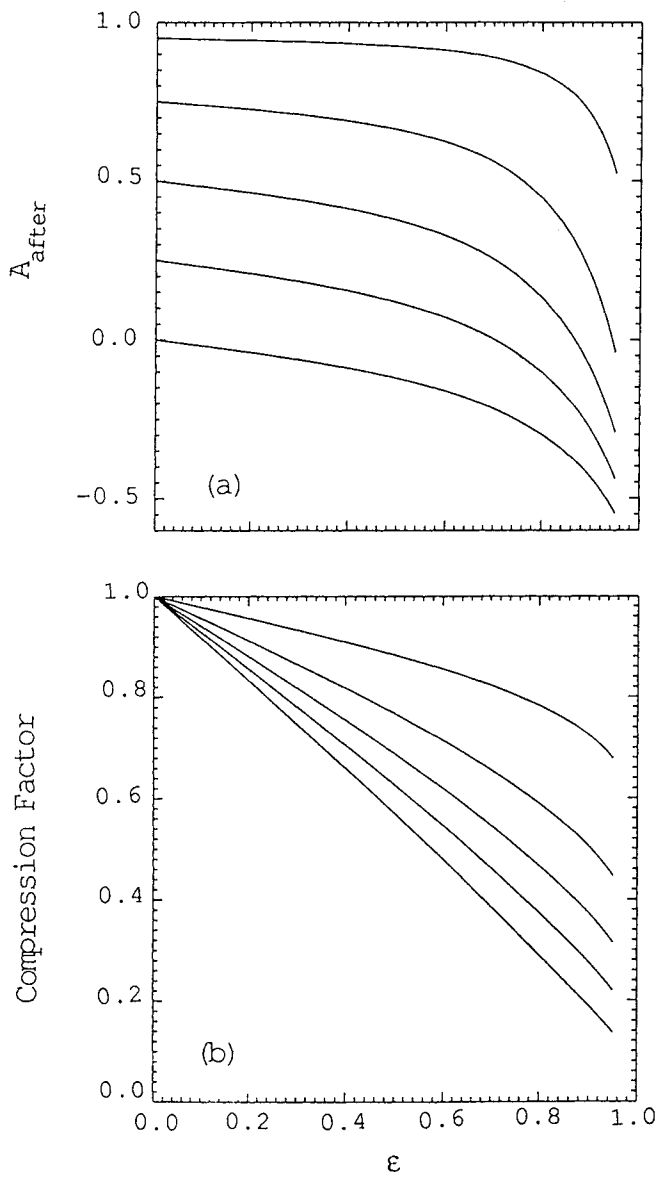


Fig. 2

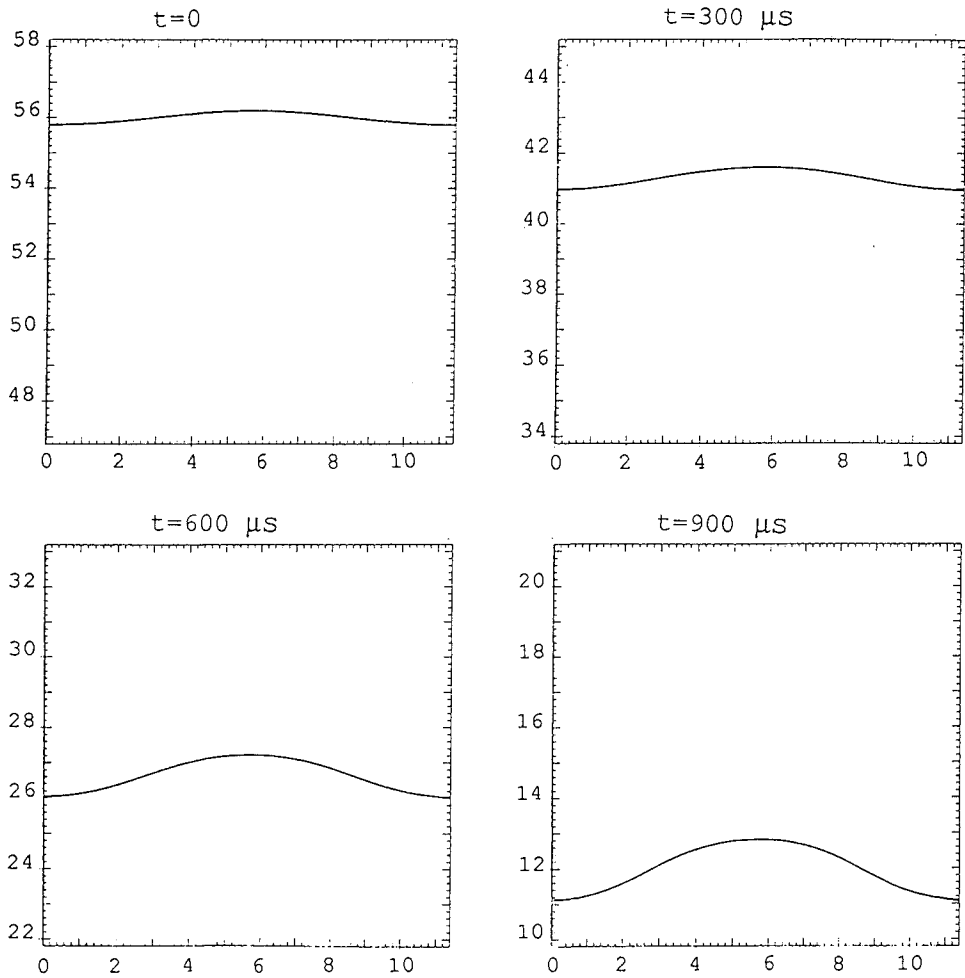


Fig. 3

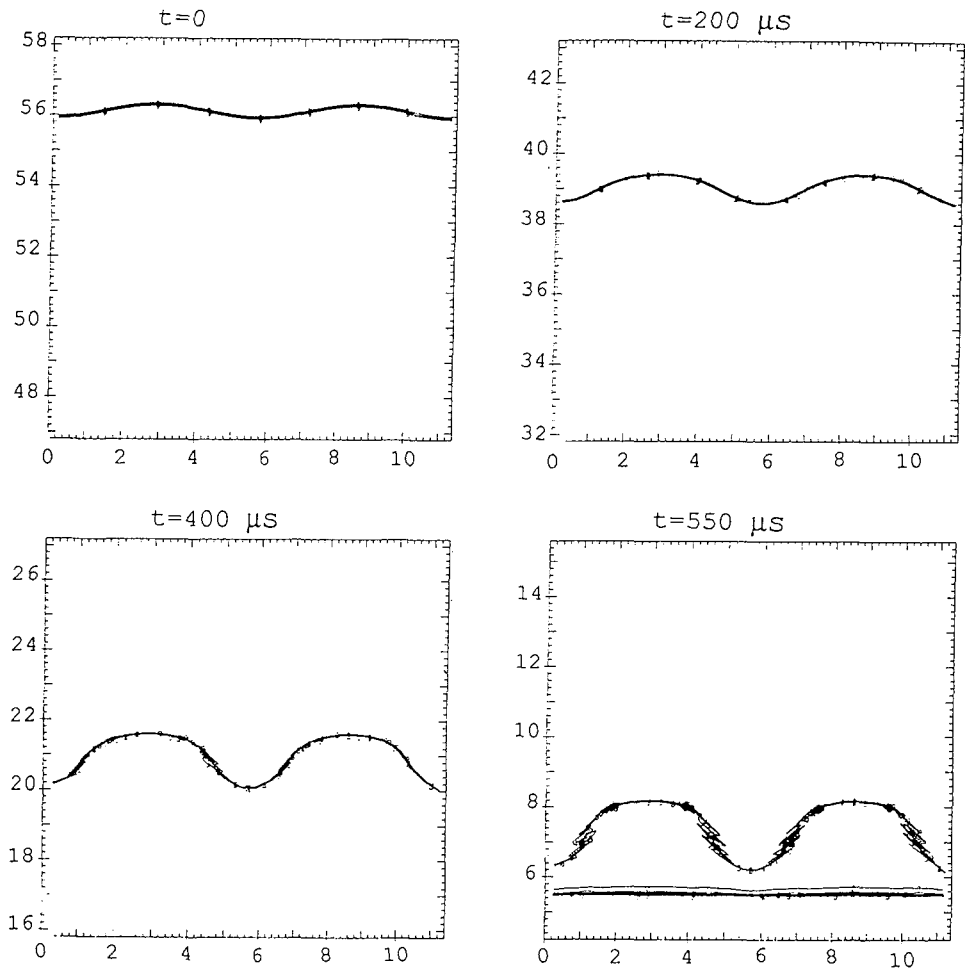


Fig. 4

Non-Linear Stage in Development of Perturbations of Interfaces between Liquids under Joint Action of Impulsive and Constant Accelerations.

V.YE. Neuvazhayev, I.E. Parshukov
Institute of Technical Physics, Chelyabinsk-70, Russia

To study two-dimensional flows of ideal incompressible liquids in [1,2] one can find method based on the consideration of liquid interface by vortex sheet. The method is modified [3] by means of integrands smoothing in the equations of motion with the help of "vortex blobs" permitting to determine characteristics of the interface development at the stage of rollup. The study was made of a behaviour of liquid interface in stationary gravitational field (Rayleigh-Taylor instability [1,3], surface waves [2] and so on). Method application for the case of impulsive gravitational field which approximately corresponds to shock wave passing through interface (Richtmyer-Meshkov instability) is substantiated and shown in [4].

The first part gives the study of liquid interface behaviour under the joint action of impulsive and constant accelerations. The second part gives consideration of a question on technique applicability to real gas-dynamic flows description and gives comparison of calculated and experimental (obtained by means of shock tubes) results. Meshkov's experiments [7] studying linear and the beginning of non-linear stages of gas interface development at small values of Mach number ($M \sim 1$) of shock wave incident on it are used in our work as test ones. Of interest are experiments of Zaitzev [8] ($M=3.5$) and Vasilenko [9] (where a decelerating wave of unloading with $M \sim 3$ forms the situation of combined effect of R-T and R-M instabilities) following the evolution of interface up to the stage of developed turbulence.

I Joint action of impulsive and constant accelerations.

1. Statement of the problem. Linear approximation. Let's consider a two-dimensional problem on the behaviour of interface between two infinite deep ideal incompressible liquids in gravitational field. Let's introduce rectangular coordinate system (x,y) and assume that straight line $y=0$ is the unperturbed interface and the densities of liquids occupying half-spaces $y < 0$ and $y > 0$ are ρ_1 and ρ_2 , respectively.

Full acceleration effecting the liquids has the following form:

$$\hat{g}(t) = U\delta(t) + g,$$

where $\delta(t)$ - Dirac function, $g = \text{const}$. U - full increment in velocity due to the impulsive acceleration. $g > 0$ corresponds to acceleration effect in the direction opposite to axis y , and $U > 0$ corresponds to the case when shock wave passes from lower half-plane into upper one in the direction of axis y .

At moment $t=0$ the interface has the form $y = a_0 \cos(kx)$. According to linear theory ($ak \ll 1$) interface amplitude growth in the case constant g satisfies the known equation:

$$da^2/dt^2 = -\omega^2 a$$

where $\omega^2 = Agk$, $A = (\rho_1 - \rho_2) / (\rho_1 + \rho_2)$ - Atwood number.

Impulsive acceleration acts at the moment $t=0$ and determines initial nonzero rate of the perturbation amplitude growth. Thus, the initial conditions of the problem are

$$a|_{t=0} = a_0, \quad da/dt|_{t=0} = -kAUa_0.$$

For the case $Ag > 0$ the solution has the following form

$$a(t) = a_0 (\cos(\omega t) - UV\sqrt{Ag/g} \sin(\omega t)),$$

where $\omega = \sqrt{Agk}$, i.e. $a(t)$ amplitude is limited and one can speak that it is a stable case.

When $Ag < 0$

$$a(t) = a_0 (\text{ch}(\omega t) - UV\sqrt{-Ag/g} \text{sh}(\omega t)),$$

where $\omega = \sqrt{-Agk}$, i.e. $a(t)$ grows without limit in time and the interface is instable.

Four situations are possible: 1) $AU < 0$, $Ag > 0$, 2) $AU > 0$, $Ag > 0$, 3) $AU < 0$, $Ag < 0$, 4) $AU > 0$, $Ag < 0$. It is evident that cases 3,4 are instable, because constant acceleration effect only increases the development of the instability that initially appeared due to impulsive acceleration (Vasilenko's experiments [9] correspond to case 4). It remains to consider cases 1 and 2 when constant acceleration effects in stabilizing manner and to clear non-linearity effect on interface development.

2. The results of numerical calculations. At first calculations were made for the cases with fixed values A , U , g and with changing values of initial perturbation amplitude a_0 . Under relatively small values a_0 one observes good agreement of calculated results with linear theory. The increasing of initial amplitude shows that non-linearity effect displays first of all in the distortion of interface sinusoidal profile and in the increasing of its fluctuation period as

compared to linear theory. Fig.1 shows the results of calculation for case $A=0.33$, $U=-1$, $g=0.1$, $a_0=0.5$ (situation 1). It is seen that limitless growth of interface width is absent; in late time moments one observes the beginning of rollup, inherent in the K-H instability.

Considering this case one can speak of interface stability. But decreasing of constant acceleration as compared to impulsive one causes longer period of R-M instability effect with the picture of the interface development becoming more complicated. For fixed values A and a_0 under a certain ratio of U and g vortexwise structure develops before the beginning of first decreasing of interface amplitude under the effect of gravity force (see fig.2 where the case $A=0.33$, $U=-10$, $g=0.1$, $a_0=0.5$ is presented). This makes impossible to describe further the development of the interface by used method, because under surface compression and phase changing the picture of flow is complicated incommensurately due to inevitable obtaining of self-crossing interface; that means the appearance of isolated liquid bubbles and the destruction of perturbation initial structure.

The further increasing of the ratio U and g under fixed A and a_0 leads to the fact, that the beginning of turbulence stage (when the initial notion of interface loses its meaning) takes place earlier than one notes the effect of constant component of acceleration. It is necessary to do further consideration of the problem on the development of turbulent layer the effect of gravitation force for whose study one needs absolutely different models. The technique which was used may give only initial data (layer width and kinetic energy) for a given problem. However, interface stability may be achieved under given ratio A , U , g and k by decreasing of initial perturbation amplitude a_0 that is seen in fig.2a, where one can find additional result of calculation for the case $A=0.33$, $U=-10$, $g=0.1$, $a_0=0.005$.

It is known [9] that for R-T and R-M instabilities non-linear stage of interface development with distinct vortex structures begins under $a/\lambda \sim 1$. If in cases 1 and 2 this condition is fulfilled before constant acceleration has the time to stop the growth of interface width caused by the effect of impulsive acceleration one can speak about the beginning of turbulent stage. Considering linear formula and described above interface behaviour dependences on the initial data one can introduce into consideration dimensionless ratio $a_0 U \sqrt{AK/g} / \lambda$ whose critical value has the magnitude of the order of 1. Under smaller values of this parameter one can speak about interface stability and under greater values gravitation force has not enough

time for distinct display of its stabilizing effect before the beginning of turbulent stage. This is confirmed by our calculations.

For case 2 calculation results show the same regularities as in previous case, the difference lies in the only fact that interface development begins with amplitude decreasing.

II Comparison with experiments.

1. Some notes. In all cases, described below one considers shock wave passage through contact boundary separating two equilibrated gases with different density. The values of shock wave velocity D incident on the interface and velocity U gain caused by it as well as Atwood number value on the interface if they are not known beforehand, are taken from one-dimensional calculation of corresponding problems for ideal polytropic gases. Recall that the basis for this method is the model of ideal incompressible liquids where shock wave is simulated by impulsive acceleration $g(t)$.

The initial perturbation of the interface has the following form $y = a_0 \cos(kx)$. Interface amplitude decreases for the case of shock wave passage from light substance into the heavy is considered by the formula [5]

$$a_0^* = a_0 (1 - U/D)$$

and for the case - from heavy into light [6]

$$a_0^* = a_0 (1 - U/2D).$$

Zero time moment is taken as a moment of final passage of shock wave through the interface. The form of result representation is similar to the used one in [7-9] respectively.

2. Meshkov's experiments. The behaviour of interface between helium and air under Mach numbers $M \sim 1$ of shock wave incident on it is considered ($a_0 = 2$ mm and $\lambda = 40$ mm). For the case of shock wave passage from light substance into heavy flat stationary shock wave incident on the gas interface is characterized by the following values of calculated parameters: $D = 1.25$ mm/mcs, $U = 0.198$ mm/mcs. After shock wave passage through interface the value of Atwood number $A = -0.7767$ is settled. The results of calculation are presented in fig.3a in the form of plot of full (double) interface amplitude versus time. For comparison one can find the results of calculation from [6] and experiment [7]. Experimental results have satisfactory agreement with the calculation by method of vortex blobs (the value of parameter $\delta = 0.1$ was selected as the one providing the best agreement with the

results of other gasdynamic calculations of test problems). It is seen that in the experiment the interface develops a bit slower than in calculation.

The case of shock wave passage from heavy into light is characterized by the following values: $D=0.502$ mm/mcs, $U=0.801$ mm/mcs, $A=+0.802$. The results of calculation are presented in fig.3b. Though this case is more complicated than the previous and the formula allowing for initial interface compression which is used has semi-empirical character nevertheless one observes rather a good agreement of experimental and calculated results.

Thus, Meshkov's experiments studying linear and the beginning of non-linear stage of interface development are satisfactorily described by the technique used by us that confirms once more its feasibility for the problems of such kind.

3. Zaitzev's experiments. The set up and the results of experiments are described in [8]. Argon and xenon were taken as operating gases. Initial interface perturbation amplitude was $a_0=5$ mm. Shock wave with $M=3.5$ passes from argon to xenon, i.e. from light into heavy and is characterized by the following values: $D=1.273$ mm/mcs, $U=0.764$ mm/mcs. After shock wave passage through interface the value of Atwood number $A=-0.45$ is settled.

Fig.4a shows the plots of gases penetration into each other versus time for the case with $\lambda=36$ mm, and fig.4b shows the position of interface at some time moments (method of vortex blobs with $\delta=0.1$ was used). The method gives on the whole correct qualitative picture of interface evolution, but there is quantitative discrepancy with experimental results. Unlike the results of Meshkov's experiments calculation here the interface in the experiment grows much quicker than in the calculation. The reasons of such discrepancy are not quite clear and this question needs refinement.

4. Vasilenko's experiments. The set up and results of experiments are described in [9]. In gases there was a propagation of decelerating shock wave with $M\sim 3$ passing from crypton into helium (from heavy into light). At the interface the wave of unloading creates approximately constant acceleration determining flow deceleration, i.e. it is the case of joint action of impulsive and constant accelerations. Parameters had the following values [9]: $D=0.8114$ mm/mcs, $U=0.94$ mm/mcs, $g=-10^{-3}$ mm/mcs², $A=0.8644$.

The calculation of the case with $a_0=1$ mm and $\lambda=50$ mm is given in fig.5 as compared with linear theory and experimental results. Or

the similar plot in [9] the growth of interface amplitude is shown up to the moment 150 mcs though in the experiments one observes the development of flow up to turbulent stage. Averaged values of interface amplitude for later time moments and unpublished results of calculation for this experiment by gas dynamic technique TIGR [10] were given to us by Vasilenko and Kuz'min and also shown in the figure.

Satisfactory agreement of experimental and calculation results on non-linear stage is observed (up to the moment 150 mcs), therewith the interface in the experiment is developed a bit slower than in the calculation by nonviscous technique but a bit quicker than in the case of vortex blobs usage. The further discrepancy of experimental and calculation results needs additional study and refinement. Let's note that our results on the whole have good quantitative agreement with the results obtained by the technique considering gas compressibility and are closer to experimental data that is an argument in favour of confirming the possibility to use our method to calculate such problems as well (with $M \sim 3$).

Conclusions

On the base of numerical investigation of liquid interface behaviour under joint action of impulsive and constant accelerations for non-linear case at $Ag > 0$ it is possible to state that the deduction of linear theory on the determining influence of constant acceleration component on interface stability is true only in a certain range of initial data change (over limited interval of parameter $a_0 U V (AR/g) / \lambda$ change). Non-linearity influence reveals here in sufficient distortion of initially sinusoidal profile of interface and gradually increasing of its oscillation period as compared to linear theory. Going beyond said interval leads to the fact that transition to the turbulent stage takes place earlier than the effect of constant acceleration becomes distinct.

Vortex method permits to retrace linear and non-linear stages of one-mode interface development after single flat shock wave passage through it in the case of compressible gases. For R-M instability at small Mach numbers (Meshkov's experiments) satisfactory agreement was obtained with the experiment results and other two-dimensional calculations.

For great Mach numbers ($M \sim 3$) at linear and non-linear stages of interface development calculation results agree with the results of

Vasilenko's and Zaitzev's experiments. Some quantitative discrepancy of experimental and calculation results for non-linear stage needs further study.

References

1. Baker G.R., Meiron D.I., Orszag S.A. Vortex simulation of the Rayleigh-Taylor instability // *Phys.Fluids*.- 1980.- v.23.- p.1485-1490.
2. Baker G.R., Meiron D.I., Orszag S.A. Generalized vortex method for free-surface flow problem // *J.Fluid Mech.*- 1982.-v.123.-p.477-501.
3. Kerr R.M. Simulation of Rayleigh-Taylor flows using vortex blobs // *J.Comp.Phys.*- 1988.- v.76,- N.1.- p.48-84.
4. Neuvazhaev V.E., Parshukov I.E. Study of Richtmyer-Meshkov instability by vortex method // *Mathematical Modelling and Applied Mathematics*, A.A.Samarski and M.P.Sapagovas (Editors), IMAGS - 1992.- p.323-335.
5. Richtmyer R.D. Taylor instability in in shock acceleration of compressible fluids // *Commus.Pure and Appl.Math.*- 1960.- v.13,- N.2.- p.297-319.
6. Meyer K.A., Blewett P.J. Numerical investigation of the stability of a shock-accelerated interface between two fluids // *Phys.Fluids*- 1972.- v.15, N.5.- p.753-759.
7. Meshkov E.E. Some results of experimental investigations on gravitational instability of interfaces for media with different density // *Study of hydrodynamic stability by means of computer* // edited by Babenko K.I.- M., 1981, -. 163-190.
8. Alyoshin A.N., Lazareva E.V., Zaitzev S.G. et al. Study of linear, non-linear and transition stages of Richtmyer-Meshkov instability// *Doklady akademii nauk SSSR*, 1990.,-v.310,- N.5.- p.1105-1108.
9. Rozanov V.B., Lebo I.G., Zaitzev S.G. et al. Experimental investigation of gravitational instability and turbulent mixing of stratified flows in acceleration field in the context of inertial thermonuclear fusion // *Preprint N 56- M: FIAN*, 1990.,- p.32-51.
10. Bisyarin A.Yu., Gribov V.M., Zubov A.D. et al. TIGR complex for two-dimensional mathematical physics problems calculation // *Voprosy atomnoi nauki i tekhniki, seriya "techniques and programs of numerical solutions of mathematical physics problems"*- 1984, N.3.(17).,- p. 34-41.

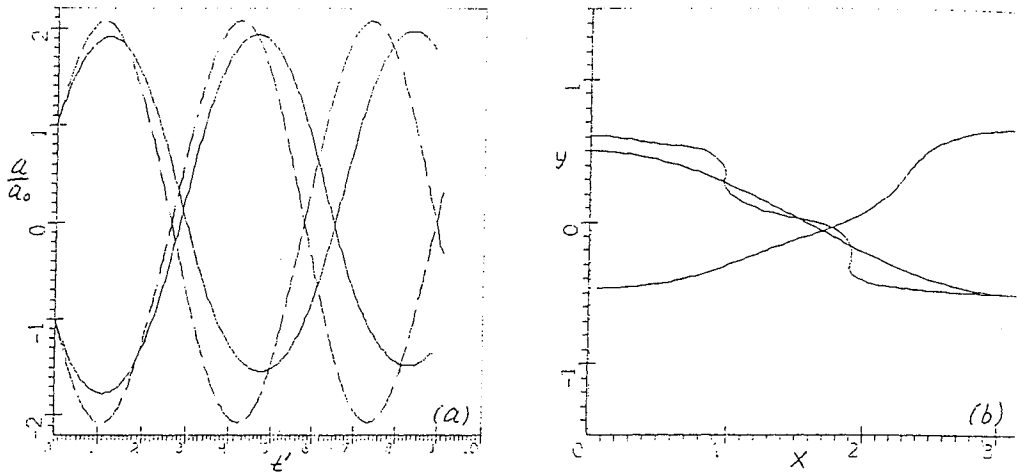


Fig.1 Case $A=0.33$, $U=-1$, $g=0.1$, $a_0=0.5$: (a) the dependence of initial interface position extremum points in coordinates a/a_0 on $t'=\sqrt{(Akg)t}$. - - - linear theory, — calculation with $\delta=0.1$ (b) interface position at the moments $t=0, 20, 40$

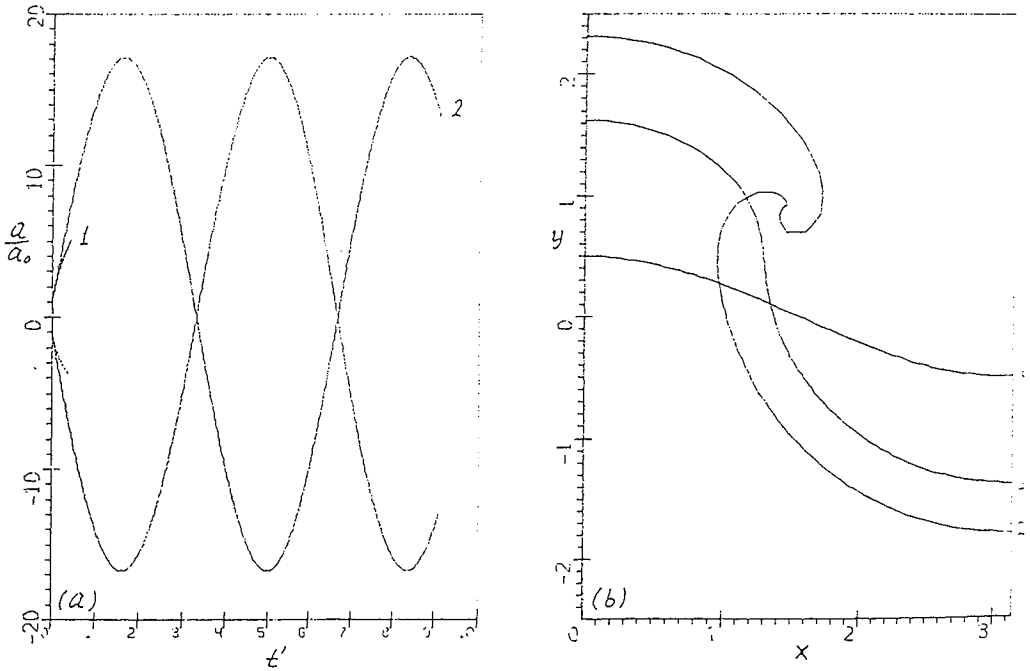


Fig.2 Case $A=0.33$, $U=-10$, $g=0.1$: (a) the dependence of a/a_0 on t' 1 - $a_0=0.5$, 2 - $a_0=0.005$; (b) interface position for the case $a_0=0.5$ at moments $t=0, 1, 2$

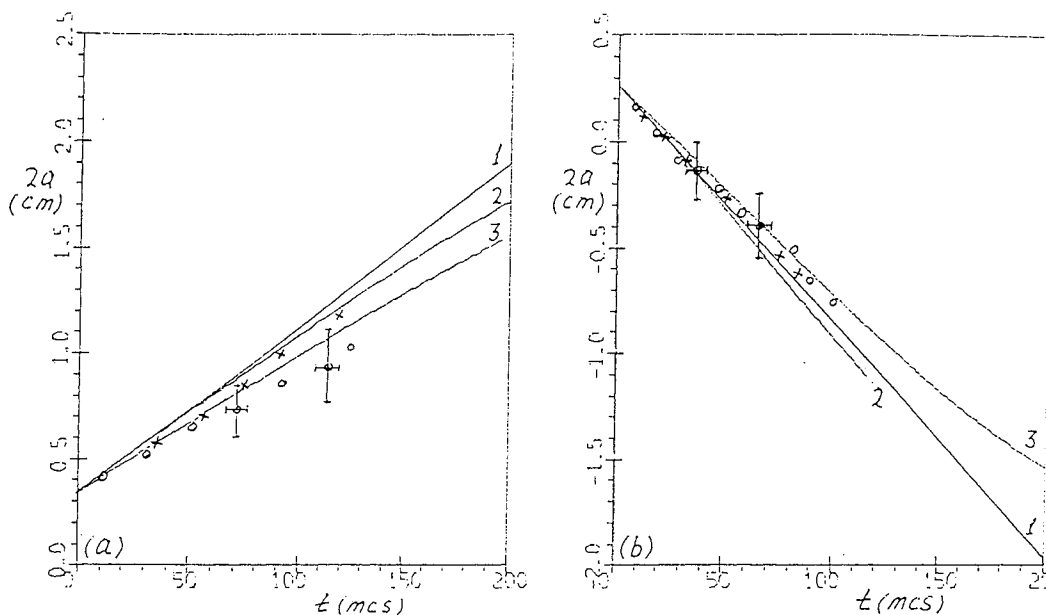


Fig.3 The dependence of interface amplitude on the time for Meshkov's experiments: (a) shock wave passage from light into heavy (b) from heavy into light. 1 - linear theory, 2 - calculation with $\delta=0$, 3 - with $\delta=0.1$, x - results from [6], O - experimental results.

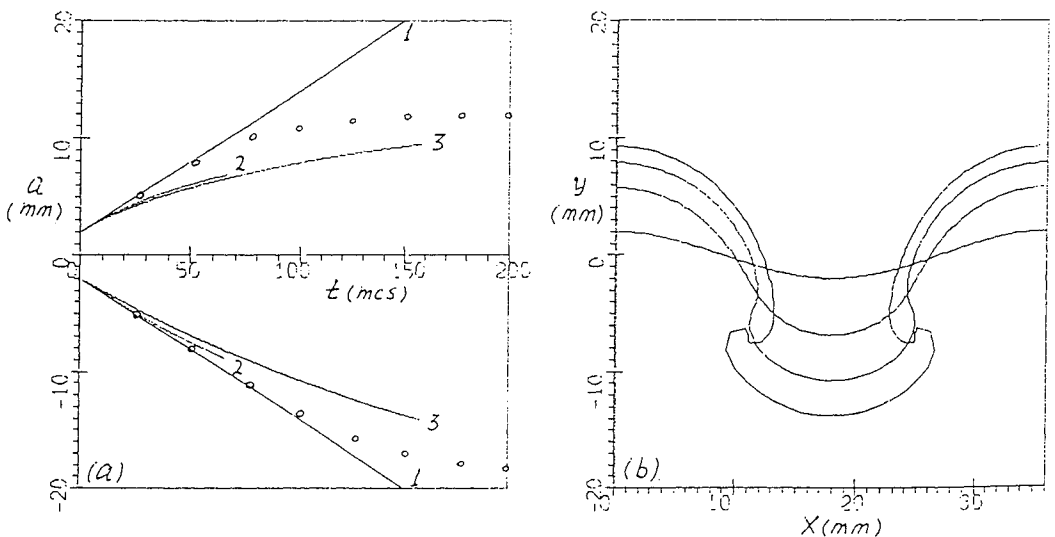


Fig.4 Zaitzev's experiment: (a) the dependence of "spike" and "bubble" coordinates on time. 1 - linear theory, 2 - calculation with $\delta=0$, 3 - calculation with $\delta=0.1$, o - experimental results; (b) position of the interface at the moments $t=0, 50, 100, 150$ mcs.

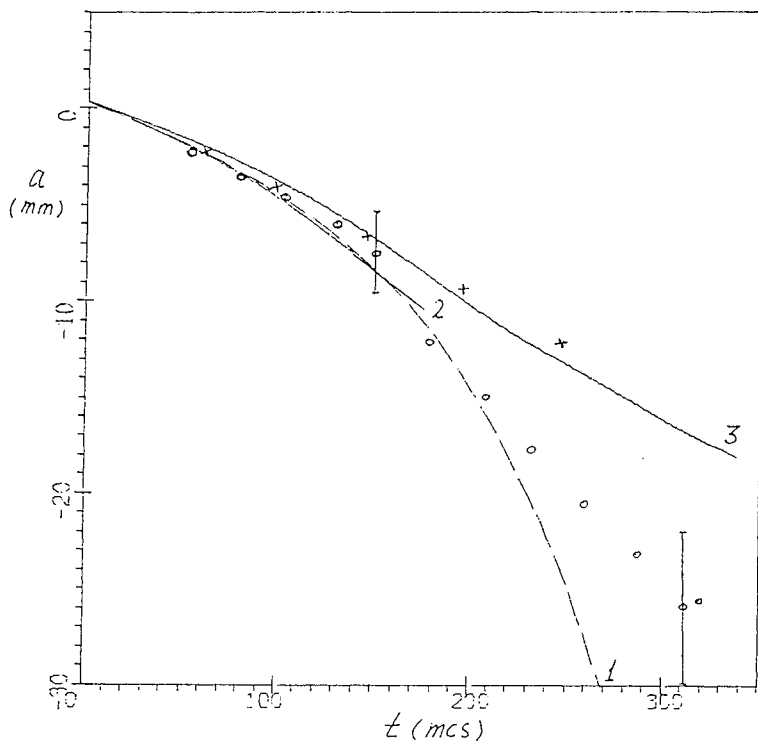


Fig.5 The dependence of interface amplitude on time for Vasilenko's problem ($a_0=1\text{mm}$, $\lambda=50\text{mm}$): 1 - linear theory, 2 - calculation with $\delta=0$, 3 - calculation with $\delta=0.1$, o - experimental results, x - calculation by TIGR.

RICHTMYER-MESHKOV INSTABILITY IN A VERTICAL SHOCK-TUBE

G. Rodriguez, I. Galametz, H. Croso and J.-F. Haas
 Commissariat à l'Energie Atomique, Centre d'études de Vaujours-Moronvilliers
 BP7, 77181 Courtry, France

1. Abstract

We describe shock-tube experiments performed since the Royaumont workshop on Compressible Turbulent Mixing¹ on the behaviour of heavy/light gas interfaces submitted to acceleration by an incident shock wave and decelerations by several shock waves reflected from the tube end wall. The interface, separating two gases of very different density: sulphur hexafluoride (SF₆)-air or xenon-air, is subjected to the Richtmyer-Meshkov instability (RMI) at the passage of the shock waves. The instability is due to vorticity creation by the vector product of local density (interface) and pressure gradients (shocks). This instability leads to the interpenetration of the two gases, and in some cases to turbulent mixing. The initial interface can be either continuous or discontinuous, planar or with large perturbations. Schlieren images of the flow are recorded by a high speed camera and flash X-ray photographs are made in the xenon-air case for density measurements. We compare the experimental results on perturbed interfaces to the linear theory² of the RMI and two-dimensional simulations³ while the results on planar interfaces are used to test turbulent mixing models such as the k- ϵ model⁴ imbedded in one-dimensional codes.

2. Shock tube and interface preparation

In a vertical shock tube (length 380 cm and cross section 8 cm by 8 cm) we create *upward* propagating shock waves (typically Mach number 1.45 in SF₆ or 1.4 in Xe initially at atmospheric pressure). The strength and the velocity of the shock waves are measured with flush mounted piezoelectric transducers on the shock tube side walls. Initially, i.e. prior to the arrival of the incident shock wave, the horizontal interface can be either discontinuous (the gases are separated by a 0.5 μm thick microfilm), or continuous, i.e. the gases have diffused into each other over a few centimeters after the retraction of a separating plate (time between full retraction and shock arrival 0.7 s.). In the experiments described here, the plate is retracted along a direction orthogonal to the optical axis, as in ref.⁵, whereas in ref.¹, it was retracted in parallel to the optical axis. When a pneumatic jack is used to retract the blade in about 2 s. (average speed 4 cm/s, but in fact slower at the beginning and faster at the end), the continuous interface presents small two-dimensional perturbations due to the wake instability, which become visible on a fraction of the shock tube width only after interaction with the first reflected wave. If an electric step motor is used (retraction time 5 s, constant velocity 1.6 cm/s) the diffusion zone remains planar. Discontinuous interfaces can be either planar or bulged due to slightly different pressures on both sides of the membrane, but only the planar case is shown here.

3. Schlieren observations

The observation of air-helium and SF₆-air interfaces has been performed previously^{1,5} with single shot schlieren, i.e. only one high resolution picture is recorded in a shock tube run. As the complete evolution of the interface (and shock) motion was recorded over many runs by varying the firing time of the spark-gap light source, the results suffered from unperfect reproducibility of shock wave strength and initial interface conditions. We now use a high speed motion picture camera (Cordin 350) which records about 200 smaller images in a shot where the interface dynamics is observed for 4 ms.

In the test with *planar* interfaces, the length of the air section between initial interface position and end-plate is 30 cm.

Figures 1a and 1b are schlieren photographs of a planar continuous SF6-air interface (Mach 1.43), respectively before interaction with the first reflected shock and after passage of the second reflected shock. Figure 1c shows a continuous Xe-air interface at a late time (Mach 1.4). Some perturbations on the interface and wall jets below the interface are visible on figures 1b and 1c. The SF6-air mixing zone trajectory appears on figure 1d and thickness for both cases on figure 1e. The thickening rate of the SF6-air interface is small and the Xe-air interface does not thicken at all. One likely reason is that whatever random small scale interface perturbations which may initially exist cannot grow into turbulence, another is that the mixing zone is stretched thinner by entrainment into the boundary layers. This effect is stronger in the Xe-air case possibly because of a different mode of interaction of the reflected shock with the boundary layer with SF6 (polyatomic gas, $\gamma = 1.09$) vs. Xe (monoatomic gas, $\gamma = 1.645$). The same phenomena were observed in the Caltech vertical shock tube in which the shock wave initially propagates downward^{2,6}.

In the case of initially planar discontinuous interfaces, the membrane break-up leads to small scale perturbations ensuring a rapid transition to turbulent mixing. Figures 2a and 2b are schlieren photographs of the discontinuous SF6-air interface (M=1.44) and figure 2c represents the discontinuous Xe-air interface (M=1.38). The trajectory and the width of these approximately planar turbulent layers are compared to the results from the $k-\epsilon$ turbulence model⁴ on figures 2d-e (SF6-air) and 2f (Xe-air). For these preliminary calculations, we choose (as done in ref.¹) the same coefficients in front the terms which model the Rayleigh-Taylor instability as those used to reproduce, with the model, the length of bubble penetration in the heavy fluid ($L_b = 0.06 Agt^2$) in a generic constant acceleration experiment. The initialization of mixing zone thickness and turbulence intensity is chosen in order to obtain approximately the measured thickness just after the first reflected shock. In both cases, the experimental and numerical growth rates agree between first and second reflected shock but seem to diverge after, especially in the xenon-air case, where the experimental mixing zone penetrates further in the air side (fig. 2f).

Figures 3a-c show the instability of a *perturbed* SF6-air continuous interface seen after each reflected shock. The incident Mach number in SF6 is 1.38 and the separating blade is located at a distance $L=15.5$ cm from the shock tube end plate. Its fast retraction to the left by a pneumatic jack created gravity waves occupying at the time of shock wave arrival about 60% of the shock tube width. The initial geometry of these waves is not measured but the dominant wavelength λ after the first reflected shock is 1.55 cm. The measured amplitude on the air (upper) side is shown on figure 3d while figure 3e shows the overall width (interpenetration length) of the mixing zone in the left (perturbed) side as well as the thickness in the right (unperturbed) side.

We compare the measured amplitude (figure 3d) with the linear theory for the RMI of a continuous interface (equation (3) of ref.²) subjected to one incident and several reflected shock waves in order to estimate the initial (peak to zero) amplitude. The growth rate for each phase (between two consecutive shock wave-interface interactions) is:

$$\frac{d\eta}{dt} = k \frac{\eta_i A_i \Delta U_i}{\psi_i} \quad (1)$$

where η_i , A_i , ΔU_i and ψ_i are respectively the amplitude, Atwood number, velocity jump and growth reduction factor after the interaction i and k is the wave number. The growth reduction factor $\psi = f(At, \delta, \lambda)$ is estimated with constant λ (15.5 mm), several values for the thickness δ_i (16.34 mm before incident shock, 11.6 mm measured after incident shock, 7.35, 6.68, 6.35 mm after first, second and third reflected waves) and two values for the Atwood number A_i (-0.69 after incident shock, 0.72 after the first reflected wave) which yields $\psi_0 = 2.76$ after the incident shock wave and $\psi_i = 2.07, 1.92$ and 1.9 after the successive reflected waves. Using (1), we obtain $\eta_0 = 0.063, 0.15, 0.248$ mm from the comparison with the

measured growth rate for each phase (fig. 3d). This dispersion indicates a poor match between linear law and experiment. Note that a shape reversal has taken place between incident and first reflected shocks.

The question arises whether the growth rate after the interaction N should be the sum of the individual growth rates as proposed in equation (3) of ref.²:

$$\frac{d\eta}{dt} = k \sum_{i=0,N} \frac{\eta_i A_i \Delta U_i}{\psi_i} \quad (2)$$

Again, using (2), $\eta_0 = 0.049, 0.065, 0.045$ mm from the comparison with the measured growth rate for each phase. These values, now with less dispersion, appear to be in the same range as those given for SF6-air experiments in tables II and III of ref.² where a top retraction speed of 10 cm/s was mentioned.

A preliminary 2D simulation with the EAD code (as in ref.³) was performed over half the wavelength (computational domain 30 cm in x by 0.775 cm in y) with an initial thickness $\delta_0 = 2$ cm and an initial amplitude $\eta_0 = 0.5$ mm. The continuous diffusion zone was discretized in 5 intermediate layers of 0.4 cm thickness and air concentration 0.15, 0.3, 0.5, 0.7 and 0.85. In the region of interest, the computational cells are square of size 0.025 cm, thus the half wavelength is well resolved (31 cells) but not the amplitude (only 2 cells). Figures 4a, b, c are density maps from the simulation at about the same time as the experimental photographs. The numerical shapes appear much more non-linear than the experimental ones, where the details may have been smoothed out by optical integration of 3D perturbations. Consequently, the numerical amplitudes on air or xenon side are much higher than the experimental ones. However, the overall mixing zone thickness from the simulation (obtained with 5% and 95% thresholds on y averaged concentration profiles), is in good agreement with the measured one (figure 4d). This was achieved with two (respectively ten) times the initial amplitude estimated using (1) (resp. (2)) from the third measured growth rate. Taking in account the facts that the instability has entered the nonlinear phase (with a growth slower than the linear one) and that the numerical growth rate is small due to the coarse mesh size, the comparison seems to favor the application of (1).

4 X-ray measurements

In an ideal 2D flow, the optical density on the schlieren photographic film is proportional to the optical refraction index gradient. In a real flow, the integrated signature across the shock tube width with 3D perturbations and mixing in the boundary layers doesn't allow to recover a mean index, hence density or concentration gradients. In many cases, even the approximate measurement of mixing zone thickness becomes problematic. Thus we are developing two other methods: differential interferometry and flash X-ray photography, both aimed at obtaining a density field in the mixing zone. The first method is in preparation and we describe below the second technique which is being used now on the shock tube.

For the flash X-ray technique, which was pioneered on the Caltech vertical shock tube⁶, one of the gases in the mixing zone must be xenon because of its high absorption coefficient, and the other must be quasi transparent to the soft X-ray photons. Considerable care has been taken in the design of the X-ray source in order to optimize the spectrum (centered at 30 keV) and obtain an irradiation on the test section as uniform as possible. Figure 5a is a sketch of the experimental set-up. The X-ray source is positioned at 1.3 m from the shock tube. The shock tube windows are made of two thin carbon plates stiffened by a steel honeycomb structure. A wedge-shaped calibration cell with carbon windows containing pressurized xenon to create a linear areal density profile is positioned next to the shock tube. We use standart X-ray film (XM type) with scintillation screen (T16 from 3M) and only one image is recorded in a shock tube run. The major length (238 cm) of the shock tube test section is filled with SF6 and the (expensive) xenon occupies the last 27 cm below the interface of interest. As these two gases (initially separated by a 1.5 μ m mylar membrane) have similar acoustic impedances, the transmitted shock Mach number in xenon is 1.4 and waves reflected from the SF6-xenon interface are weak. The shock tube end plate lies 30 cm above the

xenon-air diffusion zone. Tests with cells with known xenon-air mixtures allow to estimate the error in the measurement of xenon partial density at 5%.

In the experiments completed so far, xenon is separated from air by a *planar* diffusion zone (about 2 cm thick). Figure 5b is a 3D plot of optical density recorded at 1.34 ms (after passage of the first reflected wave) showing from top to bottom a high plateau corresponding to air, the diffusion zone, a low plateau corresponding to xenon shocked twice, the curved reflected shock and an intermediate plateau for singly shocked xenon. One also sees the trace of the honeycomb pattern. Figure 5c was obtained at late time (2.74 ms) with two mixing zones: on the top, the air-xenon mixing zone with an air wall jet or vortex, on the bottom, the more perturbed xenon-SF6 mixing zone with an important xenon jet or vortex on the wall. Such large perturbations cannot be induced by the RMI (the densities of xenon and SF6 are similar) but are created by the rupture of the relatively strong mylar membrane.

Except for the edges, the mixing zone appears one-dimensional. Therefore we average the optical density profiles over 2/3 of the shock tube width and by calibration with the profile from the prismatic cell obtain an average profile of partial xenon density from each X-ray film. Figure 6a is a 3D plot of the time evolution of the xenon partial density profiles in the xenon-air mixing zone showing the apparition of the wall jet after the second reflected shock wave. From each profile, we deduce a mixing zone thickness using the 10% (air side) and 90% (xenon side) levels of the difference of xenon partial density (fig. 6b). After the apparition of the wall jet, another (lower) value is obtained from the 10% and 90% levels between air and the local maximum. The first and second values respectively greatly overestimate and slightly underestimate the thickness to be expected in the absence of wall effects.

The evolution of the mixing zone thickness (fig. 6c) indicates that the only significant growth is due to the wall jet or vortex on the xenon side after the bifurcation at the time of the second reflected shock. As in Caltech⁶, where the incident shock went from air to xenon, the mixing zone itself is thinner than observed from schlieren photograph (fig. 1f) and very little growth due to the reflected shocks is observed.

Experiments on discontinuous xenon-air interfaces are now in progress. Preliminary results indicate a thin planar mixing zone at early time and thick, perturbed one at late time.

5 Acknowledgements

We thank G. Delouis, P. Fouquart, G. Fournier, M. Hyvernage, C. Rayer, M-H. Thorembey and J-C. Valleron for their participation in the laboratory and M. Roussel for his help on the simulations.

6 References

1. C. Cavailler et. al., Results from the Vaujours vertical shock tube, proceedings of the 3rd International Workshop on the Physics of Compressible Turbulent Mixing (Royaumont, June 1991), CEA DAM (1992).
2. M. Brouillette and B. Sturtevant, Richtmyer-Meshkov instability at a continuous interface, 17th ISSWST (Bethlehem, 1989), YW Kim ed., AIP conference proceedings 208, New-York (1990).
3. R. Benjamin, D. Besnard and J-F. Haas, Richtmyer-Meshkov instability of shocked-gaseous interfaces, in Shock Waves, proceedings of the 18th ISSWST (Sendai, 1991), K. Takayama ed., Springer Verlag (1992).
4. M. Bonnet and S. Gauthier, A k-ε model for turbulent mixing in shock-tube flows induced by Rayleigh-Taylor instability, Phys. Fluids A2(9), September 90.
5. C. Cavailler et. al., A new vertical shock-tube built for Rayleigh-Taylor instability measurements, 17th ISSWST (Bethlehem, 1989), YW Kim ed., AIP conference proceedings 208, New-York (1990).
6. R. Bonazza and B. Sturtevant, X-ray densitometry of shock-excited Richtmyer-Meshkov instability at an air-xenon interface, in Shock Waves, proceedings of the 18th ISSWST (Sendai, 1991), K. Takayama ed., Springer Verlag (1992).

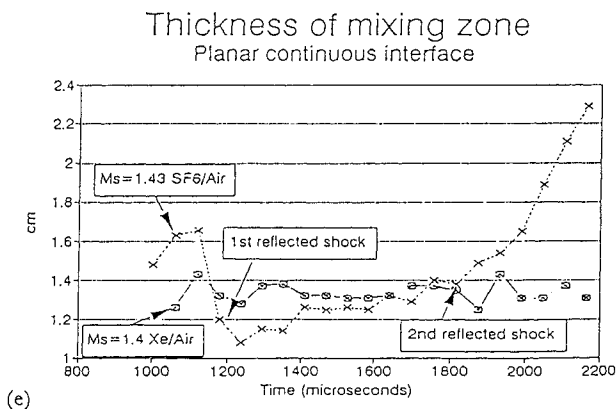
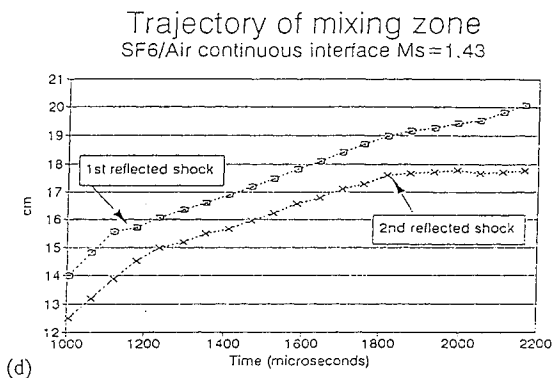
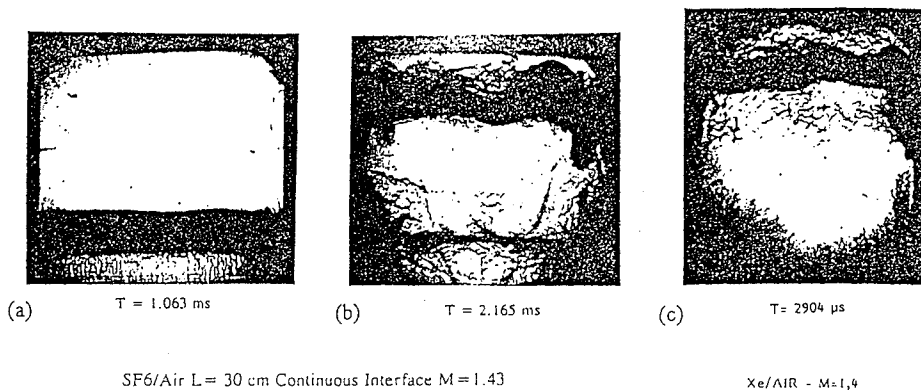
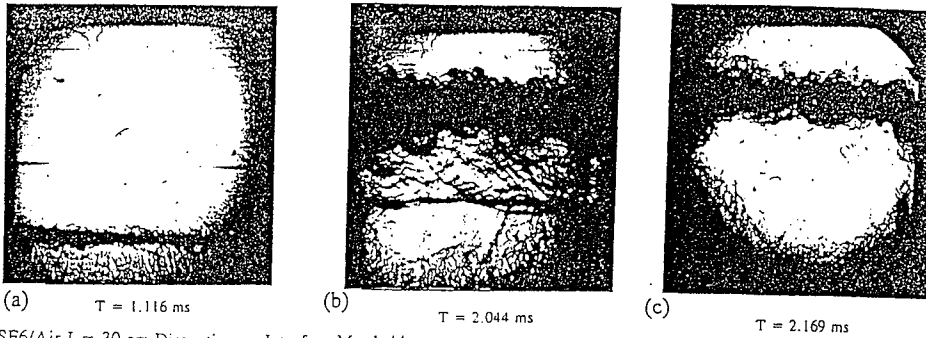


Figure 1: Planar continuous interfaces : (a, b) Schlieren photographs SF6-air, (c) Schlieren photograph Xe-air, (d) SF6-air mixing zone trajectory, (e) mixing zone thickness



SF6/Air L = 30 cm Discontinuous Interface M = 1.44

Xe/Air L = 30 cm Discontinuous Interface M = 1.385

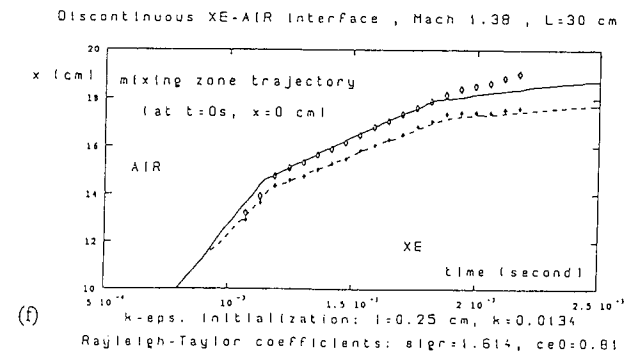
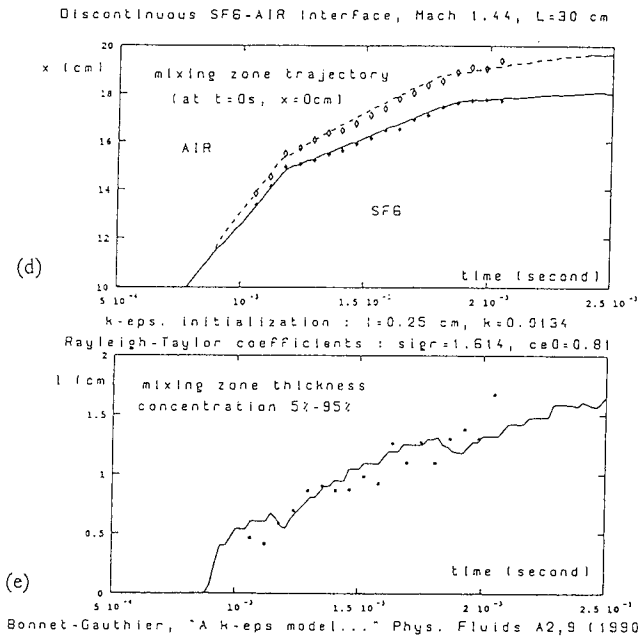
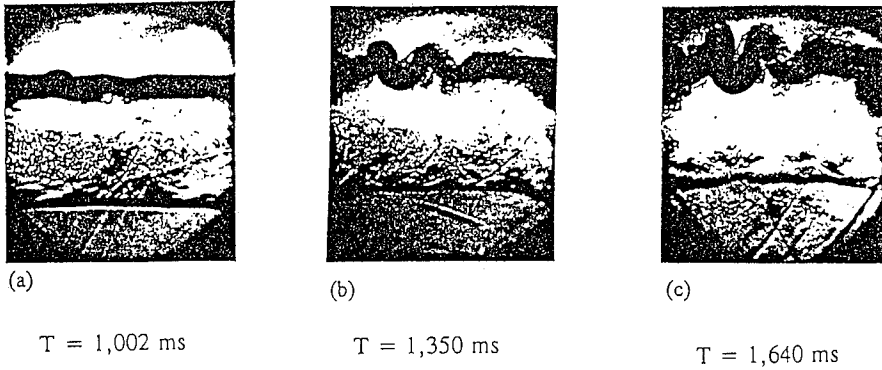
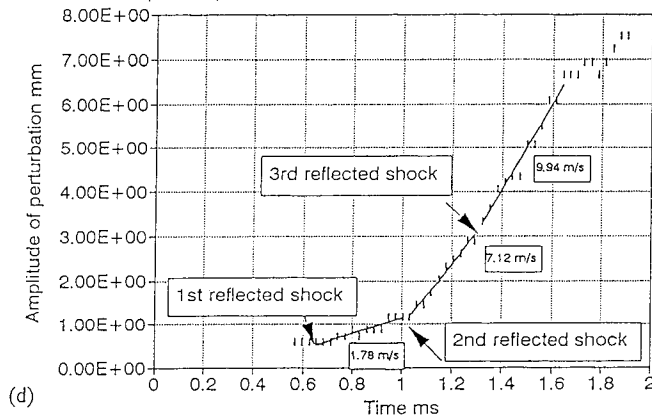


Figure 2: Planar discontinuous interfaces : (a, b) Schlieren photographs SF6-air, (c) Schlieren photograph Xe-air, (d, e) SF6-air mixing zone trajectory and thickness, (f) Xe-air trajectory



Amplitude of perturbation vs time

SF6/Air $Ms=1.38$ $L=15.5$ cm



Thickness of interface vs time

SF6/Air $Ms=1.38$ $L=15.5$ cm

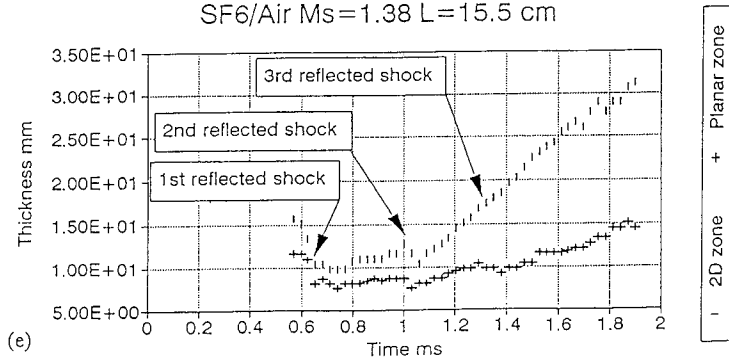


Figure 3: Perturbed continuous interfaces SF6-air: (a, b, c) Schlieren photographs, (d) perturbation amplitude air-side, (e) mixing zone thickness in the perturbed and unperturbed regions.

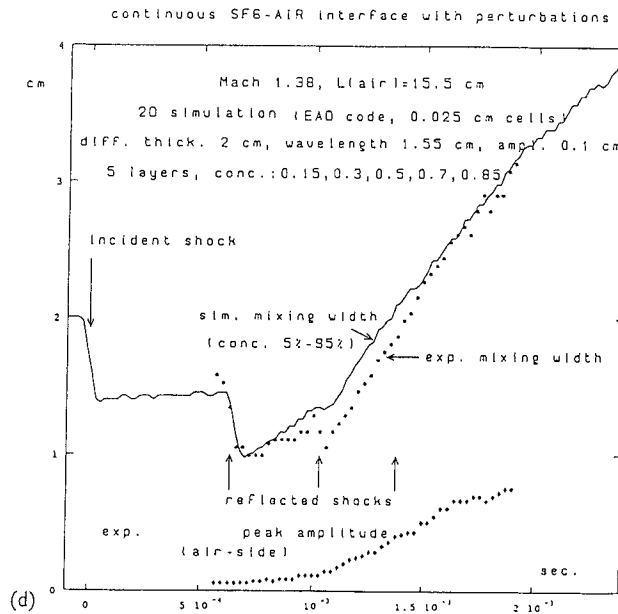
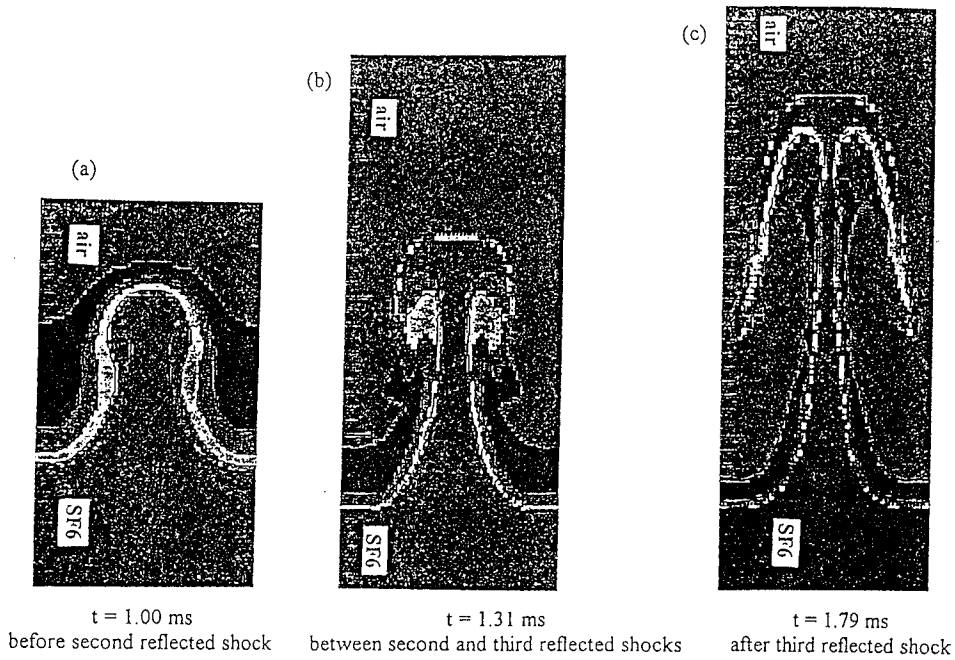


Figure 4: Simulation of single wave continuous interface: (a, b, c) density maps, (d) comparison of the numerical and experimental mixing zone thicknesses.

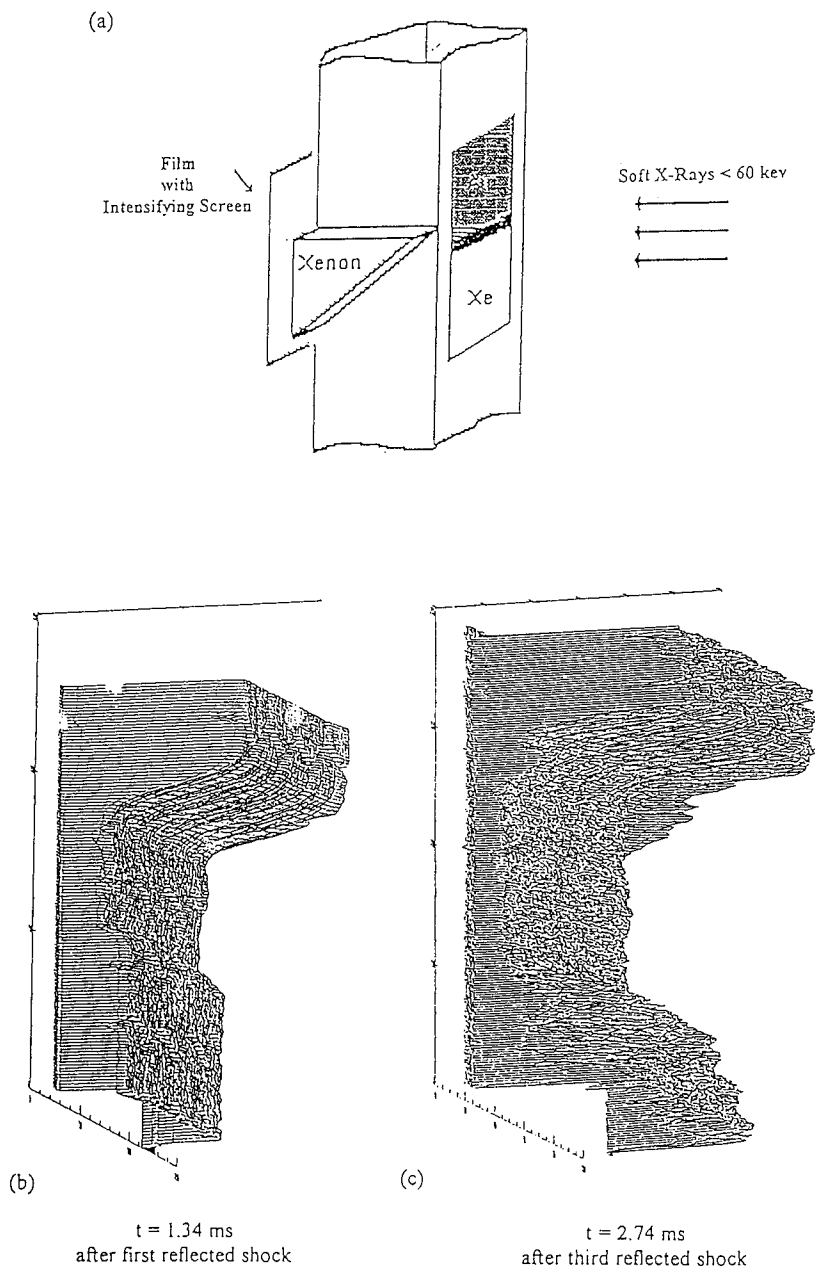


Figure 5: X-ray measurements: (a) experimental set-up, (b, c) 3D optical density plot at early and late time.

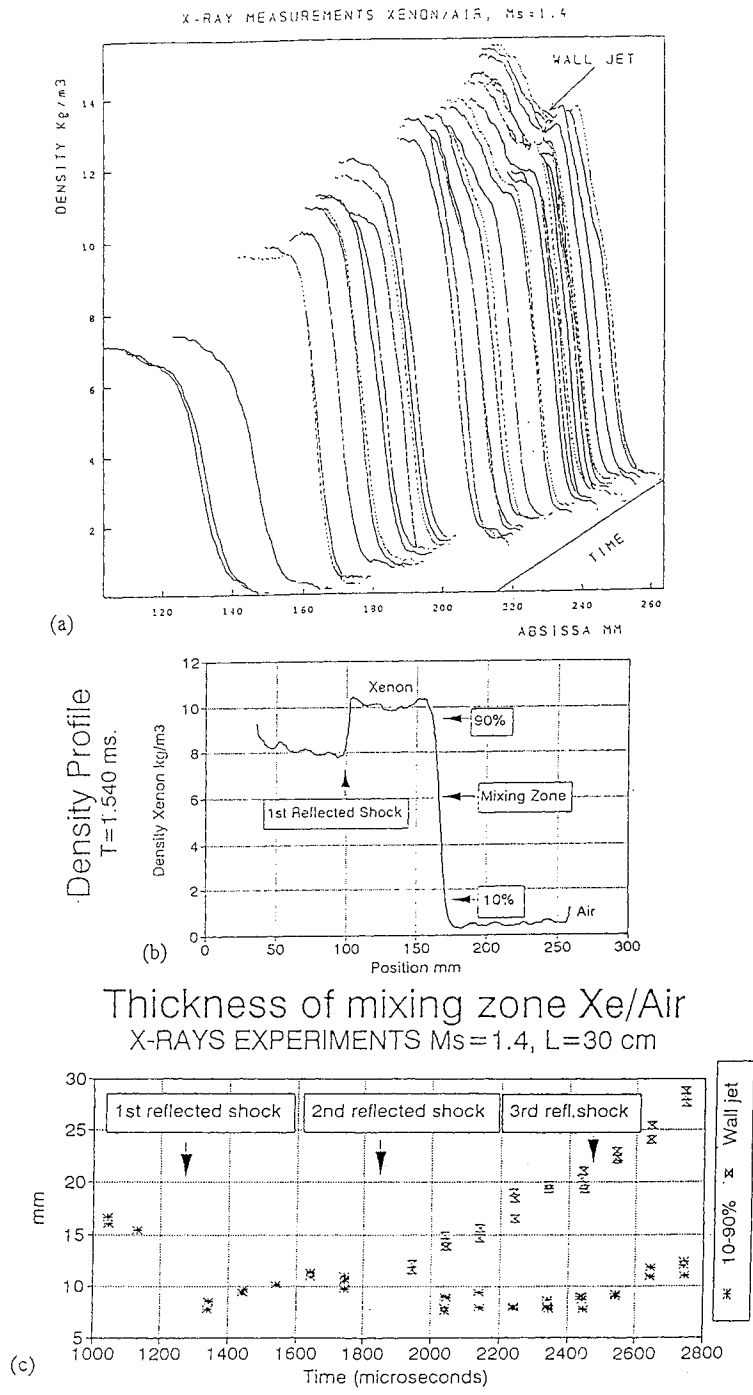


Figure 6: X-ray measurements: (a) time evolution of Xe partial density profile, (b) mixing zone thickness definition, (c) time evolution of mixing zone thickness.

Multidirectional laser technique for Richtmyer-Meshkov mixing experiments

A. Touat, I. Chemouni, G. Jourdan, L. Labracherie and L. Houas
 Université de Provence - Lab. IUSTI - CNRS ura 1168 - Dept. MHEQ
 Faculté Saint Jérôme 13397 Marseille cedex 20 - France

Introduction

Most of experimental works carried out in the framework of the Richtmyer-Meshkov instability give only qualitative informations of turbulent mixing zones. To determine thermodynamic parameters within a mixing, new techniques are presently undertaken in low Mach number shock tube experiments, such as X-ray densitometry (Bonazza¹ et al. and Rodriguez² et al.). In the present high Mach number experimental study, a multidirectional laser absorption technique (Wang³, 1976) is developed for a simultaneous determination of temperature and concentration in a Richtmyer-Meshkov gaseous mixing zone. The birth and growth of such a mixing is originated from the shock wave acceleration of a plane interface which initially separates two gases of different densities. Previous measurements have been done (Houas⁴ et al., 1987), and temperature and concentration have been determined within a CO₂/Ar mixing zone. But these thermodynamic parameter profiles were integrated through the mixing zone, along a thin cylinder which represents, in fact, the laser beam across the test section, and therefore provide averaged temperature and concentration within the mixing zone. We have previously determined average thickness by a strioscopic Schlieren method (Houas⁵ et al., 1991), but this way gives qualitative results, which are not sufficient to describe the evolution of the physical phenomena. Using the multidirectional absorption method, we give in this paper the two dimensional shape of the mixing zone before its interaction with the reflected shock.

1. Experimental apparatus and procedure

Experiments are performed in a double diaphragm shock tube. The test chamber is about 8.5 cm by 8.5 cm cross section and about 9m total length. The test section length is variable from 135 to 160 cm long. This allows to separate much better the film from the interface, which provides an easier analysis of the signals. The two test gases are CO₂, because of its spectroscopic properties, and argon because it presents no infrared absorption in the domain of our experiments. They are initially separated by a thin plastic membrane (1.5 μm thickness). Calibration tests are presently done for determining suitable conditions. As the mixing zone is nonhomogeneous, we have divided the test chamber cross section into 9 regions where, in each one, we suppose the mixing to be homogeneous (see Figure 1). Then, absorption coefficients α_{0i} ($i=1, 2$) of two characteristic vibrational-rotational lines of the CO₂ bending mode will be determined from absorption signals measured using a continuous wave CO₂ laser as a diagnostic probe. Temperature and concentration within each region of

the mixing zone are calculated from a couple of measurements by solving each of the 9 systems

$$\begin{cases} \alpha_{01} = \alpha_{01}(\rho, T, v_1) \\ \alpha_{02} = \alpha_{02}(\rho, T, v_2) \end{cases}$$

for a known line profile. The measurements must be solved in a definite order. For example, in the arrangement, regions (1,1), (1,3), (3,1) and (3,3) can be solved independently, but the other zones (2,3), (1,2), (2,1), (3,2) than (2,2) may only be solved after. For this, a theoretical model of the CO₂ absorption coefficient, taking into account both a collisional profile and the hot bands of CO₂ has been developed. Figure 2 shows the different configurations. In the first configuration the laser beam was directed across the (1,1) and (3,3) corners with the help of ZnSe mirror and ZnSe 50/50 beam splitter at 135 degrees, so this configuration permits exploitation of the (1,1) and (3,3) zones. The principle is the same for 2nd, 3rd, and 4th configurations, but the 5th configuration permits to exploit the (2,2) zone and to examine the validity of the method because, in this configuration, we determine the absorbed energy signals of the same zone through two different optical ways.

2. Preliminary results

The initial conditions of the experiments presented in this work are :

Couple of test gas : CO₂/Ar, Mach number about 5, turbulent mixing velocity : 1100m/s, initial pressure : P(CO₂)=P(Ar)=2000 Pa; thickness of the membrane : 1.5 μm; temperature of CO₂ : 1000 K, temperature of Ar : 2400 K, density of CO₂ : 0.3 Kg/m³, and the measurement abscissa at 54 cm from the initial interface position.

We can see in figure 3 unprocessed signals, simultaneously recorded from two beams crossing opposite corners (configuration 2). The mixing zone is the drop at 1.05 ms (clean signal). The negative peak of the noisy signal is due to membrane fragments, which makes the mixing zone not measurable. The rise at 1.37 ms is due to the arrival of helium driver gas, therefore this figure shows the membrane influence on the measurement. Figure 4 gives information on the important wall boundary layers (Mach about 5). The clean signal is from the beam through center (configuration 5, far from walls), and the perturbed signal from the beam near the wall (configuration 3). Recorded signal amplitude depends on laser frequency used, as the CO₂ molecule absorption depends on quantical transitions. In our experimental conditions, absorbed energy is important when we select rotational lines near P30 and R30⁶. Figure 5 shows absorbed energy recorded signals for two different rotational lines (thick line P20, thin line P18) we can note easily the importance of the rotational line choice. In figure 6 we summarize the preliminary results from a small number of experiments obtained by averaging 5 measurements in the center and 2 in the corners, we can note that the mixing zone is thinner in the center than near the walls and corners. This is because measurements in the corners take into account wall macroscopic vorticies at the end the mixing zone. Thus,

we can say that the effective thickness of the mixing zone is better recorded in the center of the mixing, because we are far from wall effects.

3. Discussion on the work in progress

We have found that this technique requires particular conditions : The incident shock Mach number in CO₂ has to be about 4 in order to reduce wall effects, so we can obtain a "clean" information from the center of the tube. Good mixing test gases are CO₂ and argon (Argon diffuses less than helium through the 0.5 μm membrane), to prevent membrane particles disturbance of the mixing zone during the measurement (absorption and/or deviation of the laser beam), the initial pressure has to be in the range of 3000 Pa, and the membrane thickness which initially separates the test gases has to be about 0.5 to 1 μm thick, because a thicker membrane introduces more perturbations, and therefore more difficulties in obtaining some information about the mixing.

Aknowledgments

This work is supported by the C.E.A. Centre d'Etudes de Limeil-Valenton on contract N° 1253/S 766 II Y.

References

1. R. Bonazza and B. Sturtevant , X-ray densitometry of shock-excited Richtmyer-Meshkov instability at an air-xenon interface, in Shock Waves, proceedings of the 18th ISSWST(Sendai, 1991), K. Takayama ed., Springer Verlag (1992).
2. G. Rodriguez, I. Galametz, H. Croso and J.F Haas; Richtmyer-Meshkov instability in a vertical shock-tube, proceedings of the 4th IWPCTM, (Cambridge,1993), P. Linden ed.,
3. J. W. Wang (1976), Laser absorption method for simultaneous determination of temperature and species concentrations through a cross section of a radiating flow. Applied Optics, vol 15 No 3.
4. L. Houas, A. Farhat, A.Ramdani, J Fortes, and R Brun, Concentration and temperature profiles in a shocked gaseous interface, proceedings of the 16th ISSTW (Aachen, 1987), H. Grönig Ed.,
5. L. Houas, I. Chemouni, A. Touat and R. Brun, Experimental investigation of Richtmyer-Meshkov induced turbulent mixing over long distances, proceedings of the 3rd International Workshop on the Physics of Compressible Turbulent Mixing(Royaumont,1991), CEA DAM (1992).
6. O.V. Atchakov, N.N. Kundriatsev, S.S Novikov, R.I. Solourim, N.A. Fomin, Diagnostica Neravnovesneir v Moleculiarneir Laserar, Minsk, Nauka I Ternika, (1985).

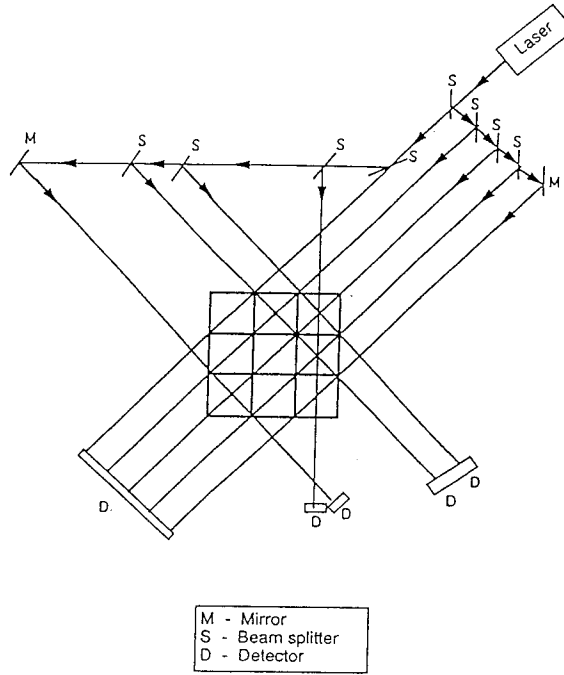


Figure 1 : Sketch of multibeam geometry (from WANG, 1976)

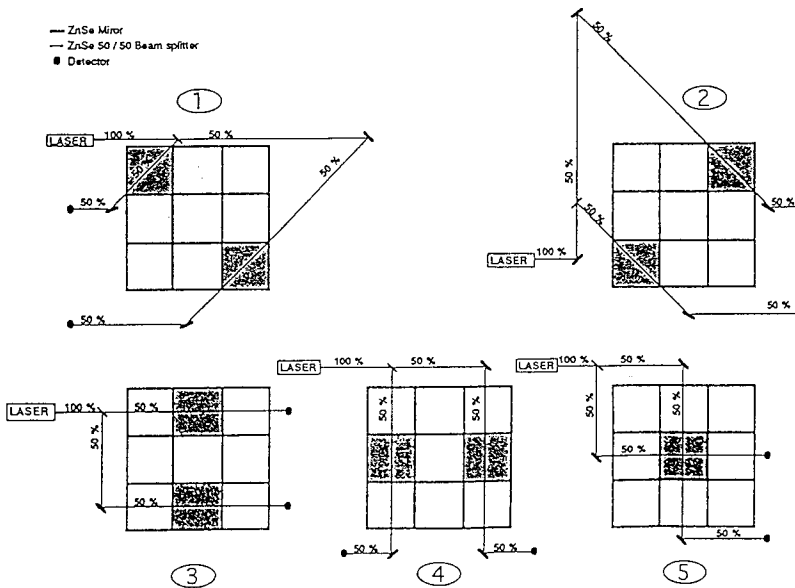


Figure 2 : Cross beam configurations through the shock tube cross section

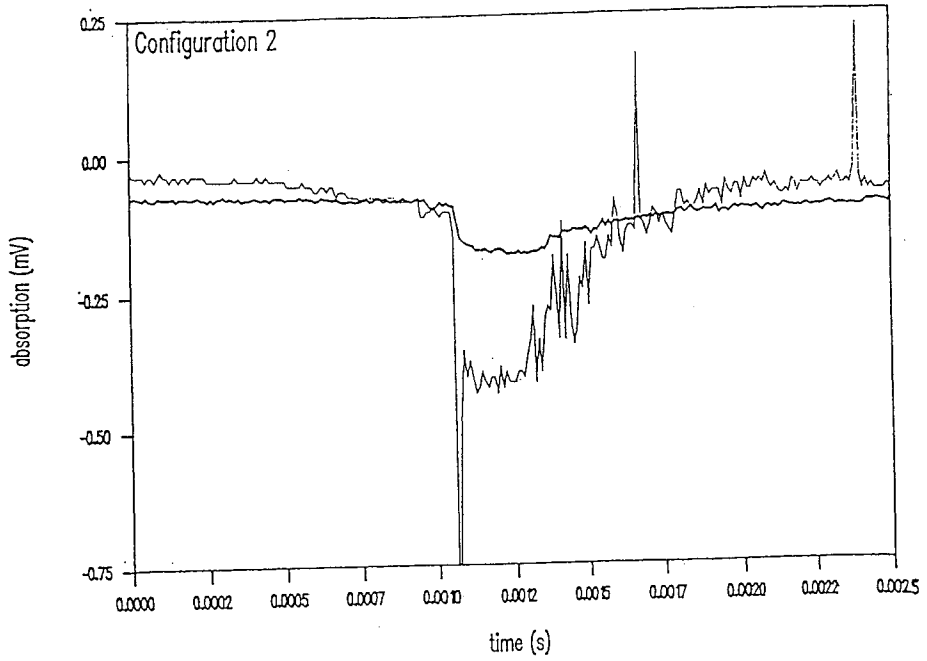


Figure 3 : Unprocessed signals simultaneously recorded from two beams crossing opposite corners

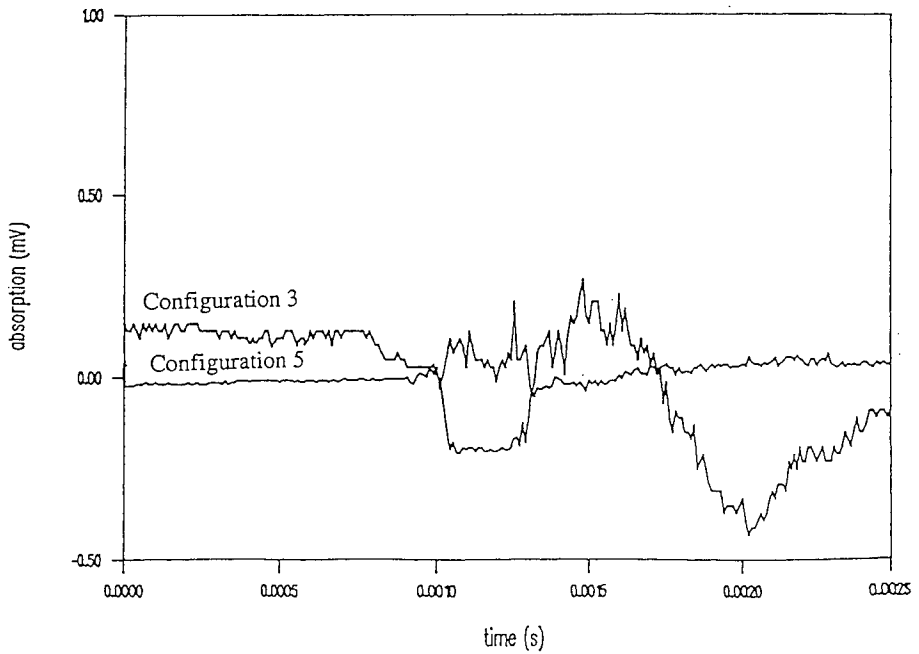


Figure 4 : Comparison of signals from two different configurations

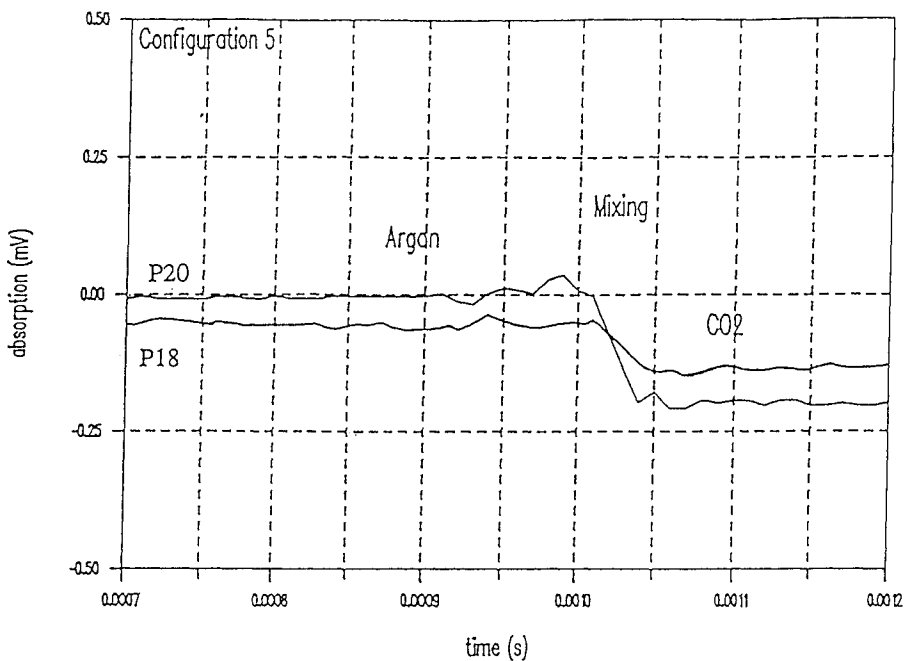


Figure 5 : Unprocessed signals from two beams in configuration 5 recorded with the same detector but with two different rotation lines on different shots (thick line P20, thin line P18). The enlarged time scale shows the mixing zone.

60,1	53,45	48,7
	36,5	
40,1	57,25	57,25

Figure 6 : Averaged thickness in different sectors of the mixing zone (mm)

Vortex deposition and evolution of perturbed 3D Richtmyer-Meshkov environments

Norman J. Zabusky and Ravi Samtaney
 Department of Mechanical and Aerospace Engineering, and CATP Center
 Rutgers University, Piscataway, NJ 08855

Abstract

We present numerical simulations of perturbed 3D Richtmyer-Meshkov environments, including single- and-multiple modes on vertical and inclined planar interfaces. We present analytical expressions (where applicable) for the initial vorticity deposited on the interface based on a generalized shock polar analysis including quantifying the growth rate of the mixing width based on the initial circulation on the interface. We also examine compressibility effects. Numerical simulations were done with a second-order Godunov method with interface tracking on the NCSA CM/5 and the PSC CM/2.

Objective

- To quantify and model the vorticity deposition in 2D and 3D Richtmyer-Meshkov environments.
- To quantify growth rate of a *single mode* in Richtmyer-Meshkov instability from vorticity considerations.
- To quantify the evolution of coherent structures into a preturbulence state.

Previous Work

- R. Samtaney and N.J. Zabusky, "On shock polar analysis and analytical expressions for vorticity deposition in shock-accelerated density-stratified interfaces", Phys. Fluids A 1993 (in press).
- R. Samtaney and N.J. Zabusky (Bull. of APS 1991, 1992).
- X. Yang, I-L. Chern, N.J. Zabusky, R. Samtaney and J.F. Hawley (Phys. Fluids 1992).
- N.J. Zabusky and J.F. Hawley (PRL 1989).
- Richtmyer (Comm. Pure Appl. Math. 1960), Meshkov (NASA Tech. Report 1970).
- J-F. Haas and B. Sturtevant (JFM 1987, Private Comm. 1988).
- K.O. Mikaelian (Phys. Rev. 1985, Physica D 1989).
- L.D. Clutman and M.F. Werner (Phys. Fluids 1992).
- K.A. Meyer and P.J. Blewett (Phys. Fluids 1972).
- L.F. Henderson (JFM 1966, 1989).

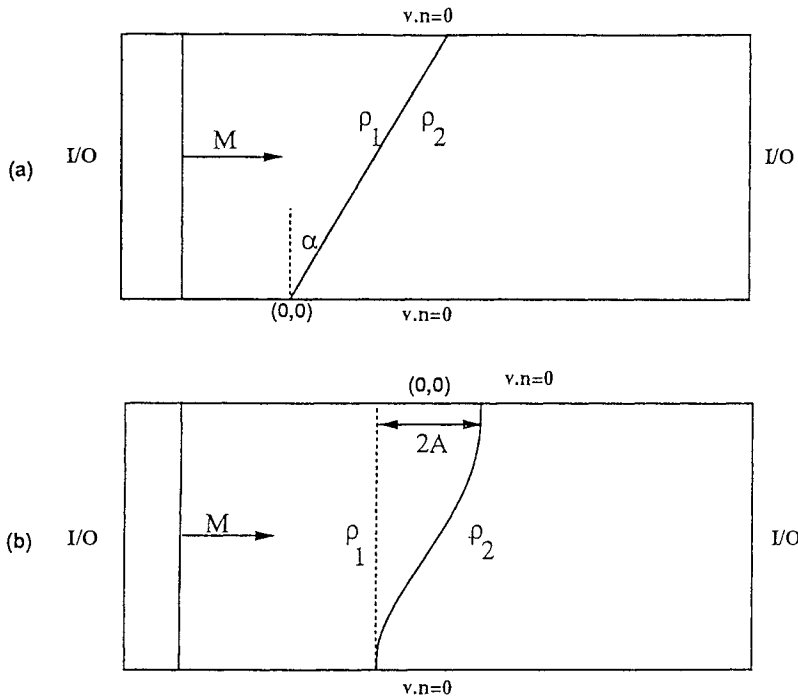


Figure 1: Schematic of physical domain and parameters in shock-interface interactions.

Physical Domain and Parameters

- M : Mach number characterizing the strength of the incident shock.

$\eta = \rho_2 / \rho_1$: Density Ratio.

- Geometry of the interface

$$x = x_0 - A \cos(ky) \cos(kz) \quad (3D), \text{ or } x = x_0 - A \cos(ky) \quad (2D)$$

$$x = x_0 - y \tan \alpha \quad (2D)$$

Assumptions

- Inviscid flow.
- Both gases are perfect with different γ .

Numerical Method

- Second-order Godunov method with pde coupled interface tracking.
- Boundary Conditions: Inflow/Outflow in streamwise direction; Reflecting at top/bottom walls.
- Galilean transformation after t_b .
- Initial conditions:
 - $p = 1.0$ in both gases.

- $\rho = 1.0$ in gas1; $\rho = \eta$ in gas2.
- $\gamma_1 = 1.4$ in air; $\gamma_2 = 1.172, 1.0935$ in R22/SF6.
- Sharp Density Interface interpolated over 2-3 zones.
- Shock initialized 8-10 zones to the left of the interface.
- $\psi(x, t) = \pm 1$ in gas1/gas2 ($\psi(x, t) = 0$ defines the interface).
- Computations performed on PSC CRAY 90, PSC CM2 and NCSA CM5.
- Grid Size: (a) 128x64x64 for 3D runs; (b) 80 zones in y-direction for 2D runs. The grid size was varied in the x-direction depending on the geometry.

Visiometric Methods

- Quantification of circulation deposited on the interface is done when shock traverses the interface completely. The sum is performed where $|\psi(i, j)| < 1$.

$$\hat{\Gamma} = \sum_{i,j} \hat{\omega}(i, j) \Delta x \Delta y \tag{1}$$

Space-time diagrams; Coherent structures (Moments, Elliptical quantification).

Equations of Shock Polar Analysis (SPA)

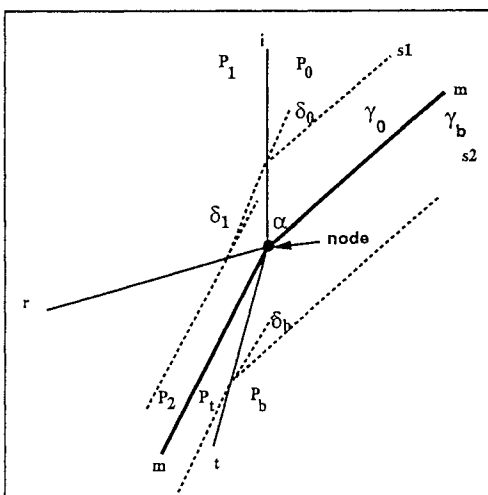


Figure 2: Schematic of regular refraction at a fast-slow interface.

$$\tan \delta_i(p) = \frac{p/p_i - 1}{1 + \gamma_i M_i^2 - p/p_i} \left[\frac{(1 + \mu_i^2) M_i^2 - \mu_i^2 - p/p_i}{\mu_i^2 + p/p_i} \right]^{\frac{1}{2}} \tag{2}$$

where $i = 0, 1, b$ for the incident, reflected and transmitted shock and $\mu^2 = \frac{\gamma - 1}{\gamma + 1}$,

$$\frac{P_1}{P_0} = 1 + (1 + \mu^2)(M^2 - 1), \quad \frac{P_t}{P_b} = \frac{P_2}{P_0} = \frac{P_2}{P_1} \frac{P_1}{P_0} \quad (3)$$

$$\frac{1 + \frac{\gamma-1}{2} M_0^2}{1 + \frac{\gamma-1}{2} M_1^2} = \frac{1 + \mu^2 \frac{P_1}{P_0}}{1 + \mu^2 \frac{P_0}{P_1}} \quad (4)$$

$$M_0 = M \sin^{-1} \alpha, \quad M_b = M_0 \eta^{1/2} \frac{\gamma_b}{\gamma_0} \quad (5)$$

Circulation per unit *original length* (SPA)

$$\Gamma' = \frac{1}{\sin \alpha} \left(\left[\gamma_0 M^2 + \frac{\gamma_b}{\gamma_b - 1} \left(\frac{1 - \Psi(p_2, \mu_b)}{\eta} \right) \sin^2 \alpha \right]^{1/2} - \left[\gamma_0 M^2 + \frac{\gamma_0}{\gamma_0 - 1} (1 - \Psi(p_2/p_1, \mu_0)) \Psi(p_1, \mu_0) \sin^2 \alpha \right]^{1/2} \right) \frac{\cos \alpha}{\cos(\alpha - \delta_b)} \quad (6)$$

$$\Psi(p, \mu) \equiv \frac{1 + \mu^2 p}{\mu^2 + p} p \quad (7)$$

Exact expression is valid only for $\alpha \leq \alpha_{cr}(M, \eta)$.

Fundamental Scaling

$$\Gamma' = \frac{2\gamma^{1/2}}{\gamma + 1} (1 - \eta^{-1/2}) \sin \alpha (1 + M^{-1} + 2M^{-2})(M - 1) \quad (8)$$

Approximations of SPA

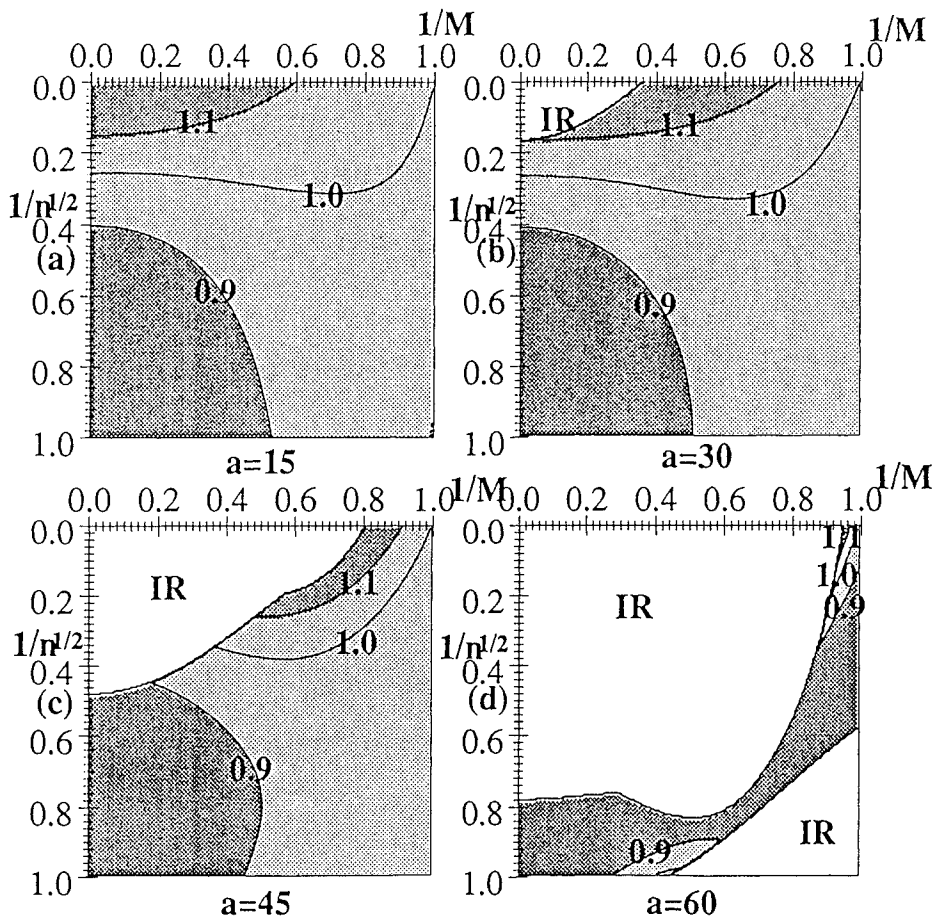
- Asymptotic series expansion of circulation per unit *original length*

$$\Gamma' = \Gamma'_1 \sin \alpha + \Gamma'_3 \sin^3 \alpha + O(\sin^5 \alpha) \quad (9)$$

$$\Gamma'_1 = \frac{1}{\gamma_0^{1/2} M} \left(\frac{\gamma_b}{\gamma_b - 1} \frac{1 - \Psi(p_{2,0}, \mu_b)}{\eta} - \frac{\gamma_0}{\gamma_0 - 1} (1 - \Psi(p_{2,0}/p_1, \mu_0)) \Psi(p_1, \mu_0) \right) \quad (10)$$

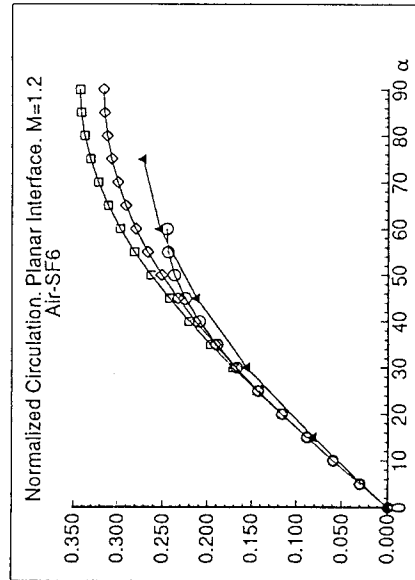
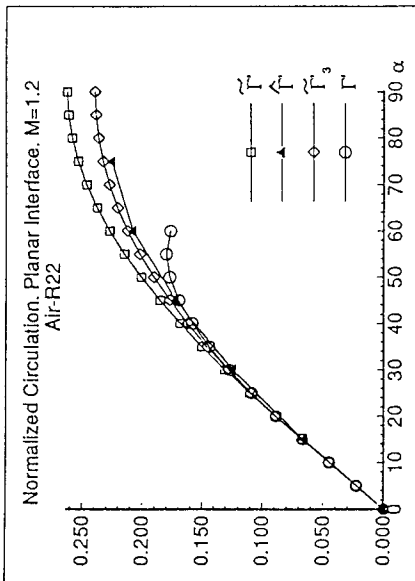
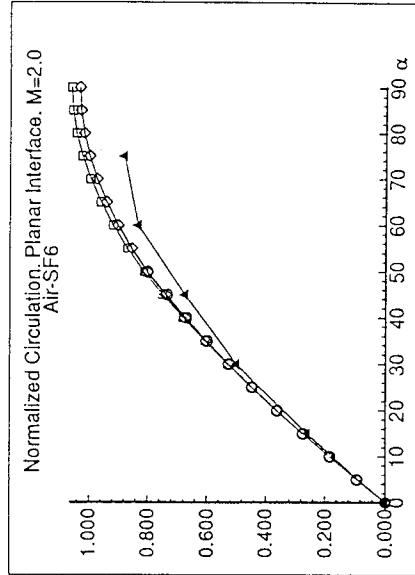
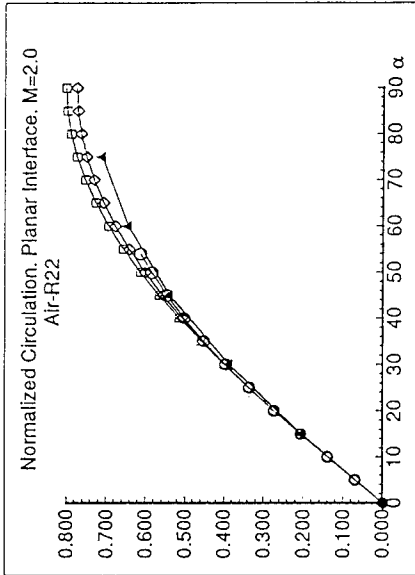
- Γ'_1 and Γ'_3 can be evaluated for $0 \leq \alpha \leq \pi/2$
- Γ'_3 does not contribute significantly to the circulation.
- Higher order terms may be complex for $\alpha > \alpha_{cr}$.

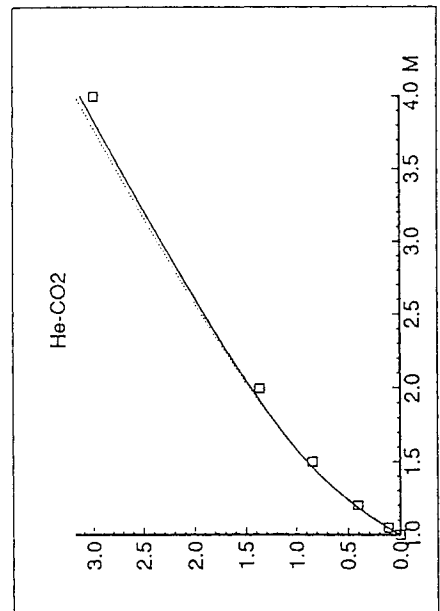
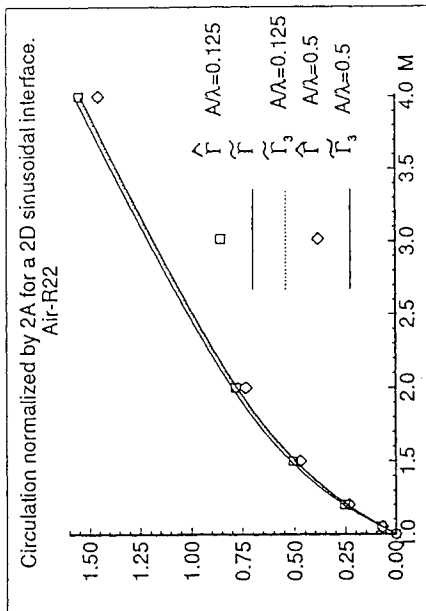
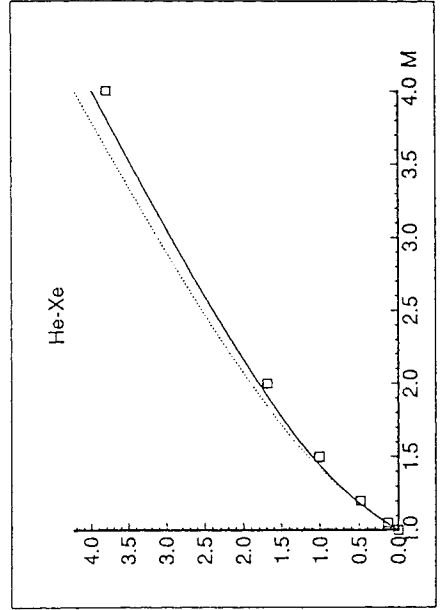
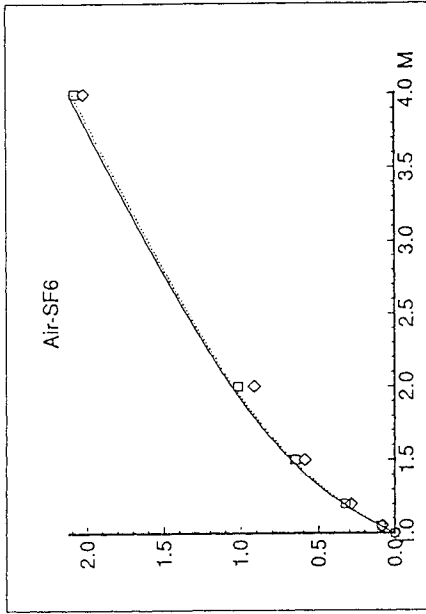
- Validation: Comparison with DNS Quantifications
 - Air-R22 ($\eta=3.0$, $\gamma_{0,b}=1.4$, 1.172), Air-SF6 ($\eta=5.04$, $\gamma_{0,b}=1.4$, 1.0935)
 - $M=1.2, 2.0$
 - $\alpha=15^\circ, 30^\circ, 45^\circ, 60^\circ, 75^\circ$
 - At large angles the difference between DNS quantification and analytical results increases as the vortex layer has evolved dynamically. The difference increases with increase in η and α and decreases with increase in M .



Parameter Space for Circulation Scaling Laws

M =Mach Number
 n =Density Ratio
 a =angle





2D Non-Planar Interface

- Interface $x=f(y)$, total circulation (up to third order); ΔX is the range of x .

$$\tilde{\Gamma}_3 = \Gamma'_1 \Delta X + \Gamma'_3 \int_0^{\Delta X} \frac{dx}{1 + \left(\frac{dx}{dy}\right)^2} \tag{11}$$

- Vorticity distribution

$$\tilde{\omega}(x, y) = \Gamma'_1 f'(y) \delta(x - f(y)) + O(\Gamma'_3) \tag{12}$$

2D Sinusoidal Interface

- Interface: $x = A \cos(ky)$ where $\alpha_{\max} = \tan^{-1}(Ak)$.
- Total circulation

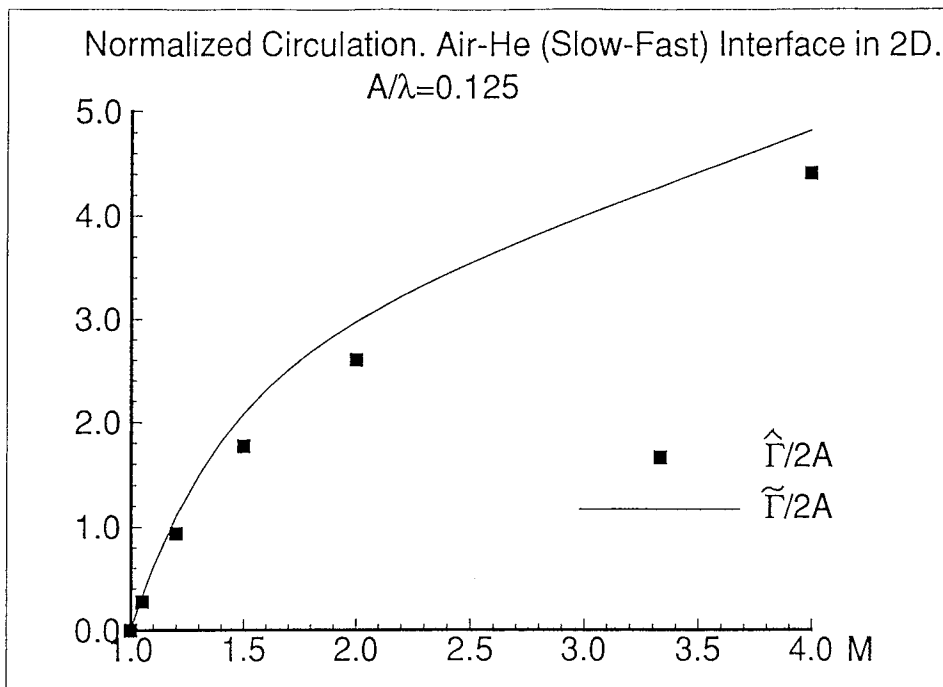
$$\frac{\tilde{\Gamma}}{2A} = \Gamma'_1 + \Gamma'_3 - \Gamma'_3 \frac{1}{4kA(1+k^2A^2)^{1/2}} \log \left[\frac{(1+k^2A^2)^{1/2} + kA}{(1+k^2A^2)^{1/2} - kA} \right] \tag{13}$$

- For slow-fast interfaces

$$\frac{\tilde{\Gamma}}{2A} = \frac{1}{\gamma_0^{1/2} M} \left(\frac{\gamma_b}{\gamma_b - 1} \frac{1 - \Psi(p_{2,0}, \mu_b)}{\eta} - \frac{\gamma_0}{\gamma_0 - 1} \left(1 - \Psi(p_1, \mu_0) \left(\frac{p_{2,0}}{p_1} \right)^{\frac{\gamma_0 - 1}{\gamma_0}} \right) \right) \tag{14}$$

- Validation: Comparison with DNS quantification.
 - Air-R22 ($\eta=3.0, \gamma_{0,b}=1.4, 1.172$), Air-SF6 ($\eta=5.04, \gamma_{0,b}=1.4, 1.0935$), He-CO₂ ($\eta=11.0, \gamma_{0,b}=1.667, 1.297$) and He-Xe ($\eta=32.7, \gamma_{0,b}=1.667, 1.667$)
 - $M=1.05, 1.2, 1.5, 2.0, 4.0$
 - $A/\lambda=0.125, \alpha_{\max}=38^\circ$ (regular). $A/\lambda=0.5, \alpha_{\max}=72^\circ$ (irregular).
- Vorticity distribution

$$\tilde{\omega}(x, y) = -\Gamma'_1 A(0-) k \sin ky \delta(x - A(0-) \cos ky) \tag{15}$$



3D Non-Planar Interface

- Interface $x=f(y,z)$. Vorticity distribution to first order

$$\tilde{\omega}(x, y, z) = \Gamma_1' \delta(x - f(y, z)) (f_y \hat{j} - f_z \hat{k}) \tag{16}$$

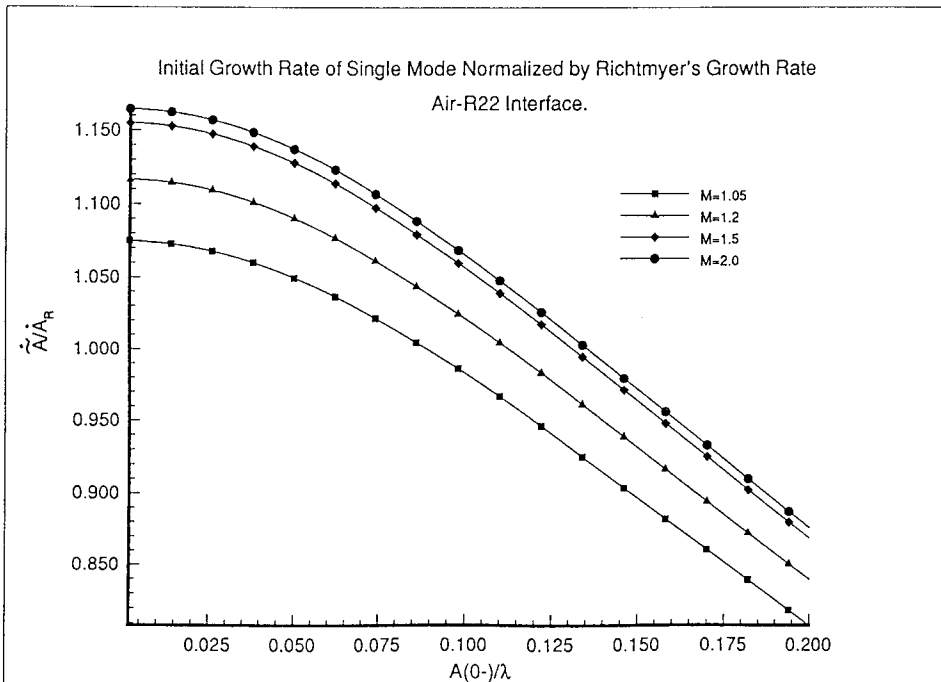
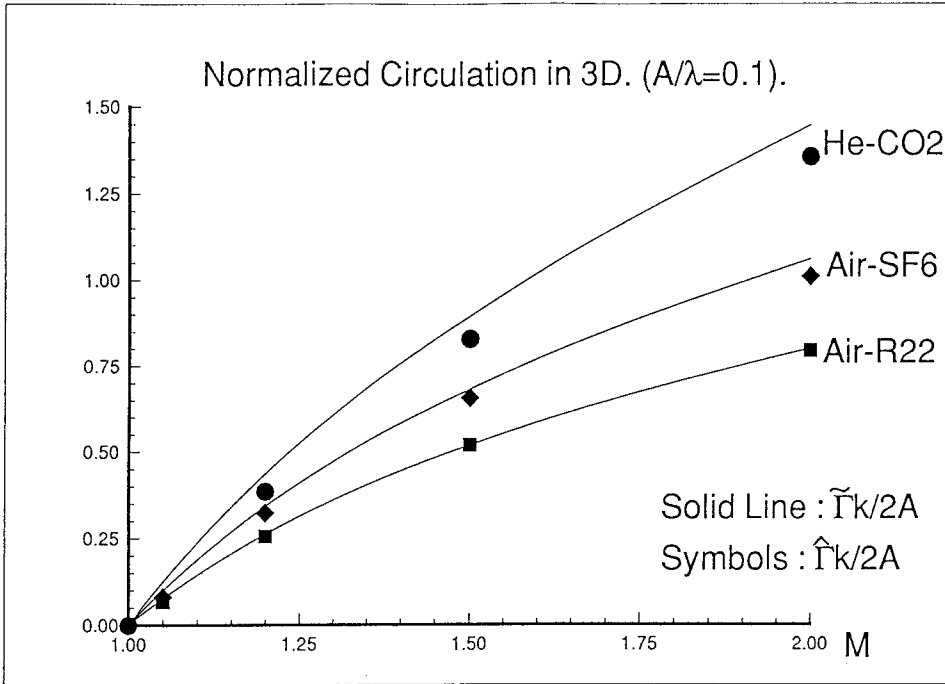
- Interface $x = x_0 + A \cos(ky) \cos(kz)$
- Diagnostics

$$\tilde{\Gamma}_{(2)} = \int_0^{\lambda/2} \int_{-\infty}^{\infty} \tilde{\omega} dx dy = 2A\Gamma_1' \cos(kz) + O(\Gamma_3') \tag{17}$$

$$\tilde{\Gamma} = \int_0^{\lambda/4} \int_0^{\lambda/2} \int_{-\infty}^{\infty} \tilde{\omega}(x, y, z) dx dy dz = 2A\Gamma_1'/k + O(\Gamma_3') \tag{18}$$

$$\tilde{\Omega}_e = \int_0^{\lambda/2} \int_0^{\lambda/2} \left(\int_{-\infty}^{\infty} \tilde{\omega} \right)^2 dy dz = A^2 \Gamma_1'^2 \pi^2 / 4 \tag{19}$$

- SPA does not predict initial longitudinal vorticity component.
- Validation: Comparison with DNS quantifications.
 - Air-R22 ($\eta=3.0$), Air-SF6 ($\eta=5.04$), He-CO₂ ($\eta=11.0$)
 - $M=1.05, 1.2, 1.5, 2.0$
 - $A/\lambda=0.1$.



Growth Rate of a Single Mode

"...there is slipping along the interface. This effect will not concern us directly" - R.D. Richtmyer (1960).

- Single mode evolution from Biot-Savart (incompressibility) (assuming the vorticity distribution remains sinusoidal for $t < \epsilon$)

$$\dot{\hat{A}}_{2D} = \frac{\Gamma_1' k A|_{0-}}{4\pi} k \int_{-\infty}^{\infty} \frac{\xi \sin \xi d\xi}{A(t)^2 k^2 (1 - \cos \xi)^2 + \xi^2} \quad (21)$$

- Initial growth rate assuming $Ak \ll 1$ is

$$\dot{\hat{A}}_{2D} \Big|_{0+} = \frac{1}{2} \Gamma_1' k A|_{0-} \quad (22)$$

- Vortex paradigm for growth rate of a single mode in 3D

$$\dot{\hat{A}}_{3D} = \frac{\Gamma_1' k A|_{0-}}{4\pi} \int_{-\infty}^{\infty} \frac{\xi \sin \xi \cos \eta d\xi d\eta}{\left(A(t)^2 k^2 (1 - \cos \xi \cos \eta)^2 + \xi^2 + \eta^2 \right)^{3/2}} \quad (23)$$

- Assuming $Ak \ll 1$

$$\dot{\hat{A}}_{3D} \Big|_{0+} = 2^{-1/2} \Gamma_1' k A|_{0-} = 2^{1/2} \dot{\hat{A}}_{2D} \Big|_{0+} \quad (24)$$

- Comparison with Richtmyer linear theory.
 - Linear growth rate by Richtmyer theory

$$2\dot{\hat{A}}_R = \left(k A \Delta U \frac{\eta - 1}{\eta + 1} \right)_{0+} \quad (25)$$

where $\Delta U(M, \eta, \gamma)$ is the change in the mean velocity of the interface and

$$A|_{0+} / A|_{0-} = 1 - \Delta U / W_s$$

- Growth rate from vorticity considerations (equation 21) is *nonlinear* in amplitude.

Observations

- Total circulation and initial vorticity distribution agrees with analytical prediction.

$$\dot{\hat{A}} \Big|_{0+} > \dot{\hat{A}} \Big|_{0+} \quad (\text{numerical})$$

- In 3D computations we observe significant growth of longitudinal vorticity. This may lead to a lessening of the growth rate according to the vortex paradigm.

Interface	M	A/λ	$2\hat{A}$	$2\check{A}$	$2\dot{A}_R$	\hat{A}/\check{A}	$A/\Delta x$
Air-R22	1.05	0.05	0.022	0.023	0.022	0.95	12
Air-R22	1.2	0.05	0.070	0.080	0.074	0.88	12
Air-R22	1.5	0.05	0.129	0.159	0.141	0.81	12
Air-R22	2.0	0.05	0.176	0.245	0.216	0.72	12
Air-SF6	1.24	0.064	0.107	0.154	0.129	-	12
Air-R22 (3D)	1.5	0.064	0.212	-	0.258	-	8
Air-SF6 (3D)	1.24	0.064	0.115	-	0.183	-	8
Air-SF6 (3D)*	1.24	0.064	0.067	-	0.183	-	8

Table 1: Comparison of initial growth rate of a single mode

*: Cloutman and Werner; Phys. Fluids A (4), 8, 1992.

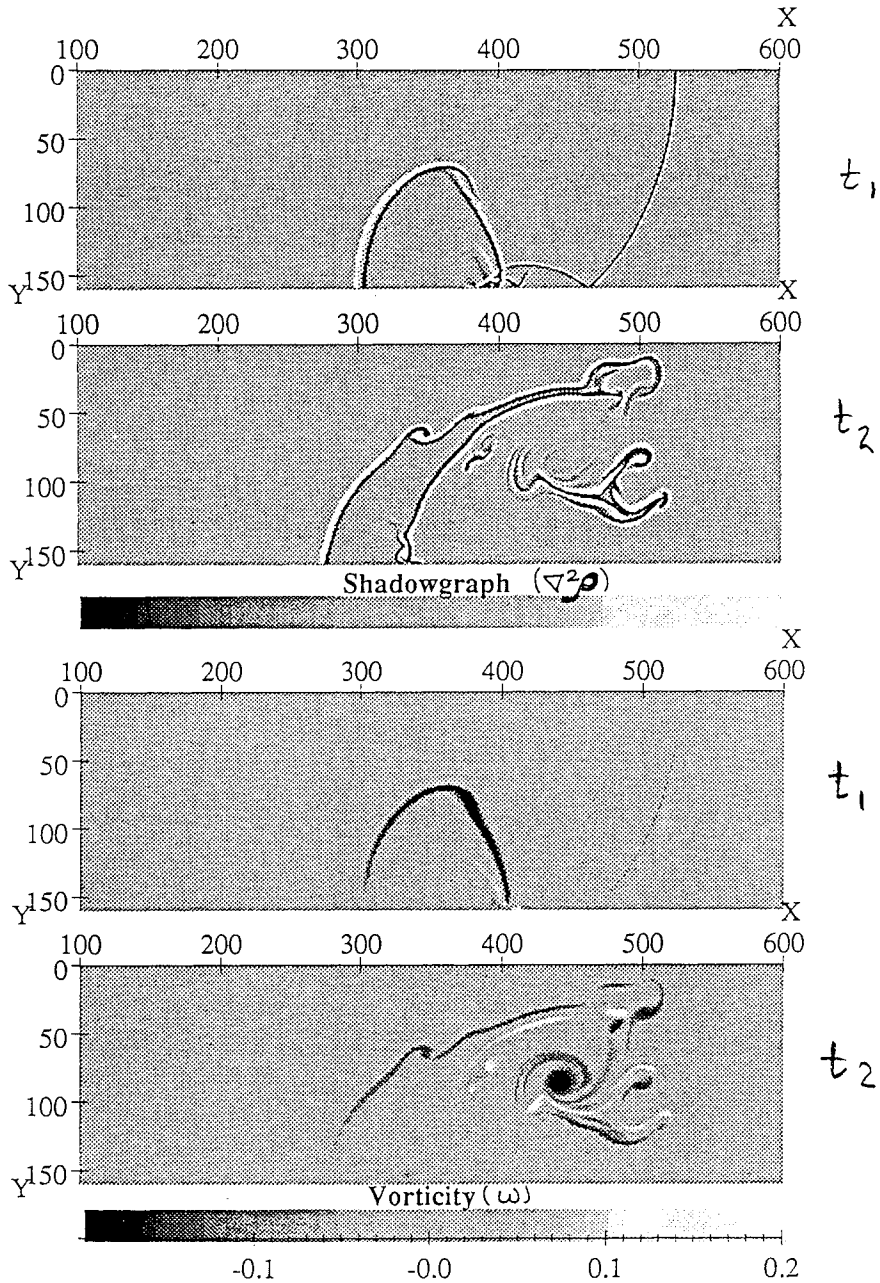
Multiply \hat{A} above by $c\gamma^{-1/2}$ to convert to dimensional units. c is the sound speed in the incident gas.

Conclusion

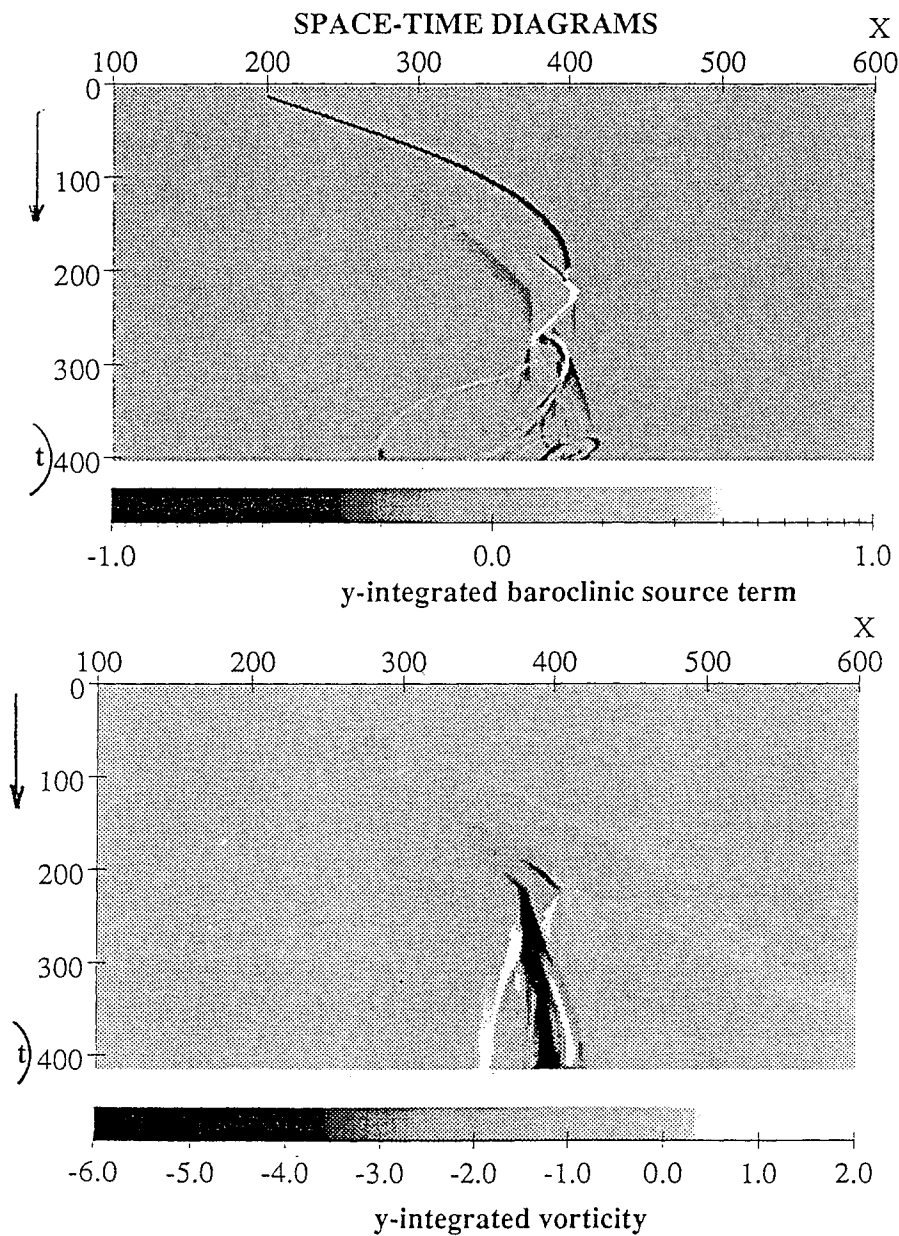
- Asymptotically motivated expressions for vorticity deposition on shock accelerated interfaces were derived.
- Scaling laws were proposed for circulation per unit *original* length on planar interfaces and the parameter space of validity was explored. Γ' scales as $(1 + M^{-1} + 2M^{-2})(M - 1)$; $1 - \eta^{-1/2}$ and $\sin \alpha$.
- Good agreement between analytical and numerical results for total circulation on single mode sinusoidal interfaces in 2D and 3D.
- Growth rate derived from Biot-Savart law overpredicts the numerically observed values. Is the incompressibility assumption justified?
- Preliminary quantification of compressibility effect on growth rate.
- In single and multiple mode 3D simulations, significant increases in longitudinal vorticity is observed.

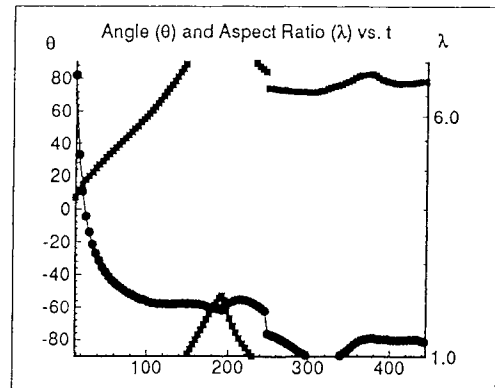
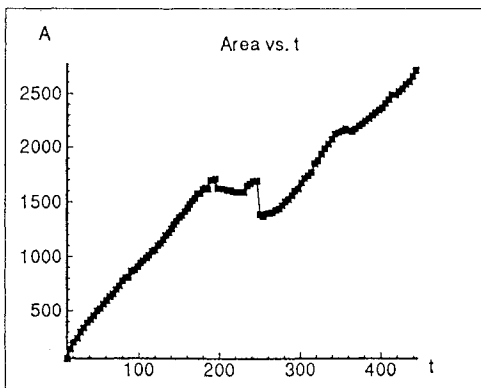
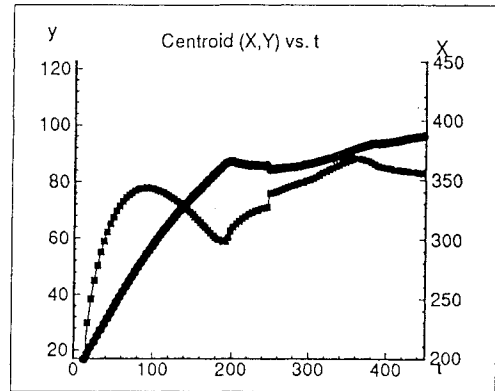
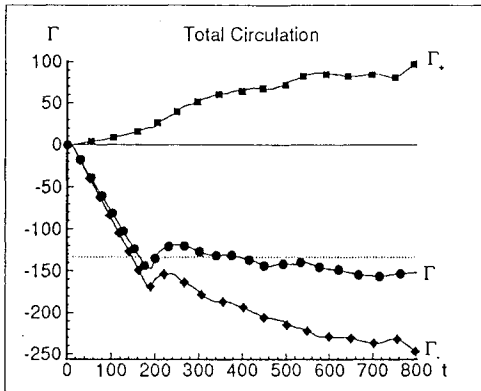
Future Work

- Increase the resolution of 3D computations to 512x128x128 on massively parallel machines (CM2, CM5).
- Quantify the effects of compressibility.
- Quantify the vorticity in the coherent structures in 3D.
 - Spacetime diagrams, ellipsoidal quantification, feature tracking *etc.*
- Symmetry breaking perturbations; turbulent mixing.



Visiometric Examples: Visualization and Some Quantification of 2D Shock Bubble Interaction Air-R22, $M=2.0$





Richtmyer-Meshkov instability for two- and three-dimensional interfaces.

S. Zaytsev, A. Aleshin, E. Lazareva

The Krzhizhanovskiy Power Institute, Leninsky Pr.19, Moscow, 117071, Russia

V. Rozanov, I. Lebo

The Lebedev Physical Institute, Leninsky pr. 53, Moscow 117333, Russia.

Abstract

The experimental study of 2D and 3D interfaces disturbed by a shock passage has been carried out. Into a special section of a driven section of the shock tube, a flange was inserted, with a thin nitrocellulose film (about $0.5 \mu\text{m}$ thick) pasted on it. Thin lavsan threads were fastened on the flange to divide the square of $7.2 \times 7.2 \text{ cm}^2$ in 4 equal parts. The 1-2 mm Hg difference in pressure between the two parts of the driven section filled with argon or xenon allowed to obtain a 3D interface with $\lambda_x = \lambda_y = 3.6 \text{ cm}$. We used two orientations of a shock wave with respect to the interface. In the first case, the shock hits the interface on the side of crests formed along the threads (the curvature was maximal). In the second case, the shock hits the interface on the side of the bulges (in the environment of bulge the curvature was minimal). The growth rates of interpenetrating of one gas into the other for both variants of 3D interfaces at the shock passage from argon to xenon have been determined. The experimental data obtained for 3D interface ($\lambda = 3.6 \text{ cm}$) were compared to those obtained for a 2D interface ($\lambda = 3.6 \text{ cm}$).

1. Introduction

The problem of hydrodynamic instability concerning the task of target compression in inertial confinement fusion is a classical one. The most important aspect is the evolution stage of the process, when substances of different density contacting with each other are penetrating one into the other. Hydrodynamic instabilities are excited by the disturbances in the interface between the substances of different density and by nonuniform laser illumination. That is why the predictions of mixing zone (interface), and, respectively, the decrease of neutron output based on the use of the auto modelling of the turbulent model of the process, considerably differ from experimental data [1,2]. On the ground of ideas on the evolution stage, it has been suggested [3,4] that the development of instability and the early stage of mixing for 3D perturbations in interface may significantly differ from those for 2D. Numerical calculations confirm that the pattern of development of 3D perturbations considerably differ from 2D, because 3D perturbations are less affected by the Kelvin-Helmholtz instability and can promote the more extensive mixing than the 2D perturbations.

This report represents the experimental study on the evolution of 2D and 3D perturbations of the interface under a shock front passage, i.e. Richtmyer-Meshkov instability.

2. Experimental set-up

The study has been carried out on the shock tube. An interface separating inert gases of different densities was prepared with a $0.5 \mu\text{m}$ thick nitrocellulose film. Constructions of 2D and 3D interfaces are represented in Fig. 1. To obtain a 3D

interface, the film was fastened on a special flange (1) (Fig. 1a), inserted in the driven section of the shock tube. Thin threads (2) were fastened on the flange. Such a construction provided a separation of gases filling the driven section. Previous to experiment both parts of the driven section were pumped out to 0.1 mm Hg. After the pumping, both parts of the driven section were filled with test gases. During pumping and filling, the difference in pressure in both chambers did not exceed 1-2 mm Hg. At higher values the film was destroyed.

The initial pressure of gases was 0.5 atm, Mach number of the shock wave S_0 hitting the film approximately 3.5. The pressure in driven section adjacent to the threads stretching under the film, was reduced by 0.5 mm Hg before the experiment. This resulted in deformation of the film leaning on the threads, which produced a 3D surface, schematically shown in Fig. 1a. A shock wave hit the interface either from the side of "crests" (points C in Fig. 1a) - variant 1, or from the side of the "bulges" (points B) - variant 2. The total length of the field of view along the channel was 11 cm.

The 2D interface was generated by fastening the film to the flange 1 of a certain shape (Fig. 1b). In this case the form of the interface in XY plane was sinusoidal-like. The plane 1 (Fig. 2b) was 0.4 cm distant from the field of view. To separate gases for 2D case, a 2 μm thick lavsan film was used. The study of the shock wave interaction with the 2D film described above [6] has shown that the film did not affect the interface evolution.

The diagnostics of the process was carried out by shlieren method. The light was directed along the axis Z . Ruby laser working in the mode of modulated accuracy was used as a light source. Laser generated series of sequential 0.1 μs flashes with approximately 10^5 Hz frequency. A detailed description of the set-up can be found in [6].

3. Results

The study of the shock wave passage from Ar to Xe through 3D and 2D interfaces has been performed. Fig. 2 represents the scheme of experiment for 3D interface (variant 1). S is the front of a shock wave, K is the section of interface by the plane $Y=1.8$ cm (Fig. 1), S and R are refracted and reflected shock waves, respectively, after the shock passage. A number of Topler pictures corresponding to this variant is shown in Fig. 3a. Topler pictures were used to determine the motion paths of the characteristic points of the interface, its amplitude $a_k(t)$ and the path of the refracted wave.

In this experiment a light gas(Ar) invaded into a heavy one (Xe) in the section of interface with a relatively low curvature (the vicinity of point B). The heavy Xe invades into the light gas in the place of "spike"-shaped interface (the vicinity of point C, Fig. 2a.). The paths of the interface points B and C in the region $0.4 \text{ cm} < x < 11.4 \text{ cm}$ were straight lines, within the limits of the measurement accuracy. These curves were extrapolated, to determine the amplitude at the end of diffraction ($t=0$, $a_{k0}=5$ mm). The velocities of points B and C in the system of coordinates related to the particles beyond the refracted shock wave S were 45 and 113 m/s, respectively. The velocity of the front S in the region $0.4 \text{ cm} < x < 11.4 \text{ cm}$ was 782 m/s. The design value for the gas particle velocity beyond S was 557 m/s.

Fig. 2b demonstrates a scheme of experiment for a shock wave hitting the interface from the side of the "bulges" (the vicinity of point B, variant 2). In this case the velocities of points B and C in the chosen system of coordinates were 30 and 70

m/s, respectively. Topler pictures obtained in experiment (variant 2) are represented in Fig. 3b.

Fig. 4 shows the values da_k/dt obtained for variants 1 and 2 (lines 1 and 2, respectively). The higher values of the rate of invading of one gas into the other - da_k/dt obtained for variant 1, comparing to those for variant 2, were due to the "previous preparation" for the generation of a heavy gas "spike" into the light gas and a "bubble" of the light gas into the heavy one. For variant 2, the generating of the "bubble" started in the vicinity of the point C and that of the "spike" - in the vicinity of the point B (Fig. 3b).

Fig. 3c represents the Topler pictures for the evolution of 2D perturbations ($\lambda=2.4$ cm). The value a_{k0} in this experiment was 1.0 cm, what corresponded to a^* . As can be seen from the Topler pictures for 2D perturbations, at $t=100$ μ s after the end of diffraction, the developed vortical structures are observed on the "spike" edge. For 3D perturbations, by the moment $t=100$ μ s after the end of diffraction, no vortical structures were observed on the "spike" edge. Values da_k/dt obtained for 2D perturbations at $\lambda=2.4$ cm are shown in Fig. 4 (points 3).

4. Discussion

The experimental and design data for 2D perturbations [6] have shown that the generating of the curved refracted and reflected shock waves resulted in appearance of local high pressure areas beyond the segments of front arched towards the gas flowing into the refracted or reflected front. The time required for generation of these areas was inversely proportional to the sound speed in a shock-compressed gas. The pressure amplitude in these areas was proportional to the curvature and intensity of shock front. After the pressure has reached its maximum, it started to fall, and then occurred "the outspreading" of the pressure nonuniformities generated by the curved wave. For a sufficiently high curvature of the shock front, the generation and "outspreading" of high pressure areas were accompanied by the appearance of secondary shock waves moving along the layer of shock-compressed gas. For the lighter gas, the "outspreading" went faster than for the heavier one, due to the higher sound speed. This diminished the curvature in that part of interface, beyond which a high pressure area was generated in the light gas. The diminution of the curvature was accompanied by the widening of this part of interface in a direction perpendicular to the gas flow - a "bubble" appeared. The high pressure area in the heavy gas appeared later than in the light one, and, due to the lower rate of "outspreading" and therefore to the longer period of life, caused a more local and prolonged effect on the part of interface, beyond which it has appeared. This induced the generating of a heavy gas "spike" invading into the light gas. At a certain stage of development, the "spike" edge produced a mushroom-like vortical structure (Fig. 3c). The "outspreading" of high pressure areas was accompanied by the reduction of the rate of invasion of one gas into the other. The appearance of vortical structures on the "spike" edge caused the further reduction of the invasion rate. Later, an interaction of adjacent vortical structures was accompanied by a generation of turbulent mixing zone of finite thickness L towards the motion of the flows. At the turbulent stage the rate of invasion of one medium into the other dL/dt was minimal.

The analysis of 2D and 3D one-mode interface perturbations should be performed according to the following relation:

$$K_2=1.4K_{3x}$$

where K_2 is wave number for 2D one-mode interface perturbations, $K_{3x}=K_{3y}$ is wave number for 3D one-mode interface perturbations. The experiments in this study were performed for $K_2=2,62 \text{ cm}^{-1}$, $K_{3x}=1.75 \text{ cm}^{-1}$.

The comparison of Topler pictures for evolution of 2D and 3D perturbations has shown that for variant 2 of experiment, the shape of interface changed with appearance of "bubbles" instead of "crests" and "spikes" instead of "bulges". This was qualitatively confirmed by the scenario of the interface shape generation proposed in [6] for 2D perturbations.

Unlike for 2D perturbations, the process of generation of vortical structures on 3D "spikes" was delayed.

Acknowledgement

We are very grateful to Dr J.F. Haas for the interesting discussion and the valuable comments on the manuscript.

References

1. Progress in laser fusion. Theoretical interpretation of OMEGA glass-ablator cryogenic implosion experiments. LLE Review. Quarterly Report, Apr-June 1991, Rochester, pp.117-135.
2. S. Nakai, K. Mima, H. Azeshi et al. High density compression experiments and ignition program with Gekko-XII. ILE Report, June 1991.
3. V. Rozanov. Hydrodynamic instabilities and mixing in the laser driven targets. Report at the LLNN LLE RU NPI Seminars (USA, June 1991). The 21st ECLIM (Poland). In Book of abstracts. Warsaw, 1991, pp. 1-24.
4. V. Rozanov, N. Zmitrenko. Growth rates of Kelvin-Helmholtz instabilities in the problem of laser fusion. Pre-print No. 16, The Lebedev Physical Institute. Moscow, 1992.
5. R. Benjamin, D. Besnard and J.F. Haas. Richtmyer-Meshkov instability of shocked gaseous interfaces. (Submitted to Phys. Fluids, 1992).
6. S. Zaytsev, A. Aleshin, E. Lazareva, S. Titov, E. Chebotareva, V. Rozanov, I. Lebo, V. Demchenko. Experimental investigation of Rayleigh-Taylor and Richtmyer-Meshkov instabilities. The Proceedings of the 3rd International Workshop on the Physics of Compressible Turbulent Mixing. Royaumont, France. 1991.

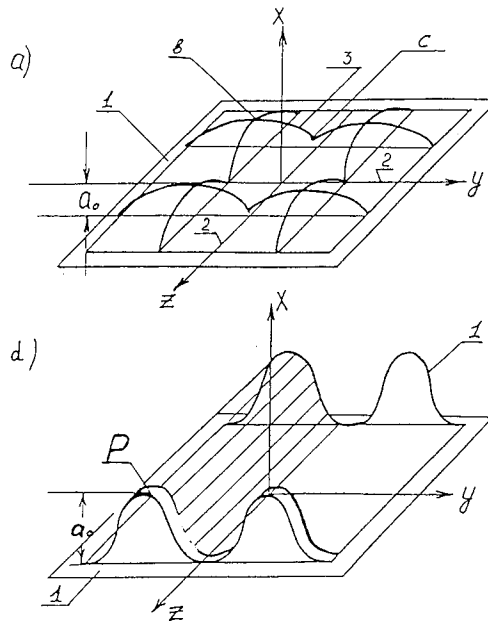


Fig. 1. The scheme of the discontinuous interfaces used. (a) 3D interface, (d) 2D interface. 1 and P - the planes of the film fastening, 2 - the line of "canyon" (towards the negative X axis of the moving shock wave, variant 2) or the line of "crest" (towards the positive X axis of the moving shock wave, variant 1), b - the bubble, a_0 - the initial amplitude.

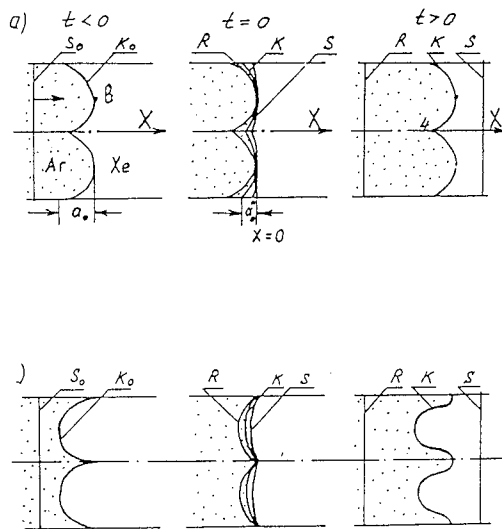


Fig. 2. The scheme of the incident shock interaction with 3D interface, (a) variant 1, (d) variant 2. S_0 - the incident shock wave, K_0 - the initial interface (cross section along $Z = \text{const.}$, for the line 3, see Fig. 1 11), S - the refracted shock wave into X_e , K - the interface between the shocked Ar and X_e , R - the reflected shock wave into Ar .

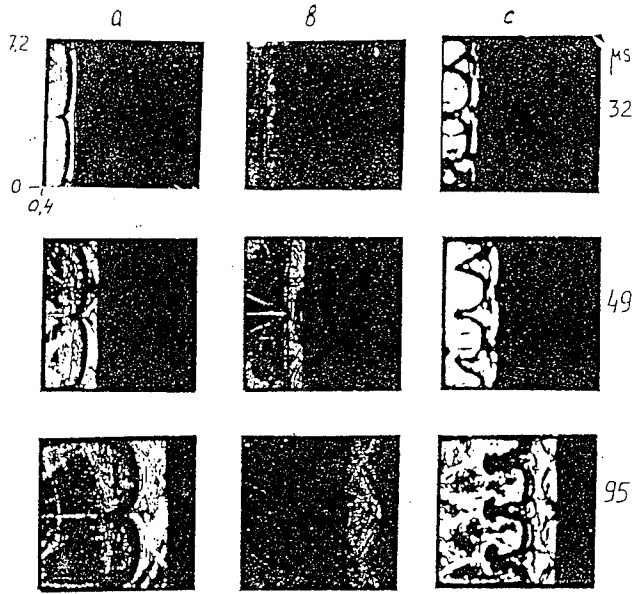


FIGURE 3: The schlieren pictures of a shock wave interaction with the interface: (a) variant 1, 3D interface; (b) variant 2, 3D interface; (c) 2D interface. The incident shock wave passed from Ar to Xe. $P_0=0.5\text{atm}$, $M_0=3.5$.

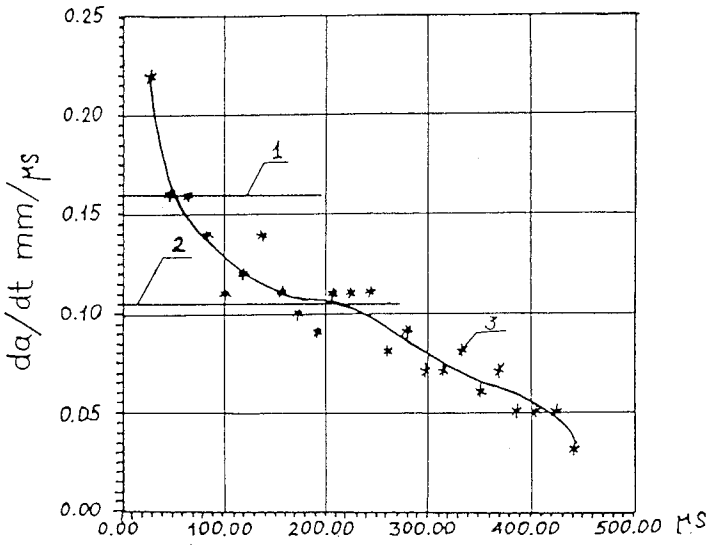


Fig. 4. The experimental growth rate of the interface perturbation da/dt versus the time: (1) 3D (variant 1); (2) 3D (variant 2); (3) 2D.

The initiation and the development of Richtmyer-Meshkov instability in continuous interface.

S.G. Zaytsev, E.I. Chebotareva and S.N. Titov

The Krzhizhanovsky Power Institute, Leninsky Pr.19, Moscow, 117071, Russia

Abstract

The experimental study of the evolution of a thick layer separating gases of different density (continuous interface) after the interaction with a shock wave has been performed. The experiments have been carried out in a horizontal shock tube. Shock wave passed from one inert gas into the other. The evolution of the process has been studied with interferometer. The growth rate of amplitude a_k of surfaces separating continuous interface from pure gas after the passage of the incident and the first reflected shock waves has been determined. The experimental data for a_k have been compared to the calculated values using a simple model proposed in [5].

1. Introduction

Theoretical study of the evolution of a continuous interface separating incompressible media of different density, drawn into accelerated motion, has been carried out in [1,2]. These studies have demonstrated that the change of discontinuous interface for a continuous one results in reduction of perturbations growth rate at initial (linear) stage of RTI evolution. The experimental study of this phenomenon for gases of different density in a gravitational field has been performed in [2].

An experimental study of evolution of interface between gases of different densities in the field of impulsive acceleration generated by a shock wave, has been carried out in [3-6]. The study [3] has been performed in a horizontal shock tube. The initial mixing zone (continuous interface) separating gases was generated by the withdrawal of a sliding plate separated the gases before the experiment. At the initial stage, evolution of continuous interface has been found to be qualitatively similar to that of discontinuous interface. The limited amount of experimental data did not allow to provide an adequately accurate determination of reduction of the growth rate of perturbations amplitude. In this study the growth rates of interface thickness were obtained for the final turbulent stage of evolution.

The studies of shock wave passage through the interface separating gases of different density have been performed in [4,5,6]. The experiments were carried out in a vertical shock tube. The relatively low Mach numbers of the shock wave did not allow the authors to detect the change of interface properties after shock passage through it. Only after the passage of a several damping waves, appeared between the interface and the end wall of the shock tube, the growth of interface thickness and the growth of perturbations on its surface have been registered.

A simple model for estimation of the reduction of the perturbations growth rate has been suggested in [5]. This model used the equation describing the development of instability in incompressible media [2].

2. Experimental set-up.

The experiments have been performed in a horizontal shock tube [3]. The channel of the driven section had a cross-section $7.2 \times 7.2 \text{ cm}^2$. The side walls of the test section Ts-2 contained the optical grade glass windows, to provide the visualisation of the process. Within the field of view, Ts-2 was equipped with a 0.2 cm thick sliding plate installed perpendicularly to the axis of the channel (X) and dividing the driven section in two parts. The construction of Ts-2 provided the vacuum-tight separation of both parts of the driven section, when the sliding plate was inside the channel, using the vacuum seal of the sliding plate with rubber washers embedded into grooves in the glass windows and the lower walls of the channel. The washer appeared in interferograms as a 0.3 cm thick stripe. The plate was withdrawn by a spring mechanism initiating the accelerated motion of the plate. The time of complete withdrawal of the plate varied in different experiments from 70 to 150 ms. During the withdrawal of the plate, an interface was being generated in the channel. Different couples of inert gases He, Ar, Kr and Xe were studied. The initial pressure of gases before the experiment was fairly the same, within 0.1-0.5 atm. The diagnostics of the process was carried out with Mach-Zehnder interferometer. Fig.1 demonstrates three types of continuous interface appearing after withdrawal of the plate. The generated interfaces are characterised by a bend near the lower wall of the channel, which is a result of gravitational instability in the interface. The interface thickness depends on the process of molecular diffusion. The undulate continuous interface is generated by a flow separation behind the edge of the plate being withdrawn. Amplitude a_k of the surface distortions depends on the speed of the plate withdrawal and on the properties of gases being in contact. The distance λ between the "crests" arisen on the surface depends on the properties of gases in contact.

At the moment of a complete withdrawal of the plate from the channel, the oxygen/hydrogen/helium mixture in driver section is ignited and 5-6 ms later the shock wave S_0 hits the continuous interface. To determine the time of evolution of continuous interface, we use high-speed schlieren motion pictures. To record the process, a laser light source generating series of sequential $0.1 \mu\text{s}$ flashes was used. Continuous recording of the process was carried out through the slit which narrowed the image of the field of view in the film, using the light source generating an approximately $500 \mu\text{s}$ flash. The film moved perpendicularly to the slit. Visualisation was carried out at different distances from the site of the plate withdrawal.

3. Results

3.1. The interaction of an incident shock wave with the interface.

The shock wave passage from a light gas to a heavy one and vice versa has been studied. Fig.2 demonstrates the interferograms of these processes and the sketches indicating the positions of characteristic lines of wave pattern recorded in corresponding interferograms. The perturbations amplitude $a_k(t) < 0.5\lambda$ grows linearly in time. For $a_k(t) > 0.5\lambda$, the amplitude growth rate decreases. This is accompanied by a generation of an interface shape, typical for non-linear stage of evolution. The tapering "spikes" are penetrating into the light gas. For $a_k(t) \approx \lambda$, a specific mushroom-like vortical structure appears at the "spike" edge (Fig.3.a). The change in amplitude $a_k(t)$ as a function of $kAut$ is represented in Fig. 4 (k is the wave

number, A is Atwood number, u is the velocity of interface relatively to the walls of shock tube). The experimental measurement of $a_k(t)$ at the linear stage was carried out in the chamber Ts-2, where the evolution of interface was recorded within $+0.15 \text{ cm} < x < +9 \text{ cm}$. The most difficult problem in recording this stage of the process was to obtain at least 3 frames with $a_k(t) < 0.5\lambda$ for the selected perturbations. The initial amplitude was determined by rectilinear extrapolation to the section, in which at the end of diffraction, the perturbation "crest" was observed.

3.2. The interaction of reflected shock wave with interface.

The study of the interaction of shock wave with interface has been carried out in test chamber Ts-3, where the plate was installed 5 cm before the field of view. The process of interface (K) motion after interaction with a shock wave S and K interaction with the wave reflected from the end wall (at distance $x=15 \text{ cm}$) were recorded within $5 \text{ cm} < x < 15 \text{ cm}$ ($x=0$ matches the position of the inserted plate). Thus, in this set of experiments the initial stage of interface K evolution was not observed. To study the interaction of a plane reflected front with an interface at the linear stage of evolution, we used the combinations of gases with lower Atwood numbers, providing the prolongation of this stage. Fig. 3b represents the interferograms of the interaction of reflected shock wave R with K . A different recording has been carried out for the evolution of interface K perturbations after interaction with S and evolution of these perturbations after interaction with the reflected shock wave R .

4. Discussion

The shock wave passage through the interface K_0 separated from the pure gases by an undulate surface, has been studied in series of experiments. The thickness of interface $\delta(y)$ (towards the normal to its surface) has been shown to depend on molecular diffusion. The shock wave S_0 passage through K_0 reduced its thickness $\delta(y)$ and the amplitude a_k^* by the value dependent on the shock front compression. The reduction of amplitude $a_k(t)$ growth rate in the linear region ($a_k(t) < 0.5\lambda$) resulted in decrease of growth reduction factor ψ_e comparing to the value given by the Richtmyer-Meshkov equation.

$$da_k/dt = a_k^* [u] Ak$$

Table 1 represents the values λ , δ , A , ψ_e obtained by the processing of experimental data. Sturtevant [5] has suggested for the shock-induced impulsive acceleration, an equation [2], which described the evolution of a layer with distribution $\rho = \rho(x)$, separating two incompressible fluids. In the field of acceleration $g = g_0$ when g_0 was replaced by $g = [u]\delta(t_i)$. The growth reduction factor, according to [5], can be determined by the eigenvalue equation.

$$\frac{d}{dx} \left(\rho \frac{du}{dx} \right) = uk^2 \left[\rho - \frac{\psi_n(A, \delta)}{Ak} \frac{d\rho}{dx} \right]$$

The values ψ_n calculated for the terms of experiment are represented in Table 1.

Table 1. The values of interface amplitude growth reduction factor ψ at the linear stage RMI ($a_k < \lambda$).

No. of exp.	Shock wave S,R passes from/to	Atwood Number A	λ (mm)	δ (mm)	kd	ψ_e	ψ_n
471	S:He/Ar	0.76	13.5	3.6	1.7	2.1	1.9
474	S:He/Ar	0.76	14.4	4.5	2.0	2.0	1.9
475	S:He/Ar	0.76	16.5	3.0	1.1	1.7	1.6
477(1)	S:He/Ar	0.76	13.1	3.0	1.4	1.3	1.6
477(2)	S:He/Ar	0.76	16.4	3.0	1.1	1.9	1.8
488	S:Ar/He	0.76	20,9	8.0	2.4	5.4	2.4
	R:He/Ar	0.76	20.9	3.0	0.9	1.5	1.5
490	S:Ar/He	0.76	30.1	3.5	0.73	3.7	1.5
	R:He/Ar	0.76					
491	S:Ar/ (He+Ar)	0.24	10.5	4.1	2.44	5.3	2.8
	R: (Ar+He)/Ar	0,23	10.5	2.9	1.58	2.9	2.3

There is a good agreement between ψ_e and ψ_n except for three cases. For 488 (S: Ar/He) and 491 (S: Ar/ He + Ar), the initial amplitude was difficult to measure. The disagreement for 490 (S: He/Ar) is not understood.

5. Conclusions

The experimental study of the shock wave interaction with the interface separating gases of different density has been carried out. It has been found that at initial stage of interface evolution ($a_k(t) < \lambda$), the amplitude $a_k(t)$ of surface separating the interface from the "pure" gases grew more slowly than for discontinuous interface in the same conditions. The decrease of the growth reduction factor ψ_e obtained in experiment has shown a good agreement with the values ψ_n calculated from the equation [5]. The evolution of the surface perturbations at non-

linear and transient stages has appeared to be qualitatively similar to the evolution of the discontinuous interface: at the non-linear stage, "spikes" and "bubbles" appeared and at the transient stage, on the "spike" edge mushroom-like vortical structures appeared.

Acknowledgement

We acknowledge with gratitude the generous help of Dr J.F. Haas in discussing and preparing the manuscript.

References

1. S. Chandrasekhar. *Hydrodynamics and hydrodynamic stability*. Oxford. 1961.
2. R.E. Duff, F.H Harlow, and C.W. Hirt. Effects of diffusion on interface instability between gases. 1962 *Phys. Fluids*, v.3, no.4, pp.417-425.
3. E.G. Gamalii, S.G. Zaytsev, I.G. Lebo, V.B. Rozanov, S.N. Titov, E.I. Chebotareva. Interaction of a shock wave with an interface between two gases of different density. 1988. *Teplofizika vysokikh temperatur*, v.26, no.5, pp.960-964.
4. M. Brouillette and B Sturtevant. Growth induced by multiple shock waves normally incident on plane gaseous interface. 1989. *Physica D*, v.37, pp.248-263.
5. M. Brouillette and B Sturtevant. Richtmyer-Meshkov Instability at a Continuous Interface. 1990. In: *Shock waves and Shock Tubes*. Ed. Yong W. Kim. Lehigh University.
6. C Cavallier, H.Croso, P.Gandebouef, J.F. Haas and G. Rodriguez. Results from the Vaujours vertical shock tube. *Proceedings of the 3rd International Workshop on the Physics of Compressible Turbulent Mixing*. Abbey of Royuamont (France), 17-19 June 1991.

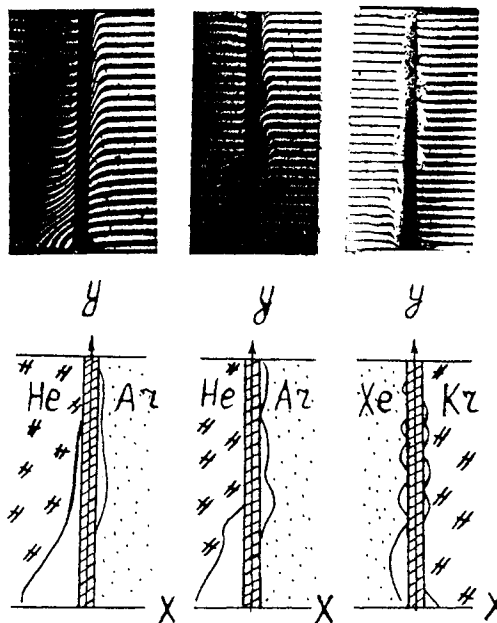


FIGURE 1: The interferograms and their sketches for different types of continuous interface. (a) $Re < 40$. (b) $Re \approx 60$. (c) $Re > 1000$. $Re = u\delta/\nu$, where u is the velocity of the sliding plate, δ is the thickness of the interface, and ν is the viscosity.

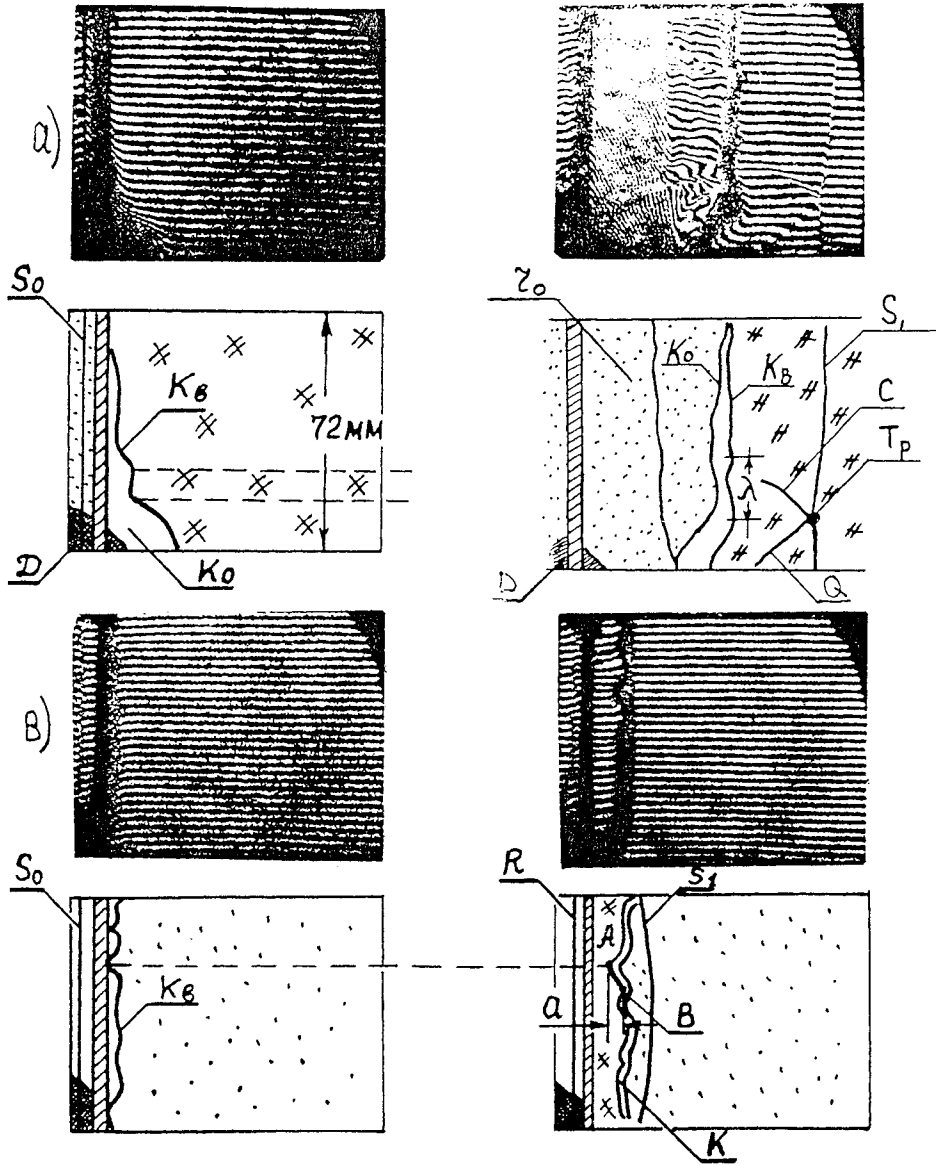


FIGURE 2: The interaction of a shock wave with the continuous interface. a,b - the interferograms and sketches for the shock passage from a light gas to the heavy one and vice versa, respectively. S_0 - the incident shock wave; K_0 - the initial continuous interface; K_a , K_b - the surface between the mixing zone and the pure gas; R - the reflected shock wave; C - the second shock wave; Q - tangential surface; r - the rarefaction wave; T_P - triple point; D - a defect of glass.

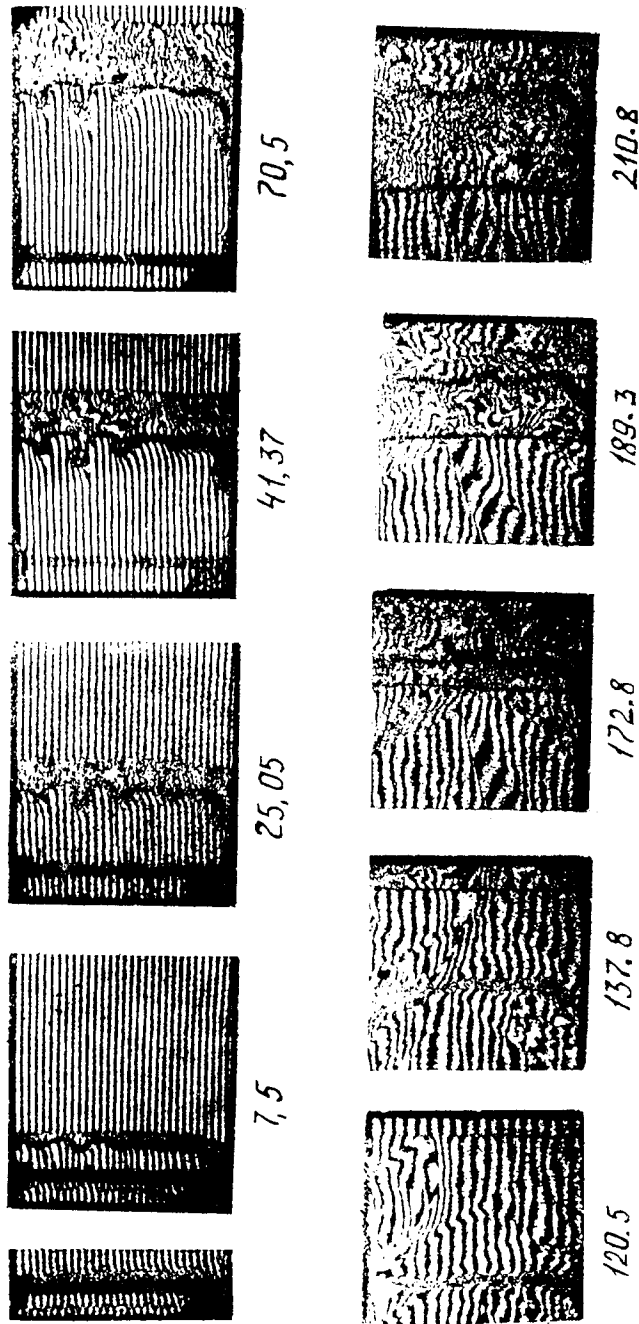


FIGURE 3: (a) The evolution of a continuous interface after the interaction with the incident shock wave passed from He to Ar. (b) The evolution of a continuous interface after the interaction with the reflected shock wave passed from He+Ar to Ar.

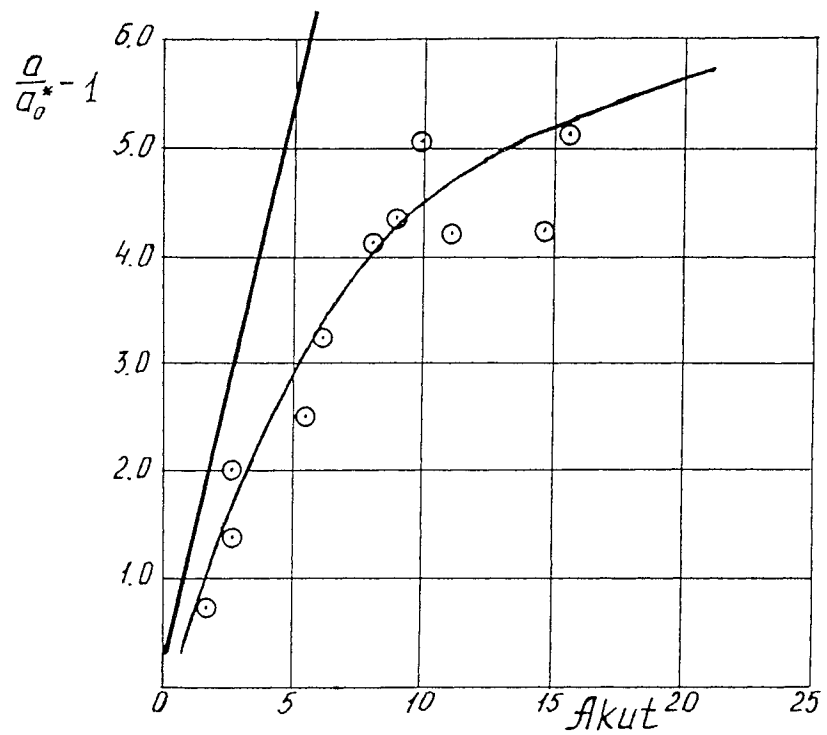


Fig. 4. The amplitude of the surface between the mixing zone and the pure gas versus $Akut$, where: A - Atwood number, k - wave number, u - velocity of the shocked gas, t - time.

III

Shear and vortex flows

THE EFFECTS OF TURBULENCE AND VISCOSITY
ON STRUCTURE OF THIN VORTEX RINGS

S.M. Bakhrakh, N.S. Darowa, G.V. Zharova, V.A. Zhmailo, V.P. Stazenko
Russian Federal Nuclear Center
Institute of Experimental Physics
Arzamas-16, 607200, Russia

ABSTRACT

We present and discuss the formulas describing the influence of turbulence and molecular viscosity on the structure of thin cylindrical and ring vortices.

The statement and results of numerical and analytical calculations of turbulent mixing in those vortices (for homogeneous fluids) are described.

The results of calculation are compared with experiments.

Formation and movement of vortex rings and cylinders are described in a lot of publications (see for example 1,2). The turbulence is very suppressed in these flows (see review 3), as it is demonstrated in the experimental works 3-5.

Here we offer some simple variants of equations (similar to 2,7) for description of turbulent mixing (TM) in cylindrical vortices and an approximate way to calculate TM in thin vortex rings by means of these equations.

Our approach includes effects of molecular viscosity too.

Let us consider the cylindrically symmetrical flow of homogeneous fluid. At first we suppose that azimuthal component of velocity $w(r,t)$ is present only. Equations, describing this flow, can be obtained as partial case of equations 8. It turns out:

$$\frac{\partial \Gamma}{\partial t} = \frac{1}{r} \frac{\partial}{\partial r} [(-r^2 R_{12}) + r^3 \nu \frac{\partial}{\partial r} (\frac{\Gamma}{r^2})] \quad (1)$$

$$\frac{\partial R_{12}}{\partial t} = \frac{M_\nu R_{22}}{2} - \frac{R_{11} M_\nu}{2} - \frac{R_{12}}{\tau_1} - R_{12} S_\nu + \text{Diff}(R_{12}) \quad (2)$$

$$\frac{\partial R_{11}}{\partial t} = M_\nu R_{12} + \frac{1}{\tau_1} (\frac{q^2}{3} - R_{11}) - S_\nu R_{11} - \frac{b q^2}{\tau_1} + \text{Diff}(R_{11}) \quad (3)$$

$$\frac{\partial R_{22}}{\partial t} = -M_\nu R_{12} + \frac{1}{\tau_1} (\frac{q^2}{3} - R_{22}) - S_\nu R_{22} - \frac{b q^2}{\tau_1} + \text{Diff}(R_{22}) \quad (4)$$

$$\frac{\partial q^2}{\partial t} = -M_1 R_{12} - \frac{3 b q^2}{\tau_1} - S_\nu q^2 + \text{Diff}(q^2) \quad (5)$$

Here :

$$\Gamma = wr, \quad 2\pi\Gamma - \text{circulation}; \quad R_{ik} - \text{components of Reynolds tensor};$$

$$q^2 = \sum R_{ii}; \quad M_\nu = \frac{2\partial\Gamma}{r\partial r}; \quad M_1 = \frac{4\Gamma}{r^2}; \quad M_1 = M_\nu - M_\nu = 2r \frac{\partial}{\partial r} (\frac{\Gamma}{r^2});$$

$$\text{Diff}(q^2) = \frac{c_1}{r} \frac{\partial}{\partial r} (qr_1 \frac{\partial q^2}{\partial r}); \quad S_\nu = 2a\nu/\Lambda^2; \quad \nu - \text{molecular viscosity};$$

$$\tau_1 = \Lambda/q \tag{6}$$

There are expressions for the other quantities of type $\text{Diff}(R,k)$ in τ, s ; a, b - numerical coefficients.

Λ is the scale of TM. We use the simplest formula for Λ below:

$$\Lambda = \alpha L \tag{7}$$

where α - empirical coefficient, L - characteristic scale of flow.

Considering the vortex rings, we shall assume them to be thin enough, i.e. $r_0 \gg R(t)$, where r_0 and R - radii of cross-section and ring axis correspondingly.

The flow depends on r coordinate only (as experiment ^{4,5} confirms) in this case, within distances $r \sim r_0$, but radial velocity resulting from changing ring radius $R(t)$ appears also.

Nevertheless we may use equations (1)-(7) for description of TM in that case if dependence $R(t)$ is known. Now:

$$r(r_1, t) = r_1 \frac{r_0(t)}{r_{00}} = r_1 \sqrt{R_0/R(t)} \equiv r_1 f(t),$$

where r_1 is initial coordinate of considered point r ; R_0, r_{00} - initial values of corresponding radii.

Then equations (1)-(7) keep their form being written as function of r_1 and :

$$\tau = \int_{t_0}^t f^2(t') dt'$$

(instead of r and t), but an additional term appears in equation (5), namely : $3df^2/dt^2 (q - R_{11} - R_{22})$. Besides, new functions $\tilde{R}k(r_1, \tau), \tilde{\Lambda}(\tau)$ appear instead of Rk and Λ :

$$\tilde{R}k(r_1, \tau) = Rk(r, t) f^2(t) ;$$

$$\tilde{\Lambda}(\tau) = \Lambda(t)/f(t)$$

(further we omit the symbol $\tilde{}$).

Solving the system (1)-(7) becomes more simple if we neglect the terms, connected with diffusion and nonstationarity. Then this system converts to algebraic one.

New system both simplifies numerical calculations and allows to analyze the influence of rotation and viscosity on TM in considered flows. The solution of these simplified equations has a form :

$$R_{12} = \frac{M_1 q^2 \tau^2 \mu}{2\tau_1 (1 + S_0 \tau_2^2)} \tag{8}$$

where :

$$1/\tau_2 = 1/\tau_1 + S_\nu$$

$$S_0 = M \nu M_\nu, \quad \mu = 1/3 - b$$

We can use formulas (7), (8) for solving equations (1), (5) (that corresponds to model 1, the most general of our models).

Model 2 is yet simpler. It uses equilibrium condition for q^2 also when equation (5) is solved. It gives for τ_1 :

$$12b + 4\tau_1 S_\nu = \frac{2\mu M_1^2}{S_\infty + (\frac{1}{\tau_1} + S_\nu)^2} \tag{9}$$

So, this model needs solution of one differential equation (1) only, where R_{12} is found from (8) and (9). It follows from (9) that its real positive solution has a form ($b=1/12$):

$$\frac{1}{\tau_1} = 2[(\frac{G_1}{3} + S_\nu^2)^{1/2} \cos(\frac{\pi-\Phi}{3}) - S_\nu] \tag{10}$$

where:

$$G_1 = G_\infty - S_\infty; \quad G_\infty \equiv M_1^2/2; \\ \cos\Phi = S_\nu(S_\infty + G_\infty + S_\nu^2)/(G_1/3 + S_\nu^2)^{3/2},$$

This solution exists if $\cos\Phi \leq 1$. In our case ($S_\nu^2/G_1 \ll 1$) last condition may be written as:

$$G_1^{3/2} (G_\infty + S_\infty)^{-1} \geq m\Omega_\infty/Re, \tag{11}$$

where Reynolds number $Re = \Omega_\infty r_0^2/\nu$; $m = 2a_3^{3/2}/\alpha^2$; Ω_∞ - characteristic value of angular velocity.

For an ideal fluid ($Re \rightarrow \infty$) we have, using (8), (10):

$$q^2 = \Lambda^2/\tau_1^2 \quad \Lambda^2 (\frac{\mu M_1^2}{6b} - S_\nu) = 4\Lambda^2 [\frac{\mu}{3b} (r \frac{\partial \Omega}{\partial r})^2 - \frac{1}{r^3} (\frac{\partial \Gamma^2}{\partial r})] \tag{12}$$

$$R_{12} = \frac{M_1 q^2}{8\tau_1 (S_\infty + 1/\tau_1^2)} = \frac{\Lambda^2}{G_\infty} G_1^{3/2} \mu M_1; \quad \Omega \equiv \Gamma/r^2 \tag{13}$$

If $G_1 < 0$, then: $q^2 = R_{12} = 0$, i.e. turbulence is suppressed when $Re \rightarrow \infty$ even.

Note that solution of equilibrium equation (2) for R_{12} has a form in "isotropic" case ($R_{22} = q^2/3$):

$$R_{12} = -\frac{\mu M_1 q^2 \tau_1^2}{2\tau_1} \tag{14}$$

and:

$$q^2 = \frac{\Lambda^2 M_1^2}{3} \tag{15}$$

instead of (12).

Comparing (12) and (15), we see that an account of Reynolds tensor anisotropy leads to appearing $S_\infty = \frac{4}{r^3} \frac{\partial \Gamma}{\partial r}$ in the formulae for q^2 . The sign of $\frac{\partial \Gamma}{\partial r}$ determines stabilizing or destabilizing role of rotation.

Note that relation (13) naturally yields a method (see ⁶) to account rotation effects which is generally used to match the theory with experimental data on circular flows

$$\Lambda = \Lambda_\infty (1 - \beta \frac{w \partial w}{r \partial r}) \tag{16}$$

where $\beta = 4/7$ - empirical coefficient. This expression is a consequence of (13), (14) when $|\frac{w}{r \partial w / \partial r}| \ll 1$.

We checked the models 1 and 2 by comparing their results with

some experiments 4,5 and other (more complex) models 5,7 .

There are measurements 5 of velocity profiles for the pair of aircraft tail vortices. As it follows from this data , the flow within a small distance from vortex axis ($r \leq 20m$) is cylindrically-symmetric ($t < 60 \div 70$ sec). It is also seen that radial and axial components of the velocity are negligible (i.e. $f(t)=1$ in our formulae). Re is about 10^7 , therefore viscosity effects don't take place (see (10), (11)).

At first we used simple model 2 to describe this experiment. The equations (1), (13) can be written in a standard form:

$$\frac{\partial \omega}{\partial \tau} = \frac{1}{y} \frac{\partial}{\partial y} (y D \frac{\partial \omega}{\partial y}) \quad ; \quad (17)$$

$$D = \frac{y \varepsilon^{3/2}}{\varepsilon_0} \quad , \quad y > y_1(t);$$

$$D = 0 \quad , \quad y \leq y_1(t);$$

$$\varepsilon = \varepsilon_0 - \frac{1}{y} \frac{\partial \gamma^2}{\partial y} \quad ; \quad \gamma \equiv y \omega \quad ;$$

$$\varepsilon_0 = (y \frac{\partial \omega}{\partial y})^2 \quad ; \quad y \equiv (\frac{r}{r_0})^2 \quad ;$$

$$\tau \equiv 8 \Omega_0 \mu \Lambda^2 (\frac{2\mu}{3b})^{1/2} t / r_0^2 \quad ;$$

$$\omega \equiv \Omega / \Omega_0 \quad ;$$

Here $b = 1/12$, $y_1(t)$ - the boundary of mixing zone - is determined from condition $\varepsilon(y_1, t) = 0$.

Following 5 we assumed $\Lambda(t) = 0.18 r_0$ and $\Omega_0 r_0^2 = 100$ m²/sec, $r_0 = 4m$. Boundary conditions were specified as form:

$$D \frac{\partial \omega}{\partial y} \Big|_{y \rightarrow 0} \rightarrow 0 \quad , \quad \gamma(y) \Big|_{y \rightarrow \infty} \rightarrow 1$$

Initial conditions (according to 5 for the initial moment $t_0 \approx 11$ sec):

$$\gamma(y, t_0) \equiv \gamma_0(y) = 1 - e^{-y}$$

Equation (17) was numerically solved using 1xD variant of method 10 .

Results of calculations and corresponding experimental data for circulation profiles are compared in the figures 1a,b,c,d (for some moments t). As it is seen, these calculations agree with experiment as close as those, carried out more complex model 5 .

The same calculations were done with model 1. In this case (according to 5) $\Lambda = 0.75m$, $q^2(t_0) = 1m^2/sec^2$. The results are near identical to previous ones.

For its simplicity model 2 can be used for clearing some basic features of considered flows. For this purpose we shall get approximate solution of (17). It is naturally to assume the function $\gamma(y, \tau)$ to be independent on r_0 when $y \gg 1$, $\tau \gg 1$, i.e. the solution is self-similar: $\gamma = \gamma(\eta)$, $\eta = y / \sqrt{\tau}$. It turns out (when $\eta \gg 1$):

$$\gamma = \gamma_2(y, \tau) = \frac{\eta^2}{\eta^2 - 1}$$

On the other hand, when $y \geq y_1(\tau) < 1$ we suppose $\varepsilon = 0$, therefore:

$$\gamma = \gamma_1(y, \tau) \equiv (y/y_1)^k \gamma_0(y_1) \quad , \quad k = 2 - \sqrt{3} \quad ,$$

where $\gamma_0(y_1)$ is initial value of $\gamma(y)$ at $y = y_1(\tau)$.

We shall assume

$$\begin{aligned} \gamma &= \gamma_1(y, \tau) \quad ; \quad y_1 \leq y \leq y_2(\tau) \quad ; \\ \gamma &= \gamma_2(y, \tau) \quad ; \quad y > y_2(\tau) \quad . \end{aligned}$$

The values of $y_1(\tau)$, $y_2(\tau)$ and $\gamma(y_2, \tau) \equiv \max\{\gamma(y, \tau)\}$ at time τ can be found by substituting (18) in the total moment conservation law:

$$\int_{y_1(\tau)}^{\infty} (\gamma(y) - \gamma_0(y)) dy = 0 \quad .$$

The results of this calculation are presented in fig.1(b,c). It's seen, there is a rather acceptable accordance with the numerical solution of equation (17). It turns out, further, that $y_1(\tau)$ - radius of laminar core - decreases with time (if $y_1 \ll 1$, $y \gg 1$) as:

$$y_1(\tau) = [y_2^k (1 - \frac{2}{\lambda})^{\frac{\xi}{k-1}}] \quad ; \quad \xi = \frac{1}{k-1} \quad ; \quad \lambda = 18 \quad ;$$

where $y_2(\tau) = \sqrt{\lambda \tau / 2}$ - is the point, where $\gamma(y)$ is maximal and equals $\gamma(y_2) = 1.12$.

The effects of Reynolds tensor anisotropy are illustrated by fig. 1d where circulation profile, calculated using isotropic variant of model 2, i.e. (14),(15). We see that mixing rate is considerably greater than experimental one.

Consider the effects of viscosity and turbulence anisotropy in the experiment 4 with a thin vortex ring moving in water. There are measurements of velocity profiles. The flow is cylindrically-symmetrical ($0.5 \text{ sec} < t < 3.5 \text{ sec}$) near vortex core according to data of this work, and initial profile is:

$$\Omega(y, t_0) = \Omega_0 \frac{1}{y} (1 - e^{-y}) \quad ,$$

where $\Omega_0 = 330 \div 350 \text{ sec}^{-1}$; $r_0 = 0.35 \text{ cm}$; $t_0 = 0.5 \text{ sec}$, i.e. $Re \approx 4 \cdot 10^3$.

Measured velocity profiles at $t = 0.5 \text{ sec}$ and $t = 3.5 \text{ sec}$ are shown in fig.2 (curves 1 and 2 accordingly). Curve 3 in this figure is result of simplest calculations which ignore viscosity and turbulent anisotropy (according to (14),(15) at $\tau_1 = \tau_2$). Here $t = 3.5 \text{ sec}$, $\alpha = 1/6$, $a = 3$, $L = r_0$, $f(t) = 1$. Comparing curves 2 and 3 we can conclude about considerable increase of TM when these effects are ignored. The curve 4 in fig. 2 was obtained by means of the complete model, i.e. using (1),(8),(10). We see that TM effects are suppressed enough in this model and there is reasonable agreement with experiment. Some additional calculation was done to clear role of the viscosity in that suppressing, namely, we assumed $S_0 = 0$ in equation (10) ("isotropic" approach). This run produced curve 5 in fig.2. We can conclude that curve 2 (experiment) and 5 are close and rather disagree with 3 in basic part of the flow.

It means that the role of viscosity and circulation in suppressing of turbulence is significant and comparable in such flow although Re is rather great ($Re \approx 4 \cdot 10^3$), their common effects can be described only if Reynolds tensor anisotropy is accounted.

References

1. M.A. Lavrentjev, B.V. Saabat, Problems of hydrodynamics and their mathematical model ("Science", Moscow, 1973) (in russian)
2. A.T. Onufriev, About turbulent moving in vortex ring core, Dynamical processes in gases and solid bodies (physical mechanics), vyp. 4, LGU, pp. 31-70 (in russian) (1980)
3. D.G. Akhmetov, O.P. Kisarow, Hydrodynamical structure of circular vortex, Journal prikladnoj mekhaniki i tekhnicheskoy fiziki, No4, pp. 120-123 (in russian) (1966)
4. T. Maxworthy, Some Experimental Studies of Vortex Rings, J. of Fl. Mech., vol. 81, Pt. 3. (1977)
5. A.M. Hecht, A.J. Bilanin, J.E. Hirsh, Turbulent Trailing Vortices in Stratified Fluids, AIAA J., No 6, pp. 691-698. (1981)
6. Turbulence, ed. by P.M. Bradshaw, Mashinostroenie, Moscow (in russian) (1980)
7. K.P. Donaldson, Calculation of turbulent flows in atmosphere and isolated vortex, Raketnaja tekhnika i kosmonawtika, vol. 10, No1, pp. 4-14 (in russian) (1972)
8. W.S. Lewellen, M.E. Teske, K.P. Donaldson, Calculation of density inhomogeneous flows by closing second moments equations of turbulent movement, Raketnaja tekhnika i kosmonawtika, vol. 14, No3, pp. 115-122, (in russian) (1976)
9. W.A. Wladimirow, B.A. Lugowtsew, W.F. Tarasow, Suppression of turbulence in cores of concentrated vortices, Journal prikladnoj mekhaniki i tekhnicheskoy fiziki, No5, p.9 (in russian) (1980)
10. G.W. Zharowa, W.A. Zaguskin, Calculation of heat conductivity on nonorthogonal grids, Woprosi mekhaniki i prikladnoj matematiki, Ed. Rostow university, p.54-60 (in russian) (1976)

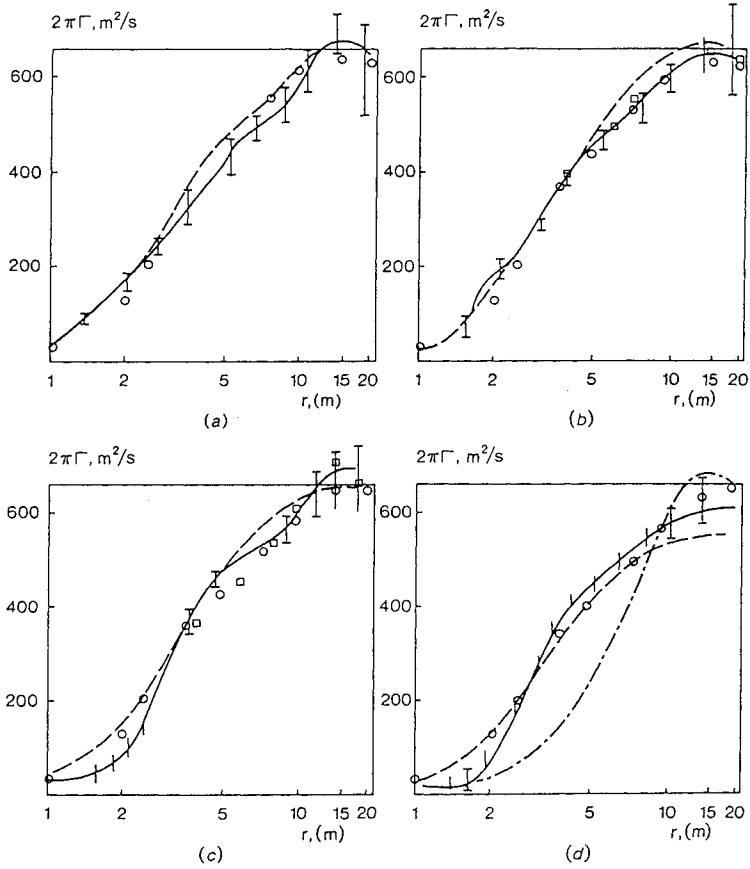


Fig. 1 Profiles of velocity circulation in cylindrical vortex for some t : a - 18 s, b - 25 s, c - 39 s, d - 55 s;
 — experimental data; O - model 2; - - - model [5]; □ - approximate solution;
 - · - isotropic model with viscosity.

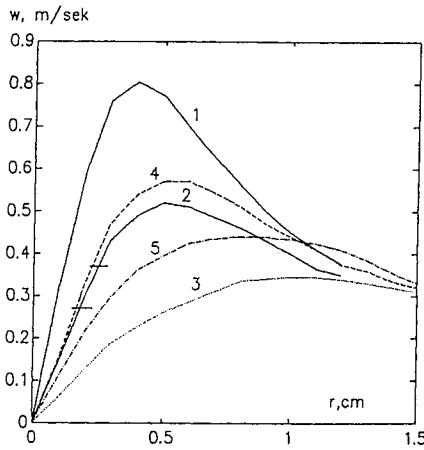


Fig.2. Rotational velocity in vortex ring

Simple models of stratified and compressible entrainment

Robert E. Breidenthal

Department of Aeronautics and Astronautics, University of Washington, Seattle 98195

Abstract

A simple, physical model for stratified entrainment is compared with a related one for compressible turbulence. Both models assume that an eddy must complete one rotation to engulf fluid, and that the engulfment process is intrinsically nonsteady. Depending on the Reynolds, Richardson, and Schmidt numbers, the model for stratified turbulence predicts six different entrainment regimes over the entire parameter range. Several of these regimes match earlier proposed models, such as that of Linden. At large Reynolds number, the particular regime depends on the size of the eddy whose Richardson number is unity, since this determines the ability of eddies to complete a rotation. Transitions between regimes occur when the largest and the smallest eddies have unity Richardson number. Another transition between regimes is expected when the entrainment rate associated with the diffusive Taylor layer equals that of the Batchelor layer, i.e., when the Richardson number equals the Schmidt or Prandtl number. This is in accord with the observations of Turner. The model for compressible turbulence presumes that only those eddies which are capable of responding to nonsteadiness during one rotation can engulf fluid. The largest such eddies take the largest gulps of engulfed fluid and therefore dominate the entrainment process. Their rotational Mach number is unity. According to the model, such sonic eddies control the mixing process. They are predicted to be three-dimensional, since only nearby disturbances can influence the nonsteady engulfment process during one vortex rotation. This is consistent with recent shear layer observations.

1. Introduction

Stratified and compressible turbulence have several obvious similarities. First, there is a wave speed in both cases, so one expects something important to occur when the eddy rotation time is equal to the

wave transit time across the eddy diameter. For compressible flow, this ratio is the eddy Mach number, and for stratified flow, the ratio is the inverse square root of the eddy Richardson number.

The second obvious feature is that as both the Mach and Richardson numbers increase, the entrainment rates decline dramatically. Third, one expects a transition when the aforementioned numbers are about unity. In compressible flow, there is a transition in entrainment rate when the large eddy Mach number is about one (Papamoschou and Roshko 1986). In stratified flow, there is a transition when the large eddy Richardson number is about one (Turner 1973).

This paper explores some recent theoretical notions about compressible and stratified entrainment. The treatment is incomplete, at best, since the effects of waves on entrainment are ignored.

2. Compressible entrainment

The central notion is that entrainment is intrinsically nonsteady. There is evidence that nonsteadiness is a requirement for entrainment. The remarkable discovery of zero shear layer growth by Oster and Wygnanski (1982) can be interpreted to mean that all entrainment ceases if the vortices are steady. Their vortices, which were steady in the region of zero growth, continued to rotate even though the Reynolds stresses and the molecular mixing vanished (Roberts, 1985). Their discoveries would seem to have a powerful message about vortices and entrainment. Here the message is taken to be that nonsteadiness is required for entrainment.

If true, then an eddy can only actively participate in the entrainment process if the signal from a nonsteady event can propagate to an appropriate region within an appropriate time. The only available scales are the eddy diameter and rotation period. If the information of a nonsteady event at one edge of an eddy can not propagate across the eddy diameter during one eddy rotation, then any nonsteadiness can not have influenced the eddy behavior. According to this argument (Breidenthal, 1992a), there can then be no entrainment by that eddy.

It follows that there must be a distinguished eddy size for which the nonsteady signal just arrives at the other side of the eddy in one vortex rotation. It seems natural to call this a sonic eddy. Define an eddy Mach number to be the eddy (rotational) speed divided by a reference speed of sound. Choose the dimensionless coefficient so that the sonic eddy has an eddy Mach number of unity.

For simplicity, assume a Kolmogorov inertial spectrum exists for all eddies smaller than the sonic eddy. Then the rotational Mach number of these eddies is less than one; they are subsonic in the sense of their rotational speed. Of course, they may be convected downstream at a highly supersonic

speed. However, the vortex dynamics can only depend on the *rotational* Mach number of an eddy, not on the relative speed of an arbitrary inertial observer.

If, as inferred below, the largest scale eddies are temporally and spatially unorganized, the mean velocity profile will be roughly equal to any instantaneous one. It follows that in a shear flow of thickness δ and velocity jump ΔU , the sonic eddy size λ^* is approximately

$$\frac{\lambda^*}{\delta} = \frac{a^*}{\Delta U} = M^{-1}. \quad (1)$$

Here a^* is a reference speed of sound and M is the rotational Mach number of the largest eddies.

The sonic eddy divides the turbulent vortices into two groups. Eddies larger than λ^* are supersonic. They are not capable of internal communication during one of their own rotations, the time of Roshko's engulfment (Roshko 1976). Consequently, they are steady; like Oster and Wygnanski's vortices, they can not entrain. Eddies smaller than λ^* are subsonic. As a first approximation, they are taken to be completely incompressible.

In incompressible turbulence, the largest eddies control the entrainment rate. They engulf the largest volume of entrained fluid at each rotation. Even though their rotation period is greater than that of smaller eddies, their larger gulps more than compensate.

In compressible turbulence, the largest eddies are supersonic, and thus presumed to be completely impotent at entrainment. The largest, non-supersonic eddy, which is capable of entrainment, is the sonic eddy. The entrainment rate is determined by it. This is analogous to choking in a channel flow, where the conditions at a sonic throat determine the mass flow along the channel.

The transition from incompressible to compressible entrainment occurs when the Mach number of the largest eddies is unity. The model assumes this transition is sharp for simplicity. Above the transition, the model predicts that the entrainment rate should be independent of Mach number, at least until the next transition. The reason for this is that the sonic eddy entrainment time is the ratio λ^*/a^* , which from eq. (1) is independent of the speed of sound a^* and hence Mach number. Another consequence of this argument is that the structures responsible for entrainment must be three-dimensional, since there is not enough time for nonsteady information to propagate more than the diameter of the sonic eddies.

As the Mach number increases, the sonic eddy size shrinks, according to eq. (1). At some point, it becomes equal to the smallest possible eddy size, the Kolmogorov microscale. Assuming that the subsonic eddies obey a Kolmogorov spectrum based on the sonic eddy, this occurs when

$$M = \text{Re}^{1/2}, \quad (2)$$

where Re is the (large scale) Reynolds number. Here the Kolmogorov microscale is also just equal to the mean free path of the gas l .

At higher Mach numbers, all eddies are now supersonic. Therefore the entrainment rate is controlled by the characteristic time at scale l ,

$$\tau_l = \frac{l}{a^*} = \frac{M^2}{\text{Re}} \frac{\delta}{\Delta U}. \quad (3)$$

Consequently, the entrainment rate should go as Re/M^2 in this regime.

A further transition is expected at extreme Mach numbers when the mean free path of the gas becomes equal to the global eddy scale, at

$$M = \text{Re}. \quad (4)$$

Above this final transition, no eddies are possible. Without any length scale in the problem, the entrainment rate can only depend on the speed of sound, so that the spreading angle should vary inversely with Mach number.

Figure 1 is a schematic showing the different entrainment regimes according to the model. The entrainment rate is indicated within each regime. The double line between regimes I and II indicates a discontinuity.

Comparison with experiment

There seems to be general agreement between this model and experiment in supersonic flow. The shear layer measurements of Papamoschou & Roshko (1986), however, reveal a gradual rather than a sharp transition at about unity Mach number. Clemens & Mungal (1978) have confirmed that the supersonic structure is three-dimensional, in sharp contrast to the subsonic case. Von Gierke *et al.* (1952) found that the noise spectrum of a jet could be explained by noise-producing eddies corresponding to the sonic eddy of the model. Hypersonic wake growth (Finson 1973) seems to be described by a simple turbulent diffusion argument based on the properties of the sonic eddy.

One prediction of the model not yet tested is the effect of the Mach number on the concentration field of an inert scalar. The model predicts that the instantaneous concentration pattern should be a series of steps across a shear layer, each step the size of the sonic eddy.

3. Stratified entrainment

Consider turbulence generated below a stratified interface. The model neglects the effects of stratification until the Richardson number Ri of the impinging large eddies is equal to one. At larger Ri , the largest eddies are "stratified." The smallest eddies will become stratified when the Richardson number at the Kolmogorov microscale is one. Assuming a Kolmogorov spectrum, this occurs when

$$Ri = Re^{1/4}. \quad (5)$$

For even stronger stratification, then the interface is essentially flat, so that the entrainment rate can no longer depend on the Richardson number. The problem is analogous to heat transfer at a solid surface. Clearly the relevant diffusivity must enter the problem. Surface renewal theory (Cohen 1983) then is appropriate, but there are two possible eddy scales to choose from, the largest and the smallest.

Persistence

It has been recently suggested (Cotel & Breidenthal 1993) that another parameter, persistence, determines which eddy to choose. If the large eddy pattern is sufficiently persistent, so that the large scale vortices make many rotations while remaining in one place, then it should not matter whether small scale eddies are present or not. This is because the stationary process by which a fluid element is ultimately convected away from the interface requires a sequence of events, the slowest of which will be rate-limiting. The large eddies have the largest rotation period, so they are the ones which enter the surface renewal theory if persistent.

On the other hand, if the number of rotations the large eddies make while residing in one place is small enough, then a fluid element initially near the interface need not wait until it is transported away from the interface by the large eddies. The process is no longer a stationary sequence, so the parcel can be removed by the smallest eddies. In other words, now the eddies with the smallest speed control entrainment instead of the ones with the longest rotation period. Surface renewal theory applies with Kolmogorov microscale eddies.

Persistence also seems to play a role at lower stratification, when the interface is convoluted. Various measurements of stratified entrainment yield a general dependence on Richardson number to the power α . Measurements of α in different turbulent flows have been reported (Fernando 1987, Maderich *et al.* 1992, Piat & Hopfinger 1981, and Price 1979). In stirred grid experiments, Turner (1968), Linden (1973), and Shy (1990) all find $\alpha = -3/2$, at least if the stratification is due to salt in water. Turner (1968) reports that if the stratification is due to heat in water, the observations obey $\alpha = -1$ for Richardson numbers greater than about seven.

In other experiments such as Baines (1975), the measurements indicate $\alpha = -1/2$. It is natural to look for simple explanations to such a pattern.

Schmidt number

The results of Turner (1968) unambiguously indicate that Schmidt number must play a role, not just when the interface is flat as discussed above, but even when it is highly convoluted. It has been suggested (Breidenthal 1992b) that a transition between regimes should occur when $Ri = Sc$ or Pr if the stratification is due to heat. According to this model, a transition from $\alpha = -3/2$ to $\alpha = -1$ occurs when small eddy "nibbling" of the Taylor layers associated with Linden's rebound process (Linden 1973) first becomes important.

Another transition has recently been suggested, when persistence effects enter the problem (Cotel & Breidenthal 1993). According to the latest version of the model, a transition occurs when $Ri = T$, where T is the dimensionless persistence time, equal to the number of rotations a large scale vortex makes before it moves a distance equal to its own diameter. For $Ri \geq T$, the flow is nonpersistent and $\alpha = -3/2$, while for $Ri \leq T$, the flow is persistent and $\alpha = -1/2$. Just as in the case of a flat interface, the entrainment rate jumps at this transition.

Figure 2 is a schematic diagram taken from Cotel & Breidenthal showing the different regimes for stratified entrainment. As in figure 1, the double lines again signify a discontinuity at a transition. The interface is flat in regimes V and VI. A turbulent flow is nonpersistent if the persistence parameter T is small, of order one. On the other hand, no matter how large a fixed value T acquires, as in a stationary impinging jet, according to this model the flow will nonetheless become nonpersistent at sufficiently large Reynolds and Richardson numbers. This is because in this limit, the small eddies become so slow at transporting fluid parcels that even after a considerable number of rotations, the large eddies have moved somewhere else before the small eddies have accomplished their transport.

Comparison with experiment

The stratified model seems to be accord with almost all the observations. One would expect stirred grid turbulence to be highly nonpersistent, so that $\alpha = -3/2$. Recent measurements of a persistent, impinging jet yields $\alpha = -1/2$ as well as a sudden jump at about $Ri = Re^{1/4}$ to an entrainment rate independent of Ri (Cotel & Breidenthal). Heat transfer measurements at solid surfaces are also consistent with the model in the limit of large Ri (Dowling *et al.* 1990).

However, one experiment seems to be at variance with the model. Baines (1975) measured the entrainment rate of an apparently stationary impinging plume. He found $\alpha = -3/2$, in contrast to the expected value of

$\alpha = -1/2$, as had been observed for the jet. A possible explanation is that the plume may have larger fluctuations than the jet, making the plume effectively nonpersistent. The question remains open.

4. Conclusions

This paper has discussed the use of simple models in an attempt to describe the basic features of compressible and stratified entrainment. Similar notions about the entrainment process led to schematic diagrams outlining different entrainment regimes. Transitions occurred between regimes when the Mach or Richardson number of the largest and the smallest eddies became unity. While not identical, the two diagrams become more alike for the case of unity Schmidt and persistence numbers.

ACKNOWLEDGMENTS

The author would like to thank Aline Cotel, Marcia Baker, Jakob Keller, Ben Saylor, Hamid Johari, Perry Meyer, David Dowling, Bob Abel, Roger Campbell, Anatol Roshko, Godfrey Mungal, Michael Finson, Steve Crow, and Linda Hedges for their insightful comments. This work was supported by NSF ATM - 8611225A02 and AFOSR-87-0366.

REFERENCES

- Baines, W.D. 1975 Entrainment by a plume or jet at a density interface, *J. Fluid Mech.* **68**, 309-320.
- Breidenthal, R.E. 1992a Sonic eddy - a model for compressible turbulence, *AIAA J.* **30**(1), 101-104.
- Breidenthal, R.E. 1992b Entrainment at thin stratified interfaces: The effects of Schmidt, Richardson, and Reynolds numbers, *Phys. Fluids A*, **4**(10), 2141-2144.
- Clemens, N.T. & Mungal, M.G. 1978 Two- and three- dimensional effects in the supersonic mixing layer *AIAA Paper* 90-1978, July, Orlando, FL.
- Cohen, Y. 1983 Mass transfer across a sheared, wavy air-water interface, *Int. J. Heat Mass Transfer* **26**(9), 1289-97.
- Cotel, A.J. & Breidenthal, R.E. 1993 Persistence effects in stratified jet entrainment, submitted to *Phys. Fluids A*.
- Dowling, D.R., Buonadonna, V.R. & Breidenthal, R.E. 1990 Temperature transients in a cylindrical pressure vessel filled from vacuum, *J. Thermophysics and Heat Transfer*, **4**(4), 504-511.

- Fernando, H.J.S. 1987 Turbulent mixing in the presence of a stabilizing buoyancy flux, *Stratified Flows*, Proceeding of the Third International Symposium on Stratified Flows, ed. E.J. List and G.H. Jirka, Caltech, 447.
- Finson, M.L. 1973 Hypersonic wake aerodynamics at high Reynolds numbers *AIAA J.* **11**(8), 1137-1145.
- Kantha, L.H., Phillips, O.M. & Azad, R.S. 1977 On turbulent entrainment at a stable density interface, *J. Fluid Mech.* **79**:753-768.
- Landau, L.D. & Lifshitz, E.M. 1959 *Fluid Mechanics*, Pergamon Press, 122.
- Linden, P.F. 1973 The interaction of a vortex ring with a sharp density interface: a model for turbulent entrainment, *J. Fluid Mech.* **60**, 467-480.
- Maderich, V.S., Konovalov, O.M. & Konstantinov, S.I. 1992 Mixing efficiency and processes of restratification in the stably stratified medium, *J. Marine Hydrophys.* **6** (in Russian).
- Oster, D. & Wygnanski, I. 1982 The forced mixing layer between parallel streams, *J. Fluid Mech.* **123**, 91-130.
- Papamoschou, D. & Roshko, A. 1986 Observations of supersonic free shear layers, *AIAA Paper* 86-0162.
- Piat, J.-F. & Hopfinger, E.J. 1981 A boundary layer topped by a density interface, **113**, 411-432.
- Price, J.F. 1979 On the scaling of stress-driven entrainment experiments, *J. Fluid Mech.* **90**, 509-529.
- Roberts, G.A. 1985 Effects of a periodic disturbance on structure and mixing in turbulent shear layers and wakes, Ph.D. Dissertation, California Inst. of Technology, Pasadena, CA.
- Roshko, A. 1976 Structure of turbulent shear flows: A new look *AIAA J.* **14**, 1349-1357.
- Shy, S. S. 1990 A chemically reacting, turbulent stratified interface, Ph.D. Thesis, University of Washington.
- Turner, J.S. 1968 The influence of molecular diffusivity on turbulent entrainment across a density interface, *J. Fluid Mech.* **33**:639-56.
- Turner, J.S. 1973 *Buoyancy Effects in Fluids*, Cambridge University Press, 291.

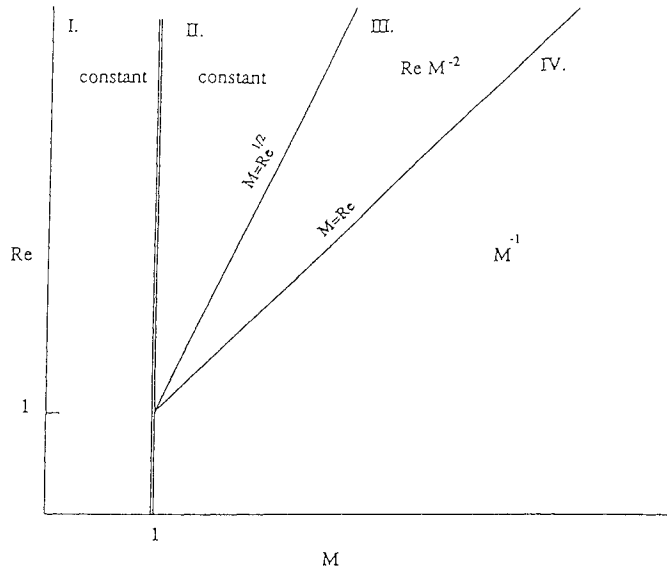


Figure 1. Schematic of the regimes of compressible entrainment.

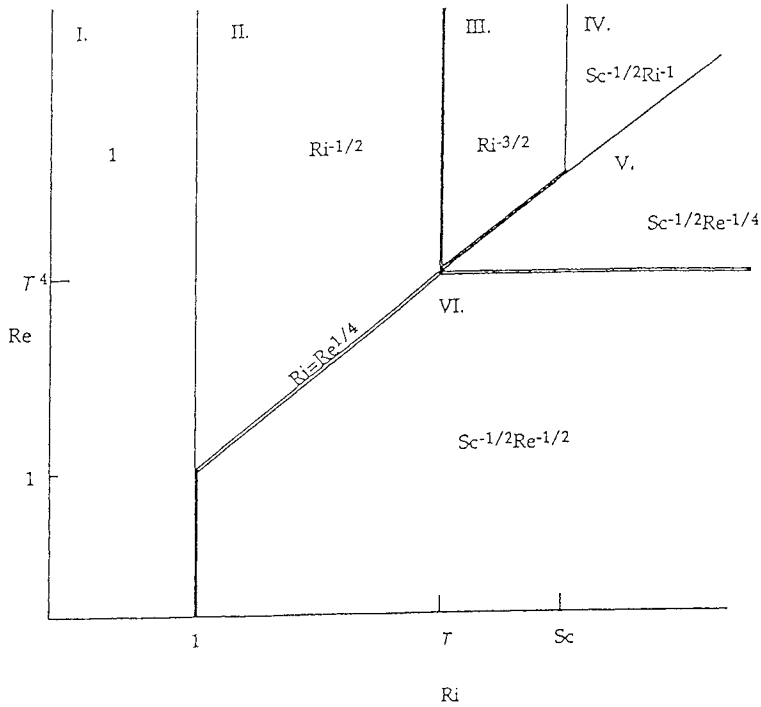


Figure 2. Schematic of the regimes of stratified entrainment.

A COMBINED THEORETICAL AND NUMERICAL STUDY OF THREE DIMENSIONAL JET MIXING

by

E. F. Brown
J. E. Burr
S. L. Huang
T. B. Mutter

Virginia Polytechnic Institute and State University

Blacksburg, VA

The purpose of this work is to increase the level of our understanding of the enhanced entrainment exhibited by elliptical jets and to investigate the role played by combustion in this process. Two approaches were used in this study, numerical simulation and linear stability analysis. The numerical simulations were obtained with the MILES algorithm, a monotone integrated LES algorithm developed by Jay Boris and his collaborators at the Naval Research Laboratory in Washington, DC, and the linear stability analysis was carried out with the MATRIX program which we developed. Both the numerical simulations and the linear stability analysis were carried out on state-of-the-art super computers, the CM-2 at the Naval Research Laboratory in Washington DC and the Cray YM-P at the National Center for Supercomputing Applications in Champaign-Urbana, Illinois. We were aided in this work by a powerful numerical flow visualization software package called FAST developed at the NASA Ames Research Center.

Allow me to again state the objective of our work. It is to combine the results of numerical simulations and linear stability theory to produce a phenomenological description of the mixing processes in elliptical jets which accounts for their substantially increased entrainment in comparison with their circular counterparts. Furthermore, we hope to be able to use this understanding to further enhance the entrainment process and thereby to suggest ways of minimizing the acoustical, thermal, and kinematic signatures of aircraft and ships, to permit the design of more compact and efficient heat exchangers, combustors, and chemical reactors, and to offer the possibility of minimizing the environmental impact of thermal and chemical discharges. I will first discuss the results of our numerical simulations followed by a discussion of the insight provided by our linear stability analysis, then present the results of some recent simulations, and finally describe our plans for future work. The results of our numerical simulations are clearly more general

than the results of our linear stability analysis because they include nonlinear effects and are therefore not limited to only the region in close proximity to the nozzle exit.

Our simulations were produced by helically exciting elliptical and circular jet flows and observing the differences between them. First of all we found that the elliptical jet displays a filament-like nature unseen in the circular jet simulations (Fig. 1). In other words at the same time step the elliptical jet retained far more of its original shape. Upon undertaking a spatial FFT analysis of these structures, we found the small wave numbers were much less densely populated in the case of the elliptical jet than in the case of the circular jet, and in the case of the elliptical jet the small wave numbers were much less densely populated in the major axis plane than in the minor axis plane (Fig. 2). Thus, in addition to the structure being finer in the elliptical jet than in the circular jet, the structure is finer on the major axis than on the minor one. This is not inconsistent with the experimental observations of Ho and Gutmark which showed that the entrainment is greater on the minor axis than on the major axis. (We will shortly see from the results of linear stability analysis that the increased entrainment and larger structures on the minor axis are connected with a locally greater value of the growth rate there.) The more filamentous nature of the elliptical jet simulation is also brought out in contours of streamwise vorticity which show clear strands of concentrated downstream vorticity in the case of the elliptical jet in contrast with the lower levels and more diffuse distribution of the streamwise vorticity in the case of the circular jet (Fig. 3).

Our attempts at identifying the mechanisms for the increased entrainment of the elliptical jet from the results of the numerical simulations were not successful. We have concluded that at least part of our failure was due to the fact that the far field region is exceedingly complex from a topological point of view. It seemed appropriate therefore to pursue its analysis from the standpoint of linear stability analysis. In addition, since fine grid simulations can easily require tens of hours of Cray YM-P time we were also motivated to pursue linear stability analysis in an attempt to economically perform an investigation of the parameters which influence the mixing process. I believe that we have been quite successful in this regard.

First of all, allow me to describe MATRIX, our linear stability analysis program. In these calculations it is assumed that the basic flow is inviscid and parallel; however, the flow is allowed to be compressible and swirling. For high resolution in the near field, we use generalized nonorthogonal elliptical coordinates and discretize the governing equations by means of a combined Chebyshev/Fourier spectral collocation method. The resulting algebraic eigenvalue problem is solved by a combination

of the Q-R and power methods. Both axisymmetric and azimuthal modes have been calculated for a wide variety of circular and elliptical jet geometries including various aspect ratios, both thick and thin shear layers, uniformly and nonuniformly azimuthally-distributed shear layer thicknesses, compressible and incompressible flow, and both with and without the presence of swirl. We found that without exception nonuniformly distributed shear layers, swirl, and increasing aspect ratios contribute increased azimuthal nonuniformity both in terms of the distribution of the eigenfunction as well as in the growth of the shear layer. We speculate that when enhanced mixing occurs, it is this enhanced asymmetry (and not the growth rate, which decreased in all cases) which accounts for the increased mixing.

Focusing for a moment specifically on the elliptical jet, we found that the eigenfunction of the first azimuthal (sine) mode possesses a maximum on the minor axis and that the growth rate of that mode is much greater than the growth rate of the cosine mode, which has a maximum on the major axis. In addition we found that the phase speed of the cosine mode is much greater than the phase speed of the sine mode. The greater growth rate on the minor axis explains the larger structure the minor axis mentioned in connection with the numerical simulations. In addition, the higher phase speed of the cosine mode (which has a maximum amplitude on the major axis) is consistent with the observation of Hussein that the portion of the vortex ring lying along the major axis leads the portion of the vortex ring located along the minor axis. It is this out-of-plane motion of the vortex ring which accounts for the phenomena of axis switching which has long been associated with the behavior of elliptical jets. Finally we have discovered that in the case of the elliptical jet most modes, particularly in the presence of swirl, have more or less the same growth rates. This competition among the various modes provides a convincing explanation for finer overall structure exhibited by elliptical jets.

These observations were drawn from more than 100 calculations. Space permits us to substantiate only a few of these observations. In the upper third of Fig. 4 are the axial velocity eigenfunction contours of the uniform-shear-layer, nonswirling circular ($AR = 1$) and elliptical ($AR = 2$) jets. The clear asymmetry of the elliptical jet case is easily seen as is the decreasing growth rate (in the middle third of the right-hand panel) as the aspect ratio increases. The azimuthal nonuniformities in the shear layer thickness explored in the left-hand panel serve to further decrease the growth rate. Swirl (left-hand panel of Fig. 5) accentuates the nonuniformity by moving the maximum in the eigenfunction from the minor axis and driving its value to nearly zero on the major axis. Compressibility has little effect on the nature of the eigenfunction but decreases the growth rate sharply (right-hand panel of figure).

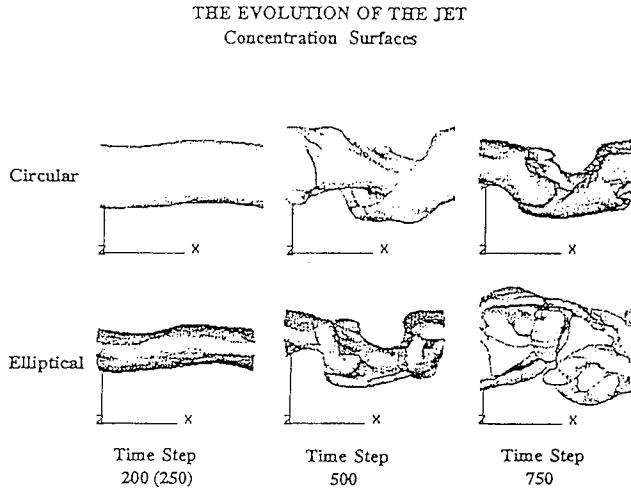


Figure 1. A Comparison of the Concentration Surfaces in Elliptical and Circular Jets.

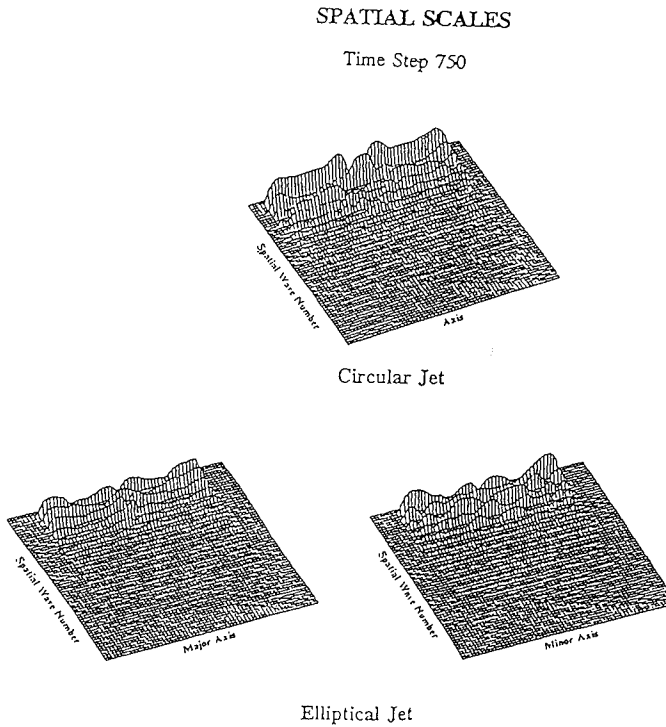
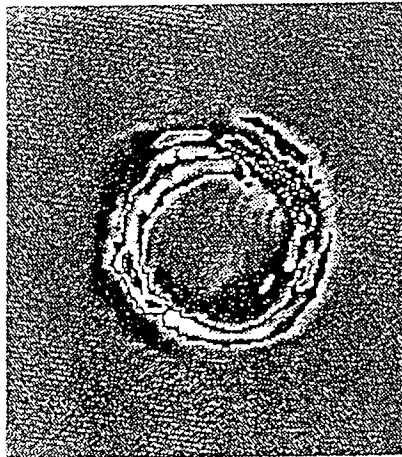


Figure 2. A Comparison of Spatial Wave Numbers.

STREAMWISE VORTICITY CONTOURS



Circular Jet --- Time Step 200



Elliptical Jet --- Time Step 250

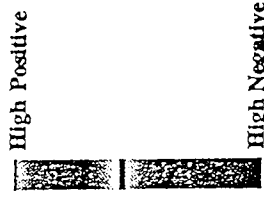


Figure 3. Evolution of Streamwise Vorticity.

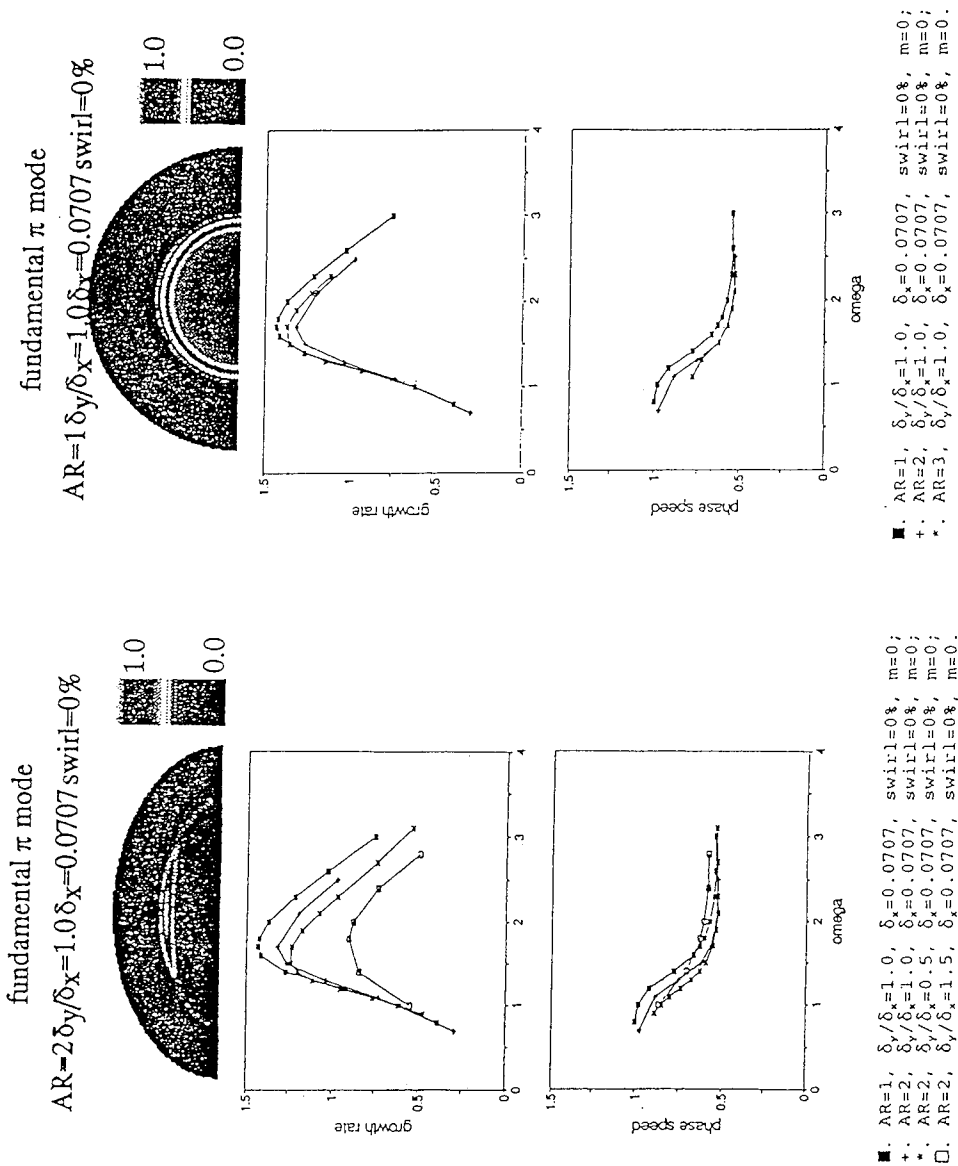


Figure 4. The Effects of Geometry.

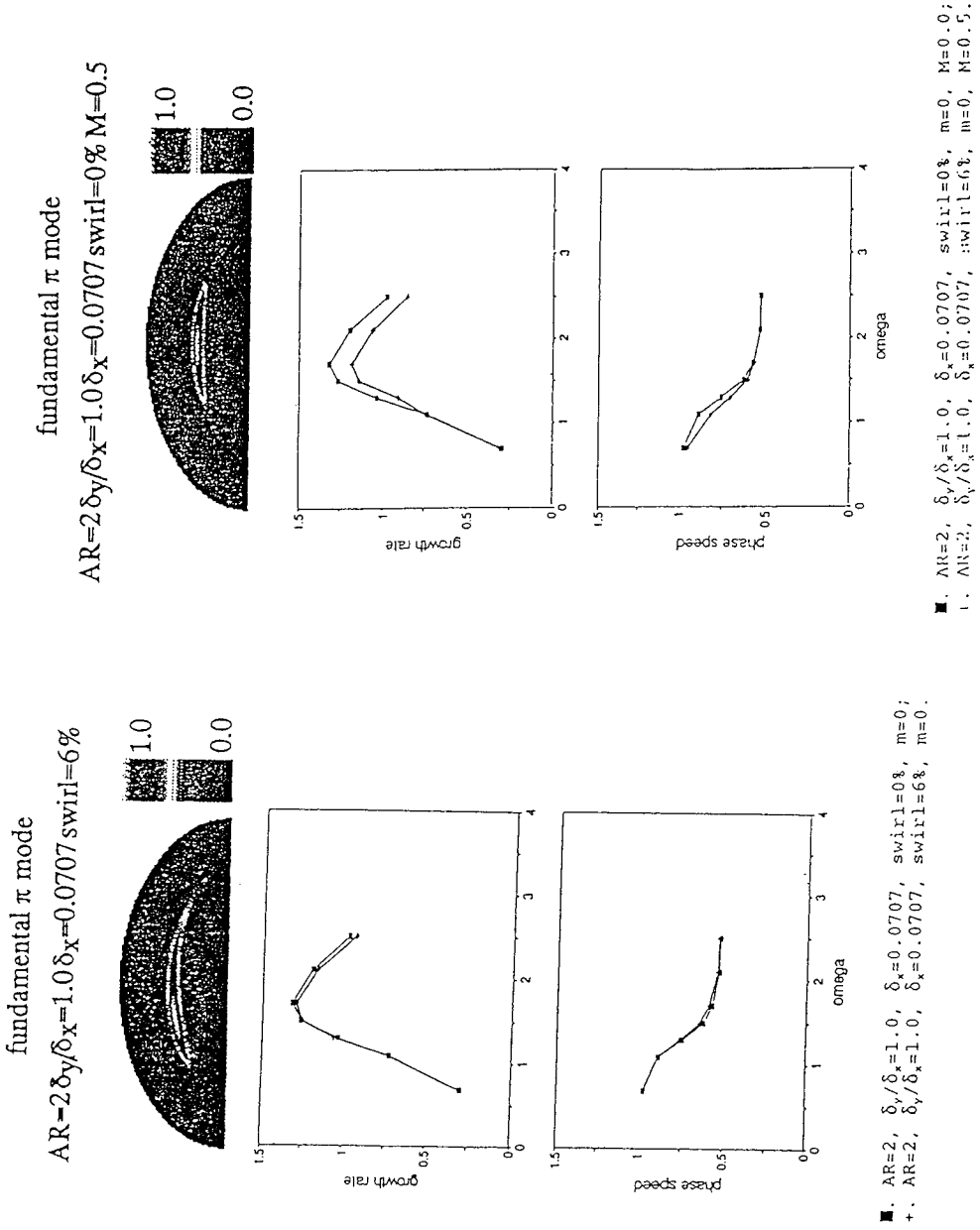


Figure 5. The Effects of Swirl and Compressibility.

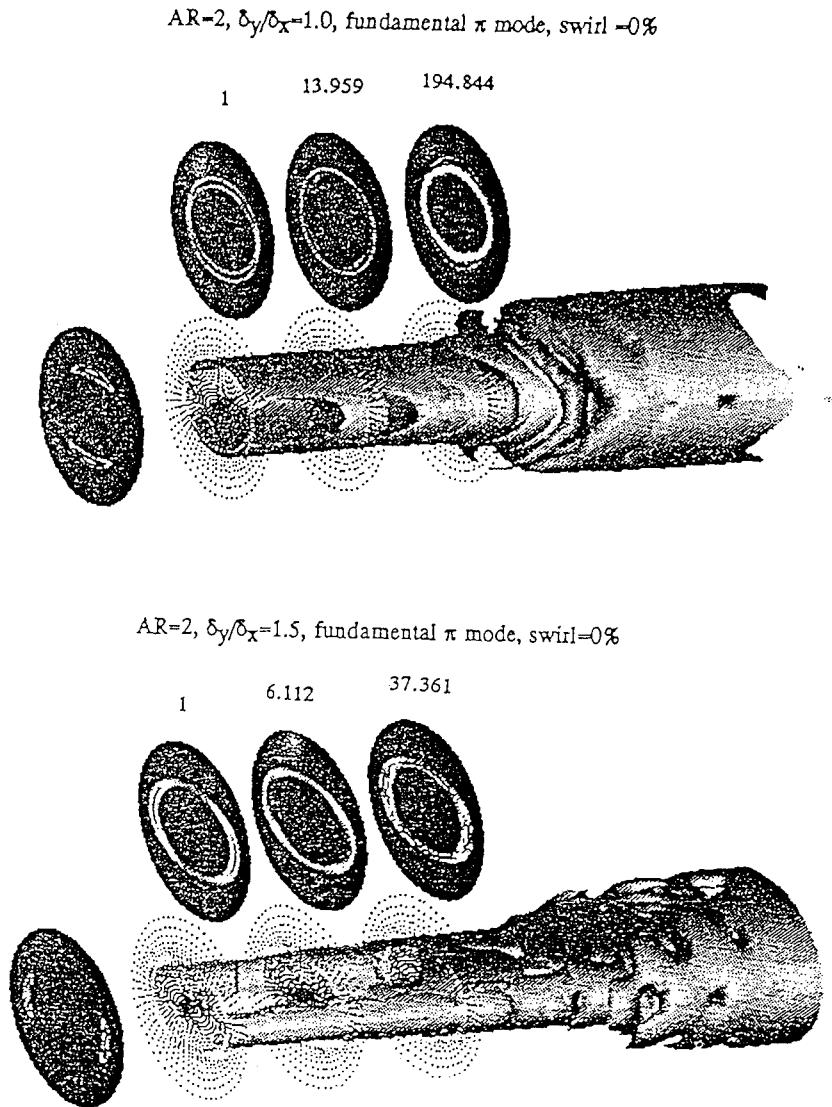


Figure 6. A Demonstration of Asymmetry.

Circular Jet
Large Eddy Simulation
Vorticity Magnitude after 1500 Time Steps
 $R/\theta = 5$, Nonuniform Grid

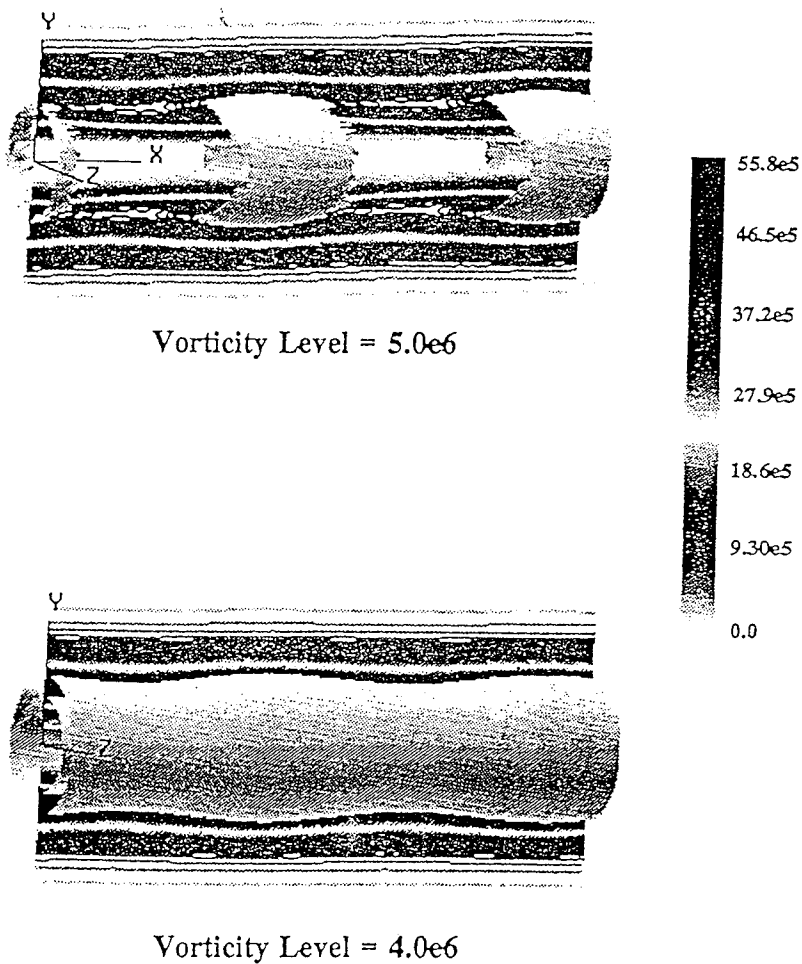


Figure 7. Early Stages of Roll-Up.

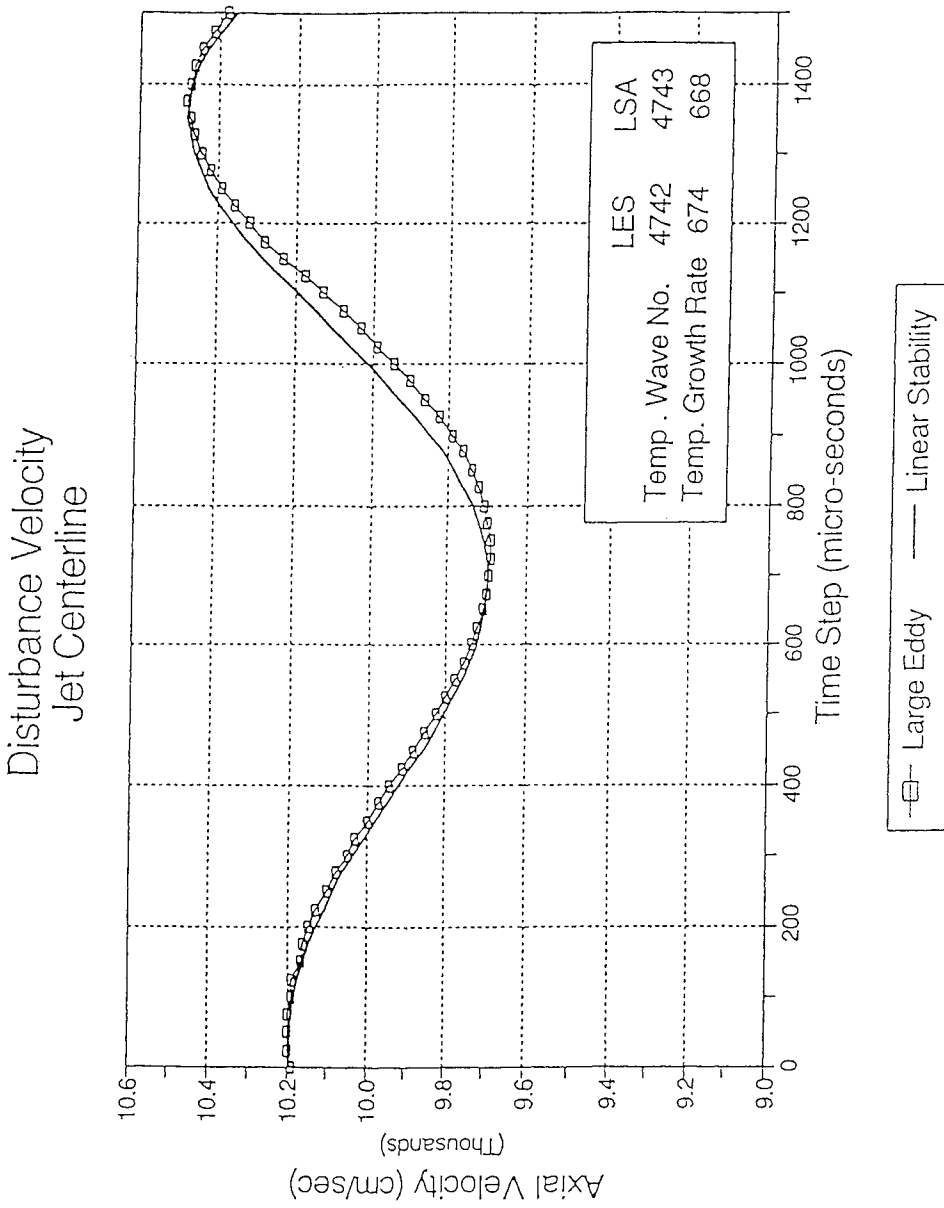


Figure 8. Agreement with Linear Stability Theory.

DIRECT SIMULATION OF A SHOCK-INDUCED MIXING LAYER

*Jeffrey A. Greenough ***John B. Bell **Lawrence Livermore National Laboratory
Livermore, CA 94550

ABSTRACT

The interaction of a shock wave with a dense fluid layer in three dimensions is investigated using direct numerical simulations. The underlying numerical method is a second-order Godunov scheme. This is coupled to an implementation of Adaptive Mesh Refinement (AMR) which is used to manage the hierarchical grid structure. An anomalous shock refraction is formed as the initiating shock wave impinges on a quiescent thin dense gas layer. One of the two resulting centered waves from the refraction, the contact surface, serves as the site for initial deposition of primarily spanwise vorticity and represents the primary mixing layer instability. The other wave, the transmitted shock wave, through repeated interactions with the free-surface, forms a cellular structure within the dense layer. The initial interaction introduces three dimensional perturbations onto the slip surface. These perturbations are selectively enhanced, due to favorable velocity gradients over part of the cellular structures, and form large-scale counter-rotating streamwise vortical structures. The structures characterize the secondary instability of this mixing layer. These vortices are quite unstable and transition to small-scales within a distance spanned by two of the cellular structures behind the initiating shock. The transition location has been verified in physical experiments. The fine-scale structure contains evidence of hairpin vortices.

The evolution of a conserved scalar is used to monitor mixing progress. Increases in the rate of mixing are directly tied to intensification events associated with the streamwise vortices. Overall the large-scale streamwise structures provide an efficient mechanism for mixing the light and dense fluids.

Analysis of time-series data from the calculation shows evidence of what are termed energetic small-scales. This is the characteristic signature of the hairpin vortices undergoing intensification. Also, the primary dominant frequency for the system agrees with that found in the experiments. The power spectrum shows an emergence of a well-resolved inertial range having a f^{-3} frequency dependence.

1 Introduction

The passage of a shock wave over a thin dense layer leaves in its wake a flow field where shock physics and mixing layer development are interrelated. In terms of the shock physics, this type of flow represents the degenerative, glancing incidence, fast-slow anomalous shock refraction. The non-glancing case has been the subject of extensive experimental and numerical studies by [1, 5, 6, 7]. In the present case, the density interface is not clearly defined by a membrane inclined at some angle less than ninety degrees to the horizontal, but rather is a slightly diffuse mixed region separating stably stratified dense and light

*This work of these authors was performed under the auspices of the U.S. Department of Energy by the Lawrence Livermore National Laboratory under contract No. W-7405-Eng-48. Support under contract No. W-7405-Eng-48 was provided by the Applied Mathematical Sciences Program of the Office of Energy Research and by the Defense Nuclear Agency under IACRO 92-825 and IACRO 93-817.

gases. A typical gaseous system might be air and FREON. The refraction for the fast-slow case is so termed because the speed of sound is faster in air than it is in the denser gas. Hence the speed of the shock wave is retarded in the dense gas relative to its speed in air. An anomalous refraction refers to all refractions that are not regular, i.e., all refractions not resulting in a planar three wave system. Here there is curvature of the initiating shock wave due to a train of expansion waves in the post-shock air.

At the point of impingement of the shock wave with the dense layer, two centered waves result. One is the deflected density interface, or contact surface, and the other is a transmitted (into the dense layer) shock wave. The latter wave is transmitted obliquely into the dense gas.

The first of the resultant waves, the slip surface, is primarily two dimensional and due to baroclinic production of vorticity is the site of spanwise vorticity deposition. In the context of mixing layers, this two dimensional organization of spanwise vorticity constitutes the primary instability of this mixing layer.

The transmitted shock wave plays a dual role in this problem. First, it provides large three dimensional perturbations to the mixing layer. It is reflected by the lower wall and interacts with the two dimensional mixing layer. Through this interaction, large perturbations are introduced into the primarily two dimensional flow. Second, the subsequent interactions downstream set up a characteristic cellular structure within the dense layer. The development of the three dimensional perturbations and the cellular pattern in the dense layer are intimately related. Streamwise and vertical velocity gradients are induced in the flow by the cellular structures. Over portions of a cell, they are found to be positive (or negative). As the perturbations are swept downstream, these gradients selectively enhance, where they are favorable, streamwise and vertical vorticity by vortex stretching. Hence, there is the appearance of large-scale counter-rotating vortical pairs, due initially to the perturbations introduced into the two dimensional layer by the transmitted wave, and subsequently enhanced by velocity gradients induced by the cellular structures formed by free-surface/transmitted wave interactions. In terms of mixing layer instabilities, these large-scale vortical structures represent a different manifestation of secondary instability than is found in low speed plane mixing layers [9], where in the present case, the flow field features are dominated by the large-scale streamwise vortical structures.

These large-scale structures provide an efficient means for mixing the light and dense gases. By monitoring the evolution of a function of the conserved scalar, the mixing can be monitored over time. The behavior of the function is correlated to the development and intensification events associated with the large-scale structures. It will be seen that the largest increases in mixing occurs as the streamwise vorticity is intensified.

As a transitional flow, this flow field breaks down to small-scales quite rapidly. There have been some previous numerical studies of this type of flow in two dimensions [8], as well as preliminary laboratory data for an Air/FREON system [10]. Two-dimensional calculations of this problem are lacking in that the important three dimensional vortical features generated by vortex stretching and turning are neglected. With the current numerical model, the three dimensional structure can be directly observed and a unique opportunity is provided to greatly enhance and augment the measured experimental data and two dimensional schlieren flow visualizations.

The current work is aimed at studying the three dimensional aspects of this type of flow in light of the previous two-dimensional work. For all of the calculations to follow, a density variation comparable to that for an air/FREON system will be used assuming a single gaseous system. The model equations and the assumptions made in this study are presented in section 2. Also, a brief description of the numerical scheme and its implementation will be given.

Section 3 is devoted to analysis of the three dimensional problem. Flow field visualizations will be the primary tool for understanding the dynamics. They will be used to discuss the mechanisms responsible for developing the three dimensional large-scale streamwise structures. The effect of the large-scale structures on the mixing process, as modelled by a conserved scalar formulation, will be given.

The structure of the flow field after transition will be provided through volume renderings of the

vorticity field. Analysis of sampled time series data from the three dimensional calculation show that there is a peak frequency for the flow. An interpretation of this frequency consistent with, and in terms of, the physical quantities of the flow will be given.

The primary sites of intensification occur at the tips of so-called hairpin vortices. In the spectra, these energetic small-scales will be shown to have a characteristic signature. Also, the spectra shows the emergence of a well-resolved Kolmogorov spectrum with a $(-5/3)$ frequency decay rate.

2 Methodology

The governing equations are taken to be the inviscid equations for gas dynamics with a perfect gas equation of state. In conservative form this system is written as

$$q_t + \nabla \cdot (A) = 0 \tag{2.1}$$

and the ideal gas equation of state,

$$p = (\gamma - 1)\rho e \tag{2.2}$$

The state vector, $q = (\rho, \rho u, \rho E)$, has components density, momentum vector and total energy per unit volume. The matrix A is the usual flux matrix in three dimensions and will not be given here.

Mixing is monitored by a conserved scalar formulation. This amounts to solving an additional equation for an advected quantity, ϕ , that takes the form

$$(\rho\phi)_t + \nabla \cdot (\rho\phi u) = 0 \tag{2.3}$$

where ϕ is defined as

$$\phi = C_a - C_b \tag{2.4}$$

for C_a and C_b the mass fractions of reactant species a and b . The reaction kinetics for this model system are assumed to be single step and irreversible with no heat release and have an infinite rate of reaction. This is given as



With the above assumptions on the kinetics and with the constraint that $\sum C_i = 1$, either of the mass fractions can be obtained from the computed value of ϕ . In particular, the assumptions of infinite rate and irreversibility imply that species C_a and C_b cannot coexist in any given cell, hence, given the value of ϕ , the concentrations of the reactants are known and the constraint equation determines the mass fraction of product.

The numerical integration scheme is centered around an operator-split Godunov method which is second order in space and time [4]. This scheme uses a type of artificial viscosity that in some sense provides for subgrid-scale dissipation. This is the mechanism responsible for the mixing between C_a and C_b . The evolution of C_p will be used as a qualitative measure for the mixing that occurs between the reactants.

On top of this basic integrator is an object-orientated language (C++) implementation of Adaptive Mesh Refinement (AMR)[2]. This methodology provides for a hierarchically refined grid structure to be overlaid on the computational domain. For this problem, the instabilities and the large-scale structures are confined to a thin layer slightly larger than the initial dense layer. Also, it is the propagation of the shock wave and resulting shock refraction that is driving the flow field development. Therefore, the refinement is restricted to a region containing the important flow development as well as the shock wave.

The real experimental system consisting of two distinct gases, air and FREON, is modelled as a single gas system having a hyperbolic tangent density variation. Implicit in this formulation is that ratios of specific heats for the two gases are assumed equal.

A random perturbation will be superimposed on this profile in the three dimensional simulations. This models the physical roughness of the porous plate on the bottom of the shock tube and the experimental uncertainty in the initial profile, and provides a mechanism for breaking the two dimensional symmetry of the propagating planar shock wave.

3 Three-Dimensional Aspects

3.1 Computational Parameters

The model chosen is similar to that used in the experiments and described in [10]. A numerical test section consisting of the last 20cm of the computation domain is used for visualization and to sample data over time at fixed stations. The physical dimensions of the domain are 65cm in the x direction by 7.5cm vertically by 4cm wide. The number of points in the lowest level grid is 194 by 20 by 12. Two levels of refinement are used with a refinement ratio of 2 at each level. Approximately 35% of the domain was refined to the highest level.

The initial conditions are defined for a $M = 1.38$ shock wave in air with the pre-shock state at 1atm and room temperature. Lab-fixed coordinates are used and the shock wave is initialized in air and allowed to propagate down the numerical shock tube and pass over the dense gas. The value for ρ_{FREON} is taken to be four times that of air. A random perturbation with magnitude 10% of ρ_{FREON} is imposed on the dense layer.

3.2 Flowfield Overview

Figure 1a,b shows the density and pressure fields at a fixed spanwise location. The main features of the anomalous refraction are evident. There is the curved shock wave impinging on the dense layer as well as the resulting slip surface and transmitted wave. Note the misalignment of the density and pressure gradients along the slip surface. This allows for baroclinic generation of spanwise vorticity along this surface and represents the primary mixing layer instability. Downstream of the refraction, the characteristic cellular structure forms. It is the result of regular wall reflections and interactions of the transmitted wave with the free-surface. The constrictions in the dense layer, separating the cellular structures, correspond to interaction zones, where focused compression waves interact with the free-surface.

3.3 Vortical Features

Snapshots in time of renderings of the magnitude of the vorticity field are shown in figures 2a,b,c. The view is of the numerical test section from slightly above the layer. The first frame corresponds to the shock wave having just passed from left to right out of the numerical test section. The deflected slip surface is seen as a predominantly planar surface with some slight spanwise striping. This rendering technique does not show the bounding walls, but the first interaction zone, where the reflected transmitted shock wave interacts with the free-surface, is evident. This region contains the peak vorticity magnitude anywhere in the test section, at this point in time. The interaction introduces three dimensionality into the vorticity field in the form of relatively small streamwise and vertical vortical perturbations as compared to the dominant spanwise component.

On the downstream, relative to the shock refraction, side of the first cellular structure, it is seen that streamwise vortical structures appear and that they are inclined to the horizontal in figure 2a. This would imply that the streamwise structures are actually a combination of streamwise and vertical vorticity components as they are aligned more or less in the x-y plane.

On the backside of the second cell it is clear that the streamwise structures dominate the flow field. Spanwise slices of the vorticity field are shown in figures 3a,b,c. Dark corresponds to negative values and light corresponds to positive values. It is seen that there are large-scale counter-rotating vortical pairs in both

the streamwise and vertical components. In fact, these two components are of the same order of magnitude and have grown larger than the spanwise vorticity which is the initially dominant component.

The spanwise component has changed configuration dramatically from its initial primarily planar configuration. In addition to the three dimensional structure, there is the presence of counter-sign spanwise vorticity.

The corresponding product field, figure 3d, shows that mushroom shapes have developed. In this rendering, the colormap is chosen to highlight the secondary structures and the dark portions correspond to the highest concentrations of product. The structures are formed primarily due to the pumping of fluid between the counter-rotating streamwise vortices. Similar structures have been observed in experiments [3] and in incompressible simulations of secondary instability [9]. Upstream the mixing region is primarily planar, but here is fully three dimensional. It is dominated by the mushroom structures, and appreciable amounts of product are being formed. Note also that the pockets of counter-sign spanwise vorticity correspond spatially to the lobes on the mushrooms, also locations of the highest concentration of the product. This counter-sign production is due to local baroclinic generation. Note that the mushroom structures are topped by cups of negative spanwise vorticity.

The transition to small-scales occurs in the calculation on the downstream portion of the second cellular structure. In all of the calculations done to present, this seems to be a consistent flow feature. Different conditions for Mach number or dense layer perturbation or changes in the resolution seemed to have no effect on the location of the transition. This would imply that there may be some critical condition that is consistently exceeded by this point in the flow and leads to transition. The critical condition could be the amplitude of the streamwise vortices, and once it is exceeded, the kinking imposed in the interaction zone forces the coherent structures to breakdown into fine-scale structures. The physical experiments performed by Reichenbach at EMI reveal that transition occurs in generally the same location.

Figure 2b, the second in the ray traced vorticity magnitude renderings, shows the flow field after the main cellular structures have moved out of the test section. It is seen that the large-scale coherent streamwise structures breakdown in this interaction zone and emerge as fine-scale vortices. The emergence of hairpin vortices is seen downstream of this transition.

The last of the vorticity magnitude renderings, figure 2c, is near the end of the numerical experiment. The vortical structures have become much more dense and intertwined in the layer. Some hairpin vortices are well defined within the field, although the arrangement of the structures appears quite complicated. Note that the largest magnitude of vorticity occurs at the hairpin tips, the bright spots in the rendering.

3.4 Mixing Enhancement

The conserved scalar formulation can be used as a mixing monitor. With regard to the model chemical reaction given above, the integrated product as a function of time will depend strongly on the large-scale features of the flow. At a fixed location in space, $x = 45cm$, the quantity

$$\bar{C}_p(t) = \int_y \int_z C_p(x, y', z', t) dz' dy' \quad (3.1)$$

is computed using the data at the finest level available. In figure 4, the integrated product is shown over time. The quantity, $\bar{C}_p(t)$, is scaled by the integrated pre-shock amount of \bar{C}_b in the slab. This number provides a normalization where 1.0 corresponds to the consumption of all of the limiting reactant.

All of the key features of the flow field are evident in this plot. There is an initial jump from the small pre-shock value. The short period of time after the arrival of the shock, shows the formation of product along the slip surface. The small oscillations are due to the concentration of product in the cores of the small spanwise vortices associated with the primary instability.

After the first interaction zone, there is an increase in product formation, a leveling off, and then a more rapid increase. This is the production that occurs over the first cell. By reference to figure 2a,

the streamwise vortices only become of appreciable size on the backside of the cell. This is also when the formation of product increases most rapidly. In fact, the rate of production is decreasing up to the cell peak, coincident with a deintensification of the streamwise vorticities due to unfavorable velocity gradients. Where these vortical structures are enhanced, the rate of production increases. Over the upstream portion of the second cell, there is formation of product primarily because the streamwise vorticities are already established and hence less sensitive to the effects of the velocity gradient. But on the downstream, or backside, portion of this cell, the rate of product formation increases greatly. The bulk of C_p production occurs over the second cell, accounting for consumption of almost 40% of the available limiting reactant. It is clear from this plot that the counter-rotating vortical structures provide an efficient means for mixing the reactants.

After transition, the amount of product essentially oscillates about the value obtained up to transition. There is a general upward trend, however, and at late times, as the vortical field intensifies, most of the remaining reactant is consumed. The point in time when there is a final increase in product formation roughly corresponds to the time when the vorticity magnitude begins to increase due to the vortical field beginning to intensify.

3.5 Time Series Analysis

The refinement strategy guarantees that the dense layer is completely contained by the finest level grid. Hence, the data sampled at points within the layer will have the greatest possible time resolution. The frequency resolution is determined based on the timestep on the finest grid. Letting Δ denote the finest grid timestep, the Nyquist frequency is given as

$$f_c = 1/(2\Delta), \quad (3.2)$$

where Δ is approximately $0.9\mu\text{sec/sample}$, so $f_c = .55\text{MHz}$.

Two analysis procedures are applied to the sampled data as a consistency and accuracy check. One is Fast Fourier Transforming (FFT) the time data using a standard overlapped windowing procedure and the other is the Maximum Entropy Method (MEM). Typically, there were 1000 data points in the sample. In the FFT method, this gave about 10 windows of 128 points and with MEM, 60 to 80 poles were used. In general, both procedures differed by only a constant normalization factor. Representative raw data and the corresponding power spectrum for kinetic energy at three vertical locations, in the center of the test section span, are shown in figures 5a,b, respectively.

In the raw data, the jump in kinetic energy signals the passage of the shock wave. The trace appears to be roughly periodic with a dominant low frequency of approximately 7kHz . Good agreement with estimates of the dominant low frequency in the physical experiments, approximately 8kHz , is obtained.

At the mid-range frequencies, less than 100kHz , there are a number of small local peaks that represent higher harmonics of the low frequency. There also appears to be a fairly strong dependence of the spectrum on the vertical location. At the lowest location, near the wall, the spectrum decays more rapidly between 105kHz and 125kHz than at the other locations. This could be due to wall effects. As the probe is moved upward, the spectrum levels out over this mid-frequency range, and there is the emergence of an inertial range. The straight line gives a $(-5/3)$ frequency decay for comparison. This inertial range is considered well resolved, with approximately 35 frequencies contained within it.

Near the Nyquist frequency and for sampling locations within the mixing region, a tail in the spectrum appears. At first glance, it might be thought that this is just the high frequency pile-up of energy due to the numerics. But the strong dependence of the tail on vertical location would imply that this is a feature of the flow and not merely an artifact of the numerics. Structures that would appear at these frequencies have associated length scales that are a small integer multiple of the finest level grid spacing. This is precisely the length scale of the fine-scale vortical structures that are so prevalent in the flow field after transition. So it is proposed that the spectral tails are really the characteristic signature of the fine-

scale vortical structures and are termed energetic small-scales. The source of this energy would be the intensification that is observed to occur at the tips of hairpin vortices.

4 Conclusions

The interaction of a shock wave with a thin dense layer in three dimensions is studied using a higher order Godunov method coupled into AMR. The shock refraction is identified as being of the anomalous type. The resultant waves of the refraction, the slip surface and the transmitted shock wave, form the essential features for the subsequent development and transition. The transmitted wave is trapped within the dense layer, and through regular reflection with the wall and the free-surface, forms a characteristic cellular pattern.

In three dimensions, the slip line becomes generalized to a slip surface and is the site of primarily spanwise vorticity deposition by baroclinic generation. In particular, spanwise striping signals the primary two dimensional Kelvin-Helmholtz instability. The transmitted wave's interaction with the slip surface excites three dimensional perturbations that grow rapidly. The perturbations are converted and selectively enhanced by favorable velocity gradients, on the backside of the cellular structures, into large-scale counter-rotating streamwise and vertical vortical pairs. The streamwise vorticity is enhanced by the streamwise velocity gradient and the vertical vorticity is enhanced by the vertical velocity gradient. The streamwise vortices are the dominant vortical features in the flow. Just prior to transition, mushroom structures appear in the product field, which are characteristic of secondary instability. The lobes of these secondary structures are the sites of production of counter-sign spanwise vorticity as well as the spatial location of the highest product concentrations. There is a transition to small-scales following the second cell. This is in qualitative agreement with the observed location of transition observed in experiments.

In the fully developed flow regime, the fine-scale vortical structure is characterized primarily by a complicated hairpin arrangement with intensification occurring at the tips.

The large-scale streamwise vortical structures are quite efficient at mixing the two streams. Before transition, 60% of the limiting reactant is consumed. In fact, the intensification that occurs over the backside of the second cell accounts for 35% of the total mixing. The point at which essentially all of the remaining reactant is consumed corresponds to when $|\omega|$ begins to increase.

Time series analysis of sampled data shows a dominant frequency that agrees quite well with that obtained in physical experiments. Also, there is the emergence of a well resolved Kolmogorov spectrum exhibiting a classical $f^{-5/3}$ decay rate. At the Nyquist frequency, within the dense layer, there is the signature of what are termed energetic small-scales. The intensification of the fine-scale (of size on the order of a small multiple of the finest grid spacing) vortical structures are thought to give rise to this feature of the spectra as opposed to being merely a numerical artifact. A possible explanation for this feature of the small-scale vortical structures could be the direct result of compressibility effects.

References

- [1] Abdel-Fattah, A.M. & Henderson, L.F. 1978 shock waves at a fast-slow interface. *J. Fluid Mech.* 86, 15-32.
- [2] Berger, M.J. & Colella, P. 1989 Local adaptive mesh refinement for shock hydrodynamics. *J. Comp. Phys.* 82, 64-84.
- [3] Bernal, L.P. 1981 The coherent structure of turbulent mixing layers. I. Similarity of the primary vortex structure. II. Secondary streamwise vortex structure. Ph.D. thesis, California Institute of Technology, Pasadena.
- [4] Colella, P. 1990 Multidimensional upwind methods for hyperbolic conservation laws. *J. Comp. Phys.* 87, 171-200.

- [5] Henderson, L.F. 1989 On the refraction of shock waves. *J. Fluid Mech.* 198, 365-386.
- [6] Henderson, L.F., Colella, P. & Puckett, E.G. 1991 On the refraction of shock waves at a fast-slow gas interface. *J. Fluid Mech.* 86, 15-32.
- [7] Jahn, R.G. 1956 The refraction of shock waves at a gaseous interface. *J. Fluid Mech.* 1, 457-489.
- [8] Kuhl, A.L., Reichenbach & H., Ferguson, R.E. 1991 Shock interactions with a dense-gas wall layer. *LOGICON RDA Report RDA-TR-2-1263-2201-002.*
- [9] Metcalfe, R.W., Orzag, S.A., Brachet, M.E., Menon, S. & Riley, J.J. 1987 Secondary instability of a temporally growing mixing layer. *J. Fluid Mech.* 184, 207-243.
- [10] Neuwald, P., Schatzle, W., Gehri, W. & Reichenbach, H. 1992 Preliminary Measurements applying the LDV system at the EMI Shock Tube. *Ernest-Mach-Institut Technical Report.*

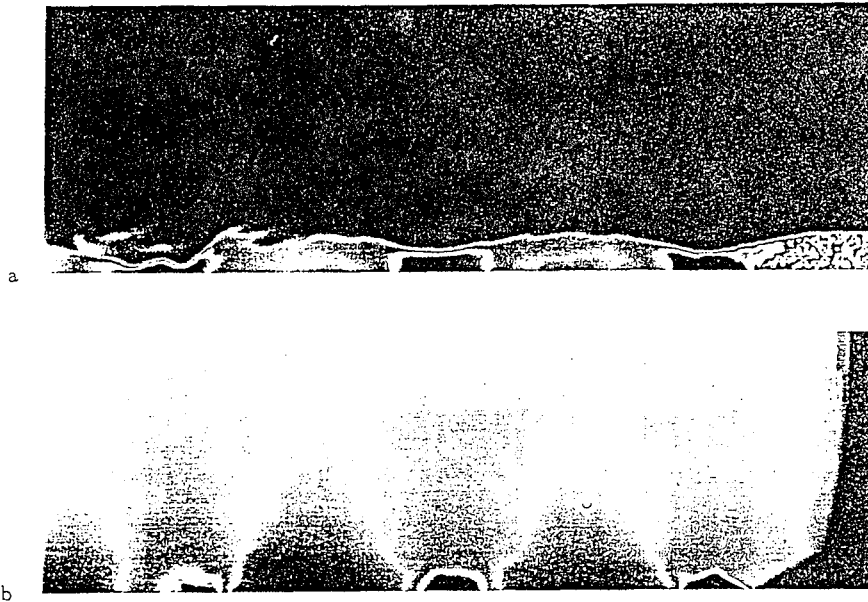


Figure 1. Streamwise slices of (a) density and (b) pressure fields for $M = 1.38$ case showing the shock refraction and induced cellular structures within the numerical test section.

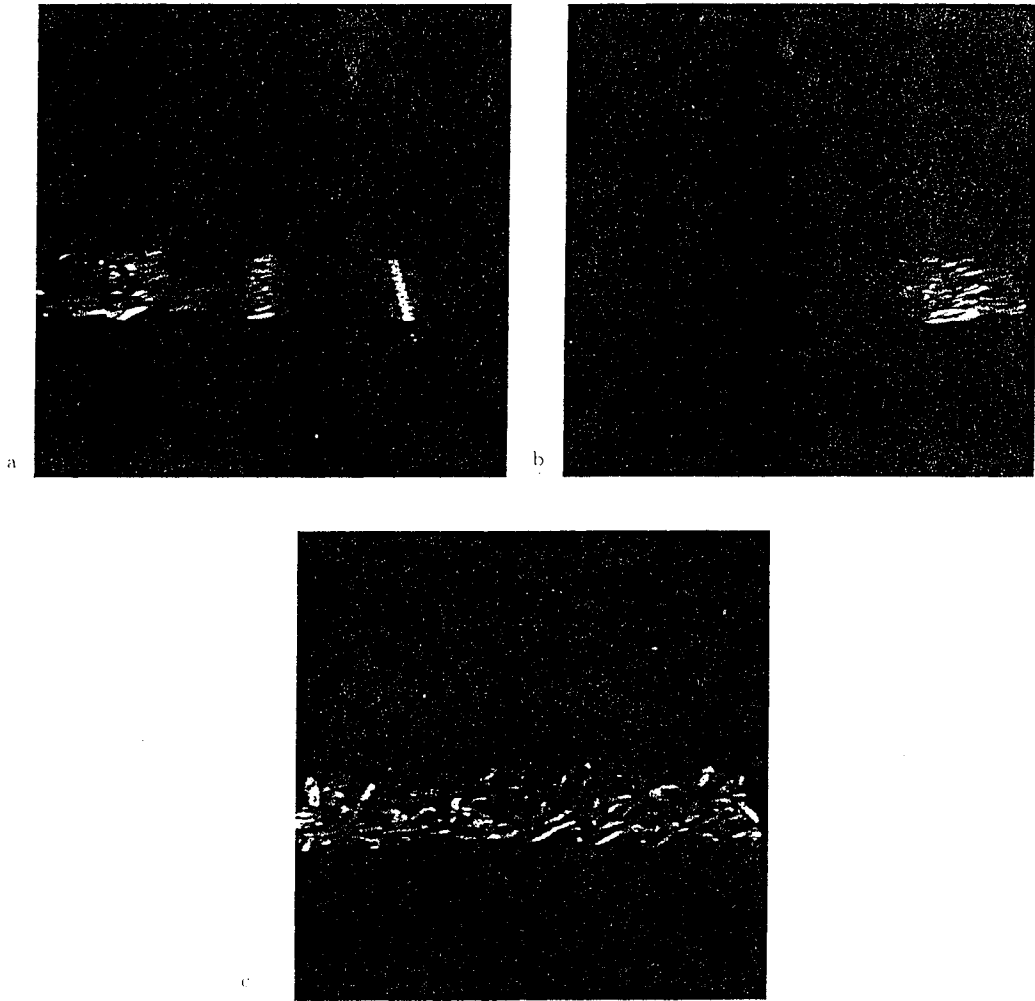


Figure 2. Ray traced volume rendering of the vorticity magnitude field within the numerical test section at (a) 330 time steps, (b) 400 time steps, and (c) 500 time steps.



Figure 3. Spanwise slices of the vorticity vector fields, (a) ω_x , (b) ω_y , and (c) ω_z , and (d) C_p field in the downstream portion of the second cellular structure at 330 time steps.

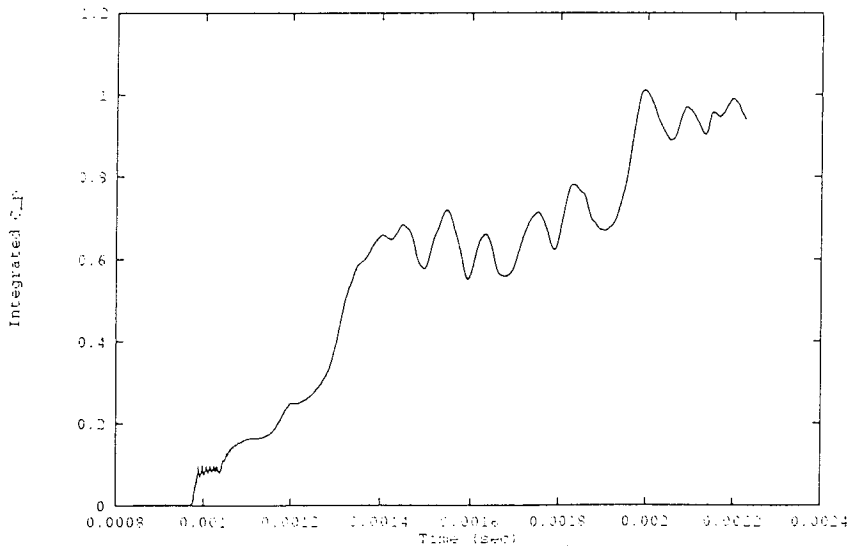


Figure 4. $\bar{C}_p(t)$ time evolution.

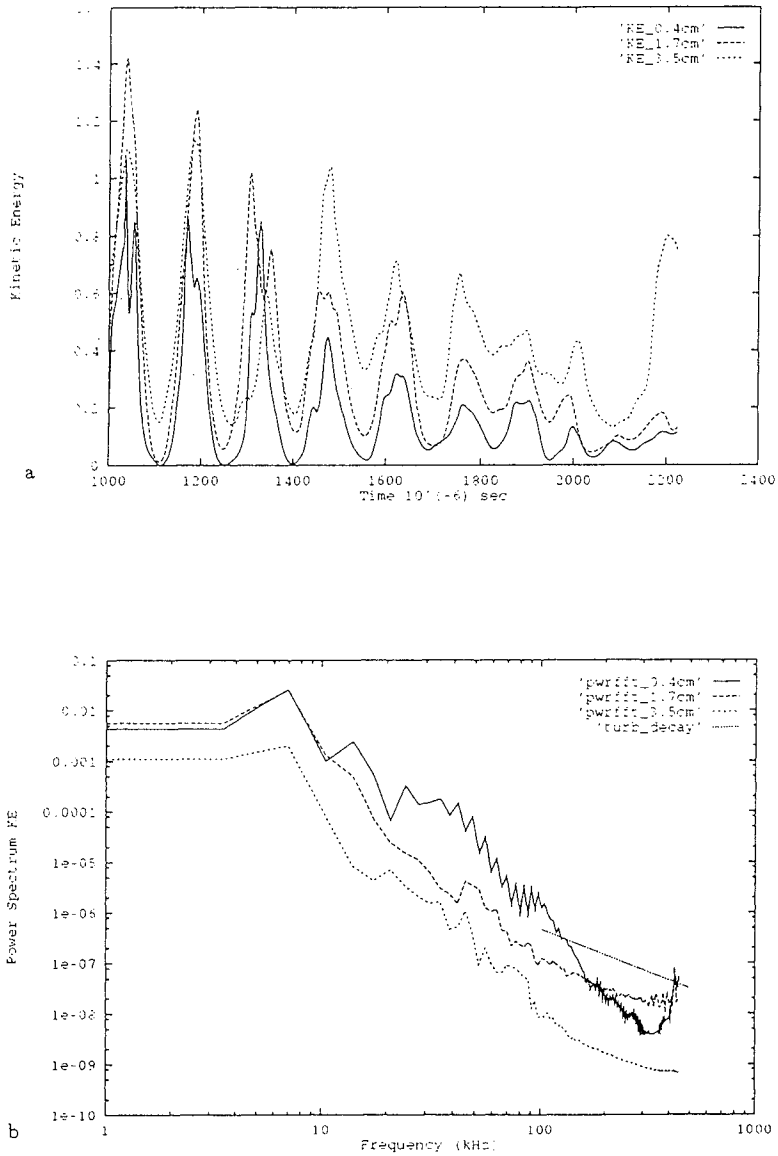


Figure 5. Center span traces of (a) raw Kinetic Energy at three vertical heights and corresponding (b) Power Spectra.

RESPONSE OF A SHEARED DENSITY INTERFACE TO PERIODIC FORCING

G. A. Lawrence¹, L. G. Guez², F. K. Browand², and S. P. Haigh¹

¹ Departments of Civil Engineering and Mathematics, University of British Columbia, Vancouver, Canada

² Department of Aerospace Engineering, University of Southern California, Los Angeles, USA.

ABSTRACT

The results of laboratory experiments in which a mixing layer is subject to small two-dimensional perturbations are compared with an analysis of the linear stability of a shear layer where the thickness of the density interface is initially much thinner than, and displaced with respect to, the velocity interface. Besides traditional statically stable mixing layer experiments the sheared Rayleigh-Taylor instability was investigated. Two layers of water were brought together downstream of a thin splitter plate with the upper layer being slightly more dense than the lower layer. In the absence of forcing sheared Rayleigh-Taylor instabilities grow at the same rate as in more traditional Rayleigh-Taylor experiments. However, these instabilities are initially suppressed when appropriate two-dimensional perturbations are applied to the flow.

INTRODUCTION

An understanding of the stability of a sheared density interface is sought after in many branches of science and engineering, since it is fundamental to the generation of turbulence and mixing. We study this problem using piecewise linear approximations to the velocity and density profiles and complement our theoretical investigations with laboratory experiments.

The present paper is an extension of the work of Lawrence et al. (1991) who performed experiments in the mixing layer channel depicted in figure 1. In these experiments instabilities formed at the interface between two layers of water of slightly different density as they merge downstream of a thin splitter plate. The most important parameter in determining the growth of these instabilities is the Richardson number:

$$J = g'h/\Delta U^2 \quad (1)$$

where the modified gravitational acceleration, $g' = g(\rho_2 - \rho_1)/\rho_2$; the velocity difference, $\Delta U = |U_2 - U_1|$; the vorticity thickness, $h = \Delta U/(dU/dz)_{\max}$; and the densities and velocities of the upper and lower layers are ρ_1 , U_1 and ρ_2 , U_2 respectively.

In a departure from previous studies Lawrence et al. (1991) studied the statically unstable case ($J < 0$) as well as the statically stable ($J > 0$) and homogeneous ($J = 0$) cases. Quantitative observations of the mean growth of the mixing region over a wide range of Richardson numbers ($-0.5 \leq J \leq 0.2$) are given in figure 2. The horizontal axis is the distance downstream from the splitter plate, normalized by the initial vorticity thickness and the velocity ratio, $R = \Delta U/(U_1 + U_2)$. The inclusion of R is necessary to properly scale experiments having different velocity ratios, see Ho & Huerre (1984). The vertical axis is the thickness of the mixing layer, η , normalized by the initial vorticity thickness, h .

For small, statically unstable, density differences, there is an initial region of growth comparable to the unstratified case, as one would expect. In fact, for sufficiently small values of J , the sign of J is initially unimportant, and the experimental results display this symmetry. The development of instabilities in a flow with $J = -0.03$ is shown in Fig. 3. Near the origin (Figs. 3 a-f), the flow develops Kelvin-Helmholtz billows as if it were a statically stable shear layer, but

eventually buoyancy forces enhance rather than retard the growth. When the scale of the structure is sufficiently large for buoyancy to become important, the upper layer fluid being entrained by the vortices simply continues its downward motion and ultimately becomes a large mushroom-shaped structure reminiscent of the Rayleigh-Taylor instability (Fig. 3 g-l).

Downstream there is a transition to a more rapid rate of growth, which occurs progressively closer to the origin as J takes on larger negative values. For $J = -0.43$ and -0.5 , the flow has completely departed from the homogeneous behaviour, and the mixing layer growth is given by:

$$\eta = 0.035 g' t^2 \tag{2}$$

Experiments over a larger range of J would be needed to give more confidence in the numerical value of the constant in (2). However, it is very encouraging to note that Read (1984) recommends the same value on the basis of experiments on the Rayleigh-Taylor instability performed under very different conditions. Read (1984) subjected fluids with ρ_1/ρ_2 from 1.6 to 600 to accelerations of up to 75g. Thus, it seems that mixing layer experiments may be useful in the study of sheared Rayleigh-Taylor instabilities.

THEORETICAL BACKGROUND

The experimental set-up depicted in Fig. 1 results in flows with a density interface that is much thinner than, and displaced with respect to, the velocity interface. The piecewise linear approximations to this profile are given in Fig. 4. The advantage of piecewise linear profiles is that an eigenvalue equation can be derived analytically from the Taylor-Goldstein equation. Using the techniques outlined in Drazin & Reid (1981, §23) we obtain the eigenvalue equation:

$$c^4 + a_1c^3 + a_2c^2 + a_3c + a_4 = 0 \tag{3}$$

The complex wavespeed $c = 2(c_r^* - \bar{U})/\Delta U$, where the dimensional complex wavespeed is $c^* = c_r^* + ic_i^*$, and the mean velocity, $\bar{U} = (U_1 + U_2)/2$; the instability wavenumber $\alpha = kh$, where $k = 2\pi/\lambda$, and λ is the wavelength of an instability; the Richardson number, $J = g'h/\Delta U^2$; and the profile asymmetry, $\epsilon = 2d/h$. The coefficients a_n in (3) are functions of α , J and ϵ .

Solutions to (3) for $\epsilon = 0.5$ and 1.0 are presented in Fig. 5. The experiments of Lawrence et al. (1991) verified the above solutions to the extent that the wavenumber of the instabilities corresponded closely to that with the maximum predicted growth rate αc_i . In the present study we investigate the the behaviour of the mixed layer when we forced the flow at other than the maximum amplified wavenumber. We also attempt to test the curious prediction of stability for a range of negative Richardson numbers when $\epsilon = 1$.

RESPONSE TO PERIODIC FORCING

To input small two-dimensional perturbations into the flow at other than the most amplified wavenumber we oscillated a thin strip of metal attached to the trailing edge of the splitter plate. We input perturbations over a range of wavenumbers into flows with $J = 0.15$, $J = 0.0$, and $J = -0.015$ to test the theoretical predictions. In general the response was consistent with predictions for a profile asymmetry $\epsilon \approx 0.5$. A limitation of our experimental set-up was that we were not able to measure ϵ accurately. On the other hand figure 6 shows that the predicted growth range is not particularly sensitive to ϵ except at high wave numbers. Furthermore, some of the predictions of instability are suspect, since viscosity is ignored in the analysis given above.

The various responses of the mixing layer to forcing when $J = 0.15$, $J = 0.0$, and $J = -0.015$ are presented in figures 7, 8, and 9 respectively. In each case the mixing was suppressed, at least

initially, whenever the flow was forced at other than the most amplified wavenumber, α_m . In figure 7 the flow was visualised by injecting a thin stream of dye just above the splitter plate. This reveals the presence of concentrated spanwise vorticity in the dominant upper layer. These vortex tubes remain above the interface and cause the interface to cusp, but not necessarily billow, into the upper layer. When the flow is unforced (Fig. 7a) small background perturbations of the most amplified wavenumber dominate. When the flow is forced at $\alpha = 0.34$ (Fig. 7b) the resulting long waves are not amplified, despite the prediction of weak amplification. This is probably due to viscous effects which are ignored in the analysis. By the downstream end of the test section the flow is similar to the unforced case. When $\alpha \approx \alpha_m$ (Fig. 7c) the response is almost immediate and a regular stream of spanwise vortices forms. When $\alpha > \alpha_m$ (Figs. 7d & 7e) the forced instabilities do not grow. Again the theory predicts some amplification, but for these short wavelengths viscous damping appears to be very important.

The results for homogeneous flows ($J = 0$) are presented in figure 8. In this case the flow has been visualised using laser induced fluorescence. Again the most dramatic response occurs when $\alpha \approx \alpha_m$, see figure 8b. For $J = 0$ the theoretical prediction is that the flow is stable for wavenumbers greater than about 1.3 no matter what the value of ϵ . There does, however, appear to be some amplification at higher wavenumbers. However, if the layers are not of exactly the same density (due either to temperatures differences or the introduction of a small quantity of dye into the lower layer), then $J \neq 0$ and instability is generally predicted.

The results for the statically unstable flows ($J = -0.015$) are presented in figure 9. Again the most dramatic response occurs when $\alpha \approx \alpha_m$, see figure 9b. Waves forced at $\alpha = 2.0$, (figure 9c) decay as predicted for $\epsilon = 1$, but not for $\epsilon = 0.5$. It should be stressed that even though stability may be predicted at high wavenumbers the instability at low wavenumbers is high and unforced perturbations with $\alpha \approx \alpha_m$ quickly dominate. The downstream conditions are little different for forcing at $\alpha = 2.0$ than in the unforced case (figure 9a). Clearly, further work needs to be done to explore the potential for suppressing Rayleigh-Taylor instabilities by forcing the flow.

CONCLUSIONS

Observations of the development of mixing layers are consistent with predictions obtained from an analysis of their linear hydrodynamic stability. Observations of statically unstable flows indicate that mixing layer experiments are useful in the study of the sheared Rayleigh-Taylor instability. Two-dimensional forcing of the flow can dramatically change the development of the mixing layer. Besides providing insight into the mechanisms of instability our results should provide direction for future theoretical, numerical, and laboratory investigations.

ACKNOWLEDGEMENTS

Financial support from the United States Office of Naval Research's Fluid Mechanics and Oceanography Programs and the Canadian Natural Sciences and Engineering Research Council is gratefully acknowledged.

REFERENCES

- Drazin, P. G. & W. H. Reid 1981 *Hydrodynamic Stability*, Cambridge.
- Lawrence, G. A., F.K. Browand & L.G. Redekopp 1991 The stability of a sheared density interface. *Physics of Fluids A: Fluid Dynamics*, **3**(10):2360-2370.
- Read, K. I. 1984 Experimental investigation of turbulent mixing by Rayleigh-Taylor instability. *Physica*, **12D**, 45-58.

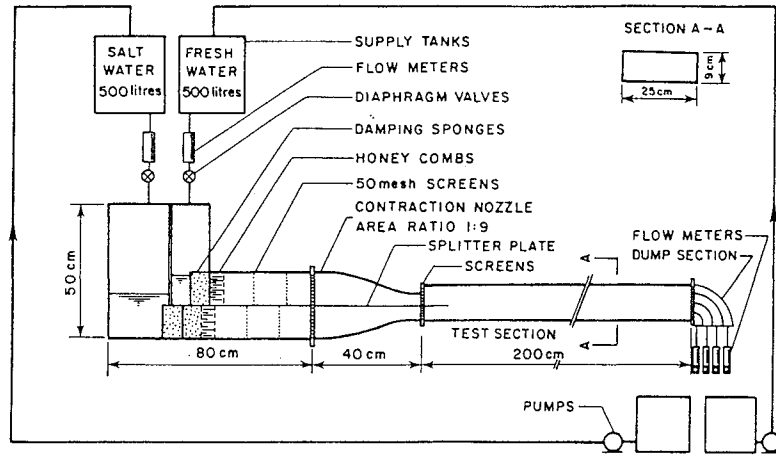


Fig. 1 Experimental apparatus.

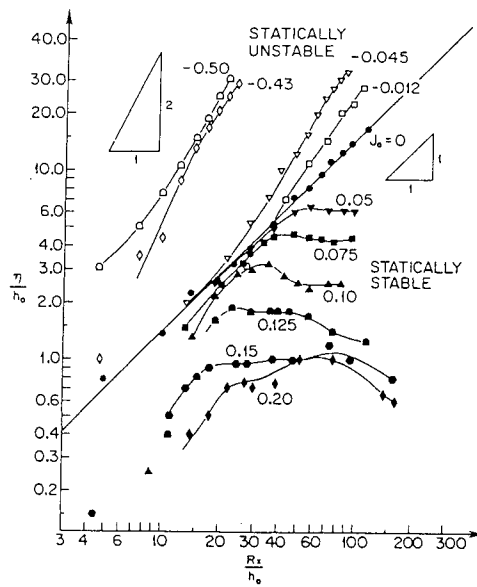


Fig. 2 Measurements of growth rates in both stably and unstably stratified shear layers.

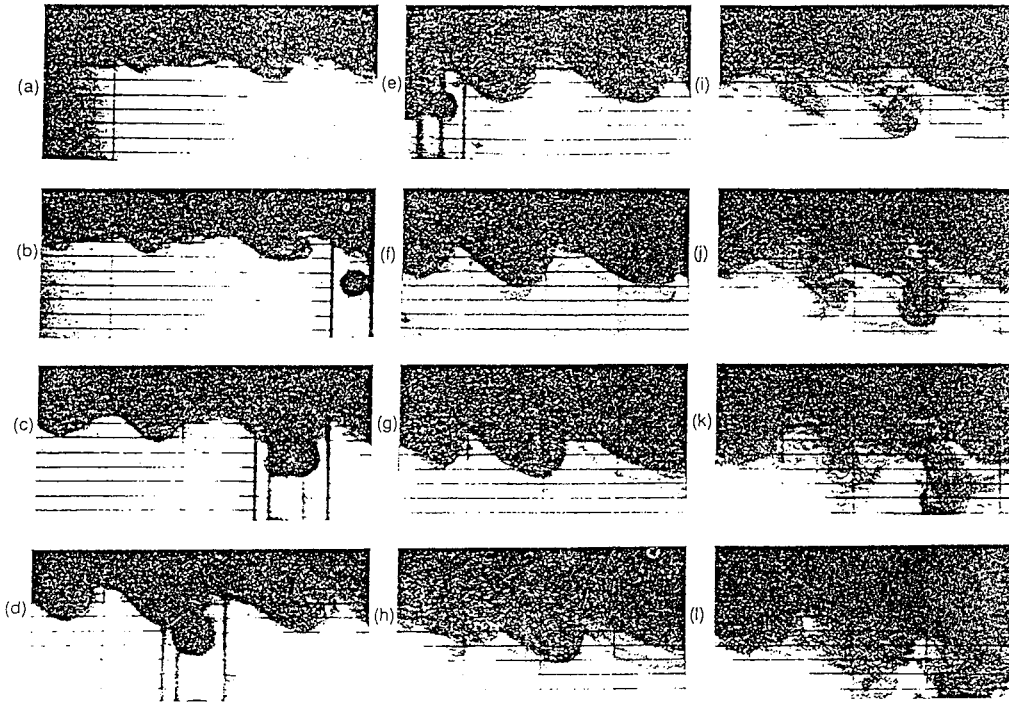


Fig. 3 Development of instability in a flow with $J_0 = -0.03$. The fluid in the upper layer is slightly heavier than that in the lower layer. The camera is moving at approximately the mean velocity, so that the development of individual billows can be observed. The flow is left-to-right, with the lower layer moving faster.

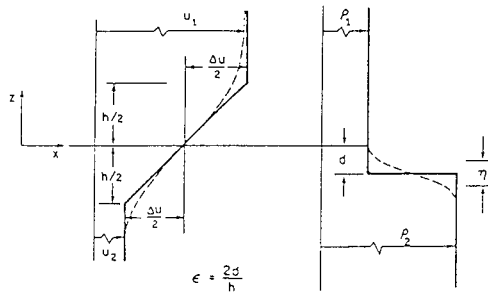


Fig. 4 Definition diagram for the piecewise linear approximations of the velocity and density profiles.

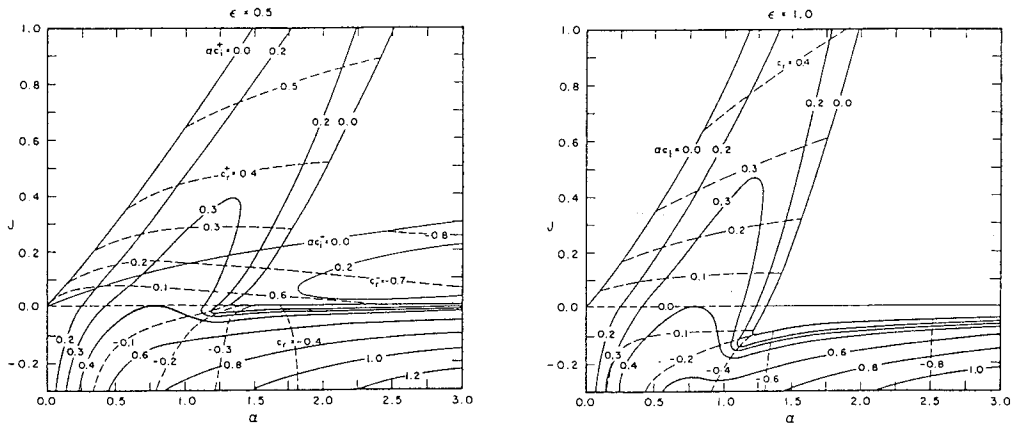


Fig. 5 Stability diagrams for asymmetric flows: (a) $\varepsilon = 0.5$; (b) $\varepsilon = 1.0$. — Contours of constant amplification rate, αc_i ; - - - Contours of constant phase speed, c_r .

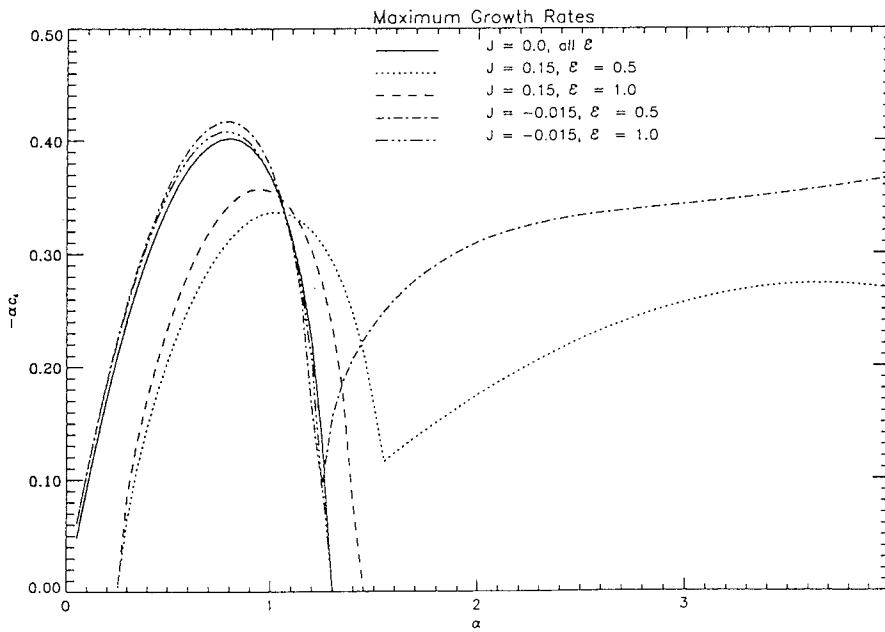


Fig. 6 Plots of growth rates obtained from linear inviscid stability theory.

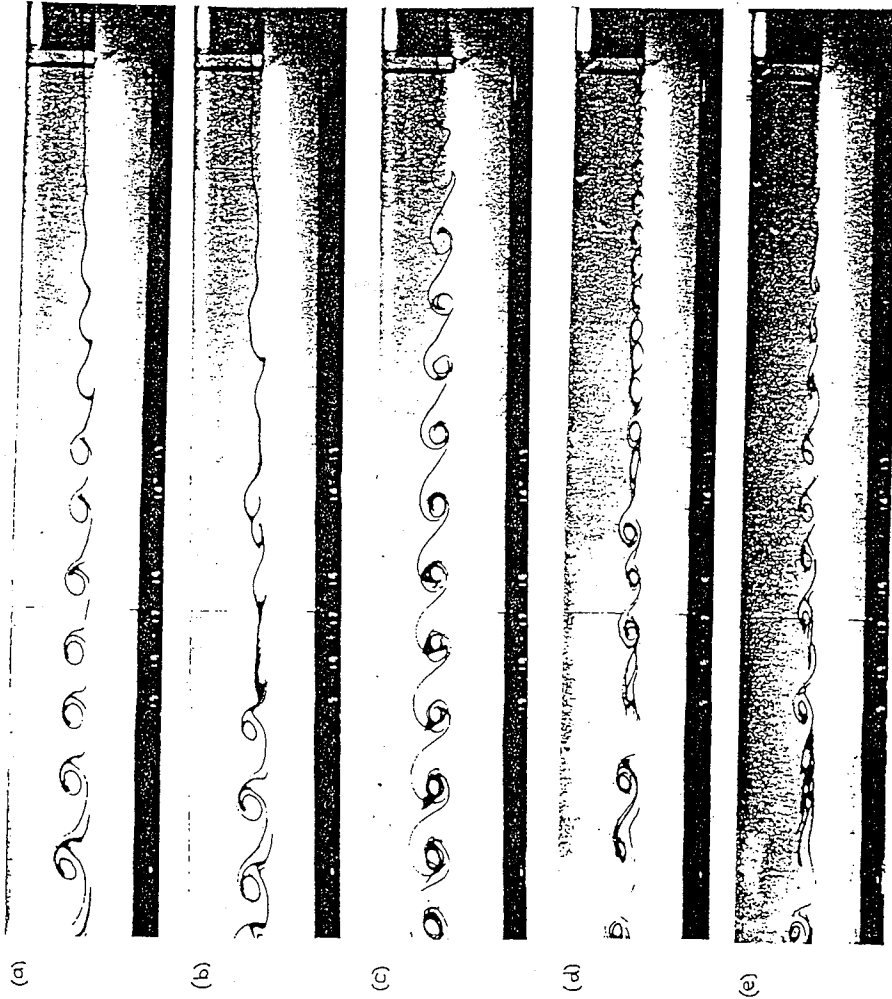


Fig. 7 Response of a statically stable ($J = 0.15$) shear layer to periodic forcing: (a) no forcing; (b) $\alpha = 0.34$; (c) $\alpha = 1.1$; (d) $\alpha = 1.8$; (e) $\alpha = 3.2$.

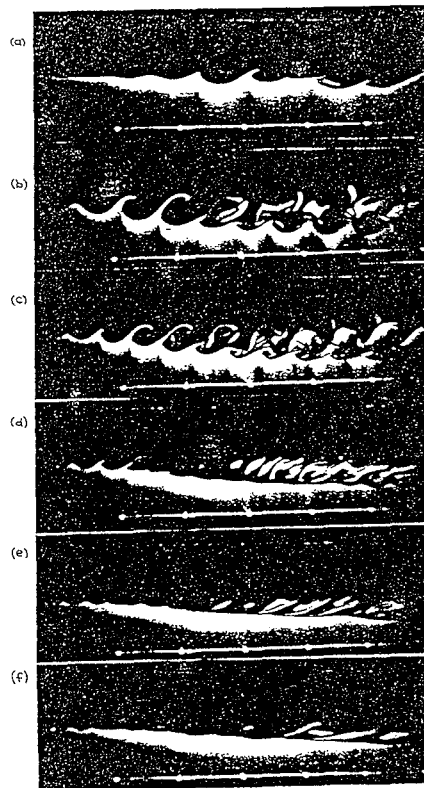


Fig. 8 Response of a homogeneous ($J = 0.0$) shear layer to periodic forcing: (a) no forcing; (b) $\alpha = 0.9$; (c) $\alpha = 1.2$; (d) $\alpha = 1.4$; (e) $\alpha = 1.5$; (f) $\alpha = 1.6$.

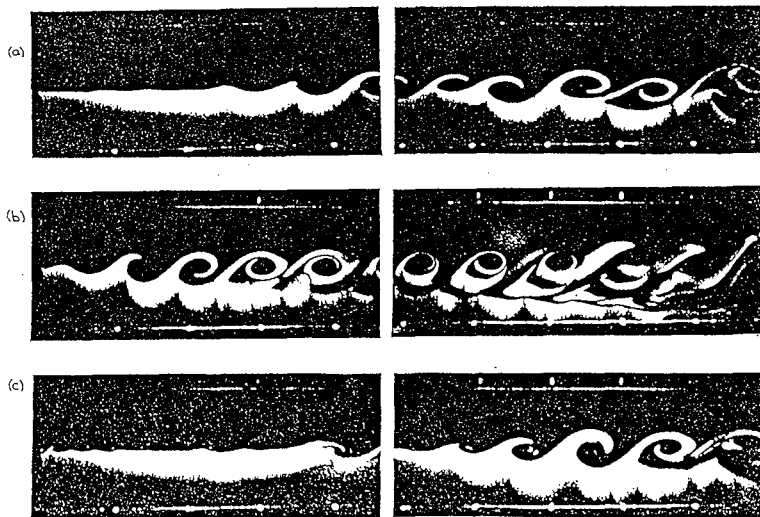


Fig. 9 Response of an unstably stable ($J = -0.015$) shear layer to periodic forcing: (a) no forcing; (b) $\alpha = 0.9$; (c) $\alpha = 2.0$.

COMPRESSIBILITY EFFECTS ON THE DYNAMICS OF SHEAR LAYERS

Marcel LESIEUR, Pierre COMTE and Yves FOUILLET*

*Institut de Mécanique de Grenoble (L.E.G.I.)***

B.P. 53 X, 38041 Grenoble-Cedex, France

Abstract

In this paper, we study the dynamics of compressible shear layers with the aid of direct-numerical simulations, or large-eddy simulations. We focus on the coherent vortices, and consider both free-shear and wall-bounded flows. We look first at the incompressible mixing layers, and study the effects on the flow of two types of initial perturbations superposed upon the basic shear: a quasi two-dimensional perturbation, where straight Kelvin-Helmholtz billows are observed, and a three-dimensional perturbation, where a helical pairing is observed. Afterwards, we study the effect of compressibility on the mixing layer, by increasing the convective Mach number M_c . It is shown that the helical pairing is suppressed above $M_c = 0.7$, and that the flow evolves towards large staggered Λ vortices. This structure is analogous with the one found in the supersonic compressible boundary layer on an adiabatic flat wall (Mach number 5), and the subsonic heated boundary layer. Details on the large-eddy simulation procedure are given in the appendix.

1. Introduction

Let us start by a few words on coherent vortices, which will be considered in most of this paper. Usually, coherent vortices are pressure lows. Indeed, they correspond to a vorticity concentration in space. Hence, from Stokes circulation theorem, the fluid will circulate around the vortex, being

* Lecture given at the 4th International Workshop on the Physics of Compressible Turbulent Mixing, Cambridge, 29 March-1 April 1993.

** *Institut National Polytechnique de Grenoble (INPG), Université Joseph Fourier (UJF) and Centre National de la Recherche Scientifique (CNRS).*

in approximate balance between the centrifugal force and the pressure gradient. This is no more true when compressibility is high, as will be seen below, and also when the fluid is submitted to a solid-body rotation: in this case, Coriolis force must be accounted for.

One of the simplest ways to generate coherent vortices is through Kelvin-Helmholtz instability, where a vortex sheet, corresponding to the interface between two layers of different (but parallel) velocity will roll up into two-dimensional spiral vortices. Laboratory experiments (Winant and Browand, 1974; Brown and Roshko, 1974), as well as numerous numerical simulations, show also that the vortices undergo successive pairings, which contribute to the spreading of the mixing layer. Various numerical illustrations of Kelvin-Helmholtz instability and of the pairing are provided in Lesieur (1990). The numerical simulations do show also that the coherent vortices are local concentrations of vorticity and low pressure, around which the transported quantities (dye, passive temperature) wind.

Other types of coherent vortices are the longitudinal hairpin vortices. In shear flows, they correspond to three-dimensional instabilities where vortex filaments in a shear, submitted to a weak vertical oscillation in the spanwise direction, are stretched longitudinally by the basic shear. It yields longitudinal hairpin vortices of opposite sign. Due to self-induction effects, they are usually inclined approximately 45° with respect to the horizontal plane defined by the streamwise and spanwise directions.

An important feature for the organization of the vortex topology is the relative phase of the perturbed vortex filaments: if they are in phase in the streamwise direction, the resulting hairpins will have a global in-phase sinusoidal oscillation, as in the so-called aligned Klebanoff's mode in the boundary layer (Klebanoff et al., 1962), and the translative instability (Pierrehumbert and Widnall, 1982) in the mixing layer. In this situation where the hairpin vortices are in phase, low and high-speed streaks should be very elongated. This was the case for the experiment of Klebanoff et al. (1962) in a forced transitional boundary layer. If the initial spanwise perturbations are out of phase, the flow will give rise to hairpin vortices staggered in the streamwise direction. This vortex topology corresponds to the so-called staggered

mode in the boundary layer (Herbert, 1988) and to the helical-pairing mode (Pierrehumbert and Widnall, 1982) in the context of the mixing layer.

The “helical pairing” (this terminology is borrowed from Pierrehumbert and Widnall, 1982, who used it in the context of secondary instability of the mixing layer) is obtained in the following way in the staggered case: when the tips of the hairpins come close to each other, and if the vorticity carried by the vortices is high enough, there will be a local roll up and pairing. This may occur in free-shear flows, as will be shown below.

2. Mixing layers

2.1 Incompressible case

We have carried out 3D direct-numerical simulations of a temporal mixing layer (periodic in the streamwise and spanwise directions), using pseudo-spectral methods (128^3 points). The initial flow is a parallel hyperbolic tangent basic velocity profile, plus a weak random perturbation which may be a white noise or peak in the large scales (harmonic or subharmonic). When the perturbation is quasi two-dimensional, one observes the emergence of spiral quasi two-dimensional Kelvin-Helmholtz vortices. One notices also the appearance of weak longitudinal hairpin vortices, of vorticity about 1/10 of the initial maximal spanwise vorticity (Comte et al., 1992). The same vortex topology, with thin longitudinal modes stretched between quasi two-dimensional large vortices, was observed for spatially-growing mixing layers by various experimentalists such as Breidenthal (1981), Lasheras and Choi (1988), or Bernal and Roshko (1986). It was also found in the temporal mixing layer simulations of Metcalfe et al. (1987). Notice that our direct-numerical simulations are at moderate Reynolds number, and the longitudinal vorticity stretched is low. In fact, large-eddy simulations of a periodic wake show more intense longitudinal vortices. We have carried out large-eddy simulations of the wake using the same pseudo-spectral code, at a resolution of 48^3 points, and with a quasi two-dimensional forcing (for details on the large-eddy simulations, see the appendix). Figure 1 shows the iso-surface of the vorticity modulus corresponding to a value of half the maximum initial vorticity ω_i . Figure 1a corresponds to a direct numerical

simulation (no subgrid model) at a Reynolds number of 200: for such a threshold, no longitudinal vortices appear. Here, the maximum vorticity is $\approx \omega_i$, and oriented in the spanwise direction. Figure 1b corresponds to the structure-function model (Métais and Lesieur, 1992) using an eddy-viscosity scaling on the local velocity second-order structure function of turbulence. Longitudinal vortices stretched between the Karman billows do appear, of maximum vorticity $2.22\omega_i$. Figure 1c corresponds to Smagorinsky's model: the maximum vorticity is slightly reduced ($2.13\omega_i$), but the large primary vortices are less important than with the structure-function model. Finally, figure 1d shows the vorticity modulus isosurface $0.83\omega_i$ for a subgrid model replaced by an iterated laplacian $\nu(\nabla^2)^8$. The stretching is even more intense than for the structure-function model, with vorticity peaks at $\approx 4\omega_i$. The secondary longitudinal vorticity fields shown in the large-eddy simulations of figures 1b and 1d are quite realistic, by comparison with the very high Reynolds number cavitating wake experiments presented on figure 2 (taken from Franc et al., 1982). Intense vortices are low-pressure regions, marked by cavitation bubbles. Thus, the side view of figure 2 shows Karman vortices reconnected by the longitudinal hairpin vortices.

Let us come back to the mixing layer. When the initial perturbation is three-dimensional (but still of low amplitude), on the contrary, a helical pairing is observed (Comte et al., 1991, 1992). This is shown on figure 3, presenting a top view of both the low-pressure field (fig. 3a) and the vortex lines (fig. 3b) in a direct-numerical simulations (spectral methods, resolution 128^3). One observes a good correlation between depressions and intense vortices, except in the central region of the domain, where a hairpin is stretched between the two concentrations of vorticity: this hairpin has one leg ($\approx \omega_i$) more intense than the other one, which is not seen on the low-pressure plot. Here, it is in the region of vortex reconnexion that the vorticity attains its maximal stretching, of the order of $4\omega_i$. It has to be mentioned that a spatially growing calculation forced upstream by a white noise still exhibits the helical pairing, but with a weaker amplitude (see Comte et al., 1992). This is certainly the explanation for the symmetry breaking of the large vortices observed experimentally by Browand and Troutt (1980).

In this helical-pairing situation, the kinetic-energy spectra display a one-decade $k^{-5/3}$ Kolmogorov law in the large scales (for the direct-numerical simulation). The probability density functions (pdf) of pressure is highly skewed towards the low values (with an exponential wing), while it is gaussian for high values (see Comte et al., 1992). This tendency for the pressure to take very low values for rare events is an indicator of large-scale intermittency, and is obviously associated with the existence of coherent vortices.

2.2 Compressible mixing layer

We consider here a mixing layer in an ideal gas, between two streams of same density at infinity. We have looked at the influence of compressibility upon the mixing layer, with the aid of direct-numerical simulations using finite-difference methods of the predictor-corrector type (fourth-order in space for the nonlinear terms). Here, the hyperbolic-tangent velocity profile is perturbed by a weak three-dimensional white noise. The relevant Mach number, called convective, M_c , is built up with the relative velocity between one of the two streams and the coherent vortices. At a $M_c = 0.3$, the same helical-pairing structure as in the incompressible case is recovered, as can be seen on figure 4, which represents a top view of the resulting vortex lines in this case. Since the calculation is done with other numerical schemes than in the incompressible case (which uses pseudo-spectral methods), this validates the incompressible results. Now, we increase the Mach number. Above $M_c = 0.6 \approx 0.7$, one observes that the helical pairing is inhibited, yielding large Λ -shaped vortices staggered in the streamwise direction, and inclined with respect to the horizontal. They carry a vorticity of the order of the initial spanwise basic vorticity, but the intense stretching observed in the incompressible case is suppressed. This vortex structure is shown on figure 5a ($M_c = 1$). Preliminary simulations in the spatially-growing case confirm the change of topology, from the $M_c = 0.3$ case where large Kelvin-Helmholtz vortices oscillate quasi two-dimensionally and are submitted to dislocations, to the $M_c = 1$ case where turbulence consists of large and very elongated staggered Λ vortices. In the laboratory experiments of Papamoschou and Roshko (1988), it was shown that the spreading rate of the layer decreased

when the convective Mach number was increased, from the incompressible value at $M_c = 0.3$ to about 40% of this value above $M_c = 1$. For $M_c > 1$, the spreading rate was Mach number invariant. This might be an indicator of the bifurcation from the low to high Mach number vortex topology of turbulence. Another interesting result in the temporal compressible mixing layer case concerns the pressure, which ceases to follow the vorticity and reconnects longitudinally when the helical pairing has been inhibited (see figure 5b). Our temporal simulations at Mach numbers 0.8 and 1 are in good agreement with the results of Sandham and Reynolds (1991). The latter, however, did not find the helical pairing at $M_c = 0.4$. This is certainly ascribable to the fact that they used other types of initial conditions.

3. Compressible boundary layer

We have done large-eddy simulations of the transition to turbulence in the compressible spatially-developing boundary layer above an adiabatic flat wall, with the same numerical methods as above for the compressible mixing layer. A preliminary Mach 5 calculation using the structure function model (see Normand and Lesieur, 1992) displays a staggered pattern of large elongated Λ vortices, very similar to those observed for the compressible mixing layer at $M_c = 1$. The trouble with the structure-function model is that it is too dissipative in low Mach number boundary layers, and prevents turbulence to develop. Therefore, we have implemented a selective version of the structure-function model, which is applied selectively in regions where the flow presents a sufficient degree of three-dimensionality. The latter is measured in terms of the mean angle between the vorticity at a given grid point and the vorticity of the neighbouring points. If this angle exceeds the most probable value obtained in simulations of isotropic turbulence at an equivalent resolution, the subgrid model is turned on. Otherwise, it is only molecular dissipation which acts. This selective structure-function model has been applied successfully to the simulation of an isothermal boundary layer at a temperature three times larger than the temperature at infinity (David, 1993): the flow is uniform upstream ($M_\infty = 0.5$), with a small three-dimensional random white-noise perturbation superposed upon it, and the

plate is inclined 10° with respect to the incoming velocity. The calculation uses the same numerical methods as for the flat plate case mentioned above, except for the fact that a curvilinear system of coordinates is used. The resolution is $237 \times 30 \times 32$ grid points respectively in the streamwise, transverse and spanwise directions. Here, the heating accelerates the transition, due to the generalized inflexion-point criterion. Figure 6 shows the vorticity modulus, which displays again staggered Λ vortices.

Appendix: large-eddy simulations

In order to increase the Reynolds number in the simulations, it is necessary to introduce a subgrid-scale model representing the action of scales smaller than Δx , the computational mesh, upon the explicitly resolved scales. The formalism of the large-eddy simulations proceeds as follows: one considers a spatial filter F of width Δx , which filters out the *subgrid-scales* of wavelength $< \Delta x$,

$$\bar{u}_i(\vec{x}, t) = F\{u_i(\vec{x}, t)\} \quad ; \quad u_i = \bar{u}_i + u'_i \quad , \quad (1)$$

where the u'_i are the velocity fluctuations. Applying the filter to Navier-Stokes equations, it is obtained:

$$\frac{\partial \bar{u}_i}{\partial t} + \bar{u}_j \frac{\partial \bar{u}_i}{\partial x_j} = -\frac{1}{\rho_0} \frac{\partial \bar{p}}{\partial x_i} + \frac{\partial}{\partial x_j} \left\{ \nu \left(\frac{\partial \bar{u}_i}{\partial x_j} + \frac{\partial \bar{u}_j}{\partial x_i} \right) + T_{ij} \right\} \quad (2)$$

with

$$T_{ij} = - \left(\overline{u'_i u'_j} + \overline{\bar{u}_i u'_j} + \overline{u'_i \bar{u}_j} + \overline{\bar{u}_i \bar{u}_j} \right) \quad . \quad (3)$$

This has formal similarities with the Reynolds equations for the mean flow, except for the form of subgrid-scale stress tensor T_{ij} . Still, an eddy-viscosity assumption is done for the latter:

$$T_{ij} = \nu_t \left(\frac{\partial \bar{u}_i}{\partial x_j} + \frac{\partial \bar{u}_j}{\partial x_i} \right) + \frac{1}{3} T_{ll} \delta_{ij} \quad . \quad (4)$$

The filtered Navier-Stokes equation writes

$$\frac{\partial \bar{u}_i}{\partial t} + \bar{u}_j \frac{\partial \bar{u}_i}{\partial x_j} = -\frac{1}{\rho_0} \frac{\partial \bar{P}}{\partial x_i} + \frac{\partial}{\partial x_j} \left\{ (\nu + \nu_t) \left(\frac{\partial \bar{u}_i}{\partial x_j} + \frac{\partial \bar{u}_j}{\partial x_i} \right) \right\} \quad , \quad (5)$$

where \bar{P} is a filtered pressure including the $T_{ll} \delta_{ij}$ contribution and determined by the filtered continuity equation $\partial \bar{u}_j / \partial x_j = 0$.

In Smagorinsky's model (1963), the eddy-viscosity is given by

$$\nu_t \sim (\Delta x)^2 \left[\left(\frac{\partial \bar{u}_i}{\partial x_j} + \frac{\partial \bar{u}_j}{\partial x_i} \right) \left(\frac{\partial \bar{u}_i}{\partial x_j} + \frac{\partial \bar{u}_j}{\partial x_i} \right) \right]^{1/2}. \quad (6)$$

We have adopted a different point of view, based on the spectral eddy-viscosity concept:

A.1 Spectral eddy-viscosity

Let us consider isotropic turbulence in Fourier space: the filter F is now a sharp filter which cancels out the modes larger than the cutoff wavenumber $k_c = \pi/\Delta x$. Let $E(k_c)$ be the kinetic energy spectrum at k_c . An "à la mixing length" theory, assuming that the integral scale of the subgrid turbulence is $\sim k_c^{-1}$ and its characteristic velocity $v(k_c) \sim \sqrt{k_c E(k_c)}$ gives

$$\nu_t \sim k_c^{-1} v(k_c) \sim k_c^{-1} \sqrt{k_c E(k_c)} = C \sqrt{\frac{E(k_c)}{k_c}}. \quad (7)$$

Nonlocal expansions based upon the EDQNM theory, plus assumption of a $k^{-5/3}$ spectrum for $k > k_c$, yield for $k \ll k_c$ (Chollet and Lesieur, 1981)

$$C = 0.44 C_K^{-3/2}, \quad (8)$$

where C_K is the Kolmogorov constant). When k is close to k_c (in practice, it corresponds to $k > 0.3 k_c$), a k dependance is found for the eddy-viscosity, with a cusp behaviour (Kraichnan, 1976, Lesieur, 1990). This is the so-called Chollet and Lesieur's model. A simplified version of it is the averaged spectral eddy viscosity (without cusp), where the constant in the eddy-viscosity is adjusted by assuming a subgrid-scale flux equal to ϵ in an infinite Kolmogorov cascade $E(k) \sim \epsilon^{2/3} k^{-5/3}$. It is found

$$C = \frac{2}{3} C_K^{-3/2}. \quad (9)$$

The spectral eddy-viscosity gives fairly good results for isotropic turbulence, but with a spectrum closer to k^{-2} than $k^{-5/3}$. However, kinetic-energy decay is in good agreement with theoretical predictions at high Reynolds number as checked in Métais and Lesieur (1992).

A.2 The structure-function model

When working in physical space, however, this spectral eddy-viscosity is difficult to employ in cases of strong inhomogeneity and intermittency: the spectral eddy viscosity will be calculated from an average of turbulence upon the whole domain. It will be obviously too high in the regions where the flow is quasi-laminar, or where instabilities develop. In this case it is preferable not to use any additional damping due to an eddy viscosity. On the other hand, the eddy-viscosity will be too low in regions of strong turbulent activity. The idea of the structure-function model (Métais and Lesieur, 1992) is to introduce a local kinetic energy spectrum $E_{\vec{x}}(k_c)$, which is used for the evaluation of the eddy-viscosity. This spectrum is calculated in terms of the local second-order velocity structure function

$$F_2(\vec{x}, \Delta x, t) = \langle \|\vec{u}(\vec{x}, t) - \vec{u}(\vec{x} + \vec{r}, t)\|^2 \rangle_{\|\vec{r}\|=\Delta x} \quad (10)$$

using “Batchelor-Orszag’s formula”

$$F_2(\vec{x}, \Delta x, t) = 4.82 C_K (\epsilon \Delta x)^{2/3} \quad , \quad E_{\vec{x}}(k_c) = C_K \epsilon^{2/3} \left(\frac{\pi}{\Delta x} \right)^{-5/3} \quad (11)$$

which yields

$$E_{\vec{x}}(k_c) = \frac{1}{4.82} \pi^{-5/3} \Delta x F_2(\vec{x}, \Delta x, t) . \quad (12)$$

Expressing the structure function of the filtered field, \bar{F}_2 , in terms of the total structure function¹, it is obtained

$$\nu_t(\vec{x}, \Delta x, t) = 0.105 C_K^{-3/2} \Delta x [\bar{F}_2(\vec{x}, \Delta x, t)]^{1/2} , \quad (13)$$

where the spatial average in the structure-function is taken upon points $\vec{x} + \vec{r}$, a distance Δx apart of \vec{x}).

An analogous eddy-conductivity is built up taking a turbulent Prandtl number equal to 0.6, as given by the isotropic incompressible studies. Afterwards, these eddy-coefficients are incorporated with the viscous coefficients into the Navier-Stokes equations. For isotropic decaying turbulence, a very

¹ This is done assuming that the small-scale turbulence follows a Kolmogorov cascade (see Métais and Lesieur, 1992, for details).

good Kolmogorov spectrum is obtained for the velocity in the neighbourhood of the cutoff wavenumber k_c . For non-isotropic turbulence, the use of the structure-function model may be justified by the fact that small scales are less anisotropic than large scales: the anisotropy of the latter is directly taken into account by the simulation. The model works very well for the backward-facing step flow (Silveira-Neito et al., 1991, 1993) where it predicts a reattachment length and pressure coefficients in good agreement with experiments in the low-step case. For the high step, the calculation shows a vortex structure close to the structure obtained in experimental mixing layers, with quasi 2D primary Kelvin-Helmholtz vortices shed behind the step, and stretching longitudinal vortices inbetween. Applied to the problem of initially 3D isotropic turbulence submitted to rotation, the structure-function model shows how, for certain regimes of rotation, turbulence is reorganized into a few cyclonic vortices parallel to the rotation axis (Bartello et al., 1993).

Aknowledgements

The authors are indebted to E. David, E. Lamballais and M. Silvestrini for contributing to the large-eddy simulations presented here. The support of CCVR, CNRS, Dassault/CNES and DRET is acknowledged.

References

- Bartello, P., Métais, O. and Lesieur, M., 1993, "Coherent structures in rotating three-dimensional turbulence", submitted to *J. Fluid Mech.*
- Bernal, L.P. and Roshko, A., 1986, *J. Fluid Mech.*, **170**, 499.
- Breidenthal, R., 1981, *J. Fluid Mech.*, **109**, 1.
- Browand, F.K. and Troutt, T.R., 1980, *J. Fluid Mech.*, **93**, 325.
- Brown, G.L. and Roshko, A., 1974, *J. Fluid Mech.*, **64**, 775.
- Comte, P., Fouillet, Y., Gonze, M.A., Lesieur, M. and Normand, X., 1991, in *Turbulence and Coherent Structures*, Kluwer Publishers, O. Métais and M. Lesieur eds, 45.

- Comte, P., Lesieur, M., and Lamballais, E., 1992, *Phys. Fluids A*, **4**, 2761.
- David, E., 1993, PhD, National Polytechnic Institute, Grenoble.
- Franc, J.P., Michel, J.M. and Lesieur, M., 1982, C.R. Acad. Sci. Paris, Ser II, **295**, 773.
- Herbert, T., 1988, *Ann. Rev. Fluid Mech.*, **20**, 487.
- Klebanoff, P.S., Tidstrom, K.D. and Sargent, L.M., 1962, *J. Fluid Mech.*, **12**, 34.
- Kraichnan, R.H., 1976, *J. Atmos. Sci.*, **33**, 1521.
- Lasheras, J.C. and Choi, H., 1988, *J. Fluid Mech.*, **189**, 53.
- Lesieur, M., 1990, "Turbulence in Fluids" (second revised edition), Kluwer Publishers, Dordrecht.
- Métais, O. and Lesieur, M., 1992, *J. Fluid Mech.*, **39**, 157.
- Metcalf, R.W., Orszag, S.A., Brachet, M.E., Menon, S. and Riley, J., 1987, *J. Fluid Mech.*, **184**, 207.
- Normand, X. and Lesieur, M., 1992, *Theor. and Comp. Fluid Dynamics*, **3**, 231.
- Papamoschou, D. and Roshko, A., 1988, *J. Fluid Mech.*, **197**, pp 453-477.
- Pierrehumbert, R.T. and Widnall, S.E., 1982, *J. Fluid Mech.*, **114**, 59.
- Sandham, N.D. and Reynolds, W.C., 1991, *J. Fluid Mech.*, **224**, 133.
- Silveira Neto, A., Grand, D., Métais, O. and Lesieur, M., 1991, *Phys. Rev. Letters*, **66**, 2320; see also "A numerical investigation of the coherent vortices in turbulence behind a backward-facing step", to appear in *J. Fluid Mech.* (1993).
- Smagorinsky, J., 1963, *Mon. Weath. Rev.*, **91**, **3**, 99.
- Winant, C.D. and Browand, F.K., 1974, *J. Fluid Mech.*, **63**, 237.

Figure captions:

Figure 1: isosurface of the vorticity modulus in a periodic wake, corresponding to $s\omega_i$, where ω_i is the maximum initial vorticity ; a) direct-numerical simulation at Reynolds 200 and $s = 1/2$; b) large-eddy simulation using the structure-function model, $s = 1/2$; c) LES with Smagorinsky's model, $s = 1/2$; d) iterated laplacian, $s = 0.83$.

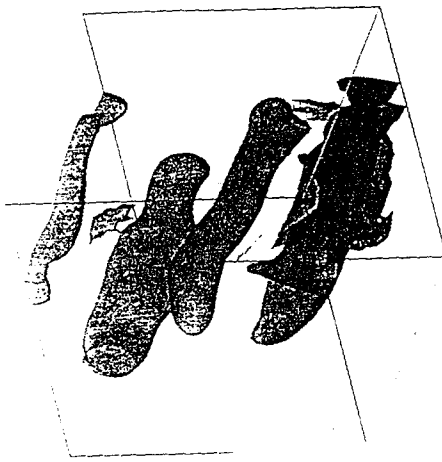
Figure 2: side-view of a cavitating wake at Reynolds 180 000 (from Franc et al., 1982).

Figure 3: top view of the incompressible periodic mixing layer undergoing a helical pairing; a) low pressure, b) vortex lines (from Comte et al., 1992).

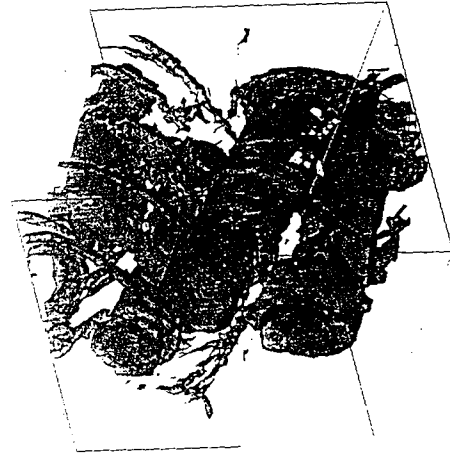
Figure 4: top view of the vortex lines in a compressible periodic mixing layer at a convective Mach number 0.3.

Figure 5: top view of the vortex lines (a) and low pressure (b) in a compressible periodic mixing layer at $M_c = 1$.

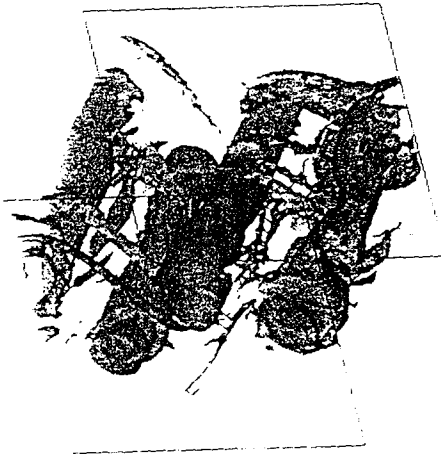
Figure 6: large-eddy simulation of transition in a Mach 0.5 boundary layer above a heated plate inclined 10° with respect to the upstream velocity. The isosurface of vorticity norm corresponding to 30% of the maximum is shown (from David, 1993).



(a)



(b)



(c)



(d)

FIGURE 1

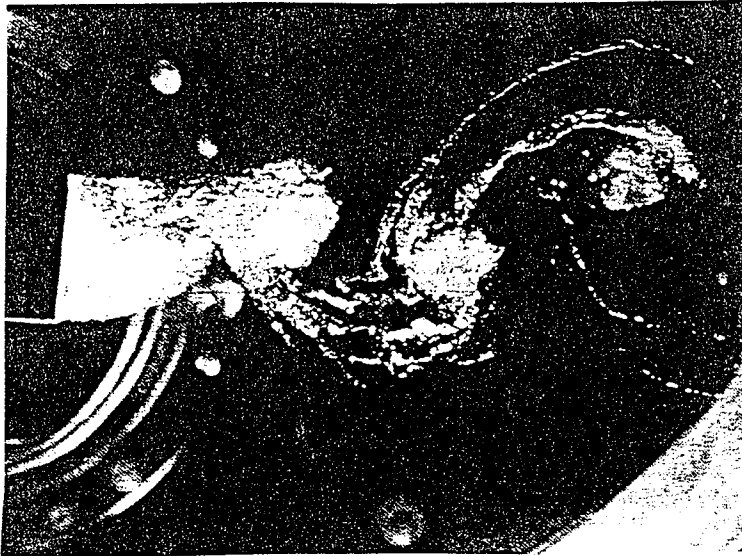
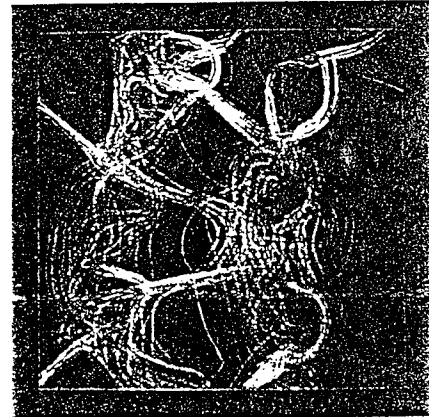


FIGURE 2



(a)



(b)

FIGURE 3

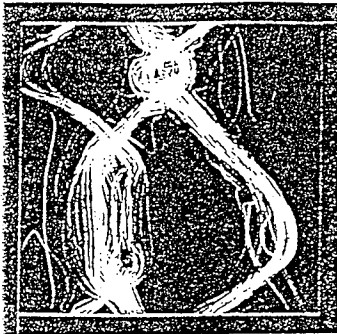
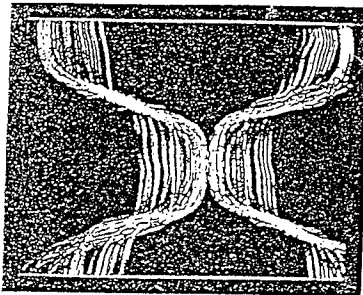
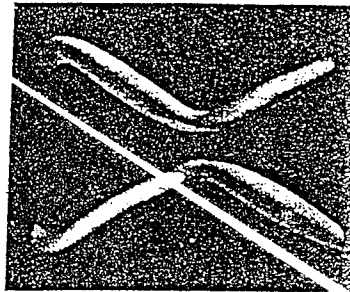


FIGURE 4



(a)



(b)

FIGURE 5

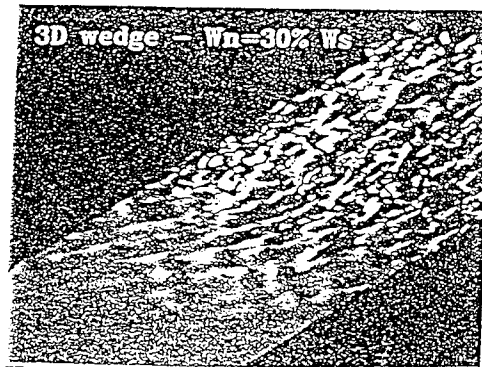


FIGURE 6

LATE-TIME TURBULENT MIXING OF A HIGH DENSITY GAS
 BUBBLE IN A SHOCKED AIR FLOW ($M_s = 1.14$)

M Philpott
 A V Smith
 AWE, Foulness, UK

N W Cowperthwaite
 D L Youngs
 AWE, Aldermaston, UK

INTRODUCTION

A series of shock tube experiments is described which investigates the interaction of a shock wave with a bubble of dense gas (freon-12) in air. The Mach number of the incident shock is $M_s \sim 1.14$. The main purpose of the experiment was to study the late-time turbulent mixing of the freon with the surrounding air which occurs after shock passage. Comparisons have been made with two-dimensional direct numerical simulations in axisymmetric geometry. There is a significant disagreement between simulation and experiment. The two dimensional calculation has recently been repeated with a turbulence model to represent the effect of three dimensional turbulence. The experimental results are described in [1].

COMPARISON WITH DIRECT 2D NUMERICAL SIMULATION

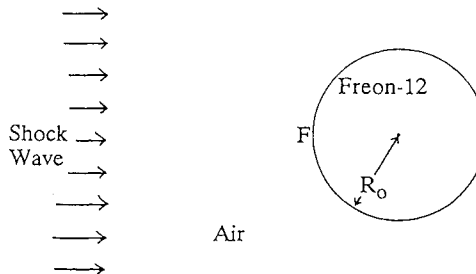


Figure 1: The initial configuration for the experiment

The experiment is illustrated in figure 1. R_0 , the initial radius of the freon sphere is in the range 12 to 19 mm. U denotes the velocity of the air behind the shock and X denotes the displacement of the front surface (F). 2D direct numerical simulation has been carried out in axisymmetric geometry with $R_0 = 15$ mm and mesh size $\Delta r = \Delta z = 0.3$ mm (further details are given in [1]). For the purpose of comparing with experiment X/R_0 is plotted against Ut/R_0 , see figure 2. The calculated bubble displacement is less than observed, particularly at late time. Figure 3 includes results for a 2D calculation with a coarser mesh ($\Delta r = \Delta z = 0.6$ mm). Refining the mesh does not have a large effect on the displacement. Agreement with experiment is, in fact, worse for the finer mesh calculation. Hence there is a definite disagreement between 2D simulation and experiment. Figure 4 shows comparisons of observed (shadowgraph) and calculated (freon volume fraction

contours) bubble shapes. At early time there is quite good agreement. However, at late time there appears to be more fine scale mixing on the downstream side of the bubble in the experiment than in the simulation.

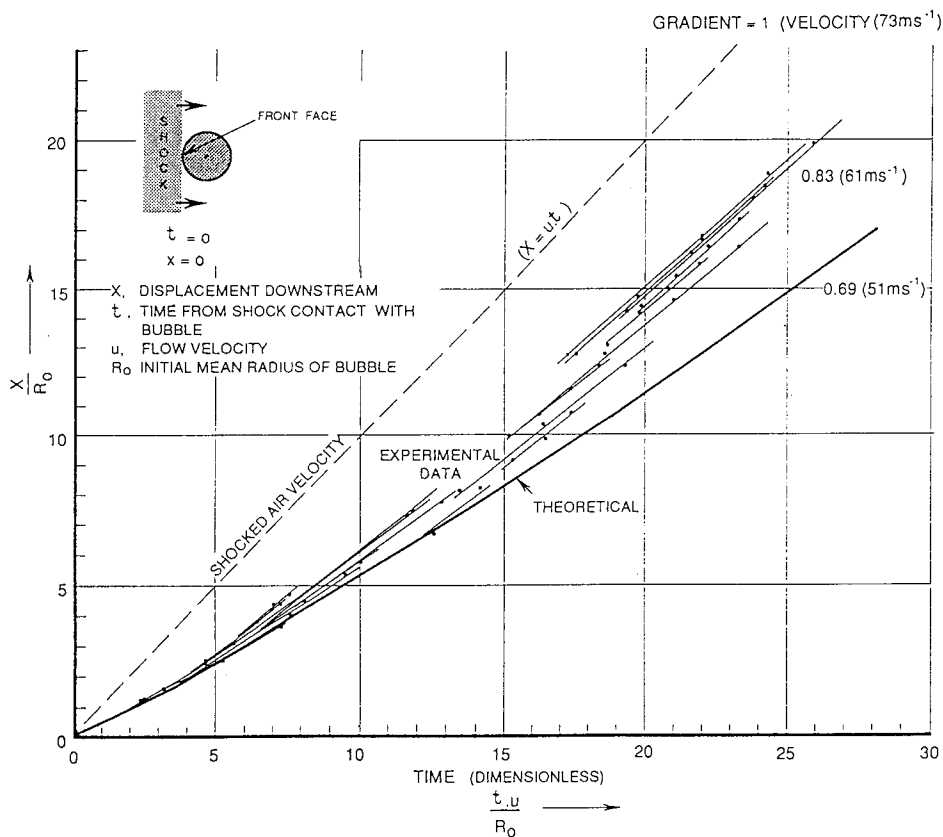


Figure 2: Bubble displacement versus time

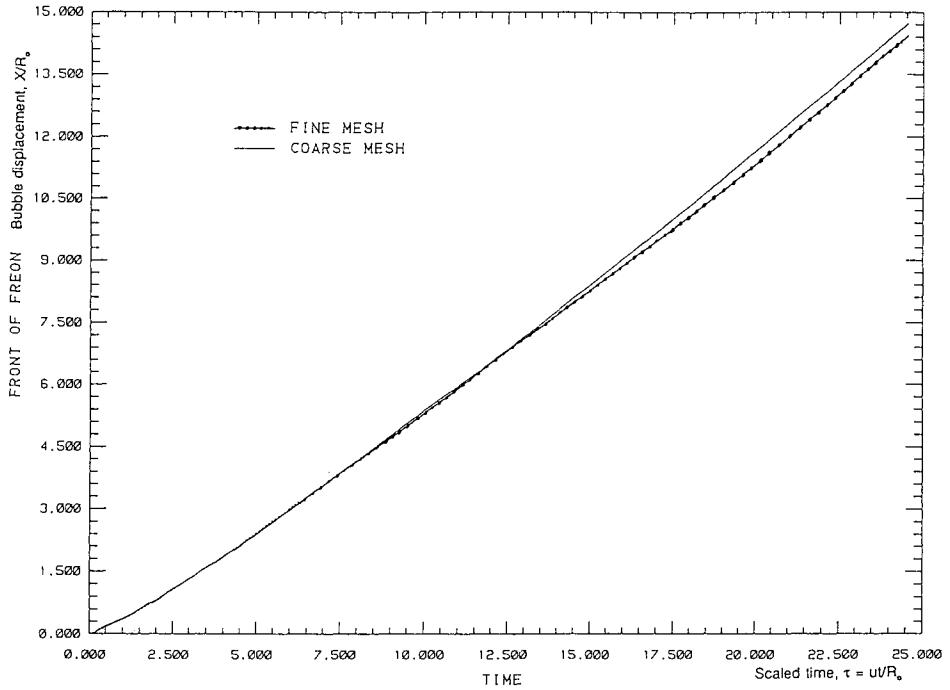


Figure 3: Calculated bubble displacement: effect of mesh size

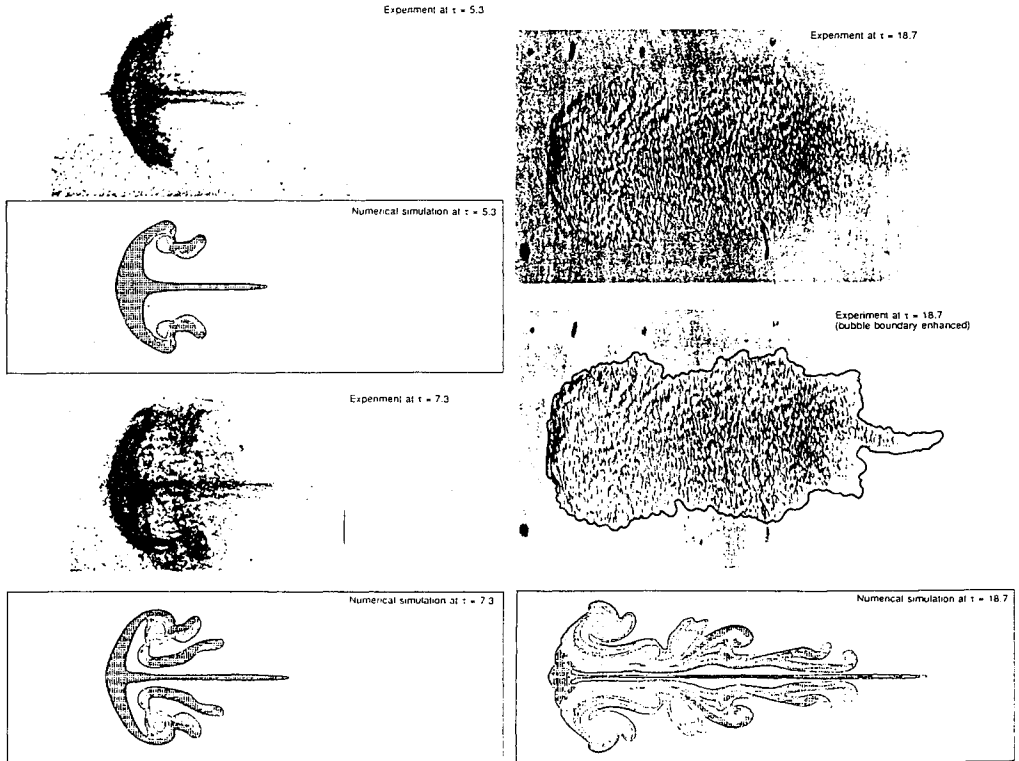


Figure 4: Observed and calculated bubble shapes.

VORTEX RING MOTION

The 2D simulation shows that the velocity field is dominated at late time by a single vortex ring which moves at the same velocity as the front of the bubble. The radius of the core of the vortex ring is about $1.3 R_0$; its distance from the front surface is about $1.25 R_0$.

According to Batchelor [2], the velocity of a vortex ring relative to the ambient fluid is given approximately by

$$V = \frac{1}{2} \frac{T}{P} \quad \text{where} \quad T = \text{kinetic energy, } P = \text{impulse}$$

At late time, the front surface of the bubble moves with velocity $U-V$; the rear surface moves with velocity close to U . As time proceeds the bubble elongates but does not increase in width. In the 2D simulation the front surface of the bubble moves at a velocity less than observed. This implies that the value of V in the simulation is greater than in the experiment, ie, the calculated vortex is too strong. A likely explanation is that, in the experiment, there is significant dissipation of kinetic energy due to the effect of three-dimensional turbulence.

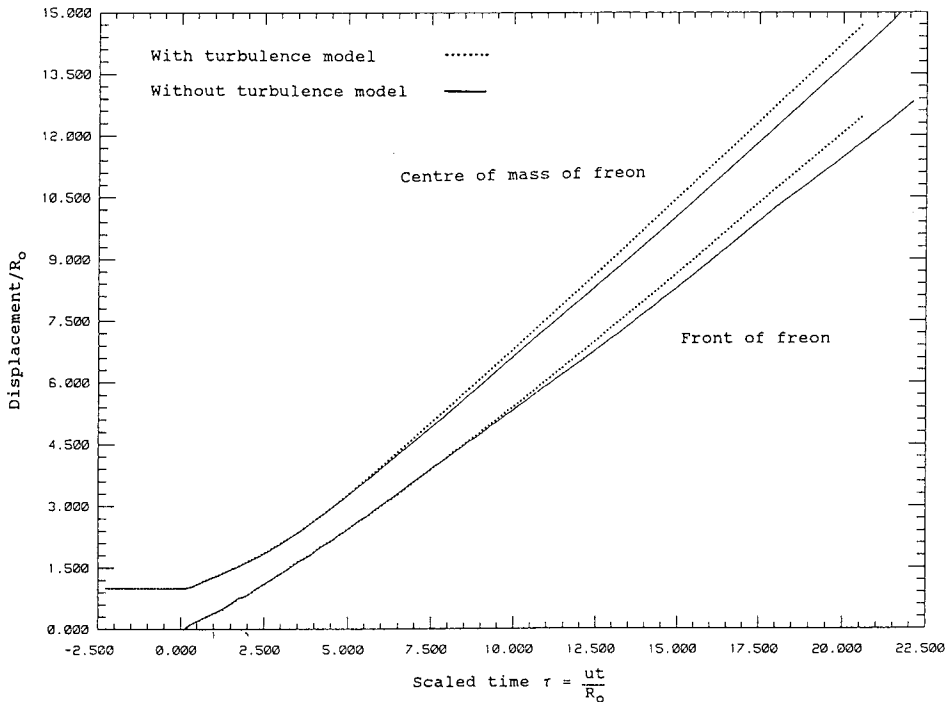


Figure 5: Calculated bubble displacement: effect of including the turbulence model

APPLICATION OF A TURBULENCE MODEL

In an attempt to resolve the discrepancy between simulation and experiment the 2D calculation has been repeated with a turbulence model included. A summary of the turbulence model is given in [3]; the same model coefficients are used here as in [3]. The bubble displacement is slightly greater in the calculation with the turbulence model, see figure 5. Hence agreement with experiment is improved. However, the effect is not large enough to explain the difference between simulation and experiment. Bubble shapes obtained for the turbulence model calculation are shown in figure 6. The bubble is now more diffuse and the shape is in much better agreement with experiments.

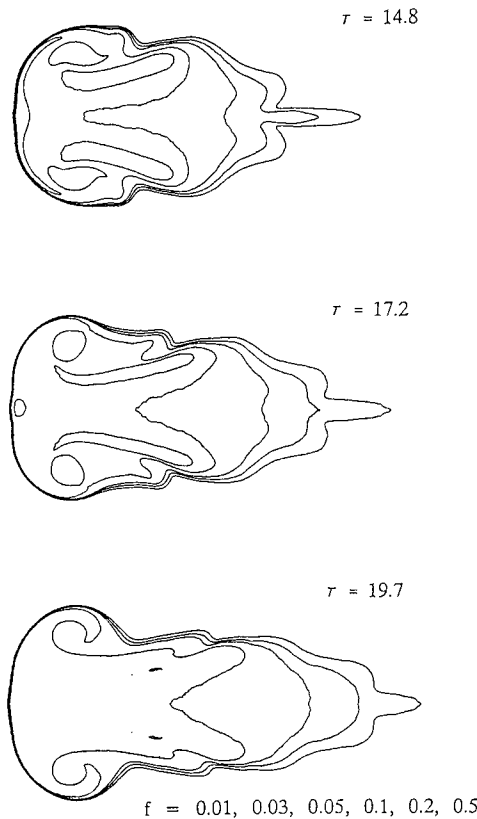


Figure 6: Volume fraction countours for calculation with turbulence model.

REFERENCES

1. M Philpott, A V Smith, N W Cowperthwaite and D L Youngs: "Late-time turbulent mixing of a high density gas bubble in a shocked air flow ($M_s = 1.14$)", AWE Report No. O8/92 (1992)
2. G K Batchelor: "An introduction to fluid dynamics", Cambridge University Press (1967)
3. D L Youngs, B C Hankin, N W Cowperthwaite: "Application of a two-dimensional turbulence model", these proceedings

On Shock Polar Analysis and Analytical Expressions for Vorticity Deposition in Shock-Accelerated Density-Stratified Interfaces

Ravi Samtaney and Norman J. Zabusky

Department of Mechanical and Aerospace Engineering, and CAIP Center
Rutgers University, Piscataway, NJ 08855

Abstract

Vorticity is deposited due to baroclinic effects on the surface of a density-stratified interface accelerated by a shock. We present an analytical expression, derived from shock polar analysis, for circulation per unit length on a fast-slow planar density interface inclined at an angle to the incident shock. The analytical expression is compared with numerical simulations for planar interfaces. The analytical expression is simple enough to be integrated to yield total circulation on nonplanar interfaces (sinusoidal and semicircular interfaces) accelerated by shocks. The analytical results agree very well with numerical experiments using a second order Godunov hydrodynamic code.

1 Introduction

A fundamental interaction in compressible hydrodynamics is that between a shock wave and a density inhomogeneity. Furthermore, the elemental processes that occur are of practical interest in combustion and inertial confinement (laser driven fusion). Of special interest is the “early-time” stability and growth rate for shock-accelerated interfaces which may be explained from the point of view of vortex dynamics¹. As a result, accurate quantification of vorticity generation is a very important goal. We present analytical expressions for circulation at fast-slow planar gas interfaces using shock polar analysis (SPA). Using these results we predict analytically the circulation on non-planar interfaces (sinusoidally perturbed interfaces and bubbles). The analytical results agree very well with numerical experiments.

The physical picture may be characterized by a shock wave propagating in a rectangular shock tube, through a gas of density ρ_1 and an interface separating a gas of density ρ_2 . Fig. 1 shows a schematic of three possible physical situations: planar interface inclined at an angle, α ; a sinusoidally perturbed vertical interface with amplitude, A , and wave length, λ ; or a bubble of radius, r_0 . The essential parameter space is three dimensional: the strength of the shock characterized by the Mach number M , the density ratio $\eta = \rho_2/\rho_1$, and the geometry of the density interface characterized by α or r_0 or by A/λ . Effects of viscosity and changes in specific heat ratio are omitted, as they play a minor role in this parameter domain.

Two generic classes of interactions exist: one in which the shock crosses into a fluid with a higher sound speed, $\eta < 1$ (the “slow/fast” or s/f interac-

tion), and the case where the shock passes into a region with a lower sound speed, $\eta > 1$ ("fast/slow" or f/s). In this letter, we consider only $\eta > 1.0$.

Vorticity layer generation and late time evolution of coherent vortical structures in shock-interface interactions have been investigated by Hawley and Zabusky¹; Yang, Zabusky et. al. and Samtaney, Zabusky et. al.^{2,3,4}. Experimental work on shock-interface interactions was done by Jahn⁵, Abdel-fattah and Henderson⁶, Haas and Sturtevant⁷; and many others. For a limited parameter range, Yang, Zabusky et. al.² quantified the circulation at a f/s interface using SPA and numerically; and validated the performance of their code.

2 Circulation at a Fast-Slow Gas Planar Interface

Fig. (2) shows a schematic of a regular refraction of a shock wave at a fast/slow interface. In SPA one assumes a frame of reference which is stationary with respect to the *node* where all the shocks meet. Furthermore, we assume that initially both gases are perfect, inviscid and of constant identical specific heat ratio (γ). In Fig. (2), *mm* is the interface; *i*, *r*, *t* are the incident, reflected and transmitted shocks, respectively; *s*₁ and *s*₂ are the streamlines in the incident and transmitted media; δ_0 and δ_1 are the deflections of *s*₁ due to *i* and *r*, respectively and δ_b is the deflection of *s*₂ due to *t*. p_0 and p_b are the initial pressures in the incident and transmitted gases respectively; p_1 , p_2 and p_t are respectively the pressures behind the incident, reflected and transmitted shocks. M_0 and M_b are the free stream Mach numbers in the incident gas and transmitted gas respectively. Follow-

ing Henderson ⁸, we may write three equations of the shock polars for the incident, transmitted and reflected shocks as

$$\tan \delta_i(p) = \frac{p/p_i - 1}{1 + \gamma M_i^2 - p/p_i} \left[\frac{(1 + \mu^2)M_i^2 - \mu^2 - p/p_i}{\mu^2 + p/p_i} \right]^{\frac{1}{2}}, \quad (1)$$

where $i = 0, 1, b$ for the incident, reflected and transmitted shock and $\mu^2 = \frac{\gamma-1}{\gamma+1}$. The following equations are also obtained from the conservation laws:

$$\frac{p_1}{p_0} = 1 + (1 + \mu^2)(M^2 - 1), \quad (2)$$

$$\frac{1 + \frac{\gamma-1}{2}M_0^2}{1 + \frac{\gamma-1}{2}M_1^2} = \psi \left(\frac{p_1}{p_0} \right), \quad (3)$$

where $\psi(p) = p(1 + \mu^2 p)/(\mu^2 + p)$ and $M_0 = M \sin^{-1} \alpha$. Since the velocity of the node is the same in both media, we have $M_b = M_0 \eta^{\frac{1}{2}}$. To solve for the pressure p_2 , the following compatibility equations hold:

$$\delta_0(p_1) - \delta_1(p_2) = \delta_b(p_t) \quad (4)$$

$$\frac{p_t}{p_b} = \frac{p_2}{p_0} = \frac{p_2 p_1}{p_1 p_0}. \quad (5)$$

For simplicity, we assume that initially $p_b = p_0 \equiv 1$. For regular refraction, and fixing γ, M, α , and η , one can solve the above equations for p_2 and the velocity jump (Δv) across the interface. The magnitude of the circulation (vorticity deposition) per unit length of the *shocked* interface is:

$$\frac{d\Gamma}{ds'}(M, \alpha, \eta, p_2, \gamma) = \Delta v \equiv (v_t(M, \alpha, \eta, p_2, \gamma) - v_2(M, \alpha, \eta, p_2, \gamma)) \quad (6)$$

In Eq. (6), v_t and v_2 are the tangential velocities on either side of the perturbed interface. To get the circulation per unit length of the *original* interface we multiply Eq. (6) by the factor $ds'/ds = \cos \alpha / \cos(\alpha - \delta_b)$

which accounts for the instantaneous change in length of the interface due to the shock. Thus we get $\Gamma' = \Delta v \cos \alpha / \cos(\alpha - \delta_b)$. The expression for Γ' reduces to

$$\Gamma' = - \left(\frac{2\gamma}{\gamma - 1} \right)^{\frac{1}{2}} \frac{\cos \alpha}{\cos(\alpha - \delta_b)} \left(\left[\frac{\gamma - 1}{2} \frac{M^2}{\sin^2 \alpha} + \frac{1 - \psi(p_2)}{\eta} \right]^{\frac{1}{2}} - \left[\frac{\gamma - 1}{2} \frac{M^2}{\sin^2 \alpha} + 1 - \psi(p_2/p_1)\psi(p_1) \right]^{\frac{1}{2}} \right). \quad (7)$$

To obtain an approximate expression for circulation on the interface, we expand Γ' in Eq. (7) as a series in $\sin \alpha$ about $\sin \alpha = 0$. Thus we have,

$$\Gamma' = - \left(\frac{\gamma^{\frac{1}{2}}}{(\gamma - 1)M} \right) \left(\frac{1 - \psi(p_{2,0})}{\eta} - 1 + \psi(p_{2,0}/p_1)\psi(p_1) \right) \sin \alpha + O((\sin \alpha)^3) \quad (8)$$

where the limiting pressure behind the reflected shock $p_{2,0} = \lim_{\alpha \rightarrow 0} p_2$.

3 Numerical Experiments

As described earlier^{2,3}, we use a second order Godunov scheme to simulate 2D compressible Euler equations on a uniform grid with $\Delta x = \Delta y = 0.25$ with shocktube width 20, and a shock about 10 grid zones to the left of the density interface (starting at $x = 25$) which is spread over to 2-3 grid zones.

The boundary conditions were reflecting in the y-direction and inflow/outflow in the x-direction. We made several runs with different density ratios and different angles. Using the feature tracking mode in DAVID⁹ enables us to track coherent vortex structures which lie above a specified threshold value. This is used to measure the vorticity deposition after the the shock crosses

the interface completely.

In Fig. (3) we have shown the normalized circulation per unit length of the interface using Eq. (7), Eq.(8) and the numerical result for $\eta = 3.0$ and $M = 1.05, 2.0$. It is apparent that the exact result (Eq. 7) terminates at a certain critical angle while the approximate result (leading term in the series in Eq. (8) can be extended to $\alpha = \pi/2$. The analytical expressions agree very well with each other and with the numerical result up to moderate values of α . For large α , the approximate result overpredicts significantly when compared with the numerical result. Also, the agreement is better for moderate to large M than for small M at large α . Similar observations hold for larger η which are not reported here. We identify the sources of error for this discrepancy: the analytical expression is for an instantaneous vorticity deposition while the real vortex layer is evolving with time; and numerical diffusion spreads the vortex layer. Hence the for larger α the error is expected to be larger.

4 Circulation for Non-planar Interfaces

Consider a fast-slow interface which is nonplanar and can be described by the equation $x = f(y)$. We have an approximate expression for circulation (Eq. 8) which is of the form

$$\frac{d\Gamma}{ds} = -\Gamma'_1 \sin \alpha \quad (9)$$

where Γ'_1 depends only upon η and M . For planar interfaces the angle, α is constant. For an arbitrary interface $\alpha = \alpha(s)$, i.e. the angle between the

shock and the interface is a function of arclength, s . If α does not change sign along the interface, i.e. $f(y)$ is a monotonically decreasing or increasing function of y and at no point along the interface is $\alpha > \pi/2$, then we may integrate Eq. (9) to get the total circulation on the interface simply as $\Gamma = -\Gamma'_1 A_e$, where A_e (see Fig. 1) is the effective amplitude (crest to trough distance).

4.1 Sinusoidally Perturbed Interface

The equation of the interface is: $x = A \cos(ky)$. See Fig. (1) (b) for a schematic of the perturbed interface. Using the above result we get the circulation on one half-wavelength sinusoidally perturbed interface, (Γ_p) as $\Gamma_p = -2A\Gamma'_1$. For this case, the largest angle between the shock and the interface occurs at the $(0, -\lambda/4)$ and is given by $\tan \alpha_{max} = Ak$. Comparison between numerical simulations and the above expression is shown in Fig. 4 for $A/\lambda = 0.125$ and 0.5 . For $A/\lambda = 0.125$, the refraction of the shock at the interface is regular at all times while for $A/\lambda = 0.5$, $\alpha_{max} = 72^\circ$, for which the refraction is irregular. The agreement is very good, especially for small A/λ ratios.

4.2 Circular Interfaces

We use $\Gamma = -\Gamma'_1 A_e$ to get the circulation on surface of the bubble until the shock has reached the top of the bubble. For a circular bubble of radius r_0 the circulation (Γ_b) on the "uside" of the bubble is given by $\Gamma_b = -\Gamma'_1 r_0$. For numerical experiments we use $r_0 = 25$. Fig. 4 shows the magnitude of

circulation (normalized by τ_0) obtained numerically and analytically for the bubble. Note that in the case of a bubble we have angles between the shock and the density interface varying from 0 to $\pi/2$.

5 Conclusion and Future Work

In this letter, we have presented exact and approximate analytical expressions for circulation deposited on a fast-slow interface accelerated by a shock. We have obtained analytical expressions for vorticity deposition on sinusoidally perturbed and circular interfaces that are in good agreement with numerical results. A similar expression for slow-fast interfaces yields larger error and will be reported in the future.

In the future we will show that changes in γ across the interface do not significantly affect the circulation. Also, in the future we will use the analytical expressions to develop models to predict the vorticity deposition in shock-bubble interactions. For sinusoidally perturbed interfaces, we will use the expression for circulation and relate it to the growth rate of perturbations in the Richtmyer-Meshkov instability environment.

Acknowledgments

This work was supported in part by the National Science Foundation, Grant No. DMS-8901900. RS was supported by a fellowship from the IBM Corporation. We thank Xiaolong Yang for his useful comments.

References

- ¹ J. F. Hawley and N. J. Zabusky, "Vortex Paradigm for Shock-Accelerated Density-Stratified Interfaces," *Phys. Rev. Lett.* Vol. 63, pp 1241-1244, (1989)
- ² X. Yang, I-L. Chern, N. J. Zabusky, R. Samtaney, J. F. Hawley, "Vorticity Generation and Evolution in Shock-Accelerated Density-Stratified Interfaces," *Phys. Fluids A*, Vol. 4, No. 7, pp. 1531-1540,(1992)
- ³ N. J. Zabusky, R. Samtaney, X. Yang, I-L Chern, J. F. Hawley, "Vorticity deposition, evolution and mixing for shocked density-stratified interfaces and bubbles," *Shock Waves, The 18th International Symposium on Shock Waves, Sendai, Japan*, ed. K. Takayama, pp 19-28, 1991. Springer-Verlag.
- ⁴ R. Samtaney , N. J. Zabusky , X. Yang, I-L. Chern, "Evolution of vortex structures in shock-accelerated density-stratified interfaces," *Conference on Nonlinear Analysis and Computation, SUNY Stony Brook, November 21-22, (1991)*
- ⁵ R. G. Jahn, "The Refraction of Shock Waves at a Gaseous Interface," *J. Fluid Mech.*, vol. 1, pp. 457-489, (1956)
- ⁶ A. M. Abd-El-Fattah and L. F. Henderson, "Shock Waves at a Fast-Slow Gas Interface," *J. Fluid Mech.*, vol. 86, pp 15-32, (1978)
- ⁷ J-F Haas and B. Sturtevant. *CalTech Report*, (1985, unpublished)
- ⁸ L. F. Henderson, "The Refraction of a Plane Shock Wave at a Gas Interface," *J. Fluid Mech.*, vol. 26, pp 607-637, (1966)

⁹ F. Bitz and N. J. Zabusky, "David and 'Visiometrics': Visualizing, Diagnosing and Quantifying Evolving Amorphous Objects," *Computers in Physics*, pp. 603-614. Nov/Dec (1990)

Figure Captions

Fig. 1. Schematic of physical domain and parameters in shock accelerated density stratified interfaces. a) Planar interface; b) Sinusoidally perturbed interface; and c) Circular interface.

Fig. 2. Schematic of regular refraction with three shocks at a fast-slow interface. i, r, t are the incident, reflected and transmitted shocks, respectively.

Fig. 3. Circulation per unit original length, Γ' for $\eta = 3.0$. for $M = 1.05$ and $M = 2.0$ normalized by $(M^2 - 1)/M$. "○" = exact circulation, "◇" = approximate circulation, and filled "□" = numerical circulation.

Fig. 4. Circulation for a sinusoidal interface, $\Gamma_p/(2A)$ and the "uside" of a circular bubble Γ_b/r_0 for $\eta = 1.2, 3.0, 6.0, 15.0$. "□" = Sinusoidal interface, with amplitude $A = 10$ and wavelength $\lambda = 80$. Filled "□" = Sinusoidal interface, with $A = 40$ and $\lambda = 80$. "○" = Circular bubble. Solid Line = Analytical result ($\Gamma_p/(2A)$) or Γ_b/r_0 .

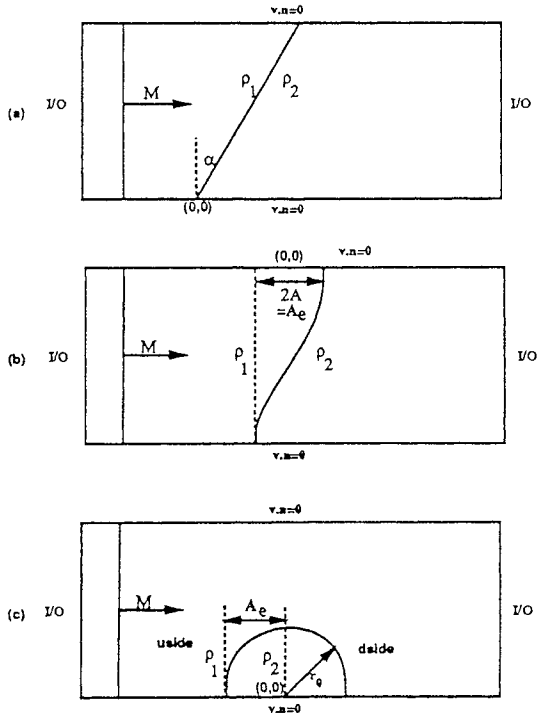


Figure 1:

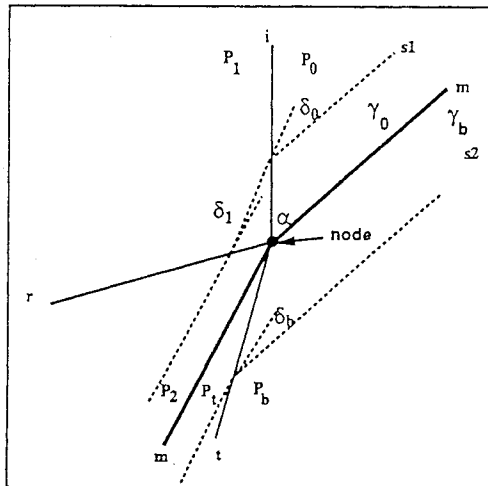


Figure 2:

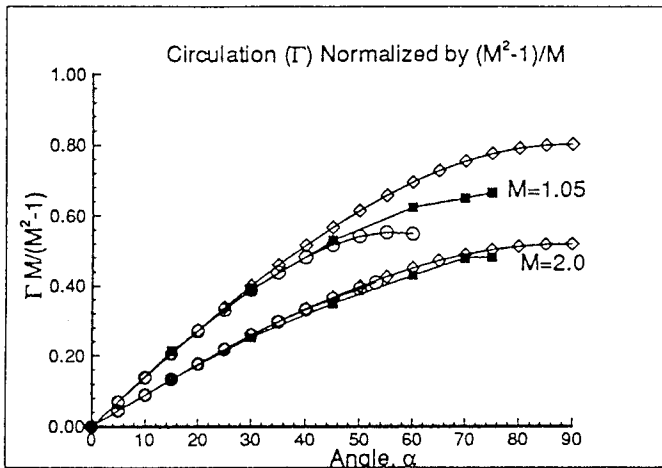


Figure 3

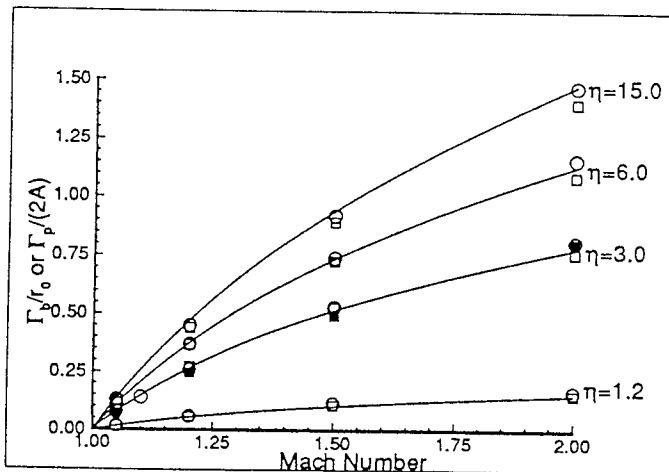


Figure 4

IV

Theoretical and empirical models

MODELING TURBULENT MIXING WHERE DO WE STAND?

D. Besnard
 Centre d'Etudes de Limeil-Valenton
 94195 Villeneuve-St-georges Cedex FRANCE

1-INTRODUCTION

If Kelvin-Helmholtz instability induced mixing has already been studied for quite a few years, it was only recently that interest grew about the role of Rayleigh-Taylor and Richtmyer-Meshkov instabilities as drivers towards mixing. The obvious reason is that there are applications, such as inertial confinement fusion, which require some control over these instabilities. Modeling such flows is a difficult task: They are turbulent, highly nonstationary, and involve several compressible media. Solving the problems associated to each of these aspects is in itself a challenge. However, a number of approaches have been considered, which are reviewed in this paper.

There are two main classes of problems to be addressed when modeling turbulent mixing. The first type pertains to the understanding of the hydrodynamics of non-stationary turbulent mixture flows. The second one is related to the modeling of mixing patterns induced by hydrodynamic instabilities, and their relationship to other physical processes. The first class has been approached with already well-known techniques, but generalized to multi-material flows. In Section 2, we summarize some of the results obtained from theoretical work, that should help for deriving engineering models, such as single-point closure modeling of turbulent correlations. In Section 3, we mainly investigate one-field models, such as "k- ϵ " models and two-field models. In particular, we describe here the different types of closure and their domain of application. We then analyze the different choices of closures and discuss their advantages.

It is well-known that such models implicitly assume an underlying spectral equilibrium. For unsteady flows, with sudden changes imposed upon, single-point models may be unsuited. To address these problems, and improve currents models, spectral models are currently under investigation. This is described in Section 4, with a two-point closure approach, that reduces to single point models through wavenumber averages. However, the type of closure they use assumes that the flow is already turbulent, and therefore cannot deal with the early phase of the mixing. That is why they require an initialization procedure, a very difficult problem that is considered in this paper. One way to alleviate it is to use a two-field model, by which the early, ordered interpenetration of the two fluids is clearly separated from the later turbulent mixing phase.

The second class is by far not as much developed than the first one. In fact, although multiphase flow has been of considerable interest for the past twenty years in the nuclear engineering community, interface dynamics is such a complex, nonlinear problem that very little results were obtained before the advent of the most recent computers, allowing for very detailed numerical experiments. These in turn suggest possible models. Up to now, no statistical knowledge was obtained about mixtures induced by Rayleigh-Taylor and Richtmyer-Meshkov instabilities. However, if such a distribution of one fluid in the other assumes a specified form, it may be possible to calculate some mean values, for such a quantity as the opacity of the mixture. A very brief review of the present results constitutes the Section 5 of this paper.

2-THEORETICAL RESULTS

2.1-Rayleigh-Taylor instability induced mixing

The non-linear and turbulent stages of Rayleigh-Taylor instability induced mixing have been the subject of a renewed interest, starting a few years ago, due to two factors: It was shown experimentally ^{1,2,3,4} that RTI mixing layers grow in a self-similar fashion, at least for a large range of parameters. This suggested that it should be possible to model such a process with rather simple models (i.e. involving a limited number of equations). On the other hand, the availability of more powerful computers and of new, more sophisticated numerical algorithms allowed for detailed simulations, way in the non-linear regime of RT (and RM) instability. Indeed, it was shown ^{5,6,7,8} using both simulations and modeling that RT mixing layer growth follows the power law $\alpha g t^2$, as observed in experiments ^{1,3}. It should be emphasized that the above mentioned simulations pertain to the nonlinear regime, that shows nevertheless the same feature of a rather well-defined self-similar regime. Initial conditions might therefore be forgotten if the acceleration lasts long enough (i.e. compared to the other time scales in the problem), which would greatly simplify the difficulties associated with modeling. These results suggest that it should be possible to derive relatively simple models with accurate prediction capabilities.

2.2-Richtmyer-Meshkov instability induced mixing

In contrast with RTI induced mixing, Richtmyer-Meshkov instability induced mixing does not offer as clear a picture. Due to its impulsive nature, RMI does not induce a well defined, self-similar law of interpenetration. In fact, it was suggested ⁹ that the fluctuating energy contained in the interpenetration zone might depend on initial conditions, at least in a statistical sense. More precisely, this energy would be proportional to a power of the interface roughness (in fact to the interface rms). The associated power law for the mixing layer growth is $t^{2/3}$, to be compared to another prediction ¹⁰, of a linear growth, with no initial condition dependence (for "small" initial perturbations). Detailed numerical simulations ^{11,12} seem to confirm the first prediction, at least in the limit of the times that were considered for the simulations.

It was also shown experimentally that, for a single mode perturbation, the ratio of the perturbation amplitude to the mode wavelength is a "universal" function of Richtmyer formula ¹³, even in the non linear regime.

The above mentioned work was done for discontinuous interfaces separating two fluids. Some additional work was done regarding the interaction of shocks and continuous interfaces, showing a reduction of the interpenetration growth rate when compared with the discontinuous case ^{14,15}.

3-SINGLE-POINT CLOSURE MODELS

We concentrate here on the engineering modeling of multimaterial compressible turbulent flows; the different materials are not necessarily mixed initially, which brings in the additional complexity of the modeling of the mixing process itself. The applications range from volcanic eruptions, where a plume of hot air (mixed with ashes) mixes with the surrounding cold air, to laser-implosed pellets, where the mixing of the outer shell and the inner fuel may lead to a significant decrease in the neutron yield ¹⁶.

All these applications have the common features of being highly unsteady, and involving multimaterial flows. They bring in a major difference with the usual field of application of transport models; one has here to address the problem of initialization of transport models, or of the modeling of the different phases of the mixing occurring between the materials; the model has to mimic successively the linear, nonlinear (two-field interpenetration), and turbulent phases of the mixing.

3.1-Two-field models

We consider here flows consisting of several different materials, denoted by α . In each field, conservation laws read ¹⁷

$$\frac{\partial}{\partial t}(\rho^\alpha f^\alpha) + \nabla \cdot (\rho^\alpha f^\alpha v^\alpha + j^\alpha) = \rho^\alpha r^\alpha$$

to which one has to add interfacial relationships between materials, $\sum_\alpha [f^\alpha] = 0$ on Σ , with $[f^\alpha] = \rho^\alpha f^\alpha (v^\alpha \cdot n^\alpha) - j^\alpha \cdot n^\alpha$. f^α is respectively 1, the velocity, and the total energy of field α ; r^α is the production rate of f^α , and $-j^\alpha$ is a flux; v^α is the interface velocity, and n^α is the unit vector orthogonal to Σ at point x .

We consider now circumstances when the material interpenetrate each other or already form a heterogeneous mixture. However, we assume here we only have a statistical knowledge of this multifield flow; for example, if we consider the case of Rayleigh-Taylor instability induced mixing of two materials, we assume we do not have control over the perturbations of the interface separating them (we might only know its rms); in the case of particles in a carrier fluid, the initial locations and/or number of the particles is not known, only the particle volume fraction. We therefore define an averaging procedure over a set of possible realizations of the flow. If the Reynolds number is high enough, the flow may turn turbulent, and another average be defined: it is the usual Reynolds ensemble averaging technique. The corresponding set is used as the basis for obtaining ensemble averaged quantities.

This approach leads to two-phase models ^{2,18,19}, upon which turbulence is superimposed. The two-phase part of the models describes the laminar interpenetration of the two materials, occurring in a well-defined direction. In other words, the interpenetration is highly anisotropic. It is also useful to emphasize that, due to a differential acceleration, the two fluids might have different velocities along the interpenetration direction, which supports the two-field approach. The interaction between fluids is modeled as a drag term, which transfers energy from the large scale anisotropic motion into the small scale turbulent part of the flow, if the Reynolds number is large enough. The turbulence is described by additional equations. They range from a k-L model ² to second order models ^{18,19}. Note that the turbulent fields might not be in equilibrium with each other, therefore suggesting the use of separate variables for the two turbulent kinetic energies ¹⁸.

An interesting feature of these models is that they do not offer any difficulty regarding their initialization. Indeed, differential acceleration leads to interpenetration, and therefore fluctuating energy that, in turn, may be transformed into turbulent kinetic energy: These models mimic the transition phase from laminar to turbulent patterns. This is achieved through two different choices of closures (corresponding to two different sets of realizations for the flow) for the statistical correlations appearing in the models. The underlying idea is that some of the modes (the larger ones) are still in their linear phase, while smaller scales have already turned turbulent, i.e. the spectrum of the flow can clearly be separated, at any given time, into a well developed part, and a discrete one.

2.2-Single field modeling

Another possible approach is to use the mixture local variables $\rho = \sum_\alpha \chi^\alpha \rho^\alpha$, $u = \sum_\alpha \chi^\alpha v^\alpha$, $e = \sum_\alpha \chi^\alpha e^\alpha$, $j = \sum_\alpha \chi^\alpha j^\alpha$, and $r = \sum_\alpha \chi^\alpha r^\alpha$. This does not necessarily mean that the two-field processes described above are neglected here. Rather, the idea here is to keep the same framework as most large hydrodynamic multimaterial

codes. If "k-e" models were considered^{9,20}, it was early recognized that more sophisticated models are necessary, in order to address the problems of RM induced turbulence^{21,11}.

The underlying assumptions for such models have been analyzed¹¹ and may be listed in the following way:

-The goal is to study instability induced mixing, and, as a first step, we consider that part of the spectrum of scales for which microscopic diffusion is small compared to the macroscopic perturbations created during the development of the instabilities inducing this mixing;

-It is also assumed that the Mach number of the velocity fluctuations ($M' = \sqrt{k}/c$, where c is the sound speed in the mixture) is small. This is equivalent to assume (for example through an expansion in M') that the divergence of the velocity is negligible (this excludes supersonic slip in a flow); therefore, there is a local equilibration of the pressures in the different materials. However, nothing is implied in terms of temperatures. Their equilibration depends upon the turbulent and molecular Prandtl numbers. Notice here that the two length scales -turbulence length scale and mixture length scale- are strongly linked, because the very process of the mixture formation is due to instability development and the subsequent turbulence. In terms of a transport model where one considers only one mean scale for the turbulence, this means that the turbulence length scale cannot be much smaller than the mixture length scale. This is exemplified by the choice of certain models² of a constant ratio of those two quantities;

-This assumption breaks down in the vicinity of shocks. Consider for example a shock interacting with a perturbed interface separating two fluids. An early pressure map would show that there is no pressure equilibration on the interface perturbation length scale, as expected. Also, due to our ensemble averaging procedure, we cannot describe the detailed distortions of the shock passing through a macroscopic mixture. All we can hope for is to obtain a good estimate of the density, energy, and fluctuating energy jumps across the shock. As a simplifying assumption, we neglect the self consistent interaction of the shock and the fluctuating field.

Our hypothesis of negligible microscopic interfacial exchanges and of local pressure equilibrium implies that fluctuations in density, pressure and internal energy occur only through intermittency. In fact, we obtain this result because only mean scales for the mixture and the velocity fluctuations (respectively L_m and L_t) were considered. We have

$$L_m/c_s \ll L_t/\sqrt{k},$$

where c_s is the mixture sound speed, and k is the local fluctuating energy.

However, the mixing of the two fields induces the generation of an entire spectrum of sizes for eddies and droplets of different materials; for a given size, the absence of pressure fluctuations within each field is true, only if

$$L_m\delta/c_s \ll L_t\delta/\sqrt{k\delta},$$

where δ denotes a specific range of entity sizes.

We therefore recognize the possibility of large scale fluctuations (compared to the mean two-field length scale), and that is why we model the term PV , that takes these fluctuations into account. However, we fully use our above assumption to obtain a simple mixture equation-of-state, that depends only upon intermittency, and not explicitly upon turbulence energy.

Within the limits defined by these assumptions, these models can adequately describe some of RTI and RMI induced flows. They differ quite markedly from single material flow models, due to the occurrence of additional source terms due to the interaction of shocks and accelerations with the density inhomogeneities existing in the flow. These interactions are

mean flow gradients driven, but here pressure and density gradients are involved, in place of mean velocity gradients. It is the modeling of these processes that differentiates models^{9,20}. Models of the "k-ε" family show a source term directly proportional to the tensor $\partial P/\partial x_i \partial \rho/\partial x_j$. Second order models show evolution equations for second order correlations^{11,21}, that, due to the choice of closures, allow for the description of the laminar phase of the interpenetration. Indeed, it is demonstrated in²² that one can draw an equivalence between the two-field approach and the single field approach, provided that evolution equations are kept for second order correlations, and that a careful choice is made for closing triple correlations. Moreover, second order models can deal with RMI mixing, through the coupling of the turbulent kinetic energy to the density self-correlation, which may be associated to interface corrugation, in the early phase of the interpenetration, and density inhomogeneities later in the process. An asymptotic analysis of such models show that they simplify into models of the "k-ε" family²³, and show an additional source term proportional to the tensor $\partial P/\partial x_i \partial P/\partial x_j$ (this result was obtained earlier by Andronov et al.²¹). This demonstrates the possibility of two-phase interpenetration in the absence of mean density gradients, such as in the case of fluidized dust beds.

Figure 1 shows the results obtained with one of these models¹¹, which are compared to the experimental results of Read¹.

Such models have been used for analyzing such problems as bringing an initially accelerated interface back to rest with as little turbulence energy production as possible^{24,25}.

4-TOWARDS SPECTRAL MODELS

3.1-Why a spectral model ?

In Section 2, are shown a number of difficulties associated to single-point models of turbulent mixing. If some of these are specific to the mixing problem, most arise in fact for single field turbulent flows. They are :

-Modeling multimaterial flows in real circumstances does not allow for simple gradient closures of second order correlations. More precisely, it is better to keep evolution equations for the components of the turbulent mass flux and the density self-correlation. This in turn leads to complex models. Moreover, dissipation equations have to be derived for each of the statistical correlations mentioned above, or a closure has to be found^{11,21};

-Multimaterial flow models therefore show a large number of "universal" constants that have to be estimated through comparison with experiments. The underlying assumption for doing so is that the physics not explicitly described by the model is dealt with by the coefficients is not an important part of the description of the flow (they are of order one); the another assumption is that one can identify each physical process with a specific term in the model, and that there is not a strong coupling between them. One then gathers experimental results for well defined experiments that involve only one physical process (e.g. shearing), simplifies the model and solves it, to obtain algebraic equations for the unknown constants. One eventually solves the system of equations obtained for a large enough number of experiments²⁶. But too often, experimental data are scarce or not completely reliable : there might be a lack of consistency between different experiments, which does not allow for going through the entire program of finding the coefficients associated to multimaterial flow models;

-Compressibility effects, although not crucial in many applications, may become important in some circumstances, such as supersonic slip, or shock/turbulence interaction. Most current models^{2,9,11,21} for compressible mixtures assume that the turbulent Mach number (that is, based on the fluctuating velocity and the sound speed \sqrt{k}/c) is small. This in effect couples the turbulent field only to the mean flow pressure gradient. Interaction with the

entropy field is not taken into account^{27,28}; this assumption prevents noise production and propagation description. It remains to be demonstrated that current models can reproduce the increase in turbulence intensity due to the passage of a shock through a patch of turbulence, as reported in²⁹;

-Rayleigh-Taylor and Richtmyer-meshkov instability induced turbulent mixing needs specific modeling for both laminar interpenetration and fully turbulent phases. Models have to mimic the transition from laminar to turbulent and therefore rely on different closures for the two phases;

Most applications envisioned here, such as ICF flows, involve shocks, interactions, and sudden accelerations. In other words, they are not in spectral equilibrium, which in part precludes the use of single point closure models, that do not take any change in spectra into account, for accurate prediction. It is indeed well known that "k-ε" models rely on a spectral equilibrium assumption, which cuts down the number of variables needed to describe the turbulent flow to which it is applied;

-These mixing models must also provide formulations for mixture equations of state, or thermodynamics relationships between pressures and temperatures in the case of multifield models. Whenever hydrodynamics calculations are coupled to such other processes as thermal conduction or radiative transfer, mixture thermal diffusivity or opacity must also be provided.

Single point closure models do provide partial answers to the above mentioned difficulties, as illustrated in Section 2. However, their recurrent problems are consistency and spectral equilibrium. A possible answer is to use spectral transport modeling. In this case, spectral information is kept via the use of an equation for the two-point Reynolds stress $R(x,y) = \overline{u'(x)u'(y)}$. Moreover, all the information provided by the model is obtained through a single equation, that is the turbulent kinetic energy density equation. Its advantages are obvious :

- there is only a limited number of parameters to be determined;
- through two-point closures, one keeps all the necessary information on spectra and their evolution with time;
- the derivation of single point closure transport models is simple, and is achieved through the calculation of moments of the model equations. One can therefore evaluate the accuracy of these simpler models and their limits. Moreover, through a careful study of the solutions to the full model, it is possible to improve single point closure models, and to take some of the spectral changes into account;
- there is a full consistency between equations obtained through this procedure : all these equations come from the same spectral model equation, and the coefficients that appear in them are limited to those of the spectral model; some additional dependence with spectra may take place.

3.2-Derivation and modeling

To discuss this type of approach, we present here such a model. Starting from Navier-Stokes equations, velocity and pressure fields are then divided in mean and fluctuating parts. The most general second order correlation that can be considered here involves velocities at two different points and two different times; to deal with flows far from equilibrium, one has to keep some information on fluctuations both in physical space and in wavenumber space. If $C(x_1,x_2)$ denotes such a correlation, the above constraint means that we must know the dependence of C both with regard to $(x_1+x_2)/2$, and (x_1-x_2) . An evolution equation is therefore derived³⁰ for a generalized Reynolds tensor defined as

$$R_{ij}(x_1,x_2) = \overline{u'_i(x_1)u'_j(x_2)} .$$

These correlations vanish at finite distance, of the order of the characteristic scale of turbulence, and a Fourier transform of the equation obtained for R_{ij} is used to obtain a spectral model. For the sake of simplicity, the resulting equation is averaged over wavevector angles, and the model describes therefore the evolution of the turbulent kinetic energy density in physical space and wavenumber space, defined as

$$E_{ij}(x,k,t) = \frac{1}{2} \int R_{ij}(x,k,t) k^2 \frac{d\Omega_k}{(2\pi)^3} .$$

Integrating the trace of this tensor over wavenumber, one obtains the density of turbulent kinetic energy at point x . The usual Reynolds tensor is therefore

$$R_{ij}(x,x,t) = 2 \int_0^\infty E_{ij}(x,k) dk .$$

Obtaining an evolution equation for E_{ij} relies on the formal expansion of the initial equation in a series of differential operators, for which it is very difficult to prove convergence. However, it is intuitively plausible that the terms of order n are proportional to the ratio $(L_T/L_u)^n$, where L_T is the characteristic scale of turbulence and L_u is the gradient length of the flow velocity. The ration of these two quantities may be assumed to be small, meaning that fluctuations vary at a smaller scale than those of the mean flow. This hypothesis suggests to keep only low order terms in the above mentioned expansion. Reference ³⁰ retains first order terms. At this point, there are still some unknown correlations in the equation that have to be modeled. This is done using known variables, and the criteria is to take the simplest formulations, namely linear or quadratic, that are dimensionally correct and have the required invariance properties (for example, translational invariance), and the specific properties of the original correlations. One obtains an equation which, in its simplest form ³⁰, writes

$$\begin{aligned} \frac{\partial E_{ij}}{\partial t} = & -(1 - c_B) \left(E_{in} \frac{\partial u_j}{\partial x_n} + E_{nj} \frac{\partial u_i}{\partial x_n} \right) - \frac{2}{3} c_B \delta_{ij} E_{mn} \frac{\partial u_m}{\partial x_n} - E_{nj} \frac{\partial u_i}{\partial x_n} + \frac{1}{2} \nu \nabla^2 E_{ij} \\ & - 2 \nu k^2 E_{ij} + c_M k \sqrt{kE} \left(E \frac{\delta_{ij}}{3} - E_{ij} \right) + c_D \frac{\partial}{\partial x_n} \left(\nu_t \frac{\partial E_{ij}}{\partial x_n} \right) \\ & - c_1 \frac{\partial}{\partial k} \left(k^2 \sqrt{kE} E_{ij} \right) + c_2 \frac{\partial}{\partial k} \left(k^3 \sqrt{kE} \frac{\partial E_{ij}}{\partial k} \right) \end{aligned}$$

where u_i is the mass averaged velocity, E is the trace of E_{ij} , and the turbulent viscosity ν_t is defined as

$$\nu_t = \int_0^\infty \frac{\sqrt{kE(x,k)}}{k^2} dk .$$

There are five phenomenological constants in this model, c_B , c_D , c_1 , c_2 , and c_M . For this model to have a reasonable degree of universality, these coefficients have to stay constant for all the flows we are interested in. They are obtained through theoretical reasoning and comparisons with experiments. It is shown in ³⁰ that c_1 and c_2 are related

to the Kolmogorov constant C_K through the relationship $c_1 + \frac{5}{3} c_2 = C_K^{-3/2}$. Moreover, the ratio c_1/c_2 may be taken to be equal to 2 if one uses the so-called equirepartition of energy property of triple correlations³¹. Analysis of the model in the circumstances of turbulence undergoing homogeneous irrotational strains suggests also³² $c_1 = \frac{6}{11} C_K^{-3/2}$, $c_2 = \frac{3}{11} C_K^{-3/2}$, and $c_M = \frac{26}{33} C_K^{-3/2}$.

Each of the terms in the model equation can be associated with a well defined physical process which affects the evolution of the turbulence spectral density. Turbulence is transported by mean-flow, including shears $\left(E_{in} \frac{\partial u_j}{\partial x_n} + E_{nj} \frac{\partial u_i}{\partial x_n} \right)$. However, these terms are separated from the total derivative of E along the mean flow to be interpreted as a source of energy to the mean flow. If the flow is incompressible, it is possible to show that the correlation relating pressure and velocity do not furnish any energy to the system; rather, they induce a relaxation of the flow into an isotropic state. They are usually modeled through two terms; the first one is independent of the mean flow, persisting in homogeneous circumstances; the second one includes mean flow shear effects : they are the terms respectively proportional to c_M and c_B . Viscous effects appear in the terms proportional to ν ; one notices direct dissipation into heat and diffusion in physical space. Triple correlations arise in the derivation of the model, demonstrating a non-linear, non-local effect of the turbulence on itself. They are modeled as diffusion in physical space

(i.e. $c_D \frac{\partial}{\partial x_n} \left(\nu_t \frac{\partial E_{ij}}{\partial x_n} \right)$). The last terms that are not yet commented in the above equation do not involve mean variables; they correspond therefore to a physical process which is characteristic of homogenous turbulence. It is the well-known nonlinear coupling between modes in the spectrum of turbulence. Even though it is widely recognized that this transfer is non-local, it was chosen in³⁰ an approximation based on and its two first derivatives, - $c_1 \frac{\partial}{\partial k} (k^2 \sqrt{kE} E_{ij}) + c_2 \frac{\partial}{\partial k} \left(k^3 \sqrt{kE} \frac{\partial E_{ij}}{\partial k} \right)$. It was demonstrated³⁰ that this approximation gives excellent results.

It is worthwhile mentioning earlier work on the modeling of energy transfer terms. For homogeneous isotropic turbulence, they may be divided into three categories:
 - heuristic and phenomenological closure of moment equations, e.g. EDQNM³³;
 - direct derivation from Navier-Stokes equation, e.g. DIA^{34,35,36};
 - derivation from other equations, such as the Langevin or Fokker-Planck equation³⁷.
 The shear complexity of Navier-Stokes equation is diminished in these models in two ways : either the non-locality of transfer terms is preserved but interactions between modes are simplified (DIA, EDQNM, RCM), or local approximations are proposed^{38,39,30}.

Extensions have also been proposed for non homogeneous flows such as boundary layer flows. Bertoglio and Jeandel⁴⁰ proposed a model in which third-order correlations are closed through EDQNM, and where a self-similar spectrum, not used in the model, is assumed to exist. This is to be put in contrast with the model we described above, that includes a self-description of turbulent spectra.

3.3-Examples

It is worthwhile emphasizing that there is a good agreement between a local model such as BHRZ³⁰ and a non-local model such as EDQNM. This is illustrated on Figure 2 by the two sets of curves defining the path of spectra towards self-similarity. As

expected, the $k^{-5/3}$ inertial range are identical, as well as the low k part of the spectra, which can be demonstrated analytically. What is more interesting is that the agreement on the dissipation range, which shows over seven decades. However, recent work by Clark and Zemach⁴¹ demonstrated that the time rates at which the self-similar regime is attained with BHRZ are off with respect to EDQNM.

Self-similar behaviors were also explored for a large range of flows : turbulence undergoing homogeneous mean flow velocity gradient constraints (e.g. irrotational strains), turbulence in free shear layers, and freely decaying anisotropic turbulence. The crucial result is that turbulence spectra approach self-similarity, but in each case reach different spectra. These spectral forms are independent from the intensity of shearing and straining, but depend on the structure of the mean-flow velocity gradient tensor (when it is non-vanishing). This demonstrates that it is not possible to use a two-equation model such as "k- ϵ " to accurately predict this range of flows, and that single-point closure models must include some additional knowledge about velocity gradient effects on turbulence spectra. To test the ability of BHRZ spectral models to reproduce sudden changes in driving forces, experiments by Gence⁴² and Gence and Mathieu⁴³ were simulated. In these experiments grid generated turbulence is submitted to two successive plane strains, with principal axes of the second strain aligned, or opposite, to those of the first strain. The case of two identical plane strains, then return to isotropy was also explored⁴⁴, as well as axisymmetric contraction by Uberoi and Wallis⁴⁵. The results show a sensitivity of the rate of return to isotropy on the spectral distribution, which implies constraints on the mean-flow coupling terms. These terms must "generate" the correct anisotropy spectra during the straining phase for the free decay to be accurately predicted. Overall, BHRZ predictions are in good agreement³² with experiments, an example of which is shown on Figure 3.

3.4-Derivation of single-point closure models.

As stressed above, it is easy to derive single-point closure models from a spectral model. To do so, one first averages over spherical shells in Fourier space. This eliminates the imaginary part of the complex valued functions that appear in Reynolds components and triple correlation terms. One then obtains the m^{th} order moment equation by integrating the spectral equation over k , after a multiplication by k^m . This procedure leads to "k- ϵ " like models, or more complex ones, depending on the number of moments that are considered. The number of moments to be retained might be larger than two in some instances, in view of §3.3. Otherwise, one obtains a poor approximation of non-equilibrium spectra⁴⁶. If one chooses to integrate the spectral model over intervals of wavenumber space, one obtains multi-group (or multi-scale) models. The interesting result is that full consistency between the group equations is retained, provided that one works with self-similar forms for spectra within the entire set of moment equations. This was not the case in earlier work^{47,48} which leads to the above mentioned consistency difficulties.

Renormalization group theory was also used for deriving a "k- ϵ " model⁴⁹. As an example, we derive it starting from a spectral model³⁰, and show how well coefficients are predicted, compared to what are the most widely accepted ones⁵⁰. Note first that, as the limit of the dissipation range,

$$\epsilon(x,t) = 2\nu \int k^2 E dk \quad \text{and} \quad \epsilon(x,t) = \lim_{k \rightarrow kd} (-c_1 k^{5/2} E^{3/2} + c_2 k^{7/2} E^{1/2} \partial E / \partial k) .$$

The crucial assumption here is that the flow is in a self-similar regime (without stating which one). One then assumes that the following ansatz holds for E and the deviatoric part $E^{d_{ij}}$ of the Reynolds stress tensor :

$$E = K(x,t) L(x,t) f(kL(x,t)) , E^d_{ij} = K_{ij}(x,t) L(x,t) f^d(kL(x,t)) ,$$

where K is an energy, L a length scale, and f is the dimensionless spectrum of turbulence

($\int f d\xi = 1$). One then computes the m^{th} order moment of the model equation ³⁰, and,

by vertu of the definition of ϵ , one obtains an evolution equation for the dissipation rate ϵ of the turbulent kinetic energy. The last step is to use a Boussinesq approximation, which expresses equilibrium between the production of energy and decay of turbulent kinetic energy.

$$\frac{\partial K}{\partial t} + u_n \frac{\partial K}{\partial x_n} = - 2 g_{\epsilon 1} u_{n,m} - \epsilon + g_D \frac{\partial}{\partial x_n} \left(\frac{K^2}{\epsilon} \left(\frac{\partial K}{\partial x_n} \right) \right)$$

$$\frac{\partial \epsilon}{\partial t} + u_n \frac{\partial \epsilon}{\partial x_n} = - 3 g_{\epsilon 1} u_{n,m} - g_{\epsilon 2} \frac{\epsilon^2}{K} + g_D \frac{\partial}{\partial x_n} \left(\frac{K^2}{\epsilon} \left(\frac{\partial K}{\partial x_n} \right) \right)$$

$$- \frac{g_D}{3} \left(\frac{K^2}{\epsilon^2} \left(\frac{\partial \epsilon}{\partial x_n} \right)^2 + (2-3m) \left(\frac{K}{\epsilon} \frac{\partial \epsilon}{\partial x_n} - \frac{3}{2} \frac{\partial K}{\partial x_n} \right)^2 \right)$$

In these equations, the coefficients g_m , $g_{\epsilon 1}$, $g_{\epsilon 2}$, and g_D depend on the spectral equation coefficients as well as on integrals of moments of the spectral shape function f . With the choice of a spectral ansatz, obtained in the case of homogeneous isotropic turbulence, it was shown ³⁰ that they are in very good agreement with the coefficients currently considered for the incompressible, high Reynolds number limit, "k- ϵ " model ⁵⁰.

5-STRUCTURE OF RTI AND RMI INDUCED FLOWS

It was emphasized in the introduction that turbulent mixing models are to be used in conjunction with other physical processes in a number of applications, e.g. in ICF flows, or climate modeling (where buoyancy forces are important). This shows directly in the models in the choice of mean equation-of-state to be used. Indeed, the mean flow pressure is a nonlinear function of the mean flow quantities, as well as, in principle, of the turbulent correlations. In most cases, it is modeled ^{11,20} as a function of density, internal energy, and concentrations only. To do this, it is necessary to use an additional thermodynamic assumption (pressure equilibrium, or temperature equality), to close unknown correlations. More formal approaches, such as pdf techniques, might be worthwhile exploring.

An example of such a modeling is the use of local approximations for general equations of state ¹¹. For most materials and equations-of-state, the stiffened gas EOS is a very good local approximation, as long as the coefficients in that equation are adjusted. Let us consider this approximate EOS, involving the two coefficients γ and P_0

$$I = \frac{P + \gamma P_0}{(\gamma - 1)\rho}$$

This type of equation degenerates naturally into a perfect gas EOS and gives a good answer in a wide range of densities and pressures. From it it is easy to obtain a mixture EOS. Combining two such equations (for materials 1 and 2), and using a pressure equilibrium assumption, we obtain for the mixture an equation of the same type, and its two coefficients γ and P_0 are

$$\frac{1}{\gamma - 1} = \frac{\alpha_1}{\gamma_1 - 1} + \frac{\alpha_2}{\gamma_2 - 1},$$

and

$$\frac{\gamma P_0}{\gamma - 1} = \frac{\alpha_1 \gamma_1 P_{01}}{\gamma_1 - 1} + \frac{\alpha_2 \gamma_2 P_{02}}{\gamma_2 - 1},$$

where α_1 and α_2 are the volume fractions of materials 1 and 2.

Another field of investigation is particle transport through non-homogeneous media ⁵¹. This is of interest in climatology, regarding the modeling of radiative transfer through clouds. This is also an important feature in astrophysical flows. Up to now, it has been possible to derive effective cross-sections, starting from assumed chord length distribution functions. However, there is very little available for circumstances such as RTI or RMI induced flows.

For any such coupling, one therefore has to calculate effective mixture coefficients, based on the structure of the mixture. It is worthwhile mentioning some pioneer work done for RT flows by Redondo and Linden ⁵². This experimental and theoretical work paves the way for determining the most significant parameters of these flows, such as Hausdorff dimension, self-similar spectrum power law, and their relationship. Additional information was provided using detailed numerical simulations ⁵³, that explore RM flows and show that chord length statistics might be different from the ones used elsewhere ⁵¹.

6-CONCLUSION

From what was presented here, it is clear that current single-point models are still far from adequate. The problems still to be solved, or points to be improved, were listed in Section 3. Some of the current efforts, and new possible directions, even though not yet successful, are emphasized as a conclusion to this review :

It was demonstrated ^{54,55} that, using Large Eddy Simulation, it is possible to simulate the transition to turbulence in a backward facing step flow. Although mesh requirements are rather severe for LES calculations, the advent of ever more powerful computers should allow such models for simulating RT and RM flows, therefore offering an alternative for modeling transition.

The highly nonlinear character of shock/turbulence interaction might delude any attempt to develop a predictive theory. Once again, turning to detailed simulations should help, as already demonstrated ²⁹.

It was demonstrated³⁰ that it is possible to model off-equilibrium spectra, and to evaluate or improve single-point models in the case of incompressible flows. Current effort is geared at generalizing this model to the case of several incompressible materials²⁶.

Spectral models lead to fully consistent single-point models, with a limited number of coefficients. Their evaluation is currently underway, as well as their generalization.

Much more work is needed regarding RT/RM flow structure. This implies more detailed numerical simulations, along the same line of work than what was presented at Royaumont, but with a stronger emphasis on adequate numerical diagnostics.

REFERENCES

- 1-Read K.I., *Physica* 12 D, (1984) 45-58.
- 2-Youngs D.L., *Physica* D 37, (1988) 270.
- 3-Vasilenko A.M., et al., "Advances in Compressible Turbulence", Proceedings of the Princeton International Workshop on the Physics of Compressible Turbulent Mixing, (1988) 581-606.
- 4-Kurenchenko Y.A., et al., in Proceedings of the 3rd International Workshop on the Physics of Compressible Turbulent Mixing, June 17-19, 1991, Royaumont, France, Besnard, Haas, Sitt & Wilke Eds., (1992) 427-454.
- 5-Glimm J., Sharp D.H., *Physical Review Letters* 64, (1990) 2137. See also J. Glimm et al., *Phys. Fluids* A2, (1990).
- 6-Orszag S.A., preprint.
- 7-Anuchina N.N., et al., in Proceedings of the 3rd International Workshop on the Physics of Compressible Turbulent Mixing, June 17-19, 1991, Royaumont, France, Besnard, Haas, Sitt & Wilke Eds., (1992) 305-323.
- 8-Geleznikoff F., private communication.
- 9-Leith, C.E. LLNL report UCRL-96036, (1986).
- 10-Mikaelian K.O., *Phys. Fluids* A, 2, 4, (1990) 592-598.
- 11-Besnard D., Haas J.F., and Rauenzahn R.M., *Physica* 37 D, (1989), 227-247.
- 12-Anuchina N.N., Volkov V.I., in Proceedings of the 3rd International Workshop on the Physics of Compressible Turbulent Mixing, June 17-19, 1991, Royaumont, France, Besnard, Haas, Sitt & Wilke Eds., (1992) 315-323.
- 13-Richtmyer R.D., *Comm. Pure and Appl. Math.*, 12, 2, (1960) 297.
- 14-Saffman P.G., and Meiron D.I., *Phys. Fluids* A1, 11, (1989), 1767.
- 15-Phan T., PhD Thesis, California Institute of Technology, (1990).
- 16-Holstein P.A., et al., in Proceedings of the 3rd International Workshop on the Physics of Compressible Turbulent Mixing, June 17-19, 1991, Royaumont, France, Besnard, Haas, Sitt & Wilke Eds., (1992) 251-275.
- 17-Ischii M., "Thermo-Fluid Dynamic Theory of Two-phase Flow", Eyrolles, Paris, (1975).
- 18-Besnard D., and Harlow F.H., *Int. J. Multiphase Flow*, 14, 6, (1988) 679-699.
- 19-Cranfill C., preprint.
- 20-Polyonov A.V., in Proceedings of the 2nd International Workshop on the Physics of Compressible Turbulent Mixing, November 1989, Pleasanton, USA, (1989).
- 21-Andronov V.A., et al., *Dokl. Akad. Nauk. SSSR* 264, (1982) 76-82.
- 22-Besnard D., et al., Los Alamos National Laboratory report LA-12303-MS, (1992).
- 23-Besnard D., Haas J.F., and Rauenzahn R.M., "Advances in Compressible Turbulence", Proceedings of the Princeton International Workshop on the Physics of Compressible Turbulent Mixing, (1988) 349-376.
- 24-Hoffman N., in Proceedings of the 3rd International Workshop on the Physics of Compressible Turbulent Mixing, June 17-19, 1991, Royaumont, France, Besnard, Haas, Sitt & Wilke Eds., (1992) 177-185.

- 25-Colvin J.D., in Proceedings of the 3rd International Workshop on the Physics of Compressible Turbulent Mixing, June 17-19, 1991, Royaumont, France, Besnard, Haas, Sitt & Wilke Eds., (1992) 97-102.
- 26-Besnard D., et al., in Proceedings of the 3rd International Workshop on the Physics of Compressible Turbulent Mixing, June 17-19, 1991, Royaumont, France, Besnard, Haas, Sitt & Wilke Eds., (1992) 187-199.
- 27-Chu B.T., and Kovaszny L.S.G., *J. Fluid Mech.*, §, (1957), 494-514.
- 28-Buckingham A., in Proceedings of the 3rd International Workshop on the Physics of Compressible Turbulent Mixing, June 17-19, 1991, Royaumont, France, Besnard, Haas, Sitt & Wilke Eds., (1992) 155-166.
- 29-Rotman D., *Phys. Fluids A*, 3, 7, (1991).
- 30-Besnard D., et al., Los Alamos National Laboratory report, LA-11821-MS, (1990).
- 31-Lee T.D., *Quart. Appl. Math.*, 10, 1, (1952) 69-74.
- 32-Clark T., PhD Thesis, Los Alamos national Laboratory report LA-12284-T, (1992).
- 33-Orszag S.A., *J. Fluid Mech.*, 41, 2, (1970) 363-386.
- 34-Kraichnan R.H., *Phys. Rev.*, 109, 5, (1958) 1407-1422.
- 35-Kraichnan R.H., *Phys. Fluids*, 7, 7, (1964) 1030-1049.
- 36-Kraichnan R.H., *Phys. Fluids*, 8, 8, (1965) 575-598.
- 37-Kraichnan R.H., *J. Math.Phys.*, 2, 1, (1961) 124-128.
- 38-Leith C.E., *Phys. Fluids*, 10, 7, (1962) 1409-1416.
- 39-Kovaszny L.S.G., *J. Aeronaut. Sci.*, 15, (1948) 745-753.
- 40-Bertoglio J-P., and Jeandel D., in "Turbulent Shear Flows", Durst et al. Eds., Springer-Verlag, (1987) 19-30.
- 41-Clark T.T., Zemach C., private communication.
- 42-Gence J.N., Thèse de Doctorat es Sciences, université Claude bernard, (1979).
- 43-Gence J.N., and Mathieu J., *J. Fluid Mech.*, 93, 3, (1979) 501-513.
- 44-Gence J.N., and Mathieu J., *J. Fluid Mech.*, 101, (1980) 555-566.
- 45-Uberoi M.S., and Wallis S., *Phys. Fluids*, 12, 7, (1969) 539-543.
- 46-Jeandel D., Brison J.F., and Mathieu J., *Phys. Fluids*, 21, 2, (1978) 169-182.
- 47-Shiestel R., *Phys. Fluids*, 30, 3, (1987) 722-731.
- 48-Hanjalic K., Launder B.E., and Schiestel R., in "Turbulent Shear Flows-2", Bradbury et al. Eds., Springer-Verlag, (1980) 36-49.
- 49-Dannevik W.P., Yakhot V., and Orszag S.A., *Phys. Fluids* 30, 7, (1987) 2021-2029.
- 50-Launder B.E., Reece G.J., and Rodi W., *J. Fluid Mech.*, 68, 3, (1975) 537-566.
- 51-Malvagi F., and Pomraning G.C., *Nuclear Science Eng.*, 111, (1992) 215-228.
- 52-Redondo J.M., and Linden P.F., in Proceedings of the 2nd International Workshop on the Physics of Compressible Turbulent Mixing, November 1989, Pleasanton, USA, (1989).
- 53-Viecelli J.A., in Proceedings of the 2nd International Workshop on the Physics of Compressible Turbulent Mixing, November 1989, Pleasanton, USA, (1989).
- 54-Metais O., and Lesieur M., *J. Fluid Mech.*, 239, (1992) 157-194.
- 55-Neto S., Grand D., and Lesieur M., *Int. J. Heat Mass Transfer*, 34, 8, (1991) 1999-2011.
- 56-Lesieur M., and Schertzer D., *J. Mécanique*, 17, (1978) 609-646.

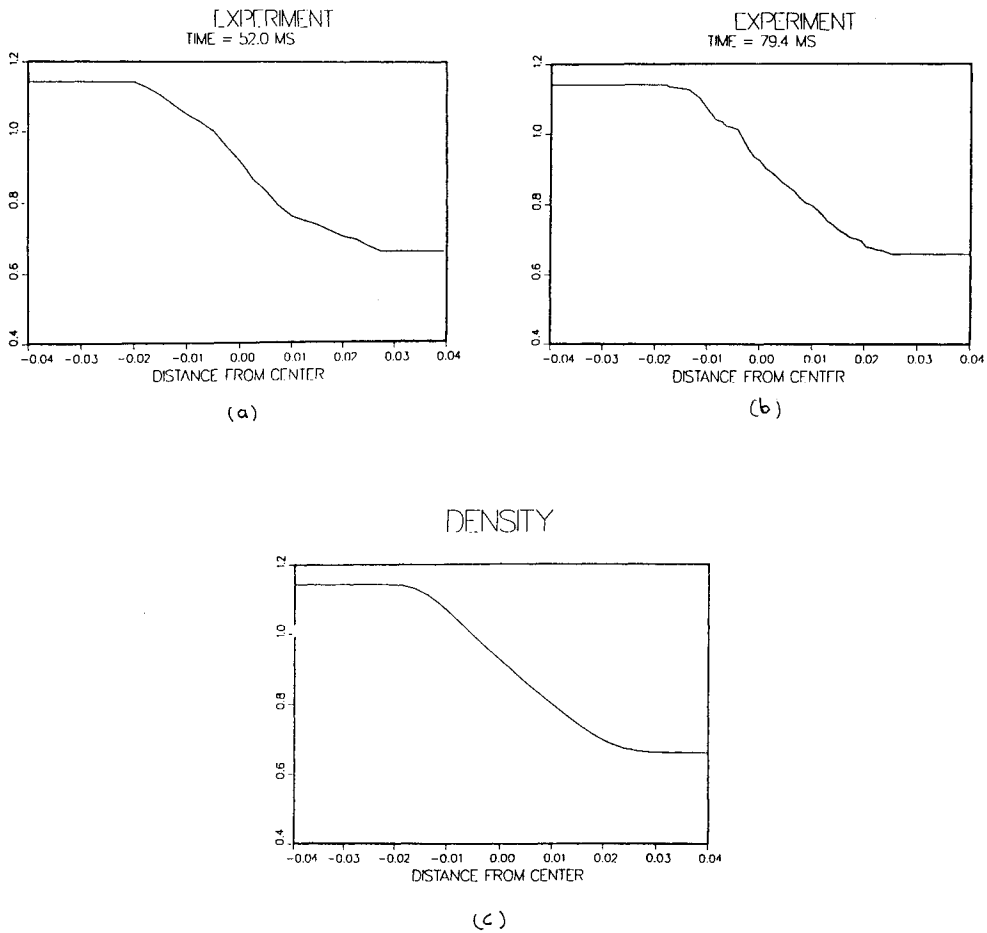


Figure 1: Figures 1a and 1b show RTI induced mixing layer density mean profiles in a rocket-rig experiment by Read ¹. The spatial variable is the reduced, self-similar variable $\xi = x/gt^2$ Figure 1c shows the same density profile obtained with a calculation for the same experiment performed with BHR ¹¹ model.

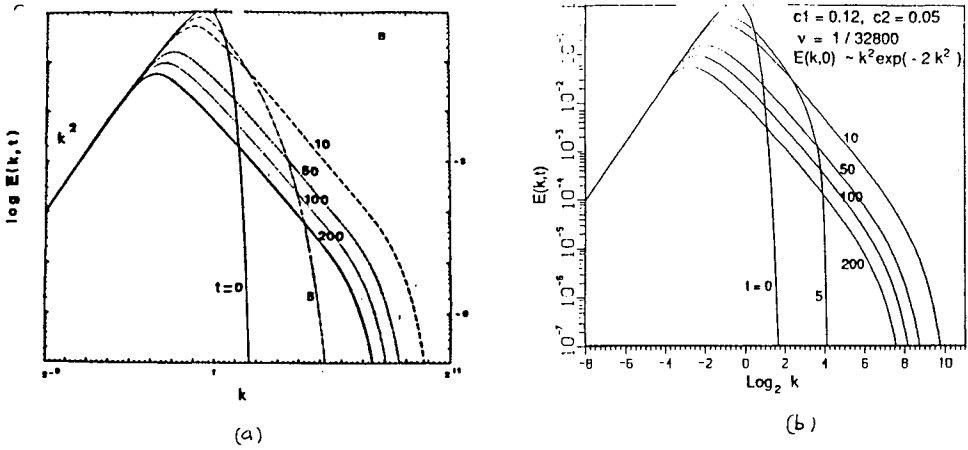


Figure 2 : Figure 2a is an EDQNM calculation by Lesieur and Schertzer ⁵⁶ of a homogeneous isotropic decay. Figure 2b is a calculation in the BHRZ ³⁰ model with the same initial conditions and viscosity, and with parameters chosen to match the data of Figure 2a at large times.

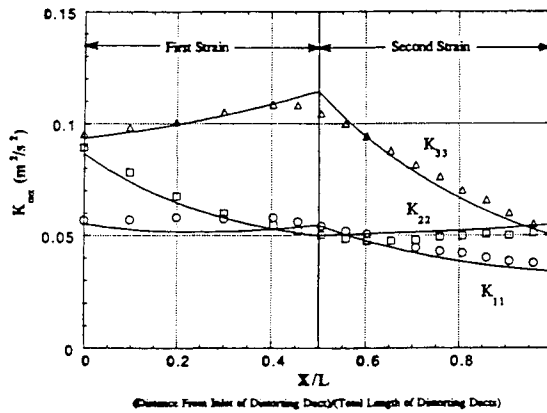


Figure 3 : The evolution of the principal components of the Reynolds tensor $K_{\alpha\alpha}$ while undergoing two opposite plane strains, with BHRZ model ³². Experimental data (symbols) from Gence ⁴².

TOWARDS A BETTER HYDRO FOR DYNAMIC MIX CALCULATIONS

Judith Binstock
Los Alamos National Laboratory

ABSTRACT

A difference equation technique suitable for clean, dynamic mix, and turbulence Lagrangian calculations is shown. This new technique is compared to the standard one for clean one-dimensional calculations of the Noh, Sedov Blast Wave, and Strong Shock Tube test problems, and for a one-dimensional two-phase flow dynamic mix calculation of a modified Noh problem, all test problems involving shocks. The new technique is shown to dramatically reduce the noise in the calculated hydrodynamic quantities of pressure, density, specific internal energy, and Lagrangian interface velocity.

I. INTRODUCTION

Since dynamic mix hydrodynamic calculations typically use a driving term involving the gradient of the pressure, and turbulence calculations depend on gradients of pressure, density and velocity, clearly the less spatial noise there is in a calculation, the more believable are the results. We therefore show in this paper a difference equation technique suitable for clean, dynamic mix, and turbulence calculations, that has a smoothing effect on pressure, density and mean flow velocity. In the next section, we show the effect on clean calculations. In the section following that we extend the technique to mixed problems, and show the effect on a two-phase-flow dynamic mix calculation.

All calculations and equations are for one-dimensional Lagrangian hydrodynamics, with an even-time difference scheme. For simplicity, all equations-of-state (EOS) used in the clean examples are analytic $\gamma = 5/3$ gamma laws, and the mixed example uses a tabular $\gamma = 5/3$ gamma-law EOS. The technique, however, is more general and works for any tabular or analytic EOS.

II. CLEAN CALCULATIONS

A. The Basic One-Dimensional Lagrangian Difference Equations

Let:

a = acceleration	v = velocity
P = pressure	r = radius of Lagrangian interface
Q, AQ = artificial viscosity terms	E = specific internal energy
A = area	V = zone volume
m = zone mass	t = time

subscript i = designator of a boundary-centered quantity, i^{th} interface
 subscript $i-\frac{1}{2}$ = designator of a zone-centered quantity, between the $(i-1)^{th}$
 and i^{th} interfaces

Then the basic difference equations are:

$$a_i = -2[(P_{i+1/2} + Q_{i+1/2} - P_{i-1/2} - Q_{i-1/2})A_i + (AQ_{i+1/2} + AQ_{i-1/2})]/(m_{i+1/2} + m_{i-1/2}) \quad (1a)$$

$$dv_i = a_i dt \quad (1b)$$

$$dr_i = v_i dt \quad (1c)$$

$$m_{i-1/2} dE_{i-1/2} = -(P_{i-1/2} + Q_{i-1/2}) \left(\frac{dV}{dt}\right)_{i-1/2} dt + AQ_{i-1/2}(v_i + v_{i-1}) \quad (1d)$$

$$\left(\frac{dV}{dt}\right)_{i-1/2} = v_i A_i - v_{i-1} A_{i-1} \quad (1e)$$

For the even-time scheme, predictor-corrector form, the times at which the above terms are to be evaluated are illustrated in Fig. 1. First evaluate P, Q, AQ, A at t_n , then calculate a at t_n , then advance v and r to $t_{n+1/2}$, for the predictor step. For the corrector step re-evaluate P, A at $t_{n+1/2}$, calculate a at $t_{n+1/2}$, re-advance v to $t_{n+1/2}$, advance E to t_n , then advance r to t_n , and then advance v to t_n . Note how E, r and v are all advanced from t_n to t_{n+1} , making this an even-time scheme, as opposed to the time-staggered scheme shown in Fig. 2. While the examples in this paper are all calculated with the two-step even-time scheme of Fig. 1, a simpler one-step even-time scheme could also have been used.

It is critical, however, just how P^n and $P^{n+1/2}$ (the values at t_n and $t_{n+1/2}$) are evaluated, for use in Eqs. (1a) and (1d). We will now discuss two possibilities, the standard form and the extrapolated (P^*) form.

B. Standard Form

For the even-time scheme, standard form, the pressure used in the basic equations is $P = P(\theta, \rho)$ where ρ = density, θ = temperature, so that table look-ups (or analytic EOS functions) give

$$P^n = P(\theta^n, \rho^n) \quad (2a)$$

$$P^{n+1/2} = P(\theta^{n+1/2}, \rho^{n+1/2}), \quad (2b)$$

where

$$\theta^{n+1/2} = \theta^n + \left(\frac{d\theta}{dt}\right)^{n-1/2}(t_{n+1/2} - t_n) \tag{2c}$$

$$\rho^n = m/V^n, \rho^{n+1/2} = m/V^{n+1/2} \tag{2d}$$

and with volume V evaluated from r at the specified time. Note that we have dropped the zonal subscript $i-1/2$.

C. Extrapolated Form (P^*)

For the even-time scheme, extrapolated form, we use a different assumption, namely

$$P^n = P^{n+1/2} = P^* \tag{3}$$

in the basic Eqs. (1a) through (1e), to advance all quantities from t_n to t_{n+1} , where $P^n, P^{n+1/2}$ correspond to Fig. 1, and where P^* is the pressure extrapolated from t_n to t_{n+1} using Eqs. (4a)-(4e):

$$E^{n+1} - E^n = -(P^n + P^*)(V^{n+1} - V^n)/2m \tag{4a}$$

$$P^* - P^n = (\gamma - 1)m(E^{n+1}/V^{n+1} - E^n/V^n) \tag{4b}$$

$$\Delta = 1 - (\gamma - 1)\rho E^n/P^n \tag{4c}$$

$$V^{n+1} = V^n + \left(\frac{dV}{dt}\right)^n(t_{n+1} - t_n) \tag{4d}$$

$$\gamma - 1 = \left(\frac{\partial P^n}{\partial \theta}\right)_\rho / \rho \left(\frac{\partial E^n}{\partial \theta}\right)_\rho \tag{4e}$$

where the subscript $i-1/2$ applies to all quantities. Note that Eq. (4a) is the Hugoniot relation across a shock.

Note also that γ corresponds to the standard specific heat ratio γ of a gamma-law equation-of-state if

$$P = (\gamma - 1)\rho E \tag{5a}$$

$$E = E(\theta) \tag{5b}$$

hold, in which case $\Delta = 0$. However, γ is still defined by Eq. (4e) for more complex or tabular equations-of-state, in which case it may not correspond exactly to the standard specific heat ratio.

Solving Eqs. (4a)-(4e) for P^* , and reinserting the subscript $i-1/2$,

$$P_{i-1/2}^* = \left\{ P \left[1 - \frac{(\gamma - 1)dV}{2V} + \Delta \frac{dV}{V} \right] / \left[1 + \frac{(\gamma + 1)dV}{2V} \right] \right\}_{i-1/2}^n \tag{6a}$$

where

$$\left(\frac{dV}{V}\right)_{i-1/2}^n = (v_i^n A_i^n - v_{i-1}^n A_{i-1}^n)(t_{n+1} - t_n)/V_{i-1/2}^n \tag{6b}$$

Thus P^* is the pressure extrapolated from t_n to t_{n+1} , using quantities evaluated at t_n , the beginning of the time-step.

D. Comparison of the Standard and Extrapolated (P^*) Forms

To see the advantage of the extrapolated form (P^*) over the standard form, for even-time hydrodynamics, we look at the results for three standard test problems for which analytic solutions are known. For simplicity, we use analytic $\gamma = 5/3$ gamma-law equations-of-state for these clean calculations, and zero in on the noise in the figures. The only difference between the standard and extrapolated (P^*) calculations is in the replacement of $P^n, P^{n+\frac{1}{2}}$ with P^* for the latter.

1. Noh Problem (See Appendix A). We see in Figure 3(a) that for a given form of artificial viscosity, namely the Von Neumann form, the effect of replacing the standard evaluation of pressure ($P^n, P^{n+1/2}$) with the extrapolated value (P^*) is to smooth out the noise in the density without shifting the curve up or down. The solid line is the analytic solution. Similarly in Fig. 3(b), we see the same effect, this time with a covariant tensor viscosity. This illustrates the fact that the smoothing effect caused by replacing $P^n, P^{n+1/2}$ with P^* is not due to P^* mimicking an addition to the artificial viscosity. An actual change in the artificial viscosity causes the calculated curve to shift, as a comparison of Figs. (3a) and (3b) illustrates. For similar comparisons of pressure, specific internal energy and velocity, see Figs. 4(a) and 4(b), Figs. 5(a) and 5(b), and Figs. 6(a) and 6(b).

2. Sedov Blast Wave Problem (See Appendix B). We now use the covariant tensor artificial viscosity only, and calculate $v/v_S, P/P_S,$ and $\rho/\rho_S,$ all versus $R/R_S,$ where $v_S, P_S, \rho_S,$ and R_S are the analytic solutions of velocity, pressure, density, radius at the shock position. The standard even-time solution (Fig. 7(a)) and the extrapolated (P^*) solution (Fig. 7(b)) can be compared (Fig. 7(c)). Note that when $R/R_S = 1,$ the curves should all go through 1 for a perfect calculation. Here again the extrapolated P^* calculation smooths out the calculated curve without shifting it materially.

3. Strong Shock Tube Problem (See Appendix C). Continuing to use the covariant tensor artificial viscosity, we show in Fig. 8 the v, E, ρ, P curves versus $R.$ The solid line is the analytic solution. Here again the extrapolated P^* calculation is much smoother.

III. DYNAMIC MIX CALCULATIONS

A. Extension of Extrapolation Technique to Mixed Zones

Having smoothed out the noise in a clean calculation, we would like to try the technique in a dynamic mix problem, and see what effect the smoothing has on the calculated mixing. However, we shall first need an extension of the extrapolation scheme defined earlier, from a single material to a mixture of materials. So from Eq. (6a) we define

$$\frac{P^*}{P} = f\left(\gamma, \frac{dV}{V}, \Delta\right) \quad , \quad (7a)$$

where

$$f(\gamma, \frac{dV}{V}, \Delta) = \left[1 - \frac{(\gamma - 1)}{2} \frac{dV}{V} + \Delta \frac{dV}{V} \right] / \left[1 + \frac{(\gamma + 1)}{2} \frac{dV}{V} \right] \quad (7b)$$

Then if we have a mixed zone with two materials in pressure equilibrium, designated by a and b, we have

$$\frac{P^*}{P} = f(\gamma^a, \frac{dV^a}{V^a}, \Delta^a) \quad (8a)$$

$$= f(\gamma^b, \frac{dV^b}{V^b}, \Delta^b) \quad (8b)$$

where

$$V^a + V^b = V \quad (9a)$$

$$dV^a + dV^b = dV \quad (9b)$$

Equations 7 to 9 can then be algebraically manipulated to yield

$$\frac{dV^a}{V^a} = \frac{dV}{V} / \left[\frac{V^a}{V} + \frac{V^b}{V} g(\gamma^a) / g(\gamma^b) \right] \quad (10a)$$

where

$$g(\gamma) = \frac{(\gamma + 1)}{2} \frac{P^*}{P} + \left(\frac{\gamma - 1}{2} \right) - \Delta \quad (10b)$$

Since $\gamma^a, \gamma^b, V^a, V^b, \Delta^a, \Delta^b, V, dV$ can all be calculated at time t_n , the unknowns can now be regarded as P^* and dV^a , so that Eqs. (8a) and (10a) can be iterated to solve for P^* , in each zone.

We are now ready to see what effect the smoothing has on the calculated mixing, and shall try it out on a two-phase-flow calculation of dynamic mixing. Since the two-phase-flow equations allow both mixing and demixing, and the term driving the interpenetration velocity is linear in the gradient of the pressure, we could guess that the noise in the pressure would cancel out, at least approximately. We shall now test this speculation with another test problem, a modified Noh problem.

B. Comparison of the Standard and Extrapolated (P^*) Forms, for the Modified Noh Problem (See Appendix D).

We now examine the effect of replacing $P^n, P^{n+1/2}$ with P^* for a two-phase-flow dynamic mix calculation of a modified Noh problem. This problem is similar to the Noh problem, with tabular $\gamma = 5/3$ gamma-law equations-of-state used, except that the material is now divided into two regions, with the outer one of density 2, the inner one of density 1. Note that until the shock formed at the origin reaches the interface, the calculations are clean. While we unfortunately do not have an analytic solution for this modified Noh problem, we can still compare the standard even-time hydro calculation with the extrapolated even-time P^* calculation.

In Fig. 9 we see P , ρ , h_{mixfr} (h_{mixfr} = fraction of zone mass that is the heavier material) as calculated by the two different methods, the standard method and the extrapolated P^* method. Note that while the standard calculation continues to be noisy in pressure, the difference in h_{mixfr} as calculated by the two methods is relatively small, at least for this simple test problem.

IV. CONCLUSION

The use of the P^* extrapolation in the even-time hydro equations decreases the noise present in the standard calculation, for clean test problems involving shocks. Extension of this method to the two-phase-flow dynamic mix even-time hydro equations continues to decrease the noise in pressure, density, and Lagrangian interface velocity. For the two-phase flow problem considered here, there was little sensitivity of the mix distribution to the noise in the calculation. While the examples shown here were for a two-step (predictor-corrector) form of even-time hydro, other calculations with one-step even-time hydro are quite similar.

V. ACKNOWLEDGMENT

The suggestion that the use of the extrapolated pressure P^* would decrease the noise in even-time clean hydrodynamic calculations was made by P. P. Whalen, who has done considerable work on this scheme. He has also extended it to two-dimensional hydrodynamics. The extension of the P^* prescription to mixed zones is the author's work.

APPENDIX A

Spherical Noh Problem

Initial conditions:

- sphere of radius 1.0 m
- 100 equal-spaced zones
- density = 1.0 kg/m³
- specific internal energy = 10⁻²¹ J/kg. (We used this small finite value of specific internal energy to avoid zero temperatures.)
- velocity = -1.0 m/s, all zone interfaces

Boundary Condition:

- outer boundary velocity = -1.0 m/s at all times
- The problem was run to 0.6 second, using an analytic $\gamma=5/3$ gamma-law EOS, hydro only (no heat conduction, no radiation), for four cases:
- Von Neumann artificial viscosity, standard even-time hydro
 - Von Neumann artificial viscosity, P^* even-time hydro
 - covariant tensor artificial viscosity, standard even-time hydro
 - covariant tensor artificial viscosity, P^* even-time hydro

Discussion:

We have used

$$Q = -\rho(1.2 \frac{dV}{dt} / A)^2$$

for the Von Neumann form¹ of artificial viscosity. For the covariant tensor form of artificial viscosity, $Q_{i-\frac{1}{2}}$, $AQ_{i-\frac{1}{2}}$ correspond to the Q_j , $\Delta Q_j(A_{j+\frac{1}{2}} - A_{j-\frac{1}{2}})/2$

of Eqs. 9' and 10 on page 318 of Ref. 2. Note that we have set their $C_Q = 1.2^2$ for all zones except the inner one, for which we use $C_Q = 1.2^2/3$, following a recommendation by Ref. 3. The analytic solution to the Noh problem can be found in Ref. 4.

APPENDIX B

Spherical Sedov Blast Wave Problem

Initial conditions:

- sphere of radius 1.2 m
- 120 equal-spaced zones, of thickness .01 m
- density = 1.0 kg/m³
- specific internal energy of 10^{-21} J/kg in outer 118 zones, and 14727.34 J/kg in inner 2 zones
- velocity = 0., all zone interfaces

Boundary Condition:

- outer boundary velocity = 0. at all times
The problem was run to 1.0 second, using an analytic $\gamma = 5/3$ gamma-law EOS, hydro only, for two cases:
- covariant tensor artificial viscosity, standard even-time hydro
- covariant tensor artificial viscosity, P^* even-time hydro

Discussion:

For the analytic solution, see Ref. 5 (problem of an intense explosion). For $\gamma = 5/3$, we used a value of λ (as defined in Ref. 5) equal to 1.1517, a number calculated by Ref. 6. We then selected the product of the initial specific internal energy and volume of the central hot spot to be λ^{-5} , so that the analytic solution would go through radius = 1 at time = 1, in the appropriate units. The analytic curves we plot were provided by Ref. 7.

APPENDIX C

Strong Shock Tube Problem

Initial conditions:

- planar geometry
- 30 zones, constant mass ratio of 0.7337, density of 10^3 kg/m³, specific internal energy of 10^{11} J/kg, $r = 0.$ to 0.03m (Note mass-matching at material interface).
- 60 equal-mass zones, density of 1.0 kg/m³, specific internal energy of 10^5 J/kg, $r = 0.03$ m to 0.09m
- velocity = 0., all zone interfaces

Left and Right Boundary Conditions:

- velocity = 0. at all times
The problem was run to 6.0×10^{-8} seconds, using analytic $\gamma=5/3$ gamma law EOS, hydro only, for two cases:
- covariant tensor artificial viscosity, standard even-time hydro
- covariant tensor artificial viscosity, P^* even-time hydro

Discussion:

The test problem was devised by Ref. 8, and is discussed in Ref. 9, where the analytic solution can be found.

APPENDIX D

Modified Spherical Noh Problem

Initial conditions:

- sphere of radius 1.0 m
- 50 equal-spaced zones, density of 1.0 kg/m^3 , specific internal energy of 10^{-21} J/kg , from $r=0.$ to $r=0.5 \text{ m}$
- 100 equal-spaced zones, density of 2.0 kg/m^3 , specific internal energy of $5.0 \times 10^{-22} \text{ J/kg}$, from $r=0.5 \text{ m}$ to $r=1.0 \text{ m}$ (Note mass-matching at material interface.)
- velocity = -1.0 m/s , all zones

Boundary Condition:

- outer boundary velocity = -1.0 m/s at all times.
The problem was run to 0.6 second, using a tabular $\gamma=5/3$ gamma-law EOS, hydro only, with two-phase-flow dynamic mixing, a Newtonian drag force (with a Newtonian drag coefficient of 0.44 and a particle diameter of 3000 microns), for two cases:
- covariant tensor artificial viscosity, standard even-time hydro
- covariant tensor artificial viscosity, P^* even-time hydro

REFERENCES

1. J. Von Neumann and R. D. Richtmyer, "A Method for the Numerical Calculation of Hydrodynamic Shocks," *Journal of Applied Physics* 21 (1950), 232-237.
2. J. R. Buchler and P. Whalen, "Experiments with Artificial Viscosity," *The Numerical Modelling of Nonlinear Stellar Pulsations*, J. R. Buchler (ed.), (1990), 315-322, Kluwer Academic Publishers, The Netherlands.
3. P. Whalen, Los Alamos National Laboratory, private communication.
4. W. F. Noh, "Artificial Viscosity and Artificial Heat Flux Errors for Spherically Divergent Shocks," Lawrence Livermore National Laboratory report UCRL-89623, (1983).
5. L. I. Sedov, "Similarity and Dimensional Methods in Mechanics," translation edited by M. Holt, (1959) Academic Press, New York.
6. W. Harvey, Los Alamos National Laboratory, private communication.
7. P. Blewett, Los Alamos National Laboratory, private communication.
8. J. LeBlanc, Lawrence Livermore National Laboratory, private communication.
9. P. Whalen, W. Harvey, S. Clancy, R. Bowers, "Strong Shock Tube Problem TP37C," Los Alamos National Laboratory memo X-DO-PPW(4/90)-65, (1990).

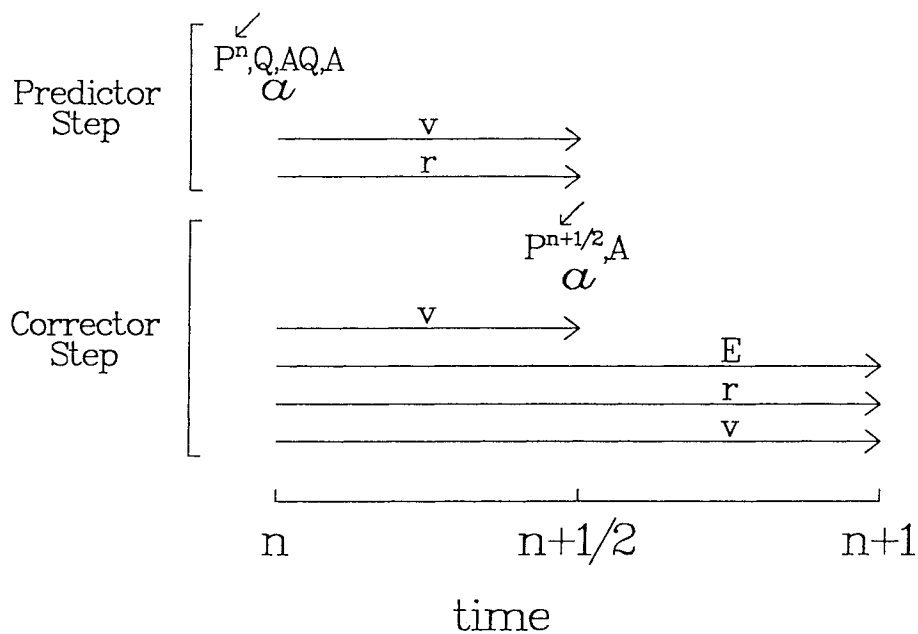


Fig. 1. Predictor-corrector even-time scheme.

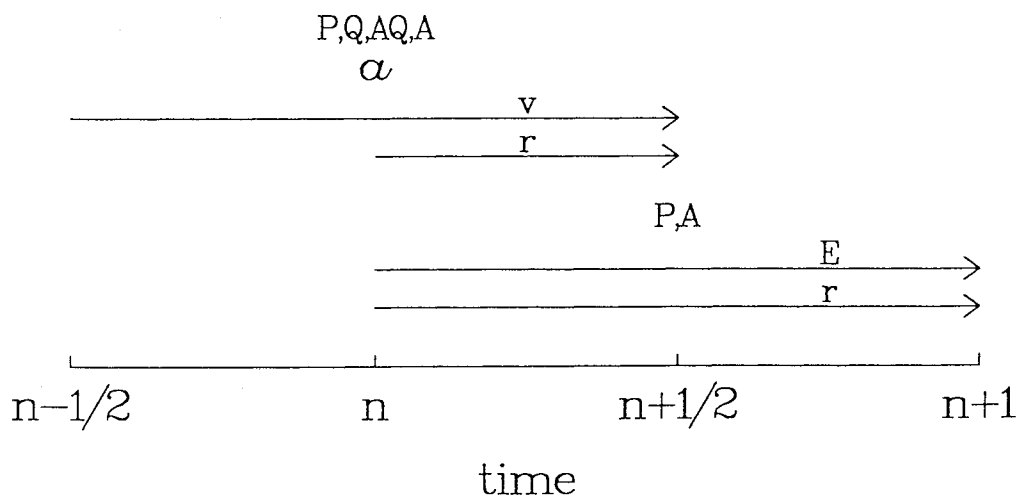


Fig. 2. Time-staggered scheme.

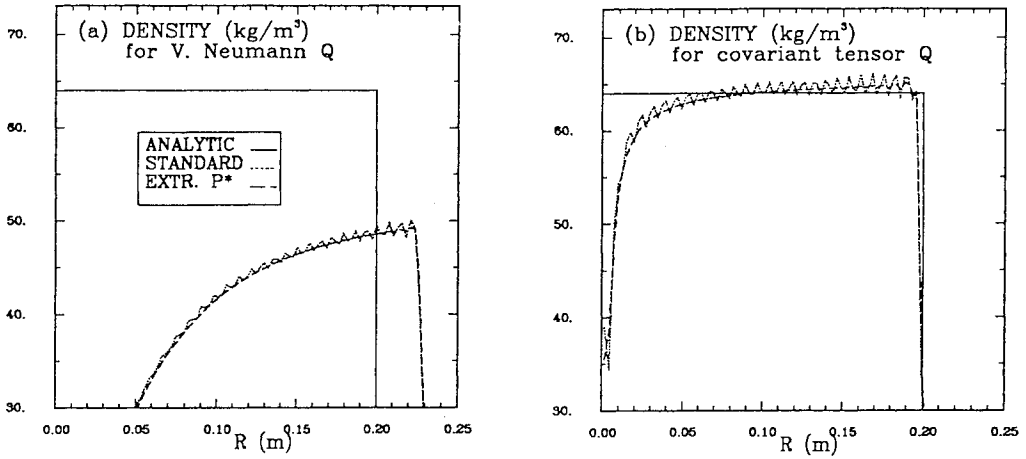


Fig. 3. Spherical Noh problem, density, at time = 0.6 second, using (a) Von Neumann artificial viscosity and (b) covariant tensor artificial viscosity.

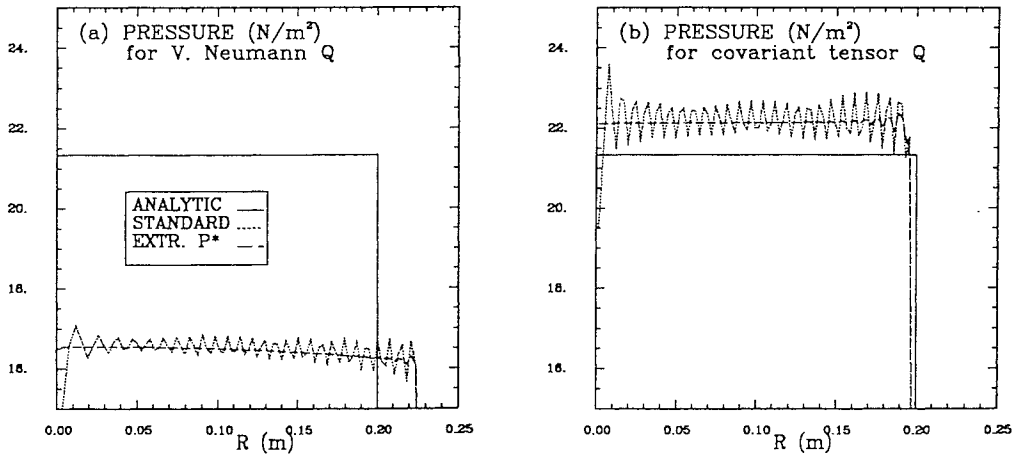


Fig. 4. Spherical Noh problem, pressure, at time = 0.6 second, using (a) Von Neumann artificial viscosity and (b) covariant tensor artificial viscosity.

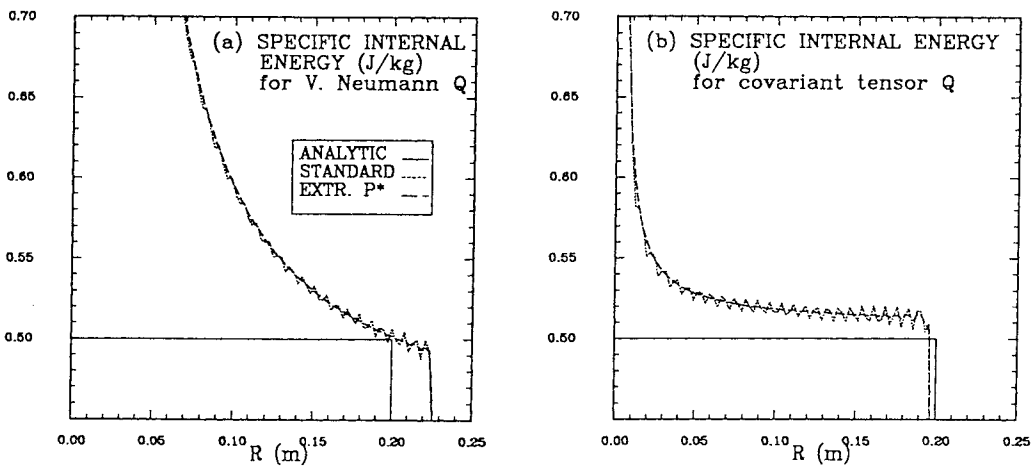


Fig. 5. Spherical Noh problem, specific internal energy, at time = 0.6 second, using (a) Von Neumann artificial viscosity and (b) co-variant tensor artificial viscosity.

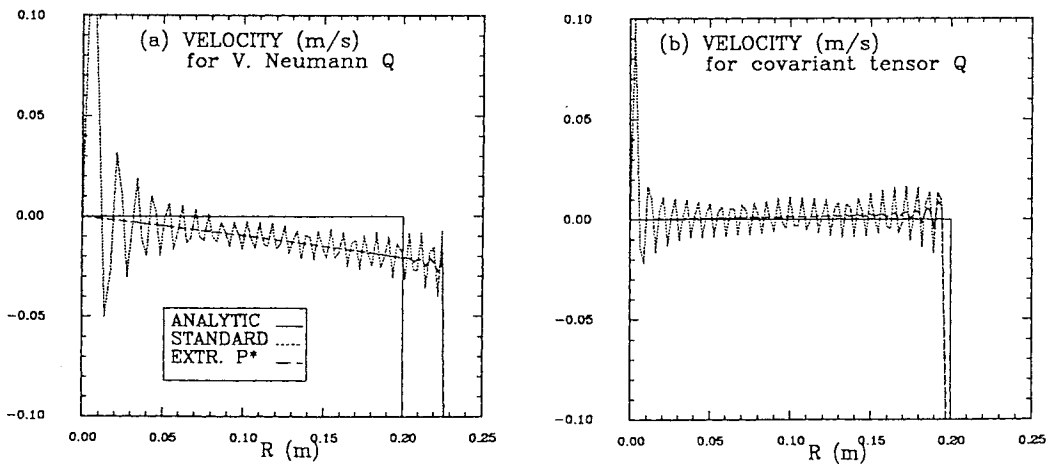


Fig. 6. Spherical Noh problem, velocity, at time = 0.6 second, using (a) Von Neumann artificial viscosity and (b) covariant tensor artificial viscosity.

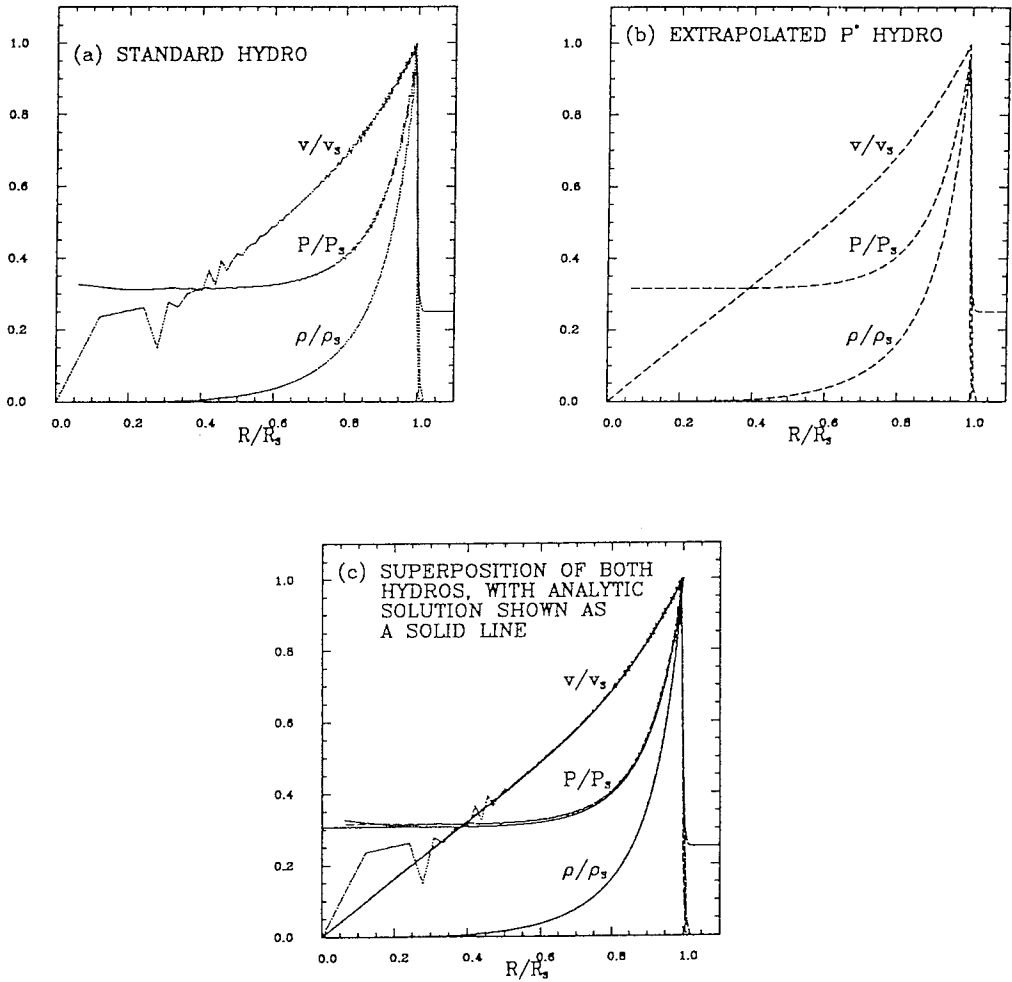


Fig. 7. Spherical Sedov Blast Wave problem, for (a) standard hydro, (b) extrapolated P^* hydro, and (c) a superposition of the two hydros with analytic solution shown as a solid line, at time = 1.0 second.

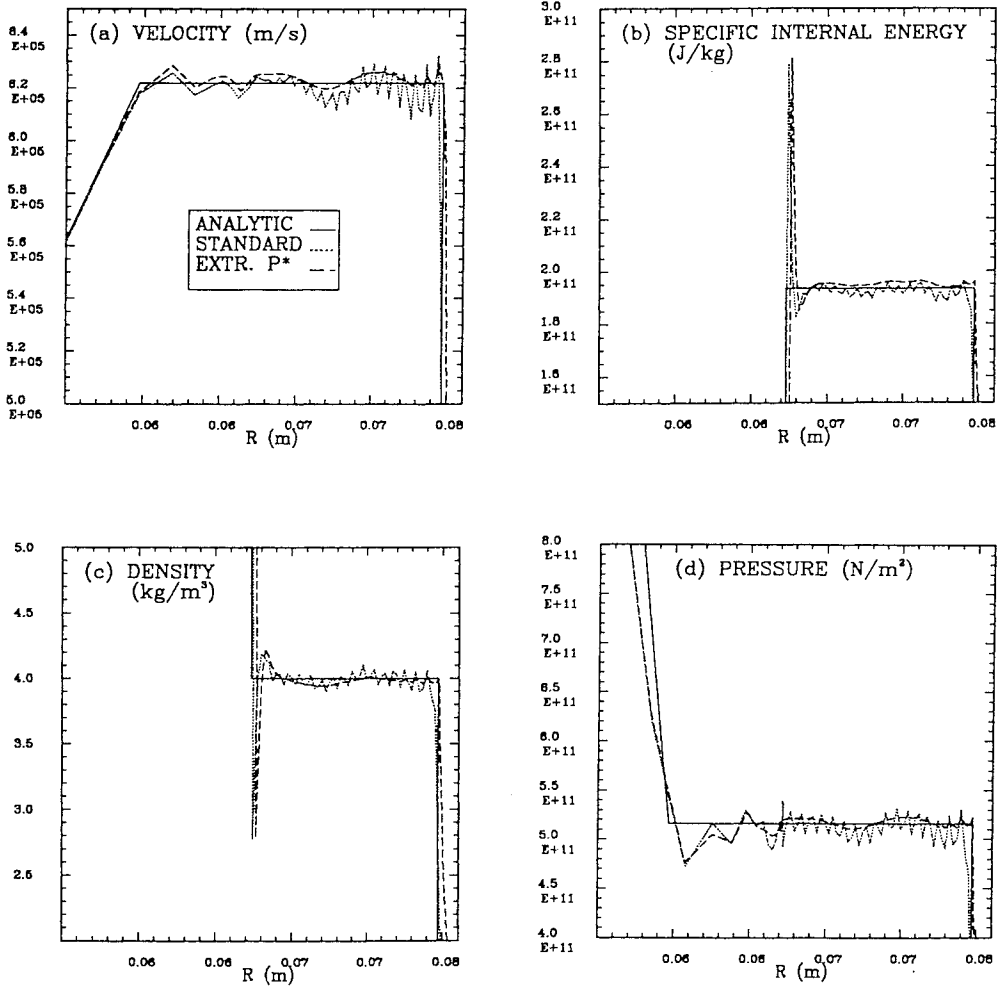


Fig. 8. Planar Strong Shock Tube problem for (a) velocity, (b) specific internal energy, (c) density, and (d) pressure, at time = 6.0×10^{-8} seconds.

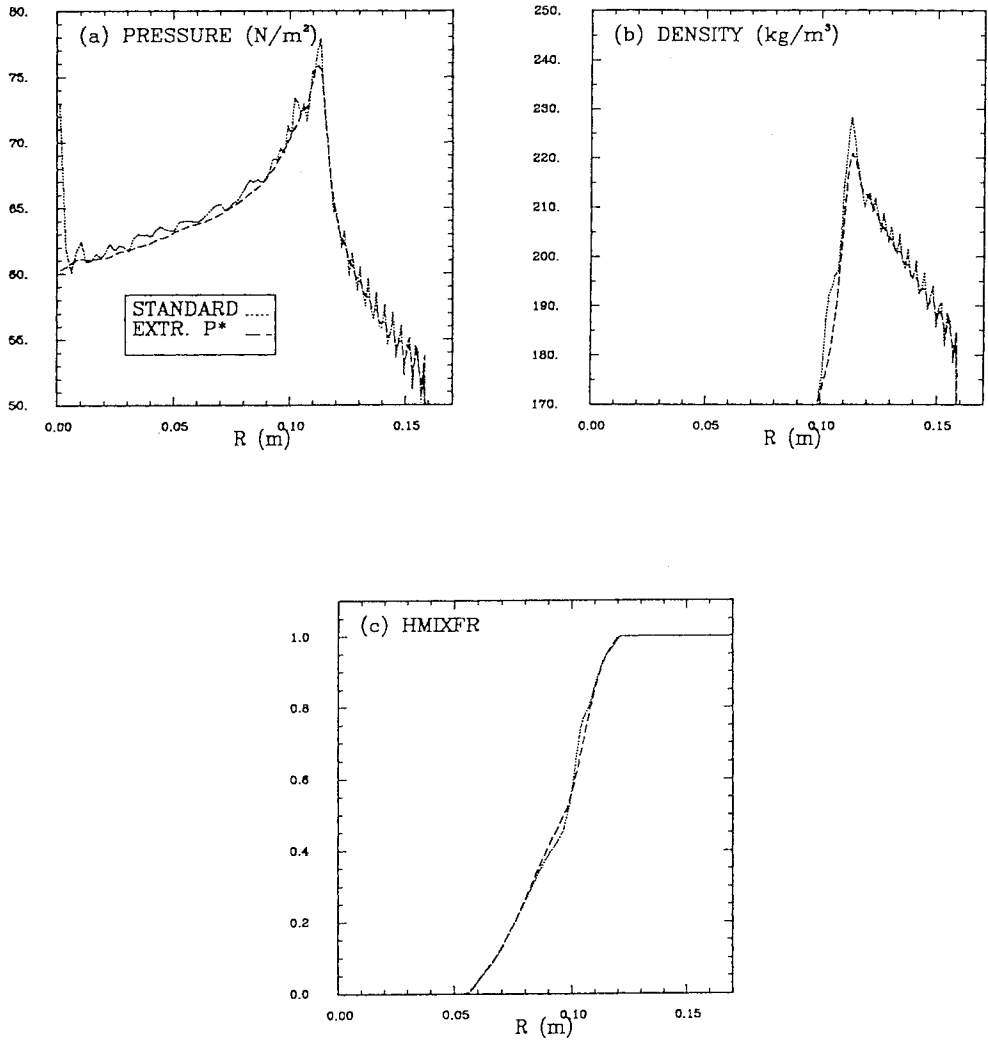


Fig. 9. Modified Noh problem, dynamical mixing, for (a) pressure, (b) density, and (c) hmixfr (fraction of zone mass that is the heavier material), at time = 0.6 second.

COMPARISON OF TWO TURBULENT DIFFUSION-DISSIPATION MODELS VIA SIMILARITY METHODS

C. CHERFILS

Centre d'Etudes de Limeil-Valenton, 94195 Villeneuve St Georges CEDEX FRANCE

Abstract

The diffusion-dissipation equations derived from two turbulent "statistic" models have been considered. The first one comes from a one equation mix length model, and the second one from a $k-\epsilon$ model.

The self similar asymptotic solutions for these two systems have been constructed by Lie group techniques. These solutions satisfy a similarity of the second type, and cannot be found analytically except for some choices of coefficients. In order to compare the general solution of the two complete systems, their asymptotic behaviour has been checked numerically. The power laws obtained for the $k-\epsilon$ model are very close to others high Reynolds number results, so we propose coefficients for the mix length model to fit the $k-\epsilon$ model. This work proves at first that the standard coefficients of these two turbulent models, that were adjusted on experiments, are not universal.

Introduction

During an implosion, Richtmyer-Meshkov instabilities appear as the shock goes through interfaces, and generate the development of a turbulent mixing layer.

In order to simulate this physical process, simple models of fully developed turbulence, a one-equation mix length model and a $k-\epsilon$ model /1,2,3/, are implemented in our compressible hydrodynamic codes. These models do not take in account transition to turbulence and need to be initialized by some procedure /3/. Unfortunately, the mix length obtained that way leading to very fine meshes, we must often turn on the models at a later time and modify the initial conditions in a appropriate manner. Noticing that the Rayleigh-Taylor instable phase which induces most of turbulence does not begin immediately after the shock's crossing, and that the effect of the Reynolds tensor is limited by a velocity nearly constant during a certain time, it is possible to reduce the models to the corresponding diffusion-dissipation equations during the same time. The initial conditions obtained suggest strongly a different behaviour of the two models. The purpose of this paper is then to determine theoretically the decay laws of the simplified models, in order to assess these one point closure models by comparison with results obtained by more elaborated models and experiments in the incompressible case.

Diffusion-dissipation equation deriving from the mix length model

The principle of the one-equation mix length model is to split variables into a mean and a fluctuating part. The mixing flow is described by evolution equations for the mean variables. The correlations between fluctuating parts are closed algebraically, except an evolution equation for the turbulent kinetic energy k defined by

$$(II.1) \quad k = u'^2$$

The diffusion-dissipation equation for k takes the form /4/

$$(II.2) \quad \frac{\partial k}{\partial t} = \frac{\partial}{\partial x} \left(\alpha h(t) \sqrt{k} \frac{\partial k}{\partial x} \right) - c \frac{k^{\frac{3}{2}}}{\alpha h(t)}$$

with an initial condition $k(x, 0) = \frac{K(0)}{h(0)} \varphi_0 \left(\frac{x}{h(0)} \right)$,

where

$$(II.3) \quad \begin{cases} \varphi_0 \in S_{[-1;+1]} ; \int_{-1}^{+1} \varphi_0(x) dx = 1 \\ K(t) = \int_{-h(t)}^{+h(t)} k(x, t) dx \quad (\text{integral turbulent energy}) \end{cases}$$

In the case without dissipation, we can obtain a self similar solution by dimensional analysis arguments /4 /. The power laws we get then are:

$$(II.4) \quad \begin{cases} h(t) = \xi_0(\alpha) K^{1/3} t^{2/3} \\ k(x, t) = \xi_0^2(\alpha) K^{2/3} t^{-2/3} \Phi \left(\frac{x}{h(t)} \right) \end{cases}$$

where $K = K(t) = K(0)$, and $\xi_0 = (135 \alpha^2 / 4)^{1/4} \therefore$

In the general case, self similar solution of this type cannot be found, because energy conservation is not verified anymore. Then we turn to self similar solutions of the second type /4,5,6,7/. Characteristic of these solutions is that the limiting passage from the non degenerate problem to the self similar one needs the definition of variables that are not proceeding directly from dimensional analysis. The power laws are then obtained by the resolution of a non linear problem of eigenvalues.

We are looking for an exponent δ that authorizes a limiting passage at $K h^\delta$ constant.

Putting $\beta = \frac{2}{\delta+3}$, and

$$(II.5) \quad \begin{cases} \zeta = \frac{x}{h} \\ h = \xi_0 t^\beta \\ k = \xi_0^2 t^{-2(1-\beta)} f(\zeta) \end{cases}$$

we get the equation

$$(II.6) \quad \alpha \frac{d}{d\zeta} \left(f^{1/2} \frac{df}{d\zeta} \right) + \beta \zeta \frac{df}{d\zeta} + 2(1 - \beta)f - \frac{c}{\alpha} f^{3/2} = 0$$

with boundary conditions

$$(II.7) \quad \begin{cases} \frac{df}{d\zeta}(0) = 0 \\ f(1) = 0 \\ \frac{df^{3/2}}{d\zeta}(1) = 0 \end{cases}$$

ξ_0 depends on the initial conditions K_0 and $a = h(0)$.

This self similar solution is not a solution of the general problem (an infinite initial energy would be needed), but conserves an asymptotic character. Indeed, the general solutions whose initial conditions verify $K_0 a^\delta = C$ are leading to the same self similar asymptot, characterized by the constant ξ_0 defined by

$$(II.8) \quad \xi_0 = C^{\beta/2} \left(\int_{-1}^{+1} f(\zeta) d\zeta \right)^{-\beta/2}$$

Diffusion-dissipation system deriving from the $k-\epsilon$ model

The one-equation model is turned into a $k-\epsilon$ model by adding an evolution equation for the dissipation rate ϵ of the turbulent kinetic energy /1,2,3/.

Let us consider the diffusion-dissipation system for k and ϵ :

$$(III.1) \quad \begin{cases} \frac{\partial k}{\partial t} = \frac{\partial}{\partial x} \left(\frac{C_D}{\sigma_k} \frac{k^2}{\epsilon} \frac{\partial k}{\partial x} \right) - \epsilon \\ \frac{\partial \epsilon}{\partial t} = \frac{\partial}{\partial x} \left(\frac{C_D}{\sigma_\epsilon} \frac{k^2}{\epsilon} \frac{\partial \epsilon}{\partial x} \right) - C_{\epsilon_2} \frac{\epsilon^2}{k} \end{cases}$$

with initial conditions

$$(III.2) \quad \begin{cases} k(x, 0) = K_0 \varphi(x) \\ \epsilon(x, 0) = E_0 \psi(x) \end{cases}$$

where φ and ψ have the same compact support $2a$.

Let T be a stretching transformation (scalings)

$$(III.3) \quad T : (t, x, k, \epsilon, K_0, E_0) \longrightarrow (Tt, Xx, Rk, S\epsilon, WK_0, QE_0)$$

(III.1) is unvarying under T iff :

$$(III.4) \quad \begin{cases} R = X^2 T^{-2} \\ W = RX \\ Q = SX \\ S = X^2 T^{-3} \end{cases}$$

As above, it is not possible to conserve the integral values K and $E = \int \epsilon(x, t) dx$, because it is not compatible with the dissipation phenomena. We have then to do a limiting passage preserving a new variable $KE^{-\delta}$, δ unknown for the moment.

This yields:

$$(III.5) \quad WQ^\delta = R\bar{S}\bar{X}^{1-\delta} = X^{3(1-\delta)}T^{3\delta-2} = 1$$

Putting $\beta = \frac{2-3\delta}{3(1-\delta)}$, the flow is thus unvarying by the stretching transformation :

$$(III.6) \quad T_1 : (t, x, k, \epsilon, K_0, E_0) \longrightarrow (1, xt^{-\beta}, kt^{2(1-\beta)}, \epsilon t^{3-2\beta}, K_0 t^{2-3\beta}, E_0 t^{3-3\beta})$$

After some algebra, we obtain the degenerate system

$$(III.7) \quad \begin{cases} \alpha_k \frac{d}{d\zeta} \left(\frac{f^2}{g} \frac{df}{d\zeta} \right) + \beta \zeta \frac{df}{d\zeta} + 2(1-\beta)f - g = 0 \\ \alpha_\epsilon \frac{d}{d\zeta} \left(\frac{f^2}{g} \frac{d\epsilon}{d\zeta} \right) + \beta \zeta \frac{dg}{d\zeta} + (3-2\beta)g - C_{\epsilon_2} \frac{g^2}{f} = 0 \end{cases}$$

where

$$(III.8) \quad \begin{cases} \alpha_k = \frac{C_D}{\sigma_k} ; \quad \alpha_\epsilon = \frac{C_D}{\sigma_\epsilon} \\ x = \xi_0 t^\beta \zeta ; \quad \zeta \in [0, 1] \\ k = \xi_0^2 t^{-2(1-\beta)} f(\zeta) \\ \epsilon = \xi_0^2 t^{2\beta-3} g(\zeta) \end{cases}$$

and with the boundary conditions

$$(III.9) \quad \begin{cases} \frac{df}{d\zeta}(0) = \frac{dg}{d\zeta}(0) = 0 \\ f(1) = g(1) = 0 \\ \frac{f^2}{g} \frac{df}{d\zeta}(1) = \frac{f^2}{g} \frac{dg}{d\zeta}(1) = 0 \end{cases}$$

β is found by the resolution of a non linear eigenvalues problem; just notice that the positivity condition imposed to f and g implies:

$$(III.10) \quad 0 < \beta < \frac{2}{3}$$

As above, the constant ξ_0 depends on initial conditions.

The solutions of III.1 whose initial conditions verify $K_0 E_0^{-\delta} = C$ are leading to the same self similar asymptot, characterized by

$$(III.11) \quad \xi_0 = C^{1-\beta} \left(\int_{-1}^{+1} f(\zeta) d\zeta \right)^{\beta-1} \left(\int_{-1}^{+1} g(\zeta) d\zeta \right)^{\frac{2-3\beta}{3}}$$

Numerical resolution

For the numerical resolution of these two systems, a shooting method is used to determine both the self similar solution and the parameter β /15/.

To avoid the trivial solution, we start from a limited development at the point 1 and we look for β giving the good boundary conditions in 0. For the k- ϵ model, a new parameter A appears during the limited development:

$$(IV.1) \quad \begin{cases} f(\zeta) = A(1 - \zeta)^{\frac{p}{\alpha_k}} + o\left((1 - \zeta)^{\frac{p}{\alpha_k}}\right) \\ g(\zeta) = A^2(1 - \zeta)^{\frac{p}{\alpha_\epsilon}} + o\left((1 - \zeta)^{\frac{p}{\alpha_\epsilon}}\right) \end{cases} \quad \left(p = \frac{\alpha_k \alpha_\epsilon}{2\alpha_\epsilon - \alpha_k} \right)$$

C_{ϵ_2}	A	β	$\eta (k = k_0 t^\eta)$	$\theta (\epsilon = \epsilon_0 t^\theta)$
1.8	11.5	0.26	-1.48	-2.48
1.9	10.5	0.305	-1.39	-2.39
2.0	8.336	0.34	-1.32	-2.32

Table 1: Similar exponents obtained for the diffusion coefficients $\alpha_k = 0.103$; $\alpha_\epsilon = 0.069$

We notice that, for our usual coefficients ($C_{\epsilon_2} = 1.9$), the power law obtained for the k- ϵ model is very close to the high Reynolds number result ($\beta = 0.31$) obtained by M.Lesieur with EDQNM, under the assumption that the spectra of turbulent energy follows a s^4 law for the small scales /8 /. We are also not very far from others numerical or experimental results /9,10 /.

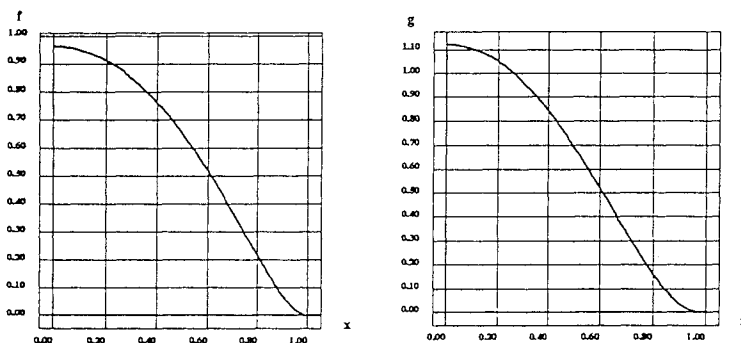


Planche 1 : f and g for standard coefficients $\alpha_k = 0.103$; $\alpha_\epsilon = 0.069$; $C_{\epsilon_2} = 1.9$

Hence, we decide to adjust our mix length model coefficients in order to find the same behaviour in the large. Our standard coefficients ($\alpha = .2, c/\alpha = 2.$) give indeed $h \sim t^{0.413}$ and $k \sim t^{-1.17}$.

To fit the previous laws $h \sim t^{0.305}$ and $k \sim t^{-1.39}$, we have to choose a couple proportional to

$$(IV.2) \quad \begin{cases} \alpha = 2. \\ \frac{c}{\alpha} = 4.46 \end{cases}$$

In fact, we want more. The important point of these self similar solutions being their asymptotic character, we have then to adjust the sets of initial conditions leading to the same asymptot *and* the corresponding constant ξ_0 . The first thing to do is to determine the invariance sets of initial conditions.

Characterization of the invariance sets of initial conditions

We assume that the turbulent mix length at the end of the non linear stage is given by

$$(V.1) \quad L_0 = 2a = 2(1+r)sA_t|\Delta u|\Delta t$$

where A_t is the Atwood number, Δu the interface velocity jump and Δt the transition time between the early linear behavior and the fully developed turbulent behavior.

r and s are given by

$$(V.2) \quad r = \left(\frac{1+A_t}{1-A_t} \right)^{0.215} ; \quad s = 0.06$$

This modelling /3/ is supported by Read's experimental results, using Young's and Mikaelian's formulae /10, 11, 12/. The evaluation of the transition time is based on Richtmyer's analysis /14/.

We suppose then that $k(x, 0)$ and $\epsilon(x, 0)$ are symmetric triangles of width L_0 and of height k_0 and ϵ_0 defined by

$$(V.3) \quad \begin{cases} k_0 = \frac{4}{3}sA_t^2(\Delta u)^2 \\ \epsilon_0 = C_2 \frac{k_0^{3/2}}{2a} \end{cases}$$

where C_2 is taken equal to 0.164.

So, the set Γ_C defined by $K_0 E_0^\nu = C$ can be parametrized by

$$(V.4) \quad \begin{cases} k_0 a^{\nu+1} \epsilon_0^\nu = C \\ \epsilon_0 = C_2 k_0^{3/2} / (2a) \end{cases}$$

After some algebra, putting

$$(V.5) \quad \mu = C_1^{\frac{\beta}{2-\beta}} \left(\frac{4}{3} (1+r)^{-1} s^{\frac{2-\beta}{2(1-\beta)}} \right)$$

we get

$$(V.6) \quad \Gamma_C : \begin{cases} \epsilon_0 = C_2 \frac{k_0^{3/2}}{2a} \\ \Delta t = \mu (A_t |\Delta u|)^{\frac{1}{\beta-1}} \end{cases}$$

Returning to the one-equation model, for which $k(x, 0)$ is defined as above, we see that the set Υ_λ of initial conditions defined by $K_0 a^\delta = \lambda$ encloses Γ_C iff C and λ satisfy

$$(V.7) \quad C^{1-\beta} = \lambda^{\frac{\beta}{2}} \left(\frac{C_2}{2} \right)^{\frac{3\beta-2}{2}}$$

It seems impossible to fit exactly the self similar solutions f_{kL} and $f_{k\epsilon}$. So we can for example adjust $f_{kL}(0)$ and $f_{k\epsilon}(0)$, which is well adapted to our initialization procedure. If we take the $k - \epsilon$ standard coefficients, we get for the one equation model

$$(V.8) \quad \begin{cases} \alpha \approx 0.057 \\ \frac{\epsilon}{\alpha} \approx 1.26 \end{cases}$$

In this case, $\int f_{kL}$ and $\int f_{k\epsilon}$ are not exactly the same.

We can also decide to adjust $\int f_{kL}$ and $\int f_{k\epsilon}$, which seems more physical. This yields to

$$(V.9) \quad \begin{cases} \alpha \approx 0.056 \\ \frac{\epsilon}{\alpha} \approx 1.25 \end{cases}$$

We can consider that these two pairs of coefficients are close *enough*. As a matter of fact, we don't know the others coefficients of the two models with great accuracy.

To adjust the complete asymptot, we have still to adjust the parameters ξ_0 . Apply II.8,III.11 and V.7 gives here in both cases

$$(V.10) \quad C_2 = 2 \left[\left(2 \int_0^1 f_{kL}(\xi) d\xi \right)^{\beta/2} \left(2 \int_0^1 f_{k\epsilon}(\xi) d\xi \right)^{\beta-1} \left(2 \int_0^1 g(\xi) d\xi \right)^{2/3-\beta} \right]^{\frac{2}{2-3\beta}} \approx 2.$$

Hence, under the condition $C_2 = 2.$, the two models have approximatively the same self similar behaviour in the large:

$$(V.11) \quad \begin{cases} \zeta = \frac{x}{h} \\ h = \xi_0 t^{0.305} \\ k = \xi_0^2 t^{-1.39} f(\zeta) \end{cases}$$

where

$$(V.12) \quad \xi_0 \approx 0.98 \left(k_0^{\beta/2} \left(\frac{L_0}{2} \right)^{1-\beta} \right) ; \beta = 0.305$$

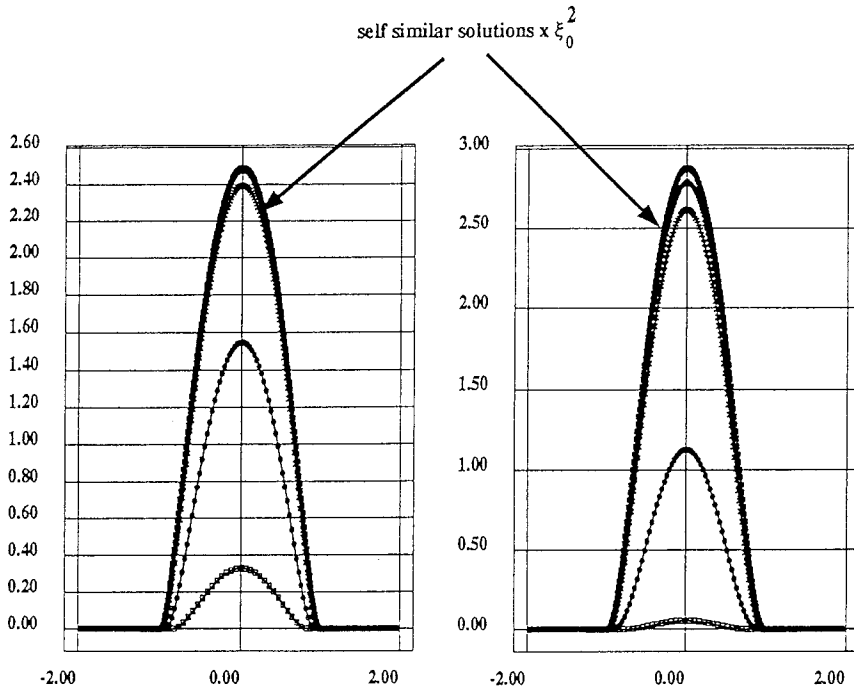


Planche 2 Convergence of the general solutions $k(x/\xi_0, t)t^{-1.39}$ and $\epsilon(x/\xi_0, t)t^{-2.39}$ towards the self similar solution normalized by ξ_0^2 (standard coefficients).

Toward a Quasi-Linear Closure for Compressible Turbulence

J. A. H. Futterman and W. P. Dannevik[†]

Center for Compressible Turbulence
Lawrence Livermore National Laboratory
P. O. Box 808, L-22 Livermore, CA 94550

Abstract

We are developing a quasilinear closure model for compressible turbulence based on a transformation of the averaged Navier-Stokes equations into a form that is at most quadratically non-linear in the mean and fluctuating variables. Following the transformation we discard third-order cumulants, in hope of arriving at a one-point closure model without adjustable parameters which will be applicable to systems undergoing rapid deformation, such as imploding Inertial Confinement Fusion capsules. This paper reports our current progress.

I. Introduction

Rapid distortion theory (RDT) as applied by Herring¹ closes the turbulence hierarchy of moment equations by discarding third-order and higher cumulants. This is similar to the fourth-order cumulant discard hypothesis of Millionshchikov,² except that the Millionshchikov hypothesis was taken to apply to incompressible homogeneous isotropic turbulence generally, whereas RDT is applied only to fluids undergoing a distortion that is "rapid" in the sense that the interaction of the mean flow with the turbulence overwhelms the interaction of the turbulence with itself. Motivated by RDT, we hope to apply a quasilinear closure to compressible, anisotropic turbulence, and eventually to the Rayleigh-Taylor and Richtmyer-Meshkov instabilities in a variety of geometries. In particular, since the quasilinear approximation should reduce in some limit to the equations of linear instability theory, we hope to gain insight into the regime between linear instability growth and fully developed turbulence.

II. Transformation of the Primitive Equations

We begin by transforming the Navier-Stokes equations into a form that is quadratically non-linear in the dynamical variables. This obviates the need for Favre averaging, and thereby provides a turbulence closure model that can more

naturally be incorporated into standard fluid mechanics codes. Using a notation in which a comma denotes differentiation, and repeated indices are automatically summed over, we write the Navier-Stokes equations as³

$$\partial_i \rho + (\rho u_j)_{,j} = 0 \tag{1}$$

$$\partial_i (\rho u_i) + (\rho u_i u_j)_{,j} + p_{,i} - \sigma_{ij,j} = \rho g_i \tag{2}$$

$$\partial_i (\rho E) + (\rho E u_j)_{,j} + (p u_j)_{,j} - (u_i \sigma_{ij})_{,j} - (\kappa T_{,j})_{,j} = \rho g_j u_j \tag{3}$$

Here σ is the tensor

$$\sigma_{ij} = \lambda u_{k,k} \delta_{ij} + \mu (u_{i,j} + u_{j,i}) \tag{4}$$

μ and λ are the so-called first and second viscosities, which are normally related by

$$\mu + \frac{3}{2} \lambda = 0 \tag{5}$$

κ is the thermal conductivity, and g_i represents a “gravitational” acceleration.

If we now change dependent variables from (ρ, u, E) to (v, u, p) where $v=1/\rho$ is the specific volume, we can use the equation of state

$$pv = (\gamma - 1) c_v T \tag{6}$$

to rewrite (1-3) as

$$\partial_i v + u_j v_{,j} = v u_{j,j} \tag{7}$$

$$\partial_i u_i + u_j u_{i,j} = g_i + v (\sigma_{ij,j} - p_{,i}) \tag{8}$$

$$\partial_i p + u_j p_{,j} = (\gamma - 1) \sigma_{ij} u_{i,j} - \gamma p u_{j,j} + \frac{\kappa}{c_v} (pv)_{,j,j} \tag{9}$$

The left-hand member of each of equation (7-9) is recognizable as a convective derivative, c_v is the heat capacity of the fluid at constant volume, and γ is the adiabatic index. We have also made the assumptions that $\lambda, \mu, \gamma, \kappa$, and c_v are constant. Equations (7-9) now form a set of “primitive” equations from which equations for the various statistical moments may be derived.

III. The Quasilinear Approximation

We now decompose the primitive variables (v, u, p) into mean $(\bar{v}, \bar{u}, \bar{p})$ and fluctuating (v', u', p') quantities, where the primitive quantity is equal to the sum of the mean and fluctuating parts, e.g., $v = \bar{v} + v'$, etc. This yields

$$\partial_t(\bar{v} + v') + \bar{u}_j \bar{v}_{',j} + u'_j \bar{v}_{',j} + \bar{u}_j v'_{',j} + u'_j v'_{',j} = \bar{v} \bar{u}_{',j} + v' \bar{u}_{',j} + \bar{v} u'_{',j} + v' u'_{',j} \tag{10}$$

$$\begin{aligned} \partial_t(\bar{u}_i + u'_i) + \bar{u}_j \bar{u}_{',i,j} + \bar{u}_j u'_{',i,j} + u'_j \bar{u}_{',i,j} + u'_j u'_{',i,j} = \\ g_i + \bar{v} \bar{\sigma}_{ij,j} + \bar{v} \sigma'_{ij,j} + v' \bar{\sigma}_{ij,j} + v' \sigma'_{ij,j} - (\bar{v} \bar{p}_{',i} + \bar{v} p'_{',i} + v' \bar{p}_{',i} + v' p'_{',i}) \end{aligned} \tag{11}$$

$$\begin{aligned} \partial_t(\bar{p} + p') + \bar{u}_j \bar{p}_{',j} + \bar{u}_j p'_{',j} + u'_j \bar{p}_{',j} + u'_j p'_{',j} = (\gamma - 1) (\bar{\sigma}_{ij} \bar{u}_{',i,j} + \bar{\sigma}_{ij} u'_{',i,j} + \sigma'_{ij} \bar{u}_{',i,j} + \sigma'_{ij} u'_{',i,j}) \\ - \gamma (\bar{p} \bar{u}_{',j,j} + \bar{p} u'_{',j,j} + p' \bar{u}_{',j,j} + p' u'_{',j,j}) + \frac{\kappa}{c_v} (\bar{p} \bar{v} + \bar{p} v' + p' \bar{v} + p' v')_{,jj} \end{aligned} \tag{12}$$

where we have used the commutativity of differentiation with bars and primes. We also neglect fluctuations in the heat capacity, the specific heat ratio, and thermal conductivity, as well as possible temporal or spatial variations in their mean quantities in this paper. If we now average (10-12) we obtain equations for the mean values of the primitive flow variables.

$$\partial_t \bar{v} + \bar{u}_j \bar{v}_{',j} = \bar{v} \bar{u}_{',j} - \overline{u'_j v'_{',j}} + \overline{v' u'_{',j}} \tag{13}$$

$$\partial_t \bar{u}_i + \bar{u}_j \bar{u}_{',i,j} = g_i + \bar{v} (\bar{\sigma}_{ij,j} - \bar{p}_{',i}) - \overline{u'_j u'_{',i,j}} + \overline{v' \sigma'_{ij,j}} - \overline{v' p'_{',i}} \tag{14}$$

$$\partial_t \bar{p} + \bar{u}_j \bar{p}_{',j} = (\gamma - 1) \bar{\sigma}_{ij} \bar{u}_{',i,j} - \gamma \bar{p} \bar{u}_{',j,j} + \frac{\kappa}{c_v} (\bar{p} \bar{v})_{,jj} \tag{15}$$

$$-\overline{u'_j p'_{',j}} + (\gamma - 1) \overline{\sigma'_{ij} u'_{',i,j}} - \gamma \overline{p' u'_{',j,j}} + \frac{\kappa}{c_v} (\overline{p' v'})_{,jj}$$

Here we see explicitly that the equations for the mean flow variables differ from the primitive equations by the introduction of averages of the products of fluctuating quantities. We can derive equations of motion for these second-order cumulants⁴ as follows. First we subtract (13-15) from (10-12) to obtain equations of motion for the fluctuating variables:

$$\partial_t v' + \bar{u}_j v'_{',j} + u'_j \bar{v}_{',j} + u'_j v'_{',j} - \overline{u'_j v'_{',j}} = \bar{v} u'_{',j} + v' \bar{u}_{',j} + v' u'_{',j} - \overline{v' u'_{',j}} \tag{16a}$$

$$\begin{aligned} \partial_i u'_i + \bar{u}_j u'_{i,j} + u'_j \bar{u}_{i,j} + u'_j u'_{i,j} - \overline{u'_j u'_{i,j}} = & -(\bar{v} p'_i + v' \bar{p}_i + v' p'_i - \overline{v' p'_i}) \\ & + \bar{v} \sigma'_{ij,j} + v' \bar{\sigma}'_{ij,j} + v' \sigma'_{ij,j} - \overline{v' \sigma'_{ij,j}} \end{aligned} \tag{17a}$$

$$\begin{aligned} \partial_i p' + \bar{u}_j p'_{i,j} + u'_j \bar{p}_{i,j} + u'_j p'_{i,j} - \overline{u'_j p'_{i,j}} = & (\gamma - 1) (\bar{\sigma}'_{ij} u'_{i,j} + \sigma'_{ij} \bar{u}_{i,j} + \sigma'_{ij} u'_{i,j} - \overline{\sigma'_{ij} u'_{i,j}}) \\ & - \gamma (\bar{p} u'_{j,j} + p' \bar{u}_{j,j} + p' u'_{j,j} - \overline{p' u'_{j,j}}) + \frac{\kappa}{c_v} (\bar{p} v' + p' \bar{v} + p' v' - \overline{p' v'})_{,jj} \end{aligned} \tag{18a}$$

We then multiply each equation by an appropriate fluctuating quantity, perform other operations, and average to obtain equations of motion for the second-order cumulants. This process will transform terms of the form $\bar{a} \overline{b'}$ in (16a-18a) into terms of the form $\bar{a} \overline{b' c'}$, which are identically zero, and terms of the form $a' \bar{b}'$ into terms of the form $\bar{a} \overline{b' c'}$, which are the third-order cumulants we plan to discard. In order to render both the following derivations and the reading thereof more bearable, we thus rewrite (16a-18a) retaining only the terms that will contribute non-zero quantities to the equations of motion for the second-order cumulants.

$$\partial_i v' + [\bar{u}_j \partial_j - \bar{u}_{j,j}] v' = [\bar{v} \partial_j - \bar{v}_{j,j}] u'_j \tag{16b}$$

$$\partial_i u'_i + [\bar{u}_j \partial_j - \bar{v} \mu \partial_{jj}] u'_i = [\bar{v} \Lambda \partial_{ij} - \bar{u}_{i,j}] u'_j - \bar{v} \partial_i p' + (\bar{\sigma}'_{ij,j} - \bar{p}_{i,j}) v' \tag{17b}$$

$$\begin{aligned} \partial_i p' + \left[\bar{u}_j \partial_j + \gamma \bar{u}_{j,j} - \frac{\kappa}{c_v} (\bar{v} \partial_{jj} + 2 \bar{v}_{j,j} \partial_j + \bar{v}_{,jj}) \right] p' \\ = [2(\gamma - 1) \bar{\sigma}'_{ij} \partial_i - \gamma \bar{p} \partial_j - \bar{p}_{i,j}] u'_j + \frac{\kappa}{c_v} [\bar{p} \partial_{jj} + 2 \bar{p}_{j,j} \partial_j + \bar{p}_{,jj}] v' \end{aligned} \tag{18b}$$

Here we have introduced $\Lambda = \lambda + \mu$, and used the identities

$$\sigma'_{ij} \bar{u}_{i,j} = \bar{\sigma}'_{ij} u'_{i,j} \tag{19}$$

and

$$\sigma'_{ij,j} = (\lambda + \mu) u'_{j,ji} + \mu u'_{i,jj} \tag{20}$$

We have also rearranged the equations to show their structure in terms of differential operators.

Writing equations (16b-18b) is equivalent to asserting that, for the domain of applicability of this approximation, terms of the form $a' \bar{b}' - \bar{a} \overline{b'}$ are small with respect to all other terms in (16a-18a). Although this means that we are discarding the turbulent Reynolds stresses from (17a), their averages are retained

in (14) and (15). Thus we are discarding some of the non-linearity the Reynolds stresses introduce into the turbulence closure problem, without discarding the Reynolds stresses themselves.

The equations of motion for the second moments of the fluctuating fields will now be closed in the sense that no higher moments of fluctuating fields are introduced. However they are not closed with respect to the increasingly higher spatial derivatives that are introduced. To resolve this problem, we expand the fluctuating fields using basis functions appropriate to a particular geometry and set of boundary conditions.

IV. A One-Dimensional Transport Model

The simplest application of the quasilinear approximation is to develop a one-dimensional transport model in Cartesian coordinates. We therefore follow Herring's approach by sketching a treatment of the compressible Rayleigh-Bénard problem in this section. Consider a compressible fluid between two infinite parallel planes oriented normal to the z-axis. We define the averaging process to be "slab-averaging" over the transverse directions, e.g.,

$$\bar{v} \equiv \bar{v}(z,t) = \lim_{a,b \rightarrow \infty} \frac{1}{4ab} \int_{-a}^a dx \int_{-b}^b dy v(x,y,z,t) \quad (21)$$

Equations for the mean fields now become

$$\partial_t \bar{v} + \bar{u}_3 \bar{v}_{,3} = \bar{v} \bar{u}_{3,3} - \overline{u'_j v'_{,j}} + \overline{v' u'_{,j}} \quad (22)$$

$$\partial_t \bar{u}_3 + \bar{u}_3 \bar{u}_{3,3} = g_3 + \bar{v} (\bar{\sigma}_{33,3} - \bar{p}_{,3}) - \overline{u'_j u'_{,j}} - \overline{v' p'_{,j}} + \overline{v' \sigma'_{ij}} \quad (23)$$

$$\begin{aligned} \partial_t \bar{p} + \bar{u}_3 \bar{p}_{,3} &= (\gamma - 1) \bar{\sigma}_{33} \bar{u}_{3,3} - \bar{\gamma} \bar{p} \bar{u}_{3,3} + \frac{\kappa}{c_v} (\bar{p} \bar{v})_{,33} \\ &\quad - \overline{u'_j p'_{,j}} + (\gamma - 1) \overline{\sigma'_{ij} u'_{,j}} - \gamma \overline{p' u'_{,j}} + \frac{\kappa}{c_v} (\overline{p' v'})_{,33} \end{aligned} \quad (24)$$

where we have used the fact that slab-averaged quantities vary only in the vertical direction, and we have transformed to a coordinate system in which the mean transverse velocities are zero.

We can Fourier analyze the fluctuating fields in the transverse directions, and expand them in the vertical direction using basis functions appropriate to the

boundary conditions. This raises the question of how to treat the boundaries for this problem.

First, consider that the temperature at each boundary is held constant. Thus, expanding the equation of state (6) we have

$$\bar{p}\bar{v} + \bar{p}'v' + p'\bar{v} + p'v' = (\gamma - 1)c_v T_b \tag{25}$$

which on averaging, yields

$$\bar{p}\bar{v} + \overline{p'v'} = (\gamma - 1)c_v T_b \tag{26}$$

Subtracting (26) from (25) gives

$$\bar{p}v' + p'\bar{v} + p'v' - \overline{p'v'} = 0 \tag{27}$$

If we remain consistent with the quasilinear approximation adopted in the previous section, we can rewrite (27) as

$$\bar{p}v' + p'\bar{v} = 0 \tag{28}$$

We now posit rigid, no-slip boundary conditions, which imply a viscous boundary layer. Making the further assumption that the layer is relatively incompressible then gives us, via (28) that both v' and p' vanish at the boundaries. This assumption also implies that the horizontal velocity fluctuations vanish at the boundaries, i.e. $u'_x = 0$ and $u'_y = 0$, and that the vertical velocity fluctuations and their vertical derivatives also vanish, $u'_z = 0$ and $du'_z/dz=0$.⁵ This allows us to expand fluctuations in the specific volume, pressure, and horizontal velocities in a cosine series, and to expand the vertical velocity fluctuations using the Chandrasekhar-Reid functions.⁶ Thus,

$$\begin{bmatrix} v' \\ p' \\ u'_1 \\ u'_2 \end{bmatrix} = \frac{\sqrt{2}}{2\pi} \sum_{n=1}^{\infty} \iint_{all\ k} d^2k e^{i(k_x x + k_y y)} \begin{bmatrix} v_{cn}(\mathbf{k}, t) \\ p_{cn}(\mathbf{k}, t) \\ u_{cn}^1(\mathbf{k}, t) \\ u_{cn}^2(\mathbf{k}, t) \end{bmatrix} \cos(a_n z) \tag{25a}$$

$$u'_3 = \frac{1}{2\pi} \sum_{n=1}^{\infty} \iint_{all\ k} d^2k e^{i(k_x x + k_y y)} [u_{cn}^3(\mathbf{k}, t) C_n(z) + u_{sn}^3(\mathbf{k}, t) S_n(z)] \tag{25b}$$

In this notation equations (16b-18b) become, suppressing the common factors, sums on n , integrals, and complex exponentials,

$$\begin{aligned} & \partial_t v_{cn}(\mathbf{k}, t) \cos(a_n z) - \bar{u}_3 v_{cn}(\mathbf{k}, t) a_n \sin(a_n z) - \bar{u}_{3,3} v_{cn}(\mathbf{k}, t) \cos(a_n z) \\ & = i\bar{v} k_j u_{cn}^j(\mathbf{k}, t) \cos(a_n z) + \bar{v} [u_{cn}^3(\mathbf{k}, t) C_n'(z) + u_{sn}^3(\mathbf{k}, t) S_n'(z)] \\ & \quad - \bar{v}_{,3} [u_{cn}^3(\mathbf{k}, t) C_n(z) + u_{sn}^3(\mathbf{k}, t) S_n(z)] \end{aligned} \quad (26)$$

$$\begin{aligned} & \partial_t u_{cn}^i(\mathbf{k}, t) \cos(a_n z) - \bar{u}_3 u_{cn}^i(\mathbf{k}, t) a_n \sin(a_n z) + \bar{v} \mu (k^2 + a_n^2) u_{cn}^i(\mathbf{k}, t) \cos(a_n z) \\ & = -\bar{v} \Lambda k_i k_j u_{cn}^j(\mathbf{k}, t) \cos(a_n z) + i\bar{v} \Lambda k_i [u_{cn}^3(\mathbf{k}, t) C_n'(z) + u_{sn}^3(\mathbf{k}, t) S_n'(z)] \\ & \quad - i\bar{v} k_i p_{cn}(\mathbf{k}, t) \cos(a_n z) \quad ; i = 1, 2 \end{aligned} \quad (27a)$$

$$\begin{aligned} & \partial_t [u_{cn}^3(\mathbf{k}, t) C_n(z) + u_{sn}^3(\mathbf{k}, t) S_n(z)] + \bar{u}_3 [u_{cn}^3(\mathbf{k}, t) C_n'(z) + u_{sn}^3(\mathbf{k}, t) S_n'(z)] \\ & \quad + (\bar{v} \mu k^2 + \bar{u}_{3,3}) [u_{cn}^3(\mathbf{k}, t) C_n(z) + u_{sn}^3(\mathbf{k}, t) S_n(z)] - \bar{v} (\mu + \Lambda) [u_{cn}^3(\mathbf{k}, t) C_n''(z) + u_{sn}^3(\mathbf{k}, t) S_n''(z)] \\ & = -i\bar{v} \Lambda k_j u_{cn}^j(\mathbf{k}, t) a_n \sin(a_n z) + \bar{v} p_{cn}(\mathbf{k}, t) a_n \sin(a_n z) + (\bar{\sigma}_{33,3} - \bar{p}_{,3}) v_{cn}(\mathbf{k}, t) \cos(a_n z) \quad ; i = 3 \end{aligned} \quad (27b)$$

$$\begin{aligned} & \partial_t p_{cn}(\mathbf{k}, t) \cos(a_n z) - \bar{u}_3 p_{cn}(\mathbf{k}, t) a_n \sin(a_n z) + \gamma \bar{u}_{3,3} p_{cn}(\mathbf{k}, t) \cos(a_n z) \\ & \quad - \frac{\kappa}{c_v} p_{cn}(\mathbf{k}, t) \left[(-\bar{v} (k^2 + a_n^2) + \bar{v}_{,33}) \cos(a_n z) - 2\bar{v}_{,3} a_n \sin(a_n z) \right] \\ & = (2(\gamma - 1) \bar{\sigma}_{33} - \gamma \bar{p}) [u_{cn}^3(\mathbf{k}, t) C_n'(z) + u_{sn}^3(\mathbf{k}, t) S_n'(z)] \\ & \quad - i\gamma \bar{p} k_j u_{cn}^j(\mathbf{k}, t) \cos(a_n z) - \bar{p}_{,3} [u_{cn}^3(\mathbf{k}, t) C_n(z) + u_{sn}^3(\mathbf{k}, t) S_n(z)] \\ & \quad + \frac{\kappa}{c_v} v_{cn}(\mathbf{k}, t) \left[(-\bar{p} (k^2 + a_n^2) + \bar{p}_{,33}) \cos(a_n z) - 2\bar{p}_{,3} a_n \sin(a_n z) \right] \end{aligned} \quad (28)$$

Here primes on the vertical basis functions denote differentiation with respect to z , and it is understood that sums involving the wavevector \mathbf{k} range from 1 to 2.

We can now exploit the orthogonality of the trigonometric and Chandrasekhar-Reid functions to convert (26-28) into equations for the individual Fourier coefficients of the fluctuating fields. Multiplying by the appropriate basis functions and integrating over z yields

IV

$$\begin{aligned} & \partial_t v_{cm}(\mathbf{k}, t) - v_{cn}(\mathbf{k}, t) a_n \langle c_m | \bar{u}_3 | s_n \rangle - v_{cn}(\mathbf{k}, t) \langle c_m | \bar{u}_{3,3} | c_n \rangle \\ & = ik_j u_{cn}^j(\mathbf{k}, t) \langle c_m | \bar{v} | c_n \rangle + [u_{cn}^3(\mathbf{k}, t) \langle c_m | \bar{v} | C'_n \rangle + u_{sn}^3(\mathbf{k}, t) \langle c_m | \bar{v} | S'_n \rangle] \\ & \quad - [u_{cn}^3(\mathbf{k}, t) \langle c_m | \bar{v}_{,3} | C_n \rangle + u_{sn}^3(\mathbf{k}, t) \langle c_m | \bar{v}_{,3} | S_n \rangle] \end{aligned} \quad (29)$$

$$\begin{aligned} & \partial_t u_{cm}^i(\mathbf{k}, t) - u_{cn}^i(\mathbf{k}, t) a_n \langle c_m | \bar{u}_3 | s_n \rangle + \mu(k^2 + a_n^2) u_{cn}^i(\mathbf{k}, t) \langle c_m | \bar{v} | c_n \rangle \\ & = -\Lambda k_i k_j u_{cn}^j(\mathbf{k}, t) \langle c_m | \bar{v} | c_n \rangle - ik_i p_{cn}(\mathbf{k}, t) \langle c_m | \bar{v} | c_n \rangle \\ & \quad + i\Lambda k_i [u_{cn}^3(\mathbf{k}, t) \langle c_m | \bar{v} | C'_n \rangle + u_{sn}^3(\mathbf{k}, t) \langle c_m | \bar{v} | S'_n \rangle] \quad ; i = 1, 2 \end{aligned} \quad (30a)$$

$$\begin{aligned} & \partial_t u_{(CS)_m}^3(\mathbf{k}, t) + [u_{cn}^3(\mathbf{k}, t) \langle CS_m | \bar{u}_3 | C'_n \rangle + u_{sn}^3(\mathbf{k}, t) \langle CS_m | \bar{u}_3 | S'_n \rangle] \\ & \quad + \mu k^2 [u_{cn}^3(\mathbf{k}, t) \langle CS_m | \bar{v} | C_n \rangle + u_{sn}^3(\mathbf{k}, t) \langle CS_m | \bar{v} | S_n \rangle] \\ & \quad [u_{cn}^3(\mathbf{k}, t) \langle CS_m | \bar{u}_{3,3} | C_n \rangle + u_{sn}^3(\mathbf{k}, t) \langle CS_m | \bar{u}_{3,3} | S_n \rangle] \\ & \quad - (\mu + \Lambda) [u_{cn}^3(\mathbf{k}, t) \langle CS_m | \bar{v} | C'_n \rangle + u_{sn}^3(\mathbf{k}, t) \langle CS_m | \bar{v} | S'_n \rangle] \end{aligned} \quad (30b)$$

$$\begin{aligned} & = -i\Lambda k_j u_{cn}^j(\mathbf{k}, t) a_n \langle CS_m | \bar{v} | s_n \rangle + p_{cn}(\mathbf{k}, t) a_n \langle CS_m | \bar{v} | s_n \rangle \\ & \quad + v_{cn}(\mathbf{k}, t) \langle CS_m | \bar{\sigma}_{33,3} | c_n \rangle - v_{cn}(\mathbf{k}, t) \langle CS_m | \bar{p}_{,3} | c_n \rangle \quad ; i = 3 \end{aligned}$$

$$\begin{aligned} & \partial_t p_{(cs)_m}(\mathbf{k}, t) - p_{cn}(\mathbf{k}, t) a_n \langle c_m | \bar{u}_3 | s_n \rangle + \gamma p_{cn}(\mathbf{k}, t) \langle c_m | \bar{u}_{3,3} | c_n \rangle \\ & \quad - \frac{\kappa}{c_v} p_{cn}(\mathbf{k}, t) [-(k^2 + a_n^2) \langle c_m | \bar{v} | c_n \rangle + \langle c_m | \bar{v}_{,33} | c_n \rangle - 2a_n \langle c_m | \bar{v}_{,3} | s_n \rangle] \\ & = 2(\gamma - 1) [u_{cn}^3(\mathbf{k}, t) \langle c_m | \bar{\sigma}_{33} | C'_n \rangle + u_{sn}^3(\mathbf{k}, t) \langle c_m | \bar{\sigma}_{33} | S'_n \rangle] \\ & \quad - \gamma [u_{cn}^3(\mathbf{k}, t) \langle c_m | \bar{p} | C'_n \rangle + u_{sn}^3(\mathbf{k}, t) \langle c_m | \bar{p} | S'_n \rangle] - i\gamma k_j u_{cn}^j(\mathbf{k}, t) \langle c_m | \bar{p} | c_n \rangle \\ & \quad - [u_{cn}^3(\mathbf{k}, t) \langle c_m | \bar{p}_{,3} | C_n \rangle + u_{sn}^3(\mathbf{k}, t) \langle c_m | \bar{p}_{,3} | S_n \rangle] \\ & \quad + \frac{\kappa}{c_v} v_{cn}(\mathbf{k}, t) [-(k^2 + a_n^2) \langle c_m | \bar{p} | c_n \rangle + \langle c_m | \bar{p}_{,33} | c_n \rangle - 2a_n \langle c_m | \bar{p}_{,3} | s_n \rangle] \end{aligned} \quad (31)$$

We are using a notation adapted from quantum mechanical matrix-elements in which

$$u_{(CS)_m}^3(\mathbf{k}, t) \equiv \begin{pmatrix} u_{cm}^3(\mathbf{k}, t) \\ u_{sm}^3(\mathbf{k}, t) \end{pmatrix}, \quad (32a)$$

$$\langle c_m | \bar{v} | s_n \rangle \equiv \int_{-1/2}^{1/2} \sqrt{2} \cos(a_m z) \bar{v}(z) \sqrt{2} \sin(a_n z) dz \quad (32b)$$

and

$$\langle CS_m | \bar{v} | s_n \rangle \equiv \int_{-1/2}^{1/2} \begin{pmatrix} C_m(z) \\ S_m(z) \end{pmatrix} \bar{v}(z) \sqrt{2} \sin(a_n z) dz, \quad (32c)$$

etc. Thus, we have chosen all vertical basis functions to be orthonormal over the interval $z = [-1/2, 1/2]$. The coefficients $a_n = (2n-1)\pi$, so that the expansions using the trigonometric functions will satisfy the boundary conditions.

The integrals over k and the complex exponentials in k can be considered to have been dropped in (29-31), although the sums on n are still implied. The vertical integrations of the matrix elements indicate that the Fourier coefficients of the fluctuating quantities depend on the mean flow in non-local manner. Such non-locality is a direct consequence of the method of averaging and the decomposition into vertical basis functions that we have chosen.

We now develop equations for the slab-averaged products of fluctuations, such as $\overline{v'v'}$ in the usual manner. We obtain, for example,

$$\begin{aligned} \overline{v'v'} &= \frac{\sqrt{2}}{2\pi} \frac{\sqrt{2}}{2\pi} \lim_{a,b \rightarrow \infty} \frac{1}{4ab} \int_{-a}^a dx \int_{-b}^b dy \sum_{p=1 \text{ all } k'} \iint d^2 k' e^{i(k'_x + k'_y)} \sum_{m=1 \text{ all } k} \iint d^2 k e^{i(k_x + k_y)} \\ &v_{cp}(\mathbf{k}', t) \cos(a_p z) v_{cm}(\mathbf{k}, t) \cos(a_m z) \quad (33) \\ &= \frac{1}{\pi} \sum_{m,p=1 \text{ all } k} \iint d^2 k e^{i(k_x + k_y)} v_{cp}(-\mathbf{k}, t) \cos(a_p z) v_{cm}(\mathbf{k}, t) \cos(a_m z) \end{aligned}$$

The slab averaging introduces a Dirac delta-function, eliminating one of the double integrals over k -space, and a double-sum on indices m and p is retained. From (33) we see that the turbulence closure problem is thus reduced to a set of 21 equations of the form

$$\begin{aligned}
 & \partial_t v_{cm}(\mathbf{k}, t) v_{cp}(-\mathbf{k}, t) - v_{cn}(\mathbf{k}, t) v_{cp}(-\mathbf{k}, t) a_n \langle c_m | \bar{u}_3 | S_n \rangle - v_{cm}(\mathbf{k}, t) v_{cl}(-\mathbf{k}, t) a_l \langle c_p | \bar{u}_3 | S_l \rangle \\
 & - v_{cn}(\mathbf{k}, t) v_{cp}(-\mathbf{k}, t) \langle c_m | \bar{u}_{3,3} | C_n \rangle - v_{cm}(\mathbf{k}, t) v_{cl}(-\mathbf{k}, t) \langle c_p | \bar{u}_{3,3} | C_l \rangle \\
 & = ik_j u_{cn}^j(\mathbf{k}, t) v_{cp}(-\mathbf{k}, t) \langle c_m | \bar{v} | C_n \rangle - ik_j v_{cm}(\mathbf{k}, t) u_{cl}^j(-\mathbf{k}, t) \langle c_p | \bar{v} | C_l \rangle \\
 & + [u_{cn}^3(\mathbf{k}, t) v_{cp}(-\mathbf{k}, t) \langle c_m | \bar{v} | C'_n \rangle + u_{sn}^3(\mathbf{k}, t) v_{cp}(-\mathbf{k}, t) \langle c_m | \bar{v} | S'_n \rangle] \\
 & + [v_{cm}(\mathbf{k}, t) u_{cl}^3(-\mathbf{k}, t) \langle c_p | \bar{v} | C'_l \rangle + v_{cm}(\mathbf{k}, t) u_{sl}^3(-\mathbf{k}, t) \langle c_p | \bar{v} | S'_l \rangle] \\
 & - [u_{cn}^3(\mathbf{k}, t) v_{cp}(-\mathbf{k}, t) \langle c_m | \bar{v}_{,3} | C_n \rangle + u_{sn}^3(\mathbf{k}, t) v_{cp}(-\mathbf{k}, t) \langle c_m | \bar{v}_{,3} | S_n \rangle] \\
 & - [v_{cm}(\mathbf{k}, t) u_{cl}^3(-\mathbf{k}, t) \langle c_p | \bar{v}_{,3} | C_l \rangle + v_{cm}(\mathbf{k}, t) u_{sl}^3(-\mathbf{k}, t) \langle c_p | \bar{v}_{,3} | S_l \rangle]
 \end{aligned} \tag{34}$$

In these equations, for each pair of indices m and p, the indices n and l are summed over. We believe these averaged equations will have less stringent requirements for discretization than (29-31).

It is evident that the resulting system of equations is closed, if formidable to compute. In practice, the integrals over k-space can be truncated at values of k corresponding to length scales at which the flow becomes viscous, i.e., at which the Reynolds number becomes low. The sums over matrix elements can likewise be truncated by limiting the number of modes to the vertical resolution desired. Further details of how to implement this model in a computer code are the subject of ongoing study.

V. Conclusion

We have presented method of developing a quasilinear one-point closure model for compressible turbulent flow. The method was specialized to the case of a fluid confined between two infinite bounding planes. The distinguishing characteristic of this model is its avoidance of adjustable parameters. This provides a somewhat "brittle" model that may be useful for flows undergoing rapid deformation.

[†] Work performed under the auspices of the U. S. Department of Energy by Lawrence Livermore National Laboratory under Contract W-7405-ENG-48.

¹ Herring, J. R., "Investigation of Problems in Thermal Convection," *Journal of the Atmospheric Sciences*, 20, 325-338, July 1963.

² Millionshchikov, M. D., "Theory of isotropic homogeneous turbulence," *Dokl. Akad. Nauk SSSR*, 32, No.9, 611-614, and "Theory of isotropic homogeneous turbulence," *Izv. Akad. Nauk*

SSSR, Ser. Geogr. i Geofiz., 5, No. 4-5, 433-446. A summary is given in Monin, A. S., and A. M. Yaglom, *Statistical Fluid Mechanics*, Vol. 2, MIT Press, Cambridge, MA, 1975, 241-260.

³ See, for example, Harlow, F. H., and A. A. Amsden, *Fluid Dynamics*, LA-4700, Los Alamos National Laboratory, 1971, 28-30, or any other introductory hydrodynamics text.

⁴ See Monin, A. S., and A. M. Yaglom, *op. cit.*, Vol 1, 222-231, for a definition and careful discussion.

⁵ Chandrasekhar, S., *Hydrodynamic and Hydromagnetic Stability*, Dover, New York, 1981, pp 21-22.

⁶ Chandrasekhar, *op. cit.*, pp 635-642 and references therein.



**Kinetic Energy of Multimode
 Rayleigh-Taylor and
 Richtmyer-Meshkov Instabilities**

Alan K. Harrison
 Center for Compressible Turbulence
 Lawrence Livermore National Laboratory
 Livermore, California, U. S. A.

4th International Workshop on the Physics of
 Compressible Turbulent Mixing
 Cambridge, England
 31 March 1993

**We need subgrid-scale models of instability
 physics to install in a turbulent hydrodynamics code**

For instance, in a K-ε model, the creation of turbulent energy may be modeled by source terms s which account for instabilities.

$$\frac{dK}{dt} = w_{turb. press} + s_{KH} + s_{RT} + s_{RM} - \epsilon$$

$$\frac{d\epsilon}{dt} = \frac{\epsilon}{K} (C_{1d} w_{turb. press} + C_{1s} s_{KH} + C_{\epsilon 1} s_{RT} + C_{\epsilon 3} s_{RM} - C_{\epsilon 2} \epsilon)$$



We need to study instability physics at arbitrary density gradients, not just at discontinuities



- Due to spatial discretization, a hydrocode cannot recognize density discontinuities *per se*.
- Even if it could reliably detect discontinuities, the abrupt appearance or disappearance of instability physics at some location in the mesh could introduce numerical instability.
- We need to account for instabilities properly even where density gradients are finite.

We will use the following profile, which is continuous and includes the small-gradient and infinite-gradient limits:

$$\rho(z) = \begin{cases} \rho_1 & (z \leq 0) \\ \rho_1 e^{\beta z} & (0 \leq z \leq \ell) \\ \rho_2 = \rho_1 e^{\beta \ell} & (\ell \leq z) \end{cases}$$



Small quantities for perturbation analysis



density	$\rho(z) + \delta\rho(x, t)$	$\langle \delta\rho \rangle = 0$
roughness	$\eta(x, t)$	$\langle \eta \rangle = 0$
pressure	$p_0(z) + \delta p(x, t)$	$\langle \delta p \rangle = 0$
fluid velocity	$\mathbf{u}(x, t)$	$\langle \mathbf{u} \rangle = 0$

Density fluctuations and roughness are equivalent ways of accounting for deviations from the unperturbed density $\rho(z)$. They are related by

$$\rho(x - \hat{e}_z \eta(x, t)) = \rho(x) + \delta\rho(x, t)$$



Spatial ODE for velocity eigenfunction W



$$D(\rho DW) + \frac{\kappa^2}{\Gamma^2}(D\rho)W - \kappa^2 \rho W = 0 \quad \kappa = \sqrt{k_x^2 + k_y^2}$$

[Originally derived by S. Chandrasekhar; see *Hydrodynamic and Hydromagnetic Stability* (Dover, New York, 1981), pp. 428-433.]

Solutions satisfy an orthogonality relation

$$\int_{-\infty}^{\infty} (D\rho)W_{\kappa m}W_{\kappa n} dz = \delta_{mn}I_{\kappa m}$$



Spatial eigenvalues for continuous density profile



The eigenvalues are

$$\Gamma_{\kappa m}^2 = \frac{2cd\kappa}{\alpha_{\kappa m}^2 + c^2 + d^2}$$

where

$$c = \kappa \ell \quad (= \text{nondimensional wavenumber})$$

$$d = \frac{1}{2} \beta \ell = \tanh^{-1}(\text{Atwood number}) \quad (= \text{nondimensional density gradient})$$

and $\alpha_{\kappa m}$ is solution m of the transcendental equation

$$\tan \alpha_{\kappa m} = \frac{2c\alpha_{\kappa m}}{\alpha_{\kappa m}^2 - c^2 + d^2}$$

We can number the solutions so that

$$m\pi < \alpha_{\kappa m} < (m+1)\pi \quad (m \geq 0; \alpha_{\kappa 0} \text{ may also be zero or imaginary})$$

[Derived by K. O. Mikaelian; see *Phys. Rev. Lett.* 48, 1365 (1982); *Phys. Rev. A* 26, 2140 (1982).]



Single-mode instability analysis (incompressible flow)



$$\rho \frac{\partial \mathbf{u}}{\partial t} = -\nabla \delta p - \hat{\mathbf{e}}_z g \delta \rho \qquad \delta \rho = -\eta D \rho$$

$$\nabla \cdot \mathbf{u} = 0 \qquad u_z = \frac{\partial \eta}{\partial t}$$

$$\frac{\partial}{\partial t} \delta \rho + u_z D \rho = 0 \qquad \text{where } D \equiv \partial / \partial z$$

Seek plane wave solutions and separate variables:

$$\eta(x, y, z, t) = A(t) W(z) e^{i(k_x x + k_y y)}$$

$$\delta \rho(x, y, z, t) = -A(t) W(z) D \rho(z) e^{i(k_x x + k_y y)}$$

$$u_z(x, y, z, t) = \dot{A}(t) W(z) e^{i(k_x x + k_y y)}$$

$$u_x(x, y, z, t) = \dot{A}(t) U(z) e^{i(k_x x + k_y y)}$$

$$u_y(x, y, z, t) = \dot{A}(t) V(z) e^{i(k_x x + k_y y)}$$

$$\delta p(x, y, z, t) = P(z, t) e^{i(k_x x + k_y y)}$$



Temporal ODE for amplitude A



$$\ddot{A} = \Gamma^2 g A = \gamma^2 A$$

eigenvalue Γ^2 (or γ^2)

RT instability $g(t) = g$ (constant)

$$A(t) = A(0) \cosh \gamma t + \dot{A}(0) \frac{\sinh \gamma t}{\gamma}$$

$$\dot{A}(t) = A(0) \gamma \sinh \gamma t + \dot{A}(0) \cosh \gamma t$$

(approximately) exponential growth

RM instability $g(t) = \Delta v \delta(t)$

$$A(t) = A(0) [1 + \Delta v \Gamma^2 t \theta(t)] + \dot{A}(0_-) t$$

$$\dot{A}(t) = A(0) \Delta v \Gamma^2 \theta(t) + \dot{A}(0_-)$$

linear growth

Larger eigenvalues correspond to larger growth rates



Spatial eigenfunctions for continuous density profile



$$W_{\kappa m}(z) = \begin{cases} e^{\kappa z} & (z \leq 0) \\ e^{-\beta z/2} \left[\cos \frac{\alpha_{\kappa m} z}{\ell} + \left(\frac{c+d}{\alpha_{\kappa m}} \right) \sin \frac{\alpha_{\kappa m} z}{\ell} \right] & (0 \leq z \leq \ell) \\ W_{\kappa m}(\ell) e^{-\kappa(z-\ell)} = e^{c-d-\kappa z} \left[\cos \alpha_{\kappa m} + \left(\frac{c+d}{\alpha_{\kappa m}} \right) \sin \alpha_{\kappa m} \right] & (\ell \leq z) \end{cases}$$

We see that $W_{\kappa m}$ is the eigenmode with m zeros, and that

$$\frac{\alpha_{\kappa m}}{\ell} \equiv \frac{m\pi}{\ell}$$

is the effective wavenumber in the z direction.



The general solution is a sum of single modes



$$\eta(x, y, z, t) = \sum_{\kappa, m} A_{\kappa m}(t) W_{\kappa m}(z) e^{i(k_x x + k_y y)}$$

$$\delta\rho(x, y, z, t) = - \sum_{\kappa, m} A_{\kappa m}(t) (D\rho(z)) W_{\kappa m}(z) e^{i(k_x x + k_y y)}$$

$$u_x(x, y, z, t) = i \sum_{\kappa, m} \frac{k_x}{\kappa^2} \dot{A}_{\kappa m}(t) D W_{\kappa m}(z) e^{i(k_x x + k_y y)}$$

$$u_y(x, y, z, t) = i \sum_{\kappa, m} \frac{k_y}{\kappa^2} \dot{A}_{\kappa m}(t) D W_{\kappa m}(z) e^{i(k_x x + k_y y)}$$

$$u_z(x, y, z, t) = \sum_{\kappa, m} \dot{A}_{\kappa m}(t) W_{\kappa m}(z) e^{i(k_x x + k_y y)}$$

($A_{\kappa m}$ depends on vector $\kappa \equiv \hat{e}_x k_x + \hat{e}_y k_y$, $W_{\kappa m}$ depends on scalar

$\kappa \equiv |\kappa| = \sqrt{k_x^2 + k_y^2}$. All sums are on vector κ .)

Initial values of coefficients are derived from position and velocity initial conditions

Use the orthogonality condition to invert the sums, and set $t=0$:

$$\begin{aligned}
 A_{\kappa n}(0) &= \frac{1}{L^2 I_{\kappa n}} \int_0^L dx \int_0^L dy \int_{-\infty}^{\infty} dz (D\rho(z)) W_{\kappa n}(z) \eta(x, y, z, 0) e^{-i(k_x x + k_y y)} \\
 &= -\frac{1}{L^2 I_{\kappa n}} \int_0^L dx \int_0^L dy \int_{-\infty}^{\infty} dz W_{\kappa n}(z) \delta\rho(x, y, z, 0) e^{-i(k_x x + k_y y)} \\
 \dot{A}_{\kappa n}(0) &= \frac{1}{L^2 I_{\kappa n}} \int_0^L dx \int_0^L dy \int_{-\infty}^{\infty} dz (D\rho(z)) W_{\kappa n}(z) u_z(x, y, z, 0) e^{-i(k_x x + k_y y)}
 \end{aligned}$$

This enables us to treat instabilities seeded by surface roughness or density inhomogeneities (RT, RM instability), or velocity fluctuations (e. g., preexisting turbulence).

We have a powerful theoretical system for the analysis of various types of instabilities

In principle, we can calculate

- mix layer thickness
- instability energy
- mass current

due to

- steady (RT)
- impulsive (RM)

acceleration of a fluid with

- an arbitrary density gradient
- a density discontinuity

initially perturbed by

- surface roughness
- turbulent velocity fluctuations
- other velocity fluctuations
- uncorrelated or correlated combinations of the above
- other density fluctuations
- shock imperfections

Limitations:

- incompressible flow approximation
- no coupling between modes
- acceleration must be parallel (or antiparallel) to density gradient

Predicted values of observables are based on eigenvalues and functionals of the eigenmodes



$$\Gamma_{\kappa m}^2 = \frac{2cd\kappa}{\alpha_{\kappa m}^2 + c^2 + d^2}$$

$$H_{\kappa m} = \int_{-\infty}^{\infty} (D\rho)W_{\kappa m} dz = \frac{2\rho_1 d}{\alpha_{\kappa m}^2 + d^2} \left\{ c + \frac{e^d \sin \alpha_{\kappa m}}{2\alpha_{\kappa m}} [\alpha_{\kappa m}^2 + (c+d)^2] \right\}$$

$$I_{\kappa m} = \int_{-\infty}^{\infty} (D\rho)W_{\kappa m}^2 dz = \frac{2\rho_1 d}{\alpha_{\kappa m}^2} \left\{ c+d + [\alpha_{\kappa m}^2 + (c+d)^2] \left(\frac{1}{2} - \frac{d \cos^2 \alpha_{\kappa m}}{\alpha_{\kappa m}^2 - c^2 + d^2} \right) \right\}$$

$$J_{\kappa q m} = \int_{-\infty}^{\infty} (D\rho)W_{\kappa m} e^{iqz} dz = \frac{2\rho_1 d}{\alpha_{\kappa m}^2 + d^2 - f^2 + 2idf} \left\{ c - if + \frac{(c+if)[\alpha_{\kappa m}^2 + (c+d)^2] e^{d+if} \cos \alpha_{\kappa m}}{\alpha_{\kappa m}^2 - c^2 + d^2} \right\}$$

where $f = q\ell$

RM and RT instability energy can be expressed as sums of single-mode energies



Since the flow is incompressible, the instability energy per unit area of the xy plane, averaged over the xy plane, is the kinetic energy

$$E = \frac{1}{2L^2} \int_0^L dx \int_0^L dy \int_{-\infty}^{\infty} dz \rho u^2$$

$$= \frac{1}{2} \sum_{\kappa, m} \frac{|\dot{A}_{\kappa m}(t)|^2 I_{\kappa m}}{\Gamma_{\kappa m}^2}$$

$$\langle E_{RT} \rangle = \frac{1}{2} g \sum_{\kappa, m} I_{\kappa m} \left[\langle |A_{\kappa m}(0)|^2 \rangle \sinh^2 \gamma_{\kappa m} t \right.$$

$$\left. + 2 \operatorname{Re} \langle A_{\kappa m}^*(0) \dot{A}_{\kappa m}(0) \rangle \frac{\sinh \gamma_{\kappa m} t \cosh \gamma_{\kappa m} t}{\gamma_{\kappa m}} + \langle |\dot{A}_{\kappa m}(0)|^2 \rangle \frac{\cosh^2 \gamma_{\kappa m} t}{\gamma_{\kappa m}^2} \right]$$

$$\langle E_{RM} \rangle = \frac{1}{2} \sum_{\kappa, m} I_{\kappa m} \left[\Delta v^2 \Gamma_{\kappa m}^2 \langle |A_{\kappa m}(0)|^2 \rangle \theta(t) \right.$$

$$\left. + 2\Delta v \operatorname{Re} \langle A_{\kappa m}^*(0) \dot{A}_{\kappa m}(0) \rangle \theta(t) + \frac{1}{\Gamma_{\kappa m}^2} \langle |\dot{A}_{\kappa m}(0)|^2 \rangle \right]$$



RM instability seeded by surface roughness



If the roughness is confined to the surface

$$\eta(x, y, z, 0) = f(x, y)$$

with a two-dimensional Fourier transform $\tilde{f}(\mathbf{\kappa})$ and a spectrum

$$s(\mathbf{\kappa}) \equiv \langle |\tilde{f}(\mathbf{\kappa})|^2 \rangle$$

then the integral expression for the initial amplitude factors into

$$A_{\mathbf{\kappa}m}(0) = \frac{\tilde{f}(\mathbf{\kappa})H_{\mathbf{\kappa}m}}{I_{\mathbf{\kappa}m}}$$

so the RM instability energy becomes

$$\begin{aligned} \langle E_{RM}(t) \rangle &= \frac{\Delta v^2 \theta(t)}{2L^2} \sum_{\mathbf{\kappa}, m} s(\mathbf{\kappa}) \frac{\Gamma_{\mathbf{\kappa}m}^2 H_{\mathbf{\kappa}m}^2}{I_{\mathbf{\kappa}m}} \\ &\equiv \frac{\Delta v^2 \theta(t) (\rho_2 - \rho_1)}{L^2 \ell} \sum_{\mathbf{\kappa}} \frac{s(\mathbf{\kappa}) c d}{c + 2d \coth d} \end{aligned}$$



Choose a perturbation spectrum and integrate on wavenumber



If, for instance, the spectrum is flat between a lower and an upper cutoff,

$$s(\mathbf{\kappa}) = \begin{cases} s & (\text{if } \kappa_1 \leq \kappa \leq \kappa_2) \\ 0 & (\text{otherwise}) \end{cases}$$

then

$$\begin{aligned} \langle E_{RM}(t) \rangle &= \frac{\Delta v^2 (\rho_2 - \rho_1) s d \theta(t)}{4\pi \ell^3} \\ &\quad \left[c_2^2 - c_1^2 - 4(c_2 - c_1) d \coth d + 8d^2 \coth^2 d \ln \left(\frac{c_2 + 2d \coth d}{c_1 + 2d \coth d} \right) \right] \end{aligned}$$

where

$$c_1 = \kappa_1 \ell, \quad c_2 = \kappa_2 \ell$$



Special cases



For a very broad perturbation spectrum we may have

$$c_1 \ll 1, d^2 \ll c_2$$

for which we get the simplified form

$$\langle E_{RM}(t) \rangle = \frac{\Delta v^2 s c_2^2 d \theta(t)}{4\pi \ell^3} (\rho_2 - \rho_1)$$

On the other hand, for a very large density ratio (Atwood number very close to unity) we may have

$$1, c_1, c_2 \ll d$$

in which case

$$\begin{aligned} \langle E_{RM}(t) \rangle &= \frac{\Delta v^2 s \theta(t)}{12\pi \ell^3} (c_2^3 - c_1^3) (\rho_2 - \rho_1) \tanh d \\ &= \frac{\Delta v^2 s \theta(t)}{12\pi} (\kappa_2^3 - \kappa_1^3) \frac{(\rho_2 - \rho_1)^2}{(\rho_2 + \rho_1)} \end{aligned}$$



More special cases



For a discontinuous interface $\ell \rightarrow 0$ we get

$$\begin{aligned} \langle E_{RM}(t) \rangle &= \frac{\Delta v^2 s \theta(t)}{12\pi \ell^3} (c_2^3 - c_1^3) (\rho_2 - \rho_1) \tanh d \\ &= \frac{\Delta v^2 s \theta(t)}{12\pi} (\kappa_2^3 - \kappa_1^3) \frac{(\rho_2 - \rho_1)^2}{(\rho_2 + \rho_1)} \end{aligned}$$

On the other hand, if $\ell \rightarrow \infty$ we find that

$$\langle E_{RM}(t) \rangle = \frac{\Delta v^2 s d \theta(t)}{4\pi \ell} (\kappa_2^2 - \kappa_1^2) (\rho_2 - \rho_1)$$



RT instability seeded by surface roughness



The RT instability energy is

$$\langle E_{RT}(t) \rangle = \frac{g}{2L^2} \sum_{\kappa, m} \frac{s(\kappa) H_{\kappa m}^2}{I_{\kappa m}} \sinh^2 \gamma_{\kappa m} t$$

which we can in principle evaluate. However, its early-time behavior is already apparent. If we can differentiate term by term, the RT instability energy and its first derivative are initially zero, but

$$\left. \frac{d^2}{dt^2} \langle E_{RT}(t) \rangle \right|_{t=0} = \frac{2g^2}{\Delta v^2} \langle E_{RM}(0_+) \rangle$$

and we have already evaluated the right hand side. This identity is the multimode analog of a single-mode relation discovered by K. O. Mikaelian [Phys. Fluids A 3, 2625 (1991)].



Net mass current in the z direction (the "mixing" current)



The mass current averaged across the xy plane is in general a function of z. But if in addition we integrate in the z direction, the result takes a simple form

$$\int_{-\infty}^{\infty} j_z(z, t) dz = - \sum_{\kappa, m} |A_{\kappa m}^*(t) \dot{A}_{\kappa m}(t)| I_{\kappa m}$$

which can be simply related to the instability energy by

$$g(t) \int_{-\infty}^{\infty} j_z(z, t) dz = - \frac{d}{dt} E(t)$$

For instance, for the RM case,

$$\int_{-\infty}^{\infty} j_z(z, t) dz = - \frac{\Delta v (\rho_2 - \rho_1) s d}{4\pi \ell^3} \left[c_2^2 - c_1^2 - 4(c_2 - c_1) d \coth d + 8d^2 \coth^2 d \ln \left(\frac{c_2 + 2d \coth d}{c_1 + 2d \coth d} \right) \right]$$

and we can make the same approximations as before.



Mix layer thickness (RM case)



By averaging η over the xy plane and the choices of initial conditions $\eta(x, y, z, 0)$, we can express the mean square mix layer thickness of the RM instability as

$$\begin{aligned} \langle \eta_{RM}^2(t) \rangle &= \sum_{\kappa \kappa \kappa'} \langle A_{\kappa \kappa}^*(t) A_{\kappa \kappa'}(t) \rangle \\ &= \frac{1}{L^2} \sum_{\kappa} s(\kappa) \left\{ \sum_m \frac{H_{\kappa m}}{I_{\kappa m}} [1 + \Delta v \Gamma_{\kappa m}^2 t \theta(t)] \right\}^2 \end{aligned}$$

The growth rate of the mixed layer is

$$\begin{aligned} \left. \frac{d}{dt} \langle \eta_{RM}^2 \rangle \right|_{t>0} &= \frac{2\Delta v}{L^2} \sum_{\kappa} s(\kappa) \left\{ \sum_m \frac{\Gamma_{\kappa m}^2 H_{\kappa m}}{I_{\kappa m}} \right\} \left\{ \sum_m \frac{H_{\kappa m}}{I_{\kappa m}} \right\} \\ &\quad + \frac{2\Delta v^2 t}{L^2} \sum_{\kappa} s(\kappa) \left\{ \sum_m \frac{\Gamma_{\kappa m}^2 H_{\kappa m}}{I_{\kappa m}} \right\}^2 \end{aligned}$$

after the time of the impulsive acceleration.



Mix layer thickness (RT case)



Using the same approach for the RT case, we find that

$$\langle \eta_{RT}^2(t) \rangle = \frac{1}{L^2} \sum_{\kappa} s(\kappa) \left(\sum_m \frac{H_{\kappa m}}{I_{\kappa m}} \cosh \gamma_{\kappa m} t \right)^2$$

At $t=0$ the mix width has the value

$$\langle \eta_{RT}^2(0) \rangle = \frac{1}{L^2} \sum_{\kappa} s(\kappa) \left(\sum_m \frac{H_{\kappa m}}{I_{\kappa m}} \right)^2$$

vanishing first derivative, and second derivative equal to

$$\left. \frac{d^2}{dt^2} \langle \eta_{RT}^2(t) \rangle \right|_{t=0} = \frac{g}{L^2} \sum_{\kappa} s(\kappa) \left(\sum_m \frac{H_{\kappa m}}{I_{\kappa m}} \right) \left(\sum_m \frac{\Gamma_{\kappa m}^2 H_{\kappa m}}{I_{\kappa m}} \right)$$



Shock-turbulence interaction



This problem can be analyzed by a similar method, except that now we are concerned with terms like

$$\begin{aligned} \langle \eta_{RM}^2(t) \rangle &= \sum_{\kappa m m'} \langle A_{\kappa m}^*(t) A_{\kappa m'}(t) \rangle \\ &= t^2 \sum_{\kappa m m'} \langle \dot{A}_{\kappa m}^*(0_-) \dot{A}_{\kappa m'}(0_-) \rangle \end{aligned}$$

which can be related to a *velocity* initial condition by

$$\dot{A}_{\kappa m}(0) = \frac{1}{L^2 I_{\kappa m}} \int_0^L dx \int_0^L dy \int_{-\infty}^{\infty} dz (D\rho(z)) W_{\kappa m}(z) u_z(x, y, z, 0) e^{-i(k_x x + k_y y)}$$

This gives us a dependence of kinetic energy on a velocity spectrum, which we take to be a typical turbulent power spectrum

$$s_T(k) = \langle |\tilde{u}(k)|^2 \rangle$$

depending on the *three-dimensional* wavevector $k = \kappa + \hat{e}_z q$. The result is

$$\langle \eta_{RM}^2(t) \rangle = t^2 \sum_{\kappa, q} s_T(\sqrt{\kappa^2 + q^2}) \left| \sum_m \frac{J_{\kappa q m}}{I_{\kappa m}} \right|^2$$



Acknowledgments



I have benefited from helpful discussions with Karnig Mikaelian.

This work was performed under the auspices of the U. S. Department of Energy by Lawrence Livermore National Laboratory under Contract No. W-7405-ENG-48.

Description of Transitional Layer Effect in Simulations with $k\varepsilon$ -Model

V. Neuvazhaev, A. Polionov, V. Yakovlev

All-Russia Research Institute of Technical Physics
454070, Chelyabinsk-70, p.o.245, Russia

Abstract

The work proposes the mode of description of the transitional layer effect by using the traditional $k\varepsilon$ -model. It needs changing the model constants to provide independence of the solution on the initial values of k and ε (k_0 and ε_0). The solution depends only on the combination $k_0^{1.5}/\varepsilon_0$ having the dimension of length which is proposed to preset proportional to the space scale of irregularities. The conducted simulations agree satisfactorily with the experiment.

The Transitional Layer (TL) is a layer with density varying along its width, placed between two layers with different densities in a gravitationally unstable system, to provide continuous distribution of density. In the case of discontinues density the turbulent mixing is developed from infinitesimal perturbations if there is no effects expressed by dimensional constants (e.g. viscosity). It stems from tending to infinity of the perturbation development increment at approaching the perturbation wave length to zero. In the case of continuous density the increment of perturbation development is limited at any wave length (e.g.^{1,2}) so development of infinitesimal perturbations requires infinite time and mixing can be only developed given the perturbations are not infinitesimal.

Placement of the TL causes a delay in development of turbulent mixing. That has been investigated experimentally in the Dr. Yu. Kucherenko's laboratory. The results have been presented in the report³. In this work the TL has been formed by mutual dissolution of two fluids at their boundary. Initial perturbations have been created by placement of solid particles in the center of the TL. It is shown schematically with some notations at Fig.1. In the experiments there has been measured the depth of penetration of the heavy fluid into the light one. The heavy spikes appeared at the boundary between the TL and the light fluid not just after applying an acceleration g but after some delay. This delay has been expressed in terms of the distance gone \hat{S} connected with the delay of time \hat{t} by the relation $\hat{S} = g\hat{t}^2/2$. The dependence obtained in the experiment are given at Fig.5. It has been taken from the paper³ with changing the coordinates.

Simulations on determination of the TL effect has been con-

ducted with using the $k\varepsilon$ -model described in the paper⁴. The model has been modified to be applied to mixing of two incompressible fluids placed in the gravitational field with the constant g . The equations of the model for this case take the following form:

$$\begin{aligned}
 (1) \quad & \rho \frac{dk}{dt} + \rho\varepsilon = \alpha_k \frac{\partial}{\partial x} \rho D \frac{\partial k}{\partial x} + g j \frac{n-1}{c+n(1-c)}, \\
 (2) \quad & \rho \frac{d\varepsilon}{dt} + c_{2\varepsilon} \rho \frac{\varepsilon^2}{k} = \alpha_\varepsilon \frac{\partial}{\partial x} \rho D \frac{\partial \varepsilon}{\partial x} + c_{1\varepsilon} \frac{\varepsilon}{k} g j \frac{n-1}{c+n(1-c)}, \\
 (3) \quad & \frac{dc}{dt} + \frac{\partial j}{\rho \partial x} = 0, \\
 (4) \quad & j = -\rho D \frac{\partial c}{\partial x}, \quad D = c_\mu \frac{k^2}{\varepsilon}, \\
 (4a) \quad & \rho = \rho_2^0 \frac{n}{c+n(1-c)}, \quad n = \rho_1^0 / \rho_2^0.
 \end{aligned}$$

Here k is a turbulent kinetic energy, ε —the rate of its dissipation, x —Euler's coordinate, c —mass fraction of the fluid 1, j —the turbulent mass flow, c_μ , $c_{1\varepsilon}$, $c_{2\varepsilon}$, α_k , α_ε are empirical constants. The boundary conditions are the zero flows of mass, turbulent energy and its dissipation.

At considering the TL we have a problem of solving the equations in the presence of the density gradient. Let us consider a small part of the TL where we could take $\nabla \rho$ as a constant. We suppose the initial values k_0 и ε_0 to be independent on space coordinate in this part of the TL. As it will have been proved further the system (1-2) allows in this case to have the decision $k(t)$ and $\varepsilon(t)$ independent on x . So we can neglect the terms with $\partial k / \partial x$ and $\partial \varepsilon / \partial x$. We assume the dissipation so small that

$$(5) \quad \varepsilon_0^2 \ll k_0^2 c_\mu \frac{\partial \rho}{\rho \partial x} \quad (\text{and as well } \varepsilon_0^2 \ll k_0^2 c_\mu \frac{c_{1\varepsilon}}{c_{2\varepsilon}} \frac{\partial \rho}{\rho \partial x}).$$

In this case we can neglect by the second terms in the left part of the equations (1-2). After the mentioned simplifications we can write the solution of the equations (1-2) in the form:

$$(6) \quad k = \left[k_0^{c_{1\varepsilon}-1} + \frac{(c_{1\varepsilon}-1) c_\mu k_0^{c_{1\varepsilon}}}{\varepsilon_0} \cdot \frac{(-g \nabla \rho)_t}{\rho} \right] \frac{1}{c_{1\varepsilon}^{-1}}$$

$$(7) \quad \varepsilon = \left[\varepsilon_0^{c_{1\varepsilon}} + (c_{1\varepsilon}-1) c_\mu \left[\frac{k_0^{c_{1\varepsilon}}}{\varepsilon_0} \right] \frac{1}{c_{1\varepsilon}} \cdot \frac{(-g \nabla \rho)_t}{\rho} \right] \frac{1}{c_{1\varepsilon}^{-1}}$$

The expression (6-7) shows the solution asymptotically does not depend on the individual values k_0 и ε_0 but does only on the combination $k_0^{c_{1\varepsilon}} / \varepsilon_0$. It is naturally to accept $c_{1\varepsilon} = 1.5$ and to consider the combination $k_0^{1.5} / \varepsilon_0$ which has the dimension of length to

be proportional to the space scale of dislocations. There have been performed two groups of simulations with the constants sets providing different rates of mixing development in the self-similar case:

$$c_{1\varepsilon}=1.5, \quad c_{2\varepsilon}=1.85, \quad \alpha_k=0.85, \quad \alpha_\varepsilon=0.5,$$

$$a) \quad c_\mu=5, \quad b) \quad c_\mu=3$$

The first set provides the same rate as the one in the paper⁴. The second set corresponds to the recommendations of the work⁵ and gives the rate 1.8 times lower.

With the mentioned sets there have been performed the simulations on mixing development in the gravitationally unstable system consisting from the two fluids of different densities with the TL. The gravitational field applied are characterized by $g=1$. The initial profile of density in the system are shown at the Fig.2,3. The initial profile of mass fractions was obtained with the expression (4a) from the density profile.

The simulations have confirmed the absence of the dependence on the initial values ε_0, k_0 if the condition (5) has been fulfilled. As a result there has been obtained the dependence of the delay on the characteristic size of dislocations which are considered to be proportional to the combination $k_0^{1.5}/\varepsilon_0$. The relation between the characteristic size of dislocations and the mentioned combination depends on the spectrum characteristic of the arose turbulence. We will assume that the dislocations spectrum character corresponds to the one of the dislocations in the turbulent region of the self similar development. Then the width of the zone of dislocations (the width of the turbulent mixing zone) connects with the combination $k_0^{1.5}/\varepsilon_0$ by the relation which can be obtained in the simulations on development of the self similar mixing:

$$L=14.3 \frac{k_0^{1.5}}{\varepsilon_0} \quad (\text{I set of the empirical constants})$$

$$L=11.0 \frac{k_0^{1.5}}{\varepsilon_0} \quad (\text{II set})$$

There have been conducted two groups of simulations for the each set of the constants. In the one group there have been assumed the dislocations with the characteristic size L has been located in the layer with the width L which has been placed in the middle of the TL. This group of simulations corresponds to the experiment so their results can be compared with the experimental data. For the more practical applying there has been performed an another group of simulations in which the dislocations with the characteristic size L has been assumed to be distributed homogeneously in the whole system.

The character of changing of the density profile at the initial stage of mixing development are shown for the two mentioned groups in the Fig.2,3. The dependence of the depth of the heavy spikes penetration on time are given at the Fig.4 for the self similar case and for the one with the TL at the different sizes

of the dislocations. It should be noted that the size of dislocations in the both groups of simulations are increasing as mixing development progresses. It seems to be plausible though this point demands an additional investigation and calibration. It should be reminded that the simulations call as well for the further investigation on reproduction of the spectrum character of the initial perturbations. As for the experiment it causes anxiety too because at the exploration of the self similar mixing development³ there has been detected the source of perturbations of an unclassified nature. It caused increased rate of mixing at the early stage of turbulence development. We cannot exclude the influence of this source on the results of the investigations of the TL effects.

The results of the simulations and the experiments are comparing in Fig.5 which shows satisfactory agreement.

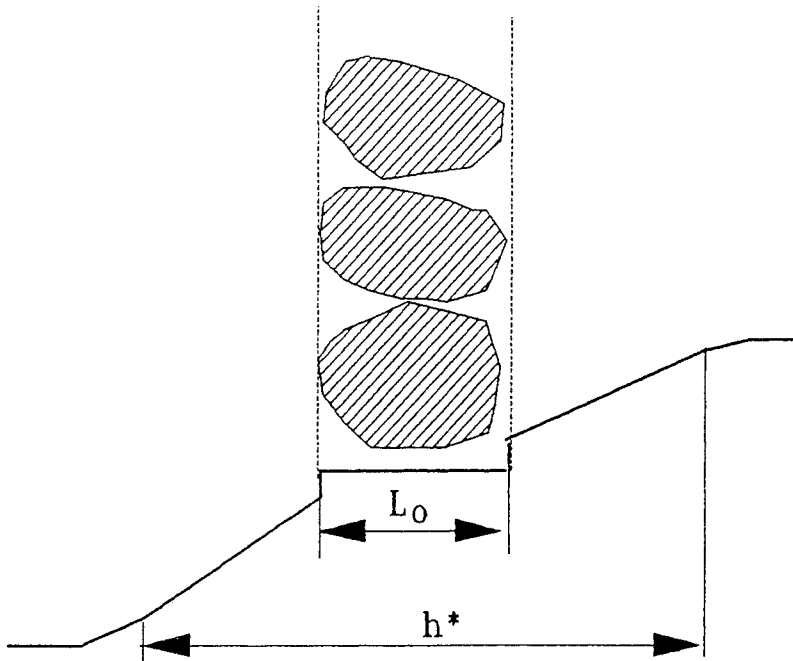


Fig.1 Structure of the transitional layer at initial moment.

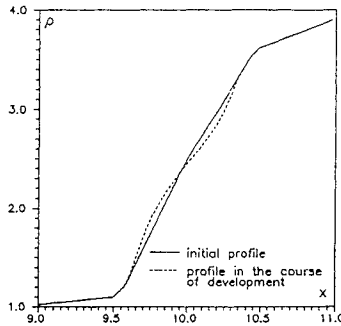


Fig.2 Changing the profile of the density at the initial stage: initial dislocations are grouped in the center of TL.

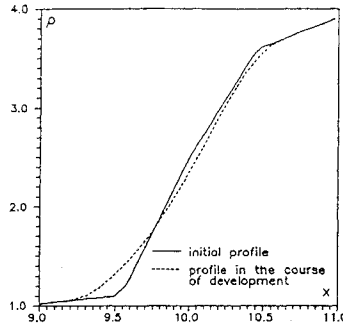


Fig.3 Changing the profile of the density at the initial stage: initial dislocations are distributed homogeneously.

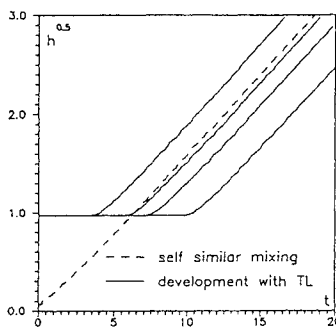


Fig.4 Dependence of the depth of penetration of the heavy spikes h on time.

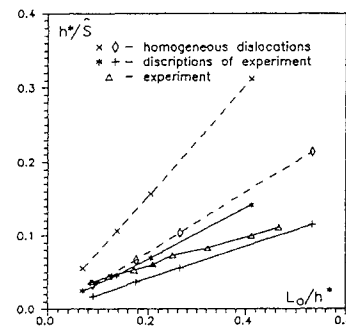


Fig.5 Delay in appearance of spikes S caused by placing the TL of the width h as a function of the size of dislocations L .

References

1. E.I.Zababahin, A.R.Ptitsin. Limitation of Convection Instability. Coll. Problems of Atom. Sci. & Engineering, Ser. Theor. & Appl. Physics, 1(1988), 4.
2. R.LeLevier, G.Lasher, F.Bjorklund. Effect of a Density Gradient on Taylor Instability. Report of LLNL. UCRL-4459, 1955.
3. Yu.A.Kucherenko, L.I.Shibarshov and others. Experimental Study of the Gravitational Turbulent Mixing Self-Similar Mode. Proceedings of the III International Workshop on Compressible Mixing, Abbey of Royaumont, France, 1991.
4. V.E.Neuvazhaev, V.G.Yakovlev. Numerical Calculation of Interface Turbulent Mixing by Rayleigh-Taylor Instability on the Basis of Semiempirical Models. Proceedings of II International Workshop on Compressible Mixing, Pleasanton, USA, 1989.
5. V.Anisimov, A.Polionov. Treatment of Experimental Data on Determination of Mixing Velocity in the Self-Similar Case. Report at the IV International Workshop on Compressible Mixing, Cambridge, England, 1993.

PROPERTIES OF THE K ϵ -MODEL FOR TURBULENT MIXING

V.E.Neuvazhayev

All-Russian Research Institute
of Technical Physics, Chelyabinsk-70

An approximate approach suggested in [1] for studying the k-model [2] of turbulent mixing of interfaces between accelerated fluids of different densities is generalized for the k ϵ -model [3,4]. In a number of cases the solutions of the problems have been obtained in an analytical form. They are: 1) the problem on mixing of two incompressible fluids under constant acceleration; 2) under impulsive acceleration; 3) the problem on "thin" layer mixing under constant acceleration. Simple analytical expressions allow to study the dependence of solution properties on empirical constants included in the model and to make their choice by way of comparison with experimental results.

I. Introduction

If there is an interface between two media and it is subjected to accelerated motion, then unstable motions can arise which lead to breaking of the interface and its turbulent mixing. Such mixing takes place if pressure in a light fluid is higher than in the heavy one. The instability of the interface is widely investigated in literature beginning with Taylor's classic work [5].

Interest to study the above-mentioned problem has increased for the last time. It is connected with the problems of inertial thermonuclear fusion where similar situations take place under compression of complicated targets for reaching high compressions and temperatures which are necessary for the following ignition of the target with thermonuclear fuel.

Turbulent mixing arising as a result of the Rayleigh-Taylor instability has a number of features, therefore special consideration of this problem was necessary for the purpose of its mathematical description. In the given work the properties of the $k\epsilon$ -model being applied to predict the process of the contact boundaries mixing are studied. The selected variant of the model [3,4] contains five empirical constants which are determined on the test problems having, as a rule, self-similar solutions. The approximate approach proposed in [1] allows to obtain solutions of these test problems in an analytical form that simplifies the analysis of the involved constants as well as their choice to a great extent.

In addition to the results of the previous publications [6,7], the significant refinement for the degree of kinetic energy attenuation without acceleration present is given alongside with consideration of the solution for a thin layer and its application for choosing the $k\epsilon$ -model constants.

II. Statement of the problem. Approximate equations.

The $k\epsilon$ -model equations can be obtained from hydrodynamics equations by substitution of $\rho = \bar{\rho} + \rho'$, $u = \bar{u} + u'$, $p = \bar{p} + p'$, and the by appropriate averaging with dropping of the third correlations and products of the second ones. According to [3,4], the final equations for average values will have the form:

$$\frac{\partial \rho}{\partial t} = \frac{\partial}{\partial x} \left[D_\epsilon \frac{\partial \rho}{\partial x} \right], \quad (1)$$

$$\rho \frac{dk}{dt} + \rho \epsilon_t = D_\epsilon g \frac{\partial \rho}{\partial x} + \alpha_\epsilon \frac{\partial}{\partial x} \left[\rho D_\epsilon \frac{\partial k}{\partial x} \right] + \frac{2}{3} k \frac{d\rho}{dt}, \quad (2)$$

$$\rho \frac{d\epsilon_t}{dt} + c_{\epsilon 2} \frac{\epsilon_t^2}{k} = c_\mu c_{\epsilon 1} k g \frac{\partial \rho}{\partial x} + \alpha_{\epsilon \epsilon} \frac{\partial}{\partial x} \left[\rho D_\epsilon \frac{\partial \epsilon_t}{\partial x} \right] + \frac{4}{3} \epsilon_t \frac{d\rho}{dt}, \quad (3)$$

Here

$$D_\varepsilon = c_\mu k^2 / \varepsilon_t, \tag{4}$$

$$\frac{d}{dt} = \frac{\partial}{\partial t} - D_\varepsilon \frac{\partial \ln \rho}{\partial x} \frac{\partial}{\partial x}.$$

Mixture density $\bar{\rho}$ is substituted by ρ , k - kinetic energy of turbulence, ε_t - rate of kinetic energy dissipation, c_μ , $c_{\varepsilon 1}$, $c_{\varepsilon 2}$, $\alpha_{\varepsilon 8}$, α_g - constants of the model, g - acceleration.

The analysis of stability on interfaces leads to the instability condition

$$g \frac{\partial \rho}{\partial x} > 0. \text{ Otherwise, the interface is stable and the}$$

generation term - the first one in right sides of Eqs. (2) and (3) - is assumed to be equal to zero.

Three problems will be considered below, viz:

- 1) $g=g_0>0$ - constant value; at $t=0: \rho=\rho_1^0$ at $x<0$; $\rho=\rho_2^0$ at $x>0$, $\rho_1^0>\rho_2^0$, $k(x,0)=\varepsilon_t(x,0)=0$.
- 2) g - Dirac function; at $t=0$:
 $k(x,0)=k_0$ at $|x|\leq L_0/2$, $\varepsilon_t(x,0)=\varepsilon_0$ at $|x|\leq L_0/2$, $\rho=\rho_1^0$ at $x<L_0/2$,
 $\rho=\rho_2^0$ at $x>L_0/2$.
 $x=\pm\infty$: $k=0$.
- 3) $g=g_0$, $\rho=\rho_1^0$ at $0\leq x\leq L_0$; $\rho=\rho_2^0$ at $x>L_0$; $x=0$: $\partial k/\partial x=0$; $\partial \varepsilon_t/\partial x=0$;
 $x=+\infty$: $k=\varepsilon_t=0$.

The first problem has a self-similar solution. For the k -model it is constructed in [8]. The mixing zone width is developed in time according to the square law.

The solution of the second problem in the limit at $L/L_0 \gg 1$ is evolving into the self-similar one, obtained for k -equations in [9]. The law of mixing in time is a power law with the power $B<1$ determined via the Atwood number

$$A = \frac{\rho_1^0 - \rho_2^0}{\rho_1^0 + \rho_2^0}$$

and the constants of the model.

The third problem is not a self-similar one but at $L/L_0 \gg 1$ it is evolving into the self-similar mode. The law of width evolution in time is linear. For the k-model the approximate solution has been constructed in [2].

Substantial simplifications in the solution of the problems above-formulated are obtained if in the turbulent mixing zone kinetic energy k and intensity ε_t are assumed to be independent of space coordinates. At it is easy to note, in this case the coefficient D_ε is dependent only on time, and the equation for density is reduced to the diffusion equation with a constant coefficient. Solutions for these three problems can be expressed in an analytical form via the probability integral Φ

$$\Phi(\eta) = \frac{2}{\sqrt{\pi}} \int_0^\eta e^{-z^2} dz,$$

where $\eta = x/(2\sqrt{\tau})$. Further, all difficulties in obtaining the solution are reduced to derivation of the relation between τ and L . For this purpose Eq. (2) and (3) are used, their approximate analogue was obtained while assuming that in the mixing zone

$$\frac{\partial k}{\partial x} = \frac{\partial \varepsilon_t}{\partial x} = 0.$$

Due to the fact that the solution for the mixture density ρ did not take into account the front determining the mixing zone, it is necessary to introduce the mixing zone width after its integral evaluation on the basis of the law of conservation of mixed mass. For this purpose we introduce the non-dimensional density δ for the problems 1 and 2:

$$\delta = (\rho - \rho_2^0) / (\rho_1^0 - \rho_2^0) \quad (7)$$

and the constants of the model.

The third problem is not a self-similar one but at $L/L_0 \gg 1$ it is evolving into the self-similar mode. The law of width evolution in time is linear. For the k-model the approximate solution has been constructed in [2].

Substantial simplifications in the solution of the problems above-formulated are obtained if in the turbulent mixing zone kinetic energy k and intensity ε_t are assumed to be independent of space coordinates. At it is easy to note, in this case the coefficient D_ε is dependent only on time, and the equation for density is reduced to the diffusion equation with a constant coefficient. Solutions for these three problems can be expressed in an analytical form via the probability integral Φ

$$\Phi(\eta) = \frac{2}{\sqrt{\pi}} \int_0^\eta e^{-z^2} dz,$$

where $\eta = x/(2\sqrt{\tau})$. Further, all difficulties in obtaining the solution are reduced to derivation of the relation between τ and L . For this purpose Eq. (2) and (3) are used, their approximate analogue was obtained while assuming that in the mixing zone

$$\frac{\partial k}{\partial x} = \frac{\partial \varepsilon_t}{\partial x} = 0.$$

Due to the fact that the solution for the mixture density ρ did not take into account the front determining the mixing zone, it is necessary to introduce the mixing zone width after its integral evaluation on the basis of the law of conservation of mixed mass. For this purpose we introduce the non-dimensional density δ for the problems 1 and 2:

$$\delta = (\rho - \rho_2^0) / (\rho_1^0 - \rho_2^0) \tag{7}$$

and for the problem 3

$$\delta = (\rho - \rho_2^0) / [\rho(0, \tau) - \rho_2^0], \quad (8)$$

where $\rho(0, \tau)$ - mixture density on the boundary of the region $x=0$. Then we shall determine the mixing front coordinate η_m by the following way:

$$\int_0^\infty \delta d\eta = \eta_m / 2. \quad (9)$$

Now we shall calculate η_m . For this we shall write down solutions for the mixture density ρ in the case of the problems 1 and 2:

$$\rho = \frac{\rho_1^0 + \rho_2^0}{2} + \frac{\rho_1^0 - \rho_2^0}{2} \Phi(\eta) \quad (10)$$

and for the problem 3:

$$\rho = \rho_2^0 + \frac{1}{2} (\rho_1^0 - \rho_2^0) [\Phi(\eta) - \Phi(\eta - L_0 / \sqrt{\tau})] \quad (11)$$

By substituting (10) and (11) into (7) and (8) we shall calculate the integral in the left side of the equality (9). We obtain that in the case of the problems 1 and 2

$$\eta_1 = 2 / \sqrt{\pi},$$

and for the problem 3

$$\eta_2 = \sqrt{\pi}.$$

After determination of the mixing front we shall obtain approximate equations for \bar{K} and \bar{E}_+ . For the problem 1 and 2:

$$\frac{dk}{dL^2} - P_0 \frac{k}{L^2} + \frac{\bar{\varepsilon}_t^2}{16\eta_1^2 c_\mu \bar{k}^2} = \frac{\Phi(\eta_1)gA}{8\eta_1^2 L}; \tag{12}$$

$$\frac{d\bar{\varepsilon}_t}{dL^2} - P_2 \frac{\bar{\varepsilon}_t}{L^2} + \frac{c_{\varepsilon 2} \bar{\varepsilon}_t^3}{16\eta_1^2 c_\mu \bar{k}^3} = \frac{\Phi(\eta_1)c_{\varepsilon 1}gA\bar{\varepsilon}_t}{8\eta_1^2 \bar{k}L}; \tag{13}$$

$$\frac{dL^2}{dt} = 16\eta_1^2 c_\mu \frac{\bar{k}^2}{\bar{\varepsilon}_t}; \tag{14}$$

where

$$P_0 = -0.5 - \Phi(\sqrt{2} \eta_1)A^2/6\sqrt{2},$$

$$P_2 = -0.5 - \Phi(\sqrt{2} \eta_1)A^2/3\sqrt{2}.$$

For the problem 3

$$\frac{d(\bar{k}L)}{dL} + \frac{\varepsilon_t^2 L^2}{2c_\mu \eta_2^2 \bar{k}^2} = gR_0, \tag{15}$$

$$\frac{d(\bar{\varepsilon}_t L)}{dL} + \frac{c_{\varepsilon 2} \bar{\varepsilon}_t^3}{2c_\mu \eta_2^2 \bar{k}^3} L^2 = \frac{c_{\varepsilon 1} \bar{\varepsilon}_t}{\bar{k}} gR_0, \tag{16}$$

$$\frac{dL}{dt} = 2c_\mu \frac{\bar{k}^2 \eta_2^2}{\bar{\varepsilon}_t L}, \tag{17}$$

where

$$R_0 = \frac{(\rho_1^0 - \rho_2^0)}{\rho_2^0 \eta_2^2} \left[1 - e^{-\eta_2^2} \right].$$

3. Problem 1: two fluids, acceleration is constant.

The set of equations (12)-(14) is integrated if acceleration is a constant value $g=g_0$. The solution is of the form:

$$\bar{k} = \frac{3\Phi(\eta_1)(c_{\epsilon 1} - c_{\epsilon 2})A\Gamma g_0}{2\eta_1^2 \left[9 - 12c_{\epsilon 2} + \sqrt{2}\Phi(\sqrt{2}\eta_1)A^2(2 - c_{\epsilon 2}) \right]}, \quad (18)$$

$$\bar{\epsilon}_t^2 = 4\eta_1^2 c_\mu \frac{9 - 12c_{\epsilon 1} + \sqrt{2}\Phi(\sqrt{2}\eta_1)A^2(2 - c_{\epsilon 1})}{3(c_{\epsilon 1} - c_{\epsilon 2})} \frac{\bar{k}^3}{L^2}, \quad (19)$$

$$L = \frac{36c_\mu \Phi(\eta_1)(c_{\epsilon 1} - c_{\epsilon 2})g_0 A t^2}{2 \prod_{i=1,2} \left[9 - 12c_{\epsilon i} + \sqrt{2}\Phi(\sqrt{2}\eta_i)A^2(2 - c_{\epsilon i}) \right]}, \quad (20)$$

where the symbol Π - product.

4. Problem 2: two fluids, acceleration is Dirac function.

The solution of this problem can be obtained if acceleration is assumed to be a step function being constant at $t \leq t_0$ and the zero one at $t > t_0$. Then, by limiting transition $\lim_{t_0 \rightarrow 0} g_0 t_0 = U_0$ one can obtain the solution sought for. It appears [7,10] that in this case the solution is essentially dependent on the initial roughness L_0 which ultimately determines a certain non-dimensional parameter β

$$\beta = \frac{U_0 t_0}{L_0}, \quad (21)$$

which is equivalent to the known Richardson number. The solution is of the form:

$$\bar{K} = \bar{K}_1(\beta) \left(\frac{L_0}{L} \right)^{2B_2} \quad (22)$$

$$\bar{\varepsilon}_t^2 = 4\eta_1^2 c_\mu \frac{18 - \sqrt{2} \Phi(\sqrt{2} \eta_1) A^2}{3(2c_{\varepsilon 2} - 3)} \frac{\bar{K}^3}{L^2}, \quad (23)$$

$$L = L_0 \left[1 + \frac{4}{L_0 B} \sqrt{\frac{3c_\mu \bar{K}_1(\beta) \eta_1 (2c_{\varepsilon 2} - 3)}{18 - \sqrt{2} \Phi(\sqrt{2} \eta_1) A^2}} t \right]^B \quad (24)$$

$$B = \frac{\frac{2}{3} c_{\varepsilon 2}^{-1}}{c_{\varepsilon 2}^{-1} + \frac{\Phi}{\sqrt{2}} (\sqrt{2} \eta_1) A^2 (c_{\varepsilon 2} - 2)} \quad (25)$$

The constructed solution must be corrected by means of making more precise the expression for the generation term. In Eqs (12), (13) it is equal to zero. However, the mixing layer being formed leads to the motion of the mixture with velocity u :

$$u = -D_\varepsilon \frac{\partial \ln \rho}{\partial x}.$$

This motion will produce an additional acceleration

$$\Delta g_0 = \frac{du}{dt},$$

which must be taken into account. In order to calculate it we find the average value of the velocity \bar{u} over the mixing zone

$$\bar{u} = - \int_{|x| \leq L/2} D_\varepsilon \frac{\partial \ln \rho}{\partial x} \rho dx / \int_{|x| \leq L/2} \rho dx = -2c_\mu \frac{\bar{k}^2}{\bar{\varepsilon}_t L} \Phi(\eta_1) A.$$

The averaged acceleration value is of the form:

$$\Delta \bar{g}_0 = -8A\Phi(\eta_1)\eta_1^2 c_\mu^2 \frac{d}{dL} \left[\frac{\bar{k}^4}{\bar{\varepsilon}_t^2 L_2} \right].$$

This additional acceleration will change the power B. For its calculation it is necessary to perform the following operations. We must solve the quadratic equation relative to x_0 :

$$x_0^2 \frac{2}{3} c_\mu^2 \Phi^2(\eta_1) A^2 \left[c_{\varepsilon 1} \left(1 + \frac{2\Phi(\sqrt{2} \eta_1) A^2}{3\sqrt{2}} \right) - \frac{2}{3} \Phi(\sqrt{2} \eta_1) A^2 \right] +$$

$$+ x_0 \left[0.5 - \frac{\Phi(\sqrt{2} \eta_1) A^2}{18\sqrt{2}} + \frac{c_\mu \Phi^2(\eta_1) A^2}{12\eta_1^2} (c_{\varepsilon 1} - c_{\varepsilon 2}) \right] + \frac{\left[1 - \frac{2}{3} c_{\varepsilon 2} \right]}{16\eta_1^2 c_\mu} = 0.$$

Then the corrected value of the power B is found:

$$B_y = \frac{\left[1 + \frac{4}{3} c_{\varepsilon 1}^2 c_\mu^2 \Phi^2(\eta_1) A^2 x_0 \right] 24\eta_1^2 c_\mu x_0}{\left[1 + \frac{4}{3} c_{\varepsilon 1}^2 \Phi^2(\eta_1) A^2 x_0 + \frac{\sqrt{2}}{9} \Phi(\sqrt{2} \eta_1) A^2 \right] 24\eta_1^2 c_\mu x_0 + c_{\varepsilon 2}} \quad (27)$$

The expression for the power is rather cumbersome. If the power B was previously determined via the constant $c_{\varepsilon 2}$ and the Atwood number A, here other model constants c_ε , and c_μ have been included. However, the corrected value agrees better with the exact solution in a full substitution without the above-made assumptions. At the limiting values of the Atwood number equal to 0 and 1 we have:

$$B_y(A=0) = \frac{2}{7} ; \quad B_y(A=1) = 0.36 .$$

Here the following constants from [8] were used.

$$c_\mu = 3.505; \quad c_{\varepsilon_1} = 1.43; \quad c_{\varepsilon_2} = 1.852; \quad \Phi(\eta_1) = 0.89; \quad \Phi(\sqrt{2} \eta_1) = 0.98.$$

Problem 3. Thin layer mixing

Eqs. (15)-(17) have an accurate solution

$$\bar{K}_O = gR_O \left[1 - \frac{c_{\varepsilon_1}}{c_{\varepsilon_2}} \right] , \tag{28}$$

$$(\bar{\varepsilon}_t L)^2 = 2c_\mu \eta_2^2 g^3 R_O^3 \frac{c_{\varepsilon_1}}{c_{\varepsilon_2}} \left[1 - \frac{c_{\varepsilon_1}}{c_{\varepsilon_2}} \right]^2 , \tag{29}$$

$$L = L_O + \sqrt{\frac{2c_\mu c_{\varepsilon_2}}{c_{\varepsilon_1}}} \sqrt{1 - e^{-\eta_2^2}} \left[1 - \frac{c_{\varepsilon_1}}{c_{\varepsilon_2}} \right] \sqrt{\frac{(\rho_1^O - \rho_2^O)L_O g}{\rho_2^O}} t . \tag{30}$$

This solution is approximately in accordance with the asymptotic one to which the problem 3 solution of the input set of equations (1-3) tends.

Conclusion

The obtained analytical solutions of the *ke* -equations for three problems can be used for calculation of the constants c_μ , c_{ε_1} and c_{ε_2} . The first and the third problems give expressions for the corresponding slopes $\frac{dL}{2ds}$ and $\frac{dL}{d\sqrt{2}s}$ ($s = g_0 t^2/2$), but the second problem - for the power B_y characterizing the change of the mixing zone width in time. The set-up of the appropriate experiments and processing of their results according to formulae (20), (27) and (30) determine the set of the constants c_μ , c_ε and c_{ε_2} .

References

1. Neuvazhayev.V.E. Dokl. Akad. Nauk SSSR, v. 222, N5, (1975), 1053.
2. Neuvazhayev.V.E. Prikl. Mekhanika i Tekhn. Fizika, 5(1983), 81.
3. Neuvazhayev.V.E., Yakovlev V.G. Voprosy Atom. Nauki i Tekhniki, Ser. Theor. and Appl Physics, 1 (1986), 28.
4. Neuvazhayev.V.E., Yakovlev V.G. Proceedings of the Soviet Union - Japan Symposium on Computational Fluid Dynamics, Khabarovsk, Ed. P.I. Chushkin, V.P.Korobeinikov, 2 (1989), 76.
5. G.I.Taylor, Proc. R.Soc. London, Ser. A 201 (1950), 192.
6. Neuvazhayev.V.E. Development of turbulent mixing induced by Richtmyer-Meshkov instabilities, Preprint N2, VNIITF (1991).
7. Neuvazhayev.V.E., Matematicheskoe Modelirovanie 3,7 (1991), 10.
8. Neuvazhayev V.E., Yakovlev V.G. Voprosy Atom. Nauki i Tekhniki, Series: Methods and Programs of Numerical Solution of Problems in Mathematical Physics, 2, 16, (1984), 17.
9. Neuvazhayev V.E. Prikl. Mekhanika i Tekhn. Fizika, 2, (1988), 46.
10. Neuvazhayev V.E. Prikl. Mekhanika i Tekhn. Fizika, 1, (1992), 38.

ASYMPTOTIC BEHAVIOUR OF A THIN INTERLAYER
AFTER PASSING A SHOCK WAVE

V.E. Neuvazhayev

Institute of Technical Physics, Chelyabinsk-70, Russia

I Introduction

In technical devices interfaces can exist between matters being different in properties. A layered target used in a laser thermonuclear fusion problem is one of the examples. It is known that the interfaces can be accelerated and decelerated due to gas dynamic motion and that they can be disturbed and mixed as a result of initial roughness and Rayleigh-Taylor - and Richtmyer-Meshkov instabilities.

On the basis of K and KE models for turbulent mixing, the theoretical study of the problem with one shock wave was performed in the author's work (1991) where the kinetic turbulent energy transferred to a rough boundary by a shock wave was computed. There are also some experimental works [S.O. Zaitzev et al.(1985), L. Houas et al.(1991)] in which the law of the contact boundary mixing after passing a shock wave has been derived.

In the given work the behaviour of a thin interlayer between layers is considered. A thin layer of an arbitrary density is supposed to acquire the turbulent kinetic energy

introduced by the passing shock wave. Other reasons for forming an interfacial layer can also be, for example, removing of the interlayer between gases. After passing a shock wave the interfacial layer can achieve accelerated or decelerated motion.

Some characteristic situations can arise depending on densities of an admixture and media around it. If the admixture density has an intermediate value then either an intensive mixing according to the square law in time (a heavy matter from above) or a weak mixing with the power $2/7 : 1/3$ (a light matter from above) will take place depending on the locations of light and heavy media. The admixture will spread up and down approximately according to the same law.

If the admixture is heavier than the surrounding media then, when the heavy medium is on the top, mixing takes place into the side of the heavy matter with constant velocity. An analogous action takes place if the admixture is lighter than the surrounding media. Then mixing takes place into the side of the light matter and with constant velocity as well, i.e. according to the linear law in time.

Results are obtained on the basis of K and KE models applications. The formulated problem is not a self-similar one, however, the solution assumes the self-similar character at rather large times when $L \gg L_0$ (L_0 - initial thickness of the interlayer). The approximate approach suggested

previously by the author (1975) is applied which allows to build solution in the form of analytical formulae. This helps to establish general regularities and, above all, to determine the connection with empirical constants.

II. Semiempirical K and KE models

In order to describe an arising turbulent mixing two models are applied. One model is based on the balance equation for the kinetic energy of turbulence $v^2/2$; we call it as K-model. The other KE-model comprises two equations ; in addition to the equation for the kinetic energy of the turbulence, equation for its intensity ϵ_t is formulated. These equations are obtained according to the law of conservation for the incompressible fluid by substitution of $\rho = \bar{\rho} + \rho'$; $u = \bar{u} + u'$; $p = \bar{p} + p'$ and the corresponding averaging with dropping of the third correlations and products of the second ones. From the continuity equation we have:

$$\frac{\partial \bar{\rho}}{\partial t} + \frac{\partial}{\partial x} \rho \bar{u} = 0$$

$$\bar{u} = \frac{\overline{\rho' u'}}{\bar{\rho}} .$$

Equation for the kinetic energy of turbulence follows from the continuity equation and the equation of pulse conservation (Neuvazhaev, Yakovlev (1984)):

$$\frac{1}{2} \left[\frac{\partial(\bar{\rho}v^2)}{\partial t} + \tilde{u} \frac{\partial \bar{\rho}v^2}{\partial x} \right] = - \frac{u\bar{\rho}v^3}{L} + \bar{\rho}g \frac{\rho'u'}{\bar{\rho}} + \left[\frac{5}{6} \right] \bar{\rho}v^2 \frac{\partial \tilde{u}}{\partial x}$$

By applying Prandtl-Kolmogorov's hypothesis to equations

$$\overline{\rho'u'} = - D \frac{\partial \bar{\rho}}{\partial x} ,$$

$$D = \alpha L v , \tag{1}$$

we have

$$\frac{\partial \rho}{\partial t} = \frac{\partial}{\partial x} \left[D \frac{\partial \rho}{\partial x} \right] , \tag{2}$$

$$\begin{aligned} \frac{\partial \rho v^2}{2 \partial t} + \frac{u_0 D v^2}{\alpha^2 L^2} &= \underline{\underline{Dg \frac{\partial \rho}{\partial x}}} + \beta \frac{\partial}{\partial x} \rho D \frac{\partial v^2}{\partial x} + \\ &+ \frac{D}{2} \frac{\partial \ln \rho}{\partial x} \frac{\partial \rho v^2}{\partial x} + \frac{5}{6} \rho v^2 \left[\frac{\partial \ln \rho}{\partial t} - D \frac{\partial \ln \rho}{\partial x} \right] . \end{aligned} \tag{3}$$

Here ρ - mixture density, $\bar{\rho}$ is substituted by ρ , L - effective width of the mixing region which is determined below; α , v , β - constants of the model.

The first term in the right-hand side of Eq. (3) generates turbulence if $g \frac{\partial \rho}{\partial x} > 0$. The second (diffusion) term with the coefficient β is introduced for describing the spatial spreading of turbulence. The second term with the coefficient v in the left-hand side of Eq. (3) results in turbulent energy dissipation. The form of its recording is

dictated by dimensional considerations.

As opposed to the K - model, the dissipative term is announced to be an unknown function in the KE-model, and the balance equation is formed for this function. Ultimately, instead of one equation (3) we shall have two equations for $k = \frac{v^2}{2}$ and ε_t (Neuvazhayev and Yakovlev (1988)):

$$\rho \frac{dk}{dt} + \rho \varepsilon_t = D_{\varepsilon} g \frac{\partial \rho}{\partial x} + \alpha_B \frac{\partial}{\partial x} \left[\rho D_{\varepsilon} \right] \frac{\partial k}{\partial x} + \frac{2}{3} k \frac{d\rho}{dt} \quad (4)$$

$$\rho \frac{d\varepsilon_t}{dt} + C_{\varepsilon 2} \frac{\varepsilon_t}{K} = C_{\mu} C_{\varepsilon 1} k g \frac{\partial \rho}{\partial x} + \alpha_{\varepsilon B} \left[\rho D_{\varepsilon} \right] \frac{\partial \varepsilon_t}{\partial x} + \frac{4}{3} \varepsilon_t \frac{d\rho}{dt} \quad (5)$$

Here $D_{\varepsilon} = C_{\mu} k^2 / \varepsilon_t$, (6)

$$\frac{d}{dt} = \frac{\partial}{\partial t} - D_{\varepsilon} \frac{\partial \ln \rho}{\partial x} \frac{\partial}{\partial x} , \quad (7)$$

C_{μ} , $C_{\varepsilon 1}$, $C_{\varepsilon 2}$, $\alpha_{\varepsilon B}$, α_B - constants of the model. A new function ε_t determines the dissipation velocity of the kinetic energy of turbulence. The mixing region width does not enter the KE- model in an explicit form and by this fact it is different from the K- model and allows to describe the mixing of arbitrary number of matters.

III. General statement. Initial and boundary conditions.

For two sets of equations (1) - (3) and (1), (4) - (5)

the problem is posed with the following initial data. When $t = 0$:

$$v(0,x) = v^0(x); \quad \rho(0,x) = \rho^0(x); \quad 0 \leq x \leq L_0 \quad (8)$$

We assume that the mixture is found between two fluids having densities ρ_1^0 and ρ_2^0 with $\rho_1^0 > \rho_2^0$.

Acceleration g is constant : $g = g_0 > 0$. In general case the mixture density in a layer $0 \leq x \leq L_0$ may be not connected with matters surrounding the mixture. Then such situations are possible when the mixture density ρ_0 is more than the densities of the surrounding media, is less than the latter or is found in the interval:

- a) $\rho^0 > \rho_1^0$ and ρ_2^0 ;
 - b) $\rho^0 < \rho_1^0$ and ρ_2^0 ;
 - c) $\rho_1^0 > \rho^0 > \rho_2^0$;
 - d) $\rho_2^0 < \rho^0 < \rho_1^0$.
- (9)

In the cases a) and b) the substitution of the light fluid by the heavy one meets new cases a') and b') [see Fig. 1.1.

The analysis of stability at the interface leads to the condition of instability:

$$g \frac{\partial \rho}{\partial x} > 0 .$$

Otherwise the interface is stable and the generation term is obtained to be equal to zero in K and KE models. However, availability of the diffusion coefficient $D(D_g)$ not equal to zero leads to the fact that under conditions when the

interface is stable, the turbulent flow is formed through it. This takes place in the case c) when the motion of the mixture arises under conditions of a stable stratification. This problem was studied in the author's work (1988), when the law of the mixing region change in time with the power B_0 depending on the constants α and ν was omitted. When both interfaces are unstable the case d) evolves asymptotically into the known self-similar solution for two incompressible fluids [Belen'ky and Fradkin (1976), Neuvazhayev and Yakovlev (1984)].

The mixing region of the admixture is then developing in time according to the square law.

The cases a) and b) lead to the statement of the problem when one interface with the admixture is stable but the other one is unstable. The instability of one of the interfaces depending on the position of the heavy matter ρ_1^0 and the light one ρ_2^0 may take place only up to some moment t_0 (cases a') and b') in Fig.1.). Starting from t_0 both interfaces become unstable that will be equivalent to the case d).

We shall assume the values v^0 and ρ^0 to be constant in the interval $0 \leq x \leq L_0$. We consider the solution of Eq.(1)-(3) and (4), (5) with initial conditions (8) under rather large times which can be connected with the mixing region width L . Therefore, we determine the solution

when $\frac{L}{L_0} \gg 1$.

IV. Limiting solutions in the cases a) and b).

A layer of width L_0 is placed into the lighter medium in the case a) and into the heavier one in the case b). One of the boundaries appears to be always stable and the conditions of the flow absence are specified for it. The more exact statement of the problem is obtained with the turbulent flow through the stable boundary as well, but here it is not considered. The basic problem is to determine the mixture profile under large times and the law of its continuous density profile in time.

A. K - model. Approximation $\partial v / \partial x = 0$.

Appreciable simplifications in solving the problem are obtained if in the turbulent mixing region the turbulent velocity v is assumed to be independent of the spatial coordinate. Such an approach has already been applied by the author previously (1975). It should be noted that in this case the coefficient D is only dependent on time, and equation for the mixture density is reduced to the diffusion equation with the constant coefficient by the substitution of the variable

$$\delta\tau = D\delta t \quad (10)$$

The exact solution of Eq.(2) for the mixture density having

the initial width L_0 is of the form:

$$\rho = \rho_1^0 + \frac{1}{2} (\rho^0 - \rho_1^0) \left[\Phi \left[\frac{x}{2\sqrt{\tau}} \right] - \Phi \left[\frac{x - 2L_0}{2\sqrt{\tau}} \right] \right], \quad (11)$$

where $\Phi(\eta) = \frac{2}{\sqrt{\pi}} \int e^{-z^2} dz$ - probability integral.

Here it is assumed that the turbulized layer of the initial density ρ^0 is surrounded by the light matter with density ρ_1^0 . According to Fig.1 a) the mixing will spread downwards; under $x = L_0$ the hard wall condition is specified .

For closing these equations it is necessary to determine the method for calculating the mixing region width, since from (11) it follows that the density profile has no front due to the linearity of initial diffusion equation. There are different ways for determining the effective width L . We dwell on the integral one. For this we introduce the non-dimensional density δ :

$$\delta = \frac{\rho - \rho_1^0}{\rho(L_0, \tau) - \rho_1^0} = \frac{\Phi \left[\frac{x}{2\sqrt{\tau}} \right] - \Phi \left[\frac{x - 2L_0}{2\sqrt{\tau}} \right]}{2\Phi \left[\frac{L_0}{2\sqrt{\tau}} \right]} \quad (12)$$

The value of δ is monotonically changed from 1 under $x = L_0$ to under $x = -\infty$. We introduce a new spatial variable η :

$$\eta = \frac{x - L_0}{\sqrt{4\tau}} .$$

We determine the mixing front from the equality:

$$\int_{-\infty}^{\infty} \delta d\eta = - \frac{1}{2} \eta_m \quad (13)$$

When times are large the function δ can be approximately substituted by the exponent:

$$\delta \simeq e^{-\eta^2} \quad (14)$$

It is obtained if the approximate representation of the function Φ is used in the vicinity of the points $x = L_0$ and $|x| > L_0$. By substitution of (14) into (13) we obtain

$$\eta_m = -\sqrt{\pi} ; \quad L_m - L_0 = -2\eta_m\sqrt{\tau} \quad (15)$$

Knowing the dependence of the mixing region width on τ we return to the balance equation for the kinetic energy (3) but preliminarily we substitute t by τ on the basis of (10):

$$\begin{aligned} \frac{\partial \rho v^2}{2\partial \tau} + \frac{\nu \rho v^2}{\alpha^2 L_m^2} &= g \frac{\partial \rho}{\partial x} + \beta \frac{\partial}{\partial x} \left[\rho \frac{\partial v^2}{\partial x} \right] + \\ &+ \frac{1}{2} \frac{\partial \rho}{\partial x} \frac{\partial v^2}{\partial x} - \frac{1}{3} \rho v^2 \left[\frac{\partial \ln \rho}{\partial x} \right]^2 + \frac{5}{6} v^2 \frac{\partial \rho}{\partial \tau} \end{aligned} \quad (16a)$$

By averaging the last equation over the mixing region, we integrate it for the variable x within the interval

$[-L_m, L_0]$ and substitute $\int_{-L_m}^{L_0} v^2 \rho dx = v_m^2$, where $m = \int_{-L_m}^{L_0} \rho dx$.

In this case for the mixture density we use the solution of (11) or its approximate representation in the form:

$$\rho \sim \rho_1^0 + (\rho^0 - \rho_1^0) \frac{L_0}{\sqrt{\pi\tau}} \rho^{-4\sqrt{\tau}} \frac{L_0^2}{\tau}$$

By omitting the intermediate calculation we obtain differential equation for v^2 :

$$\frac{\partial v^2}{\partial \tau} + \frac{v^2}{\tau} \left[\frac{1}{2} + \frac{v}{2\alpha^2 \eta_m^2} \right] = \frac{gR_0}{\tau} \quad (16b)$$

$$R_0 = \frac{(\rho^0 - \rho_1^0) L_0}{\rho_1^0 \eta_m^0} \left[1 - e^{-\eta_m^2} \right]$$

The constant velocity \bar{v}_∞ will be determined by solving Eq.(16)

$$\bar{v}_\infty^2 = \frac{gR_0}{\left[\frac{1}{2} + \frac{v}{2\alpha^2 \eta_m^2} \right]} = \frac{2gR_0 \alpha^2 \eta_m^2}{v + \alpha^2 \eta_m^2} \quad (17)$$

Eq.(16a) is not applicable in the vicinity of $\tau = 0$. Therefore, in order to satisfy the initial conditions when $\tau = 0$: $\bar{v}^2 = (v^0)^2$ one should return to the full statement of the problem. However, it might not be done as it is evident that whatever the behaviour of the function may be in

vicinity of function \bar{v} will tend to the constant value determined by formula (17). This tendency will be observed either from above or from below depending on the initial velocity v^0 .

By returning to Eq. (10) and (15) we obtain the limiting inclination established when $\left| \frac{L_m}{L_0} \right| \gg 1$:

$$\frac{dL_m}{dt} = 2\alpha\eta_m^2 \bar{v}_\infty = \frac{2\alpha^2 \eta_m^3 \sqrt{2gR_0}}{\sqrt{\nu + \alpha^2 \eta_m^2}}$$

or

$$\frac{dL_m}{d\sqrt{2s}} = \alpha^2 \eta_m^2 2^{3/2} \sqrt{\frac{1 - e^{-\eta_m^2}}{\nu + \alpha^2 \eta_m^2}} \sqrt{\frac{(\rho^0 - \rho_1^0)L_0}{\rho_1^0}} \quad , \quad (18)$$

where $s = gt^2/2$.

The other case b) ($\rho_0 < \rho_2^0 < \rho_1^0$) may be analogously considered. According to Fig.1 b) the mixing front of the lighter mixture spreads upwards from the stable interface being found in the point $x = 0$. For large times the profile of non-dimensional density is described by formula (14), as it has been previously done, whereas the mixing velocity is presented by formula similar to (16a) but the difference $\rho^0 - \rho_1^0$ under root should be substituted by $\rho_2^0 - \rho^0$ and in the denominator ρ_1^0 should be substituted by ρ_2^0 .

$$\frac{dL_m}{d\sqrt{2s}} = \alpha^2 \eta_m^2 2^{3/2} \sqrt{\frac{1 - e^{-\eta_m^2}}{v + \alpha^2 \eta_m^2}} \sqrt{\frac{(\rho_2^0 - \rho^0)L_0}{\rho_2^0}}$$

If the empirical constants α and v have been already chosen then we have an additional verification of their choice correctness.

B. KE - model. Approximation $\frac{\partial k}{\partial x} = \frac{\partial \varepsilon_t}{\partial x} = 0$

Solution will be present by the following relations:

$$k = gR_0 \left[1 - \frac{c_{\varepsilon 1}}{c_{\varepsilon 2}} \right] \tag{19}$$

$$(\varepsilon_t L_m)^2 = 2c_{\mu} \eta_{\mu}^2 g^3 B_0 \frac{c_{\varepsilon 1}}{c_{\varepsilon 2}} \left[1 - \frac{c_{\varepsilon 1}}{c_{\varepsilon 2}} \right]^2 \tag{20}$$

The kinetic energy is, as previously, constant but intensity is decreasing as the inverse value of width . Formula for the limiting inclination is

$$\frac{dL_m}{d\sqrt{2s}} = \sqrt{\frac{2c_{\mu} c_{\varepsilon 2}}{c_{\varepsilon 1}}} \sqrt{1 - e^{-\eta_m^2}} \left[1 - \frac{c_{\varepsilon 1}}{\varepsilon_2} \right] \sqrt{\frac{|\rho^0 - \rho_1^0| L_0}{\rho_1^0}} \tag{20a}$$

$i = 1, 2$

Modulus under the root means that formula is true in the case a) ($i = 1$) as well as in the case b) ($i = 2$).

We pay attention that here the inclination was obtained

depending on three constants c_μ , $c_{\varepsilon 1}$, $c_{\varepsilon 2}$. For their choice two tests are usually used: 1) mixing under zero acceleration; 2) mixing under constant acceleration. In the first test the constant $c_{\varepsilon 2}$ is chosen according to the condition for describing the required power in the asymptotic law for width

$$L = (t - t_0)^B$$

In the second test, by fitting c_μ or $c_{\varepsilon 1}$ one obtains the inclination

$$\frac{dL}{d2s} = f(c_{\mu 1}, c_{\varepsilon 1}) A_1$$

which is in agreement with the experimental one.

The proposed test with a thin layer allows to eliminate arbitrariness in the choice of constants c_μ and $c_{\varepsilon 1}$.

V. Conclusion

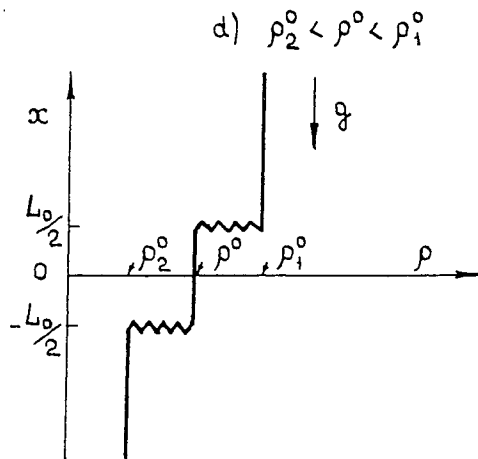
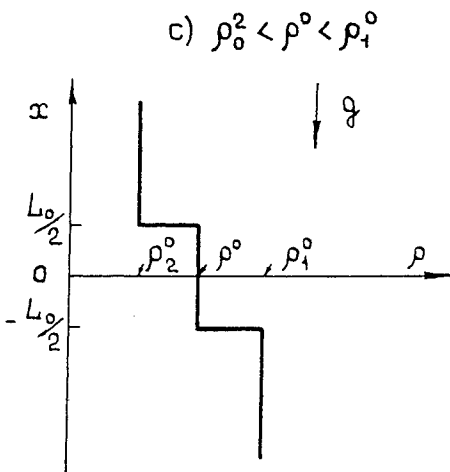
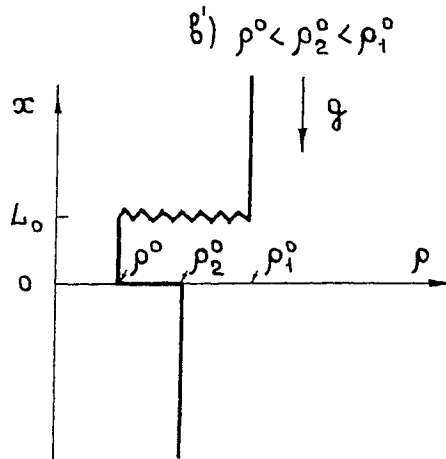
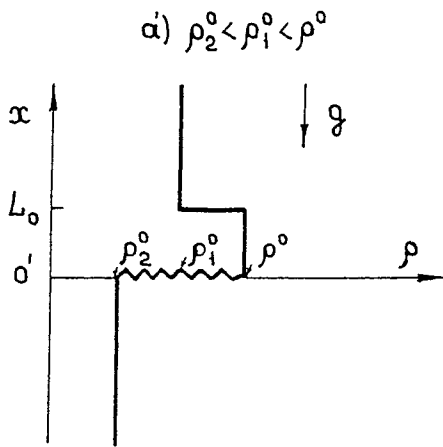
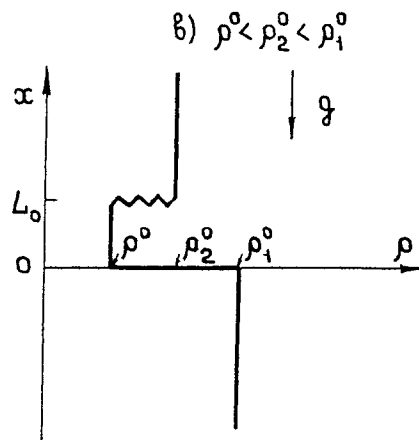
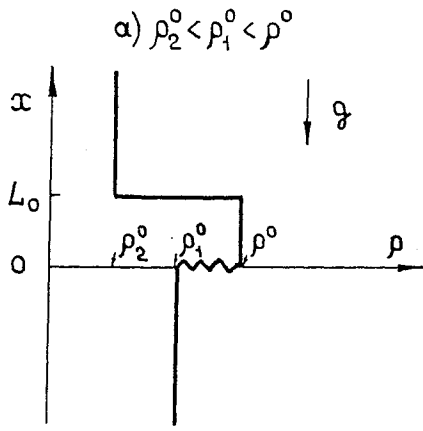
The behaviour of a thin layer turbulized initially and placed between two media of different density is considered. It is shown that three laws of the turbulent mixing zone development can be established depending on the relation between densities under constant acceleration, namely: 1) the square law when the admixture is mixed with the surrounding medium in both sides; 2) the linear law when mixing is spreading into one side; 3) the power law with the power being changed depending on the Atwood number within

the limits of $2/3 - 1/3$. In this case the mixing zone is spreading into both sides.

References

1. Andronov V.A. et al. 1976, Zhurnal Exper. i tehn. fiziki (ZHETF) v.71 N8 p. 805 -811
2. Anuchina N.N. et al. 1978, Mekhanika zhidkosti i gaza (MZHG), N8, p.157 - 160
3. Belen'kii G.Z., Fradkin E.S., 1965, Trudy fizich. inst.Ak.Nauk SSSR (FIAN) 29, 207 - 238.
4. Neuvazhayev V.E., 1975 Doklady Ak. Nauk SSSR (DAN), v.222, N5, p. 1053 - 1056.
5. Neuvazhayev V.E., 1983, Zhur. Prikl. mat. i tehn. fiziki (PMTF), issue 5, p.81 - 88.
6. Neuvazhayev V.E., 1988, PMTF, issue 2, p.(46 - 51).
7. Neuvazhayev V.E. ,1991, Matematicheskoe Modelirovanie, v.3, N7, p.10 - 28.
8. Neuvazhayev V.E.,1992, Relationship between turbulent and kinetic energy in mixed matter, PMTF, 1(191), p.38-42.
9. Neuvazhayev V.E., Yakovlev V.G.,1975, To the theory of turbulent mixing of the interface in gravitational field. PMTF, N4, p.74 - 81.
10. Neuvazhayev V.E., Yakovlev V.G.,1984,SB. Voprosy atomnoi nauki i tekhniki (VANT). Series 'Methods and Programs for Numerical solutions of the mathematical physics

- problems', 2(16),p.17-25.
11. Neuvazhayev B.E., Yakovlev., 1988, Sb.VANT, Series 'Theoretical Applied Physics', issue 1, p.28-36.
 12. Houas L., Chemouni I. and Touat A., 1991, Proc. 18th Intl Symp. on Shock waves (ed. K. Takayama) Springer-Verlag, Heidelberg.
 13. Neuvazhayev V.E. 1975 Reports of the Ac. of Sci USSR 222-5; 1053-1056.
 14. Neuvazhayev V.E. 1991. Proc.18 th Intl Symp. on Shock waves (ed. K.Takayama) Springer-Verlag, Heidelberg.
 15. Read K. 1984 Experimental investigation of turbulent mixing by Rayleigh-Taylor instability, Physica D,N12, p.45-48.
 16. Youngs D.L. 1989 Modelling of turbulent mixing by Rayleigh-Taylor instability, Physica D, N37, p.270-287.
 17. Youngs D.L. 1991 Three-dimensional numerical simulation of turbulent mixing by Rayleigh-Taylor instability, Phys. Fluids A,3,p.1312-1320.
 18. Zaitzev S.G., Lazareva E.V., Chernukha V.V. and Belyaev V.M., 1985. Intensification of mixing at the interface between media of different densities after passing a shock wave through it. DAN SSSR, 30, 579-581.



CALCULATION OF GRAVITATIONAL TURBULENT MIXING
IN NON-AUTOMODEL FLOWS

V.V.Nikiforov

All Russian Research Institute of Experimental Physics
Arsamas-16

ABSTRACT

A semi-empirical model for calculation of turbulent mixing under gravitational instability, allowing for turbulence anisotropy and non-gradient nature of mass and energy turbulent flows, and for development of turbulent mixing zone after shock-wave propagation is described in this paper. Calculation results and their comparison to experimental data are presented here.

The problem of turbulent mixing (TM) on contact boundary of media with different densities is of great interest in recent years due to ICF problems, since such mixing of thermonuclear fuel with the imploding shells' material has a significant effect on characteristics of target for thermonuclear fussion and, particularly, on neutron output.

For the first time automodel problem, concerning TM on contact boundary of two incompressible fluids of different densities in constant gravity field was presented in work / 1/. The following relation of the turbulent mixing zone (TMZ) width L_t versus deceleration way $S = \frac{1}{2} g t^2$ was obtained:

$$L_t = \alpha \frac{\delta - 1}{\delta + 1} S$$

where $\delta = \frac{\rho_2}{\rho_1} > 1$ is the density ratio of two fluids, g is the acceleration, α - is empirical constant.

However, for practical applications it not enough to solve this problem, since acceleration is rather often inconstant right up to change of sign, shock wave can propagate through TMZ in different directions. Therefore, the following works on the development of calculation methods for TMZ were aimed at the development of semi-empirical models of turbulent flows, regarding, besides the above mentioned factors, such characteristics of turbulence, occurring as a result of gravitational instability development, as turbulence anisotropy and nongradient nature of turbulent flows.

We sequentially used more sophisticated models. The first model involved one equation for turbulence energy ϵ_t with integral

definition of turbulent scale l_t : $l_t = \beta L_t$, where L_t is TMZ width, β is the empirical constant / 2 /. Gradient representation with diffusion coefficient, $D_t \simeq l_t \sqrt{\varepsilon_t}$, was used for mass and energy flows. A similar model, but with some uncertainties, is given in /3/. However, a model of integral definition of turbulence scale has a principle disadvantage, which lies in the fact, that it is not clear how to determine this scale when two or more mixing zones are joined together. To eliminate this disadvantage an equation for turbulent viscosity ν_t was added to the equation for ε_t instead of integral definition l_t / 4/. For turbulent flows, gradient representation with $D_t \simeq \nu_t$ was still used. This model is similar in concept to models of $k-\varepsilon$ type used at present.

Unfortunately such simplified models do not fit calculation of TM in sufficiently complex non-automodel flows. It is due to the fact, that semi-empirical constants involved in these models, are not in fact, constants, they are functions, depending on turbulence anisotropy and, generally speaking, on the pre-history of the flow (see below). That is why, using such models with one set of constants one fails to describe quite different TM regimes, for example, turbulent mixing under constant acceleration of interface, and further development of TMZ after acceleration removal. Besides, it should be noted, that, in the presence of significant fluctuations of density in TMZ, turbulent transfer processes under gravitational TM are essentially caused by inertial forces, that should lead to non-gradient nature of turbulent flows as compared to turbulent transfer in medium with constant density.

Taking into account all, mentioned above, we have developed a model involving equations for all second-order correlations of the interest, namely, for mean squares of the three components of fluctuating velocity $e_1 = \frac{1}{2} \langle u_1'^2 \rangle$, $e_2 = \frac{1}{2} \langle u_2'^2 \rangle$, $e_3 = \frac{1}{2} \langle u_3'^2 \rangle$, for turbulent flows of all mixture constituents $W_i = \frac{1}{\rho} \langle (\rho \mu_i)' u_i' \rangle$ (where ρ is the density, μ_i is the mass concentration i -th mixture constituent, $i = 1, n$), for energy turbulent flow $W_o = \frac{1}{\rho} \langle (\rho \varepsilon)' u_1' \rangle$ and for correlations $B_i = -\frac{1}{\rho^2} \langle \rho' (\rho \mu_i)' \rangle$, $B_o = -\frac{1}{\rho^2} \langle \rho' (\rho \varepsilon)' \rangle$ (where ε is the specific internal energy). Prime, as usual, indicates a fluctuating part of the corresponding value and $\langle \rangle$ - the mean value. We have assumed that direction of the principle one-dimensional averaged flow coincides with the direction of axis 1 (axis X). In planar and spherical geometry due to axial symmetry $e_2 = e_3$, but in cylindrical, generally speaking, it is not so. This system of equations is completed by the equation for viscous dissipation of turbulent energy $Q = \nu \langle (\partial u_i' / \partial x_k)^2 \rangle$, where

ν is the viscosity.

The complete system of equations, including gasdynamic equation for average flow has the form / 5/, / 6/ :

$$\frac{d\rho}{dt} = -\rho \cdot \text{div} \mathbf{V};$$

$$\frac{d\mathbf{V}}{dt} = -\frac{1}{\rho} \frac{\partial p}{\partial \mathbf{x}} - \frac{1}{\rho} \frac{\partial}{\partial \mathbf{x}} - 2\rho P_{11};$$

$$\frac{d\mathbf{E}}{dt} = -\frac{p}{\rho} \cdot \text{div} (\mathbf{V} - \mathbf{W}) - \frac{1}{\rho} \cdot \text{div} \rho (\mathbf{W}_0 - \mathbf{E} \cdot \mathbf{W}) + q_r + \frac{p}{e} \cdot \mathbf{Q};$$

$$\frac{dc_i}{dt} = -\frac{1}{\rho} \cdot \text{div} \rho (\mathbf{W}_i - c_i \cdot \mathbf{W});$$

$$\begin{aligned} \frac{de_1}{dt} = & \frac{\partial}{\partial \mathbf{x}} \left(3D_1 \frac{\partial e_1}{\partial \mathbf{x}} - \mathbf{W} e_1 \right) - e_1 \text{div} \mathbf{W} - 2e_1 V_{11} + \\ & + \left(1 - \frac{2}{10} \alpha k \right) f_1 W g - \gamma \left(e_1 - \frac{1}{3} e \right) - \frac{1}{3} \mathbf{Q}; \end{aligned}$$

$$\begin{aligned} \frac{de_2}{dt} = & \frac{\partial}{\partial \mathbf{x}} \left(D_2 \frac{\partial e_2}{\partial \mathbf{x}} - \mathbf{W} e_2 \right) - e_2 \text{div} \mathbf{W} - 2e_2 V_{22} + \frac{1}{10} \alpha k f_1 W g - \\ & - \gamma \left(e_2 - \frac{1}{3} e \right) - \frac{1}{3} \mathbf{Q}; \end{aligned}$$

$$\begin{aligned} \frac{de_3}{dt} = & \frac{\partial}{\partial \mathbf{x}} \left(D_3 \frac{\partial e_3}{\partial \mathbf{x}} - \mathbf{W} e_3 \right) - e_3 \text{div} \mathbf{W} - 2e_3 V_{33} + \frac{1}{10} \alpha k f_1 W g - \\ & - \gamma \left(e_3 - \frac{1}{3} e \right) - \frac{1}{3} \mathbf{Q}; \end{aligned}$$

$$\frac{dW_i}{dt} = \frac{1}{\rho} \frac{\partial}{\partial \mathbf{x}} \rho \left(2D_i \frac{\partial W_i}{\partial \mathbf{x}} - \mathbf{W} \cdot \mathbf{W}_i \right) - W_i V_{11} + 2e_1 A_i + f_1 B_i g - k_1 \frac{Q}{e} W_i;$$

$$\frac{dB_i}{dt} = \frac{1}{\rho^2} \frac{\partial}{\partial \mathbf{x}} \rho^2 \left(D_i \frac{\partial B_i}{\partial \mathbf{x}} - \mathbf{W} B_i \right) + B_i \text{div} \mathbf{W} + W A_i + W_i A - k_2 \frac{Q}{e} B_i;$$

$$i = 0, n$$

$$\begin{aligned} \frac{dQ}{dt} = & \frac{\partial}{\partial \mathbf{x}} \left(\frac{5}{3} D_1 \frac{\partial Q}{\partial \mathbf{x}} - \mathbf{W} Q \right) - Q \text{div} \mathbf{W} - Q \left[\frac{4}{3} + \beta_1 \gamma \frac{\left(e_1 - \frac{1}{3} e \right)}{e} \right] V_{11} - \\ & - Q \left[\frac{4}{3} + \beta_1 \gamma \frac{\left(e_2 - \frac{1}{3} e \right)}{e} \right] V_{22} - Q \left[\frac{4}{3} + \beta_1 \gamma \frac{\left(e_3 - \frac{1}{3} e \right)}{e} \right] V_{33} + \\ & + \frac{Q}{3e} f_1 W g + \beta_2 \left[\frac{1}{10} \alpha k f_1 W g + \gamma \frac{Q}{e} \left(e_1 - \frac{1}{3} e \right) \right] W A \frac{1+R^2}{R^2} - 2 \frac{Q^2}{ke}; \end{aligned}$$

where q_r is the heat flow due to radiation.

For short, this system of equations is given for planar case. In cylindrical and spherical geometry there appears one more series of terms while expressing corresponding divergence components of tensors of rank two and three.

In the system of equations it is defined: $e = e_1 + e_2 + e_3$;

$$\frac{d}{dt} = \frac{\partial}{\partial t} + \mathbf{V} \frac{\partial}{\partial \mathbf{x}} ; \quad \mathbf{v} = \langle u_1 \rangle + \frac{1}{\rho} \langle \rho' u_1' \rangle ; \quad c_i = \langle \mu_i \rangle + \frac{1}{\rho} \langle \rho' \mu_i' \rangle ;$$

$$E = \langle \varepsilon \rangle + \frac{1}{\rho} \langle \rho' \varepsilon' \rangle ; g = \frac{1}{\rho} \frac{\partial P}{\partial x} ; W = \sum W_i, R^2 = \sum B_i, i = 1, n;$$

V_{11}, V_{22}, V_{33} - are corresponding components of strain rates tensor.

For planar case: $V_{11} = \frac{\partial(V-W)}{\partial x}, V_{22} = V_{33} = 0 ;$

cylindrical case: $V_{11} = \frac{\partial(V-W)}{\partial r}, V_{22} = \frac{V-W}{r}, V_{33} = 0 ;$

spherical case: $V_{11} = \frac{\partial(V-W)}{\partial r}, V_{22} = V_{33} = \frac{V-W}{r} .$

$$A_i = c_i A - \frac{\partial c_i}{\partial x}, i=1, n, A = A_s + (A_t - A_s) [1 - \gamma(\phi)];$$

$$A_s = \frac{1}{\rho \lambda_1 + \frac{T}{\rho c_v}} \frac{\partial P}{\partial x} - \frac{1}{\rho} \frac{\partial \rho}{\partial x}, A_t = \frac{1}{\rho \lambda_1} \frac{\partial P}{\partial x} - \frac{\lambda_2}{\rho \lambda_1} \frac{\partial T}{\partial x} - \frac{1}{\rho} \frac{\partial \rho}{\partial x}$$

$$\lambda_1 = \frac{\partial P}{\partial \rho} \Big|_T, \lambda_2 = \frac{\partial P}{\partial \rho} \Big|_\rho, c_v = \frac{\partial E}{\partial T} \Big|_\rho, c_p = \frac{\partial E}{\partial T} \Big|_p, \lambda_3 = \frac{\partial E}{\partial \rho} \Big|_T ;$$

$$\gamma(\phi) = \frac{1}{\phi} [1 - \exp(-\phi)], \phi = \frac{\kappa_f \cdot Q}{e^2} \cdot \frac{4\sigma T^3}{\rho c_p} ;$$

κ_f - is the radiant heat conduction factor, σ is Boltzmann constant. Combination of gradients A_s corresponds to eddy adiabatic transfer of mass elements and A_t - to isothermal one.

$$A_o = EA - \frac{\partial E}{\partial x} + \rho \lambda_3 \left\{ \frac{1}{\rho \lambda_1 + \frac{T}{\rho c_p} - \lambda_2} \frac{\partial P}{\partial x} + (A_t - A_s) [1 - \gamma(\phi)] \right\} + c_v \left\{ \frac{T}{\rho c_p} - \frac{\lambda_2}{\lambda_1} \frac{1}{\rho} \frac{\partial P}{\partial x} \gamma(\phi) + [1 - \gamma(\phi)] \frac{\partial T}{\partial x} \right\}$$

Expressions for A_s, A_t, A_o we obtain while considering the transfer process of mass element, carried out by eddies, allowing for its possible heat exchange with the medium due to radiation (molecular heat conduction is ignored, since the turbulence with large Reynolds number is considered here). It should be noted, that A_o has such a structure, that, in the absence of radiation, sometimes turbulent energy flow can be directed along temperature gradient, i.e. heat is transferred from the places with lower temperature to places with the higher one. This occurs, for example, at turbulence in atmosphere, when the temperature gradient in it is smaller than its adiabatic value, i.e. $\frac{1}{T} \frac{\partial T}{\partial x} < \frac{\gamma-1}{\gamma} \cdot \frac{1}{P} \frac{\partial P}{\partial x}$ (γ is adiabatic exponent, P - pressure).

The following factors are used in equations:

$$k = 3\sqrt{3} \frac{e_1 e_2 e_3}{e}; \quad k_1 = \frac{3}{4} + \frac{1e}{6e_1} + \frac{1}{2}\gamma + \frac{1}{10}\alpha k f_1 \frac{Wge}{Q} \frac{1}{e_1}; \quad k_2 = \frac{3}{2};$$

$$\gamma = 1 + \frac{1}{2} \phi_2 + \frac{1}{2} \phi_3 + \left[\frac{\gamma^2}{4} + \frac{\phi_2^2}{4} \right]^{1/2} + \left[\frac{\gamma^2}{4} + \frac{\phi_3^2}{4} \right]^{1/2};$$

$$\phi_2 = \gamma_2 \frac{WA}{R^2} \frac{e}{Q}; \quad \phi_3 = -\gamma_3 \frac{e_1 V_{11} + e_2 V_{22} + e_3 V_{33}}{Q};$$

The choice of expression for k_1 is based on the assumption, that the energy in homogeneous, isotropic turbulence decays as t^{-1} and scalar values fluctuation - as $t^{-\alpha}$, where $\alpha = 1.5$. According to the experimental data available, a value α is in the range of 1.2-1.5. Hence, k_2 value needs further refinement. Expression for k_1 has been obtained in accordance with the requirement, that correlation coefficient between density and velocity fluctuations should no be more than a unity.

For correlations of the third order we have used a gradient presentation with the diffusion coefficient D_t , equal:

$$D_t = 4\alpha \frac{e_1 e}{k_3 Q} \frac{1}{1+b}; \quad b = \frac{k_2}{4k_3} - (\xi + |\xi|); \quad k_3 = \frac{3}{2} + \frac{e}{6e_1} + \frac{\gamma}{2}; \quad \xi = \frac{2WAe}{k_2 QR^2} - 1$$

For the case, when $W \cdot A < 0$, $D_t = 0$ is assumed. In this very case, the recalculation of mass concentrations c_i due to turbulent mass flows is not carried out.

The function f_1 is:
$$f_1 = \frac{1}{R^2} \sum_{n=2}^{n=\infty} (-1)^n \frac{\langle \rho'^n \rangle}{\rho^n} \equiv \frac{R^{\sigma}}{R^2}.$$

In the model described, we can determine f_1 , using either approximate expression $f_1 = \left[1 + R^2 - \frac{D_t}{W} \cdot \frac{\partial R^2}{\partial x} \right]^{-1}$, or, more precisely, solving the appropriate equation for R^{σ} .

The value of P_{11} in the equation for V is the corresponding tensor component $P_{ik} = \frac{1}{2} \left(\langle u'_i u'_k \rangle + \frac{1}{\rho} \langle \rho' u'_i u'_k \rangle - W_i W_k \right)$. The sum of the diagonal tensor components P_{ii} is the total kinetic energy of turbulence. In works / 5/, / 6/ the approximate expression

$$P_{11} = e_1 - 2D_t \frac{\partial W}{\partial x} - \frac{W^2}{2}$$

is used. However, this expression does not provide conservatism of the model, i.e. conservation of constancy of the sum of internal, kinetic and turbulence energies, and fits only the calculation for flows, in which the fraction of turbulence energy is sufficiently small and some violation of the total energy balance may be ignored. That is why, the following

approximation $P_{ik} = \frac{e_{ik}}{e} \cdot P$, where $e_{ik} = \frac{1}{2} \langle u'_i u'_k \rangle$, $P \equiv P_{jj}$ is the sum of the diagonal tensor components P_{ik} , has been assumed. The value of P is determined from the following equation, providing the total energy balance:

$$\frac{dP}{dt} = \frac{1}{\rho} \operatorname{div} \rho (D_i \frac{\partial P}{\partial x} - WP) - 2 (P_{11} V_{11} + P_{22} V_{22} + P_{33} V_{33}) - W \frac{dV}{dt} - \frac{Q}{e} P;$$

Two groups of semi-empirical constants appear in the system of equations. The first group involves the constants, included in tensor presentation, describing exchange interaction between components of pulsing motion - $\alpha, \gamma_1, \gamma_2, \gamma_3$, the second group - constants β_1, β_2 , included in the equation for Q . Besides, there is one more constant α_1 in D_i . For some of these constants it is possible, considering the limiting case, either to determine their limiting values, or their magnitude. Thus, considering equation for anisotropy $\kappa = e_1 / e_2$, derived from equations for e_1 and e_2 , and assuming that "generation" term should result in anisotropy increase and "dissipative" one should be always negative, we obtain: $\frac{1}{10} \alpha < \frac{1}{3\sqrt{3}}, \gamma_1 - 1 > 0$. To be concrete, similarly to / 7/, we have accepted for $\alpha, \alpha = 1$, and for γ_1 , proceeded from the assumption, that for small anisotropy ($\kappa \approx 1$), the rate of its degeneracy coincides with the rate of turbulence energy degeneracy, it was assumed: $\gamma_1 - 1 = 1$. Considering the small, fast deformation of homogeneous, isotropic turbulence, one can define, that $\frac{1}{2} \beta_1 \gamma_1 = 1 / 8$. Since $\gamma_1 = 2$, was assumed for γ_1 , then, $\beta_1 = 1$. Constants $\alpha_1, \beta_2, \gamma_2, \gamma_3$ are to be obtained from the comparison of the calculated and experimental data. According to this comparison (see below), their values of $\alpha_1 = \beta_2 = \gamma_2 = \gamma_3 = 1$ are quite satisfactory.

For the most practical applications, the above mentioned system can be simplified. If the condition $\frac{1}{P} \frac{\partial P}{\partial x} \ll \frac{1}{\rho} \frac{\partial \rho}{\partial x}$ is satisfied, then, with a sufficient degree of accuracy, the solution of the equations only for W and R^2 will be enough, which are obtained by summation of a set of equations for W_i and B_i ($i = 1, n$). Mass flows of individual mixture components and energy flow are represented after that in the form $W_i = D \cdot A_i$, where $D = W / A$, and the equations for concentrations of c_i and the term in the equation for E , describing turbulent energy transfer, are reduced to the usual diffusional form. However, if the condition

of pressure gradient infinitesimal is not satisfied, then such an approximation for turbulent flows, with a single diffusion coefficient is not suitable. For example, in a mixture of two substances, the following equalities $A_1 + A_2 = A$, $W_1 + W_2 = W$ must be, in fact, satisfied. But there may occur the condition, when, due to considerably great (inside TMZ) pressure gradient, the value of A becomes $A \approx 0$, but W and other values in these equalities are not equal to zero. If so, it is clear, that these equalities can not be satisfied using for the flows the gradient representation of the form $W_i = D_i \cdot A_i$ with similar diffusion coefficients D_i . But if this representation is still used, then $D_1 \neq D_2$ ($D_1 - D_2 = W/A_1$).

The complete system of equations given above is, in the most of their terms, accurate. However, it has four groups of terms which are essential and the form of which is assumed from physical and dimensional considerations and tensor invariance. It is an assumed form of gradient representation of the third-order correlations, describing the turbulent values' transfer, the form of dissipative terms in all equations except the equations for e_1 , e_2 , e_3 , the group of terms with β_1 , β_2 factors in the equation for Q and, at last, an assumed representation for tensor L_{ik} , describing exchange interaction between various components of pulsing motion:

$$L_{ik} = \frac{1}{10} \alpha k f_1 \sum_3 (W_i g_k + W_k g_i - \frac{2}{3} \delta_{ik} W_{jj}) + \gamma \frac{Q}{e} (e_{ik} - \frac{1}{3} e_{jj})$$

here W is the i -th component vector W , g is the k -th component vector g , $e_{ik} = \frac{1}{2} \langle u'_i u'_k \rangle$, δ_{ik} is the single tensor.

The form of these terms needs further refinement.

The system of equations given above can be simplified using different assumptions and can be finally reduced to the system of two equations for total turbulence energy and turbulence energy dissipation (model of $k - \epsilon$ type). However, these assumptions are such, that their application for calculation of sufficiently complicated non-automodel flows, raises valid doubts. The turbulent mass flow $\rho W = \rho \sum W_i$ ($i=1,n$) and energy flow ρW_0 are assumed to have gradient character. This means, that, e.g., "inertial" term $f_1 R^2 g$ is ignored in the equation for W , and only "convective" term $2eA$ is remained there, and as a result of these, there is no need of solving equations for B_i or R^2 . Then, in stationary approximation for W , ignoring the pressure gradient in

A , we obtain $W \approx - \frac{1}{k_1} \frac{e_1 e}{Q} \cdot \frac{1}{\rho} \frac{\partial \rho}{\partial x}$, or, assuming $e_2 = e_3$ (planar and

spherical geometry), $W \approx \frac{1}{k_1} \frac{\kappa}{2+\kappa} \cdot \frac{e^2}{Q} \cdot \frac{1}{\rho} \frac{\partial \rho}{\partial x}$, where $\kappa = e_1^2/e_2$. It should be noted, that for the case of constant or slightly varying acceleration g , when there is time for setting up dynamic balance of turbulence characteristics and turbulence anisotropy κ is approximately constant, then, such an approximation is justified. In this case, from the equation for R^2 , allowing for the leading terms, we have $R^2 \approx \frac{WA}{\omega}$, where $\omega = \frac{Q}{e}$. Similarly, from the equation for Q , ignoring transferring terms and terms, having V_{ik} , we can obtain $\omega = Wg/e$. Then for the term R^2g in the equation for W , we have $R^2g \approx \frac{e}{Wg} \cdot WA g = eA$, i.e., formally, this term takes the form, similar to a "convective" one. However, in real unsteady flows, g may be changed rather rapidly. Besides, there may occur a conditions when A or density gradient are small and density fluctuations are great. Then the principal term responsible for mass flow "generation" will be the "inertial" one, and the gradient representation becomes unfit. As for turbulent energy flow, negative diffusion coefficient are possible in its gradient representation, as it has already been mentioned. Then an equation for turbulence energy is obtained from the equation for P or, if the density fluctuations are neglected, by summation of equations for e . The generative term in this equation is $G \approx Wg$ or, taking into account gradient representation for W , it is $G \approx -\frac{1}{k_1} \cdot \frac{\kappa}{2+\kappa} \cdot g \cdot \frac{1}{\rho} \cdot \frac{\partial \rho}{\partial x}$, i.e. the coefficient under $g \cdot \frac{1}{\rho} \cdot \frac{\partial \rho}{\partial x}$ is the function, strongly dependent on anisotropy (allowing for the fact, that k_1 depends on anisotropy and on other parameters as well). This is due to the fact, that only one component of the three ones of fluctuating motion is responsible for mass and energy transfer. Hence, simple models of $k - \epsilon$ type fit (and are justified due to its simplicity) the description of groups of flows of similar type, where g does not undergo sharp changes, with individual selection of constants for each group.

Let us dwell on the description of turbulence development after the passage of shock wave through TMZ. The principal mechanism of variation of values, characterizing turbulence, at the shock wave front in medium with density fluctuations, is pure inertial mechanism. That is, roughly speaking, this change results from the fact, that heavier elements of medium are accelerated to lower velocities and the lighter ones - to higher velocities as compared to the increment of the average mass velocity at wave front. The system given above is not suitable for description of such processes, and additional conditions are required, connecting the characteristics of turbulence on both sides of the shock wave front. Such conditions can be obtained analytically in the extreme case of small density fluctuations before the wave front ($\frac{e'}{\rho} \ll 1$)

and the strong shock wave (in the sense that mass velocity increment at the wave front is considerably higher, than the value of fluctuating velocity). In this case all gasdynamic values may be presented as the sum of the principal part and a small addition: $\rho = \langle \rho \rangle + \rho'$, $u = \langle u \rangle + u'$, etc. Substituting these sums in the conditions of conservation of mass, pulse and energy at the wave front, taking into account fluctuations of the wave front velocity D' , neglecting the terms of the highest-order infinitesimal and assuming, that the turbulence Mach number before front $M_t \ll 1$, that allows to ignore pressure fluctuations before the front, we can solve the system of equations, that was obtained and express $\rho'_{(2)}$, $u'_{(2)}$, etc, as $\rho'_{(1)}$, $u'_{(1)}$, etc (the index 1 denote the corresponding value before the front, index 2 - behind the front). After averaging, one obtains the terms, connecting turbulence characteristics on both sides of the wave front:

$$e_1^{(2)} = a^2 e_1^{(1)} - abW^{(1)} f_1^{(1)} \Delta V + \frac{1}{2} b^2 R_{(1)}^2 (f_1^{(1)} \Delta V)^2;$$

$$e_2^{(2)} = e_2^{(1)}, e_3^{(2)} = e_3^{(1)}, B_i^{(2)} = B_i^{(1)};$$

$$W_i^{(2)} = a W_i^{(1)} - b B_i^{(1)} f_1^{(1)} \Delta V;$$

where ΔV is the increment in average mass velocity at wave front.

There, for simplicity, we assumed that the adiabatic exponents γ_i of the all mixture components are equal.

The values of a and b for the given model of strong shock wave and small density fluctuations are: $a = 1$, $b = \frac{1}{2}$. However, it is quite natural, that the series of weak shock waves ($\Delta V \rightarrow 0$), passing through TMZ should be equal to boundary braking. So, when $\Delta V \rightarrow 0$, the following condition should be fulfilled: $a \rightarrow h$, $b \rightarrow 1$, where h is the compression in a shock wave. Therefore, starting from some semi-qualitative considerations, a and b were taken in the form of the following functions:

$$a = \frac{1 + h\tau^2}{1 + \tau^2}, \quad b = \frac{1 + \tau^2}{2 + \tau^2}, \quad \text{where } \tau = \frac{P_2}{P_1} \frac{1}{P_1} \sqrt{R^2}$$

P_1 , P_2 are the pressures before and behind the wave front, respectively.

Qualitative change of e_1 and W as a function of ΔV after a strong shock wave travel through TMZ is shown in Fig.1 (here, the positive direction is the direction of the density gradient in TMZ). Fig.1 shows, that when a wave goes from a light material into heavy one, e_1 and W undergo discontinuous change (W retains the sign), that results in TMZ development intensification. When a strong wave goes from from a heavy material into a light one, e_1

is also increased, but W changes the sign. As a result of this, immediately after the wave passage, fraction separation of heavy and light materials, which have not been mixed up to molecular level, takes place, and TMZ width is efficiently reduced to some extent (in principal, if mixture in TMZ was a heterogeneous one, then the initial contact boundary will be restored for some moment). Then due to the turbulence energy, stored as the result of the wave passage, W again changes its sign (the term $2e_1 A$ in the equation for W) and TMZ development progresses. TMZ development rate, if the wave is sufficiently strong, will be close to the TMZ development rate in the case, when the wave goes from a light material into a heavy one.

The conditions obtained above connect characteristics of turbulence on the shock wave front. However, their practical application in such form is not very suitable, since in the numerical method of solution of gasdynamic equations that we have used, the wave front is "distributed" between several points. Therefore, in concrete numerical realization at the shock wave front, the same system of equations is solved, as in other regions of flow, but with some variations. That is, at the wave front, which is specified particularly, the following values $A_i^{(1)}$ ($2b - 1$), $V_{11}^{(1)}$ ($2b - 1$), $f_1^{(1)}$, $g \cdot b$ are used instead of the current values A_i , V_{11} , f_1 , g ($A_i^{(1)}$, $f_1^{(1)}$ are the values of A_i , f_1 before wave front). Solution of the system of equations whis such variations provides fulfilment of the requirements obtained for turbulence characteristics at the strong shock wave front, and, at the same time, provides equivalence of a series of weak, frequently coming shock waves, to simple braking.

Let us consider the results of some TMZ development calculations, carried out according to the model considered, and compare them to the experimental data.

In work / 8/ you can find the comparison of calculated and experimental data from / 9/ on turbulence evolution under axial symmetric deformation, which allows to check the correctness of the chosen type of the exchange interaction tensor, terms with V_{ik} in the equation for Q and γ_1 , γ_3 , β_1 constants values. In the experiment carried out, a cylindrical channel with constant cross-section S_1 , which transitted to the channel of constant cross-section $S_2 < S_1$ in the deformation region, was placed behind the turbulizing grid. Three different values of cross-section ratios $S_1 / S_2 = 4, 9, 16$ were investigated. The comparison carried out, showed that calculations gave good description of turbulence evolution through all the flow for all three cases. Calculated and experimental values of $\sqrt{2e_1} / v_0$ and $\sqrt{2e_2} / v_0$ for the case of maximum channel contraction $S_1 / S_2 = 16$ are presented in Fig.2

(e_1, e_2 are the energies of pulsing movement along and across the flow axis; V_0 is the flux velocity behind the turbulizing grid; V is the flux velocity in the given cross-section).

In work / 5/ the measurement results for TMZ width, carried out in two experiments, performed on gas models in cylindrical and plane geometry, are presented. In cylindrical geometry the inner region was filled with He and the outer - with air. A convergent cylindrical shock wave with pressure, abruptly falling behind its front, was formed on the outer air surface due to electric explosion of wires, and as result of this air-helium interface became instable immediately after the travel of this wave through the interface, and TMZ was developed on it, development rate of which was abruptly increased after the passage through it a shock wave reflected from the center. Fig.3 shows comparison between calculated and experimental data. Experiments in plane geometry were performed on a shock tube in air and helium. A shock wave generated in air passed through air-helium interface, separated by a thin film, and when it broke a "primer" TMZ was developed and then, being reflected from a rigid wall, it returned to the interface, initiating intense TM. Experimental and calculated data on TMZ width from this experiment are shown in Fig.4. In work / 10/ measurement results for the profile of air density in TMZ in this experiment are given (Fig.5). In this Fig.5 you can see the calculated profile (Fig.5 shows a relative density ρ/ρ_0 , where ρ is the average air density in TMZ, ρ_0 - is air density outside TMZ). One remark should be made, concerning this experiment. If for ideal calculation, without allowance for TM, the braking of air-helium interface is caused by a series of shock waves, then at TMZ being on interface, the accurate shock wave is only the first one, reflected from a rigid wall. Subsequent waves are not shock ones, since they are generated as a result of reflection from a "smeared" interface and during their movement from interface to the rigid wall and back, characteristics have no time to intersect and to form a shock wave, therefore, interface braking after the first shock wave is caused by variable pressure gradient. It should be noted, that TMZ growth rate after the first reflected wave passage through the interface should be defined by the value of density fluctuating in TMZ, generated after film break. Immediately after the break, air-helium mixture should be essentially heterogeneous, and then, while eddies' spectrum formation, the value of density fluctuations will gradually decrease. Therefore, one should expect change of TMZ development rate after arrival of the first reflected shock wave, depending on the distance from the interface up to rigid wall. The more is this distance and, appropriately, the time of the wave travel to a rigid wall and back and also the time for degeneration of density fluctuations in to the "primer" TMZ, the less is this TMZ development rate. That is why, it is desirable to conduct a series of similar experiments with various distances between the interface and a rigid wall. Results of such

experiments could be used to specify k_2 coefficient in the equations.

For automodel problem on TM at the boundary of two gases, having constant density with the density ratio $\delta = \rho_2/\rho_1 > 1$, existing in gravitational field with $g = \text{const}$ for TMZ width L_t , in the model described, we obtain:

$$L_t = F\left(\frac{\delta-1}{\delta+1}\right) \cdot S, \text{ where } S = \frac{1}{2} \cdot g t^2$$

The function $F\left(\frac{\delta-1}{\delta+1}\right)$ is shown in Fig.6. For $\delta \leq 10$ function F approximately is $F \approx 0.65 \frac{\delta-1}{\delta+1}$.

The calculated density profile inside TMZ is shown in Fig.7. The profile is given in nondimensional coordinates:

$$\tilde{\rho} = \frac{\rho - \rho_1}{\rho_2 - \rho_1}, \quad \tilde{x} = \frac{x}{x_{0.9} - x_{0.1}},$$

where $x_{0.9}$, $x_{0.1}$ are coordinates of points where $\tilde{\rho}$ is 0.9 and 0.1, respectively. Calculated density profile in these coordinates turned out to be independent from density ratio with the profile assymetry $L_{t1}/L_{t2} \approx 1.24$, where L_{t1} , L_{t2} is TMZ penetration depth into a light and heavy material, respectively ($L_{t1} + L_{t2} = L_t$).

The measurement results for TMZ width at the gases boundary with different density ratios, with low decreasing acceleration at the boundary are presented in / 11/. Experiments were carried out on an electromagnetic shock tube. Experimental results are given in Fig.6. Measurement results for density profile in TMZ for $\delta = 3$, which are shown in Fig. 7 are given in / 12/.

One significant contradiction in experimental data on TMZ growth rate should be noted here. It lies in the fact, that the recorded TMZ growth rates in flows, similar to automodel case, in gases (e.g. / 11/) is 2 - 2.5 times as large as in liquids (e.g. /12/,/13/) The same result is, naturally, obtained while calculating automodel problem according to our model, which was verified on gas runs / 5/ (see above). The reason for such state is not yet understandable. Perhaps, this is due to absolutely different mechanism of turbulence energy dissipation in insoluble liquids mixing (the most part of experiments). In this case, turbulence energy is mostly converted in reversible manner, without entropy increase, into free energy of the surface, separating unmixable components with potential restoration of the initial contact boundary as compared to gases, where turbulence energy is irreversibly, due to viscosity, converted into heat and restoration of the initial contact boundary can not be realized because of molecular diffusion processes. Then, the concrete value surface stress coefficient (if it is already small enough), perhaps, is not significant, likewise in gases, when turbulence

has sufficiently large Reynolds number, the concrete value of viscosity is not significant for dissipation rate, only its presence is taken into consideration. Besides, simultaneous influence of surface stress and viscosity on TMZ development rate in unmixable media is possible. In some experiments with intersoluble liquids there is its own problem, associated with the influence of a diffusion transient layer inevitably formed on the boundary upon TMZ development rate (see below). Some incorrectnesses are, certainly, likely to occur in interpreting gas experiments. This problem needs further careful investigation, however, at present we prefer to concentrate on the results of gas experiments.

Problem, concerning the effect of initial boundary disturbances on TMZ development rate and on the time when the process goes into automodel regime, is considered to be interesting. To study this problem a series of calculations have been carried out, in which at the initial time a region of Δ width was set between two substances, the density of this region was gradually varied from ρ_1 to ρ_2 . Inside this region the values of fluctuation density R^2 were set according to formula:

$$R^2 = k \cdot \frac{(\delta - 1)^2}{\delta} \cdot c(1 - c),$$

where c is mass concentration of one of substances. The value k varied from 1 to 0. The value $k = 1$ corresponds to complete heterogeneity inside region, i.e. there is pure roughness with amplitude Δ . Decrease of k corresponds to gradual diffusive smoothing of this roughness just to pure diffusive transient layer, when $k = 0$. Calculations were carried out for different ratio values of densities $\delta / 6/$. For example, TMZ widths L_t as a function of $S = \frac{1}{2} g t^2$, obtained in these calculations at different k -values for $\delta = 3$ are shown in Fig.8. It is clear, that for sufficiently high k -values TMZ growth rate at first essentially exceeds an automodel one, but as k decreases, i.e. as density disturbances decrease, the stabilizing role of the transient layer becomes more evident right up to the complete absence of TM when $k = 0$. These calculations demonstrate feasibility of application of transient layer, having small density disturbances insides, for elimination of TM effect on targets characteristics for ICF.

One more characteristic problem concerns the rate of TMZ development rate due to inertia after acceleration off-switching. According to calculations / 6/ in this case TMZ development rate of two media with constant density begins to follow asymptotic law: $L_t \approx t^\beta$ (t is the time), where β has a weak dependence on density ratio δ of the two media and changes from $\beta \approx 0.2$ when $\delta = 1.66$, and to $\beta \approx 0.26$ when $\delta = 70$.

Let us compare calculation results for TM according to the model described with the results of computational modeling in two-dimensional approximation of some turbulent flows, described

in / 14/. Two-dimensional Euler technique was used in / 14/ for calculation of flow of nonviscous, compressible media, in which for localization of contact boundaries, they have used mass concentrations and a special algorithm for counting of flows from grid meshes, containing some substances / 15/. In all calculations, carried out according to this technique, random position and amplitude distributed disturbances of density or velocity were set on contact boundaries (in two boundary meshes) to provide output from the onset and further generation of two-dimensional eddies. A series of calculations with δ varied in the range of 1.66 - 70 was carried out for automodel problem, concerning two media with constant ratio of densities δ in constant gravity field. TMZ development rate in two-dimensional calculations was slightly higher than in semi-empirical one-dimensional model described. Profile of average density in TMZ completely coincided with the profile, shown in Fig.7, and in nondimensional coordinates it also turned out to be independent on δ value. Calculations for cylindrical experiment from / 5/ have been carried out. TMZ development rate has been obtained, that is, in average, slightly higher than that of the experiment and in one-dimensional calculation. Besides, calculations of a strong shock wave propagation through medium with constant average density, but in the presence of density disturbances have been carried out, they verified the value of constant $b = \frac{1}{2}$ under conditions, connecting turbulent value from both sides of a wave front (see above). As for two-dimensional calculation, it should be noted, that Reynolds number of the generated two-dimensional turbulence relative to "schematic viscosity" must be sufficiently great. This requires essentially large number of count points as compared to ordinary gas-dynamic calculations.

Let us consider examples of more complicated flows' calculations concerning one-dimensional semi-empirical model described.

Experiments and calculations for investigation of loads affecting the walls of a closed chamber during explosion of explosive charge, taking place in this chamber, are considered in / 16/. A spherical chamber 2 m in diameter was used in the experiments. Explosive charge of a mixture type with the negative oxygen balance was placed in the center of a chamber. Pressure, affecting the chamber walls after HE explosion, was measured in these experiments. Two variants of experiment technique have been used. According to one technique, the chamber volume was filled with nitrogen, according to another - with air. After explosion TM of explosion products (EP) with gas, filling the chamber, starts, it is intensified by shock waves, generated in chamber due to reflection from chamber wall and the center. If chamber contains oxygenated gas, the TM with subsequent mixing (to molecular level) of mixture components, leads to EP after-burning and to ≈ 2.5 fold increase of the total energy output in chamber. This results in variation of the pressure

affecting the chamber wall, manifested through the change of time for shock waves' arrival to the wall and their amplitude (except the first wave). Calculations of these processes have been carried out according to the model described with additional equations, describing dynamics of mixture components' mixing to molecular level. Fig.9 shows calculated profiles of pressure at chamber wall with and without allowance for EP afterburning as the result of TM for 570 g of HE in chamber. Experimental and calculated time of three first shock waves arrival to the chamber wall as a function of HE mass, with and without EP afterburning are presented in Fig.10. As can be seen, calculated and experimental data are in good agreement.

One more model was investigated along with the model described, it was more complicated and did not use gradient presentation for correlations of any order at all. In this model the equations for the second-order correlations are just the same as before (except the transient terms, which are divergences of the third-order correlations), and for third-order correlations the corresponding equations have been obtained. The system obtained, involving $4(i+2)$ equations (i is the number of mixture components) is closed at the level of the fourth-order correlations, which are expressed in terms of the second-order correlations' products using either Millionshchicov's hypothesis, or proceeding on assumption of the complete mixture heterogeneity. However, several calculations, carried out according to this model, showed, that for most flows (of the type described above), this model does not give essentially new results. The exception, perhaps, is the possibility to describe the evolution of TMZ, developing at the beginning, after acceleration sign change, when a boundary becomes stable and some efficient decrease of TMZ width takes place. This efficient decrease of TMZ width is caused by the fact, that although the total TMZ width for the case of mixable media is not formally decreased, since even at TMZ boundaries there is a very small, but mixed to molecular level, part of mixture components, however the density gradient in TMZ center increases occurs due to separation of unmixed to molecular level components. When the mixture in TMZ is completely heterogeneous, the initial contact boundary would be restored. Time dependence of TMZ efficient width L_t (acceleration sign was changed at $t = 0.8$) calculated for this case is shown in Fig.11. There one can also see time dependences e_1 , W , R^2 in this calculation. According to Fig.11, decrease of TMZ efficient width is not too great and for practical applications, it seems quite sufficient, to use a model with gradient representation of the third-order correlations, not allowing for TMZ width decrease.

REFERENCES

1. S.Z.Belen'kiy, E.S.Fradkin, Work of the Phys. Inst.of Sov. Acad. of Science, p.207, v.29, 1965.

2. V.A.Andronov, E.E.Meshkov, V.V.Nikiforov et al, Journ. of Exp. and Theor. Phys., p.806, iss. 2(18), v.71, 1976.
3. V.E.Neuvazhaev, V.G.Yakovlev, Journ. of Appl. Math. and Techn. Phys., p.74, v.7, 1976.
4. V.A.Andronov, V.V.Nikiforov, A.V.Pevnitzkii et al, Lett. to the Journ. of Exp. and Theor. Phys., p.62, iss.1, v.29, 1979.
5. V.A.Andronov, E.E.Meshkov, V.V.Nikiforov et al, Rep. to the Sov. Acad. of Science, p.76, v.264, 1982.
- 6 V.V.Nikiforov, Quest. of Atom. Scien. and Techn. (Theor. and Appl. Phys. ser.), p.3, Iss.1, 1985.
7. B.J.Daly, F.H.Harlow, Phys. of Fluids, N 11, v.13, 1970.
8. V.A.Andronov, V.V.Nikiforov, Quest. of Atom. Scien. and Techn. (Theor. and Appl. Phys. ser.), p.34, iss.1, 1990.
- 9.M.S.Uberoi, Journ. of Aeron. Sci., p.754, N 8, v.23, 1956.
10. E.E.Meshkov, V.V.Nikiforov, A.I.Tolshmyakov, Phys. of Burn. and Expl., p.71, N 3, 1990.
11. A.M.Vasilenko, V.I.Olhovskaya, O.V.Buryakov et al, Report on 3-rd Int. Workshop on Physics of Compressible Turbulent Mixing, (Abbey of Royamont, June 17-19, 1991)
12. Y.Kucherenko, L.Shibarshov, V.Chitaikin et al, Report on 3-rd Int. Workshop on Physics of Compressible Turbulent Mixing, (Abbey of Royamont, June 17-19, 1991)
13. V.S.Smeeton, D.L.Youngs, Report on 3-rd Int. Workshop on Physics of Compressible Turbulent Mixing, (Abbey of Royamont, June 17-19, 1991)
14. V.A.Andronov, V.V.Nikiforov, Yu.V Yanilkin et al, Mechan. of Fluid and Gas, p.30, N 6, 1984.
15. S.M.Bakhrakh, Ya.P.Glagoleva, M.S.Samigulin et al, Rep. to the Sov. Acad. of Science, p.566, N 3, v.257, 1981.
16. V.A.Andronov, V.A.Mazanov, V.V.Nikiforov et al, Rep. to the Sov. Acad. of Science, p.1385, N 6, v.314, 1990.

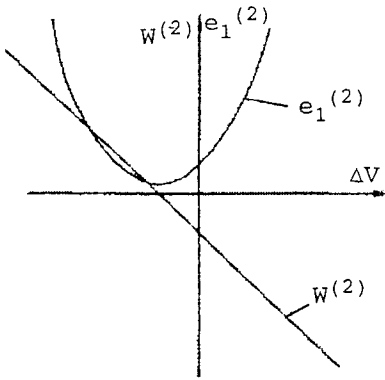


Fig.1. Characteristics of turbulence at shock-wave front.

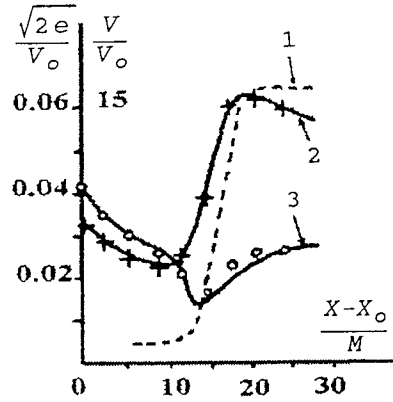


Fig.2. Turbulence energy development at axisymmetric deformation: o, + - experiment, -----, — calculation

$$\begin{aligned}
 & (1 - V/V_0, 2 - \sqrt{2e_2}/V_0, \\
 & 3 - \sqrt{3e_1}/V_0)
 \end{aligned}$$

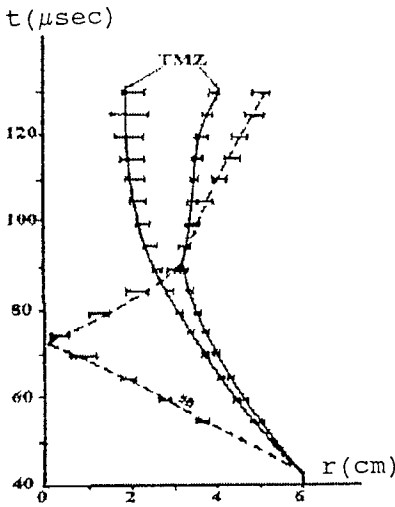


Fig.3. Cylindrical experiment "air - He".
 ←→ - exper. /5/, - - - - calc.

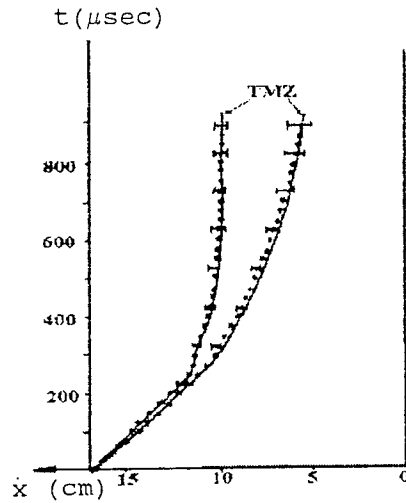


Fig.4. Plane experiment "air - He".
 ●, ←→ - exper /5/, - - - - calc.

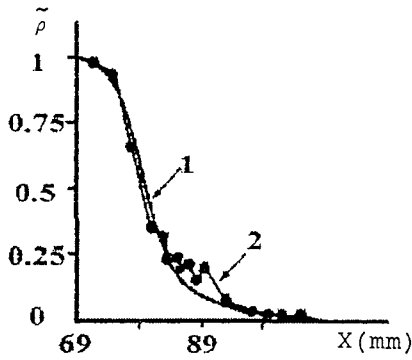


Fig.5. Profile of partial air density in plane experiment "air-He" (1 - calc., 2 - exper.).

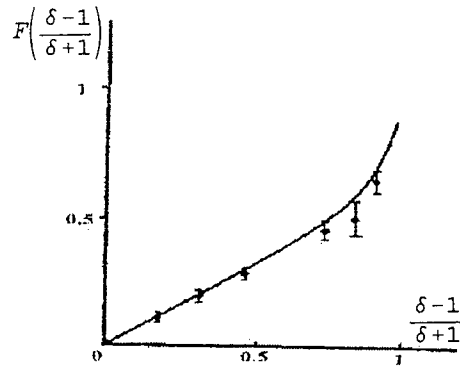


Fig.6. $F\left(\frac{\delta-1}{\delta+1}\right)$ vs $\frac{\delta-1}{\delta+1}$

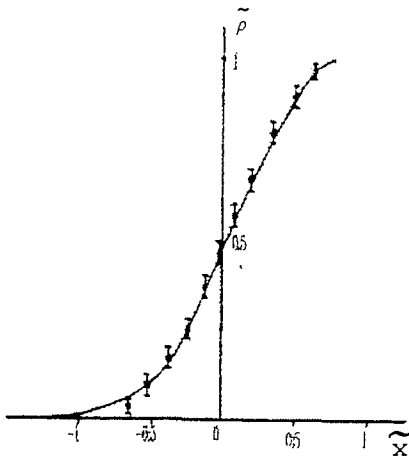


Fig.7. Profile of average density in TMZ an automodel problem.
— - calc,] - exp.

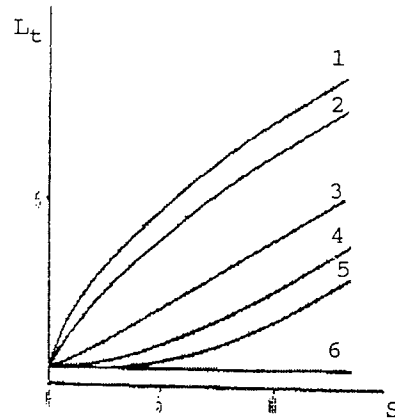


Fig.8. TMZ development rate VS density disturbances in transient layer.
(1 - $k=1$, 2 - $k=0.6$, 3 - $k=0.075$,
4 - $k=0.0075$, 5 - $k=0.00075$,
6 - $k=0$)

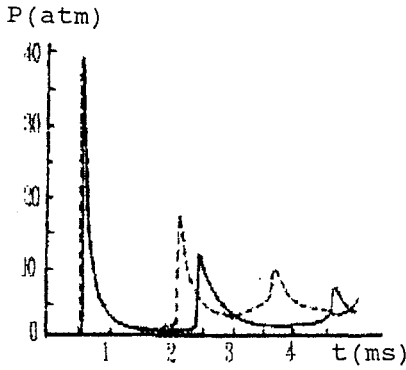


Fig. 9. Calculated relationship between the pressure at the chamber wall and the time with EPs' after-burning (----) and without EPs' after-burning (—).

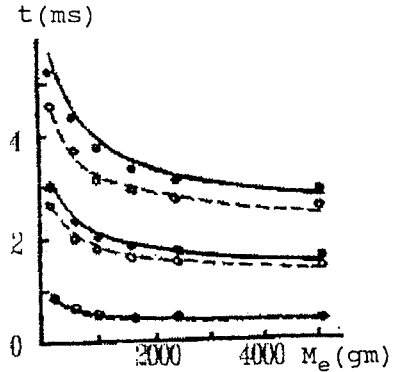


Fig. 10. Time of arrival of the first, second and third shock waves to the chamber wall as a function of HE mass, with EPs' after-burning (o - exp., ---- calc.) and without after-burning (• - exp., — calc.).

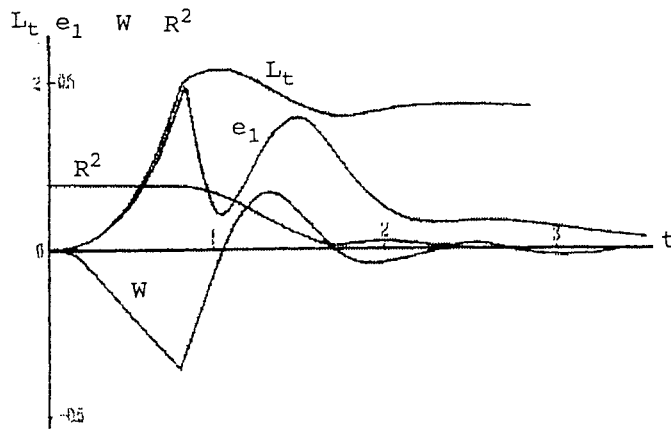


Fig. 11. TMZ width and turbulence characteristics as a function of time, when acceleration sign is changed.

Mixture Separation in the Framework of Hkε-Model

A.Polionov, V.Yakovlev

All-Russia Research Institute of Technical Physics
454070, Chelyabinsk-70, p.o.245, Russia

Abstract

There has been calibrated the equations of the Hkε-model¹ which describe a gravitational turbulent mixing. The calibration has been carried out in accordance with the experiments of Dr.D.Youngs² realizing the self-similar mixing and a mixture separation at the change of the acceleration sign.

The heterogeneous kε-model (Hkε-model) describes gravitational mixing as a turbulent diffusion however considers in contrast to the usual kε-model³ the fact that a turbulence diffusion takes place in the gravitational field. It is taken into account by the expression for the turbulent mass flow. It involves the additional term proportional to the difference of the mixture component buoyancies apart from the traditional one proportional to concentration gradient only. The Hkε-model equations has been deduced and described previously¹.

There was a prompting to create the model in an attempt to describe a separation in a shock wave by G.Rykovanov who by analogy with the consideration in ⁴ included in the turbulent mass flow an additional term proportional to the pressure gradient.

This paper considers mixing of two incompressible fluids in the gravitational field described by g. The interface between fluids are denoted by r₀ so that the fluid with the initial density ρ₁⁰ occupies the interval [r₁,r₀] and the one with ρ₂⁰ does [r₀,r₂], r₁<r₂.

Behavior of this system can be described by the equations obtained from those contained in the paper¹:

$$\begin{aligned} \rho \frac{dk}{dt} + \rho \epsilon &= \alpha_k \rho \frac{\partial}{\partial m} \rho^2 D \frac{\partial k}{\partial m} + g j \frac{n-1}{c+n(1-c)}, \\ \rho \frac{d\epsilon}{dt} + c_2 \epsilon \rho \frac{\epsilon^2}{k} &= \alpha_\epsilon \rho \frac{\partial}{\partial m} \rho^2 D \frac{\partial \epsilon}{\partial m} + c_1 \epsilon \frac{\epsilon}{k} g j \frac{n-1}{c+n(1-c)}, \\ \frac{dc}{dt} + \frac{\partial j}{\partial m} &= 0, \\ j &= -\rho^2 D \frac{\partial c}{\partial m} + \beta \rho D g \frac{c(1-c)}{k} \cdot \frac{(n-1)[c+n(1-c)]}{n}, \\ \rho &= \rho_2^0 \cdot \frac{n}{c+n(1-c)}, \quad n = \rho_1^0 / \rho_2^0, \quad dr = \frac{dm}{\rho}, \quad D = c_\mu \cdot \frac{k^2}{\epsilon}. \end{aligned}$$

Here k is a turbulent energy, ε is intensity of dissipation

of k , m is the Lagrange's coordinate, r is the Euler's coordinate, c is a mass fraction of the first component, j is a turbulent mass flow of the first component. At the boundaries r_1 and r_2 we have $j=0$ and the diffusion flow of the k and ϵ is equal 0.

The values of empirical constants c_{μ} , $c_{1\epsilon}$, $c_{2\epsilon}$, α_k , α_ϵ , β can be found from experiments. We have used the experiments of D.Youngs from the paper² on finding the rate of mixing development and on a mixture separation at the changing of the acceleration sign.

The dependence of the acceleration on time has been kindly given us by Dr.D.Youngs as following ($g_0=0.98$):

$0 \leq t < 5$	$g/g_0 = -0.084t$
$5 \leq t < 48$	$g/g_0 = -0.42$
$48 \leq t < 55$	$g/g_0 = 0$
$55 \leq t < 70$	$g/g_0 = 0.85$
$70 \leq t < 84$	$g/g_0 = 0.80$
$t \geq 84$	$g/g_0 = 0$

We have taken $r_1=0$, $r_0=35$, $r_2=70$, $\rho_1^0=1$, $\rho_2^0=1.73$. The depth of the light fluid penetration into the heavy one h_1 was found in accordance with the experiment by the volume fraction $f(h_1)=0.95$ (in this case mass fraction is $c(h_1)=0.97$).

At the performing of the simulations it has been found that the values of the constants α_k and α_ϵ should be increased to conserve the form of the average density profile as it has been accepted in $k\epsilon$ -model³ in accordance with the experiment⁵.

On the basis of comparison with the experiment the values of the model constants has been chosen as following:

$$C_{\mu}=14, c_{1\epsilon}=1.43, c_{2\epsilon}=1.54, \beta=0.06, \alpha_k=2.8, \alpha_\epsilon=1.54.$$

Fig.1 shows a satisfactory agreement of h_1 with the experiment, the profiles of an average density are given at fig.2 at different moments.

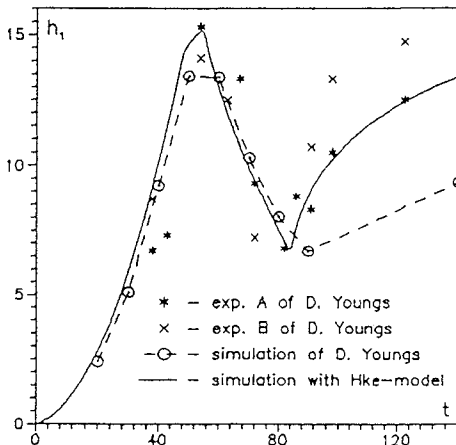


Fig.1 Dependence of zone mixing width on time

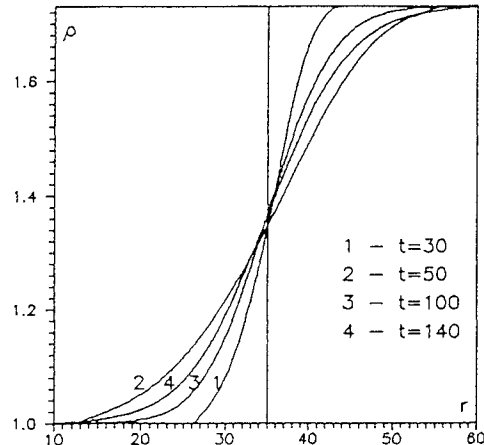


Fig.2 Profiles of density

It should be noted that the model provides the full separation of a mixture. Depending on the sign of an acceleration it means either restoration of the original positions of the fluids or the interchanging by their positions.

References

1. A.Polyonov. Heterogeneous $k\epsilon$ -model of Gravitational Mixing. Proceedings of II International Workshop on Compressible Mixing, Pleasanton, USA, 1989.
2. D.L.Youngs. Modelling turbulent mixing by Rayleigh-Taylor instability. *Physica D* 37 (1989) 279.
3. V.E.Neuvazhaev, V.G.Yakovlev. Numerical Calculation of Interface Turbulent Mixing by Rayleigh-Taylor Instability on the Basis of Semiempirical Models. Proceedings of II International Workshop on Compressible Mixing, Pleasanton, USA, 1989.
4. Y.B.Zeldovich, Yu.P.Rizer. Physics of shock waves and high temperature hydrodynamic phenomena, Moscow, 1963.
5. Yu.A.Kucherenko, L.I.Shibarshov and others. Experimental Study of the Gravitational Turbulent Mixing Self-Similar Mode. Proceedings of the III International Workshop on Compressible Mixing, Abbey of Royaumont, France, 1991.

APPLICATION OF A TWO-DIMENSIONAL TURBULENCE MODEL

D L Youngs
 B C Hankin
 N W Cowperthwaite

Atomic Weapons Establishment, Aldermaston
 Reading, Berkshire, United Kingdom

INTRODUCTION

For turbulent mixing in complex applications, direct three-dimensional simulation is impractical. For such problems it is necessary to use a turbulence model to predict the average behaviour. A two-dimensional turbulence model is used to simulate mixing of fluids by Rayleigh-Taylor, Kelvin-Helmholtz and Richtmyer-Meshkov instabilities in flows which are on average two-dimensional. The model is based on the equations of multiphase flow with turbulent diffusion effects included and is an extension to two dimensions of the one-dimensional turbulence model described in [1].

THE MULTIPHASE FLOW MODEL

A brief summary of the model is given here. Details of the equations (in 1D) are given in [1]. For each fluid for which mixing needs to be calculated, equations are solved for mass transport, momentum transport and internal energy transport. For the mixture as a whole, equations are solved for turbulence kinetic energy (k) and the length scale (L). A key part of the model is the drag between fluids in the momentum equations. The drag between fluid r and fluid s is

$$\underline{D}_{rs} = - c_1 \frac{\rho_{rs} f_r f_s}{L} \left| \underline{u}_r - \underline{u}_s - \underline{w}_r + \underline{w}_s \right| (\underline{u}_r - \underline{u}_s - \underline{w}_r + \underline{w}_s)$$

- ρ_{rs} = average density for fluid r, s
- f_r, f_s = volume fractions for fluid r, s
- \underline{u}_r = velocity of fluid r (mass weighted)
- \underline{w}_r = value of $\underline{u}_r - \bar{\underline{u}}$ expected for pure diffusive mixing
- = $-\frac{D}{\rho_r f_r} \nabla (\rho_r f_r)$

The turbulent diffusion coefficient is taken to be $D = 2\ell_t k^{1/2}$ where ℓ_t is the turbulence length scale. This is assumed to be proportional to the length scale used in the drag term ($\ell_t = c_2 L$). The model constants c_1 and c_2 are adjusted to fit Rayleigh-Taylor and Kelvin-Helmholtz mixing experiments. The constant c_2

determines the importance of diffusive mixing whereas the drag coefficient c_1 determines the importance of pressure gradient driven mixing. If c_1 is set to a high value then $\underline{u}_r - \underline{u}_s = \underline{w}_r - \underline{w}_s$ and mixing is purely diffusive. Model coefficients are chosen so that the bubble penetration for Rayleigh-Taylor mixing is given by

$$h_1 = \alpha \frac{\rho_1 - \rho_2}{\rho_1 + \rho_2} g t^2 \quad , \quad \text{with } \alpha = 0.05.$$

Three applications of the two dimensional turbulence model are considered in this paper:-

- (a) Comparison with direct 3D simulation for a problem which is on average two-dimensional.
- (b) An explosive gas/jelly experiment carried out at the Institute of Experimental Physics, Arzamas-16 [2].
- (c) A simplified Inertial Confinement Fusion implosion.

COMPARISON OF THE 2D TURBULENCE MODEL WITH 3D SIMULATION

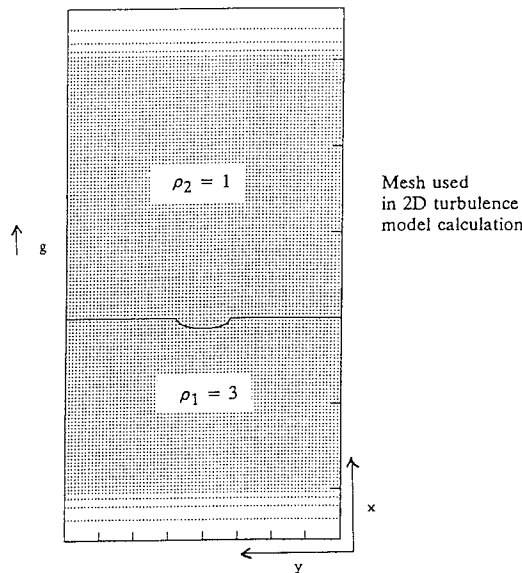


Figure 1: Initial geometry for the cylindrical groove problem.

Direct 3D numerical simulation is impractical for complex problems. However, it may be applied to simple problems which are on average two-dimensional. The results may then be used to assist in the validation of the 2D turbulence model. An example is shown here. The initial geometry (figure 1) is based on the Rayleigh-Taylor problem considered in [3]. The initial perturbation at the interface consists of a cylindrical groove plus a random short wavelength perturbation ($\lambda = 4\Delta x$ to $8\Delta x$). The depth of the groove is 0.03 and its width is 0.16. The groove evolves into a large two-dimensional structure, on which three-dimensional turbulence is superimposed. The 3D direct simulation uses $270 \times 160 \times 160$ zones. In order to compare with the 2 turbulence model, the line-averaged volume fraction

$$\bar{f}_1(x, y) = \int_{z_{\min}}^{z_{\max}} f_1(x, y, z) dz / (z_{\max} - z_{\min})$$

is calculated, where $f_1 = (\rho - \rho_2) / (\rho_1 - \rho_2)$. Contours for \bar{f}_1 are shown in figure 2(a). These may be compared with the results obtained from a 2D turbulence model calculation (figure 2(b)) using 135×80 meshes. There is good agreement at $t = 1.0$ and $t = 1.5$. At $t = 2.0$ the large bubble which forms from the initial groove is more diffuse in the 3D simulation than in the 2D turbulence model calculation.

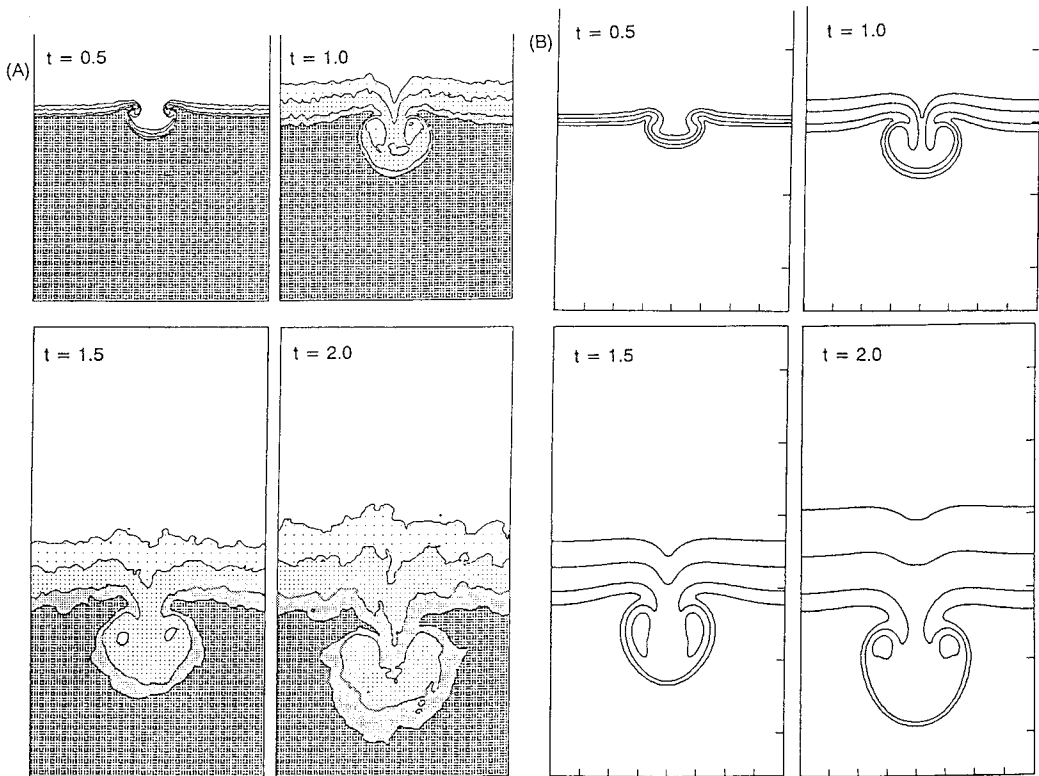


Figure 2: Volume fraction contours ($\bar{f}_1 = 0.05, 0.3, 0.7, 0.95$) for cylindrical groove problem. (A) direct 3D simulation (B) 2D turbulence model calculation.

EXPLOSIVE GAS/JELLY EXPERIMENT

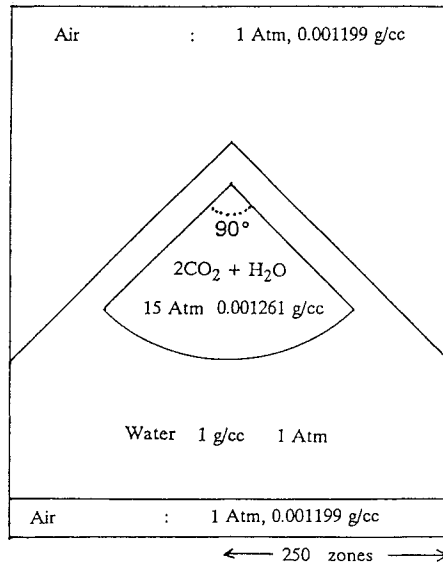


Figure 3: Initial geometry for explosive gas/jelly experiments.

The 2D turbulence model has been applied to an experiment described in Rogatchov et al [2] which used explosive gas ($C_2H_2 + 2.5O_2$) and jelly (water + gelatin). The jelly has very low strength and when the gas mixture is detonated it is assumed to behave as a liquid (water). The explosive gas products were observed to mix with the water due to RT instability. This is the process modelled in the 2D calculation. The initial geometry used is shown in figure 3. The mesh size was $\Delta x = \Delta y = 0.03$ cm. Perfect gas equations of state were used for the air ($\gamma = 1.4$) and explosive gas products ($\gamma = 1.116$). The equation of state used for the water region was

$$p = B \left(\frac{\rho}{\rho_0} - 1 \right) + \Gamma \rho \epsilon$$

with $B = 1$ kbar and $\Gamma = 0.3$. An artificially low value was used for the bulk modulus B in order to increase the computational timestep. B was high enough to ensure that the water was almost incompressible. Vaporisation of the water by the hot explosive products is not included in the computer simulation. The 2D simulation models the turbulent mixing at the explosive gas/water interface. Interface tracking, as described by Youngs [4], is used at the stable water/air interfaces. Results from the computer simulation are shown in figure 4. The corresponding experimental results, from [2], are reproduced in figure 5.

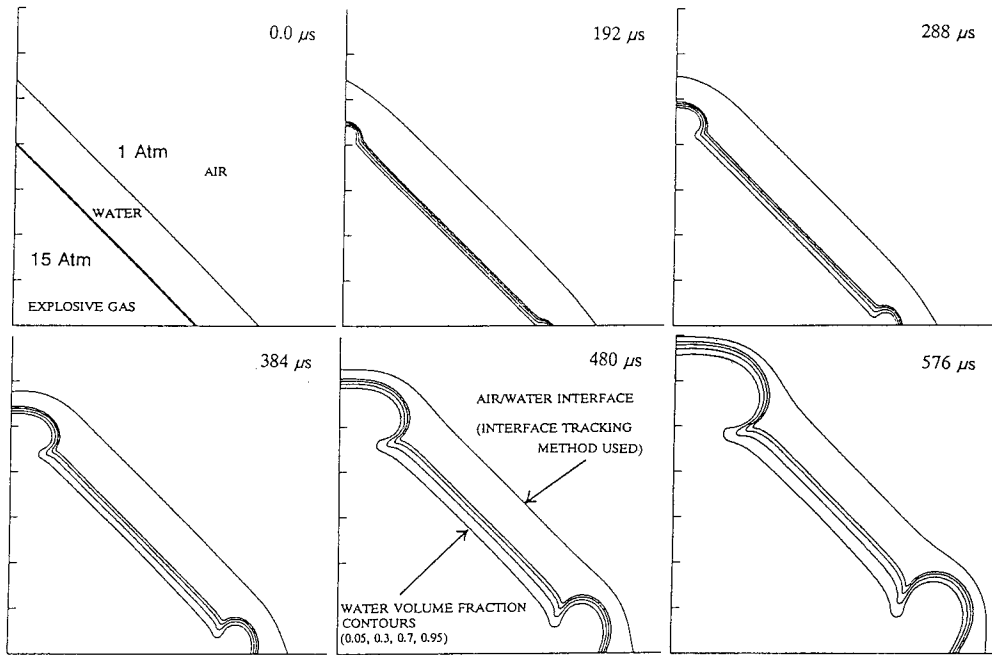
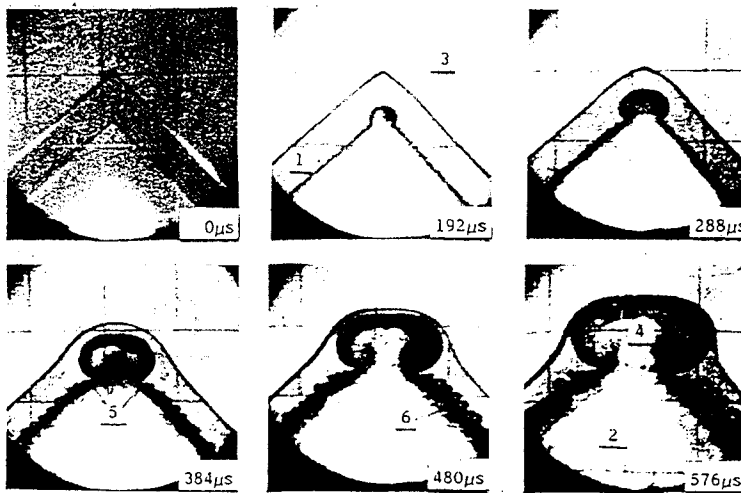


Figure 4: Explosive gas/jelly experiment. 2D turbulence model calculation.



Experimental photocronogram, $\beta=90^\circ$.
 1- accelerated layer, 2- explosion products, 3- air, -
 4- cavern, 5- new peculiarities, 6- turbulent layer.

Figure 5: Explosive gas/jelly experiment. Experimental results from reference 2.

The general features in the computer simulation agree well with the experiment. However, the displacement of the jelly layer (6) is greater in the calculation. This may be because of reduction in pressure due to vaporisation of the water. Alternatively, the difference may be due to inappropriate choices in the simulation for the initial pressure or the value of γ used for the explosive gas products. The calculated Rayleigh-Taylor instability penetration of the jelly layer (6) corresponds to $\alpha = 0.05$. This is less than observed.

AN IDEALISED ICF IMPLOSION

A test problem, taken from Town and Bell [5] is used to illustrate the application of the 2D turbulence model to an ICF implosion. The unperturbed initial spherical geometry which represents a DT/glass capsule at the end of the shell acceleration phase, is shown below.

TABLE 1. INITIAL GEOMETRY USED FOR THE IMPLOSION CALCULATION

Material	DT gas	Glass	Glass
Density (g/cc)	0.5	5	0.5
Outer Radius (μm)	130	190	300
Pressure (Mb)	20	20	20
Inward velocity (cm/ μs)	0	15	15

Realistic equations of state are used. A simple model is used for the thermal flux, $\underline{F} = -k\nabla T$ where k allows for both electron conduction and photon diffusion. Thermal smoothing reduces the density at the gas/shell interface from $\rho_1/\rho_2 \sim 10$ to $\rho_1/\rho_2 \sim 2$. This should give some reduction in the mixing predicted by the turbulence model. A two-dimensional axisymmetric implosion is obtained by perturbing the gas/glass interface at the beginning of the calculation. The perturbed radius is $r = r_0 + a_0 P_4(\cos \theta)$ where $r_0 = 130 \mu\text{m}$ and $a_0 = 0$ or $5 \mu\text{m}$.

The two-dimensional calculations used an (r, θ) spherical polar mesh with θ in the range 0° to 90° . The mesh in the radial direction moves with the mean (θ -averaged) fluid velocity, ie, a semi-Lagrangian calculation is performed. The number of meshes is 160 in the radial direction, 60 in the angular direction.

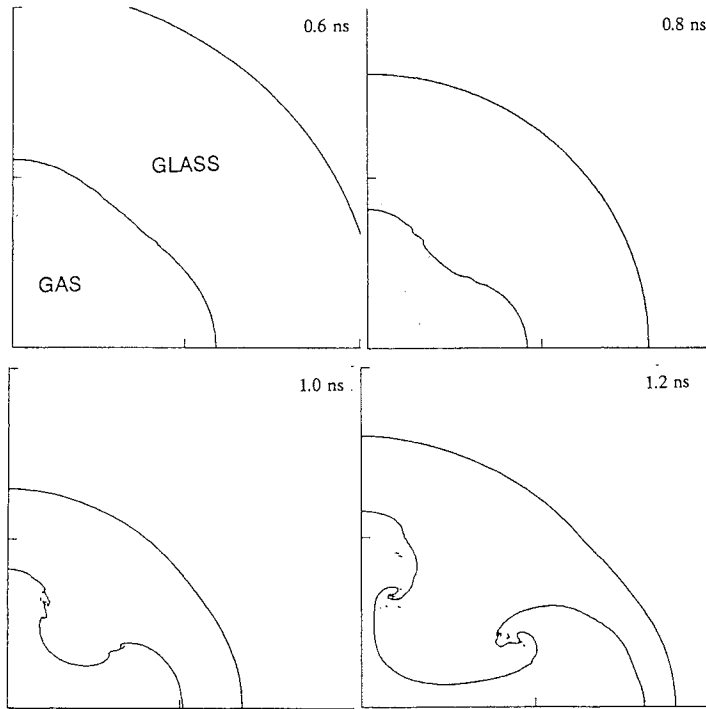


Figure 6: ICF implosion. Numerical simulation for the case $a_0 = 5 \mu\text{m}$, with interface tracking.

Figure 6 shows results for the case $a_0 = 5 \mu\text{m}$, with interface tracking at the gas/shell interface. Maximum compression of the gas occurs at about $t = 1.0$ ns. Calculations with the turbulence model activated at the gas/shell interface are shown in figure 7, for the cases $a_0 = 0$ and $a_0 = 5 \mu\text{m}$. With model coefficients adjusted to give a relatively low value of $\alpha = 0.05$, thin turbulent mixing layers are predicted.

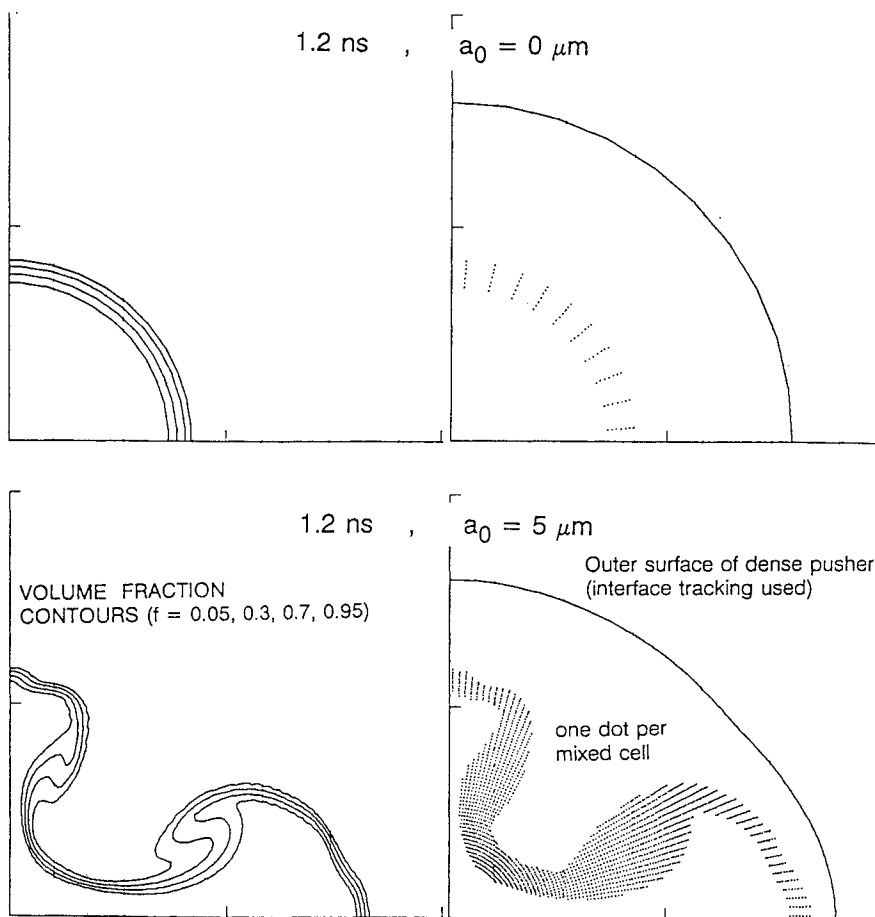


Figure 7: ICF implosion. 2D turbulence model calculations.

REFERENCES

1. D L Youngs: "Modelling turbulent mixing by Rayleigh-Taylor instability", Physica D37, p270 (1989)
2. V Rogatchov, I Zhidov, B Klopov, E Meshkov, A Tolshmyakov: "Non-stationary flows in the proximity of angular points of gas accelerated liquid layer". Proceedings of the 3rd IWCTM, Royaumont 1991
3. D L Youngs: "Direct three-dimensional numerical simulation of mixing by Rayleigh-Taylor instability", these proceedings
4. D L Youngs: "Time-dependent multi-material flow with large fluid distortion", in Numerical Methods for Fluid Dynamics, Eds, K W Morton and M J Baines, Academic Press (1982)

V

Laser-driven instability experiments

Effects of the surface finish on the hydrodynamic evolution of surfaces exposed to thermal radiation

A. CARUSO, V. A. PAIS

Associazione EURATOM - ENEA sulla Fusione
C.E. Frascati C.P. 65-00044 Frascati, Roma, Italia

ABSTRACT

2-D hydrodynamical simulations have been used to study the effects of surface finish on the evolution of planar analogs for the components of indirect driven ICF targets (cavity surfaces and capsules), when exposed to the same uniform, *assigned, temporally-profiled* thermal radiation bath. For the time dependence of the radiation temperature was assumed the one resulting from 1-D simulations of a high gain indirectly driven target. The perturbation wavelength has been taken in the interval $2.5\text{--}40\ \mu\text{m}$, as suggested by the typical lengths appearing in the 1-D hydrodynamic evolution. In this paper the results for the evolution of $300\ \text{\AA}$ initial perturbation amplitude will be presented, being the results obtained for other amplitudes (somewhat smaller or larger) qualitatively the same.

The results seem not very encouraging for the indirect drive approach, at least in the form presented in the current literature, as the simulations show the onset of fast growing hydrodynamical unstable modes, both on the capsule surface and on the cavity surface, producing dramatic effects on symmetry, energy absorption and ablation rate.

With regard to the (gold) cavity surface, for the shortest wavelengths the evolution enters in the non-linear phase in the early stages of the interaction, producing an increase in the absorbed energy by a factor as large as 10, due to surface area increase and thermal field rippling.

Similar results are obtained for the capsule surface at short wavelengths. In this case, in addition to an enhancement of the ablation rate and energy absorption, the flow behind the first shock wave turns-out to be turbulent, with "eddies" having typical products of *angular velocity* \times *time* of the order of the unity or greater.

The situation is not encouraging even for longer wavelengths; in this case, in addition to the generation of eddies in the fuel, the flow exhibits a transverse matter piling-up with consequent generation of holes in the thermal shield and premature fuel preheating.

For the tested wavelengths stabilization mechanisms due to ablative polishing, finite gradient or overpressure result to be ineffectual.

INTRODUCTION

Short wavelength stability studies with respect to imperfect surface finish of ICF targets have been performed by 2-D hydrodynamical simulations. The planar analog of a high gain target discussed in previous papers (Caruso 1988, Caruso & Pais 1988, Caruso & Pais 1992, Caruso & Pais 1992a) has been used (see Fig. 1). The choice of a planar analog is in this case justified by two circumstances:

- a) the perturbation wavelengths are assumed much smaller than the target radius;
- b) the phenomena of interest evolve in a time so short, that matter has no time to displace as a whole over a significant fraction of the target radius.

The planar analog described in Fig.1 corresponds to a capsule formed by a 85-mgr solid aluminium shell with a 4-mgr internal layer of frozen equimolar deuterium-tritium mix, the most external radius being 0.462 cm.

The corresponding cavity results formed by the inner surface of a spherical gold shell with internal radius twice the capsule radius. Thickness and structure of the shell are minor relevant parameters for the stability studies, on condition that the entire gold layer be not fully involved in the motion.

The "capsule" and "cavity" perturbed surfaces have been exposed to a thermal radiation field characterized by a temperature T_r depending on the time t as

$$T_r = \frac{0.03}{1 - \frac{t_{ns}}{27}} \text{ keV, for } t \leq t_{\max} = 25 \text{ ns;} \quad (1)$$

for $t = 25$ ns the maximum radiation temperature (≈ 0.4 keV) is achieved. Eq. 1 is a good approximation for the temperature dependence obtained in the previously quoted, 1-D, high gain, target simulations (Caruso & Pais 1988, Caruso & Pais 1992, Caruso & Pais 1992a).

With regard to the choice of *assigning* the thermal radiation temperature instead of the injected power, we note that in the framework of this model the absorbed power could, in principle, increase without limit as a result of a corresponding area or local thermal gradient growth. This point will be treated later, in the section "Conclusions".

A cartesian framework (X,Y) was chosen with the X -axis playing the role of the outward radial direction and the Y -axis that of an azimuthal coordinate, parallel to the interfaces. The zoning used in the 2-D calculations

was formed by 90 cells in the X -direction and 40 cells/wavelength in the Y -direction.

The perturbation has been introduced by keeping the density unmodified and displacing the cells vertexes position (X, Y) by a small amount ξ given by the harmonic field:

$$\xi_X = \xi_o e^{-k|X-X_o|} \cos(k Y), \quad \xi_Y = -\xi_o e^{-k|X-X_o|} \sin(k Y) \quad (2)$$

where X_o ($= 0.462$ cm for the capsule and 0.924 cm for the cavity) is the initial unperturbed external surface position. With this choice, strong mass differences between adjacent cells are avoided (as $\nabla \cdot \xi = 0$).

We have considered perturbations having wavelengths ($\lambda = 2\pi/k$) of the same order of magnitude as a characteristic scale-length of the compressed accelerated material ($\approx 10 \mu\text{m}$) (Caruso & Pais 1988, Caruso & Pais 1992, Caruso & Pais 1992a). Five cases have been processed with different λ ($2.5, 5, 10, 20, 40 \mu\text{m}$). Several values of initial amplitudes (ξ_o) have been tested (from 100 to 10000 \AA); in this paper we shall limit to present the cases for $\xi_o = 300 \text{ \AA}$ (corresponding to an "optical" finish or better), being sufficiently representative for the physical processes involved.

RESULTS

The temporal evolution in all the cases has been found to be characterized by a strong hydrodynamical instability on both the cavity and capsule surfaces.

Effects of the instability are an increase of the ablating surface area ("area effect") and a change in the power absorbed per unit area due to the thermal gradients local modification ("ripple effect"). A sensible overall measure for both, the "ripple effect" and the "area effect", are the substantial increase in the ablation rate and in the absorbed energy, when compared to the unperturbed case (up to a factor 10 for the cavity and for the capsule).

In the two plots of Fig. 2, one for the capsule and one for the cavity, the absorbed energy (E_a) is represented versus the "one-directional free streaming energy" defined as

$$E_s = \int_0^t c U dt \quad (3)$$

where c is the light speed and U the radiation energy density in the thermal bath, computed by using the temperature given by Eq. (1) ($U = 4\sigma T^4$, σ being the Stefan-Boltzmann constant). Henceforth E_s will be often used in place of t in several figures.

From this plots, we observe a decrease of E_a when the wavelength increases, with its slope ultimately saturating to that of the unperturbed case. The effective average absorbed power density, F_a , can be expressed as

$$F_a = \frac{P_\lambda}{\lambda} = \beta A_{eff} F_{unp} \tag{4}$$

where P_λ is the power absorbed over a wavelength λ , F_{unp} is the power density evaluated for the unperturbed case (1-D calculations in Caruso & Pais 1988, Caruso & Pais 1992 and Caruso & Pais 1992a), A_{eff} is the computed area ratio at the ablation front

$$A_{eff} = \frac{1}{\lambda} \int_0^\lambda \frac{ds}{dY} dY, \quad ds = \sqrt{dX^2 + dY^2} \tag{5}$$

and β takes into account for the remaining "ripple effect". The evolution of β and A_{eff} is represented in Fig. 3 for the capsule (Al) and for the cavity (Au). It is apparent the complementary behaviour of β and A_{eff} . Typically the factor β starts deviating from unity when $k\xi \geq 0.1$, reaches a maximum and then decreases to unity when the spectrum of the surface distortion becomes rich in harmonics. The area factor A_{eff} starts also deviating from unit when $k\xi \geq 0.1$ but, in the explored field, maintains an increasing, nearly monotonic character sufficient to make the product βA_{eff} a substantially non decreasing quantity.

With regard to the detailed flow structure, two different kind of evolutions have been identified, appearing preferably for the two ranges of perturbation wavelengths, short and long.

For small wavelengths the non linear growth generates a chain of decay processes in which harmonics at a half of the wavelengths are produced, whereas the amplitudes saturates (Fig. 4 for the capsule and Fig. 5 for the cavity); as a consequence, the motion behind the first shock wave becomes turbulent and the symmetry is lost. This is seen in the 2-D map (Fig. 6) for the local angular velocity perpendicular to the plane, defined as

$$\Omega = \frac{1}{2} \nabla \times V \tag{6}$$

where V is the flow velocity.

For the short wavelengths considered in this study stabilization mechanisms due to ablative polishing (Takabe et al. 1985), finite gradient (Lindl 1988) or overpressure (Nuckolls et al. 1972) are ineffectual both for the cavity and the capsule. The case of the ablative overpressure stabilization should arise as result of a fractional increase of the thermal flux on the ripples maxima, this being estimated of the order of $k\xi$. Actually violent overpressure effects are observed when ξ is already of the order of λ , the main result being the transformation of the maximum in a minimum and the generation of harmonics of the initial k .

For long wavelengths, the penetration of a thermal radiation wave into the fluid may occur before the end of the temperature pulse. The process of the premature fuel preheating, by holes formation in the shield, is due to two concurrent effects. One of these is the enhancement of the ablation process related to the increase of A_{eff} and β . The other effect, contributing to the formation of holes, is due to the important transverse motion and matter piling-up induced in the shield by the non linear growth of the instability (Figs. 7 and 8); when this happens, a substantial deformation of the DT-Al interface occurs. With regard to the evolution of Ω (see Fig. 11), it may be interesting to point-out that, as in adiabatic flows Ω is frozen in the matter, a further increase of Ω has to be expected in all the compression stages of the flow evolution (say $\Omega \propto \rho^{2/3}$).

CONCLUSIONS

In conclusion, the behaviour of material surfaces exposed to time-taylored T - radiation pulses, as that given by the Eq. 1, may be very different from the one predicted in 1-D calculations. Enhanced radiation absorption and loss of symmetry may render useless the 1-D based designs of high gain radiation driven targets.

As noted in the introduction, the model adopted here, based on an assigned time dependent temperature at the system boundary, may allow an unlimited energy absorption as result of area increase and "ripple effect". It is however reasonable to expect that, when instability enhanced absorption occurs to such a level to make the confinement parameter (Caruso 1988) of the order of unity, the ablation process will adjust in such a way to make consistent this value with the injected external power.

REFERENCES

Caruso, A. 1988, "High Gain Radiation-Driven Targets (I)", Proceedings of the International School of Plasma Physics "Pietro Caldirola" on Inertial Confinement Fusion, Varenna (Italy) 6-16 September 1988, edited by A. Caruso and E. Sindoni.

Caruso, A. & Pais, V. A. 1988, "High Gain Radiation-Driven Targets (II)", Proceedings of the International School of Plasma Physics "Pietro Caldirola" on Inertial Confinement Fusion, Varenna (Italy) 6-16 September 1988, edited by A. Caruso and E. Sindoni.

Caruso, A. & Pais, V. A. 1992, "Effect of surface finish on the stability of targets imploded by thermal radiation", Proceedings of the Japan-US Seminar on Physics of High Power Laser Matter Interactions, Kyoto (Japan), March 1992, in press.

Caruso, A. & Pais, V. A. 1992a, "Effect of surface finish on the stability of targets imploded by thermal radiation", *Laser and Particle Beams*, in press.

Lindl, J. 1988, "Introduction to the physics of ICF capsules", Proceedings of the International School of Plasma Physics "Pietro Caldirola" on Inertial Confinement Fusion, Varenna (Italy) 6-16 September 1988, edited by A. Caruso and E. Sindoni.

Nuckolls, J. et al. 1972 *Nature*, **239**, 139

Takabe, H. et al. 1985 *Phys. Fluid* **28**, 3676

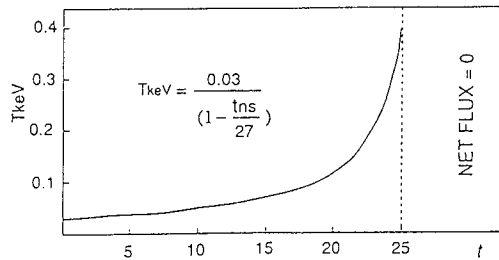
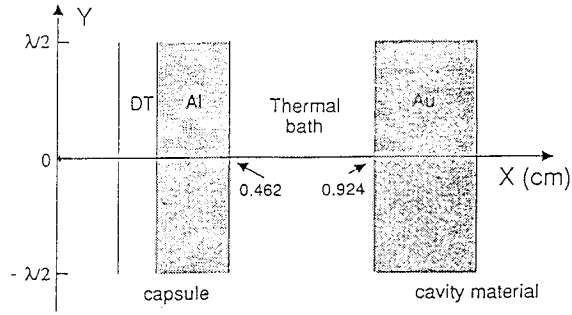


Figure 1: The planar analog for an indirectly driven, high gain thermonuclear target used in the numerical simulations.

$$\xi_0 = 300 \text{ \AA}$$

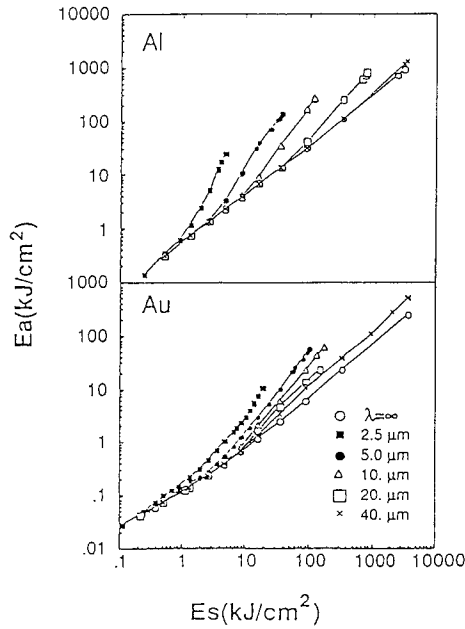


Figure 2: Absorbed energy on capsule (Al) and cavity surfaces (Au) versus the "free streaming energy" E_s (see Eq. 3), for different wavelengths.

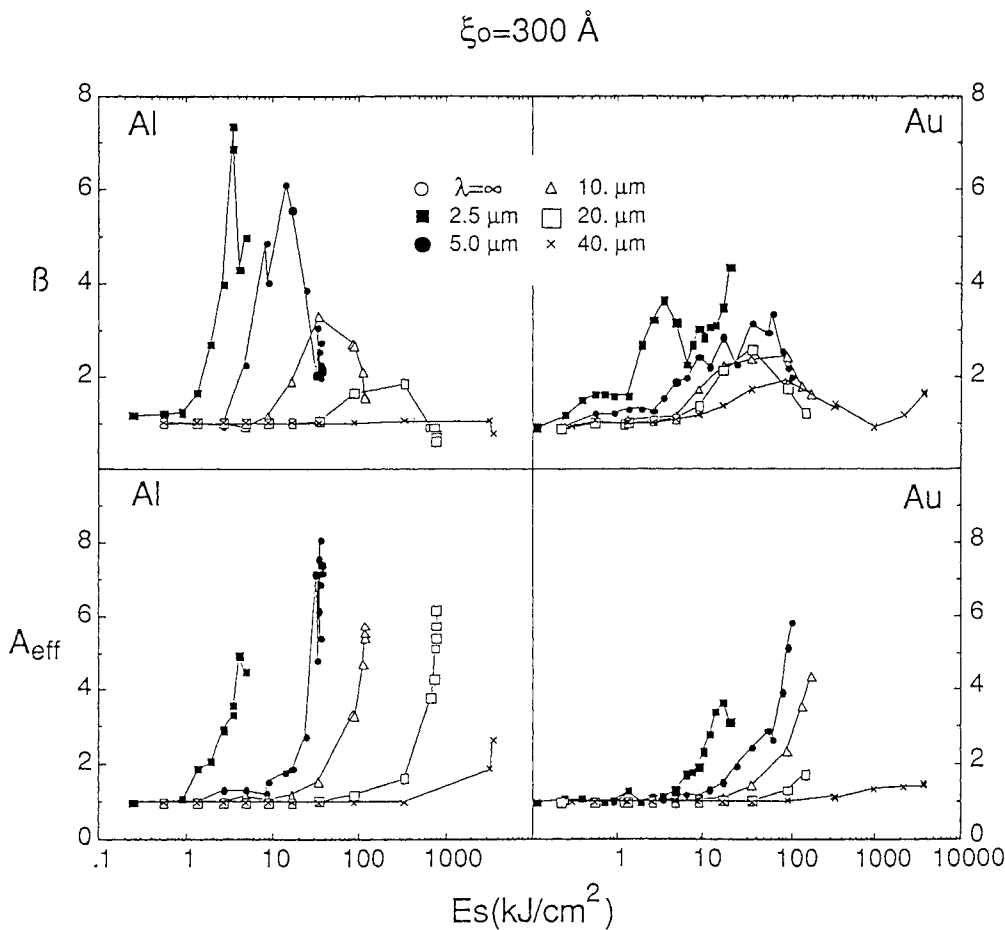


Figure 3: Behaviour of the "ripple factor", β , and of the computed area ratio, A_{eff} (Eqs. 4 and 5), as a function of the "free streaming energy" E_s , for different wavelengths, on the capsule (Al) and cavity surfaces (Au).

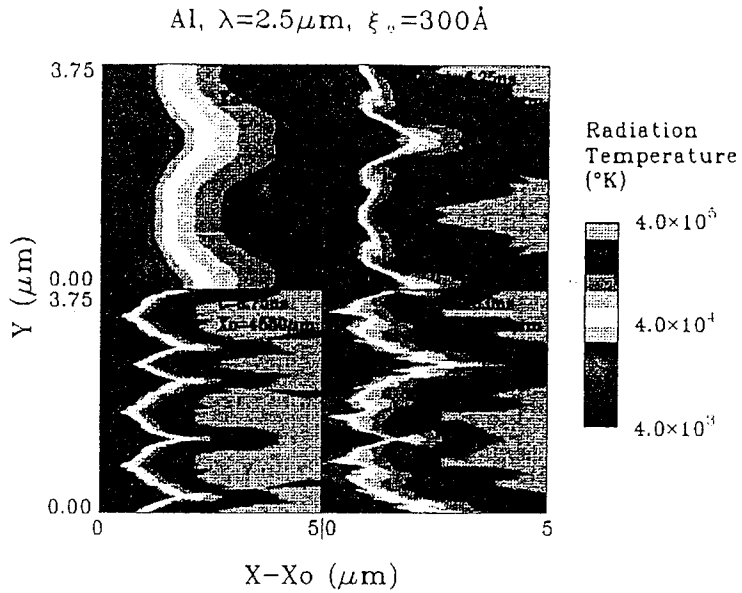


Figure 4: Ablation front evolution on the capsule (Al). 2-D maps of the radiation temperature at four different instants (t). Initial amplitude $\xi_o=300\text{\AA}$ and wavelength $\lambda=2.5\mu\text{m}$.

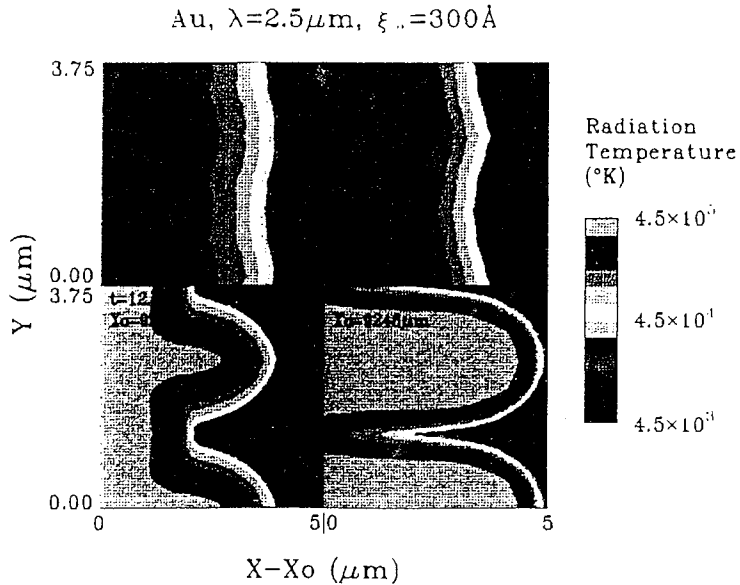


Figure 5: Ablation front evolution on the cavity surface (Au). 2-D maps of the radiation temperature at four different instants (t). Initial amplitude $\xi_o=300\text{\AA}$ and wavelength $\lambda=2.5\mu\text{m}$.

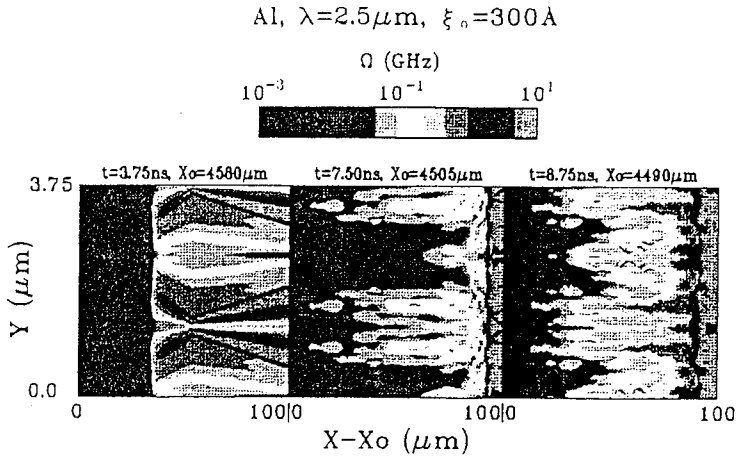


Figure 6: 2-D maps for the local angular velocity, Ω (Eq. 6), at three different instants (t) of the capsule evolution. Initial amplitude $\xi_o = 300 \text{ \AA}$ and wavelength $\lambda = 2.5 \mu\text{m}$. The dashed line indicates the DT-Al interface.

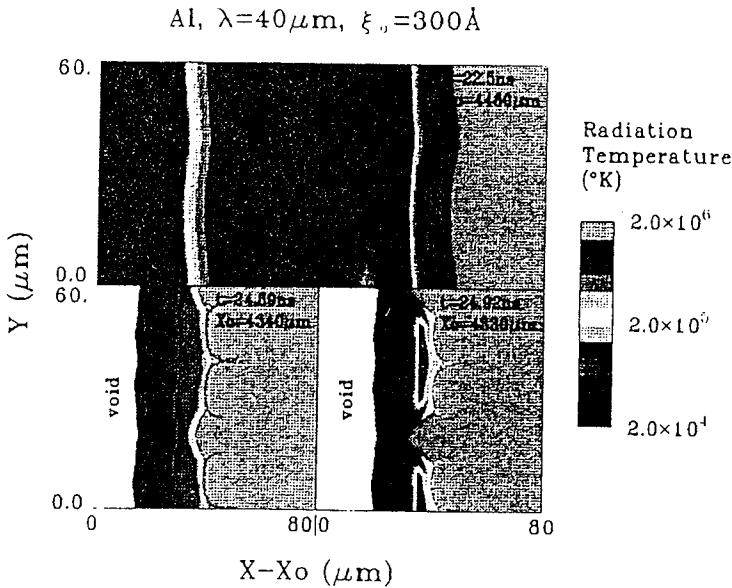


Figure 7: Ablation front and dense phase evolution for the capsule (Al). 2-D maps of the radiation temperature at four different instants (t). Initial amplitude $\xi_o = 300 \text{ \AA}$ and wavelength $\lambda = 40. \mu\text{m}$. The dashed lines indicate the void-DT and the DT-Al interfaces.

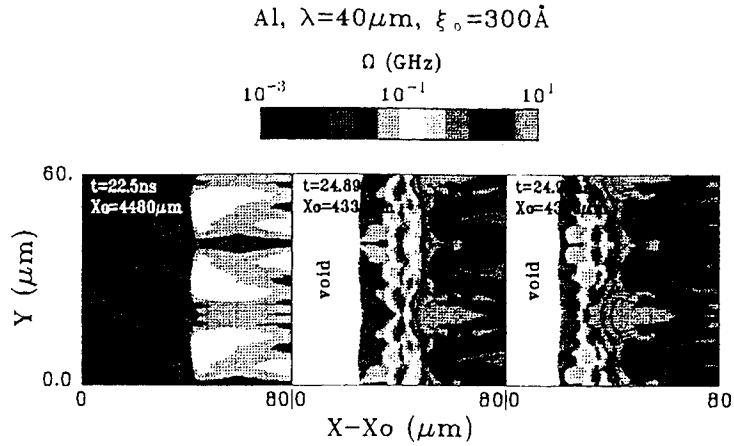


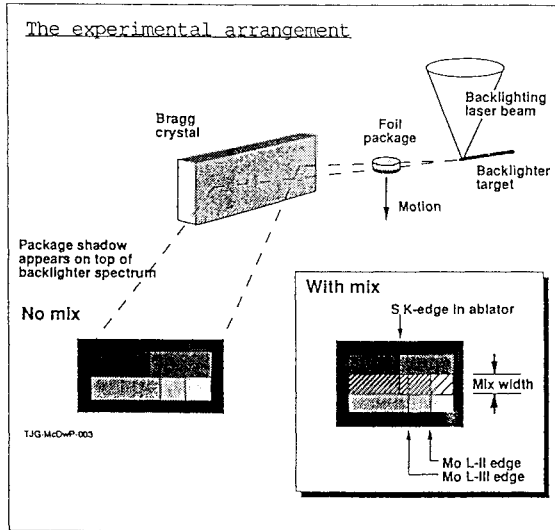
Figure 8: 2-D maps for the local angular velocity (Eq. 6) at three different instants (t). Initial amplitude $\xi_o = 300 \text{ \AA}$ and wavelength $\lambda = 40 \mu\text{m}$. The dashed lines indicate the void-DT and the DT-Al interfaces.

The AWE/LLNL NOVA Planar Foil Mix Experiment
Comparison With Calculation

N W Cowperthwaite, T J Goldsack, D L Youngs
 AWE Aldermaston, Reading RG7 4PR, England

Results of the NOVA Planar Foil Mix Experiment were presented at the 1991 Royaumont workshop. In this paper we present further comparisons between experiment and calculation. In particular, we present results of explicit 2D calculations, together with results from 1D mix models.

THE EXPERIMENTAL TECHNIQUE



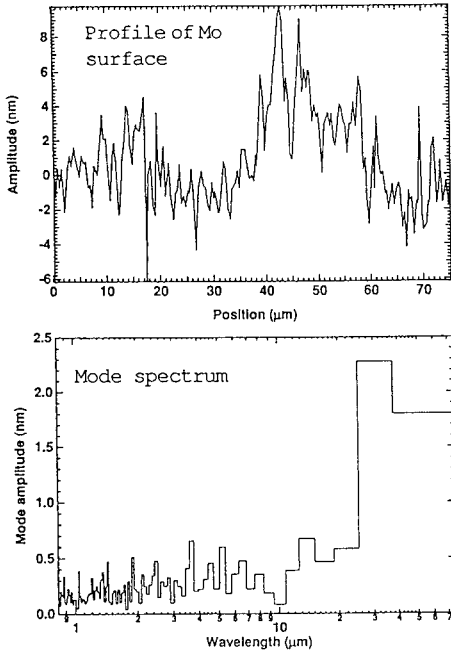
The experimental technique and the results were described at the 1991 Royaumont Compressible Turbulent Mixing Workshop¹ and are only briefly summarised here.

A two-layer sample, consisting of a poly(phenylene sulphide) ablator ($\rho = 1.36 \text{ g cm}^{-3}$) and a Mo payload ($\rho = 10.22 \text{ g cm}^{-3}$), was accelerated by indirect drive. Later, at between 4 and 9 nsec, the accelerated package was diagnosed by simple time-integrated point-projection spectroscopy, using a $\sim 200\text{ps}$ FWHM 3ω Gaussian pulse onto a Pt/Au/Bi mixture coated on a $22\mu\text{m}$ diameter Cu wire. The shadow of the package was recorded with Kodak Industrex-C film, giving spatial information in the direction of motion, and both spectral and spatial information in the perpendicular direction.

Spatial overlap of the S K-edge and Mo L-edges quantifies the mix after image analysis.

¹ T.J.Goldsack, J.C.V.Hansom, N.W.Cowperthwaite, (AWE); J.D.Molitoris (LLNL); *The AWE/LLNL Planar Foil Mix Experiment*, Proceedings of the 3rd International Workshop on the Physics of Compressible Turbulent Mixing, Royaumont, France, 1991

INTERFACE PROFILE

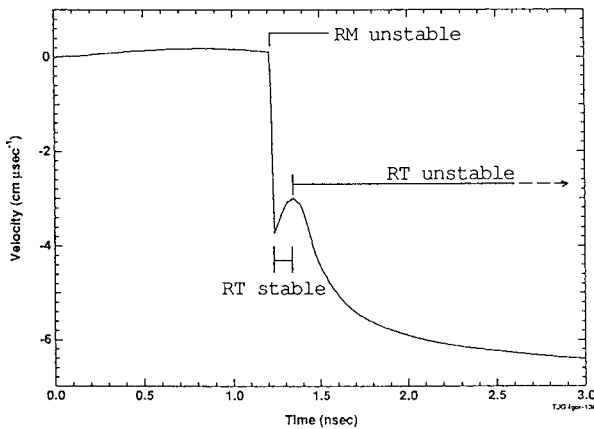


The molybdenum (high-atwood-number) or poly-chlorostyrene (low-atwood-number) payload was deposited onto the poly(phenylene sulphide) ablator by ion-beam sputtering. The interface was inaccessible, and so its profile could not be measured. The shape of the outer surface of the Mo or PCS was assumed to show a very similar shape to the interface, and so the profile of the outer surface was measured with a laser-interferometric microscope with $\sim 0.5 \mu\text{m}$ spatial resolution and about 0.2 nm vertical resolution.

A typical lineout is shown (left, top), together with the resulting mode spectrum (left, bottom). Precise details varied across and between samples, but the mode spectrum shown here is typical.

One uncertainty in the experiment is that the interface shape may be influenced by preheat before the shock reaches it.

INTERFACE DYNAMICS



The velocity of the interface from a 1-d simulation.

The interface first experiences a weak acceleration towards the laser, caused by pre-heat expansion of the Mo payload. Then, at about 1.2 ns in this calculation, the shock from the laser drive reaches the interface, causing a rapid acceleration to $4 \times 10^6 \text{ cm sec}^{-1}$. Richtmyer-Meshkov growth¹ is possible at this time. Following this, the interface once more experiences a slight acceleration towards the laser, caused this time by the decay of the pressure behind the shock, during which time the interface is RT stable. At around 1.25 ns the shock breaks out of the rear side of the Mo payload, causing a rarefaction wave to run back into the Mo, reaching the interface at about 1.3 ns. This accelerates the interface away from the laser once more, leading to Rayleigh-Taylor² growth.

1 R.D.Richtmyer, *Taylor Instability in shock acceleration of compressible fluids*, Comm. Pure. Appl. Math., 13, pp 297-319 (1960); E.E.Meshkov, *Instability of the interface of two gases accelerated by a shock wave*, Izv. AN SSSR, Mekhanika Zhidkosti i Gaza, 4, 3, pp151-157 (1969)
 2 Lord Rayleigh (Stuart), *Investigation of the character of the equilibrium of an incompressible heavy fluid of variable density*, Scientific Papers, 11, pp 200-207, Cambridge, 1900; G.I.Taylor, *The instability of liquid surfaces when accelerated in a direction perpendicular to their planes. I*, Proc. Roy. Soc. A, 201, (1950)

PASSIVE MIX MODEL EQUATIONS

The AWE passive mix model¹² solves two non linear inhomogeneous second order ordinary differential equations for h_1 and h_2 where h_i is the mix penetration of a fluid of density ρ_i .

$$\frac{d^2 h_i}{dt^2} = A \frac{1 - E_i}{1 + E_i} g_i - \frac{C_D f_i(\rho_1, \rho_2)}{(1 + E_i) R} \frac{dh_i}{dt} \left| \frac{dh_i}{dt} \right|$$

$$E_i = \exp\left(-\frac{4\beta_1 h_i}{\lambda_0}\right) \quad R = \max\left(\min(h_1, h_2), \frac{C_D \lambda_0}{2\beta_1}\right) \quad f_i(\rho_1, \rho_2) = \begin{cases} 1 & \text{if } \rho_i > \rho_{3-i} \\ \sqrt{\rho_i / \rho_{3-i}} & \text{if } \rho_i < \rho_{3-i} \end{cases}$$

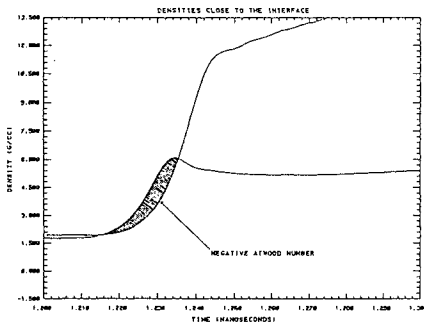
$\beta_1 = 3.83171 =$ first zero of Bessel Function J_1

For an incompressible problem with constant g and $h \gg \lambda_0$ the model gives the correct $\alpha g t^2$ law for the bubble penetration. The measured³ growth rate of $\alpha = 0.06$ is given by $C_D = 3.667$.

¹²D L Youngs, Unpublished Paper

³J C V Hanson, PA Rosen, T J Goldsack, K Oades, P Fieldhouse, N Cowperthwaite, D L Youngs, N Mawhinney, A J Baxter, "Radiation Driven Planar Foil Instability and Mix Experiments at the AWE HELEN Laser", *Laser and Particle Beams*, vol 8, pp 51-71 (1990)

³V S Smeeton, D L Youngs, "Experimental investigation of Turbulent Mixing by Rayleigh-Taylor Instability, Part 3", AWE Report 0-35/87 (1988)



NUMERICAL INTEGRATION PROBLEMS

Solving the passive mix model equations is generally straightforward, but if the calculation involves shock accelerations then the smearing out of the shock by the artificial viscous pressure can lead to spurious results. For the problem under consideration the PPS is compressed before the M_0 , leading to a non-physical reversal of the density gradient as shown to the left. This makes the results unsound and very mesh dependant, the mix width in one case being reduced from 46.4 μm to 8.2 μm at 8 ns by a halving of the cell size.

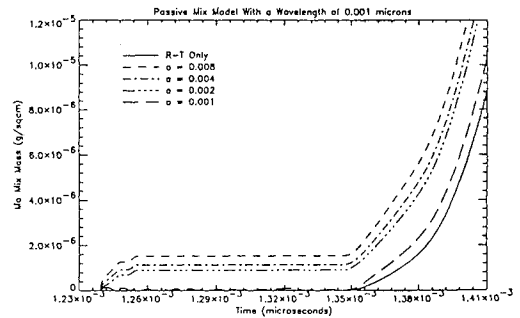
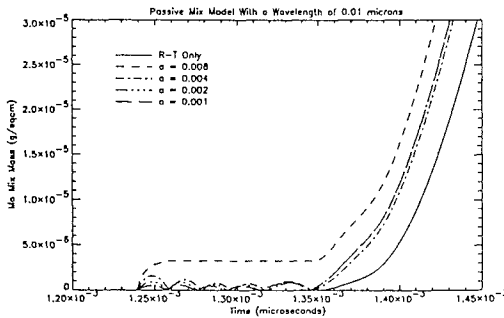
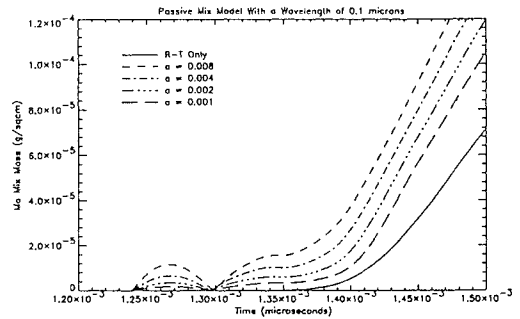
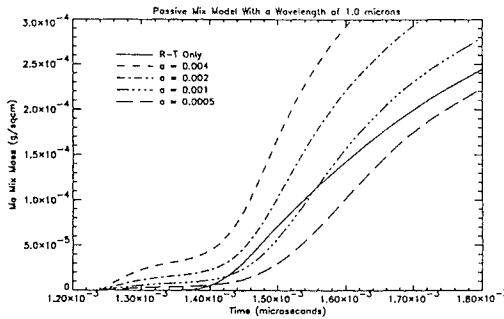
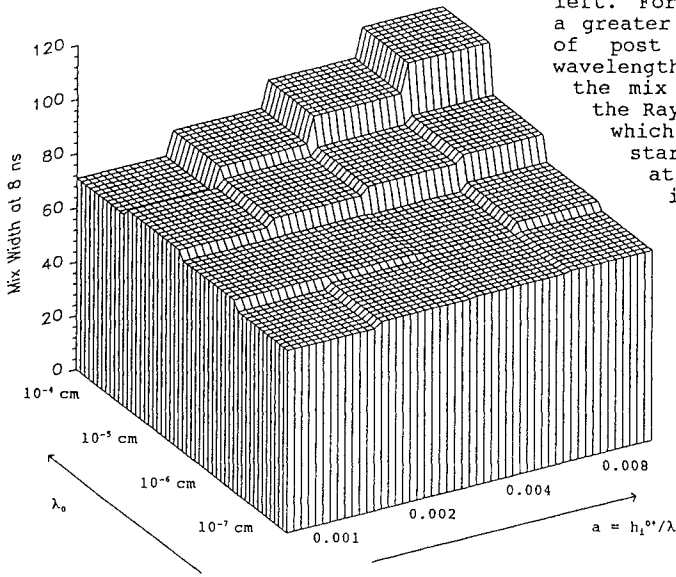
If a delta function acceleration (an idealised shock) is fed into the passive mix equations then the solution obtained in the linear regime ($h \ll \lambda_0$) is the Richtmyer formula adapted to cylindrical bubble growth.

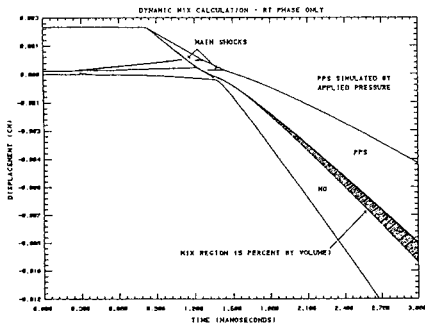
$$\frac{dh_i}{dt} = 2\beta_1 A \Delta u \frac{h_i^{0*}}{\lambda_0} = 2\beta_1 A \Delta u$$

For the passive mix calculations described here this formula was used to obtain the growth of the mix region immediately after the passage of the main shock, thus avoiding the problem described above. For the main shock in the laser target the velocity change is $\Delta u = 3.86 \text{ cm}/\mu\text{s}$ and the post shock Atwood number is $A = 0.311$.

PASSIVE MIX MODEL RESULTS

The variation of the mix width with surface finish is shown to the left. For longer wavelengths there is a greater dependence on a , the ratio of post shock amplitude to the wavelength. For shorter wavelengths the mix is due almost entirely to the Rayleigh-Taylor unstable phase which begins at 1.35 ns. By starting the passive mix model at this time with a very low initial perturbation the effect of just the Rayleigh-Taylor unstable phase can be calculated, giving a mix width at 8 ns of 66.44 μm . The foil mix mass from this calculation is compared with the calculations that included the Richtmyer-Meshkov component, at early time, on the right.



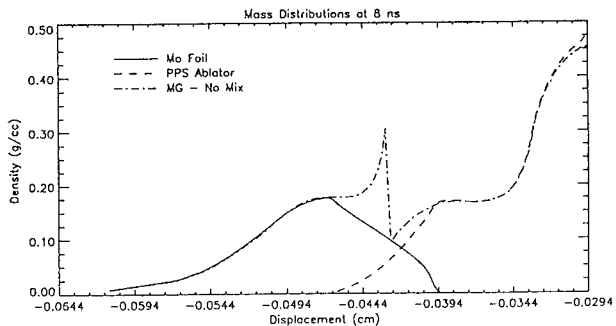


Since the dynamic mix model is incompatible with multigroup diffusion the hottest part of the PPS was not calculated directly, but was instead simulated by a time dependant boundary pressure taken from a multigroup calculation. The error resulting from this is small, as can be seen from the plot on the right.

DYNAMIC MIX MODEL RESULTS

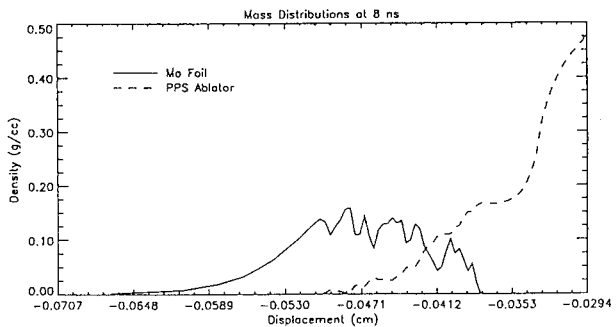
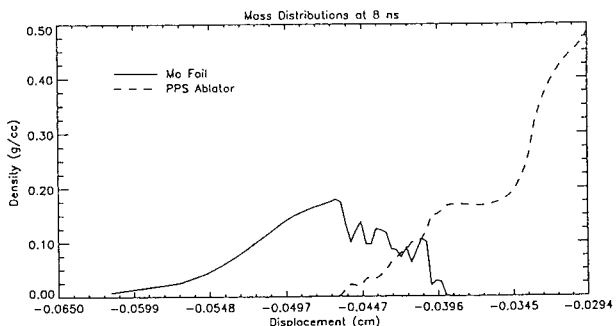
The mixing due to the Rayleigh-Taylor phase can be calculated using the AWE dynamic mix model¹. This gives a mix width (5% by volume) of 64.64 μm at 8 ns, in very good agreement with the passive mix model. Starting the dynamic mix calculation before the main shock accelerates the interface adds another 5 to 10 μm to the mix width, however this is probably mesh dependant.

¹D L Youngs, "Modelling Turbulent Mixing by Rayleigh-Taylor Instability", Physica D 37, pp 270-287 (1989)

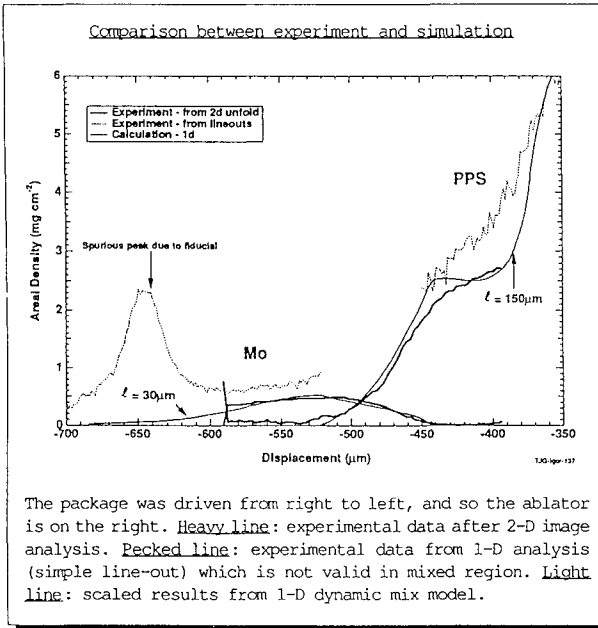


2D CALCULATION RESULTS

The growth of the mix region has been calculated using a 2D Eulerian code to simulate a 10 μm wide slice of the target. The Mo/PPS interface was perturbed by a Fourier series of 20 modes with a root mean square amplitude of 0.01 μm . The plot to the top right shows the effect of perturbing the interface after the shock passage so that only the Rayleigh-Taylor mix was calculated, whilst the mix distribution shown in the plot on the bottom right includes the effect of the Richtmyer-Meshkov mix. The mix widths (5% by volume) from these calculations are 59.68 μm and 117.15 μm respectively. As with the dynamic mix model, these calculations used a time dependant boundary pressure.



COMPARISON WITH EXPERIMENTAL RESULTS



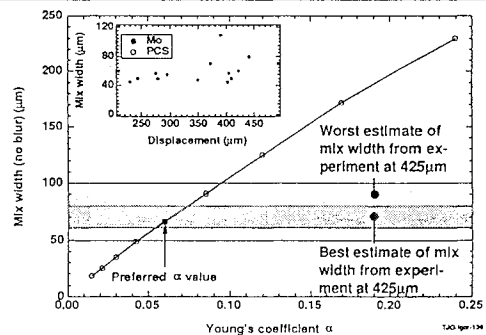
Here we compare the results of the 1-D dynamic mix model with experimental data from shot Mix 46. The experimental data were unfolded by a 2-D iterative method and show areal density (ρr) as a function of displacement.

The 1-D simulation gives density as a function of position and so in order to compare with the experimentally-measured ρr a line-of-sight distance had to be chosen. This was taken to be 30 μm in the Mo payload and 150 μm in the PPS ablator so as to normalise the peak heights. In addition, the calculated displacements were increased by 12% in order to match the observed displacements; this is a measure of the uncertainty of the drive.

Good agreement between experiment and calculation is seen.

CONCLUSIONS

- Care had to be taken when mix due to Richtmyer-Meshkov instability growth was calculated. The numerical treatment of the shock caused spurious results until it was replaced by an analytical treatment of the shock transit across the interface. It is possible that similar problems may be encountered with other mix models and also with implicit 2D and 3D hydrocode calculations.
- For the laser-driven experiments considered here, we found that the mix was caused almost entirely by Rayleigh-Taylor instability growth. This was because:
 - the interface was smooth and so the Richtmyer-Meshkov growth from the passage of the shock was small, and
 - the decaying pressure behind the shock led to a period of interface stability which restricted further growth until the rarefaction wave from the free surface reached the interface.
- Comparison of calculated density profiles, and hence mix widths, with the experimental data shows good agreement when the peak heights are normalised to those observed. Since the calculated mix width at late time varies linearly with Young's coefficient α (see sheet 5), as can be seen from the graph below, we can infer from this comparison that the value of α used (0.06) is correct to within a factor of two.



Richtmyer-Meshkov Experiments on Nova at High Compression



Guy Dimonte
Bruce Remington
Eric Frerking

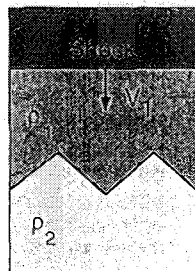
Lawrence Livermore National Laboratory

4th International Workshop on Physics of Compressible Turbulent Mixing
Cambridge, England
March 29 - April 1, 1993

Investigate Richtmyer-Meshkov Instability at Interface Between Two Fluids at High Compression



- High compression achieved with
 - Nova Laser
 - Foam Tamper $\rho_2 \sim 0.12$ g/cc
- Seed perturbations at interface
 - Control experiment and parameters
- Issues to investigate in planar geometry
 - Growth of single modes
 - Test linear theory and simulation codes
 - Multi-mode or turbulent mix



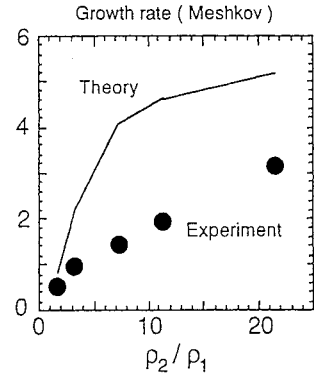
$$A = \frac{\rho_2 - \rho_1}{\rho_2 + \rho_1}$$

Why Study Richtmyer-Meshkov Instability on Nova ?

Linear growth in shock tubes disagrees with theory and simulations

$$\frac{d\eta}{dt} \sim A^* k U \begin{cases} \eta_0^* & A > 0 \\ \frac{\eta_0 + \eta_0^*}{2} & A < 0 \end{cases}$$

$$\eta_0^* \sim \eta_0 (1 - U/V_1)$$

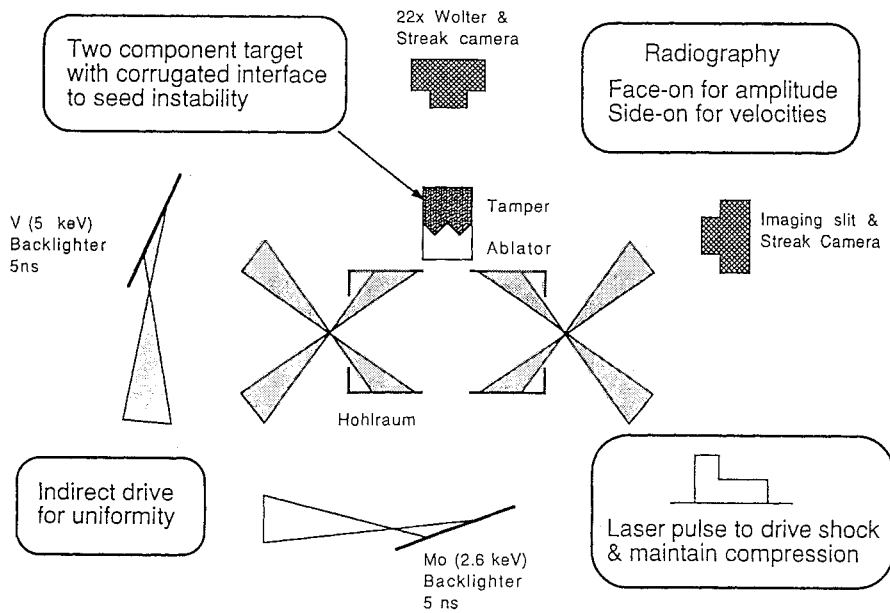


Large compression provides sensitive test

$$\eta_0^* \ll \eta_0$$

$$A^* \neq A$$

Configuration of Nova Richtmyer-Meshkov Experiment



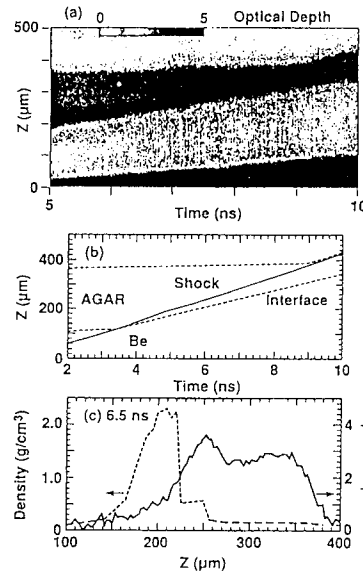
Transverse Radiograph Measures Shock Characteristics



	Be Ablator	Foam Tamper
Initial Density (g/cc)	1.7	.115
Shocked Density (g/cc)	2.2	.4 - .5
Shock Speed ($\mu\text{m/ns}$)	40	46

Interface velocity $\sim 35 \mu\text{m/ns}$

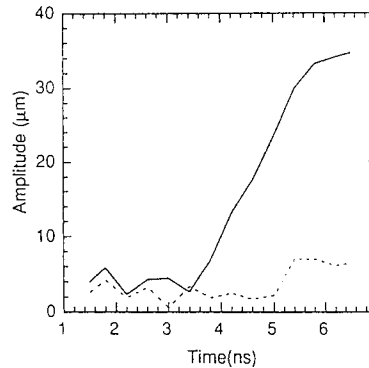
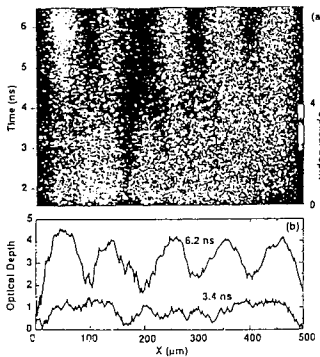
Compression = $1 - U/V_1 \sim 1/8$



Face-on Radiograph Measures Instability Growth



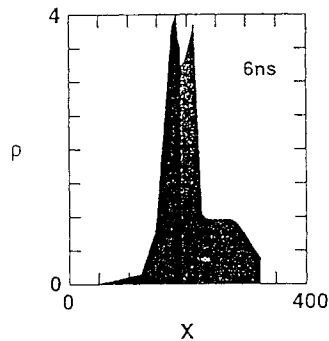
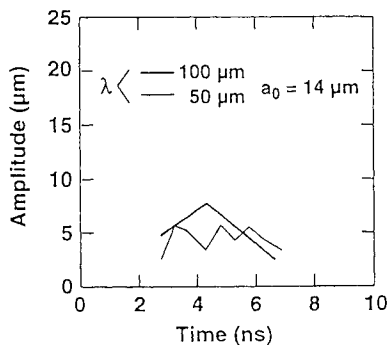
$U \sim 35 \mu\text{m/ns}$, $V_1 \sim 40 \mu\text{m/ns}$, $\lambda = 100 \mu\text{m}$, $\eta_0 = 14 \mu\text{m}$



Growth rate: $d\eta/dt \sim 11 \mu\text{m/ns}$
 Saturation: $\eta_{\text{sat}} \sim 35 \mu\text{m} \sim \lambda/3$

Differential compression can stabilize R-M instability

- Be/CH target – CH compressed more than Be
- Atwood No. reduced from $A_0 \sim 0.3$ to $A \leq 0.05$



L003-U-20787-02

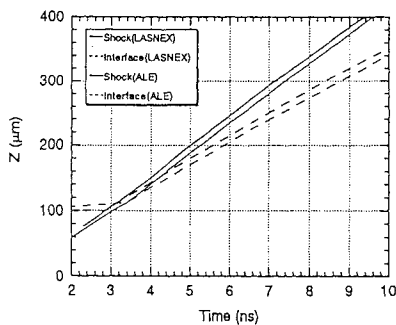
Simulate Experiments with Radiation and Hydrodynamics Codes

LASNEX calculates radiation coupling

- One dimension
- Input radiation drive
- Output pressure profile

ALE calculates hydrodynamic instability

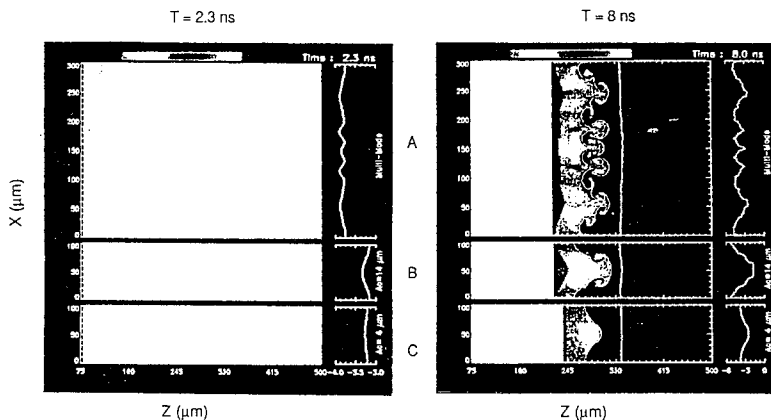
- Two dimensions
- Input pressure in stationary zone
- Output face-on & side-on "radiographs"



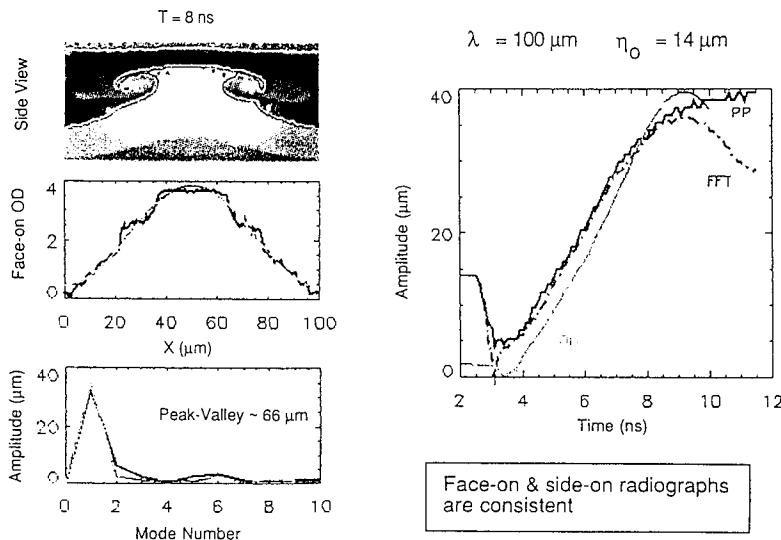
ALE Calculates Hydrodynamic Evolution of Single - mode and Multi - mode Interfacial Perturbations



	A) 10 Mode	B) Single mode	C) Single mode
λ (μm)	30-300	100	100
η_0 (μm)	0-5	14	4



ALE Code "Radiographs" are Fourier Analyzed for Spectral Evolution



V

Investigate Approach to Turbulence with Complex Initial Interfacial Perturbations



Initial spectrum with 10 modes

$$\lambda_n = 300 \mu\text{m} / n$$

$$\eta_{\text{rms}} = 3 \mu\text{m}$$

$$\text{Peak-Valley} = 22 \mu\text{m}$$

Modes saturate when $\eta \lambda \sim .15 \lambda$

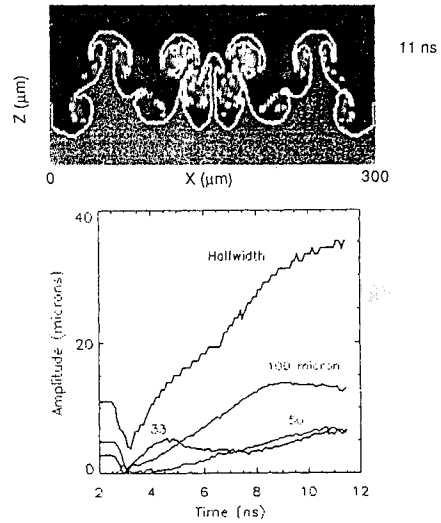
$$\text{Peak-Valley} \sim 70 \mu\text{m}$$

Mode coupling predicted

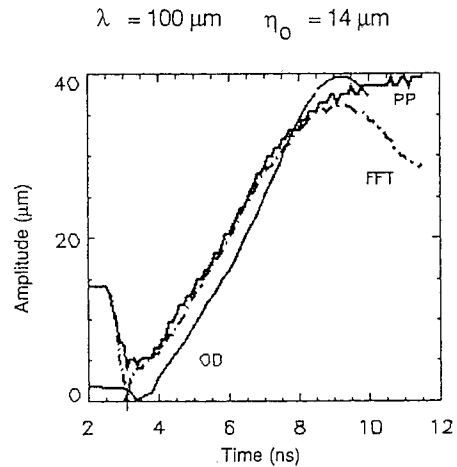
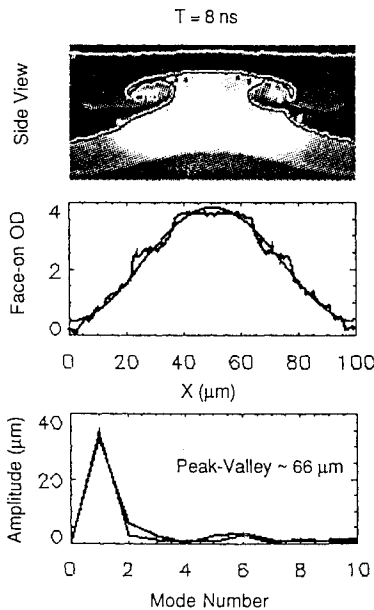
$$\lambda = 50 \mu\text{m} \text{ not initially present}$$

Experiments begin in Summer

10 different initial patterns



ALE Code "Radiographs" are Fourier Analyzed for Spectral Evolution



Face-on & side-on radiographs are consistent

Growth Rates from Experiment and ALE Simulations Agree Within 30 % and Support Meyer-Blewett Prescription for $A < 0$



Comparison of growth rates ($\mu\text{m/ns}$)

Experiment	11 ± 2
ALE simulation	8.5

$A = -0.9$
 $\lambda = 100 \mu\text{m}$
 $\eta_0 = 14 \mu\text{m}$

Richtmyer growth rate with post-shock amplitude is too small

$$\frac{d\eta}{dt} = A^* k U \eta_0^* \sim 2.5 \mu\text{m/ns}$$

$$\begin{aligned} \eta_0^* &= \eta_0 (1 - U/V_1) \\ &\sim \eta_0 / 8 \end{aligned}$$

Meyer-Blewett suggest averaging pre- and post-shock amplitudes for $A < 0$

$$\frac{d\eta}{dt} \sim A^* k U \frac{\eta_0 + \eta_0^*}{2} \sim 10.5 \mu\text{m/ns}$$

PF 15, 753 (1972)

Richtmyer-Meshkov Instability Saturates when Modal Amplitude Reaches $\sim 35\%$ of its Wavelength



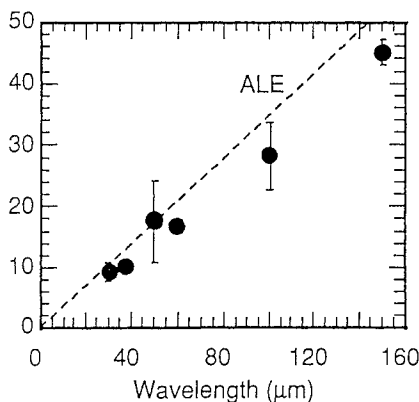
Fundamental mode saturates

$$\eta_{\text{sat}} \sim \lambda / 3$$

Bubble and spike may still grow

Reduced growth rate
 Harmonics

Saturation Amplitude (μm)



Investigate Approach to Turbulence with Complex Initial Interfacial Perturbations



Initial spectrum with 10 modes

- $\lambda_n = 300 \mu\text{m} / n$
- $\eta_{\text{rms}} = 3 \mu\text{m}$
- Peak-Valley = 22 μm

Modes saturate when $\eta\lambda \sim .15 \lambda$

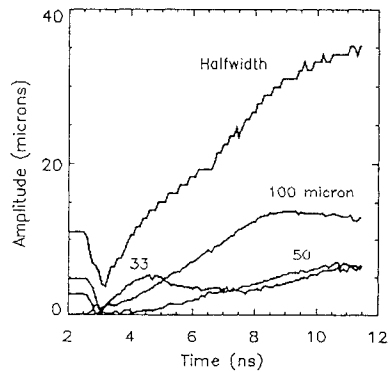
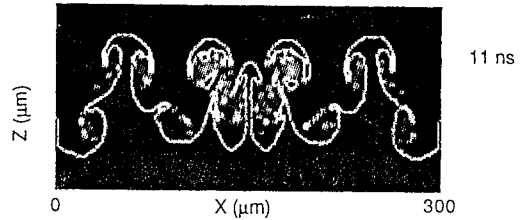
Peak-Valley ~ 70 μm

Mode coupling predicted

$\lambda = 50 \mu\text{m}$ not initially present

Experiments begin in Summer

10 different initial patterns



Summary of Richtmyer-Meshkov Experiments on NOVA Laser



- Shock characteristics agree with LASNEX (1D) simulations
- Growth rates agree with ALE (2D) simulations, and support Meyer-Blewett model for $A < 0$

$$\frac{d\eta}{dt} \sim A^* k U \frac{\eta_0 + \eta_0^*}{2}$$

Exceeds Richtmyer rate with η_0^* . Distinction important at high compression.

- Single modes saturate when $\eta \sim \lambda / 3$

Future experiments with multimode initial perturbations

Multimode and 3D Rayleigh-Taylor Experiments on Nova,* B.A. Remington, S.V. Weber, S.W. Haan, J.D. Kilkenny, and R.J. Wallace, LLNL, Livermore, CA 94550.

The basic principle behind all inertial confinement fusion (ICF) schemes, namely, ablatively accelerating a pusher, is hydrodynamically unstable in three ways. (1) During the initial shock transit through the ablator and pusher, any rippling of the shock front leads to a hydrodynamic instability of the Richtmyer-Meshkov type. (2) During the acceleration phase, the ablation front is Rayleigh-Taylor unstable, with the dense pusher fluid being accelerated by the low density hot, expanding ablation fluid. (3) During the pusher deceleration phase in the approach to peak fuel compression and stagnation, the pusher-fuel interface is now Rayleigh-Taylor unstable. The result of all three is that random surface perturbations grow, which can be deleterious to the capsule performance, especially in designs for high gain implosions. We have conducted an extensive series of experiments on the Nova laser to measure hydrodynamic instabilities under conditions similar to (1) and (2) in planar foils accelerated by x-ray ablation.¹ Single mode experiments allow a measurement of the fundamental growth rates from the linear well into the nonlinear regime; multimode foils allow an assessment of the degree of mode coupling and its effect on overall perturbation growth; and 3D experiments allow a measurement of the evolution of a completely random surface finish. Experimental results and comparisons with theory and simulations will be presented. *Work performed under the auspices of the U.S. Department of Energy by the Lawrence Livermore National Laboratory under contract number W-7405-ENG-48.

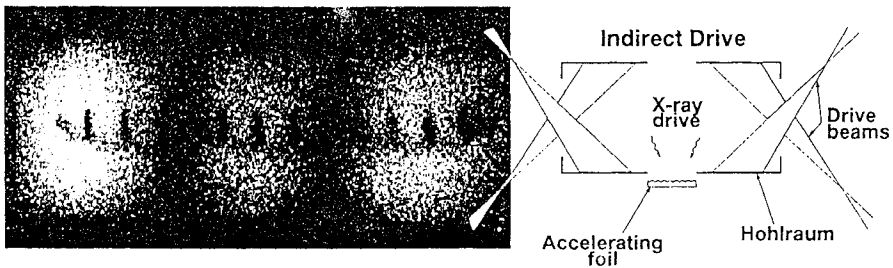
¹B.A. Remington *et al.*, Phys. Rev. Lett. **67**, 3259 (1991); *ibid*, Phys. Fluids B **4**, 967 (1992); *ibid*, Phys. Fluids B (in press, July, 1993) and UCRL-JC-111286 (1992); *ibid*, in the proceedings of the 3rd International Workshop on Compressible Turbulent Mixing, Abbey of Royaumont, France(CEA DAM, 1992), p. 225.

Multimode and 3D Rayleigh-Taylor Experiments on Nova

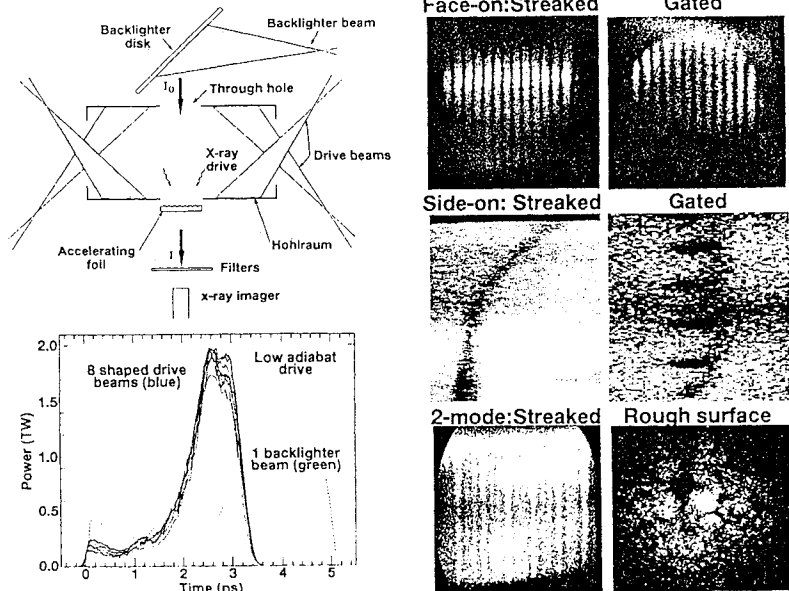
B.A. Remington, S.V. Weber, S.W. Haan, J.D. Kilkenny, and R.J. Wallace
 LLNL, Livermore, CA 94550 U.S.A.



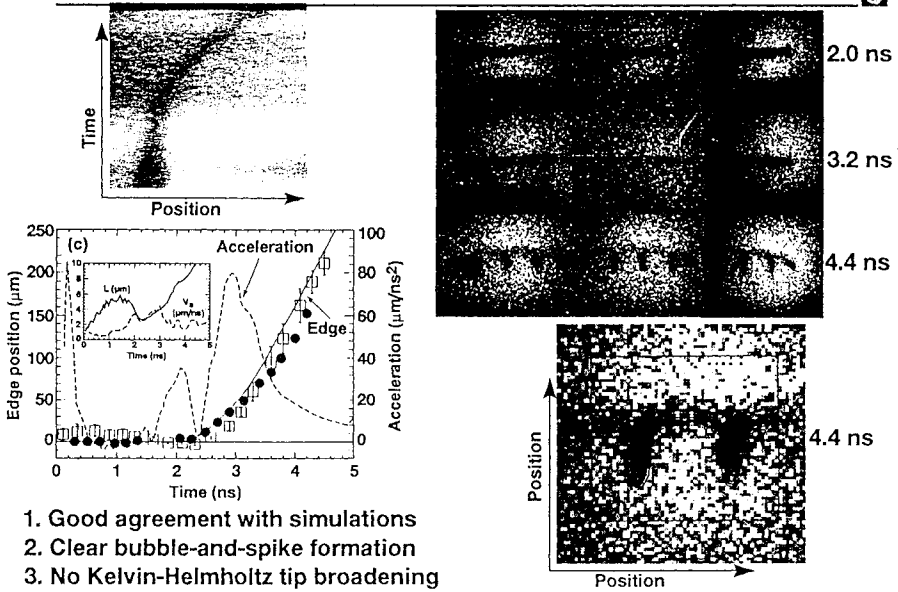
1. **Single-mode experiments with planar foils**
 [Good quantitative agreement with modeling.]
2. **2-, 8-mode perturbations experiments**
 [Mode coupling observed in nonlinear regime, in agreement with theory]
3. **Foil surface-finish experiments**
 [Smooth foils remain intact; very rough foils "break up".]



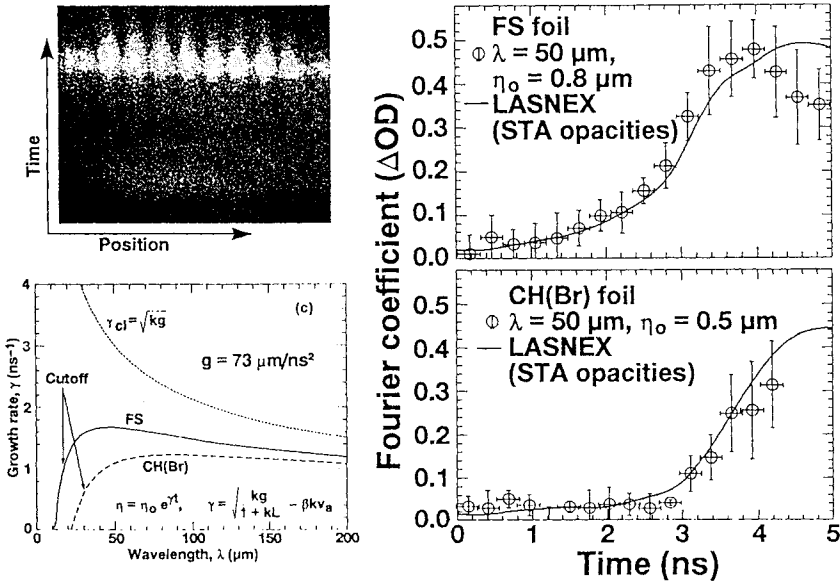
The experimental configuration allows broad access to the RT evolution



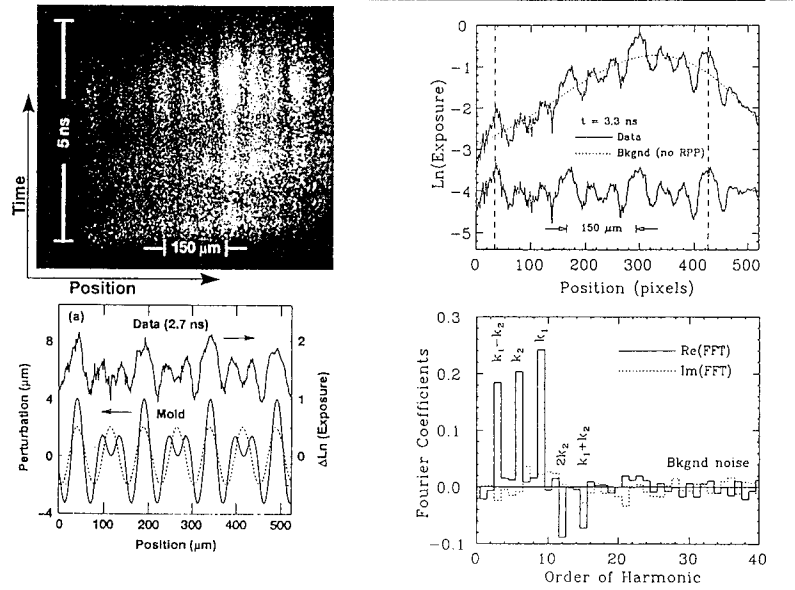
We use foil trajectory shots to calibrate the drive. Side-on gated imaging is used to see the actual shape of the perturbation.



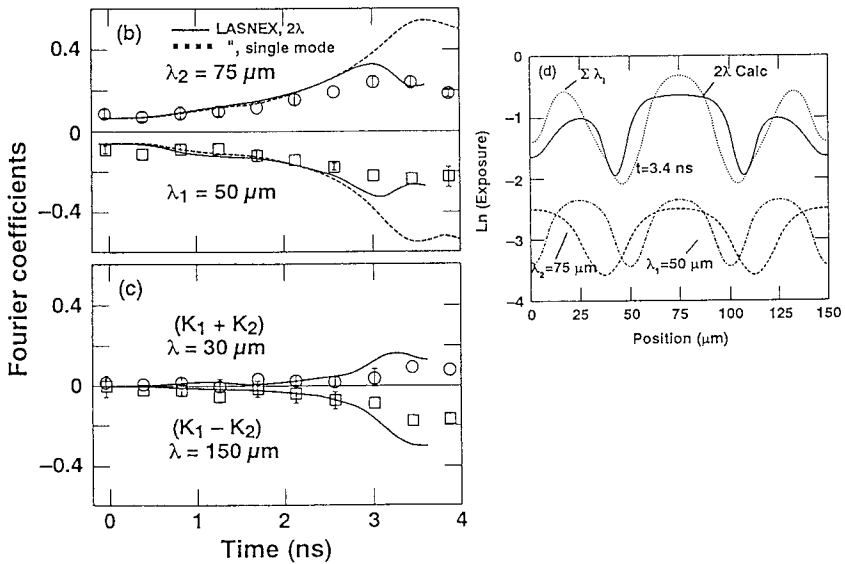
Single-mode experiments in the linear regime offer the most rigorous test of modeling: the data and theory are in good agreement.



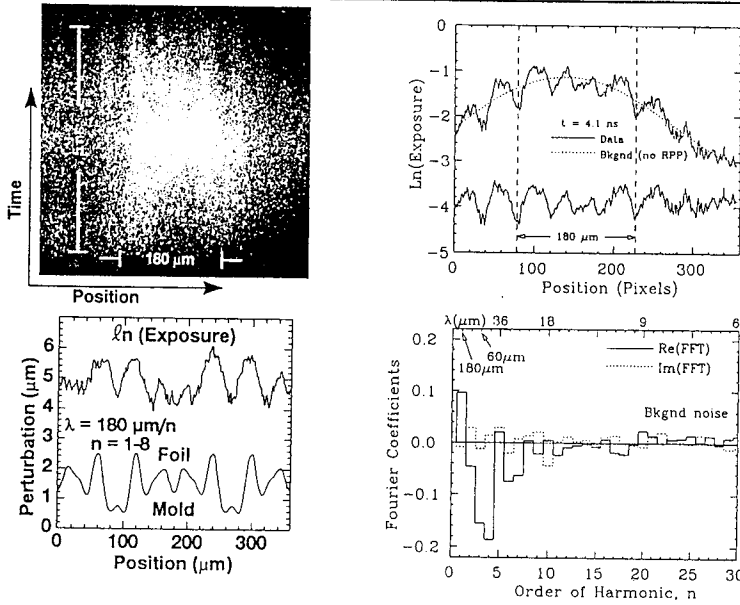
We use 2-mode experiments to study mode coupling in the nonlinear regime; the presence of λ_1 affects the evolution of λ_2



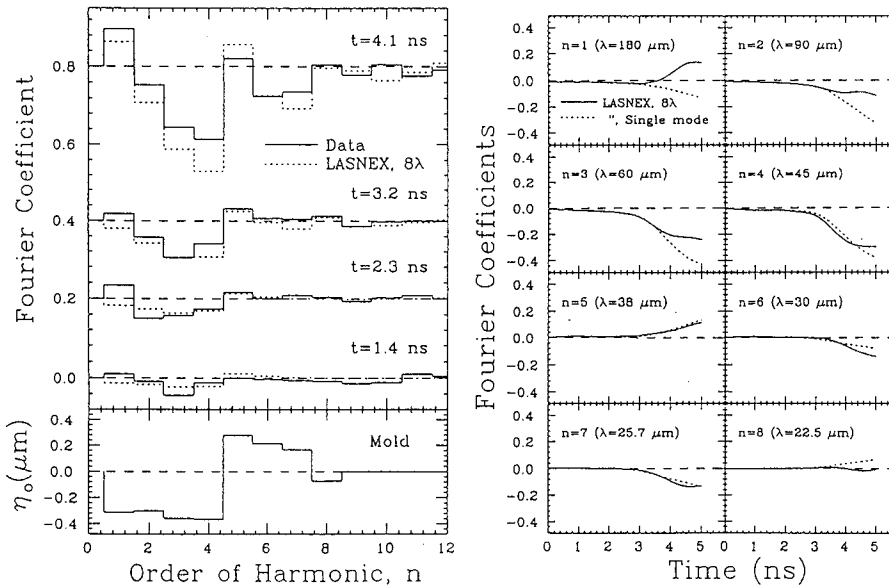
Coupling occurs late in time and leads to a broadening of the dominant bubble.



We do 8-mode experiments to study mode coupling in a more realistic situation. Coupling from the dominant modes is observed.



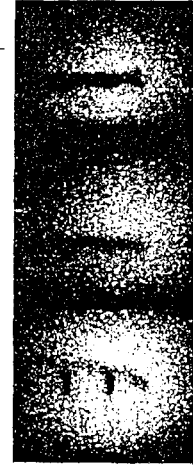
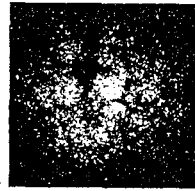
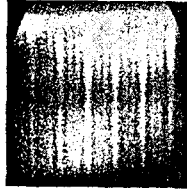
Coupling causes changes in the modal evolution, which leads to changes in shape of the perturbation.



Summary and Conclusion



1. **Single-mode experiments**
 - a. Good agreement with modeling
 - b. CH(Br) less unstable than FS due to L , v_a
 - c. No Kelvin-Helmholtz tip broadening of spike
2. **Multimode experiments**
 - a. Mode coupling evident in nonlinear regime
 - b. Presence of λ_1 affects evolution of λ_2
 - c. Good agreement with modeling
 - d. May be able to test saturation model with 8λ shots



3. **Surface finish experiments**
 - a. Smooth foils stay intact; very rough foils "break up"
 - b. Should have a good test of saturation modeling

VI

Converging flows

Hydrodynamic Instability Modeling for ICF*

S. W. Haan

Lawrence Livermore National Laboratory
Livermore, CA USA

The intent of this presentation is to review how we model instability growth in ICF targets, and identify the principal issues. Most of the material has been published in refs. 1-3, but is not familiar to many participants in the meeting.

Hydrodynamic instabilities are a key issue in ICF. Along with laser-plasma instabilities, they determine the regime in which ignition is possible. At higher laser energies, the same issues determines the achievable gain. Quantitative predictions are therefor of the utmost importance to planning the ICF program, as well as to understanding current Nova results.

The key fact that underlies all of our work is the stabilization of short wavelengths. This idea has a long history, going back to Nuckolls' original ICF paper.⁴ Recently there has come to be a consensus (from numerical work,⁵ with experimental verification⁶) that it is well described by a formula taking into account the ablation velocity (defined as $v_A = (dm/dt)\rho_{\max}^{-1}$, where dm/dt is the mass removal rate per square cm) and the scale length L at the ablation front. The growth rate is

$$\gamma = \sqrt{\frac{gk}{1+kL}} - \beta k v_a.$$

where β is a parameter between 1 and 3. This stabilization allows us to arrange our implosions so that the short wavelength growth is not important. Any interfaces with significant density steps (while in-flight) must be carefully avoided. The hydrodynamics is then essentially linear. This is corroborated by multi-mode explicit simulations, as shown in Fig. 1. We present density and temperature isocontours from simulations of an ignition target, shown at the time of ignition. The simulations used realistic initial perturbations in modes 10, 20, ..., 80; the simulation on the right had all modes' amplitudes reduced by a factor of four. It is clear that the final perturbations are nearly linear in initial amplitude. We are also working with Dahlburg and colleagues at NRL on 3D multi-mode ablative instability growth, as reported by Dahlburg at this meeting.

*Work performed under the auspices of the U. S. Department of Energy by the Lawrence Livermore National Laboratory under contract W-7405-ENG-48.

For arbitrary initial conditions, we use linear analysis based on spherical harmonic analysis (or, in planar geometry, on Fourier analysis). A series of individual code simulations gives growth factor vs. mode number. This can be combined with any initial spectrum of interest. It is important to do code simulations to get the individual modes' growth; analytical formulae are not accurate, even to an order of magnitude. An example of this is shown in Table 1.

The onset of nonlinearity, and a model for extension into that regime, is as analyzed in ref. 1. Modes do not become nonlinear when their amplitudes become comparable to their wavelength, except in the special case where no other modes are present. If other modes are present, saturation is local in space. For isotropic, random surfaces, saturation begins when modal amplitudes become comparable to $1/Lk^2$ for planar modes with

$$\text{perturbed surface } Z(x,y,t) = \sum_k e^{ik \cdot x} Z_k$$

and R/l^2 for spherical harmonic modes. Once modes get larger than this, nonlinear effects must be estimated in a way such as we have discussed in Refs. 2 and 3. This particular nonlinear model is not fundamental ICF physics and I will not emphasize it here. For most ICF problems, linear analysis is quite useful; the onset of nonlinear effects can be checked as just described.

Detailed modeling of perturbation growth in 3D remains an area of future work. Direct code simulation is becoming more and more applicable -- see, for example, the presentation by Dahlburg at this meeting. However, we are not yet in a position to simulate directly the growth of realistic 3D perturbations on real ICF targets. Hence effects must be estimated in some other way. Our baseline saturation model is oriented towards 3D perturbations, but it provides only a crude estimate of the 3D nonlinear effects. More detailed calculations are possible for very weakly nonlinear perturbations, using second order RT theory. Work on this will be reported soon.⁷ An example is shown in Fig. 2, where we used linear analysis and second order mode coupling theory to predict the size and shape of perturbations on a foil as used in Remington's experiments.⁶

In addition to calculating the size of the perturbations, we must calculate their effects. This can be done in several ways with current code capability: (i) simulations of a single spike on axis in 2D spherical geometry, which is probably the closest to the real 3D situation; (ii) simulations of curtains of material falling in near the waist plane; and (iii) a 1D mix model proposed by G. Zimmerman, in

which an extra thermal diffusivity is incorporated in the mixed region. These various models give fairly consistent results for the problems of interest, giving us confidence in them.

Experimentally testing this modeling requires testing the various ingredients. The most important issue is whether we are correctly calculating the single mode growth, and the reduction by ablation stabilization. This is being tested in the planar experiments by Remington, Glendinning, and Weber (reported on by Remington and Kilkenny at this meeting). Our LANL colleagues are attempting converging geometry single mode experiments.⁸ We also must measure perturbations resulting from realistic multi-mode initial surface perturbations. Remington reported here on some planar experiments that are beginning to give data of this sort. Also, the SSD-seeded perturbations done by Glendinning and Weber (described by Kilkenny here) show the growth of fully three dimensional randomly seeded perturbations, and will be a challenging test of our modeling capability. Implosion experiments are also being done, using spectroscopic trace emission as a diagnostic of the perturbation size in the imploded configuration. Modeling of some of these experiments requires extending our analysis into the nonlinear regime, using our saturation model from ref. 1.

Direct drive and indirect drive instability growth are qualitatively similar, although the different ablation velocities and scale lengths make for important quantitative differences. In direct drive we have the additional problem of laser-seeded irregularities, both the early time speckle and the long-time residual modulations. These can be modeled with either linear analysis or direct simulation (in full detail in 2D, and with a growing amount of detail in 3D). Conceptually, the modeling approaches and issues are very similar whether the drive is direct or indirect.

We have made remarkable progress in ICF instability modeling in the last few years. Modern code capability, along with the realization that the perturbations are nearly linear, have made the instability growth problem quite tractable, compared to a few years ago when most workers in the field regarded it as a black art. Experimental tests of the modeling are coming along very well; although they have not yet definitively verified our understanding of all the relevant issues, results are continually very encouraging and we are optimistic that definitive verification will be in hand soon.

1. S. W. Haan, "Onset of Nonlinear Saturation for Rayleigh-Taylor Growth in the Presence of a Full Spectrum of Modes," *Phys. Rev. A* 39, 5812 (1989).
2. S. W. Haan, "Weakly Nonlinear Hydrodynamic Instabilities in Inertial Fusion," *Phys. Fluids B* 3, 1992 (1990).
3. S. W. Haan, "Hydrodynamic Instabilities on ICF Capsules," prepared for submittal to *Lecture Series on Inertial Fusion*, Department of Astrophysical Sciences, Princeton University (1991).
4. J. Nuckolls, L. Wood, A. R. Thiessen, and G. Zimmerman, "Laser Compression of Matter to Super-High Densities: Thermonuclear Applications," *Nature* 239, 139 (1972).
5. H. Takabe, K. Mima, L. Montierth, and R. L. Morse, Self-consistent growth rate of the Rayleigh-Taylor Instability in an Ablatively Accelerating Plasma, *Phys. Fluids* 28(120), p 3676 (1985). M. Tabak et al, Hydrodynamic Instability and the Direct Drive Approach to Laser Fusion, *Phys. Fluids B* 2, 1007 (1990). J. H. Gardner, S. E. Bodner, and J. P. Dahlburg, *Phys. Fluids B* 3, 1070 (1991). K. O. Mikaelian, "LASNEX simulations of the Classical and Laser-Driven Rayleigh-Taylor Instability," *Phys. Rev. A* 42, 4944.
6. S. G. Glendinning et al. *Phys. Rev. Lett.* 69, 1201 (1992). B. A. Remington et al., Large Growth Planar Rayleigh-Taylor Experiments on Nova, *Phys. Fluids B* 4, 967 (1992). Also reported in this proceedings, by Remington and Kilkenny.
7. M. J. Dunning and S. W. Haan, to be published.
8. W. Hsing, private communication.

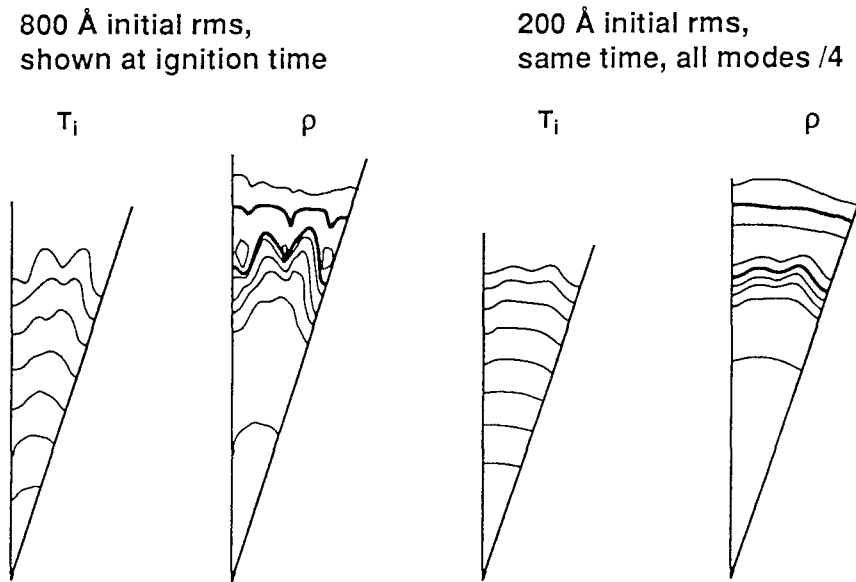


Figure 1. Density and temperature isocontours at ignition time for an ignition target, as calculated in a simulation with a multi-mode initial perturbation on the outside of the shell. Results from two perturbations are shown, which differ by a factor of four in all modes. The resulting perturbations are virtually linear. The perturbations shown on the left are marginally acceptable, with an 800 Å rms equivalent initial 3D perturbation. The perturbations shown on the right are certainly acceptable, and the initial perturbation is similar to perturbations currently measured on Nova-scale target surfaces.

"Weakly nonlinear" is $t \sim 3-4$ ns for $0.45 \mu\text{m}$ initial rms
 Contours of $\rho r = \delta(\bar{x})$ at $3.6\text{ns} \otimes \text{MTF}$, half max contour highlighted

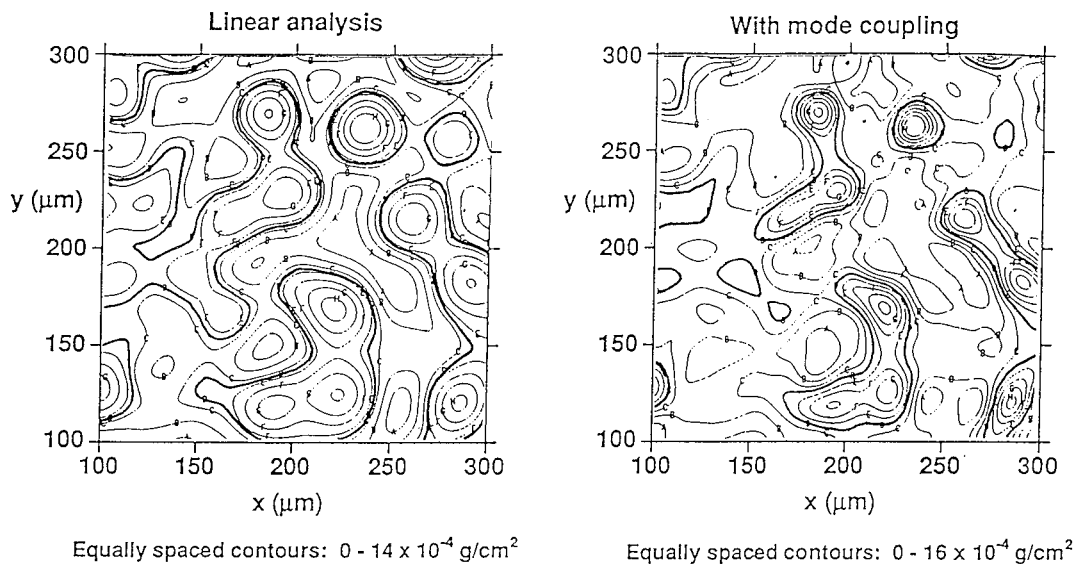


Figure 2. The effect of second order mode coupling on the shape of perturbations growing on an ablatively accelerated foil. These are contours of $\int \rho dz$ vs. x and y , for a perturbation that has grown out of a random array of bumps. The left-hand plot shows the prediction of linear analysis, with modal growth factors calculated with 2D simulations. The right-hand plot shows the effect of second order mode coupling, in that the spikes are made narrower and the bubbles broader. The half-max contour is highlighted to emphasize the spike-narrowing produced by second-order effects.

$L/\Delta R$	$v_A t/\Delta R$	$\gamma \tau$	$e^{\gamma \tau}$
0.3	0.6	4.3	75
0.2	0.4	6.6	750
0.4	0.75	2.6	14

Table 1. Predicted growth factors obtained from the ablation-stabilization formula, for various values of the ablation scale length and velocity. The wavelength is taken to be ΔR , the shell thickness, and the distance moved to be $15 \Delta R$. The scale length and velocity, relative to ΔR , are taken to be as indicated. Since the parameters cannot be estimated to better accuracy than about 25%, it is impossible to make meaningful predictions from the formula alone. Full-code simulations, with experimental verification, must be used to estimate perturbation growth.

Calculations of Instability Growth in Cylindrical Implosions

Nelson M. Hoffman, J. Bradley Beck, and Warren W. Hsing
Los Alamos National Laboratory

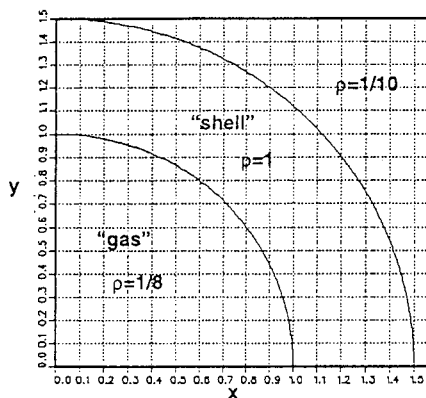
**4th International Workshop
on the Physics of Compressible Turbulent Mixing**

Cambridge University
29 March - 1 April 1993

**Cylindrical experiments are particularly suited to
address issues of fluid instability.**

- **Feedthrough of ablation front instabilities**
Cylindrical geometry diagnostic access
- **Inner-surface instability growth**
Target fabrication of perturbed inner surfaces is feasible in
cylindrical geometry
- **Coupling of low-mode asymmetry with higher modes**
Not an issue for low convergence
Observable for high convergence
- **Converging shock waves**
Instability at center of convergence

Fluid instability calculations in cylindrically converging flows are performed using 2nd-order Eulerian hydrodynamics code with Youngs interface reconstruction*.



- Materials are treated as ideal gas with $\gamma = 5/3$.
- Initial condition: inward radial velocity in cylindrical shell .
- Calculation models a 90-degree sector in Cartesian geometry.

* D. L. Youngs, "Time Dependent Multi-Material Flow with Large Fluid Distortion", K. W. Morton and J. H. Baines, ed., *Numerical Methods for Fluid Dynamics*, Academic Press (1982).

Calculations use dimensionless variables.

At $t=0$: Cylindrical shell has uniform inward radial velocity V_0
 Inner radius of cylindrical shell is R_0
 Density of cylindrical shell is ρ_0

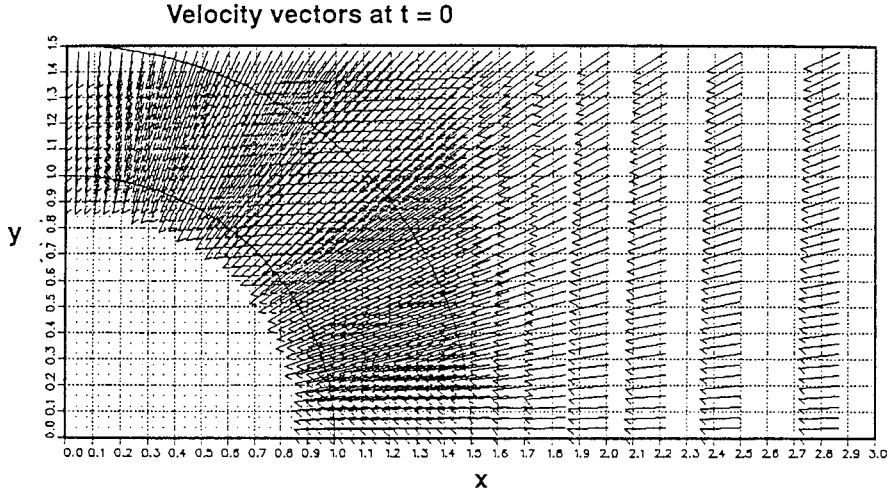
Take: velocity scale = V_0
 length scale = R_0
 density scale = ρ_0
 Then: time scale = R_0 / V_0
 pressure scale = $\rho_0 V_0^2$
 specific internal energy scale = V_0^2

The calculations use dimensionless variables that are normalized by the appropriate scale.

Initial conditions for calculations:
 Pressure in gas and shell = 1/8
 Density = 1 in shell
 3/16 in gas
 Specific internal energy = 3/16 in shell
 1 in gas
 Shell thickness = 1/5

Shell has initial inward radial velocity $V_0 = 1$.

Calculation is performed in Cartesian geometry in 6.0 X 6.0 box
 Most calculations had 150 square cells on each axis from origin to $x, y = 1.5$
 and 50 cells with ratio zoning from 1.5 to 6.0.



Shell stagnates at about $R = 1/2$ in these calculations.

For adiabatic compression in cylindrical geometry: $P \sim \rho^\gamma = \rho_0^\gamma \left(\frac{R_0}{R}\right)^{2\gamma}$

Shell comes to rest when work done on gas ~ initial kinetic energy in shell.
 Work done on gas is

$$W(R) = \int_{R_0}^R P_{\text{gas}} dv = 2\pi P_{0,\text{gas}} \int_{R_0}^R \left(\frac{R_0}{R'}\right)^{2\gamma} R' dR' = \frac{\pi R_0^2}{\gamma-1} P_{0,\text{gas}} \left[\left(\frac{R_0}{R}\right)^{2(\gamma-1)} - 1 \right]$$

Define R_{min} by $W(R_{\text{min}}) =$ initial kinetic energy in shell. Then

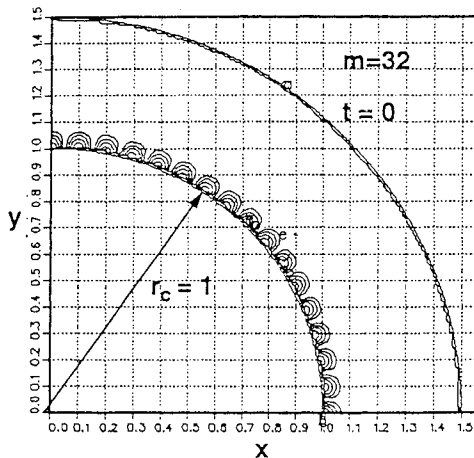
$$R_{\text{min}} = R_0 \left[1 + (\gamma-1) \frac{\rho_s V_0^2}{2P_{0,\text{gas}}} \left(\frac{R_s}{R_0}\right)^2 - 1 \right]^{-\frac{1}{2\gamma-2}}$$

Example 1: if $\gamma = 5/3$, $\rho_s V_0^2 = 1$, $P_{0,\text{gas}} = 1/3$, $R_s/R_0 = 3/2$, then
 $R_{\text{min}}/R_0 = (4/9)^{3/4} = 0.5443...$

Example 2: if $\gamma = 5/3$, $\rho_s V_0^2 = 1$, $P_{0,\text{gas}} = 1/8$, $R_s/R_0 = 6/5$, then
 $R_{\text{min}}/R_0 = (75/163)^{3/4} = 0.5587...$

Instability is initialized as a density and specific energy perturbation.

$$\rho(r, \varphi) = \rho_0(r, \varphi) \left(1 + \frac{\delta_0}{2} \cos(m\varphi) \left\{ \cos \left[m \left(\frac{r}{r_c} - 1 \right) \right] + 1 \right\} \right), \quad 1 < \frac{r}{r_c} < 1 + \frac{\pi}{m}$$



Specific internal energy is perturbed proportional to $1/\rho$, so that pressure is unperturbed.

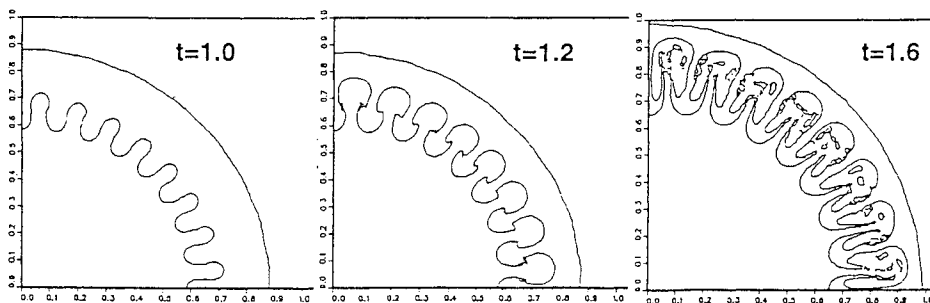
density contours

- | | | | |
|---|-------------------------|---|----------------------|
| a | 9.9000×10^{-1} | f | 1.0020×10^0 |
| b | 9.9200×10^{-1} | g | 1.0040×10^0 |
| c | 9.9400×10^{-1} | h | 1.0060×10^0 |
| d | 9.9600×10^{-1} | i | 1.0080×10^0 |
| e | 9.9800×10^{-1} | | |

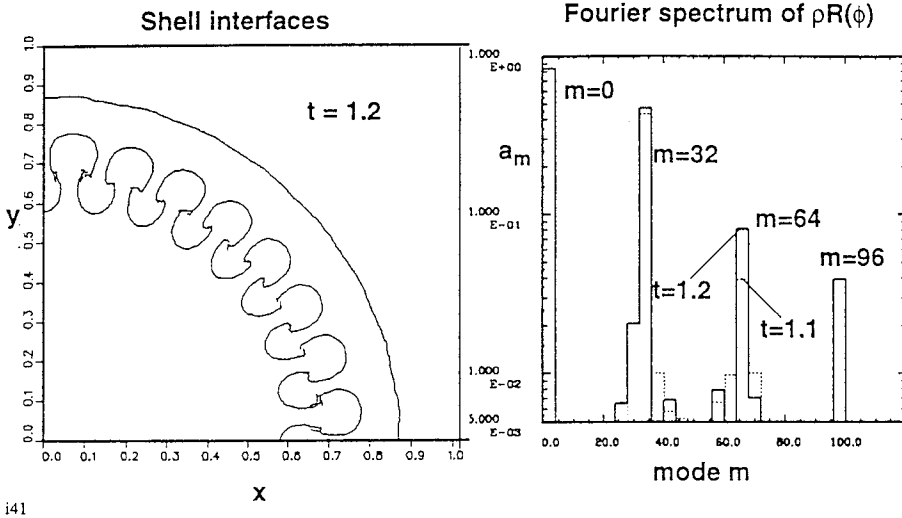
Instabilities grow as shell implodes.

Rayleigh-Taylor instability develops into “bubble-and-spike” form in its non-linear phase.

$m=32$ instability
 $P_{0g} = 1/3, P_{0s} = 2/225$



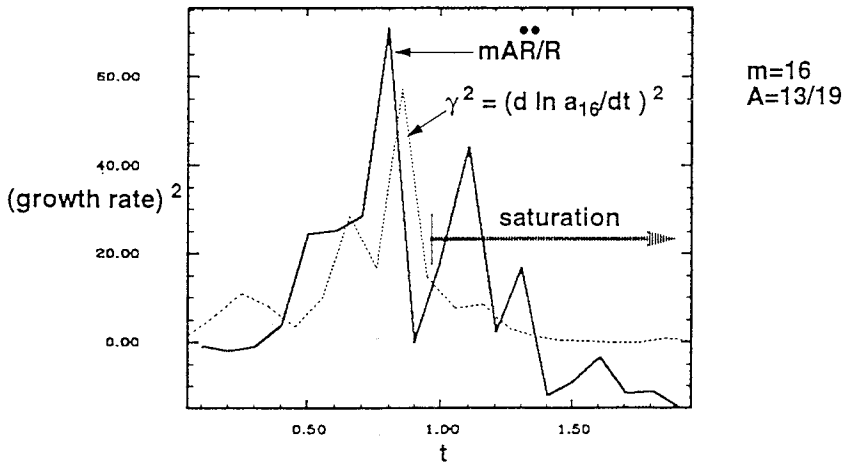
Fourier analysis of angle-dependent ρR of shell shows mode growth.



i41

Calculated growth rates show fair agreement with simple prediction for Rayleigh-Taylor instability.

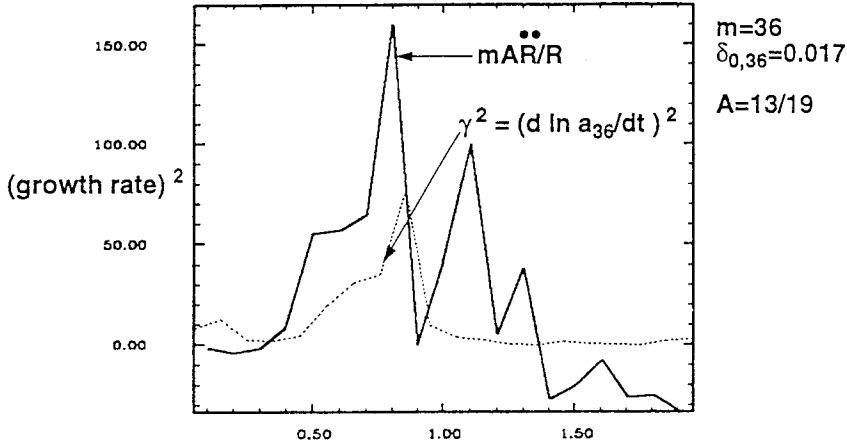
Cylinder has complicated acceleration history: several decelerating shocks traverse it.



Comparison of calculated growth rates with simple prediction is not so good for higher modes.

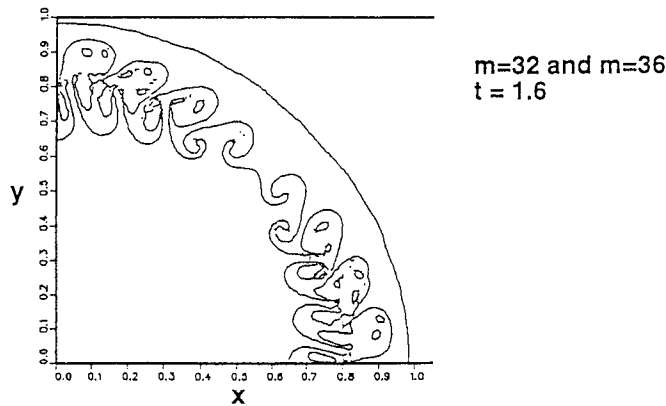
Is this because of:

- Coarse mesh effects? Density gradients?
- Cylindrical geometry, as discussed by Sakagami and Nishihara [Phys. Fluids B 2 (11), November 1990, p. 2715]?



Mode coupling can be investigated using multimode initial perturbations.

As modes grow into nonlinearity, they start to interact and affect each other's growth.*

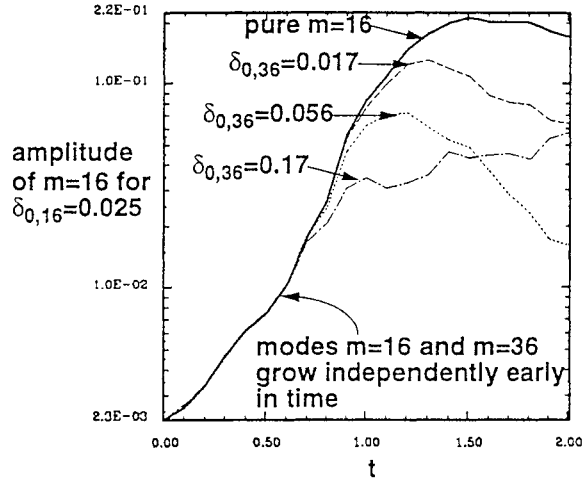


*Dahlburg, Gardner, and Emery, "Turbulent Rayleigh-Taylor Stabilization at Ablative Interfaces", 1990 APS DPP Meeting
 Ofer, Shvarts, Zinamon, and Orszag, "Mode Coupling in Nonlinear Rayleigh-Taylor Instability", preprint;

Short-wavelength mode can suppress growth of longer-wavelength mode.

Calculations with $m=16$ and $m=36$ show that amplitude of $m=16$ mode is suppressed by presence of $m=36$ mode.

Larger initial amplitudes give earlier onset of suppression.

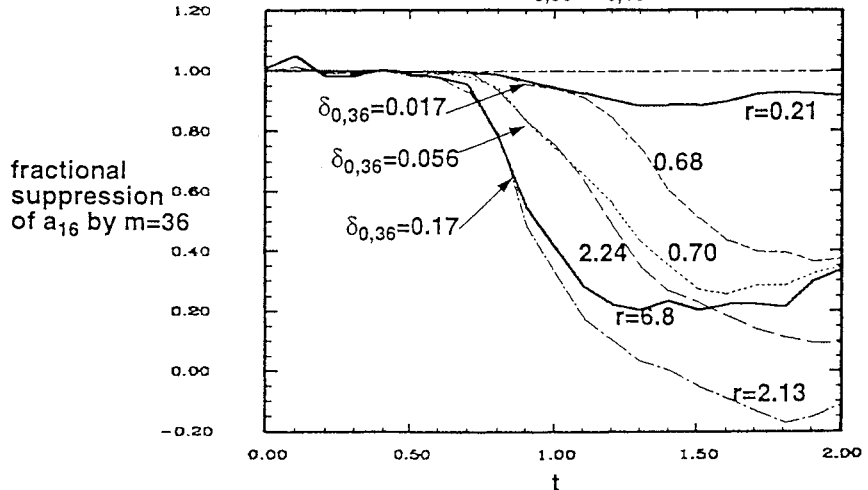


i62 63 67 68

Onset of suppression depends on amplitude of short-wavelength mode, not long-wavelength mode.

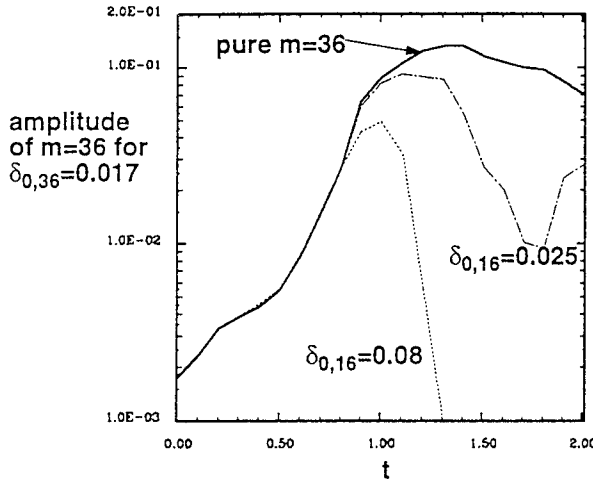
Final magnitude of suppression depends on relative amplitudes of both modes.

Define r as the ratio of initial perturbations: $r = \delta_{0,36} / \delta_{0,16}$



Long-wavelength mode can simultaneously suppress growth of short-wavelength mode.

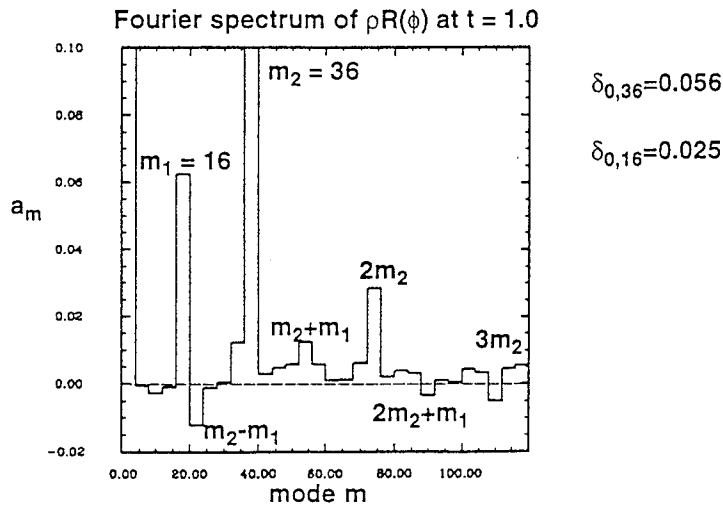
Larger initial amplitude of $m=16$ gives earlier onset of suppression.



i68 72 76

Energy removed from initial interacting modes reappears in other modes.

New modes appear which are sums and differences of fundamental modes and their harmonics.



Questions:

- How does mode coupling depend on wavelengths and amplitudes of the two interacting modes? How fast are new modes created by their interaction?
- What happens for three or more modes?
- Does a multimode mixing layer arise which grows self-similarly (i.e., independently of initial conditions)?
- How does converging flow differ from planar flow?

Three Dimensional Hydrodynamic Calculations with Adaptive Mesh Refinement of the Evolution of Rayleigh Taylor and Richtmyer Meshkov Instabilities in Converging Geometry: Multi-Mode Perturbations

Richard I. Klein

University of California, Lawrence Livermore National Laboratory and Berkeley
Department of Astronomy, U.C. Berkeley

and

John Bell, Rick Pember and Tom Kelleher

University of California, Lawrence Livermore National Laboratory

ABSTRACT

We present results for high resolution hydrodynamic calculations of the growth and development of instabilities in shock driven imploding spherical geometries in both 2D and 3D. We solve the Eulerian equations of hydrodynamics with a high order Godunov approach using local adaptive mesh refinement to study the temporal and spatial development of the turbulent mixing layer resulting from both Richtmyer Meshkov and Rayleigh Taylor instabilities. The use of a high resolution Eulerian discretization with adaptive mesh refinement permits us to study the detailed three-dimensional growth of multi-mode perturbations far into the non-linear regime for converging geometries.

We discuss convergence properties of the simulations by calculating global properties of the flow. We discuss the time evolution of the turbulent mixing layer and compare its development to a simple theory for a turbulent mix model in spherical geometry based on Plesset's equation. Our 3-D calculations show that the constant found in the planar incompressible experiments of Read and Young's may not be universal for converging compressible flow. We show the 3-D time trace of transitional onset to a mixing state using the temporal evolution of volume rendered imaging. Our preliminary results suggest that the turbulent mixing layer loses memory of its initial perturbations for classical Richtmyer Meshkov and Rayleigh Taylor instabilities in spherically imploding shells. We discuss the time evolution of mixed volume fraction and the role of vorticity in converging 3D flows in enhancing the growth of a turbulent mixing layer.

1. INTRODUCTION

The general problem of the growth of hydrodynamic instabilities leading to the formation of a turbulent mixing layer has a long history. Of particular interest has been the study of shock-interface interactions leading to the growth of both Richtmyer Meshkov and Rayleigh Taylor instabilities and the effects these instabilities have on the performance of an imploding ICF capsule (for a review of research pertaining to shock-interface interactions see Rupert, 1991). During the implosion phase of an ICF pellet, Rayleigh Taylor instabilities that may grow on both the outer and inner surface of the ablator may have deleterious effects that can potentially destroy the pellet or cause the cold main fuel to mix with a low density high temperature hot spot causing ignition failure (Lindl, McCrory and Campbell, 1992). In particular, the implosion must be maintained nearly spherical with implosion velocities uniform to $\leq 1\%$, and minimization of the mixing of fuel is necessary to successfully form the central hot spot. Thus the study of the conditions that may lead to highly non-linear development of these hydrodynamic instabilities and departure from spherical symmetry is crucial to successful design of ICF capsules.

To achieve a complete understanding of the physics of the growth of such instabilities in a realistic ICF environment requires the complication of a full radiation-hydrodynamic treatment with multi-fluid hydrodynamics in a three dimensional imploding capsule. One requires the capability of tracking the interface of the fluids accurately with a high resolution scheme that is capable of following the propagation of multi-dimensional shock waves with high precision. Following the growth of instabilities that begin as seeded perturbations of extremely small amplitude and wavelength well into the non-linear regime and accurately calculate the evolution of complex hydrodynamic structures puts extraordinary demand on the resolution capabilities of most numerical schemes. Although recently work has begun in the investigation of three-dimensional problems, (cf. Tryggvason and Unverdi, 1990; Yabe et. al. 1991; Sakagami and Nishihara, 1990; Town and Bell, 1991 and Dahlburg et. al. 1993) most of this work has suffered from extremely poor resolution making it difficult to follow the details of multi-mode perturbations for long time evolution with accuracy.

The problem of the development of multi-mode perturbations in a converging geometry brings up fundamentally important questions in their own right that pertain to the development of turbulence in mixing layers that have been initiated by shocks on unstable interfaces. How does the evolution of unstable modes merge to form a mixed layer?, how does the growth of a mixing layer evolve in time and what is the sensitivity of this growth to initial amplitudes and wavelengths of the modes?, how is turbulent energy distributed within the mixing region during growth?, how sensitive are global properties of the shell to initial perturbations?, what is the role that is played by vortex dynamics during the evolution of a turbulent mixing layer and what types of vorticity structures are formed?, are shocks that emerge from unstable interfaces in a spherically imploding geometry anisotropic and what do their three-dimensional structures look like?, can the effects of radiation and thermal conduction effectively stabilize the growth of unstable modes in multi-dimensions preventing the formation of a turbulent mixing layer.

To attempt to address these questions in detail we have begun a line of research with a new methodology in multi-dimensional hydrodynamics using high resolution hydrodynamic schemes that are capable of following the details of shock wave propagation with high accuracy coupled to local adaptive mesh refinement to provide extremely high spatial resolution in those domains where such resolution is necessary. In this brief paper we describe the results of preliminary calculations that first attempt to follow the development of multi-mode perturbations that have been placed on both the inner and outer surfaces of a pressure driven shell of dense matter that is surrounded by and envelops a low density gas. In order to assess the effects of the growth of these instabilities in a three-dimensional convergent geometry and begin a detailed study of the development of the turbulent mix layer we have begun with the simpler problem of studying pure hydrodynamic effects without the complication of radiation and thermal conduction and ablative stabilization of the capsule. In this first paper we will address a wavelength and scaling series of calculations to investigate whether the growth of a three-dimensional turbulent mixing layer is indeed forgetful of the initial perturbations. No mechanism for ablation or density gradient stabilization has been included; nevertheless we regard this as an important first step toward realistic fully three dimensional calculations with high resolution. The results that we summarize here will be discussed in more detail in Klein et. al. 1993 (in preparation). Our subsequent work will include the increasingly complex physics issues of radiation and conduction.

The structure of this paper is as follows: §2. will briefly describe the methodology of local adaptive mesh refinement and describe the initial conditions and boundary conditions that have been used in the calculations; §3. will describe the temporal evolution of a dense spherical shell seeded on its inner and outer surface with multi-mode perturbations undergoing implosion as it becomes Richtmyer Meshkov and Rayleigh Taylor unstable by using perspective volume rendered imaging of the 3D data fields. Here we investigate the growth of the turbulent mixing layer and its sensitivity to the initial multi-mode perturbations; the extent of mixing as a function of time as represented by the mixed volume fraction; the distribution of turbulent energy during

the implosion of the capsule; the relative importance of the various components of the vorticity and the role of vorticity in the generation of a turbulent mixed layer; and the sensitivity of global properties of the mixed shell during the transition to a mixed state. In §4, we summarize the key results.

2. METHODOLOGY and INITIAL CONDITIONS

Methodology

Our basic motivation is to use high resolution adaptive mesh refinement hydrodynamics in multi-dimensions to explore the fundamental physics of the nature of hydrodynamic instabilities and turbulent mixing layers in imploding convergent geometries of shock driven shells. Our goal is to develop a fully predictive capability in 3D allowing high resolution.

We solve the Euler equations of hydrodynamics in 2D cylindrical and both 3D Cartesian as well as 3D spherical coordinates. We use an operator split second order accurate Godunov integration scheme with local Adaptive Mesh Refinement (Berger and Colella, 1989) that has recently been generalized to 3D (Bell et al., 1993). For the calculations in this paper we use an ideal equation of state, although this is not a limitation. We employ a rectangular grid that first covers the computational domain (the level 1 grid). The method then constructs a hierarchical grid structure of logically composed rectangular meshes in regions where high resolution is necessary to solve the partial differential equations. In practice we have used three levels of grids, with a factor of 4 refinement in each direction. Thus a 2D a level 1 grid cell encompasses 256 level 3 cells. The decision to move to a higher level of refinement at any spatial location is based on Richardson extrapolation to estimate the local truncation error. In addition to setting the refinement level by spatial error estimation we have additional criteria to determine the maximum refinement of cells. In the present problem, we allow the dense shell material to always be treated at the highest level of refinement, whereas low density matter either outside or inside of the dense converging shell is treated at a lower refinement level. Thus we automatically have extreme refinement in the shell and in the developing mixed turbulent layer at all times without the prohibitive computational expense of having to carry this level of grid refinement throughout the entire computational domain. As we shall see this affords us an enormous savings in computational time. The main features of our code are that it employs a cell centered Godunov method that accurately captures shocks with none of the problems inherent in staggered mesh schemes. It employs a multiple grid hierarchy. It can operate either as a Cartesian geometry or a spherical geometry in 3D.

Initial and Boundary Conditions

For the 2D calculations, we studied the implosion of a thin shell with $\frac{R_i}{\Delta R} = 30$ where R_i is the initial radius and ΔR is the initial thickness of the shell. The dense thin shell was initially ~350 times the density of the low density inner gas. The perturbations on the inside and outside of the dense shell were those imposed by the tiling of a rectangular mesh on a spherical shell. We have demonstrated with a Fourier analysis that different grid resolutions represent different initial perturbations. The shell is imploded by setting a constant outer pressure over the surface boundary of the spherical shell to drive a strong shock into the dense shell. The overpressure is many times the initial pressure in the shell, which is initially set in pressure equilibrium with the low density gas encompassed by the shell. For the thin shell calculations in 2D we used an axisymmetric coordinate system. The outer pressure that is imposed on the surface of the dense capsule is used to generate an initial shock propagated into the capsule. This shock impulsively accelerates the dense shell initiating a Richtmyer Meshkov instability. The same pressure boundary condition is used to drive the implosion and trigger instabilities in our 3D calculations.

The use of this pressure boundary condition is idealized. In future work we will investigate the effects of using radiation to drive a shock into the dense shell.

For the 3D calculations which represent most of the work described in this paper, we study the implosion of a pressure driven dense shell that is moderately thick. The shell has an initial thickness to radius of $\frac{R_i}{\Delta R} = 0.1$. The shell is initially 1.25×10^2 times the density of the inner gas and the surrounding gas. We use a spherical coordinate system for the 3D calculations. This allows us to perform the calculations over a fractional patch of the full sphere to economize on computational grid cells. We perform the calculations on a domain that spans $\frac{\pi}{4} \leq \phi \leq \frac{\pi}{2}$ and $0 \leq \theta \leq \frac{\pi}{4}$ with $\frac{R_i}{\Delta R} = 10$. We used 2 levels of grid hierarchy for the 3D calculations with a factor of 4 refinement in each of the three spatial dimensions in going from level 1 to level 2. Thus our level 2 patch initially has $\theta_N=96$, $\phi_N=96$ and $R_N=34 \sim 3 \times 10^5$ cells. Since we allow grid refinement to occur wherever we have dense shell throughout the evolution of the converging shell and the development of a turbulent mixing layer, the number of level 2 cells necessary changes with time. Toward the end of the calculation when the mixed region has saturated, we have used ~ 3 million cells through the mixed shell domain. To achieve the equivalent resolution with a fixed Cartesian mesh that would have to encompass the initial shell would require 40 million cells. To achieve equivalent resolution with a fixed grid spherical code would require 25 million cells. Thus the computational efficiency of our 3D adaptive mesh refinement is enormous; at least an order of magnitude savings in computational time and memory.

For the 3D spherical calculations we imposed a multi-mode perturbation on the inner and outer surface of the dense shell. We allowed perturbations of the spherical surfaces of the form:

$$\delta r(\theta, \phi) = \frac{A}{A} P(\theta, \phi)$$

$$\text{where } P(\theta, \phi) = \sum_{l=1}^L \sum_{m=1}^M a_{lm} \cos 8l\phi \cos 8m\theta$$

and where we studied the scaling of wavelength for three cases with $\{L, M\} = (12, 24, 48)$.

The coefficients a_{lm} are randomly generated such that $\bar{A} = \max\{P(\theta, \phi)\}_{\theta, \phi}$ and $A = A_0$ or $2A_0$ for the amplitude scaling where $A_0 = 7.69 \times 10^{-3} R_i$ is the maximum amplitude perturbation.

3. RESULTS

In our first set of calculations we have performed two-dimensional calculations of the implosion of a thin spherical shell in a 2D Cartesian geometry. We used the initial conditions described in §2. Here the initial thickness of the shell is $1/30$ of its radius. The perturbations were imposed on the inner and outer surface of the shell by the projection of the shell onto the computational grid. This set of calculations were performed with a resolution of 800 level three grid cells (R_{800}) in the initial shell radius, corresponding to 1256 grid cells in each quadrant. This is equivalent to initial perturbation amplitudes that are $1.25 \times 10^{-3} R_i$ where R_i is the initial shell radius. Although we performed a detailed study of the thin shell implosion at different resolutions and established criteria for convergence, we present here only a summary of the evolution for the R_{800} case. These results and the effects of grid resolution will be discussed in more detail in Klein et. al. 1993.

In figures 1-4 we show rasterized images of density in gray scale of a half of the axisymmetric 2D shell where the left hand plane is symmetrical to the right. Darker regions indicate higher shell densities. In figure 1. we note that the appearance of the many small scale perturbations on the surface of the shell have begun to amplify due to the initial Richtmyer Meshkov instability triggered by the passage of the initial shock wave. This is caused by the large over-pressure of the low density gas outside and surrounding the high density shell. At this early time, the inner surface of the shell has not yet moved. At somewhat later time, figure 2. the shock has passed through the shell into the inner low density gas and the perturbations on the outer surface have grown substantially in amplitude with respect to wavelength due to Rayleigh Taylor instabilities well into the non-linear regime. At intermediate time, figure 3., the perturbations are far into the non-linear regime. They are many times the initial amplitude imposed by the grid. At this time significant multi-mode merges have occurred and the shell is severely fragmented and is evolving as a well developed chaotically mixed layer. The inner part of the shell has gone unstable as feedthrough of the non-linear modes from the outer surface have reached the inner surface and substantial mixing of the dense shell with the inner low density fluid has occurred. At late time in the evolution figure 4., the shell is substantially destroyed. Initial perturbations with wavelength $R_i/800$ have undergone several non-linear mode mergers with the emergence of dominant structures with wavelength $R_i/14$. There is substantial feed through of surface perturbations and growth of the inner perturbations. Significant mixing of the high and low density fluids leads to a mixed layer whose growth with respect to time can be approximately modeled by consideration of a generalization of the Plesset equation for a spherical geometry (cf. Mikaelian, 1990) this is discussed in detail in Klein et al. 1993.

We have performed these 2D calculations and analogous 3D Cartesian calculations with different grid resolutions. By examining the fourier coefficients representing the different resolutions we have established that the differing grids resolutions in fact represent different initial amplitude and wavelength perturbations. These initial calculations demonstrated that the growth of the mixing layer as a function of time first showed a linear growth in time representing the initial growth of the Richtmyer Meshkov instability makes the transition to a Rayleigh Taylor instability at intermediate time whose growth is well represented by $h(t) \sim 0.3Ag^2t$, where A is the Atwood number, and g is the effective acceleration. Our calculations indicated that the growth at late time was essentially the same for all the different grid resolutions representing different initial perturbations. Thus our preliminary conclusions were that the mixing layer loses memory of initial perturbations for the classical Richtmyer Meshkov and Rayleigh Taylor instabilities in thin spherically imploding shells.

To substantiate these preliminary results, we began a more extensive wavelength and amplitude scaling series of calculations in three dimensions with a thicker spherical shell whose initial thickness to initial radius is 0.1 and whose initial density is 1.25×10^2 times the initial density of the gas interior and exterior to the dense shell. To avoid the perturbations imposed by a Cartesian mesh on a spherically converging geometry, we solve the 3D hydrodynamics on a spherical coordinate system which allows us to more precisely control the initial perturbations on the inner and outer surface of a spherically imploding shell. As we have discussed in §2. we allow mesh refinement to occur everywhere high density shell material exists. In this way we can solve the Euler equations in 3D with high resolution. To develop a feel for the evolution of the dense shell we consider perspective volume rendered images of the density as a function of time. These images are a three-dimensional perspective view of the dense shell that allow us to look through the 3D dense structures by using different transfer functions along the line of sight of a multitude of rays through the computational domain. The rays are then reconstructed to give us a 3D view into the structure.

In figure 5. we note the initial structure at $t=0.0s$. of the low mode perturbations (12^2) on the surface of the shell. We recall that the shell is a $\frac{\pi}{4} \times \frac{\pi}{4}$ slice of the entire spherical 3D shell. In this image we view the shell at initial time at an oblique sideways angle. In figure 6. we see a side view of the low mode(12^2) perturbed shell at early time. At this time the initial shock has compressed the shell. The surface modes have begun to grow. The inner perturbed surface has not yet moved since the shock has not yet propagated far enough into the shell to trigger instabilities on the inside surface. At early time (figure 7.) we view the high frequency mode perturbations (48^2) from a perspective that is looking down on the surface of the shell. We note the extremely complex set of high frequency perturbations. At intermediate time in figure 8. just after the shock has exited from the shell into the inner low density gas, we see a side-ways view of the low mode perturbations(12^2) on the shell surface. The perturbations have grown substantially. They form 3D bubbles which are seen in the visualization as a complex network of ridges and valleys. The ridges are high density structures and the bubbles are of lower density. At intermediate time (figure 9.) we view the inside of the shell for intermediate (24^2) mode perturbations. We note an extremely complex set of ridges and bubble valleys. There is substantial feed through of the outer perturbations to the inside. Growth of the outer perturbations on the surface is apparent on the sides of the shell. At intermediate time the 48^2 mode calculation appears somewhat similar to the 24^2 mode, but the structure is far more complex (figure 10.). This is very apparent in the complex interlacing of bubbles and ridges that are combining to form a mixing layer. At this intermediate time, about 38% of the volume of the mixing layer is low density gas from the interior to the shell. At late time in the evolution the shell is well fragmented and essentially destroyed. We note in figure 11., which shows the low mode perturbations 12^2 from a view that skims the top and side of the shell that the shell has substantially thickened and broken up. Feed through of unstable modes from the outer surface is indistinguishable from growth of inner unstable modes. There is substantial mixing of the shell with the inner low density "fuel". At late time the 24^2 mode perturbation shows elongated broken shell structures (figure 12.). The shell is highly fragmented and the axis shows the location of the center of the spherical shell. Figure 13. shows the late time evolution for the high frequency perturbation which is similar to figure 12. The shell is destroyed with extremely spike-like structure. Significant amounts of mixing have occurred. At this time, 60% of the volume of the turbulent mixed layer is low density fluid.

The vorticity can play a significant role in mixing the dense shell with the low density inner gas. In the next two figures we display volume rendered images of the full 3D vorticity field, where we have calculated the magnitude of the vorticity and examine its structure. In figure 14. we view the vorticity field just after shock breakout at an oblique view of the top of the dense shell. We see the flow represented by complex baroclinically generated vortical structures in regions where the shell is starting to break apart as the low density fluid moves in between "holes" in the shell and creates shear flow layers. These calculations were for the 24^2 mode perturbations. At intermediate time, the vortical structures become elongated (figure 15.). These structures may indicate where fluid circulation is enhancing Kelvin Helmholtz instabilities on the sides of shell spikes further aiding in the breaking up and mixing in the shell. In figure 16. we examine a volume rendered image of the divergence of the fluid velocity. This is a good probe of the shock structure inside the low density gas. We note that the shock is highly crenulated in 3D. This indicates that the shock is propagating into the low density gas non-isotropically. The image shows us the inside view of an anisotropic shock surface.

A quantity of considerable importance is the growth of the turbulent mixing layer as a function of time, $h(t)$. We calculate this quantity by following shell matter with an advective marker and computing the length spanned by the 3D locus that includes 1% of the total mass of

the shell (the leading edge) to 99% of the mass of the shell (the trailing edge). In figure 17., we plot the space-time trajectory of the shell for the 24^2 mode calculation. We note that the shell is compressed by the initial shock up to about $t=1.25 \times 10^{-10}$ s, when shock breakout occurs, whereupon the leading edge begins to grow relative to the trailing edge. We can just as sensibly define the mixed layer to be that bordered by 5% to 95 % of the mass of the converging shell. In figure 18. we show the growth of the mixing layer as a function of time using the definition 5%-95% for the 12^2 , 24^2 and 48^2 mode perturbations with the initial amplitude fixed at A_0 . The mixing layer growth is remarkably insensitive to the initial wavelength perturbations throughout the duration of the implosion. The growth of the mixing layer after the shock breakout is linear and due to the Richtmyer Meshkov instability. At late time the growth is due to Rayleigh Taylor instabilities and is well fit by $h(t) \sim 0.38 A g t^2$. Figure 19. shows the growth of the mixing layer if the definition is extended from 1% to 99%. Here the leading coefficient of the quadratic growth is now 0.49. The crosses indicate the growth of a shell for which no perturbations were imposed. We see that after $t=2.25 \times 10^{-10}$ s, there is considerable departure in the growth of the perturbed shell relative to the unperturbed shell. These results add credence to our previous conclusions that the growth of the turbulent mixing layer loses memory of its initial perturbations in a converging geometry for both the Richtmyer Meshkov and Rayleigh Taylor instabilities.

As the mixing layer grows, and the shell begins to fragment, there is considerable mixing of the low density gas interior and exterior to the shell with the high density shell matter. In figure 20. we show the calculation of the volume fraction of low density gas to high density shell. We note that at late times the mixing is severe with up to 60% of the mixing volume filled by low density gas. The amount of low density gas mixed in is highest for the lowest mode perturbation presumably because these low modes represent the largest structures with the largest "holes". At late time the mixed volume fraction saturates as the fragmented shell begins to occupy a smaller volume during spherical compression. In figure 21. we show the time variation of the average density and rms density fluctuation in the shell. The shell is most compressed at time of shock breakout and undergoes a series of density fluctuations at late time. These fluctuations, most readily seen as average pressure fluctuations in the shell (figure 22.) represent a series of reflected shocks inside the shell that damp out in time. The kinetic energy in the mixing layer continues to increase until about $t=3 \times 10^{-10}$ s. when the shell begins to decelerate due to loss of pressure drive as the shell begins to fragment. At this time the mean kinetic energy in the shell decreases. After $t=2 \times 10^{-10}$ s. the kinetic energy begins to pick up a turbulent fluctuating component (figure 23.) which remains fairly constant even at late time as the shell becomes turbulent. The total kinetic energy remains dominated by its mean component. In figure 24. we display the transverse K_θ and longitudinal K_z components of the kinetic energy. These components begin to grow at about $t=2 \times 10^{-10}$ s. when the flow in the shell becomes complex. These components of the kinetic energy are only 0.02 K_r through the subsequent evolution. A measure of the vorticity is the mean enstrophy. We calculated the mean enstrophy

$$\langle \omega^2 \rangle = \frac{1}{V} \int \omega^2 dV \quad \text{where } \omega \text{ is the magnitude of the vorticity and } V \text{ is the mixing layer volume in}$$

the mixing layer as a function of time. In figure 25. we show the total enstrophy and it's individual components. The enstrophy or the vorticity has its dominant components in the plane of the converging capsule where most of the circulation is taking place. The enstrophy is fed by the buildup of shear as the gas bypasses the denser shell material. The radial component of the vorticity is dominated by these components until late time when the capsule has converged to 0.25 of it's initial radius. In figure 27. we examine the scaling of the enstrophy as a function of mode perturbation and we see an interesting cascade for the enstrophy. This wavelength scaling for the mean enstrophy shows that high frequency, small scale structures (48^2 mode perturbation) results in early vorticity build up, while low frequency (12^2 mode) perturbations representing larger scale structures increase vorticity at later times. We note that the high frequency small

scale structures show saturation of enstrophy early on. The decay of enstrophy is however fastest for the low mode perturbations.

We examined amplitude scaling of the perturbations as well as frequency scaling. In this calculation, we kept the frequency scaling as the 24^2 mode perturbations and let the initial amplitude increase by as much as a factor of 2. In figure 27, we show the results for the growth of the mixing layer for initial perturbations that are a factor of 2 larger in amplitude than our previous results. In comparing the results of the two calculations for the 24^2 mode perturbations we note that although the actual growth of the mixing layer is larger for the higher amplitude perturbations, the **rate of growth** is essentially the same for most of the convergence of the capsule. In figure 28, we plot the mix volume fraction for the different amplitude perturbations and again we see that after $t=2 \times 10^{-10}$ s, the rate of growth of the mix fractions for the two cases is the same. Combined with our results for wavelength scaling we would conclude that the growth of a mixing layer due to Richtmyer Meshkov and Rayleigh Taylor instabilities appears to lose memory of both its initial perturbations in both wavelength and amplitude for a converging geometry.

4. SUMMARY

We find several conclusions from our work.

- (1) For these initial conditions a wavelength scaling series establishes that memory loss of initial multiple wavelength perturbations occurs in the late time evolution of a turbulent mixing layer for both 2D and 3D spherically converging geometry for Rayleigh Taylor and Richtmyer Meshkov instabilities. This generalizes earlier findings for planar experiments.
- (2) For these initial conditions an amplitude scaling series establishes that the growth rate of a turbulent mixing layer loses memory of initial amplitudes in a spherically converging geometry in 2D and 3D.
- (3) The instabilities in the imploding shell considered here are violent. The shell undergoes severe break-up at $2-3 \times 10^{-10}$ s, when $R \sim R_i/4$. Feed through of unstable modes from the outer surface results in a substantial growth of a turbulent mixing layer resulting in a shell with about 3 times the nominal shell thickness without perturbations.
- (4) The break-up of the shell leads to deceleration of the shell and further enhanced Rayleigh Taylor instabilities on the inside of the shell. This results in a large increase in the mixing volume of the shell with gas that reaches 65%-80%. Shell break-up occurs before a reflected shock can cause shell deceleration. The volume fraction of mixed fluid saturates at late time and the shell compresses the low density gas very non-uniformly.
- (5) For thin shell implosions we find that $h(t) \sim 0.3Ag^2t^2$ for both 2D and 3D. This is in reasonable agreement with planar incompressible experiments of Read and Youngs (1984) for the **entire mixing region**. For thicker shells we find that the growth of the mixing region is represented by $h(t) \sim (0.38-0.49)Ag^2t^2$ depending on how the definition of the mixing region is taken. A preliminary conclusion is that the leading coefficient for the growth may not be a universal constant for spherically convergent compressible flows.
- (6) As the shell begins to fragment, kinetic energy is fed into a turbulent fluctuating component which stays relatively constant for long times as the mean kinetic energy decays.

(7) Wavelength scaling for the mean enstrophy shows that high frequency, small scale structures result in early vorticity build up, while low frequency perturbations increase vorticity at later times. The high frequency small scales saturate at earlier times. The decay of the enstrophy of low mode large scale structure are fastest.

(8) The inward moving shock has a highly crenulated 3D structure. It does not compress the inner gas uniformly. Thus different parts of the main shock reach the center of the spherical shell at different times. The crenulated structure of the 3D shock may be a result associated with our idealistic pressure boundary conditions.

Acknowledgments

Portions of this work were performed under the auspices of the U.S. Department of Energy at the Lawrence Livermore National Laboratory under Contract No. W-7405-ENG-48. The calculations were performed on the Cray YMP-8/128 supercomputer.

References

1. Bell, J., Berger, M., Saltzman, J. and Welcome, M., 1991, UCRL-JC-108794.
2. Berger, M. J. and Colella, P., 1989; *J. of Comp. Physics*, Vol. 82, p.64.
3. Dahlburg, J. P., Gardner, J. H., Doolen, G. D. and Haan, S. W., 1993, *Phys. Fluids B* 5(2), 571.
4. Lindl, J. D., McCrory, R. L. and Campbell, E. M., 1992, *Physics Today*, 32.
5. Mikaelian, K. O., 1990, *Phys. Review Letters*, Vol. 65, No. 8, 1992.
6. Read, K. I., 1984, *Physica* 12D, 45. See also Read, K. I. and Youngs, D. L., 1983 AWRE Report No. 011/83.
7. Rupert, V., 1991, 18th International Symposium on Shock Waves, Japan.
8. Sugami, H. and Nishihara, K., 1990, *Phys. Rev. Lett.* 65, 432.
9. Town, R. P. J. Town and Bell, A. R., 1991, *Phys. Rev. Lett.* 67, 1863.
10. Tryggvason, G. and Unverdi, S. O., 1990, *Phys. Fluids A2*, 656.
11. Yake, H., Hoshino, H. and Tsuchiya, T., 1991, *Phys. Rev. A* 44, 27 56.

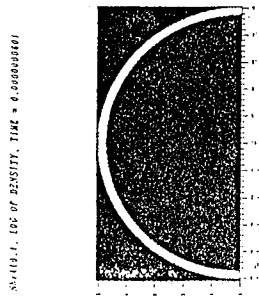


Figure 1.

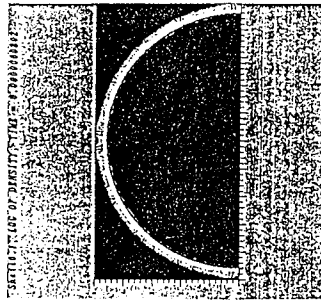


Figure 2.

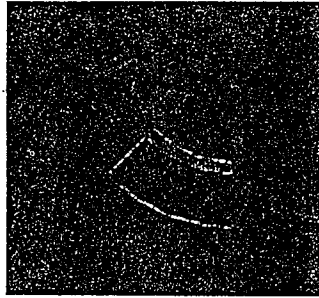


Figure 3.



Figure 4.

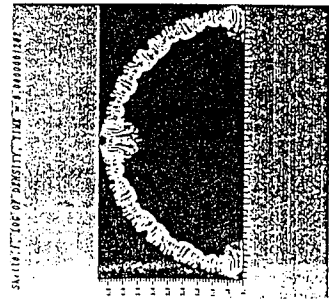


Figure 5.

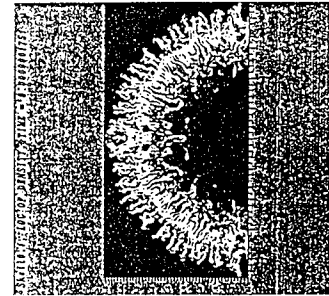


Figure 6.

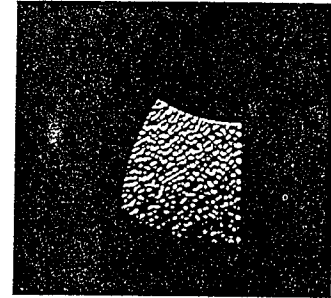


Figure 7.

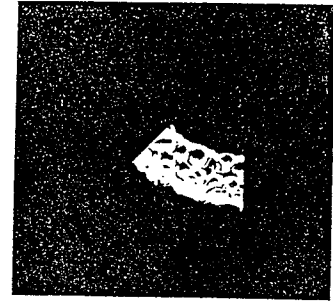


Figure 8.

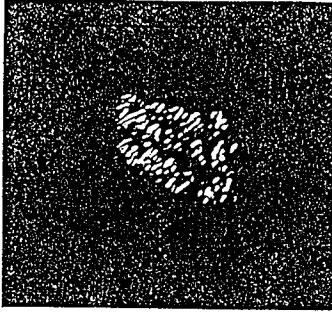


Figure 14.

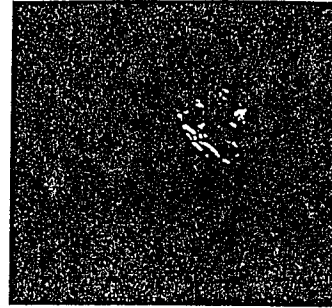


Figure 16.

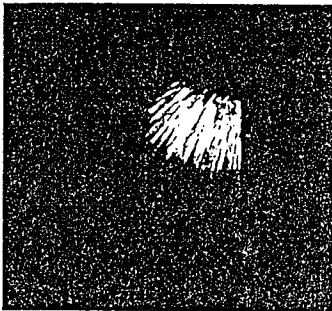


Figure 13.

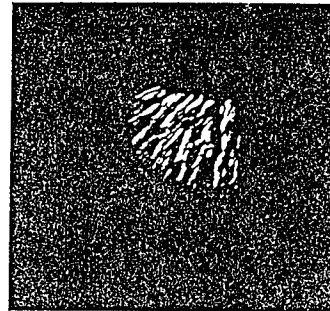


Figure 15.

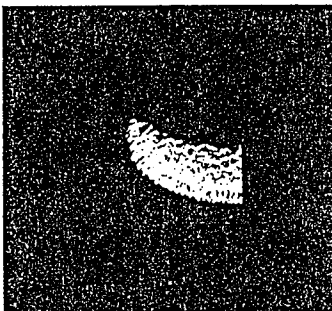


Figure 10.

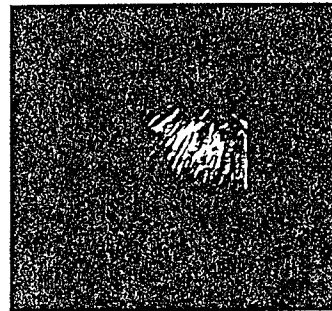


Figure 12.

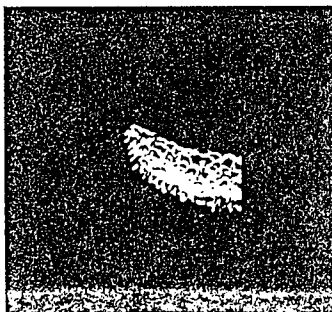


Figure 9.



Figure 11.

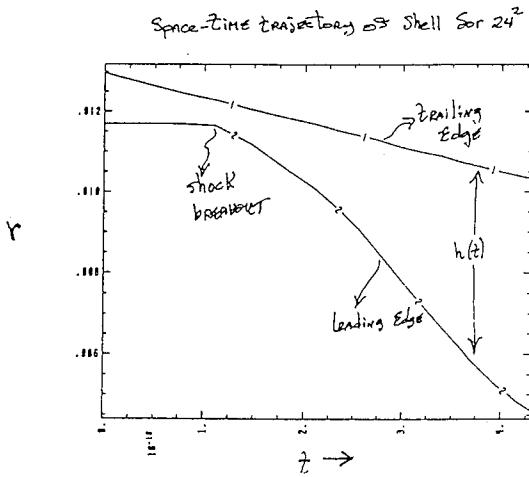


Figure 17.

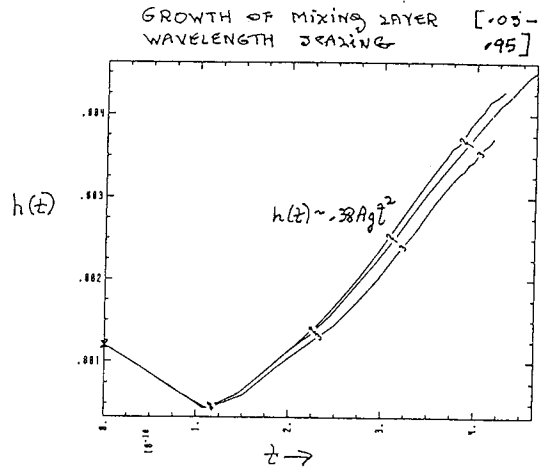


Figure 18.

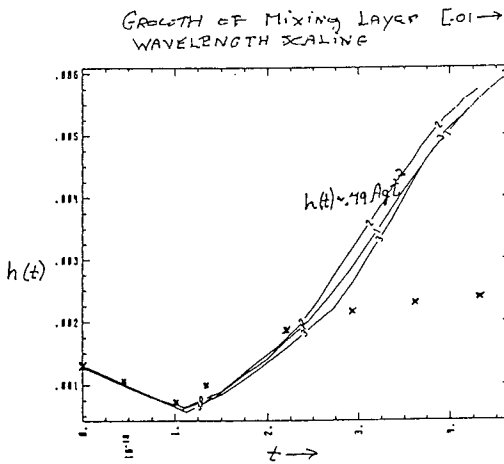


Figure 19.

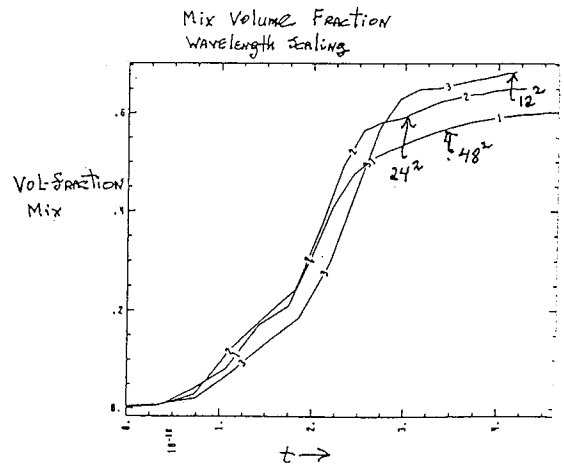


Figure 20.

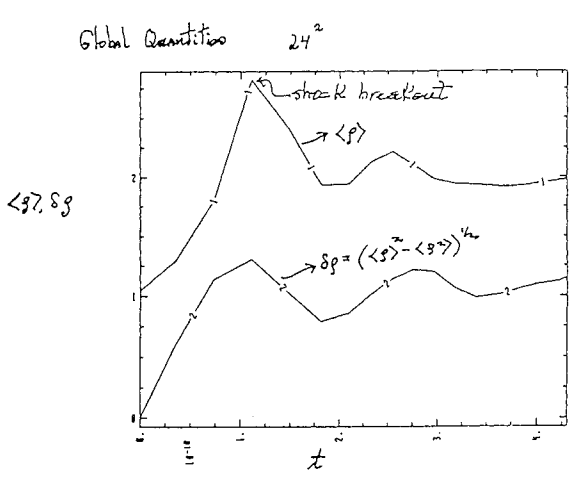


Figure 21.

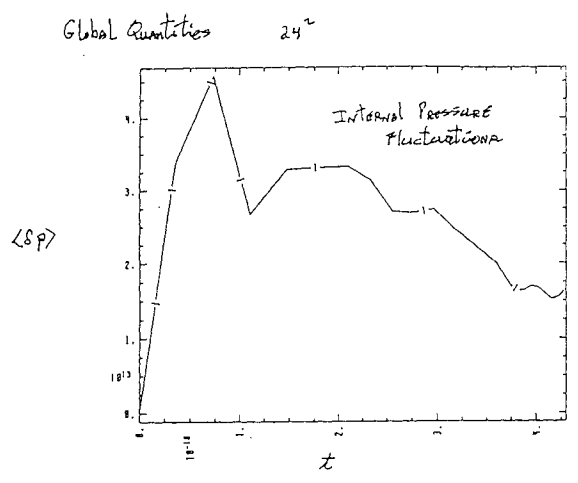


Figure 22.

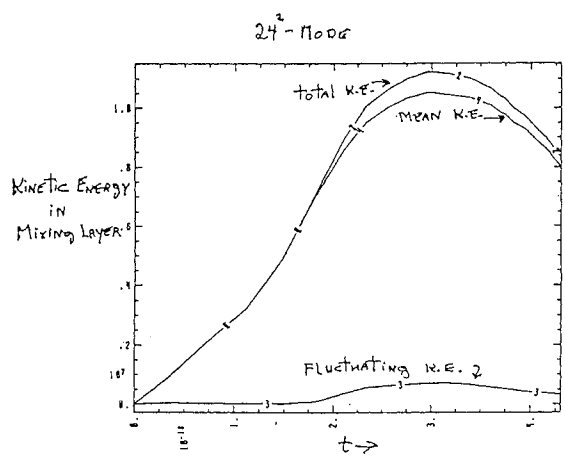


Figure 23.

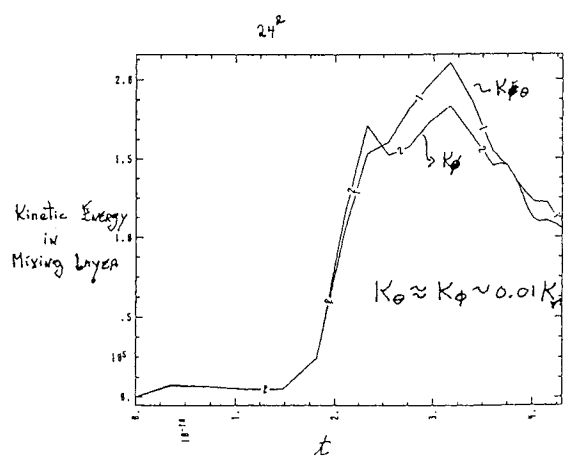


Figure 24.

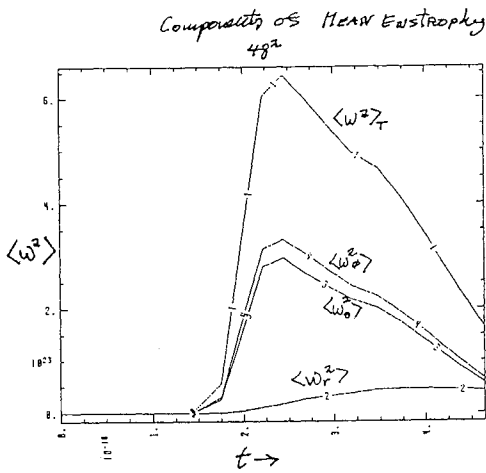


Figure 25.

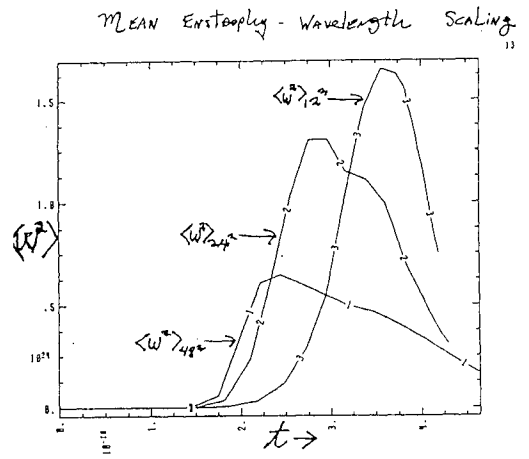


Figure 26.

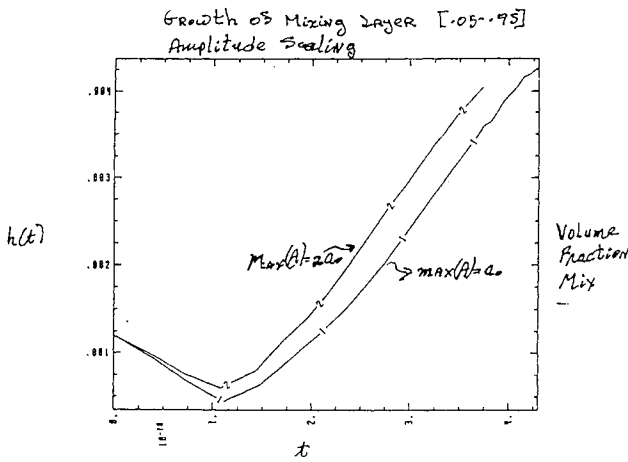


Figure 27.

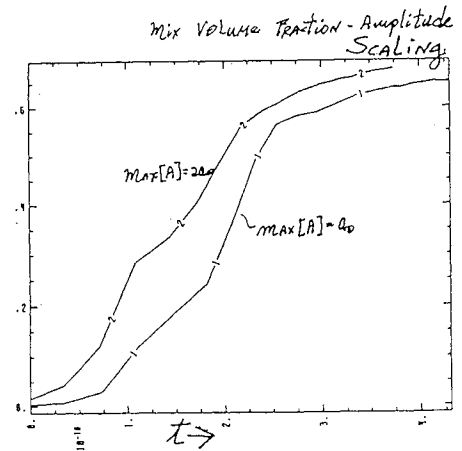


Figure 28.

RICHTMYER-MESHKOV AND RAYLEIGH-TAYLOR INSTABILITIES INDUCING A TURBULENT FLOW DURING A CYLINDRICAL IMPLOSION

Michel Legrand, Nathalie Toqué, Commissariat à l'Energie Atomique
Centre d'Etudes de Vaujours-Moronvilliers
B. P. 7, 77181 Courtry, FRANCE

1 - INTRODUCTION

Rayleigh-Taylor¹ and Richtmyer-Meshkov² Instabilities (RTI and RMI) have been widely studied because of their effect on the performance of Inertially Confined Fusion (ICF) capsules.

In the spherical configuration of an ICF capsule, direct observation of the interfaces is very difficult. Such an observation is easier in the case of an axisymmetric cylindrical geometry which can undergo a concentration phase³ and allows a radiographic observation along the axis of the cylinder.

2 - PRINCIPLE OF THE EXPERIMENT

Implosion is initiated by a cylindrical detonation wave converging in an explosive cylinder (Figure 1). The initial defect is machined at the inner face of the tin shell (external diameter: 100 mm, thickness: 4 mm) and is a combination of sinusoidal waves

$$R(\theta) = R_0 + \sum a_n \cos n\theta$$

where n is the mode order.

We aimed at obtaining a long phase during which the Rayleigh-Taylor instability could develop. This phase which is correlated to the deceleration of the metallic cylinder, is produced by the rarefaction wave following the detonation and by the counterpressure coming from the low density inner medium. With a 1D hydrodynamic code we obtained, for the central section of the cylinder, the tin/silicone interface velocity history (Figure 2).

These experiments have been used to validate the codes which compute the growth of defects in the linear and non linear phase.

More recently, we try to generate a pre-turbulent flow by using 3-modes defects⁴.

The first experiment involves the combination (13, 21, 29, $a_n = 0.5$ mm). The experimental results were very close to numerical evaluations obtained with the 2D eulerian code EAD⁵, but the flow was far from turbulence. In particular, the interface region was not exactly a mixing zone.

It is the reason why we tried to modify the spectrum of the initial defect. We have chosen to use a 1 mm amplitude for the three modes (26, 42, 58). Naturally, the meshes used in the computation had to be smaller than in the preceding one. The flow becomes very intricate much more rapidly than for the preceding case (13, 21, 29). At the end of the Rayleigh-Taylor phase, there is a real mixing zone in the interface region.

The experimental results were very close to numerical evaluations, but we didn't know the exact nature of the flow which could be laminar or turbulent.

3 - A TURBULENCE CRITERION

Turbulent flows have a unique feature: they forget initial conditions. This leads to a simple idea: a turbulence characteristic length (Turbulent Mixing Zone Width, TMZW, for example) can be related to unperturbed flow variables by means of dimensional analysis. In the case of a RTI, the flow variables are the Atwood number A_t and the interface acceleration g . Consequently TMZW is related to A_t , g and time t . The only combination of these variables which is a length is gt^2 : during the turbulent phase of a RTI, the turbulent mixing zone width can be written:

$$TMZW = f(A_t)gt^2 \quad (1)$$

$f(A_t)$ has been evaluated for various values of A_t ^{6,7}:

$$f(A_t) = \alpha (1 + \beta) A_t$$

$$\alpha = 0.07 \pm 0.01$$

$$\beta = (\rho_2/\rho_1)^{1/3}$$

ρ_1 and ρ_2 are the densities of the fluids.

Therefore, the dependence of MZW versus time during a RTI is a primitive turbulence criterion.

In the case of 3-mode experiments, the criterion leads to the following conclusion: the flow is very intricate, but not turbulent.

A turbulent flow generated during a RTI in cylindrical configuration can be obtained very simply using a "shock-tube" structure (Figure 3). This is the cylindrical counterpart of a shock tube experiment⁶.

Numerical simulations were carried out with a multimode spectrum and lead to t^2 dependence of MZW: the flows seems to be turbulent.

These results have been confirmed by biorthogonal analysis (Nadine Aubry, City College of the City University of New York): the entropy associated with a hydrodynamic variable is higher in the case of the "shock-tube" structure than in the case of the 3-mode experiments.

4 - TURBULENCE EXPERIMENTS

During 3-mode experiments, flow stays laminar: the RT phase duration Δt is smaller than the transition time τ .

The transition time is difficult to evaluate but is correlated with τ^* which is the characteristic time of the linear phase of the RTI:

$$\tau^* = \frac{1}{\sqrt{A_t kg}}$$

A_t is the Atwood number, k the wave number of the defect and g the interface acceleration.

$\Delta t/\tau^*$ is related to the turbulence tendency of the flow:

	$\Delta t/\tau^*$
3-mode experiment (26, 42, 58)	4
"shock tube" structure	13

This leads to the concept of a high explosive cylindrical experiment with $\Delta t/\tau^*$ higher than 10. Δt is fixed by the nature of the implosion system. Therefore we must shorten τ^* and use smaller defect wavelengths ($\lambda_{\min} = 0.6$ mm).

The corresponding cylindrical flow is impossible to calculate: it needs too many meshes. It is the reason why we calculate a plane approximation of the system which needs much less meshes.

Using reflection symmetries, it is possible to treat a ten modes spectrum ($0.6 < \lambda < 6.0$ mm) in an acceptable computation time.

The amplitude of each mode has been chosen at random from a gaussian distribution. Then we defined two spectra (Figure 4) leading to the same RMS amplitude of the defect (0.12 mm).

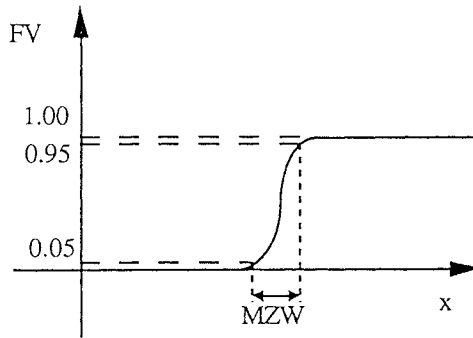
5 - NUMERICAL EVALUATIONS

Numerical simulations (2D eulerian code EAD) were carried out with the two spectra of figure 4 and the same tin/silicone interface velocity history.

The results of these computations are shown on figure 5. The patterns obtained at a given time are completely different but the mixing zone width seems very similar.

Another simulation has been carried out with spectrum 2 (Figure 4), a different interface velocity history (different g) and a different Atwood number. The results are shown on figure 6: mixing zone widths are different of those of figure 5 during the second part of the simulation (7 - 12 μ s).

Mixing zone width can be precisely defined by calculating volumic fraction of tin as a function of x :



We show on figure 7 the growth of the square root of the MZW as a function of time for the two first simulations (same tin/silicone interface velocity history). The curves are nearly identical. Moreover, we have:

$$\sqrt{MZW} = Kt + b$$

$$\text{with } K = 3.72 \cdot 10^4 \text{ c.g.s}$$

We can obtain another value for K with equation (1):

$$K = \sqrt{\alpha(1+\beta)A_s \bar{g}}$$

\bar{g} is a mean value for g which is not constant. This leads to:

$$K = 3.48 \cdot 10^4 \text{ c. g. s.}$$

These results are close to each other: flow seems to have forgotten initial conditions and could be turbulent.

These results have been confirmed by the study of the third calculation where g is different.

6- CONCLUSION

The experimental device we have chosen has shown the development of various perturbations during the pre-turbulent phase: the growth of the mixing zone is well evaluated by a 2D eulerian numerical simulation.

We have defined a simple turbulence criterion in order to select turbulent flows. This criterion has been used to test different flows initiated by different initial defects the wavelength of which have been previously determined.

This leads to the concept of an experiment using very high order modes in order to reach a final turbulent stage. This experiment will be soon carried out.

REFERENCES

- 1 - S. CHANDRASEKHAR, Hydrodynamic and Hydromagnetic Stability
Oxford Univ. Press, Oxford, 1961
- 2 - R. D. RICHTMYER, Taylor Instability in Shock Acceleration of
Compressible Fluids
Comm. in Pure and Applied Math. 13 (1960) 297
- 3 - A. I. TOLSHMIAKOV and E. E. MESHKOV, Development of
Perturbations of a Contact Boundary Accelerated by a Convergent Shock
Wave in the Cylindrical Case
1989 Plenum Publishing Corporation
- 4 - M. LEGRAND and N. TOQUE, Interface Instabilities occurring during
an explosive driven implosion
3rd International Workshop on the Physics of Compressible Turbulent
Mixing (Royaumont, FRANCE, 1991)
- 5 - C. COSTE and al. Joint CEA - LOS ALAMOS Conference on
Hydrodynamic Instabilities (LOS ALAMOS)
in Computing Methods in Applied Science and Engineering
GLOWINSKY and LYONS, North Holland 1982
- 6 - D. L. YOUNGS, Numerical Simulation of Turbulent Mixing by
Rayleigh Taylor Instability
Physica 12D (1984) 32
- 7 - K. I. READ, Experimental Investigation of Turbulent Mixing by
Rayleigh Taylor Instability.
Physica 12D (1984) 45

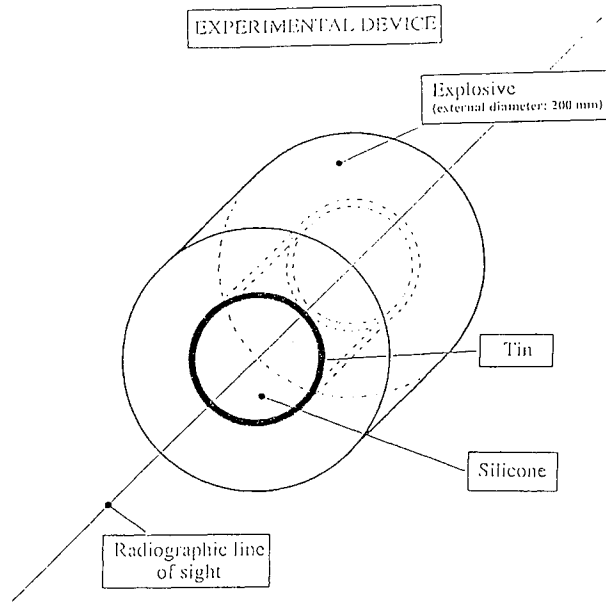


FIGURE 1

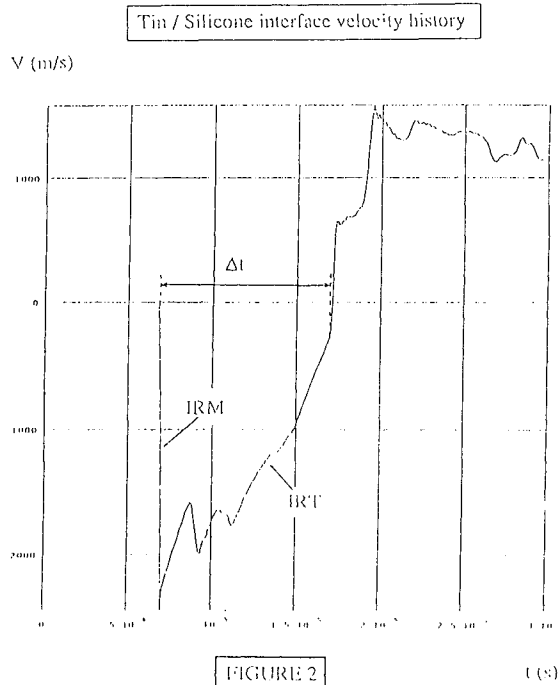


FIGURE 2

"Shock Tube" Structure

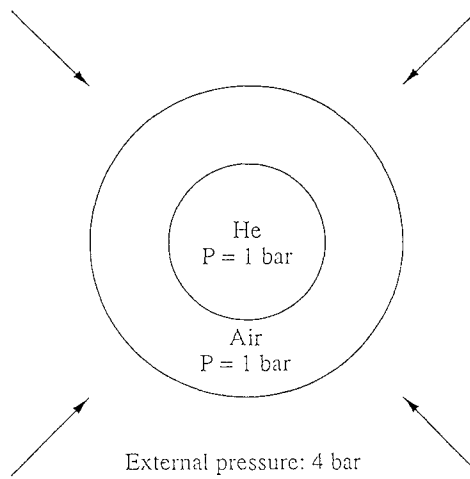


Figure 3

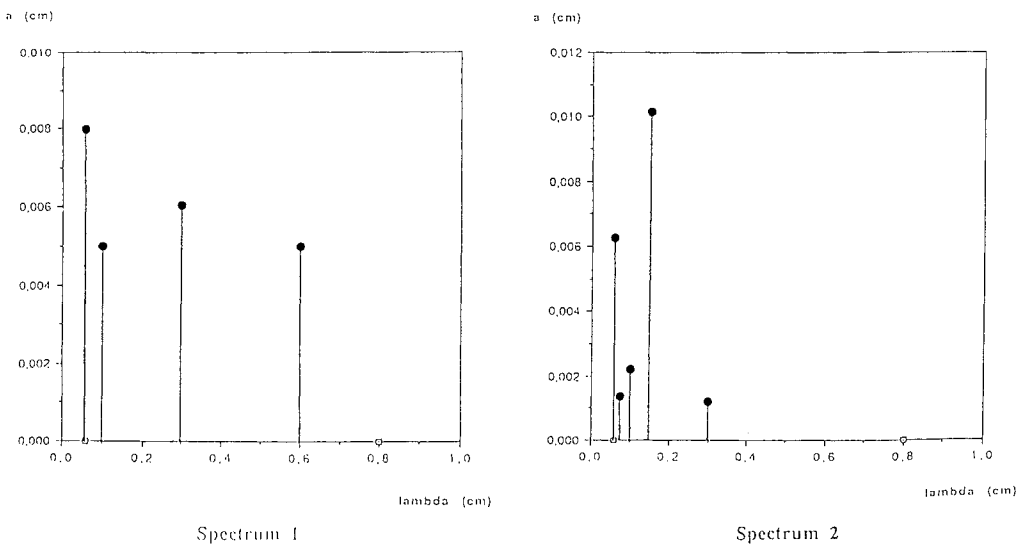


Figure 4

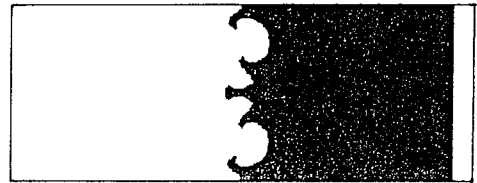
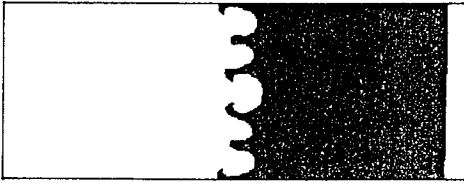
NUMERICAL SIMULATIONS
(2D eulerian code EAD)

Spectrum 1

Spectrum 2



$t = 0$



$t = 2 \mu\text{s}$



$t = 7 \mu\text{s}$



$t = 12 \mu\text{s}$

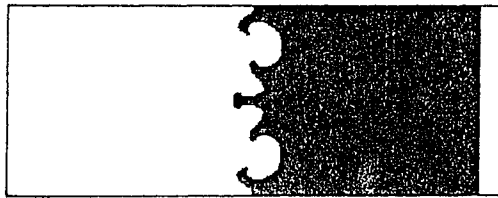
←
1 mm

FIGURE 5

NUMERICAL SIMULATION
(Spectrum 2)



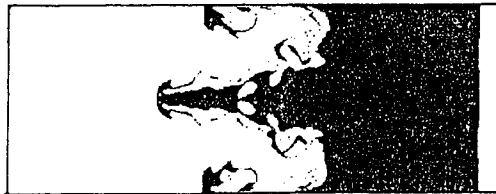
$t = 0$



$t = 2 \mu\text{s}$



$t = 7 \mu\text{s}$



$t = 12 \mu\text{s}$

←→
1 mm

FIGURE 6

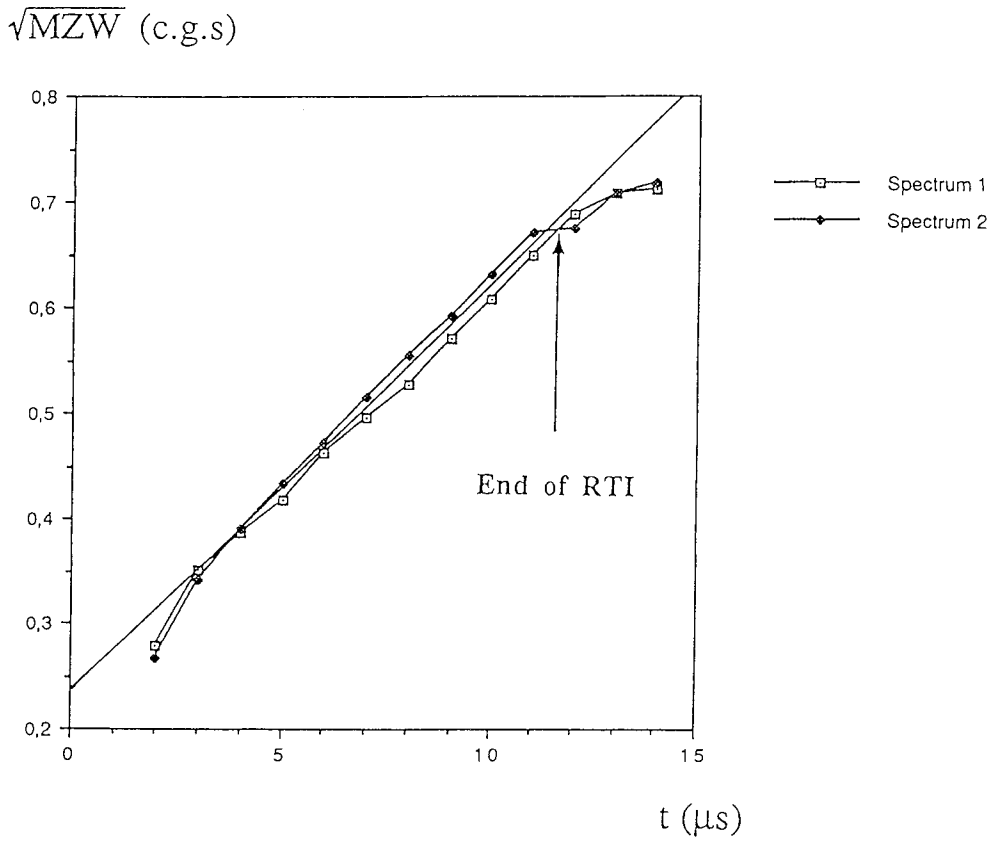


FIGURE 7

TURBULENT MIXING DEVELOPMENT INVESTIGATION WITH CONVERGING JELLY RINGS

E.E.Meshkov, N.V.Nevmerzhitsky, V.G.Rogachev, I.G.Zhidov
All-Russian Experimental Physics Institute
607200, Arsamas-16, Nizhni Novgorod region, Russia

ABSTRACT

The technique was developed to study the turbulent mixing at the unstable surfaces of converging cylindrical jelly liners accelerated by explosive gas mixture explosion products. The experimental results obtained with this technique are presented.

INTRODUCTION

In most experimental investigations of Rayleigh-Taylor instability (R-T instability)^{1,2} and associated with it turbulent mixing, a plane surface case was considered. Cylindrical case is described in a few papers. Initial perturbations and turbulent mixing zone growth on cylindrical surfaces of different densities, accelerated by a converging shock wave, are described in papers^{3,4}.

Growth of perturbations on the inner boundary of a metal shell, collapsing due to HE explosion products was studied by M.Legrand and N.Toque⁵.

Method of non-stationary hydrodynamics flow investigation, using jellies^{6,7,8}, provides wide capabilities to study R-T instability of cylindrical geometry. Specifically, jellies of gelatin water solution exhibit such strength, that allows to fabricate models of complex shape and, on the other hand, the strength of jellies, prepared by "kitchen" technology is not high, and under pressure more than 0,1+1 atm jelly loses its strength and behaves as a liquid. Jelly transparency allows to use optical methods for flow pattern recording.

Experimental results, demonstrating the capabilities of jelly technique used to study growth processes of turbulent mixing at the surfaces of jelly shell, collapsing under the pressure of gas explosive mixture (GEM) explosion products (EP), are given below.

EXPERIMENTAL

The scheme of device, used in experiments, is shown in Fig.1. The device comprises an upper (1) and lower (2) acrylic plastic plates, transparently polished, and a case ring (3) of 195 mm inner diameter and 10 mm height.

Heated gelatin solution was filled in the device without a top cover. Then it was hold in a cooler at $T=10$ °C for 2 hours. After jelly solidification a ring (4), placed concentrically to the casing (3), was cut of from the jelly total mass by a special knife. The inner and outer ring diameters were 110 mm and 80 mm, respectively (ring fabrication error <1 mm). The jelly ring height was slightly greater than the ring (3) height (about tenths of a millimeter). When the cover (1) was installed in its place, two closed sections (5) and (6) were formed. The section (5) contained air at ambient pressure and the section (6) was filled with GEM -

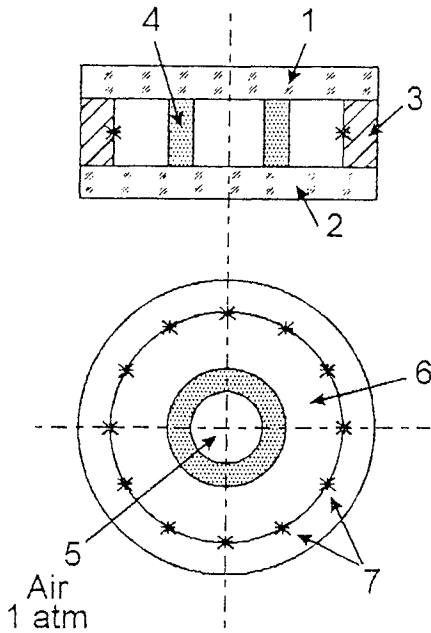


Fig.1 Scheme of experimental facility. 1,2-acrylic plastic plates, 3-case ring, 4-jelly ring, 5-inner cavity of jelly ring, filled with air ($p_0=1$ atm), 6-section filled with GEM, 7-spark gaps.

acetylene with oxygen mixture ($C_2H_2 + 2.5O_2$), through pumping the section (6) by mixture volume, which was ~ 10 times as large as section volume.

Spark gaps (40 or 12 gaps) were placed on the ring (3) inner surface (on its half-height). A detonation wave was initiated in GEM at spark gap breakdown by a high voltage pulse.

Under EP pressure, jelly ring is collapsed. Flow pattern was recorded by a high-speed camera. A flash lamp was used as a light source.

Experiments were carried out on jelly rings of various strength. Strength was changed by variation of gelatin solution concentration. To evaluate jelly strength scale, a series of compressive strength measurements were performed using cylindrical jelly samples 20 mm in diameter and of 20 mm height, fabricated by molding technique.

Measurement results are presented in Table I

Table I. Strength function of gelatin concentration.

Concentration (weight), %	4.4	8.8	13.2	17.6	35.2
Strength, atm	0.1	0.5	0.9	1.3	2.8

THEORETICAL

GEM detonation velocity is $D=2450$ m/s, sound velocity in explosion products - $C_{EP}=1040-1100$ m/s. Detonation process in the GEM takes $t = \Delta R/D = 16 \mu s$. Jelly ring is collapsed under EP pressure. Characteristic collapse velocity is 50 m/s, that is significantly less than sound velocity in EPS and in air in the ring inner cavity. To describe ring motion the simplified theoretical model was used, in which the process of pressure variation in chamber and in inner cavity was supposed to be an adiabatic one.

Calculations were performed using the following parameters:

Air - $p_0 = 1 \text{ atm}$, $\gamma = 1.4$; Jelly - incompressible liquid with $\rho = 1 \text{ g/cm}^3$, viscosity and strength properties were ignored (this approximation is valid only for jelly of small strength); GEM EPs - $p_0 = 13.5 \text{ atm}$, $\gamma = 1.24$.

Scheme for calculations is shown on Fig.2.

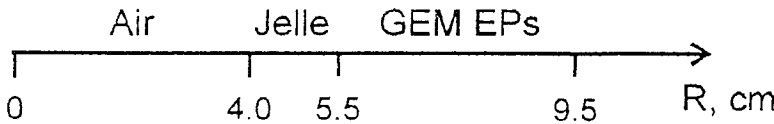


Fig.2. Scheme for calculations

Fig.3 shows a calculated R-t diagram. Figs.4-6 show inner and outer ring boundaries acceleration; velocity of inner boundary and air pressure versus time. At the initial stage of jelly cylindrical layer motion, acceleration is directed from periphery to the system center (Fig.3,4). Thus, outer boundary is unstable and the inner one is stable. After deceleration onset and change of acceleration sign, the inner boundary becomes unstable and the outer one becomes stable. The maximum acceleration value is $\sim 4 \cdot 10^6 \text{ m/s}^2$.

EXPERIMENTAL RESULTS AND DISCUSSION

The perturbation growth on unstable boundaries depends on the initial perturbation character. Two types of initial perturbation are available on outer boundary of jelly ring:

- Layer surface roughness depended on its manufacturing technology. According to visual inspection (comparison with samples, of known roughness); its initial value was $40 \div 160 \mu\text{m}$.
- Difference in acceleration dynamics (at initial stage of acceleration) at different layer surface points due to multi point GEM initiation. Detonation and shock waves collisions influence greatly the initial amplitude of perturbations⁷.

Initial perturbations at the inner boundary are depend on initial roughness. Perturbations induced by initiating system are smaller than the one at the outer boundary.

Photochronogram of the jelly layer experiment is shown in Fig.7 (gelatin concentration is 4.4 %). Initiation of GEM was performed at 40 points. Datum line radii on pictures are 15 and 35 mm. From the beginning of layer motion, a turbulent mixing zone (TZ) is formed on outer boundary of the ring. TZ length increases with time and bubbles on TZ inner edge become larger ($4 \div 5 \text{ mm}$ in diameter). After acceleration sign change ($t = 400 \text{ ms}$), bubbles begin to "force down into" reverse direction, TZ length reduces and at the moment $t = 1050 \text{ ms}$ it reaches its minimum. TZ inner edge becomes "smooth".

Layer inner boundary becomes unstable from the moment of deceleration onset, and a turbulent mixing zone of a small scale structure (zone non-transparency

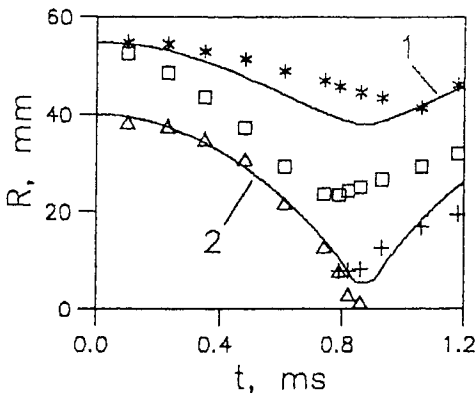


Fig.3. R-t diagram of collapsing jelly ring, 1,2-outer and inner boundaries of the ring (calculation), *, □-mixing zone surfaces at outer boundary, +, Δ-mixing zone surfaces at inner boundary of the ring (jelly ring experiment of ~0,1 atm strength).

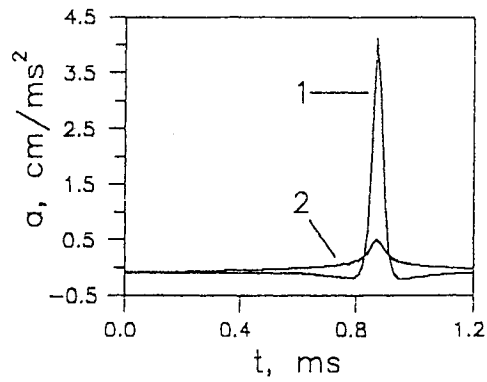


Fig.4. Calculated time function of the 1-inner and 2-outer boundary acceleration.

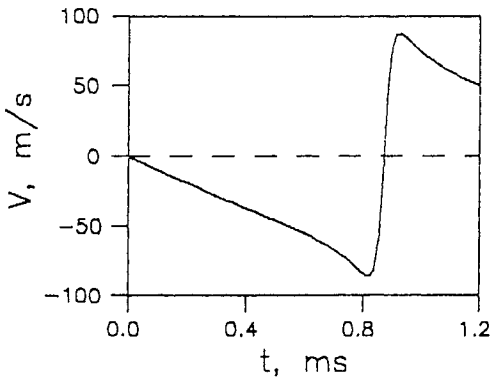


Fig.5. Calculated time function of the inner boundary velocity $V(t)$.

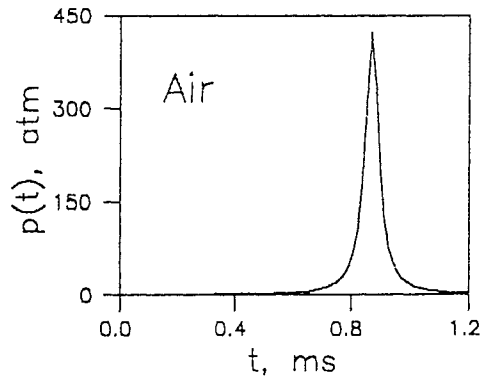


Fig.6. Calculated time function of air pressure $p(t)$.

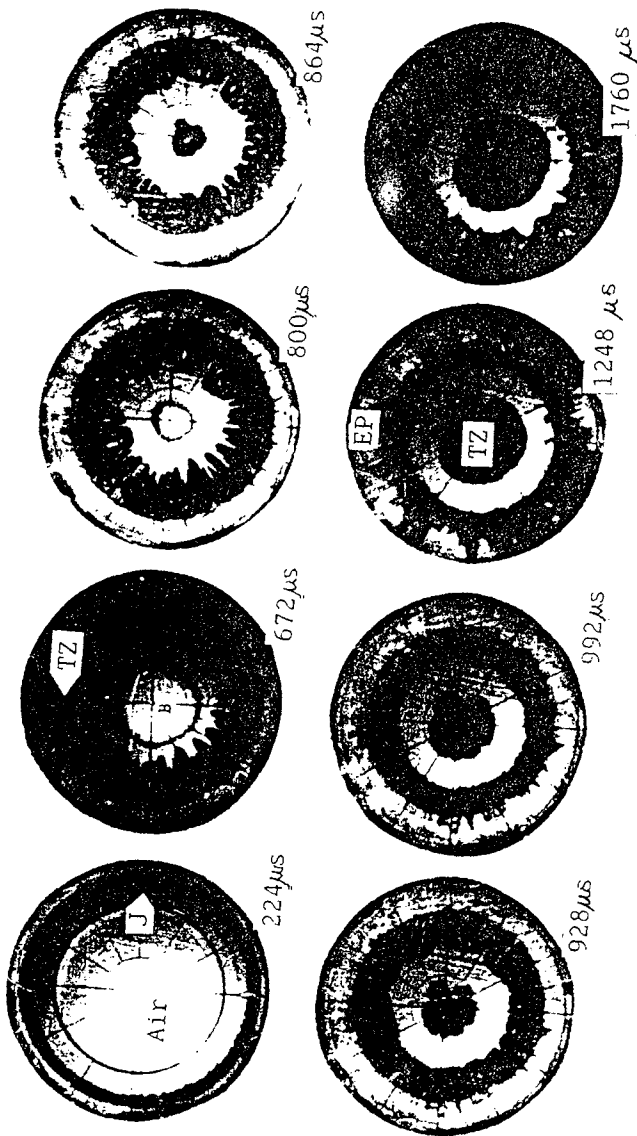


Fig. 7. Experimental photochronograms (jelly strength ~ 0.1 atm; 40 initiation points);
J-jelly ring; TZ-turbulent zone; EP-explosive products.

speaks for that fact), which can not be resolved by the optics of recording equipment (resolution ~ 0.5 mm) is rapidly formed behind it.

Photochronogram negative pictures were measured with a microscope of 0.01 mm accuracy. For each surface the measurements were made at four points. Surface radii were determined by averaging of the four given measurements.

Experimental results are given in Fig.3. There is a good agreement between the experimental and calculated data for the inner boundary at its stable portion. Fig.8 shows TZ length, L at both jelly ring boundaries as a function of time.

It may be noted that increased jelly strength significantly affects 1-D motion dynamics. As the strength increases, the characteristic collapse velocity decreases and the process is protracted. This illustrates the dependence of focusing relative time on concentration (Fig.9). Here, the focusing moment is the moment, when TZ inner edge reaches system center.

In the experiment (Fig.10) with the increased gelatin solution concentration (gelatin concentration is 17.6%), the character of instability growth changes significantly:

- jelly strength increase causes turbulent mixing zone growth suppression;
- at the same time, an intense bubble growth at detonation waves collisions at a jelly layer surface is observed (in this experiment GEM was initiated at 12 points);
- some of bubbles reach ring inner boundary and break it at the maximum compression;
- at the shell deceleration, some bubbles turn out to be "frozen" into the shell body.

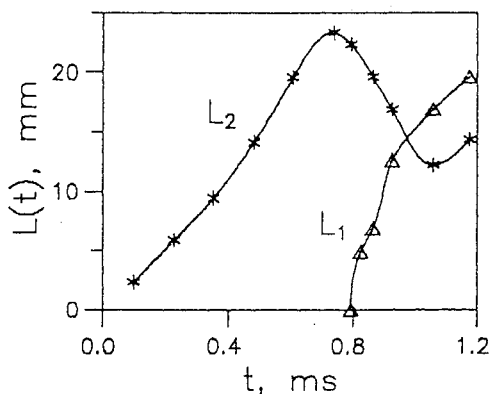


Fig.8. Time dependence of TZ-lengths.
 $L_1(t)$ - at inner boundary,
 $L_2(t)$ - at outer boundary.

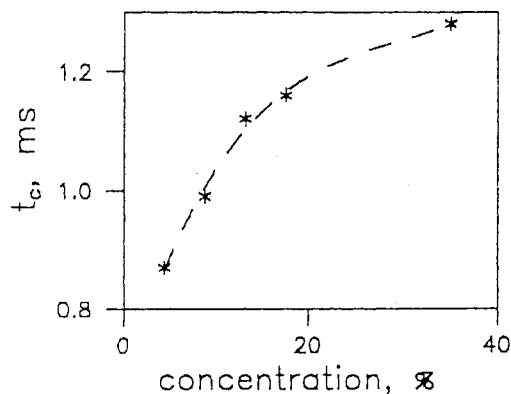


Fig.9. Dependence of the ring collapsing time t_c on the jelly concentration.

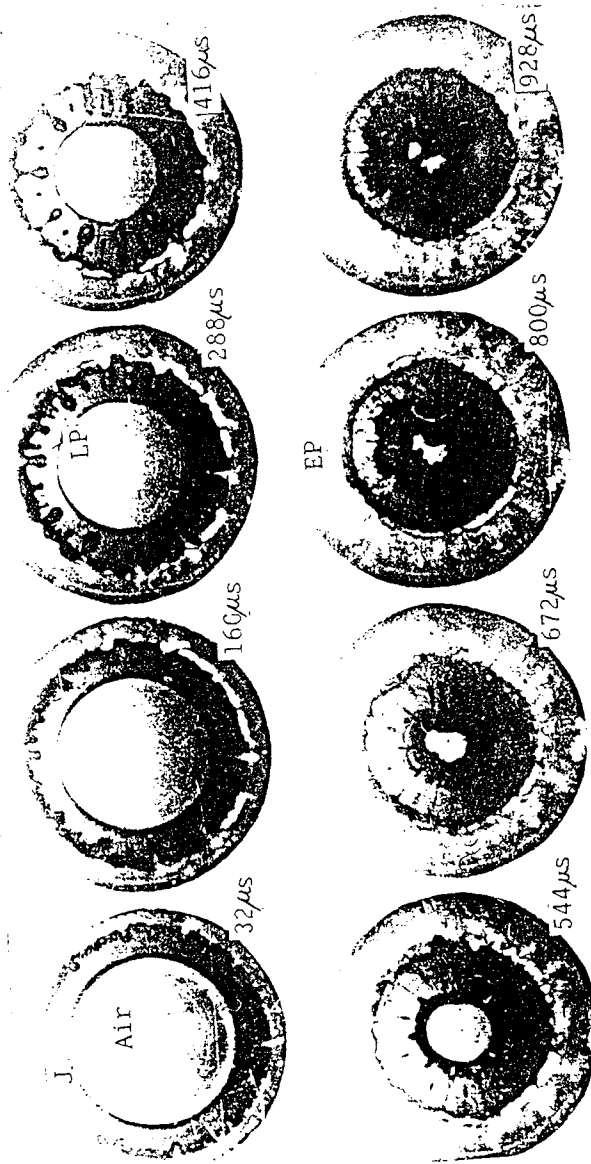


Fig. 10. Experimental photochromograms (Jelly strength ~ 0.4 atm; 12 GEM initiation points); J-jelly ring; TZ-turbulent zone; EP-explosive products; LP-local perturbations.

CONCLUSIONS

The main conclusions are:

- jelly technique developed to study the turbulent mixing at the surfaces of converging cylindrical liners is presented;
- jelly technique is very simple and optical diagnostics are suitable;
- shell strength increase leads to turbulent mixing suppression.

REFERENCES

1. Lord Rayleigh, Proc. London Math. Soc., v. 14, p. 170, 1883.
2. G.I.Taylor. The instability of liquid surfaces when accelerated in a direction perpendicular to their planes. Proc. Roy. Soc., v. A201, p. 192, 1950.
3. V.A.Andronov, S.M.Bakhrakh, E.E.Meshkov, V.V.Nikiforov, A.V.Pevnitsky, A.I.Tolshmyakov, DAN, v. 264, № 1, pp. 76-82, (1982).
4. A.I.Tolshmyakov, E.E.Meshkov, PGV, № 3, pp. 109-113, (1982).
5. M.Legrand, N.Toque. 3rd Intl. Workshop on the Physics of Compressible Turbulent Mixing, Abbey of Royaumont (France) - June 17-19, 1991, p. 9.
6. O.I.Volchenko, I.G.Zhidov, B.A.Klopov, E.E.Meshkov, V.V.Popov, V.G.Rogatchov, A.I.Tolshmyakov, AS.1026154, Byulleten OIPOTZ, № 24, (1983)
7. O.I.Volchenko, I.G.Zhidov, E.E.Meshkov, V.G.Rogatchov, Pisma v ZhTPh, v. 15, p. 47, (1989).
8. V.Rogatchov, I.Zhidov, B.Klopov, E.Meshkov, A.Tolshmyakov. 3rd Intl. Workshop on the Physics of Compressible Turbulent Mixing, Abbey of Royaumont (France) - June 17-19, 1991, p. 1.

THE IMPORTANCE OF SHEAR STRENGTH FOR DEVELOPMENT OF
DISTURBANCES AND INSTABILITY DURING ACCELERATION,
CONVERGENCE AND RETARDATION OF SHELLS

V A Ogorodnikov, A G Ivanov, G Ya Karpenko,
A D Kovtun, A A Demidov, L A Tolstikova

Russian Nuclear Centre
All-Russian Scientific-Research Institute
of Experimental Physics, Arzamas-16, Russia

Detonation of cylindrical and spherical explosive(E) charges is initiated at some points on the external charge surface synchronously, as a rule, using various layouts. This result in generation of the disturbed detonation front reaching the accelerated shells, which in its turn accounts for the prescribed disturbances on their internal surface[1]. Questions concerning the behaviour of the disturbances during the shell convergence to the centre arise, including those related with the influence of rheological properties of the shell material (strength, viscosity).

In this paper the method of pulsed radiography was used to study the behaviour of the disturbances at the internal boundary of the converging cylindrical shells accelerated by explosion energy[2]. A sectional view of the experiment is shown in Figure 1.

Detonation on the external surface of the cylindrical charge having density of $\rho = 1.72 \text{ g/cm}^3$ and detonation rate of $D = 8.15 \text{ km/sec}$ was initiated at the points disposed in vertices of squares of side 22 mm. In all the experiments the external shell of aluminium alloy (B 95) was used. The middle shell was made of steel (St. 3) and as for the inside shell, whose internal surface disturbances were studied it was made of steel (St. 3) or lead (CI). These materials having noticeably different rheological properties were allowed to be used to reveal their influence on development of disturbances.

Radiography of the internal shell boundary (ISB) form in the experiments was made at the instants of time corresponding to its

convergence to the radii: $0.5 Re$, $0.3 Re$, $0.1 Re$ and $0.07 Re$, where Re is an outside radius of the explosive charge. In special-purpose experiments it was shown that if ISB converges to $0.1 Re$ radius, the length of the shell area undisturbed due to side effects is 100 mm , which is sufficient to obtain unbiased information on the phenomenon under study.

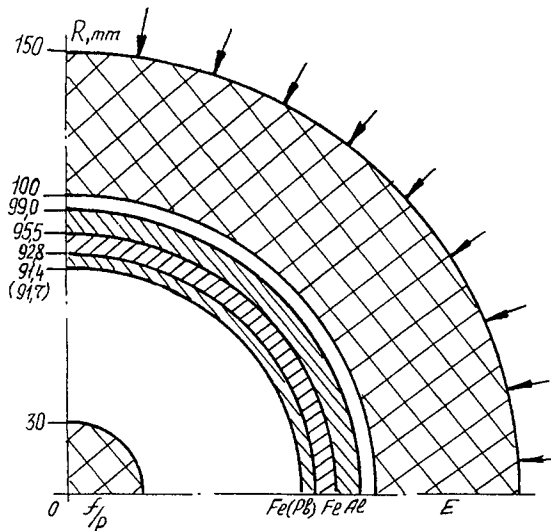


FIGURE 1: Sectional view of the experiment

Figure 2(a), (b) show experimental X-ray photos for steel and lead respectively. The dotted line marks the initial ISB position and the directions of projections for the points of detonation initiation from the external explosive charge surface to the centre of the shell symmetry are shown by the radial dot-and-dash line. The results of experimental X-ray photos processing are presented in table 1 where t is the time from the onset of ISB motion to the moment of radiography t_i ; $r_i = R_i/Re$ is a relative ISB radius at t_i (R_i was taken as a maximum radius, where from the disturbance amplitude was measured); a is a disturbance amplitude; δ , λ are shell thickness and disturbance wavelength at the present ISB radius of R_i .

TABLE 1

Shell Material	Test N	t	r_i	a	δ	λ
		μsec	-	mm	mm	mm
Steel	1	6.15	0.53	1-2	1.6	12
	2	17.90	0.32	3-4	2.6	7
	3	23.80	0.21	3-4	3.9	5
	4	26.00	0.11	-	6.5	-
	5	28.10	0.06	-	9.4	-
Lead	7	6.23	0.49	3-4	1.2	12
	8	17.90	0.30	5-6	1.9	7
	9	23.18	0.20	5-6	2.9	5
	10	27.30	0.09	5-6	5.4	3
	11	28.05	0.08	5-7	5.8	3

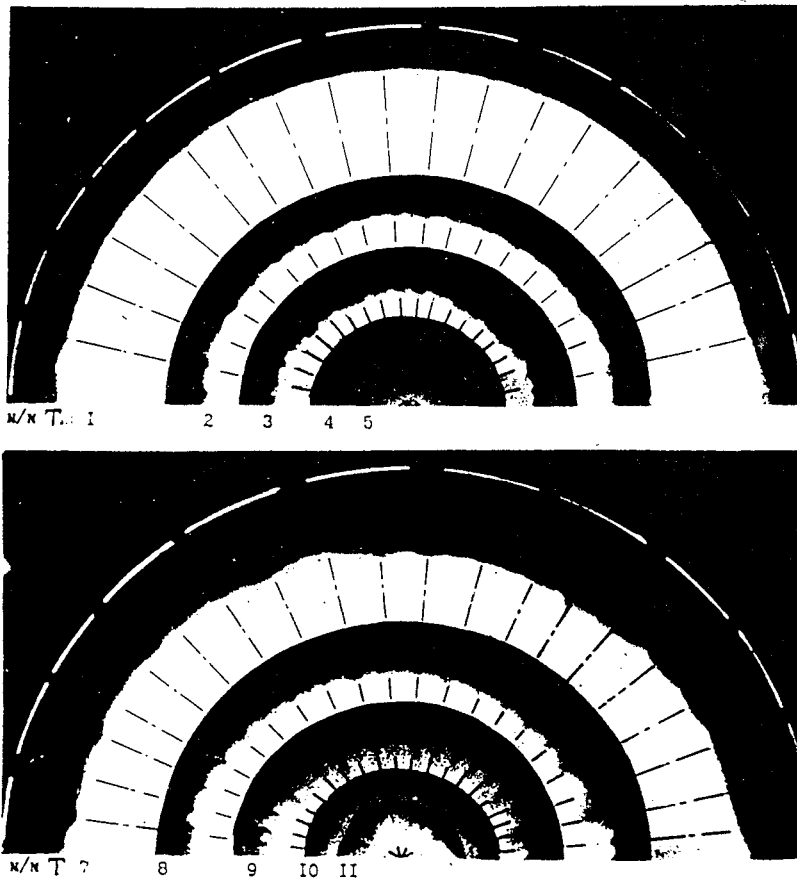


FIGURE 2: X-ray photos of ISB Position

Analysis of experimental results obtained with steel and lead shells shows that the leading disturbances at ISB in both cases generate under the projections of detonation initiation points in the explosive charge when shells are accelerated by explosion products (EP). At the same stage of shells motion disturbances practically stop to grow in amplitude.

In the inertial area of the shells motion ($r_i \leq 0.3 Re$) the amplitude of disturbances is kept the same to the radius of $\sim 0.2 Re$ for the steel shell and to that of $0.1 Re$ for the shell of lead. An approximate relation of $a \approx \text{const}$ is true. It should be noted that during convergence of steel and lead shells both at the stage of their acceleration by EP and in the inertial area of motion the sign of disturbances remains unchanged, that is they do not exhibit the oscillating character of their behaviour.

The form and the amplitude of disturbances are distinctly affected by the rheological properties of the shell material. Thus, if in case of the shell made of steel having a higher strength and viscosity the disturbance has the form of regular convexities approaching sinusoidal shape, the form of disturbances on the shell made of lead, which almost lacks strength and has a much lower viscosity, changes due to melting at a shock wave. The convexities elongate to form jets, thus pointing to the manifest non-linearity of the process. Besides the amplitude of disturbances with lead shells is 1.5 times that of shells made of steel.

Based on experimental results for the stage of shell acceleration by explosions products ($r_i = 0.5 - 0.3 Re$), estimates of velocity gradients between shell areas located in non-disturbed and disturbed zones give the following acceleration values of the disturbed regions relative to non-disturbed ones: $g = dW/dt = 1.4 \times 10^9$ cm/sec² for the steel shell and 1.1×10^9 cm/sec² for the shell made of lead, or the values of inertial forces $\sigma_F = \rho_o \cdot \delta \cdot dW/dt$ are 0.22 and 0.19 GPa respectively. The values of dynamic yield strength under these deformation conditions ($\epsilon = W/R = 2 \times 10^4$ sec⁻¹) are $\sigma_S = 1.4$ GPa for steel and $\sigma_S = 0.09$ GPa for lead. A comparison of the values

shows that for steel $\sigma_s > \sigma_F$, therefore the shear strength of the shell material produces a stabilising effect on the form and the amplitude of disturbances. For the lead shell $\sigma_s < \sigma_F$. In this case the shear strength of the material has no stabilising effect upon the growth of disturbances which turn into jets due to the prevailing influence of inertial forces though at initial stage of the shell motion they have the form similar to that of steel shell.

The experiments described above were carried out when cylindrical shells converged in air at atmospheric pressure. Consider the case when the inner cavity is filled with a low density fluid. In initial stage of the shell motion, when the pressure is rather small, distinctions of the internal boundary form can hardly be expected. However, they can occur in inertial stage of the shell motion as the pressure of the fluid increases. Its especially possible at the shell retardation in the fluid followed by its divergence from the centre. In this case conditions for the Rayleigh-Taylor instability (RT) of the interface between the shell and compressed fluid might be anticipated[3].

Although RT instability has been the objective of much research, publications on instability in solid medium are limited in number. As a result of experimental[4-6] and numerical-theoretical investigations in terms of perfect elastic[7], perfect plastic[8] and elastic-plastic[9,10] medium models, it was possible to find out that the rheological medium properties (strength, viscosity) have a pronounced stabilising effect on RT instability. Depending on the medium model used the critical wavelength λ^* [7,9], the critical initial amplitude of disturbances \dot{a} [8] or their combination[10] were taken as criteria which determined the surface transition from the stable region into instable one.

$$\lambda \geq \lambda^* = 4 \cdot \pi \cdot G/\rho \cdot g, \quad (G\text{-shear modulus}) \quad . . . \quad (1)$$

$$\dot{a} \geq \ddot{a} = \sigma_s/\rho \cdot g \quad . . . \quad (2)$$

$$\dot{a} \geq \ddot{a} = \sigma_s/\rho \cdot g \cdot (1 - \lambda/\lambda^*) \quad . . . \quad (3)$$

Considering the first stage of RT instability, since in the long run it will be just this stage which determines the maximum amount of shell material involved in the zone of turbulent mixing (ZTM), disturbances at ISB approaching sinusoidal form grow according to $a(t) = a \cdot \exp(\beta \cdot t)$ [3], where $\beta = \{(\rho_1 - \rho_2)/(\rho_1 + \rho_2) \cdot g \cdot 2\pi/\lambda\}^{1/2}$ is the increment of disturbances growth, ρ_1 , ρ_2 are densities of the shell and the low density fluid respectively. As is seen from this relation, the amplitude of disturbances grows in proportion to the initial asymmetry level at ISB. The shorter is the wavelength of disturbances, the more is the increase. From the above it follows that since the amplitude of the lead shell disturbances is 1.5 times that of the stronger steel and moreover disturbances of the former have a non-linear character, it may be concluded that the material shear strength of the shell retarding in fluid will have a stabilising effect on the magnitude and rate of disturbances growth.

For experimental check of this prediction, tests with steel and lead shells retarded by foam plastic with initial density of $\rho_0 = 0.312 \text{ g/cm}^3$. The foam was used to make a continuous cylinder which was aligned with the shells of the explosive charge described above and had an outside radius of $0.2 R_e$ (Figure 1). Pulsed radiography of ISB form was made at the stages of shell convergence (Figure 3) and divergence (Figure 4). The same figures show ISB outlines which result from mathematical computerised image processing. Figure 5 presents calculated R-T diagrams of ISB motion.

Numerical one-dimensional calculations have been made in hydrodynamic approximation. Here too the experimental points from the tests with air described above are plotted. Since it is more complicated to define ISB location at the diverging stage of motion, two extreme estimates are given. The first estimate has been made by the maximum radius, the second one - by the effective radius of the area for the outline chosen in mathematical image processing.

With reference to Figures 3 and 5, it can be seen that at the stage of shells motion to the centre the presence of foam plastic results in some balancing of ISB and virtually has no effect on their dynamics, at least at their motion from $0.2 R_e$ to $0.09 R_e$ radius. The zone of foam plastic compressed by a shock wave (SW) is clearly seen

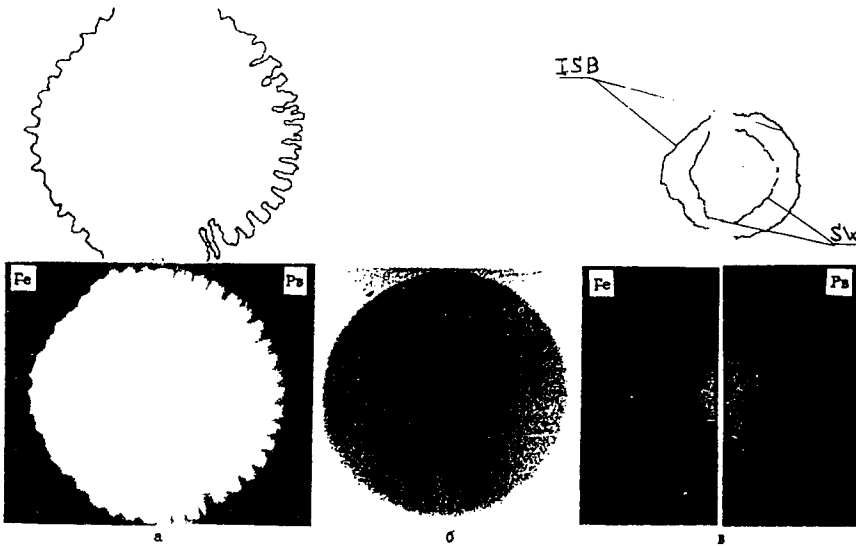


FIGURE 3

- (a) Form of ISB when reaching the radius of $0.2 Re$.
- (b) Cylinder of foam plastic with $0.2 Re$ outside radius.
- (c) Form of ISB when converging on foam plastic to $0.1 Re$ radius ($t = 27.5 \mu\text{sec}$).

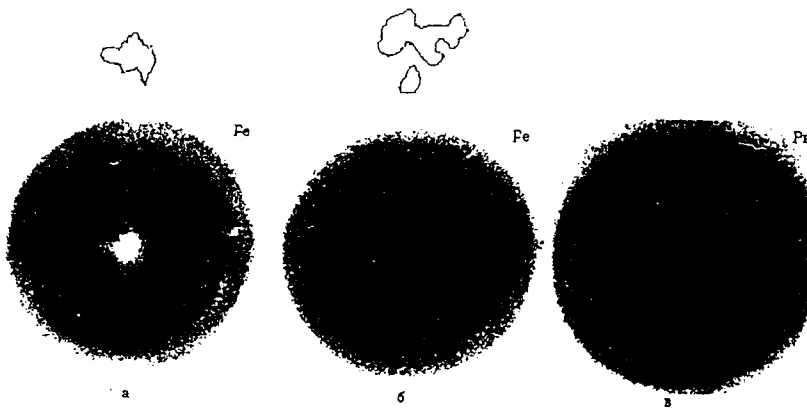


FIGURE 4

- (a) Foam of steel ISB at $t = 33.27 \mu\text{sec}$
- (b) Foam of steel ISB at $t = 35.25 \mu\text{sec}$
- (c) Form of lead ISB at $t = 35.30 \mu\text{sec}$

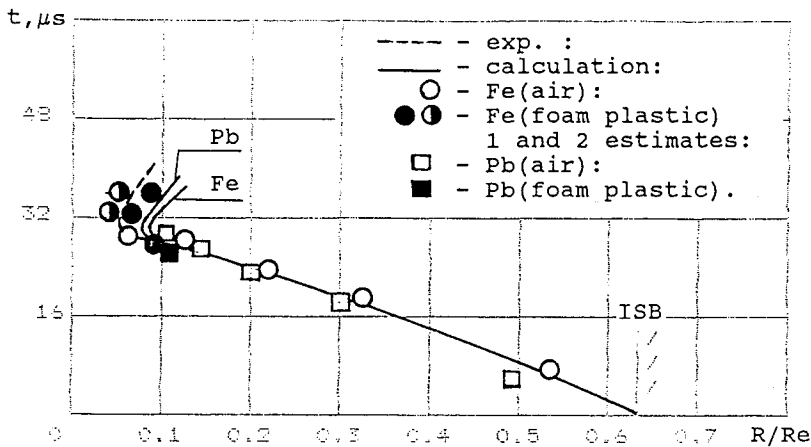


FIGURE 5: Diagram of ISB motion

in front of the shells. At the diverging stage of the steel shell motion (Figure 4(a), (b)) the initially symmetric form of ISB loses its stability and the shell material mixes with foam plastic. For the lead shell the behaviour character appears to be the same, but the stability loss begins a little earlier due to the less shear strength which results in a more vigorous mixing. At $t = 35.30 \mu s$ the distinguishing of ISB outline is no longer possible (Figure 4(b)).

It is of interest to follow the regions of disturbances stability on steel and lead shells using the criteria (1-3). To estimate the criterion values, 77 and 7 GPa shear moduli and 1.4 and 0.09 GPa dynamic yield strengths for steel and lead respectively were used. Note that the experimental points are as a whole in agreement with the calculation diagram of the shells motion (Figure 5). This gives grounds to use in estimates the values of ISB accelerations at the diverging stage of motion which are taken from calculations. For steel and lead they make up about the same value of $g = 4 \times 10^7 \text{ cm/sec}^2$. Allowance for this is included into graphical results of the estimates made which are presented in Figure 6.

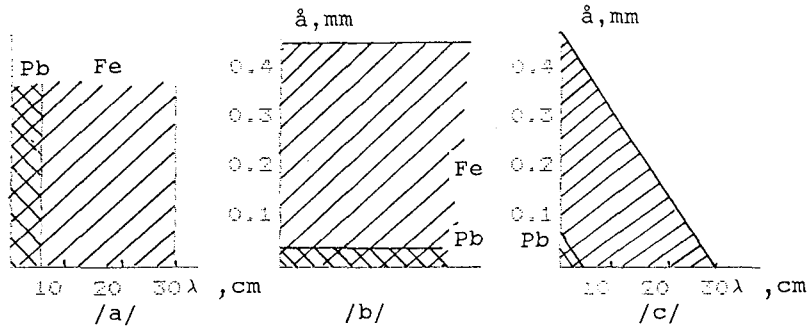


FIGURE 6: Regions of stability for steel and lead shells according to the formulae: a-(1); b-(2); c-(3).

Figure 6 shows that the region of stability for disturbances on shells made of the less strong lead are much more narrow, which is testimony to the stabilising influence of the shear strength on the growth of gravitational instability and is consistent with the experiment (Figure 4). From the tests with steel shells it follows that $\lambda < \lambda^*$, but $\lambda > \lambda^*$ ($\lambda > 1$ mm) and the disturbed boundaries are qualitatively in the instable region according to [8,10].

Thus it has been found out that in case of acceleration of relatively thin multilayered cylindrical shells using the energy of explosion, the behaviour of deterministic disturbances, if there are any at the internal boundary of the lower converging shell, cannot be described by the simplified linear theory. Among other things, the oscillating character of disturbances growth is lacking. The shear strength of the shell material has an important stabilising effect on the development of disturbances. When the shells with deterministic disturbances are retarded by the foam plastic, they can lose their stability. In this case the amplitude of disturbances which initially depends on the shear strength of the shell material is the governing value. This it has been supported that the shear strength of the shell material is a stabilising factor of the shell stability loss.

REFERENCES

- [1] V A Ogorodnikov, A G Ivanov. FGV, 1984, N3.
- [2] A G Ivanov, Ju D Lavrovskij, V A Ogorodnikov. PMTF, 1992, N5.
- [3] G I Taylor. The Instability of Liquid Surfaces when Accelerated in a Direction Perpendicular to their Planes. Proc. Roy. Soc - 1950 V 201, N1065.
- [4] J F Barnes, P J Blewitt, R G McQueen et al. Taylor Instability in Solids. J Appl. Phys, 1974, V 43, N2.
- [5] J F Barnes, D R Janney, R R London et al. Further Experimentation on Taylor Instability in Solids. J Appl. Phys, 1980, V 51, N9.
- [6] A G Ivanov, E Z Novickij, V A Ogorodnikov i dr. PMTF, 1982, N2.
- [7] J F Mills. Taylor Instability of a Flat Plate. General Atomics Rep, GAMD-7335, 1960.
- [8] D Drukker. Mekhanika Deformirueykh tverdykh tel. Napravlenija razvitija. M Mir. 1983.
- [9] S M Bakhrakh, I P Kovalev. Materialy 5 Vsesojuznoj konferencii po chislennym metodam reshenija zadach teorii uprugosti i plastichnosti. Novosibirsk, 1978.
- [10] P N Nizovtcev, V A Raevskij. VANT, Ser. TPF, 1991, V 3..

Effect of Nonuniform Implosion on High Gain ICF Targets

H. Takabe and T. Ishii

Institute of Laser Engineering
Osaka University
Suita, Osaka 565, Japan

Abstract

A high gain target design and the gain sensitivity to nonuniform implosion dynamics have been studied numerically. First of all, sensitivity of the pellet gain to the tailored pulse shape has been studied with ILESTA-1D code and the gain scaling law has been obtained through an optimization of target and laser parameters. Then, the two-dimensional code ILESTA-2D has been used to study the sensitivity of the pellet gain to the nonuniformity in the target implosion. It is found that the fire-polishing effect by the alpha particle heating drastically smooths the spark structure. The implosion mode optimized with the ILESTA-1D code is relatively sensitive to the nonuniformity and, therefore, the higher implosion velocity modes are recommended from the stability point of view.

I. Introduction

In the high gain target of the inertial confinement fusion, the compressed DT fuel should consist of a central spark region with the temperature of several keV and the density of a few hundred g/cm^3 surrounded by the main fuel of about ten times lower temperature and higher density. For such purpose, a hollow shell target is imploded with a tailored laser pulse. The tailored pulse consists of a prepulse to pre-compress the fuel and a main pulse to accelerate the shell toward the center of the target up to a velocity of $3\sim 4 \times 10^7$ cm/sec.

A typical one-dimensional simulation for the high gain is shown in Fig.1. The imploded target is made of DT solid layer of thickness of $250 \mu\text{m}$ for $2250 \mu\text{m} < r < 2500 \mu\text{m}$ contained by a polyethylene shell with the thickness of $45 \mu\text{m}$. The laser power linearly increases up to the time τ_1 and abruptly increases like (intensity) $\propto (t - \tau_1)^2$ up to the time, $\tau_1 + \tau_2$. In the simulation of Fig.1, a laser light with wavelength of $0.35 \mu\text{m}$ is irradiated and the timing of τ_1 is roughly adjusted so that the shock wave generated by the pre-pulse passes through the shell by the time of τ_1 . When the rarefaction wave is generated at the rear side of the shell, the main pulse starts to accelerate the shell.

We can enumerate a variety of parameters to control the implosion dynamics. In the high gain target design, it is required to optimize some performances, the most important one of which is the pellet gain. If we carry out such trial and error by varying all possible parameters, it is time-consuming and of non-physics approach. Our present standing point is that if by varying a few parameters in the simulation we can obtain a pellet gain which is comparable to the optimized gain predicted by a simple gain model, for example, that by Mayer-ter-Vehn [1], that design corresponds to almost the optimized one.

In obtaining the implosion mode of Fig.1, we have mainly varied two parameters τ_1 and τ_2 so that a peak gain is obtained after rough adjustment of the target layer thicknesses. In Fig.1-(a), the flow diagram of each Lagrangian grid is plotted. A trajectory of the cut-off density is also plotted until the time when the laser is turned off at $t \approx 34$ nsec. It is seen in Fig.1-(a) that the self-heating by the alpha-particles enhance the fuel burning to form a strong detonation wave near the maximum compression time. In Fig.1-(b), a snap shot of the density and ion and electron temperatures is plotted for the acceleration phase of $t = 30$ nsec. In this phase, the ablation front is unstable to the Rayleigh-Taylor [R-T] instability; however, the ablative stabilization can be expected to reduce the growth of shorter wavelength perturbations [2]. The properties of the Rayleigh-Taylor instability in

this phase have intensively studied numerically [3] and experimentally [4].

On the other hand, in the final compression phase, the rarefaction wave generated at the rear side by the pre-pulse forms a spark region and it decelerates the main fuel surrounding the spark. Then, the Rayleigh-Taylor instability appears to be important at the interface between the hot spark and the main fuel. In Fig.1-(c), a snap shot of density and temperatures at $t = 35.5$ nsec in this phase is shown, where the alpha-particle heating process is excluded in the simulation, though Fig.1-(a) does include it. Since the alpha-particle heating becomes efficient before the time of maximum compression (Fig.1-(c)) in the high gain target, it is essential to study the R-T instability in this phase by taking account of the alpha-heating effect self-consistently.

In the present paper, the high gain target design with ILESTA-1D code is described in Sec.II. A brief explanation of the physics and numerics used in the implosion codes are given in Sec.III. In Sec.IV, the effect of nonuniform implosion in high gain targets is studied by ILESTA-2D code. Gain reduction and its sensitivity to the implosion mode are described. Section V is devoted to a brief conclusion.

II. High Gain Target Design

The pellet gain is sensitive to the parameters used in the simulation conditions. A typical example for the variation of the gain is obtained when the main pulse duration τ_2 is varied as shown in Fig.2. As seen in Fig.2, the pellet gain increases by the increase of τ_2 , approaches the peak value $Q \approx 150$ and drops abruptly with the further increase of τ_2 . First of all, the abrupt decrease of the pellet gain for $\tau_2 > 15$ nsec is easily understood. The ignition and burn propagation require the spark temperature roughly more than $4 \sim 5$ keV. The spark temperature is roughly proportional to the square of the implosion velocity. Since the implosion velocity increases as the decrease of τ_2 , we need the main pulse duration τ_2 shorter than a certain value for fuel ignition. On the other hand, in decreasing the duration of τ_2 , the temperatures of the spark and the main fuel becomes higher than the optimized ones and the gain decreases gradually as seen in Fig.2.

It should be noted that as pointed out in Ref.[5], the peaked gain at $\tau_2 = 15$ nsec is also sensitive to the charge of the pre-pulse duration τ_1 . However, if we use the implosion mode with $\tau_2 = 13$, for example, the gains of roughly 100 can be maintained in relatively wide range of the pre-pulse duration [5].

It may be easy to understand that the gain prediction based on the peaked gain is not so reliable to some variance of the parameters even within the one-dimensional design. It must be more reliable if we employ the design giving the gain 100 around $\tau_2 \sim 13$ nsec instead of $Q = 150$ at $\tau_2 = 15$ nsec. In addition to such reliability consideration within the one dimensional design, we have required to study the effect of nonuniform implosion on the pellet gain.

III. ILESTA Codes

In this section, a rough explanation will be given about the one-dimensional hydrodynamic code ILESTA-1D and its two dimensional version ILESTA-2D. The physics modeled in the present high gain target design is based on the one-fluid, two-temperature fluid model with electron and ion heat conduction terms, which are given, for example, in Ref.[6]. The additional features for the ICF purpose are (parameters written below are for one-dimensional case) ;

- The classical absorption process with coefficients described in Ref.[7] is calculated for 50 laser rays.
- The flux-limited Spitzer-Harm model is used for electrons with the flux limiter $f = 0.1$, which is good for low-Z materials.
- The equation of state (EOS) is essential for high gain target design. In the present simulation, the thermodynamic variables, e.g. pressure P , is divided as $P = P_i(\rho, T_i) + P_e(\rho, T_e) + P_c(\rho)$, where P_i is the ion thermal pressure, P_e is the electron thermal pressure, and P_c is the cold pressure. The fitting formula based on the Thomas-Fermi model [8] is used to the electron component. Since the molecular bounding effect is important at the very beginning in the simulation, the model given in Ref.[9] is also used in evaluating P_c .
- The radiation transport becomes important in some case of ICF target design. In the present simulation, the photon energy $h\nu$ for $1 \text{ eV} \sim 100 \text{ keV}$ is divided into 100 groups and the multi-group flux limited diffusion model has been used.
- For the photons of $h\nu > 100 \text{ keV}$, only the loss process is modeled in the code.
- The spectral opacity and emissivity are important in radiation transport issues. The collisional-radiative equilibrium model within the average atom model has been used to obtain the non-LTE population of bound electrons with which the opacity and emissivity are directly calculated [10].
- The alpha-particle transport is also treated with the multi-group flux-limited diffusion model [11]

by dividing the energy space, $0 < \epsilon < 3.52$ MeV into 20 groups. The energy deposition rate to the ions and electrons are calculated as the result of the alpha-particle transport.

For the study of gain reduction due to the nonuniform implosion dynamics, the two dimensional version of the fluid code should be equivalent to the one-dimensional one if no asymmetry is imposed. That is, the same physics model should be installed in the two-dimensional code as in the one dimensional code. In the two-dimensional simulations shown in what follows, the final compression phase with a given nonuniformity at the void closure time has been simulated by the ILESTA-2D code with the same physics as used in the ILESTA-1D.

The axial symmetry is assumed in the 2-D simulation. The quarter of the full system is calculated, namely the simulation zone is for $0 < \theta < \pi/2$ in the spherical coordinate. In the θ -direction, 20 grids are typically used for this quarter zone and 50 grids are used for the radial direction. In the simulation, we assume that a linear deformation is generated in the acceleration phase and, therefore, the surface-mode-like deformation is given at the time corresponding to the start time (t_s) of the ILESTA-2D simulation. At first, we store the fluid variables of the ILESTA-1D at $t = t_s$. Then, the ILESTA-2D is initiated with this fluid condition with a given relocation of Lagrangian grid points according to the degree of the given nonuniformity. It is assumed that the structure of the relocation has its peak amplitude at the ablation front. In the present paper, the start time t_s for the ILESTA-2D simulation is taken to be of the void closure time, namely $t_s = 34.2$ nsec in the case of Fig.1.

IV. Two Dimensional Simulation for High Gain Implosion

First of all, the implosion given in Fig.1 is simulated. In order to see the effect of the alpha particle heating, we have carried out the simulation with and without the alpha particle transport. In Fig.3, the case when the displacement of $\ell = 8$ (ℓ ; spherical wavenumber) is imposed at t_s is shown. Peak displacement of $\delta = 5\%$ of the mean radius at the ablative front is imposed at $t = t_s$. In Fig.3-(a), the case without the alpha-particle transport is shown. From the left to the right, the figure represents the snap shots of Lagrangian mesh, the flow velocity vector at each grid point and the equi-contours of the density and electron temperature. In the equi-contours, the density and electron temperature are equally divided in the logarithmic scale with 5 zones in each order of magnitude. The

thick solid lines represents the contours of 10^{Π} . For reference, the cross sections at $\theta = \pi / 2$ (the solid line) and $\theta = \pi / 2 - \pi / 8$ (the dotted line) are plotted above the figures of the contours.

It is seen in Fig.3-(a) that the nonuniformity appears drastic at the contact surface between the spark and main fuel, the average radius of which is roughly $100 \mu\text{m}$. This is due to the Rayleigh-Taylor instability in the final compression phase. It is observed in the simulation that this nonuniformity continues to grow in the expansion phase. It is useful to point out that the phase of peak and valley at the spark-fuel contact surface is in the opposite phase against that imposed at the start of the simulation. This is easily understood as follows. The shock waves generated in the directions of $\theta = 0, \pi / 4, \pi / 2$ in Fig.3-(a) arrive faster than the other directions and the reflected jets are predominantly generated. These jets alter the phase of nonuniformity in the opposite phase. In this case, the resultant neutron yield was 9.2×10^{16} (Pellet gain $Q = 0.08$). No substantial gain is obtained because of no self-heating process.

With the same initial condition at $t = t_s$, while including the alpha particle transport, we obtain the result shown in Fig.3-(b). By comparing Fig.3-(b) with 3-(a), we can recognize a substantial smoothing at the boundary between the spark and main fuel due to the alpha particle heating. At $t = 35.0 \text{ nsec}$, the spark is already heated by the alpha particle and the temperature becomes about 20 keV . So called fire-polishing [12,13] by the alpha particle can be expected. In this case, the resultant neutron yield was 1.8×10^{20} , which is equal to the yield in the one dimensional simulation. This fact means that once the fire-polishing takes place, the gain almost equal to the one dimensional case can be maintained even with a certain degree of nonuniformity.

In order to see how high degree of nonuniformity is allowed to keep a substantial gain, we have carried out two dimensional simulations by varying the degree of nonuniformity. In Fig.4, the snapshots for the cases of $\ell = 2$ with $\delta = 10\%$ and 30% are shown. The meaning of the figures from the left to the right are the same as in Fig.3. The figures above the contours, the cross sections of the density and electron temperature at $\theta = \pi / 2$ (the solid line) and $\theta = 0$ (the dotted line) are shown. It is clear that a fairly uniform spark is formed for the case of $\delta = 10\%$ [Fig.4-(a)], although the main fuel is strongly deformed. Once the ignition takes place, the alpha heating leads the propagation of burning wave. It should be noted that the burning wave propagates predominantly in the direction where the main fuel is thin, namely the horizontal direction in this case. In this case, the total yield was $Y_N = 1.42 \times 10^{20}$ ($Q = 130$).

On the other hand, for the case when the degree of nonuniformity is 30% [Fig.4-(b)], it is found that the gain reduces by the three order of magnitude. It is clear that although the alpha-particle transport is induced in the code, the substantial spark is not formed and the burn propagation is not seen. In this case the neutron yield is 2×10^{17} ($Q=0.18$) and the three-order of magnitude less compared to the case of $\delta = 10\%$ in Fig.4-(a).

The normalized neutron yield is plotted in Fig.5 as a function of the degree in nonuniformity at $t = t_s$ ($=34.2$ nsec) for the case of $\ell = 2$ and 4. It can be concluded from Fig.5 that in order to keep the high gain, the uniformity more that about 20% is required. It is a general tendency that the reduction of the yield is less as the increase of ℓ . This is because the alpha-particle fire polishing is effective to perturbations with shorter wavelength. In addition, in case of $\ell = 4$, the total gain is slightly enhanced for the case with $\delta R/R \approx 5 \sim 10\%$.

Finally, the sensitivity to the nonuniformity as a function of the implosion mode has been studied. The implosion mode treated so far is a rather sensitive one to the nonuniformity, because the implosion velocity is adjusted so that the spark temperature is slightly above the ignition temperature. This suggests that if the spark temperature slightly drops due to the implosion nonuniformity, the ignition can not be expected, consequently leading the degrade of the fusion gain. In Fig.6, the pellet gains obtained with the ILESTA-2D code are shown for the case of $\ell = 2$ mode of the nonuniformity. The degree of nonuniformity is varied as 10, 20 and 30%. It is clear from Fig.6 that the implosion mode of $\tau_2 = 15$ nsec is very sensitive to the nonuniformity, although the highest gain is obtained within one-dimensional target design. It may be concluded from Fig.6 that within $\ell = 2$ nonuniformity study, the implosion mode with $\tau_2 \approx 13$ to 14 nsec is recommended to obtain a gain of about 100, while the level of uniformity of about 10% to 20% is required at the time of the void closure.

V. Conclusion

By using one-dimensional implosion code ILESTA-1D, we have carried out a parametric study for obtaining higher gain in the range of the laser energy of $3 \sim 4$ MJoule at 3ω . It is found that when the implosion velocity is adjusted so that the spark temperature is just above the ignition temperature, the highest gain can be obtained. We have obtained the pellet gain $Q = 150$ at 3MJoule. The sensitivity of the pellet gain to the tailored pulse shape has been shown by varying the duration of

the main pulse.

The two-dimensional implosion code which is equivalent to the one-dimensional code in symmetry condition has been developed to study the effect of nonuniformity on the pellet gain in the present high gain design. At first, it has been demonstrated that due to the alpha particle heating the nonuniform spark structure becomes fairly uniform as long as the degree of nonuniformity is not so large. So-called "fire-polishing" by the alpha particle has been demonstrated.

The sensitivity of gain reduction to the degree of nonuniformity has been studied by varying the implosion mode. It has been found that the implosion mode optimized within one-dimensional code is very sensitive to the nonuniformity. The higher implosion velocity mode is recommended to obtain a reasonable gain in 10~20% nonuniformity level at the void closure time.

References

- [1] J. Meyer-ter-Vehn, Nucl. Fusion **22**, 561 (1982).
- [2] H. Takabe, L. Montierth and R.L. Morse, Phys. Fluids **26**, 2299 (1983); H. Takabe, K. Mima, L. Montierth, and R.L. Morse, Phys. Fluids **28**, 3676 (1985).
- [3] M. Tabak, D.H. Munro and J.D. Lindl, Phys. Fluids **B2**, 1007 (1990); J.H. Gardner, S.E. Bodner and J.P. Dahlburg, Phys. Fluids **B3**, 1070 (1991); LLE Rev. Lab. Laser Energ. Univ. Rochester **37**, 2 (1988).
- [4] S.G. Glendinning et al., ICF Quant. Report, Lawrence Livermore Nat. Lab. **2**, 37 (1991); B.A. Remington et al., Phys. Fluids **B4**, 967 (1992).
- [5] H. Takabe, T. Hashimoto, K. Mima and S. Nakai, in the proceedings of IAEA Technical Committee Meeting on Drivers for ICF, Osaka, April 15-19, 1991.
- [6] S.I. Braginskii, in **Review of Plasma Physics** edited by Leontovich (Consultant Bureau, New York, 1965), Vol.1, p.205.
- [7] J.M. Dawson, in *Advance in Plasma Physics* (Interscience, New York, 1968) Vol.1; S. Skupsky, Phys. Rev. **A21**, 1316 (1980).
- [8] K. Takami and H. Takabe, Tech. Rep. Osaka Univ. **40**, 159 (1990).
- [9] R.M. More et al., Phys. Fluids **31**, 3059 (1988).
- [10] H. Takabe and T. Nishikawa, "Computational Model for Non-LTE Atomic Process in Laser Produced Plasmas". to be published.
- [11] E.G. Corman, W.E. Loewe, G.E. Cooper and A.M. Winslow, Nucl. Fusion **15**, 377 (1975).
- [12] J.H. Nuckolls, L. Wood, A. Thiessen, G.B. Zimmerman, Nature **239**, 139 (1972).
- [13] S. Atzeni, Laser Part. Beams **9**, 233 (1991).

Figure Captions

Fig.1 A typical one-dimensional dynamics of the high gain target. The imploded target is made of

DT solid layer of 250 μm in thickness contained by a polyethylene shell of 45 μm in thickness. A tailored pulse of 0.35 μs is irradiated.

(a) The r-t diagram of each Lagrangian grid. A trajectory of the laser cut-off density is also plotted.

(b) A snap shot of the density and ion and electron temperatures for the acceleration phase of $t = 30$ nsec.

(c) A snap shot of the density and temperature at $t = 35.5$ nsec of the maximum compression. The figure is obtained when the alpha-particle heating is turned off in simulation.

Fig.2 Gain sensitivity to the duration of the main pulse used in the one-dimensional target design.

The gain becomes maximum for the design where the spark temperature is slightly above the ignition temperature.

Fig.3 The snap shots near the maximum compression [$t = 35.0$ nsec] simulated with and without the alpha particle heating. In the simulations, the amplitude of the displacement at $t = t_s$ is 5% at the ablation front. The $\ell = 8$ mode of nonuniformity is imposed.

(a) The case where the alpha-particle heating is excluded in the simulation code.

(b) The case where the alpha-particle heating is included self-consistently.

Fig.4 The snap shots near the maximum compression [$t = 35.0$ nsec] for the cases where the nonuniformity of $\ell = 2$ is imposed.

(a) The case with $\delta = 10\%$ nonuniformity.

(b) The case with $\delta = 30\%$ nonuniformity.

Fig.5 The normalized neutron yield as a function of the nonuniformity imposed at the void closure time ($t = t_s$). The cases of the nonuniformity with $\ell = 2$ and 4 are studied.

Fig.6 The sensitivity of the pellet gain to the implosion nonuniformity. The solid circles are the results of ILESTA-1D as shown in Fig.2. It is seen that the implosion mode of higher implosion velocity obtained by shorter main pulse duration is relatively insensitive to the implosion nonuniformity.

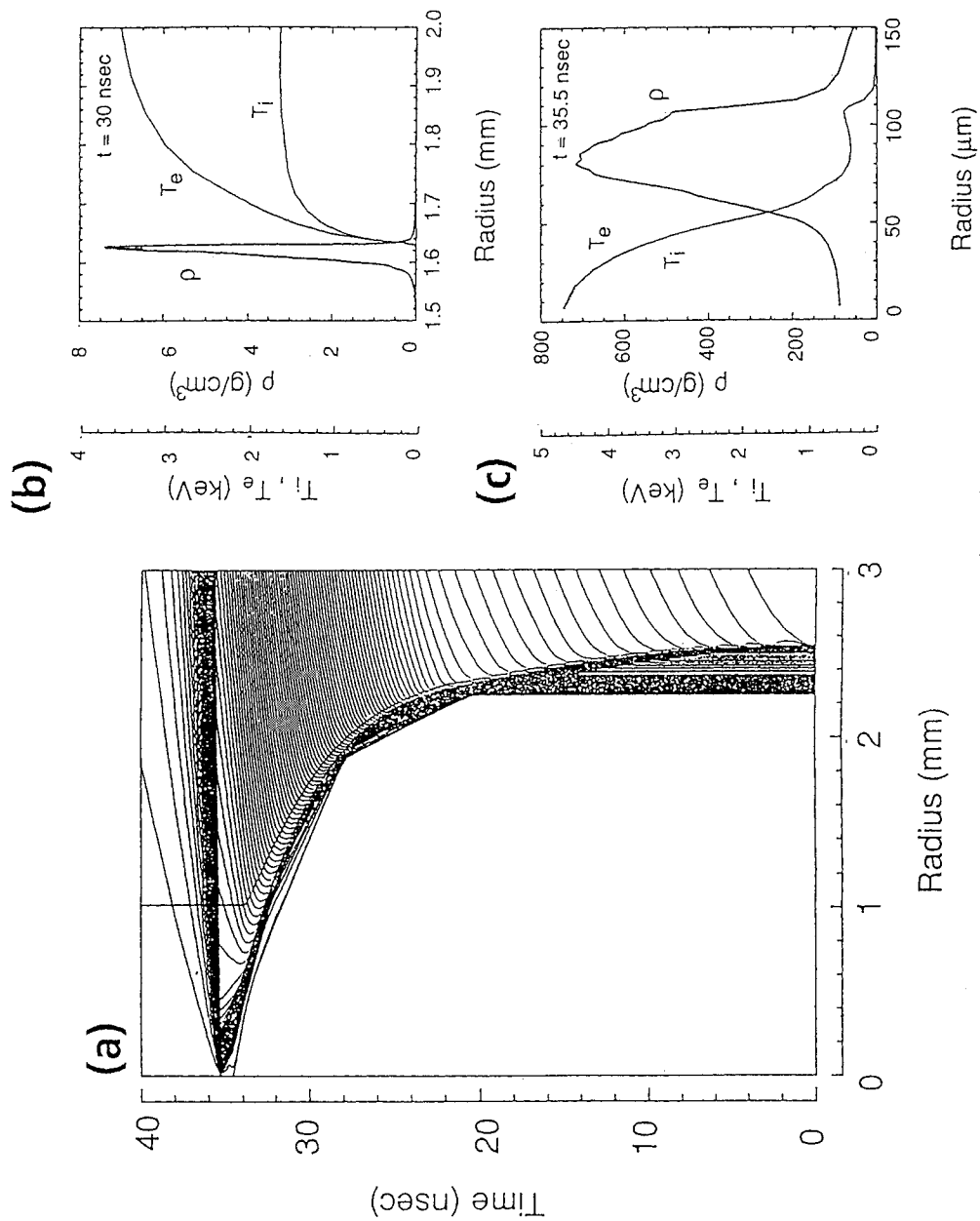


Fig.1

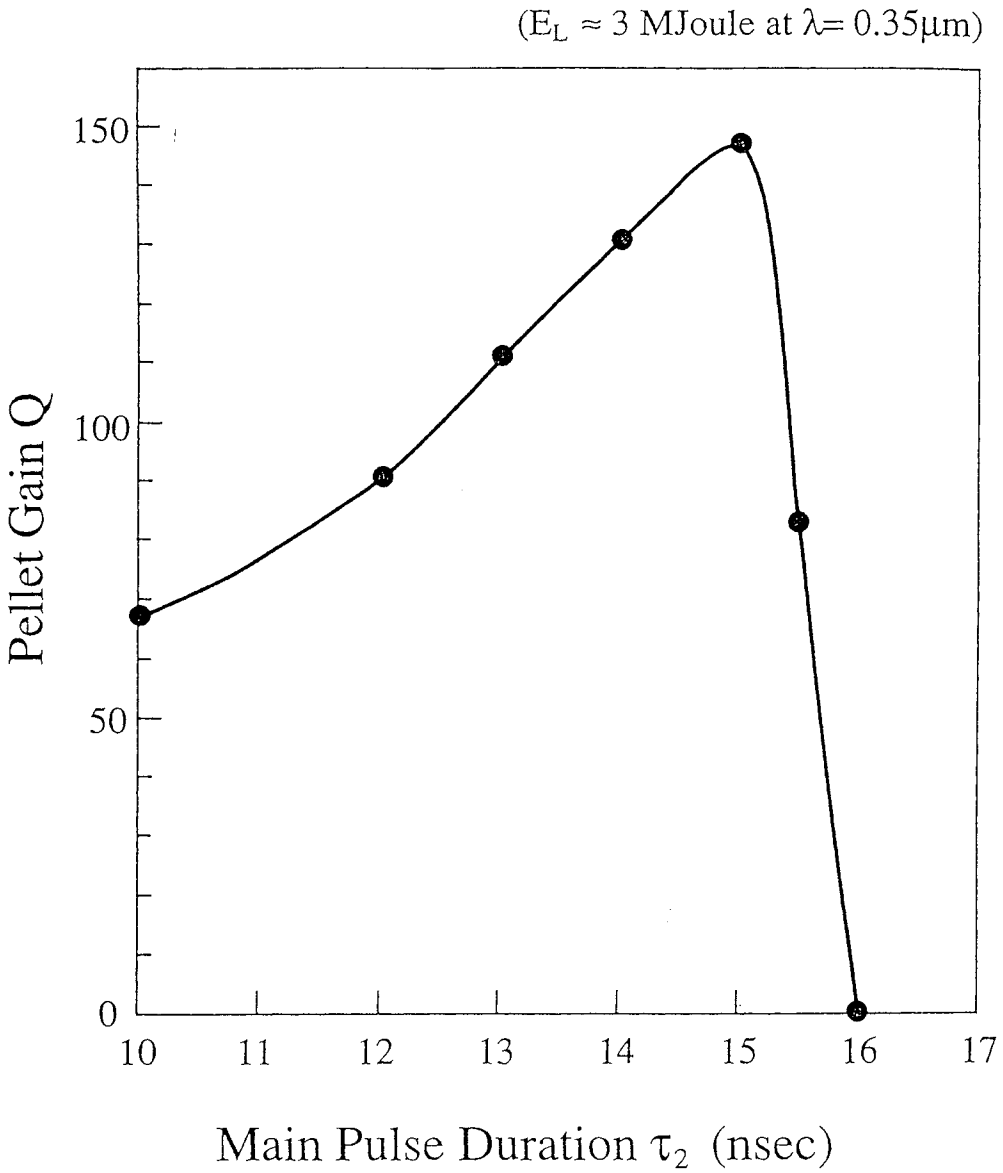
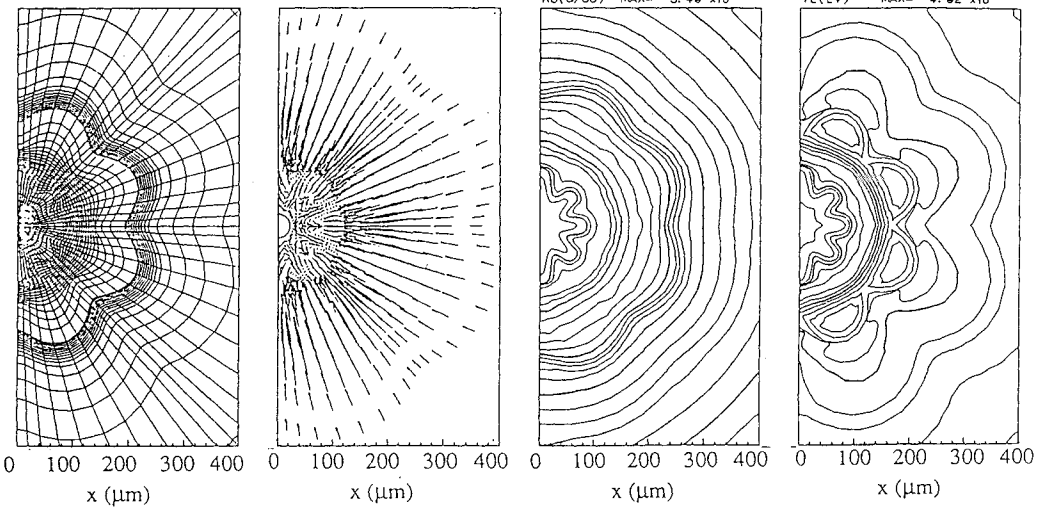


Fig.2

[$t = 35.0 \text{ nsec}$] [$\ell = 8, \delta = 5\%$]

(a) w/o α -heating



(b) with α -heating

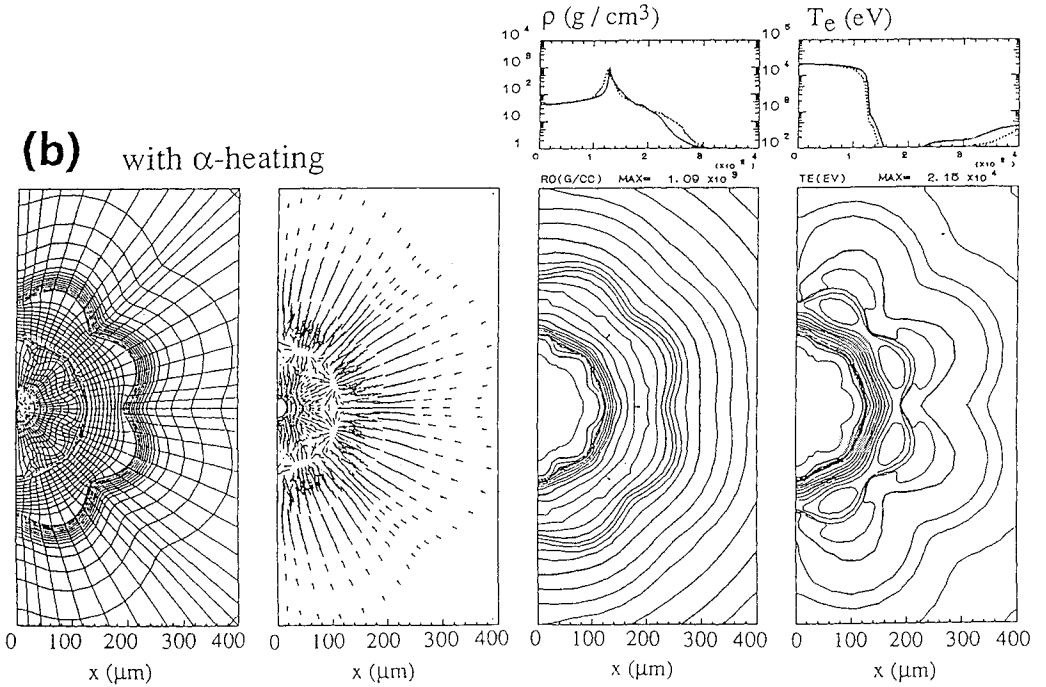


Fig.3

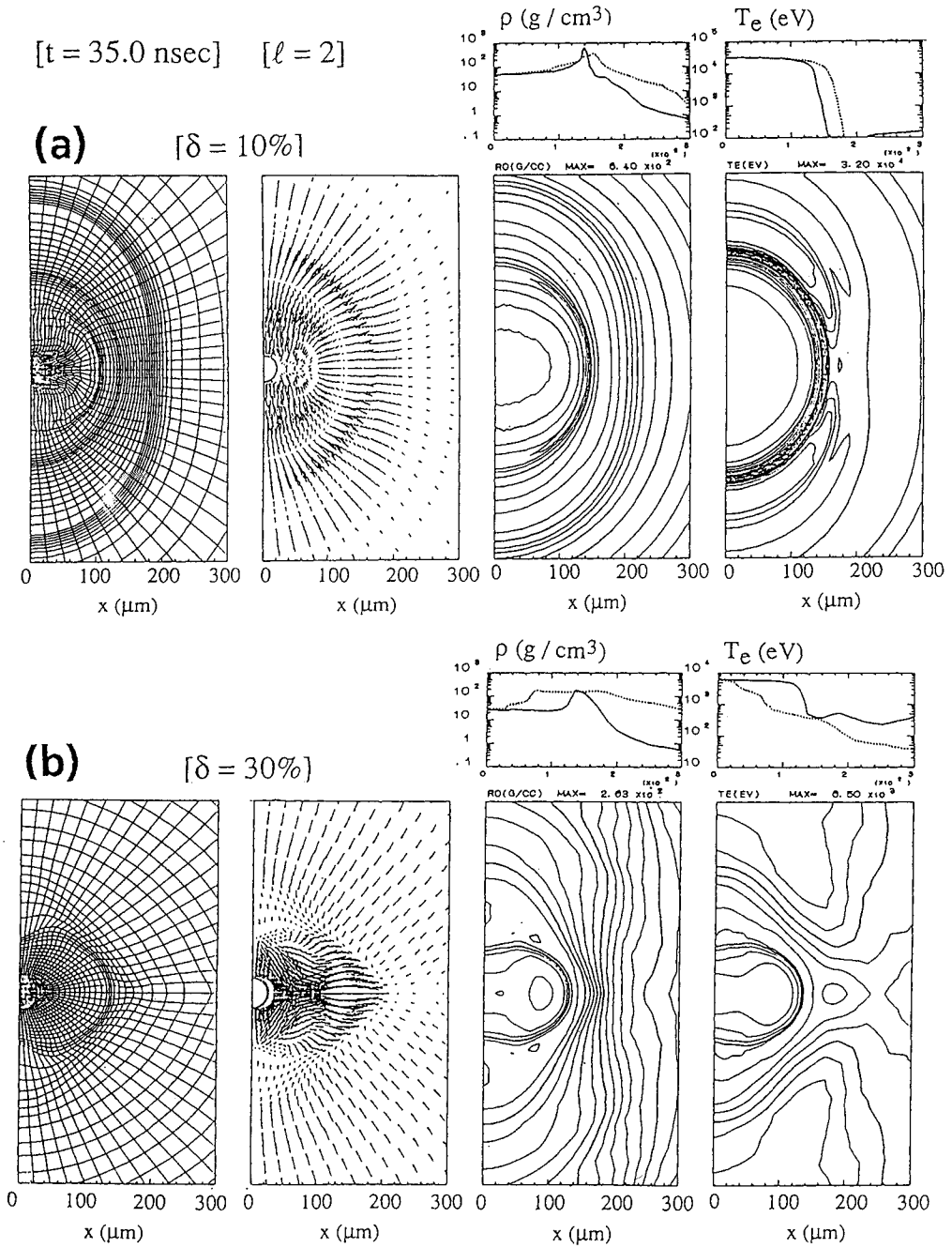


Fig.4

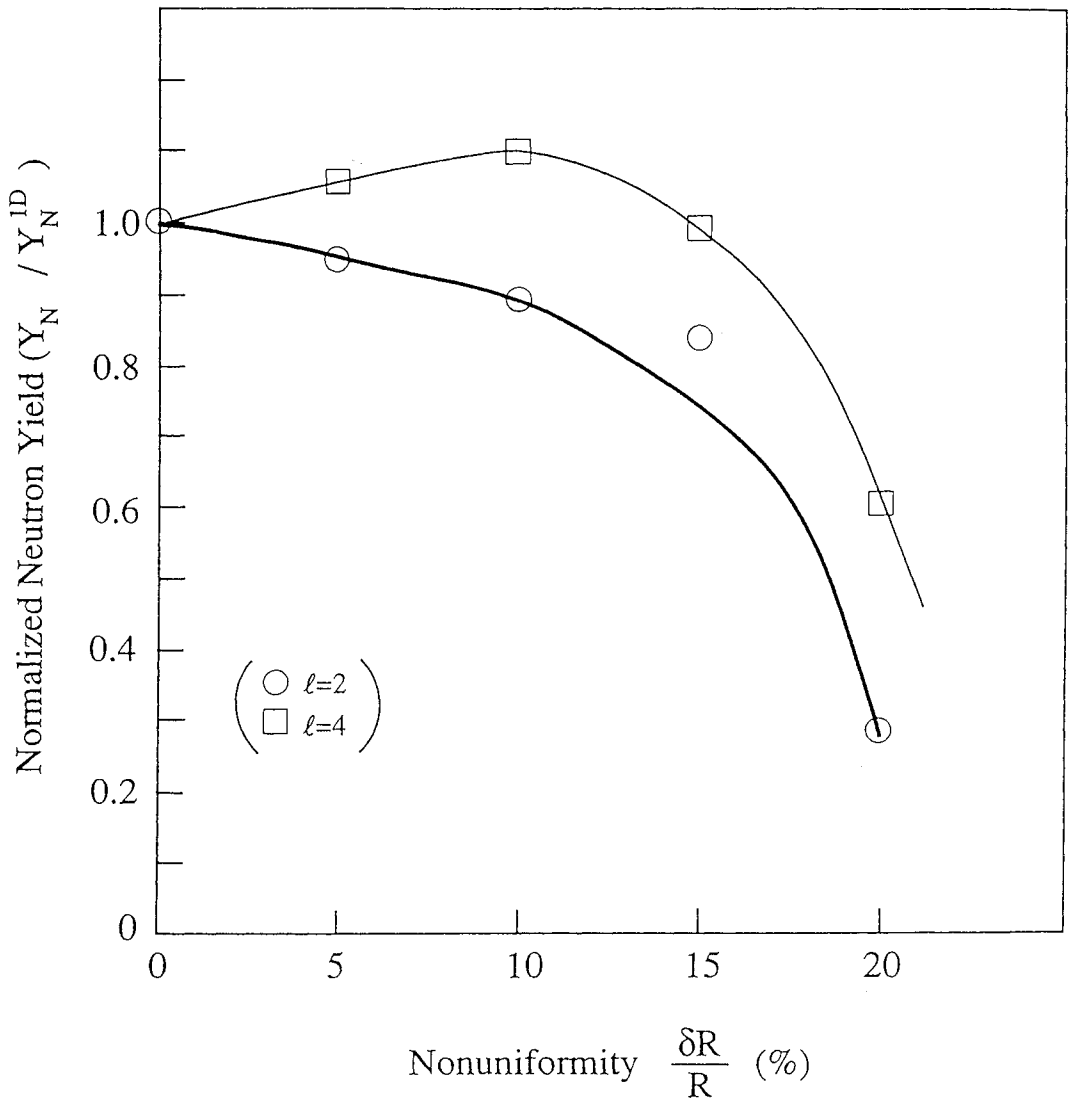


Fig.5

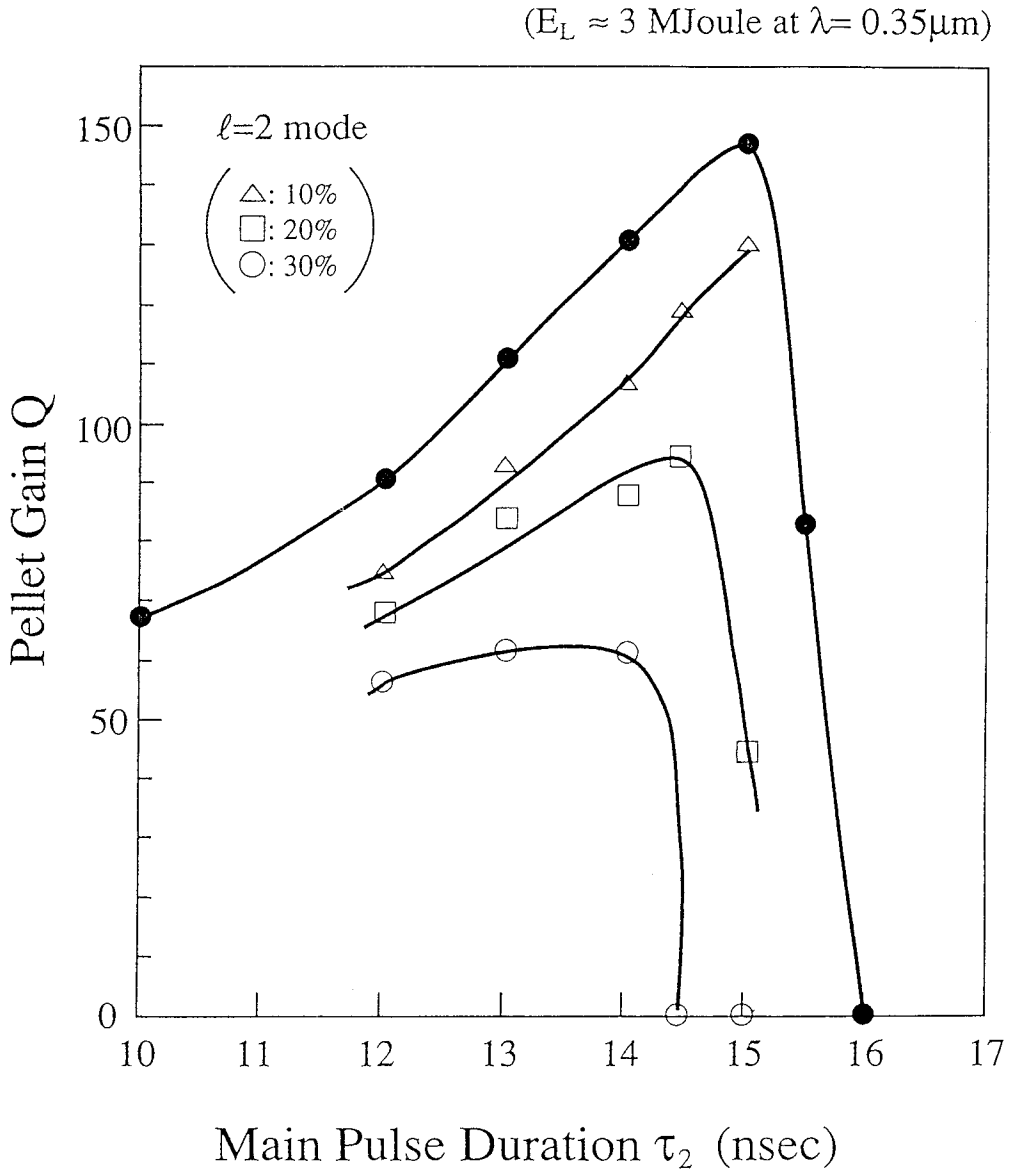


Fig.6

Author index

Aleshin, A.....	188-193
Aleshin, A.....	291-296
Andrews, M.J.	144-155
Anisimov, V.I.	1-10
Bakhrakh, S.M.....	306-312
Balabin, S.I.....	57-69
Beck, J.B.	545-553
Bell, J.B.....	332-342
Bell, J.B.....	554-567
Benjamin, R.F.	223-229
Besnard, D.....	384-398
Binstock, J.	399-412
Bonazza, R.	194-200
Boston, B.....	213-222
Breidenthal, R.E.....	313-321
Browand, F.K.	343-350
Brown, E.F.	322-331
Buckingham, A.C.....	201-206
Burke, E.....	42-49
Burke, E.....	156-166
Burr, J.E.....	322-331
Caruso, A.....	508-518
Castilla, R.	11-31
Chebotareva, E.I.....	178-187
Chebotareva, E.I.....	297-305
Chekhlov, A.V.....	50-56
Chemouni, I.....	270-275
Cherfils, C.	413-420
Chitaikin, V.I.....	129-143
Comte, P.....	351-365
Cowperthwaite, N.W.....	366-371
Cowperthwaite, N.W.....	500-507
Cowperthwaite, N.W.....	519-524
Croso, H.	260-269
Crowley, W.P.....	42-49
Crowley, W.P.....	156-166
Dalziel, S.B.	32-41
Dannevik, W.P.....	421-431
Darowa, N.S.	306-312
Demchenko, V.V.....	207-212
Demikdov, A.A.....	586-595
Dimonte, G.....	42-49
Dimonte, G.....	156-166
Dimonte, G.....	525-532
Fouillet, Y.....	351-365
Frerking, E.....	525-532
Futterman, J.A.H.....	421-430
Galametz, I.	260-269
Glimm, J.	213-222
Goldsack, T.J.....	519-524
Greenough, J.A.....	332-342
Grove, J.W.....	94-104

Grove, J.W.....	213-222
Grun, J.....	201-206
Guez, L.G.....	343-350
Haan, S.W.....	539-544
Haan, S.W.....	533-538
Haas, J.-F.....	260-269
Haigh, S.P.....	343-350
Hankin, B.C.....	500-507
Harrison, A.K.....	432-443
Hawke, R.....	42-49
Hecht, J.....	119-128
Hoffman, N.M.....	545-553
Holmes, R.....	213-222
Houas, L.....	270-275
Hsing, W.W.....	545-553
Huang, S.L.....	322-331
Inogamov, N.A.....	50-56
Ioilev, A.G.....	112-118
Ishii, T.....	596-610
Ivanov, A.G.....	586-595
Jacobs, J.W.....	223-229
Jenkins, D.G.....	223-229
Jourdan, G.....	270-275
Karpenko, G. Ya.....	586-595
Kelleher, T.....	554-567
Kilkenny, J.D.....	533-538
Klein, D.L.....	223-229
Klein, R.I.....	554-567
Kovtun, A.D.....	586-595
Kucherenko, Yu.A.....	70-80
Kucherenko, Yu.A.....	57-69
Kucherenko, Yu.A.....	129-143
Labracherie, L.....	270-275
Landeg, D.....	230-239
Lawrence, G.A.....	343-350
Lazareva, E.....	188-193
Lazareva, E.....	291-296
Lebedev, A.I.....	81-93
Legrand, M.....	568-577
Lesieur, M.....	351-365
Li, X.L.....	94-104
McAbee, T.....	105-111
McCrorry, R.L.....	119-128
Meshkov, E.E.....	112-118
Meshkov, E.E.....	578-585
Mikaelian, K.O.....	240-249
Morrison, J.....	42-49
Mutter, T.B.....	322-331
Neuvazhayev, V.E.....	70-80
Neuvazhayev, V.E.....	250-259
Neuvazhayev, V.E.....	444-448
Neuvazhayev, V.E.....	449-460
Neuvazhayev, V.E.....	461-477
Nevmerzhitsky, N.V.....	112-118

Nevmerzhitsky, N.V.....	578-585
Nikiforov, V.V.	478-496
Nisovtsev, P.N.....	81-93
Ofer, D.....	119-128
Ogorodnikov, V.A.....	586-595
Oparin, A.M.	207-212
Orszag, S.A.	119-128
Pais, V.A.	508-518
Parshukov, I.E.	250-259
Pember, R.....	554-567
Philpott, M.....	230-239
Philpott, M.....	366-371
Polionov, A.V.....	1-10
Polionov, A.V.....	444-448
Polionov, A.V.....	497-499
Ptitzyna, N.V.....	129-143
PylaeV, A.P.....	57-69
PylaeV, A.P.....	70-80
PylaeV, A.P.....	129-143
Pylev, I.G.....	112-118
Rayevsky, V.A.	81-93
Redondo, J.M.	11-31
Remington, B.A.....	42-49
Remington, B.A.....	156-166
Remington, B.A.....	525-532
Remington, B.A.....	533-538
Rodriguez, G.	260-269
Rogachev, V.G.....	578-585
Samtaney, R.	276-290
Samtaney, R.	372-383
Sharp, D.H.....	213-222
Shvarts, D.....	119-128
Smith, A.V.....	230-239
Smith, A.V.....	366-371
Smith, I.....	230-239
Snider, D.M.....	144-155
Sokolov, S.S.....	112-118
Stazenko, V.P.....	306-312
Stry, P.....	42-49
Stry, P.....	156-166
Sturtevant, B.....	194-200
Susoeff, A.....	42-49
Takabe, H.....	596-610
Titov, S.N.....	178-187
Titov, S.N.....	297-305
Tolstikova, L.A.....	586-595
Toqué, N.....	568-577
Touat, A.....	270-275
Wallace, R.J.....	533-538
Weber, S.V.....	533-538
Yakovlev, V.	444-448
Yakovlev, V.	497-499
Yang, Y.....	213-222
Youngs, D.L.....	167-177

Youngs, D.L.	366-371
Youngs, D.L.	500-507
Youngs, D.L.	519-524
Zabusky, N.J.	276-290
Zabusky, N.J.	372-383
Zaytsev, S.G.	178-187
Zaytsev, S.G.	188-193
Zaytsev, S.G.	291-296
Zaytsev, S.G.	297-305
Zhang, Q.	94-104
Zhang, Q.	213-222
Zharova, G.V.	306-312
Zhidov, I.G.	112-118
Zhidov, I.G.	578-585
Zhmailo, V.A.	306-312
Zinamon, Z.	119-128

Participants

Malcolm Andrews,
Dept. Mechanical Engineering, Mail Stop 3123
Texas A&M Univ., College Station,
TX 77843-3123, USA.
Tel: 409-845 3081
Fax: 409 847 8843
malcom@chehal.tamu.edu

Nadine Aubry
Levich Institute Room TIM
City College of the City Univ. of NY
140th Street & Convent Av. NY 10031, USA.
Tel: 212-650-6844
Fax: 212-650-6835
menna@ccnyvme

Robert Benjamin
Mailstop J970 Group M-6
LANL,
Los Alamos NM 87545 USA.
Tel: 505 667 8116
Fax: 505 665 3050

Didier Besnard
Centre D'Etudes de Limeil-Valenton
Dept. Mathematiques Appliques/MCN
94195 Villeneuve St. Georges Cedex FRANCE
Tel: 33 1 45 95 65 05
Fax: 33 1 45 95 95 55

Judith Binstock
Los Alamos Nat. Lab. X-6, MS-B226
PO Box 1663, Los Alamos,
NM 87545, USA.
Tel: 505-667-2389
Fax: 505-665-5538

Riccardo Bonazza
737 Engineering Research Bldg.
1500 Johnson Dr. Madison WI 53706
USA.
Tel: 1-608-265-2337
Fax: 1-608-262-6707
RICRDO@CONERO.NEEP.WISC.EDU

Richard Bowers
LANL
Mail Stop B259
Los Alamos
New Mexico 87545 USA
Tel: 505-667-4726
Fax: 505-665-7725

Robert Breidenthal
Univ. of Washington FS-10
Seattle WA 98195
USA
Tel: 206-685-1098
Fax: 206-685-0217
breident@aa.washington.edu

Eugene Brown
100-64 Randolph Hall,
Virginia Tech, Mech Eng
Blacksburg VA 24061-0238 USA.
Tel: 7032317199
Fax: 7032319100
FBROWN@UTVMI.CC.VJ.EDU

Alfred Buckingham
Lawrence Livermore Nat. Lab.
Mail Code L-321, PO Box 808
Livermore, CA 94551, USA.
Tel: 510-423-4828
Fax: 510-422-2851
a:fredcb@physics.llnl.gov

Don Burgess
T-3, B216 LANL,
Los Alamos NM 87545
USA
Tel: 505 667 0934
Fax: 505 665 5926
burgess@freon.lanl.gov

Eugene Burke
Lawrence Livermore Nat. Lab
PO Box 808 L-22
Livermore, CA 94551, USA.
Tel: 510-422-4613
Fax: 510-423-0925

Ian Cameron
MOD (PE) AWE
Aldermaston,
Reading, Berks. RG7 4PR
Tel: 0734 814111 ext 3763
Fax: 0734 815320

Ilan Chemouni
Univ. de Provence - Labo.JUSTI-CNRS
ura 1168 - Dept. MHEQ case 321
Faculte St. Jerome 13397 Marseille cedex 13 FRANCE
Tel: 91 28 8411
Fax: 91 28 83 22

Catherine Cherfils
Centre D'Etudes de Limeil Valenton
94195 Villeneuve St Georges Cedex
FRANCE
Tel: 45 95 68 24
Fax: 45 95 95 55

Neil Cowperthwaite
AWE Aldermaston
Building E3
Reading
Tel: 0734 814111
Fax: 0734 815320

Peter Cumber
British Gas PLC
Midlands Research Station, Wharf Lane,
Solihull, West Midlands B91 2JW
Tel: 021 705 7581
Fax: 021 704 4425

Stuart Dalziel
DAMTP
Silver Street
Cambridge CB3 9EW UK
Tel: 0223 337911
Fax: 0223 337918
sd103@uk.ac.cam.phx

Guy Dimonte
Lawrence Livermore Nat. Lab.
L-43
Livermore, CA 94550, USA.
Tel: 510-423-0596
Fax: 510-423-5998

Michael Dunning
LLNL L-35
PO Box 808
Livermore CA 94550
Tel: 510-422-3398
Fax: 510-422-3389
DUNNING@OCFMAIL.OCT.LLNL.GOV

John Futterman
Lawrence Livermore Nat. Lab.
L-22
PO Box 808, Livermore CA 94551, USA.
Tel: 510-423-4741
Fax: 510-423-0925

Ingrid Galametz
CEA
BP7
77181 Courtry, FRANCE
Tel: 33-1-49-36-80-69
Fax: 33-1-49-36-75-14

Didier Galmiche
Centre d'Etudes de Limeil-Valenton
94195 Villeneuve St. Georges Cedex
FRANCE

Pierre Gandeboeuf
Centre d'Etudes de Vaujours Moronvilliers
BP no 7
77181 Courtry, FRANCE.
Tel: 49 36 85 86
Fax: 49 36 75 20

Timothy Goldsack
AWE Aldermaston
Building N56
Reading
Tel: 0734 814111 ext 7047
Fax: 0734 815320

Bruce Goodwin
B-Division, L-35
LLNL, PO Box 808,
Livermore CA 94550, USA
Tel: 510 423 7736
Fax: 510 422 3389

Robert Gore
LANL
Group T-3, MS B214
Los Alamos NM 87545 USA
Tel: 505 665 0976
Fax: 505 665 5926

Jeffrey Greenough
7000 East Ave. PO Box 808 L-316
Livermore CA 94550
USA
Tel: 510-423-6571
Fax: 510-423-2993
greeno@bigbird.llnl.gov

John Grove
Dept. Appl. Mathematics,
Univ. at Stony Brook
Stony Brook NY 11794-3600, USA.
Tel: 516-632-8377
Fax: 516-632-8490
grove@ams.sunysb.edu

Jean-François Haas
CEA Centre d'Etudes de Vaujours-Moronvilliers
BP7
77181 Courtry, FRANCE
Tel: 33-1-49-36-83-77
Fax: 33-1-49-36-75-11

Bruce Hammel
7000 East Avenue
Livermore
CA 94550, USA.
Tel: 510-422-3299
Fax: 510-422-8395

Alan Harrison
Centre for Compressible Turbulence L-18
LLNL, PO Box 808
Livermore CA 94551-9900 USA
Tel: 510-423-5019
Fax: 510-423-5112

Nelson M. Hoffman
Los Alamos Nat. Lab.
PO Box 1663
Los Alamos, NM 87545, USA.
Tel: 505-667-3417
Fax: 505-665-3389
nmh@lanl.gov

Lazhar Houas
Universite de Provence
Labo. IUSTI CNRS ura 1168, Dept. MHEQ
case 321, Faculte St. Jerome 13397, FRANCE.
Tel: 91-28 82 54
Fax: 91-28 83 22

Julian Hunt
Meteorological Office
London Road
Bracknell
Berkshire RG12 2SZ
Tel: 0344-854600
Fax: 0344-856909

Nail Inogamov
L.D. Landau Institute for Theoretical Physics
117 940 Moscow
Kosygina Str. 2, RUSSIA.
Tel: 7-095-1373944, 9380910, 4258767
Fax: 7-095-938 20 77
ITF@IPS.AC.MSK.SU subject INOGAMOV

Jeffrey Jacobs
Dept. of Aerospace & Mech. Eng.
University of Arizona
Tucson AZ 855011
Tel: 602-621-8459
Fax: 602-621-8191

Brian Jones,
Plasma Physics Group, Blackett Lab.,
Imperial College, Prince Consort Road,
LONDON SW7 2BZ
Tel: 071-589-5111 ext. 6888
b.Jones@IC.ac.uk

Joseph Kilkenny
Lawrence Livermore Nat. Lab.
L-473
PO Box 808, Livermore CA 94550, USA.
Tel: 510-423-4213
Fax: 510-423-8395

S. Kirby
AWE
Foulness
Essex SS3 9XE
Tel: 0702 219441
Fax: 0702 219997

Richard Klein
Univ. of California, LLNL, L-58
PO Box 808,
Livermore California USA
Tel: 510-422-3548
Klein@radhydro.berkeley.edu

George Kramer
LLNL PO Box 808 L-22,
Livermore CA 94551
USA
Tel: 510-423-7787

Yury Kucherenko
Inst. of Technical Physics
454070 Chelyabinsk-70
PO Box 245,
RUSSIA
Tel: 351-72-433-69
Fax: 351-72-320-77
nto@ch 70.chel.SU(Relcom)

Allen L. Kuhl
Lawrence Livermore Nat. Lab.
2250 E. Imperial HWY (Suite 650)
El Seglindo, CA 90245, USA.
Tel: 310-615-2603
Fax: 310-615-2620
USA LA

Daryl Landeg
A6, AWE
Foulness
Essex SS3 9XE
Tel: 0702 219441 ext 3238
Fax: 0702 219997

Gregory Lawrence
Dept. Civil Engineering
Univ. of British Columbia
234 Mail Mall, Vancouver BC V6T 1Z4 CANADA
Tel: 604 822 5371
Fax: 604 822 6901

Michel Legrand
Commissariat a l'Energie Atomique
Centre d'Etudes de Vaujours-Moronvilliers
BP 7, 77181 Courtry, FRANCE
Tel: 1 49 36 86 19
Fax: 1 49 36 75 20

Marcel Lesieur
IMG-LEGI
BP 53X
38041 Grenoble Cedex FRANCE
Tel: 33 76 82 50 64
Fax: 76 82 52 71
LESIEUR@IMG>IMG>FR

Xiaolin Li
Computer & Information Sci. Dept.
Indian Univ-Purdue Univ at Indianapolis
Indianapolis IN 46202 USA.
Tel: 317 274-9745
Fax: 317-274-9742
xlli@silver.urs.indiana.edu

Paul Linden
DAMTP
Silver Street
Cambridge CB3 9EW UK.
Tel: 0223 337845
Fax: 0223 337918
pfl4@uk.ac.cam.phx

Thomas McAbee
Lawrence Livermore Nat. Lab.
L-35
Livermore, CA 94550, USA.
Tel: 510-422-7536
Fax: 510-422-3389

Evgenij Meshkov
All Russian Scientific Research Inst of Exp. Phys.
607200 Arzamas-16,
Niizhny Novogorod Region RUSSIA
Telex: 151 109 ARSA SU
Fax: 831 305 4565

Karnig Mikaelian
Lawrence Livermore Nat. Lab.
L-297
Livermore, CA 94550, USA.
Tel: 510-422-5449
510-423-7228

Paul Miller
Lawrence Livermore Nat. Lab.
L-476
PO Box 808, Livermore CA 94551, USA.
Tel: 510-423-6455
Fax: 510-423-6172
pmiller@LLNL.gov

Nakai Mitsuo
Rutherford Appleton Lab
Central Laser Facility
Chilton, Didcot, Oxon OX11 0QX
Tel: 0235 821900 ext. 6345
Fax: 0235 445888

Michel Naudy
CEL-V DLPP ELP
94195 Villeneuve St. Georges CEDEX
France
Tel: 45956157

Vladimir Neuvzhayev
Inst. of Technical Physics
PO Box 245
Chelyabinsk 454070, RUSSIA.
Tel: 351 72-3-37-72
Fax: 835172 32077
nioz@ch70 chel su Telex 124 846 SNOW SU

Valentin Nikiforov
Inst. of Experimental Physics
607200 Arzamas-16,
Nizhny Novgorod Region
RUSSIA
Tel: 831 30 5 69 74
Fax: 831 305 4565

Kevin Oades
Reading
AWE Aldermaston
Berkshire RG7 4PR.
Tel: 0734-814111 ext. 5632
Fax: 0734 815320

Jean-Marc Pace
CEA
BP7
77 181 Courtry Cedex, FRANCE,
Tel: 1-49-36-8815
Fax: 1-49-36-7524

Vicente Pais
ENEA CRE Frascati
Casella Postale 65, 00044 - Frascati
ITALIA
Tel: 39-6-9400-5731
Fax: 39-6-9400-5400
VAPAIS@IRHENE (Bitnet)

Theodore Perry
2861 Superior Dr.
Livermore CA 94550
USA
Tel: 510-443-5763 (H) 510-423-2065 (W)
Fax: 510-422-5102

Martin Philpott
AWE
Foulness
Essex SS3 9XE.
Tel: 0702-219441
Fax: 0702-219997

Arkadi Polionov
All-Russia Research Institute of Tech. Phys.,
454070 Chelyabinsk 70
PO 245, RUSSIA.
Tel: 351-72 2-39-77
Fax: 351-72 32077
Telex: 124846 snow su

Dr. V. A. Raevsky
Inst. of Exp. Physics,
607200 Arzamas-16,
Nyzhny Novgorod Region, RUSSIA
TELEX 151 109 ARSA
Fax: 831 30 54565

Bernard Rebourcet
Centre d'Etudes de Limeil-Valenton
Dept. Mathematiques Appliquet/MCN
94195 Villeneuve St. Georges Cedex FRANCE.
Tel: 33 1 45 95 65 05
Fax: 33 1 45 95 95 55

Jose Redondo
Dept. De Fisica Aplicada, Jordi Girona 31
Universitat Politecnica de Catalunya
Barcelona 08034, SPAIN.
Tel: 34 3 401 7057
Fax: 34 3 401 6090

Bruce Remington
LLNL
7000 East Avenue
Livermore CA 94550
USA
Tel: 510-423-2712
Fax: 510-422-8395

Peter Roberts
Mathematical Physics Division Bldg. E1,
AWE Aldermaston
Berks RG7 4PR
Tel: 0734 814111 ext. 7654

John Roberson
MOD (PE) AWE,
External Training, Building H11.1
Aldermaston, Reading RG7 4PR.
Tel: 0734 814111 ext 7815
Fax: 0734 815320

Girard Rodriguez
CEA
Centre d'Etudes de Vaujours-Moronvilliers, BP7
77181 Courtry
FRANCE
Tel: 33-1-49-36-80-69
Fax: 33-1-49-36-75-14

Vladimir Rogatchev
Inst. of Experimental Physics
607200 Arzamas 16,
Nizhnij Novgorod region
RUSSIA
Tel: 831 30-11978
Fax: 831-305-4565
zvz@mathdep.expphys.nnov.su

Vladislav Rozanov
P.N. Lebedev Inst.
Leninsky pr. 53
117924 Moscow, RUSSIA
Tel: 095-132-11-96
Fax: 095-135-78-80
rozanov@sci.fian.msk.su

R. Saunders
AWE
Foulness
Essex SS3 9XE
Tel: 0702 219441
Fax: 0702 219997

Rodney Schults
Group X-2, MSB220, LANL,
PO Box 1663 Los Alamos NM 87544
USA
Tel: 505 667 8931
Fax: 505 665 4080

Irina Shubina
Inst of Technical Physics PO Box 245
Chelyabinsk 70
454070 RUSSIA
Telex: 124846 SNOW SU

Dov Shvarts
Physics Department
Necular Research Centre Negev
PO Box 9001
Bear-Sheva
ISRAEL
Tel: 972-57-568736
Fax: 972-57-554848

Alan Smith
AWE Foulness
Essex SS3 9XE
Tel: 0702 219441
Fax: 0702 219997

Ian Smith
AWE, Foulness
Essex SS3 9XE
Tel: 0702 219441
Fax: 0702 219997

Denis Souffland
CEA
Centre d'Etudes de Limeil-Valenton
94195 Villeneuve-Saint-Georges Cedex,
FRANCE.

Peter Stry
Lawrence Livermore Nat. Lab.
A Division L-22
Livermore, CA 94550, USA.
Tel: 510-423-2360

Hideaki Takabe
Inst. of Laser Engineering
Osaka Univ. Suita,
Osaka 565, JAPAN
Tel: 81-6-877-5111 Ext. 6553
Fax: 81-6-877-4799

Kazuyoshi Takayama
Tohoku University
Institute of Fluid Science
2-1-1 Katahira Aoba Sendai, JAPAN.
Tel: 81-22-263-0895
Fax: 81-22-227-7390

Nathalie Toqué
Commissariat a l'Energie Atomique
Centre d'Etudes de Vaujours-Moronvilliers
BP 7, 77181 Courtry, FRANCE.
Tel: 1 49 36 82 05
Fax: 1 49 36 75 20

Abdelkader Touat
Univ. de Provence - Labo JUSTI-CNRS
ura 1168, Dept. MHEQ case 321
Faculte St Jerome 13397 Marseille cedex 13 FRANCE
Tel: 91 28 84 11
Fax: 91 28 83 22

Michel Valadon
Centre d'Etudes de Limeil-Valenton
94195 Villeneuve Saint Georges Cedex
FRANCE

Deborah Wojtowicz
Lawrence Livermore Nat. Lab.
L-22, PO Box 808
Livermore, CA 94551, USA.
Tel: 510-423-9000

David Youngs
AWE
Building E3
Aldermaston, Reading RG7 4PR.
Tel: 0734-814111 ext. 6766
Fax: 0734-815320

Norman Zabusky
Rutgers University
Dept. M&AE, PO Box 909,
Piscataway, NJ 08855-0909
Tel: 908-932-5869
Fax: 908-932-5313
nzabusky@vizlab.rutgers.edu

Sergey Zaytsev
Krzhizhanovsky Power Engineering
Institute (ENIN)
Leninsky Pr. 19, 117071 Moscow, RUSSIA.
Tel: 995-31-07
Fax: 197-095-954-25-13

© 1993, The contributing authors.

Provided due credit is given to authors of these papers, this work may be copied and reproduced freely for the purposes of education and scientific research.